X 005581

AGARD-AG-238

AGARD-AG-238

AGARD

ADVISORY GROUP FOR AEROSPACE RESEARCH & DEVELOPMENT

7 RUE ANCELLE 92200 NEUILLY SUR SEINE FRANCE

AGARDograph No. 238

Design Manual for Impact Damage Tolerant Aircraft Structure

NORTH ATLANTIC TREATY ORGANIZATION

**DISTRIBUTION AND AVAILABILITY
ON BACK COVER**

NORTH ATLANTIC TREATY ORGANIZATION

ADVISORY GROUP FOR AEROSPACE RESEARCH AND DEVELOPMENT

(ORGANISATION DU TRAITE DE L'ATLANTIQUE NORD)

AGARDograph No.238

DESIGN MANUAL FOR IMPACT DAMAGE

TOLERANT AIRCRAFT STRUCTURE

by

John G.Avery
Boeing Military Airplane Company
Research and Engineering
P.O.Box 3707, M/S 41-10
Seattle, Washington, USA 98124

This report has been prepared at the request of the Structures and Materials Panel of AGARD.

THE MISSION OF AGARD

The mission of AGARD is to bring together the leading personalities of the NATO nations in the fields of science and technology relating to aerospace for the following purposes:

— Exchanging of scientific and technical information;

— Continuously stimulating advances in the aerospace sciences relevant to strengthening the common defence posture;

— Improving the co-operation among member nations in aerospace research and development;

— Providing scientific and technical advice and assistance to the North Atlantic Military Committee in the field of aerospace research and development;

— Rendering scientific and technical assistance, as requested, to other NATO bodies and to member nations in connection with research and development problems in the aerospace field;

— Providing assistance to member nations for the purpose of increasing their scientific and technical potential;

— Recommending effective ways for the member nations to use their research and development capabilities for the common benefit of the NATO community.

The highest authority within AGARD is the National Delegates Board consisting of officially appointed senior representatives from each member nation. The mission of AGARD is carried out through the Panels which are composed of experts appointed by the National Delegates, the Consultant and Exchange Programme and the Aerospace Applications Studies Programme. The results of AGARD work are reported to the member nations and the NATO Authorities through the AGARD series of publications of which this is one.

Participation in AGARD activities is by invitation only and is normally limited to citizens of the NATO nations.

PREFACE

Aircraft must maintain structural integrity relative to many sources of damage such as, for example, fatigue cracking or corrosion. Military aircraft must also withstand, as far as is practicable, damage inflicted by hostile military weapons. The resistance of the structure to the impact of projectiles is an important parameter in considerations of vulnerability. It is necessary to determine the impact failure characteristics of the structure under load, and its residual strength after damage. The detail design features of the structure are important in determining the spread of the damage. Where neighbouring systems or fuel tanks are vulnerable, the degree of penetration of the projectile into the structure is important. Blast and fragmentation effects must be considered.

This Design Manual has therefore been produced by the Structures and Materials Panel to aid the designer in making assessments of the tolerance of the structure to various threats and the probability of the aircraft surviving the impact, completing the mission and returning safely to base. It describes methods which exist to determine both the damage resulting from the impact of various types of projectiles and the resulting capabilities of the damaged structure. It also embraces an analogous problem, arising mainly on transport aircraft, of the resistance of the structure to impact of debris from engine disintegration.

The Manual is divided into three Sections, Section I dealing with the projectile threats, Section II with analysis methods and Section III with design guidelines.

The Structures and Materials Panel was very fortunate from the outset in securing the services, as Coordinator, Compiler and Editor of the Manual, of Mr John G.Avery of the Boeing Company, Seattle, who is world renowned as an expert in the field of impact damage tolerance of structures. An essential feature of AGARD activities is the pooling of relevant knowledge with the NATO community aided by the bringing together of specialists for informed discussions. This occurred both within the Working Group on Impact Damage Tolerance of Structures and also at the Specialists' Meeting held in Ankara in September 1975 (see AGARD Conference Proceedings CP-186). The Panel is therefore deeply indebted not only to Mr Avery, for his outstanding efforts, largely single-handed, in compiling this Manual, but also to all those others who have provided valuable information and contributions, especially those listed by name in the preliminary pages.

N.F.HARPUR
Chairman, Working Group
on Impact Damage Tolerance
of Structures

CONTENTS

CONTENTS
(CONTINUED)

CONTENTS
(CONCLUDED)

AUTHOR'S NOTE

This Design Manual was prepared as the primary task of the Impact Damage Tolerance Working Group formulated by the Structures and Materials Panel, with N. F. Harpur of British Aerospace serving as the originator and guiding light of the effort. The objective of the Manual is to describe a methodology for incorporating projectile impact damage tolerance into structural design, with the aim of improving inherent survivability. The scope of the work includes military projectiles and engine debris.

As its title implies, the Design Manual is intended for structural designers and technologists having little prior knowledge of projectile impact phenomena and weapon effects. An early goal was to avoid the necessity of security classification, as it was felt that this would restrict its accessibility to designers. As a result, the data presented is limited in scope. Within this context, the user should regard the Manual as a guide in defining methods and identifying the type of data required for impact damage tolerant design, rather than as a source of data pertaining to the nature and effects of specific threats.

The Manual was prepared in three sections using information available to the author, most of it developed under the sponsorship of the U.S. Department of Defense. Each section was separately submitted for public release approval and distributed to Working Group members for technical review. This process began in 1977, and has only recently been concluded following fairly major revisions undertaken in 1980 to satisfy release requirements. Mr. Keith I. Collier, Deputy Director of the Flight Dynamics Laboratory, AFWAL, coordinated the final release activity and deserves special thanks for his interest and effort.

The author would like to thank all those who read the manuscripts and submitted review comments. Mr. D. W. Voyls of AFWAL spent many hours reviewing the entire Manual and the implementation of his suggestions has made a significant contribution in content and releasability. Mr. K. T. Shaw of the RAE provided detailed commentary which resulted in substantial improvements to Section I. Special thanks is also extended to Messrs. J. Olsen, C. Wallace, and L. Kelly of AFWAL, and W. Kirkby and R. Anstee from the Structures Department of the RAE. Because of the urgencies of the printing schedules, some excellent recommendations for improvement could not be implemented, including the reduction of duplication between Sections I and II.

With regard to preparing the Manual, I would like to acknowledge the contributions of Mr. T. R. Porter of the Boeing Military Airplane Company. Much of the format, content, and philosophy of the Manual remains from his prior efforts. The same comments apply to Mr. R. J. Bristow, also of Boeing, whose early work established the approach used for later developments in ballistic damage prediction and residual strength assessment. Ms. S. J. Bradley, again of Boeing, has been instrumental in preparing the Manual from all standpoints, including technical contributions, editing, formatting and reviewing. The notable work of Messrs. M. J. Jacobson and M. M. Ratwani, and their coworkers at Northrop Corporation, J. R. Yamane and J. Brass, provided valuable source material for portions of the Manual, as did the work of E. A. Lundstrom of Naval Weapons Center, D. McCarthy of Rolls-Royce, and P. C. Huang of NSWC. Several researchers were particularly supportive of the activity, including J. Massmann of IABG, D. F. Haskell of BRL, and R. W. Lauzze and D. O. Fearnow of AFWAL. The technical communications contributed by Mr. Massmann were of great value to the effort. Considerable information presented in the Manual was developed under contractual programs managed by A. J. Holten formerly of AFWAL, and Drs. A. Somoroff and D. Mulville of Naval Air Systems Command. Special appreciation is extended to the Boeing Military Airplane Company, particularly Mr. D. E. Strand, for supportive interest in the activity.

John G. Avery   8/1/81
Manager, Survivability/Vulnerability
Research and Engineering
Boeing Military Airplane Company
Seattle, Washington 98124

INTRODUCTION

Aircraft must maintain structural integrity relative to many types of damaging mechanisms including for example, fatigue, non-detectable initial defects and in-flight damage such as that inflicted by military weapons or by debris from disintegration of an engine. While the design methodology for some of these is well established within the structural design disciplines, that for in-flight damage has not been widely distributed to designers.

The resistance of the structure to the impact of projectiles is an important parameter in consideration of the vulnerability of military aircraft. Information on this subject is contained in AGARD Advisory Report AR-47 "Physical Vulnerability of Aircraft". However there is a need for considerable augmentation of this information, extending the scope to include design methodology. The Structures and Materials Panel of AGARD, recognizing this need, commissioned the preparation of this Design Manual.

The overall objective of the Manual is to inform designers of the general character of projectile threats and available analysis methods for predicting damage and strength degradation, and to outline a methodology for incorporating projectile damage tolerance into the structural design of aircraft. Toward this end, the Manual contains three major sections:

Section I - Description of Projectile Threats

Section II - Analysis Methods for Predicting Structural Response to Projectile Impact

Section III - Design Guidelines for Impact Damage Tolerance

Section I describes projectile types, important encounter parameters, and typical terminal effects, written primarily for the aircraft designer rather than the vulnerability or weapons effects specialist. The intent is to provide a very general overview useful to an individual having little familiarity with projectiles and their effects. Vulnerability and weapons effects specialists have more specific and often classified data, and should be consulted as required in design applications.

Section II presents analysis methods and data available for predicting the response of metal and fiber composite structure to projectile impact. The analysis methods discussed are applicable to impacts by small arms projectiles, missile warhead fragments, and the fragmentation and blast effects of high-explosive projectiles. The responses addressed include penetration capability, damage size and type, strength and stiffness degradation of damaged structure, and internal load redistribution.

Section III summarizes a design methodology for implementing projectile damage tolerance within structural design disciplines, developing methods and requirements within a format that is compatible with existing damage tolerance procedures.
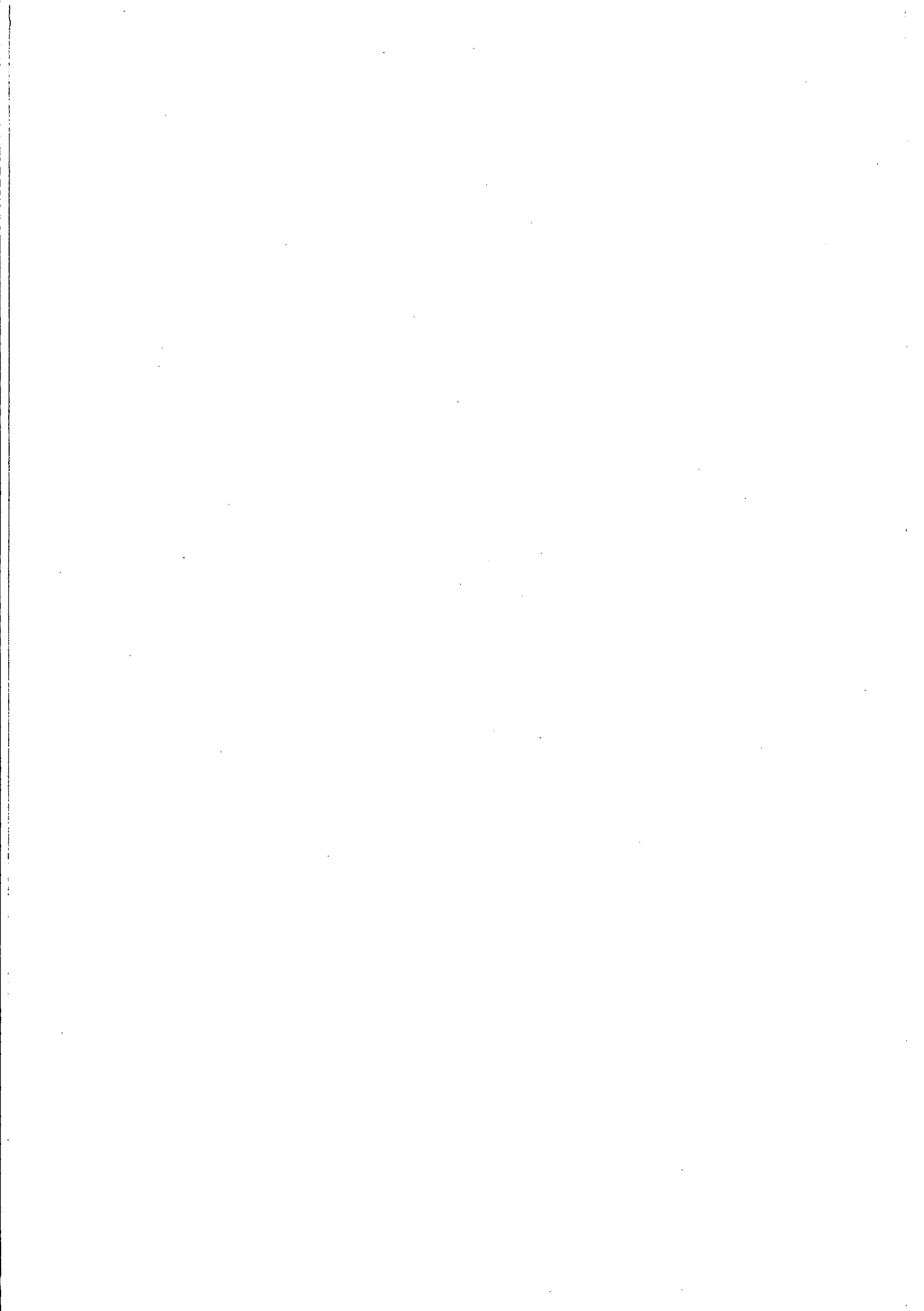
SECTION I

DESCRIPTION OF PROJECTILE THREATS
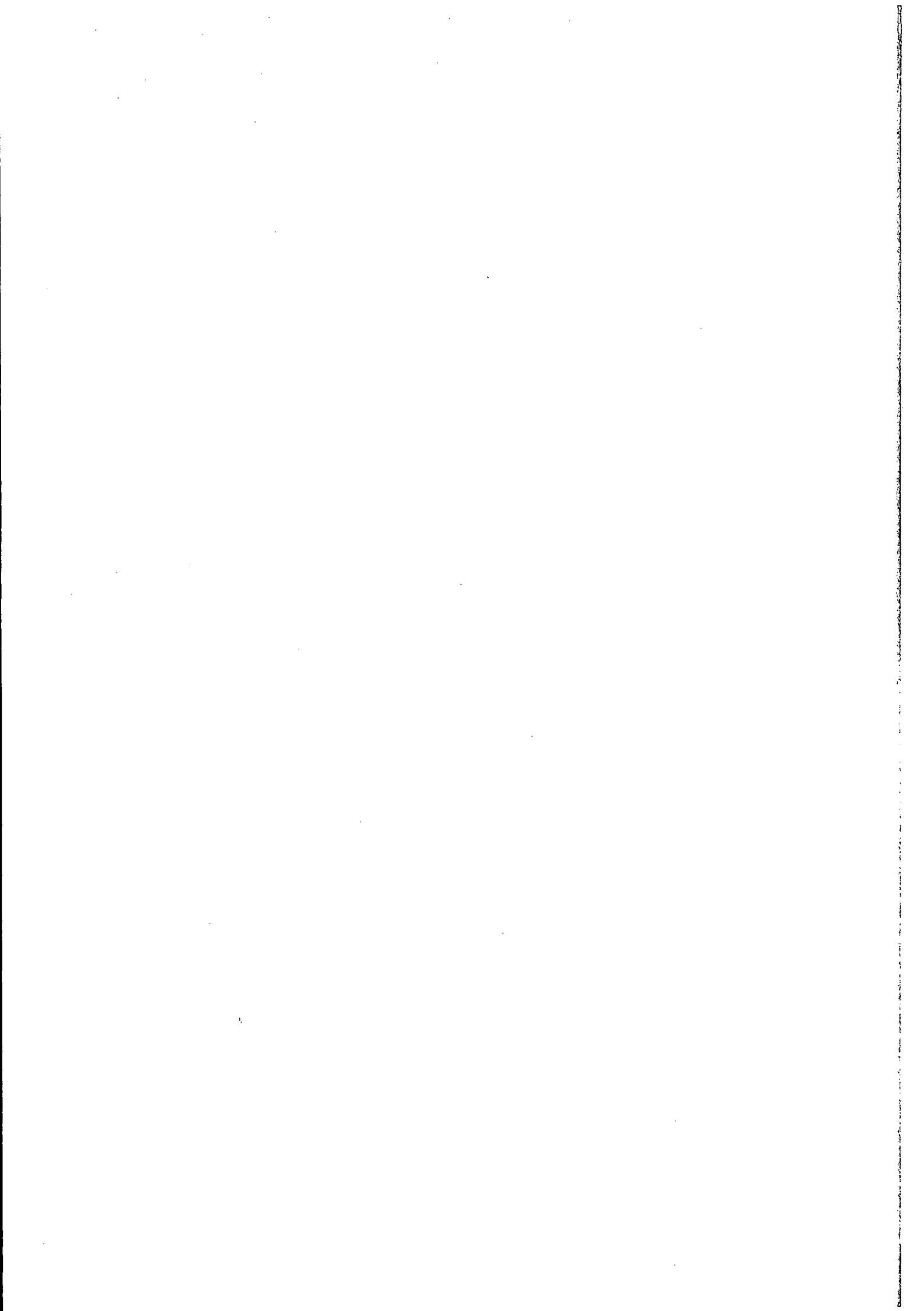
SECTION I

1.0 DESCRIPTION OF PROJECTILE THREATS

Evaluating the degradation of aircraft structure resulting from projectile impact requires a knowledge of the threat and encounter conditions. This is necessary in understanding the failure mechanisms and structural response modes induced by the various types of threats. The objective of this Section is to acquaint the aircraft structural designer with projectile types, important encounter parameters, and typical terminal effects. The section provides basic information that will be helpful in understanding the analysis of structural response to impact and the design guidelines for impact damage tolerance presented in Sections II and III.

Following the overall objective of the Manual, this Section is written for the aircraft designer rather than the vulnerability or weapons effects specialist. The intent is to provide a very general overview useful to an individual having little familiarity with projectiles and their effects. Vulnerability and weapons effects specialists have more specific and often classified data, and should be consulted as required in design applications.

The subsequent discussion is organized as shown below, reflecting the two categories of projectiles addressed in the Manual: military projectiles and engine debris. Military projectiles of concern in aircraft design can be loosely cataloged into two generic types:

(a) Non-exploding projectiles;
(b) Exploding projectiles.

The non-exploding projectile is typically a penetrator that strikes the aircraft exterior intact and produces no accompanying blast effects. Examples of military non-exploding projectiles include small-arms projectiles, certain AAA (Anti-aircraft Artillery) projectiles, and missile warhead fragments. An exploding projectile contains an explosive charge and a fuzing mechanism, and both fragment penetrators and blast overpressures are generated. Exploding projectiles are fired from AAA weapons.

Engine debris projectiles are formed from the structural failure of rotating engine components, with subsequent escape from the engine case. These projectiles can resemble fragments generated from military threats, but have unique characteristics which require separate consideration.

This section is organized as follows:

1.1 MILITARY PROJECTILES

1.1.1 Non-Exploding Projectiles

1.1.1.1 Types

An important category of non-exploding projectiles are the "small-arms" projectiles, primarily the 7.62-mm, the 12.7-mm, and the 14.5-mm. These projectiles consist of a solid metal core (often called the "penetrator") usually surrounded by a thin metal jacket. Non-exploding projectiles of caliber greater than 14.5-mm are generally classified as AAA (Anti-aircraft Artillery) or cannon projectiles. The most notable of these is the 23-mm.

There are several types of non-exploding projectiles including: ball (B), armor piercing (AP), incendiary (I), and tracer (T). Ball projectiles, typically available in 7.62-mm only, have a relatively soft core designed to deform at impact, and are intended for use against personnel. In forward area combat situations, however, they may be fired against aircraft. Armor piercing projectiles have a hardened steel core designed for penetrating hard targets, including aircraft. Incendiary projectiles contain a thermally active filler that functions at impact and can ignite on-board flammables such as fuel or hydraulic fluid. Tracers contain material that burns brightly along the flightpath for assistance in aiming and sighting. Many projectiles combine some of the above capabilities. For example, the 7.62-mm API is armor piercing-incendiary, and the 23-mm API-T is armor piercing-incendiary-tracer.

Photographs of typical small-arms projectiles are contained in Figures 1-1, 1-2, and 1-3. These figures show sectioned projectiles, illustrating the relationship between jacket, core, and incendiary. In addition, Table 1-1 shows typical weight and size characteristics of representative small-arms and AAA non-exploding projectiles. In most instances, small-arms fire emanates from ground based weapons. 7.62-mm projectiles (both ball and armor piercing) are typically fired by infantry using assault rifles or bipod mounted machine guns. The machine guns, in particular, can have a high rate of fire and are a threat to slow and low flying aircraft within range. The 12.7-mm threat typically consists of a carriage mounted heavy machine gun with quad barrels providing a fairly high rate of fire. Another anti-aircraft defense weapon, the 14.5-mm heavy anti-aircraft machine gun, has been known to be effective against aircraft flying at moderate subsonic speeds. The larger caliber projectiles are most frequently fired from ground-based weapons (AAA), but may also be fired from airborne cannon. The 23-mm armor-piercing incendiary, fired from radar controlled AAA guns having a very high rate of fire, is a significant threat.

The final type of non-exploding military projectile—missile warhead fragments—emanate from surface-to-air missiles (SAM) or air-to-air missiles (AAM). Missile fragmentation warheads often consist of an explosive charge surrounded by a wall of preformed metal fragments, or a prescored or solid metal casing. Figure 1-4 shows some warhead assemblies using preformed fragments.
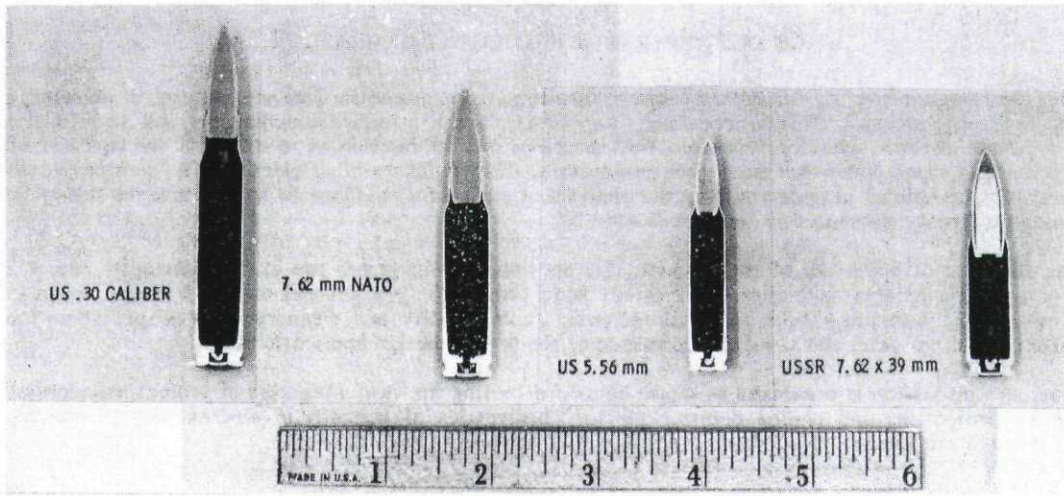
Figure 1-1. Sectioned 7.62-mm Projectiles
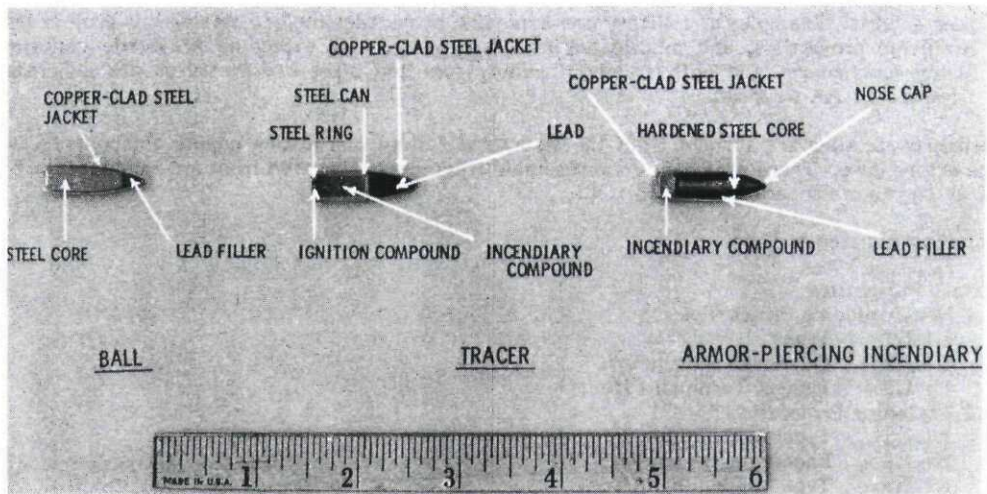
Figure 1-2. Typical Small-Arms Projectiles
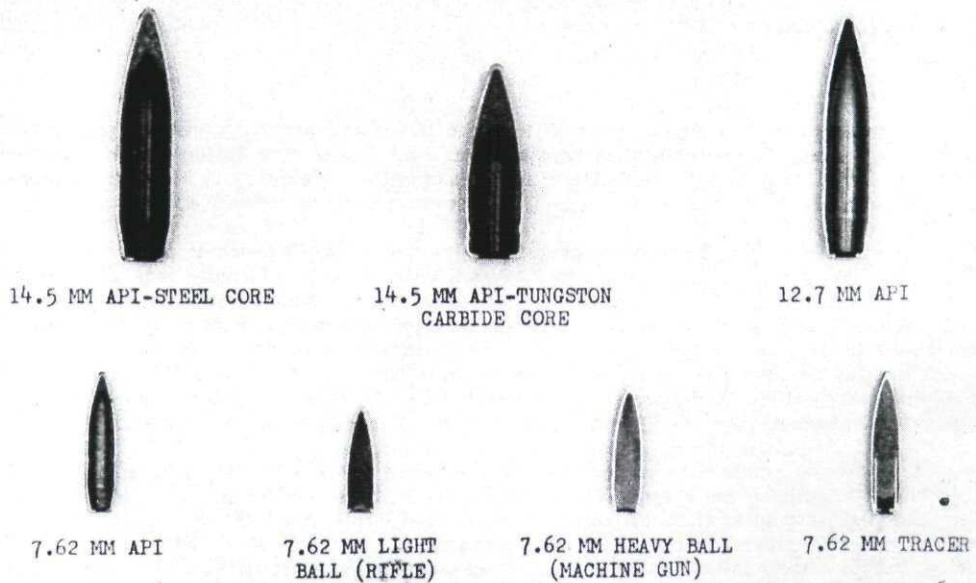
Figure 1-3. Typical Soviet Small-Arms Projectiles

Table 1. Characteristics of Small-Arms Projectiles

Projectile	Weight (gr)	Length (in)	Materials
7.62-mm API	120	1.08	Gilding metal-clad steel jacket, steel core, lead sleeve, incendiary charge filler
12.7-mm API	736	2.5	Same as above
14.5-mm APIT	919	2.68	Brass-clad steel jacket, steel core, lead sleeve
23-mm APIT	3000	3.91	Steel body and armor-piercing core; no jacket
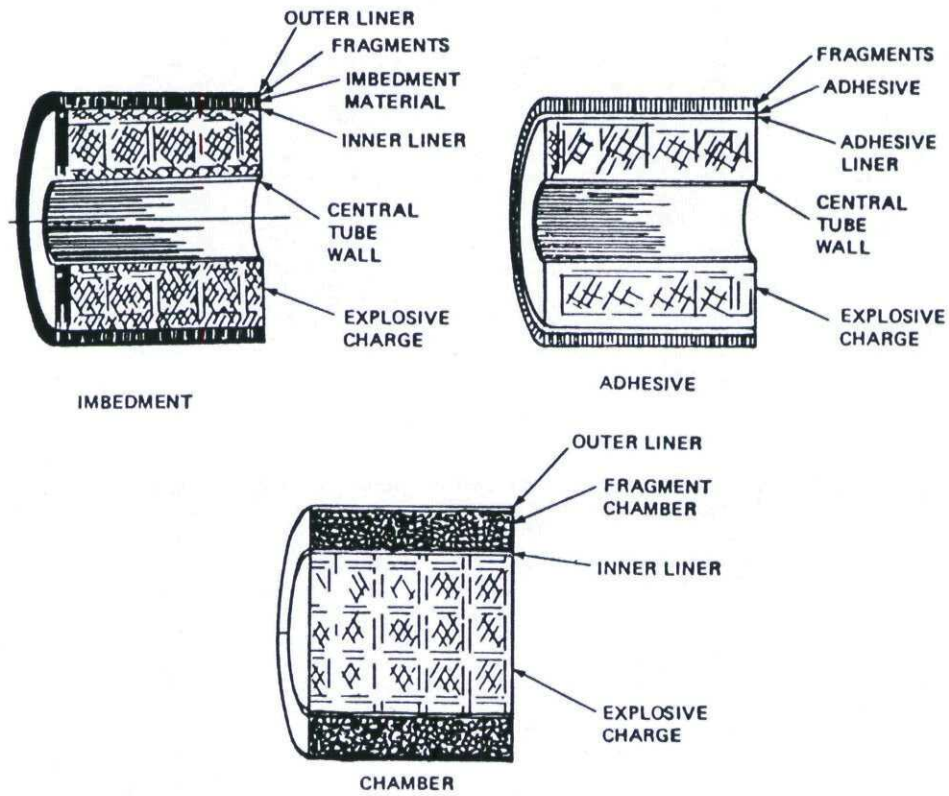
Figure 1-4. Several Warhead Assemblies Using Preformed Fragments
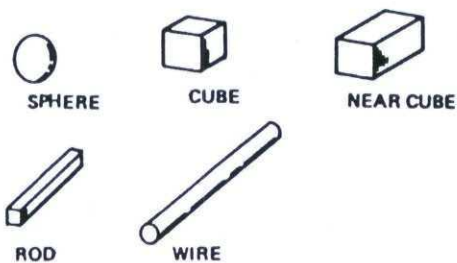
Figure 1-5. Several Fragment Shapes From Missile Warheads

The warheads generally have a proximity fuze. At detonation, the fragments are propelled outward at high velocities (10,000 feet per second in static detonation is not uncommon). The shape and weight of individual fragments depend on the warhead type. Figure 1-5 shows some preformed fragment shapes. Cubical or diamond-shaped fragments, ranging in weight from approximately 50 to 200 grains, represent typical warhead fragment threats.

Although missile warhead fragments are treated here as non-exploding penetrators, they may be accompanied by blast overpressure from the detonation. The intensity of the overpressure depends on the warhead miss-distance. In addition, it should be clear that warhead encounters invariably result in multiple fragment impacts, providing the potential for interacting effects between impacts, and for damaging several structural members.

1.1.1.2 Encounter Parameters

Striking velocity, projectile attitude (yaw), and angle of obliquity are the encounter parameters that must be specified in order to assess penetration and damage capability. These parameters are illustrated in Figure 1-6 and defined below. Missile warhead fragments, representing multiple impact encounters, are additionally characterized by fragment impact density; i.e., the number of fragments impacting per unit area.
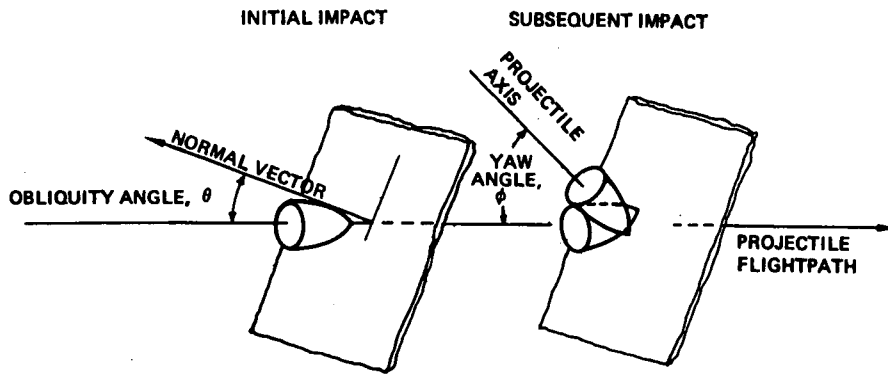
Figure 1-6. Definition of Encounter Parameters

Striking Velocity

The striking velocity is the relative velocity between projectile and aircraft at the instant of impact. Figure 1-7 shows a typical "range-velocity" chart for several small-arms projectiles. These curves are developed from ballistic trajectories obtained from solutions to the equations of motion, given an angle of trajectory, an initial (muzzle) velocity, and a ballistic coefficient. Once the striking velocity has been specified, the kinetic energy of the impacting bullet can be found conveniently using the impact energy nomograph shown in Figure 1-8.
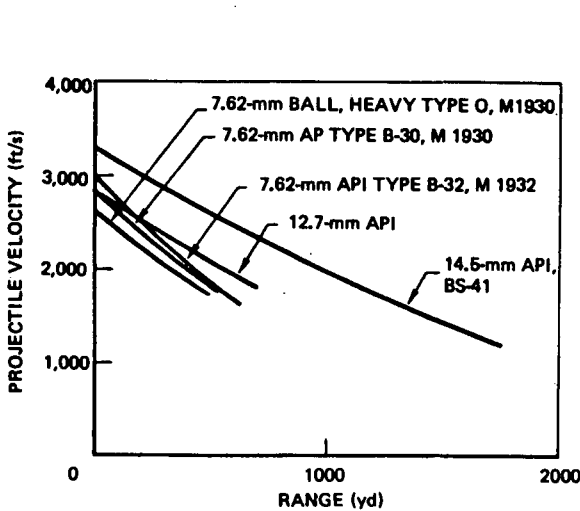
Figure 1-7. Projectile Velocity as a Function of Range
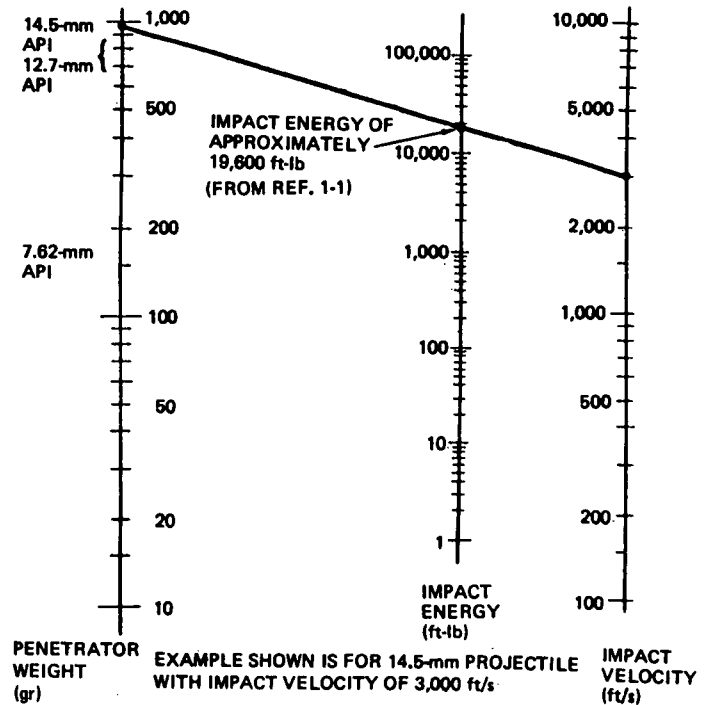
Figure 1-8. Penetrator Impact Energy Nomograph

Projectile Attitude (Yaw)

The projectile attitude or yaw is the angle between the projectile longitudinal axis and the projectile flight path, and varies from "aligned" (0-degree) to "fully tumbled" (90-degrees).

Angle of Obliquity

Angle of obliquity refers to the angle between a normal to the target surface and the projectile flight path. For example, an angle of obliquity approaching 90-degrees represents a "grazing" impact. The terms "angle of obliquity" and "impact angle" have often been used interchangeably.

A frequent application of encounter parameters in design is to specify them as part of the design criteria, often reflecting anticipated typical or worst case conditions. For example, a typical encounter condition criteria for a low-flying aircraft might read:

Striking velocity:	2,000 feet per second,
Angle of obliquity:	Normal impact,
Projectile attitude:	Aligned or fully tumbled.

An alternate approach is to determine encounter conditions from operational analyses wherein the aircraft is flown through a postulated mix of weapon threats. These "end game" analysis results can be used to provide the most probable conditions for use as design criteria.

Since both aircraft and projectile are moving at the time of impact, encounter parameters must be assessed "relative to" the aircraft. For example, the relative velocity between aircraft and projectile introduces a yaw with respect to the relative flightpath, even though the projectile may be unyawed with respect to its own flightpath. Figure 1-9 shows a useful geometry for defining encounter conditions, specifying the projectile flightpath by azimuth and elevation angles. In Figure 1-10, equations derived from the flight path/trajectory geometry are used to solve for the encounter parameters in a sample problem. The resulting values for striking velocity, obliquity angle and yaw can be used for component penetration and damage assessment, since they are expressed in a reference system within the aircraft.

PLAN VIEW
PROJECTION
OF PROJECTILE
FLIGHTPATH

RELATIVE PROJECTILE
FLIGHTPATH
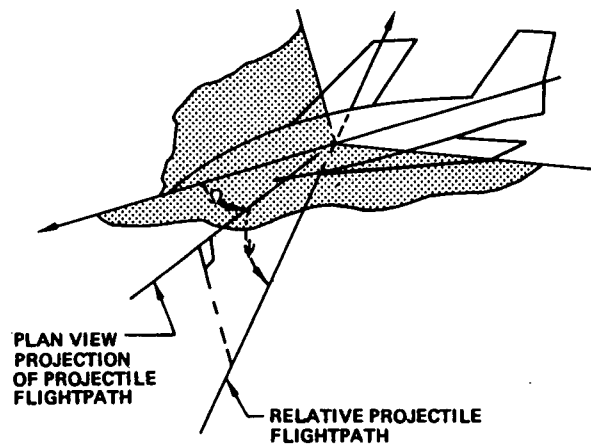
Figure 1-9. Geometry for Establishing Encounter Conditions
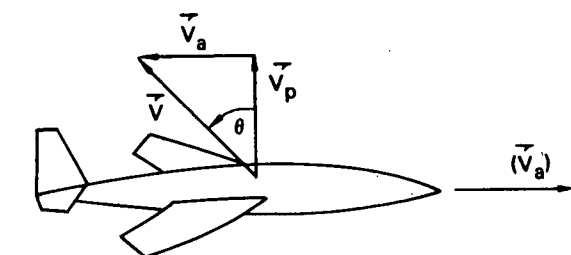
$\vec{V}_a$ = AIRCRAFT VELOCITY

$\vec{V}_p$ = PROJECTILE VELOCITY

$\vec{V}$ = VELOCITY OF PROJECTILE RELATIVE TO AIRCRAFT

GIVEN:

AIRCRAFT VELOCITY = 400 nmi/h; HORIZONTAL FLIGHTPATH (587 ft/s)
PROJECTILE VELOCITY = 2,000 ft/s; VERTICAL TRAJECTORY
$\Omega = 0$, $\psi = 90$

FIND:

PROJECTILE STRIKING VELOCITY, ANGLE OF OBLIQUITY, AND ATTITUDE (YAW), RELATIVE TO THE AIRCRAFT COMPONENT IMPACTED.

$$V = V_a \cos \Omega \cos \psi + \sqrt{V_p^2 - V_a^2 (1 - \cos^2 \Omega \cos^2 \psi)} \tag{1}$$

SUBSTITUTING INTO EQUATION (1) YIELDS THE STRIKING VELOCITY:

V = 1,912 ft/s

THE ANGLE OF OBLIQUITY, θ, IS CALCULATED FROM: (2)

$\tan \theta = V_a/V_p = 587/2,000 = 0.29$

$\theta = 16$ deg

ASSUMING THE PROJECTILE IS NOT YAWED WITH RESPECT TO ITS OWN TRAJECTORY, THE APPARENT YAW ANGLE CAN BE CALCULATED FROM:

$$\phi = \arccos \left[\frac{V^2 + V_p^2 - V_a^2}{2 V V_p} \right] = 17 \text{ deg} \tag{3}$$

Figure 1-10. Sample Problem Solving for Encounter Parameters Relative to Aircraft

The encounter parameters described above (striking velocity, yaw, and angle of obliquity) are applicable to all projectile impact encounters. An additional parameter, fragment density, is significant for missile warhead encounters. Figure 1-11 is a schematic representation of a fragment spray pattern resulting from a warhead detonation. The angular extent of the fragment pattern is determined by the characteristics of the warhead and the terminal velocity of the missile. The corresponding area enclosing fragments increases with distance from detonation. Thus, the number fragments impacting per unit area of aircraft surface is primarily dependent upon miss-distance; i.e., the distance between missile and aircraft at detonation.
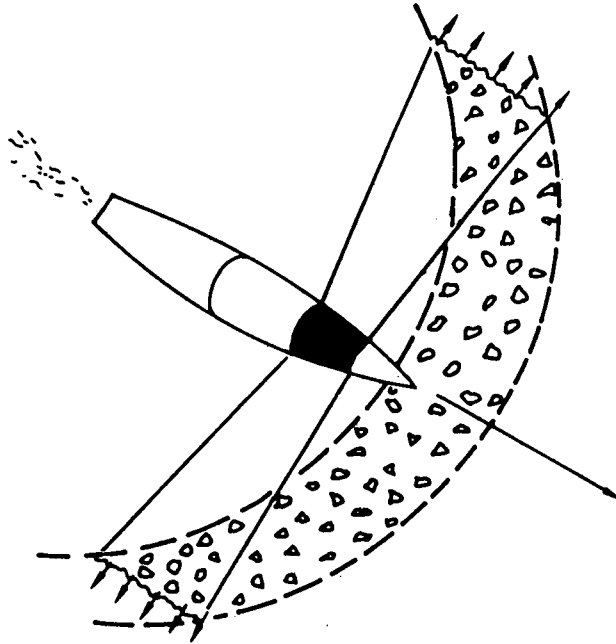
Figure 1-11. Schematic Representation of Missile Warhead Detonation

1.1.1.3 Typical Terminal Effects

Military projectiles have considerable capability to penetrate typical aircraft structure, and they will at least partially penetrate even the heaviest component. This penetration capability is illustrated in Figure 1-12 for a .50 caliber armor-piercing projectile impacting steel or aluminum sheet. The ordinate of this curve is the V_{50} ballistic limit, meaning the impact velocity at which 50-percent of the impacts result in complete penetration. The curve indicates that one-half inch aluminum plate can be penetrated at velocities as low as 1100 feet per second.

Projectile penetration damage consists of cracking and material removal including front and rear surface spallation. A special case arises when the projectile enters a cell containing liquid, since the impact shock and the dissipation of kinetic energy as the projectile slows down within the liquid leads to "hydrodynamic ram" pressures acting against the cell walls. These pressures often result in additional structural damage.

Penetration damage has diverse characteristics depending on the projectile, the configuration of the structure, and the encounter conditions. Damage can range from dents, cracks, and holes, to large petalled areas accompanied by extensive out-of-plane deformation. The diverse character of projectile damage raises questions: How can it be quantified? What should be measured?

Although there are several meaningful measures of penetration damage, lateral damage is the measurement that has been found most useful for vulnerability analysis. Lateral damage, as shown in Figure 1-13, is defined as the diameter of an imaginary circle that just encloses the limits of cracking, perforation or spallation in the plane parallel to the original surface of the sheet. The terms "lateral damage", "damage size", and sometimes simply "damage" are used synonomously.

A second significant measurement when stressed panels are impacted is the component of lateral damage transverse to the applied load. This index is referred to as transverse lateral damage, often abbreviated as TLD.

Certain characteristics of projectile impact damage are described in the following pages, organized into three major topic areas:

(a)   Non-Exploding Penetrators Impacting Metallic Structure;

(b)   Non-Exploding Penetrators Impacting Advanced Fiber Composite Structure;

(c)   Projectile Penetration into Fluid-Filled Containers.
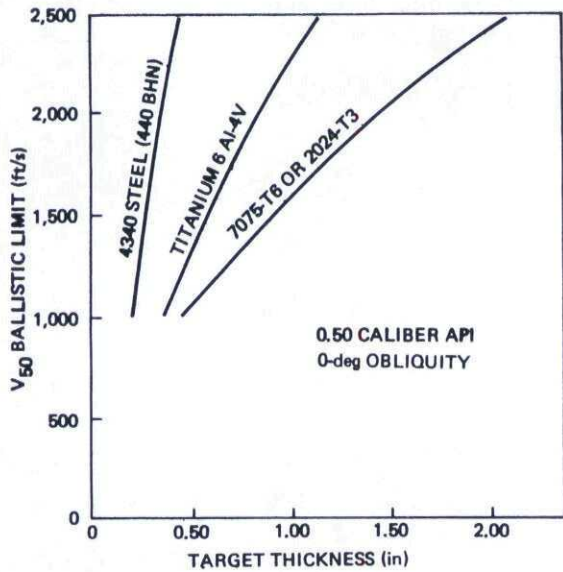
Figure 1-12. *Penetration Capability of Small-Arms Projectiles Against Typical Aircraft Structural Materials*
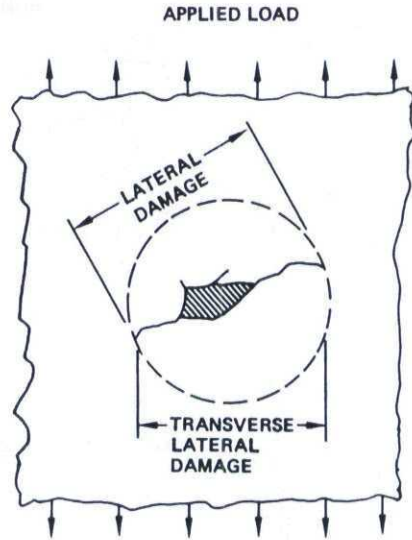
Figure 1-13. *Lateral Damage Definition*

1.1.1.3.1 Non-Exploding Penetrators Impacting Metallic Structure

The impact damage response of metals depends upon many interrelated parameters. Because of this, there is appreciable scatter in the test data, and it is often difficult to isolate and quantify the effect of individual parameters. An extensive investigation of impact damage induced in metals by small arms projectiles and fragments is reported in Reference 1-2. This reference discusses types of damage and the parameters that influence damage. Some results from that study are summarized in the following paragraphs.

Damage Type

Impact damage in metal sheet and plate can be cracks, spallation, petals, holes, dents or gouges. For a given target material, the damage type depends on the sheet thickness, and the projectile velocity and angle of obliquity. This is illustrated in Figure 1-14.
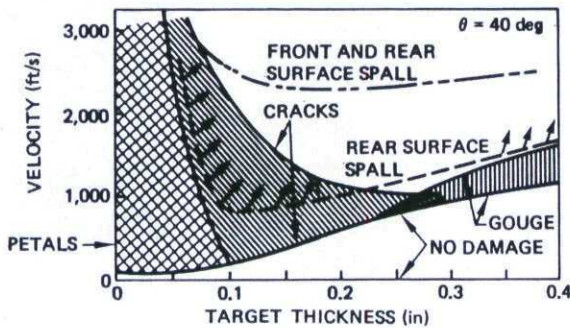
Figure 1-14. *Damage Type Regime Diagram, .30 AP, 7075-T6*
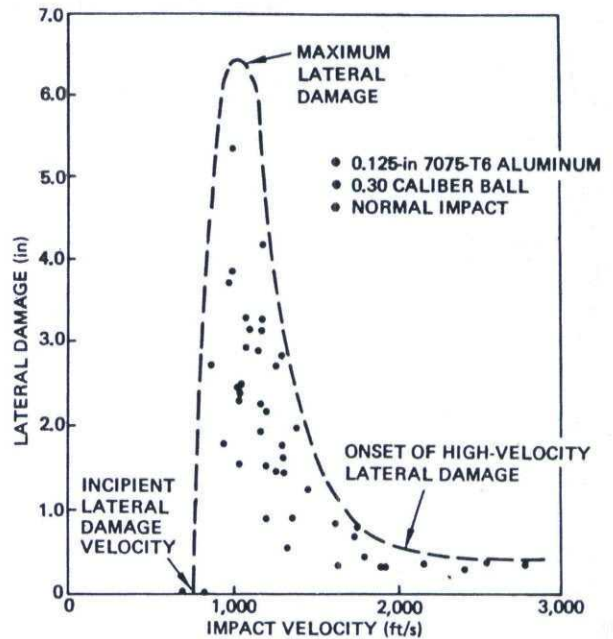
Figure 1-15. *Typical Variation of Damage Size With Projectile Velocity*

Effect of Projectile Velocity

For a given target sheet and projectile obliquity, the variation of projectile striking velocity can result in the response shown in Figure 1-15, which also illustrates the concepts of incipient damage, maximum damage and high-velocity damage. This response is characterized by a maximum lateral damage size that occurs just above the ballistic limit. Further increases in projectile velocity result in lesser damage, until a plateau is reached called the high-velocity lateral damage. Velocity increases beyond this limit do not produce any significant change in damage size, unless velocities can be reached that result in appreciable projectile break-up. The size differential between the maximum damage and the high velocity damage depends primarily on sheet thickness.

8

Figure 1-16 is a photograph showing the effects of projectile velocity for .30-caliber AP impacting 0.090-inch 7075-T6 sheet. The increase in damage with reduced velocity is evident.
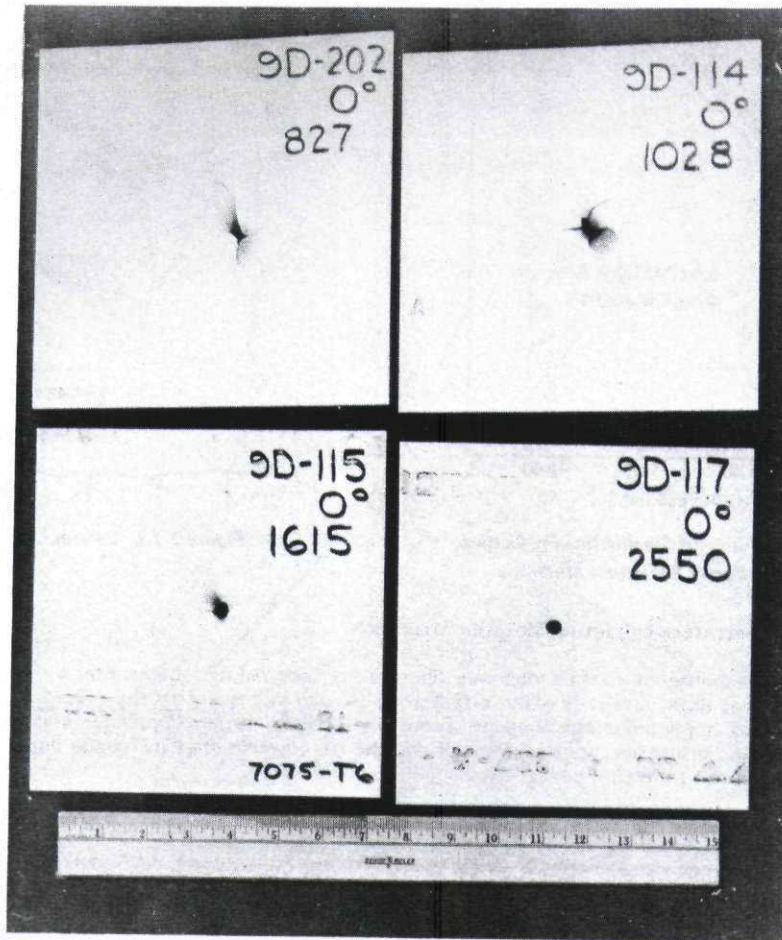
Figure 1-16. Effect of Projectile Velocity on Damage Size
(0.90 7075-T6 Impacted by .30 AP)

Effect of Projectile Obliquity

The angle of obliquity (or impact angle) has a pronounced effect on damage size. The following are generally true regarding obliquity effects:

1. When impact angles are increased and other conditions held constant, the maximum lateral damage will also increase as long as penetration occurs.

2. The velocities required for incipient lateral damage, maximum lateral damage and the onset of high-velocity lateral damage increase directly with obliquity increase.

Figure 1-17 illustrates this response schematically, and Figure 1-18 is a photograph showing 0.090-inch 7075-T6 impacted at several obliquities with velocity held constant. There is a dramatic reduction in damage size caused by projectile ricochet as the impact angle increases from 60 to 70-degrees.

Effect of Projectile Type

When projectiles are similar in shape and construction but differ in size, it is generally found that larger projectiles produce greater damage. When this similarity is not present, however, it is not possible to make lateral damage predictions based only on projectiles size. Projectile type must also be considered. A distinction must be made between ogive bullets and compact fragments, for example. Spin-stabilized ogive projectiles can exert significant in-plane wedging forces that contribute to panel cracking during projectile penetration. Compact fragments tend to punch through the panel, even at relatively low impact velocities, causing a different mode and size of damage as illustrated in Figure 1-19.

Effect of Sheet Thickness

Damage size is highly dependent on sheet thickness. A convenient thickness parameter is the ratio of thickness to projectile presented length (t/L_p). Typically, as t/L_p ratios are increased beyond 0.1, the maximum lateral damage size increases from a projectile-sized hole to a relatively large damage area. The maximum damage occurs at t/L_p values between 0.3 and 0.4 for aluminum and titanium alloys. Increasing t/L_p ratios beyond 0.4 reduces the lateral damage to a projectile-sized hole that may be accompanied by significant amounts of spallation.
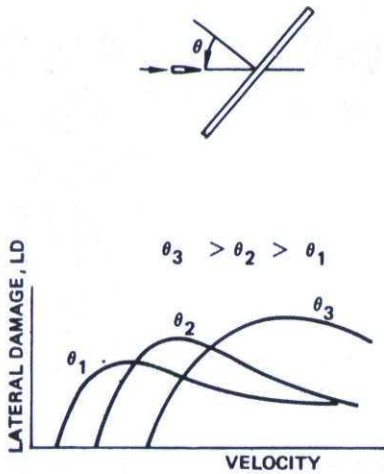
Figure 1-17. Typical Effect of Obliquity on Damage Size
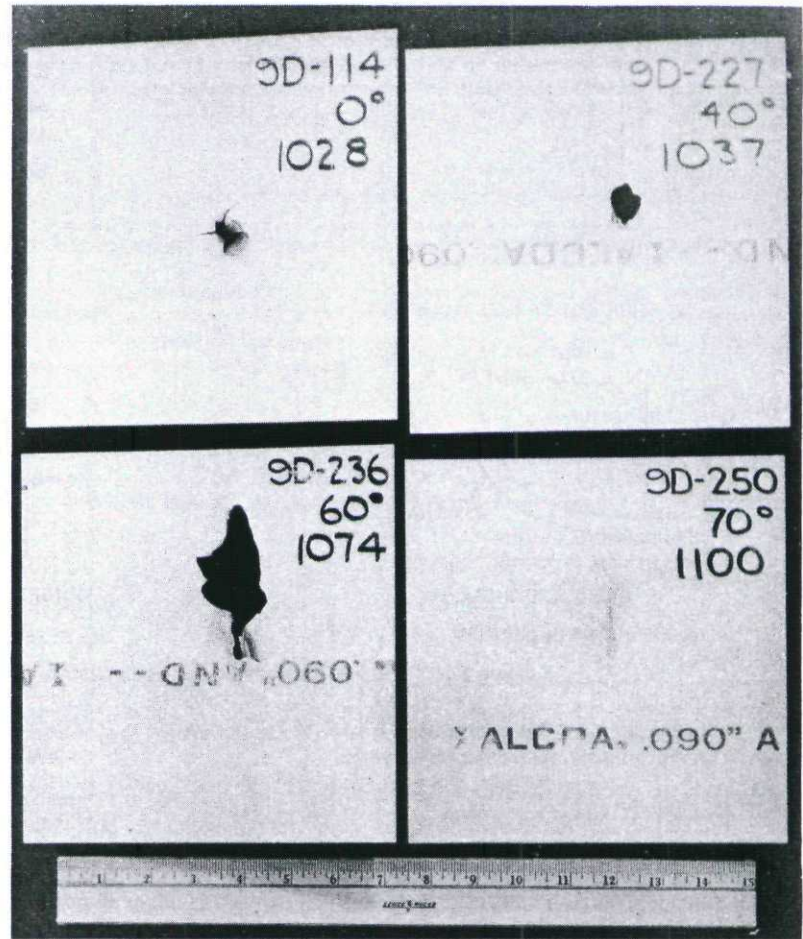
Figure 1-18. Effect of Impact Angle on Damage Size
(0.90 7075-T6 Impacted by .30 Caliber AP)
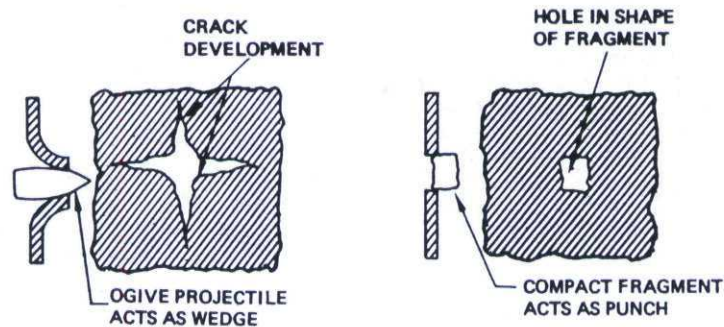
Figure 1-19. Example of Effect of Projectile Type on Character of Damage

The typical response is shown graphically in Figure 1-20(a). It should be kept in mind that since lateral damage also depends on projectile velocity, this figure shows the largest damage (i.e., the maximum lateral damage) that occurs for each given t/L_p ratio. The remaining illustrations in Figure 1-20 demonstrate the parametric effects discussed previously, namely: the effect of projectile velocity, obliquity, and projectile type.

Effect of Sheet Material

The choice of material will have a marked effect on the resulting size and type of damage, since materials differ in their resistance to impact damage. A comparison of damages produced under identical impact conditions, changing only target material, will show large differences in damage size. It was shown in Reference 1-2 that the damage sizes for 2024-T3, 2024-T81 and 7075-T6 aluminums have the ratios 1, 2.2 and 5.1, respectively. On the same basis, the ratio for 6A1-4V titanium was found to be 1.8 with regard to damage resistance, these materials rank in the order shown below, with the first having the highest damage resistance:

1. 2024-T3;
2. 6A1-4V;
3. 2024-T81;
4. 7075-T6.
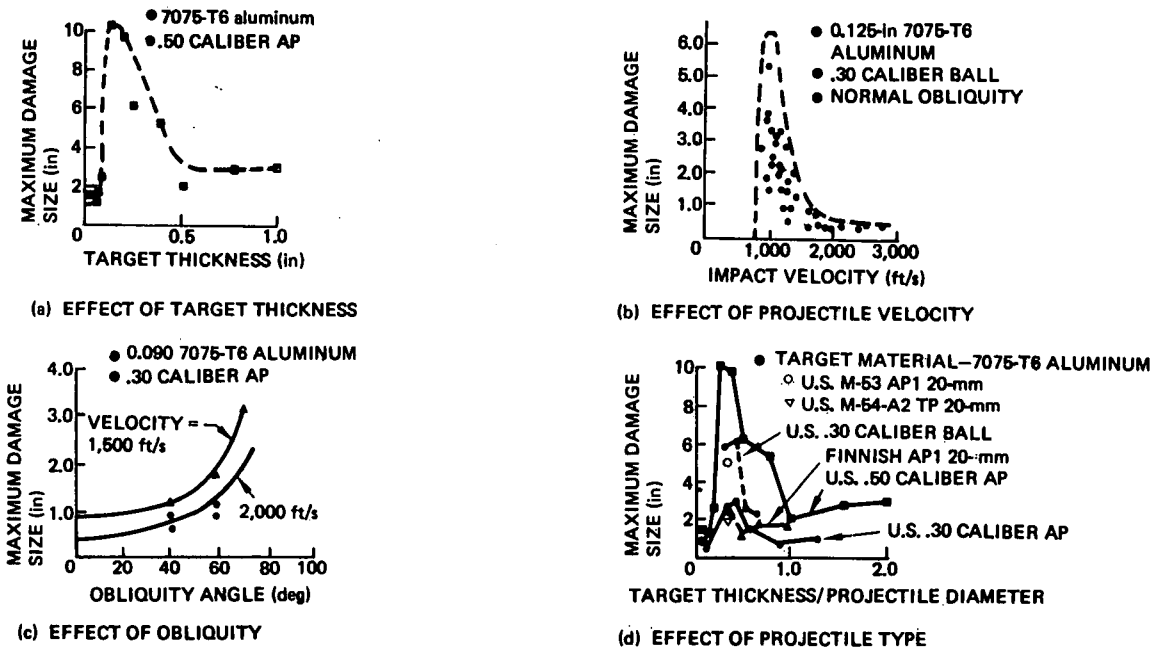
Figure 1-20. Effect of Several Parameters on Gunfire Damage of Metal Structure

Since damage tolerance also depends on material properties, material selection is an important means of reducing structural degradation due to battle damage.

Effect of Applied Stress

If the tensile stress level is sufficiently high, unstable crack propagation may occur at impact, resulting in an extension of damage beyond that obtained from lower stressed panels. Often, the stress level causing impact fracture (called "impact fracture strength" or "threshold stress") is lower than the stress required to fracture the panel containing equivalent damage inflicted without applied stress. Applied stress levels below this value may have a small influence on damage size and orientation; however, the extent of these effects has not yet been established.

1.1.1.3.2 Non-Exploding Penetrators Impacting Fiber Composite Structure

There have been a number of programs investigating the response of advanced fiber composite structure (primarily graphite/epoxy) to projectile impact (Ref. 1-3 for example). These studies have shown that the unique characteristics of composite materials can have a significant influence on damage response. Some of the properties that influence projectile damage are (1) the orthotropic strengths and stiffness of the plies, (2) the low ductility of the fibers, (3) and low interlaminar strength. Characteristic damage responses observed in fiber composite structural configurations are discussed in the following paragraphs.

Damage Type

The results of examining graphite/epoxy laminates damaged by small arms projectiles and fragments are reported in Reference 1-3. The damage modes illustrated in Figure 1-21 were noted from this examination including perforation, delamination, peeling, fiber fracture and gouging.
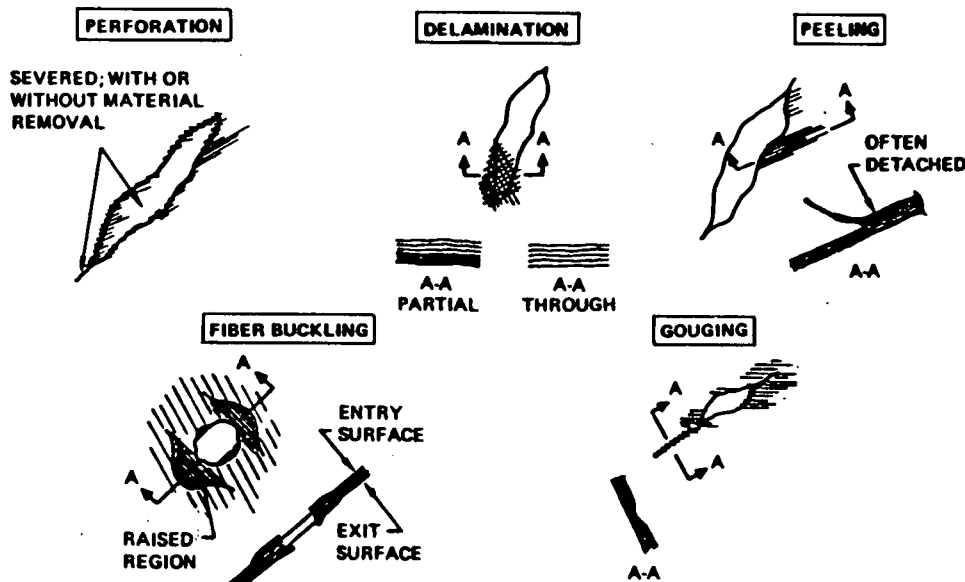
Figure 1-21. Typical Ballistic Damage in Fiber Composites

Projectile damage in fiber composites tends to conform to the contour of the projectile more closely than experienced in most metals, which often exhibit considerable cracking emanating from the primary perforation. In composites, damage is more likely to be confined to a region of perforation surrounded by delamination. There is often peeling of the surface layers, but this may not be structurally significant relative to the penetration damage.

Effect of Projectile Velocity

Considerable testing with small arms projectiles and fragments fired into fiber composite laminates has shown that visual damage size is relatively insensitive to projectile velocity. Figure 1-22(a) is representative of the results obtained in thin laminates. These data were obtained for impact conditions well above the ballistic limits of the laminates.

Results of recently conducted tests with thick graphite/epoxy (Ref. 1-3), shown in Figure 1-22(b), indicate that while the damage size increases rapidly for velocities up to $V/V_{BL} = 1.3$ (Velocity/Ballistic Limit Velocity), it remains relatively constant for higher V/V_{BL} ratios. This is in contrast to metals, where the maximum damage occurs at velocities near the ballistic limit and diminishes before leveling at high velocities (Ref. 1-2).
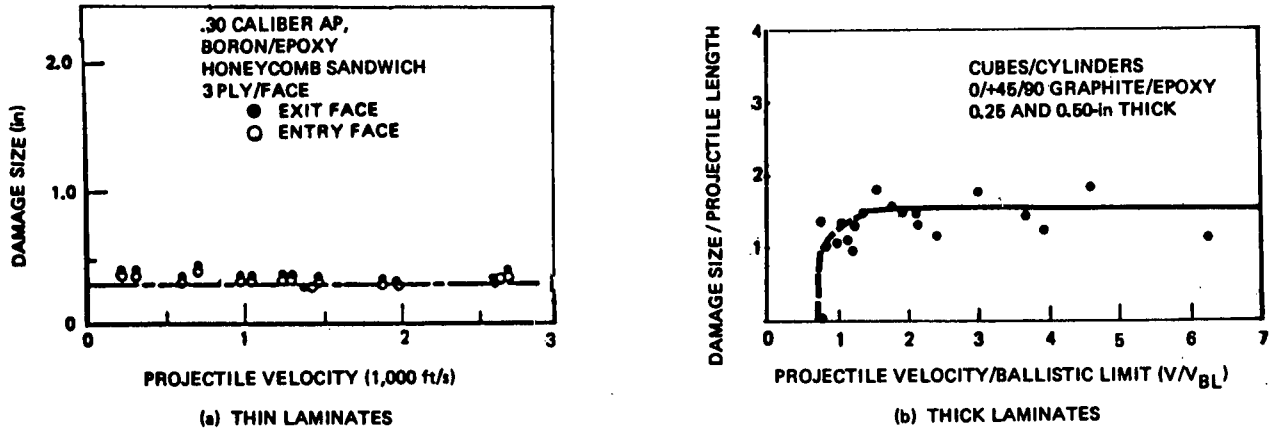
Figure 1-22. Effect of Projectile Velocity on Damage Size in Advanced Fiber Composites

Effect of Projectile Obliquity

As with metals, damage size in fiber composites varies with the obliquity angle at impact. This effect is shown in Figure 1-23(a) for thin laminates and 1-23(b) for thick laminates.
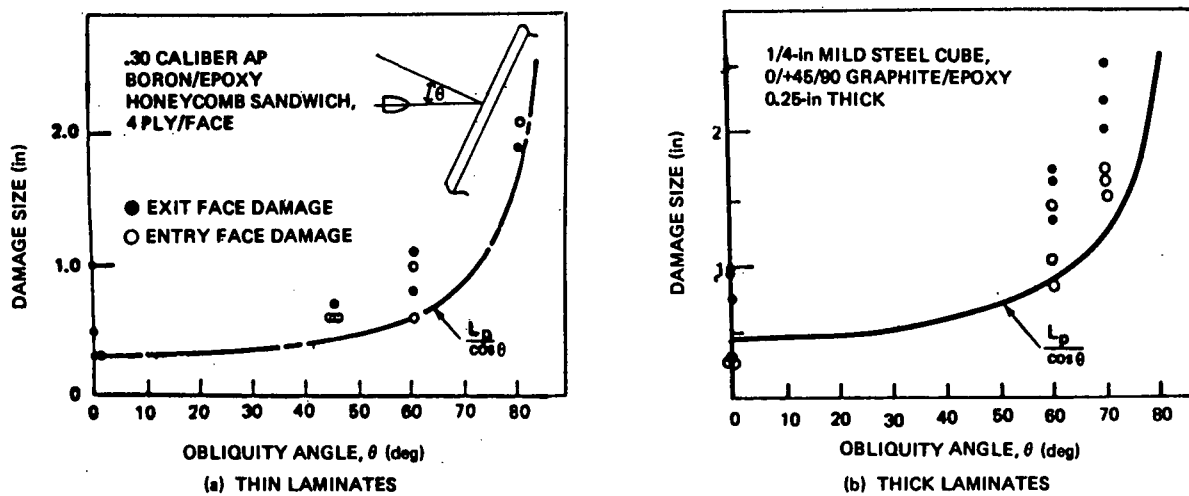
Figure 1-23. Effect of Obliquity Angle on Damage Size in Advanced Fiber Composites

Effect of Sheet Thickness

Laminate thickness has a significant effect on damage caused by penetrators. Damage size in thin composite laminates tends to conform to the projected size of the projectile in the plane of the impacted laminate. This behavior does not extend to thicker laminates, because the exit face damage can be extensively increased by delamination, sometimes appearing as rear surface spallation. This is shown in Figure 1-24. As with metals, the ratio of thickness to projectile presented length appears to be a useful parameter in describing thickness effects, as shown in Figure 1-25 for a typical graphite/epoxy.

Figure 1-24. Ballistic Penetration Damage in 0.50-in Thick Graphite/Epoxy, Exit Surface
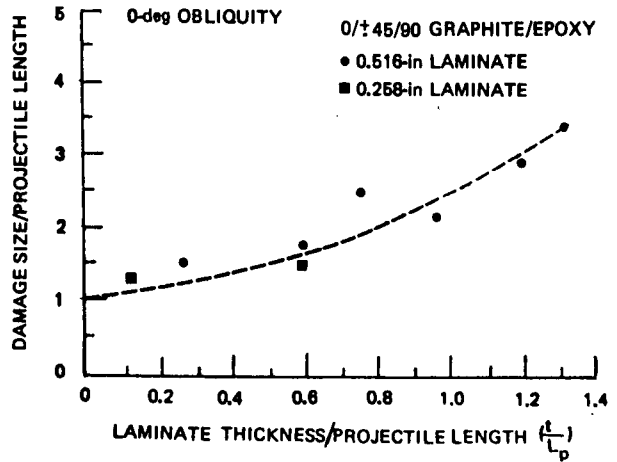
Figure 1-25 Effect of Laminate Thickness and Projectile Size on Damage in Graphite/Epoxy

1.1.1.3.3 Projectile Penetration Into Fluid Filled Containers

In many aircraft, the structure serves the additional function of fuel containment, so that a penetrating projectile enters a fluid medium after passage through an adjacent element of structure. The term "hydrodynamic ram" refers to the dynamic pressures generated within the fluid as a result of energy imparted by a penetrating projectile. These pressures are transmitted to the walls of the fuel tank, and they can cause severe structural damage.

The initial impact and penetration of the entry wall generates a spherical shock wave in the fluid. The shock pressures dissipate with distance from the entry wall, but significant damage may be inflicted by this "shock" phase of the ram phenomena, particularly to the entry wall.

Figures 1-26 and 1-27 show the second phase of the hydrodynamic ram effect, referred to as the "drag" phase. In Figure 1-26 the projectile is rapidly losing velocity as it travels in the fluid, and this rate of loss is augmented by tumbling. Figure 1-27 illustrates the corresponding pressure pulse acting on the tank walls, resulting from the conversion of projectile kinetic energy to fluid kinetic and potential energy.
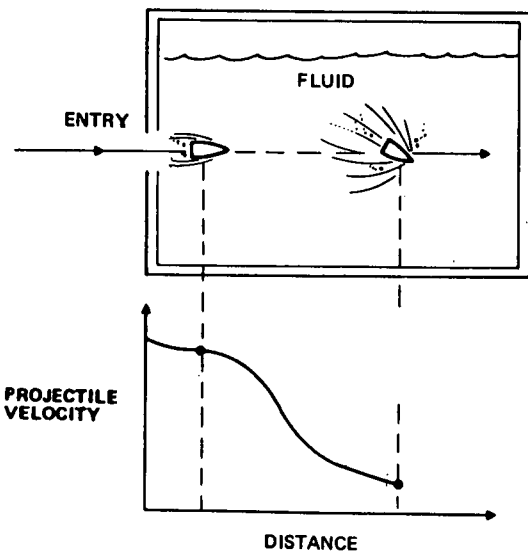
Figure 1-26. Projectile Slowing and Tumbling Within Fluid
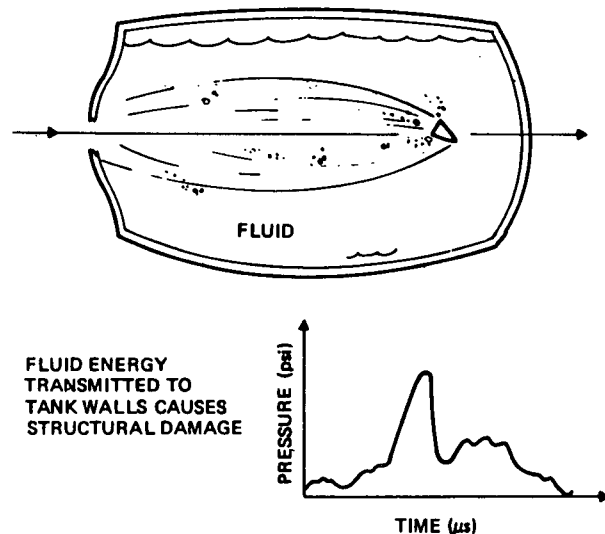
Figure 1-27. Pressure Pulse Acting on Tank Walls

Hydrodynamic ram must be considered as a damage mechanism for any structural element that is wetted by fluid, or any element that is separated from fluid by a pressure transmitting component such as a flexible bladder. The structural damage caused by ram consists of bulging and tearing, and fastener failure is common. Damage is especially severe at entrance and exit walls because the internal pressures extend the damage caused by penetration. Hydrodynamic ram damage due to fragments and small-arms projectiles can be extensive and potentially catastrophic as suggested by Figure 1-28.
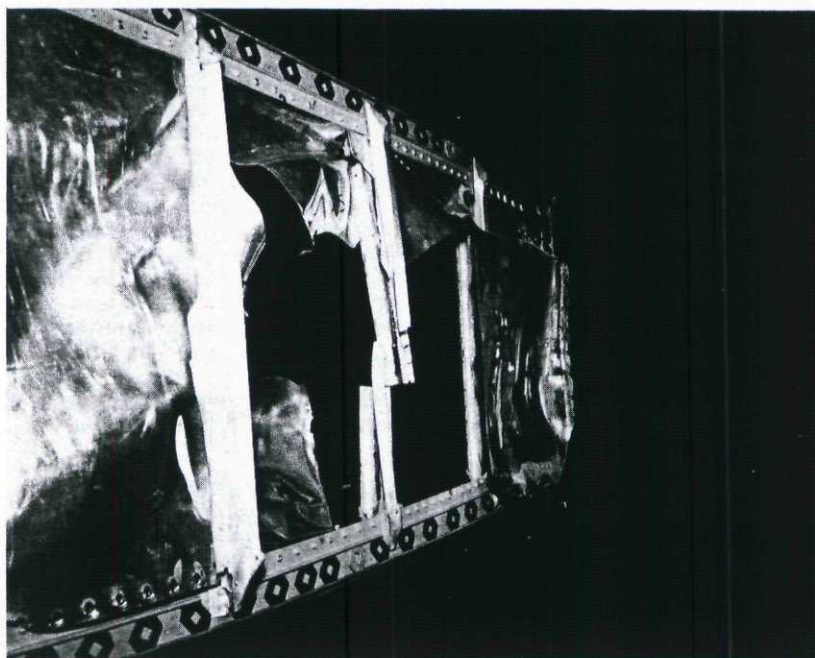
Figure 1-28. Hydrodynamic Ram Damage in Fuel Tank
Caused by Small Arms Projectile

1.1.2 Exploding Projectiles

High-explosive (HE) projectiles contain an explosive charge that is activated by impact. The detonation can occur almost immediately (superquick fuze), or it may be delayed (delay fuze). The superquick fuzed projectile initiates detonation at the external side of the entry skin, whereas detonation is usually initiated inside the aircraft with the delay fuzed round.

1.1.2.1 Types

Common high-explosive threats for aircraft are the 23-mm HEIT, 30-mm HEI, 37-mm HEIT, and 57-mm HE. Larger projectiles are still in use (though limited), but are generally not considered in structural analysis. The most frequent weapon deployment consists of vehicle-mounted AAA guns in the forward area or in defense of missile sites. In addition, the smaller calibers (20 to 30-mm) may be fired from airborne cannons.
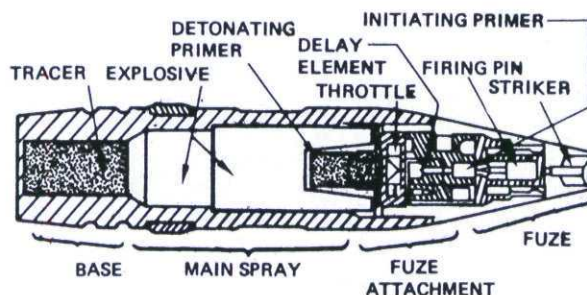
Figure 1-29. Cross Sectional View of Typical HEI Projectile

Figure 1-29 shows a cross section of a typical HEI-T AAA projectile and identifies several of the components. The projectile consists of a time varying fuze mechanism, explosive charge, tracer element, and the outer casing surrounding the explosive charge. The tracer acts as a pyrotechnic indicator of the projectile trajectory. The fuze functions when the projectile impacts a surface. Momentum drives the striker which impels the firing pin into the initiating primer. Gases escaping from the initiating primer may be channeled through a delay element before permeating the throttle and igniting the detonating primer, thus creating a time delay.

1.1.2.2 Encounter Parameters

The appropriate encounter parameters for high-explosive projectiles are identical to those for non-exploding projectiles, namely: striking velocity, obliquity, and attitude.

1.1.2.3 Typical Terminal Effects

The damage from high-explosive projectiles results from the combined effects of fragment impacts and blast pressures. These effects are discussed in the following paragraphs.

1.1.2.3.1 Fragment Effects

Detonation of the explosive charge causes rupture of the outer casing at extremely high pressure and temperature, creating fragments of various sizes and accelerating them to high velocities. Due to the configuration of the projectile, the fragments can be categorized into major groups. For example, fragments from the fuze section and the projectile base are generally expelled axially forward and aft (relative to the projectile), respectively, while the fuze attach section and main spray are ejected primarily radially. The spray of fragments emanates from the point of detonation, forming a cone of fragments. The angle of divergence relative to the projectile flightpath depends on the velocity of the projectile and the fragment ejection velocity. This latter velocity is characteristic of the projectile and can be obtained from stationary detonations. The influence of projectile velocity on fragment cone formation is shown in Figure 1-30. The cone is formed by superimposing the fragment ejection velocity (static detonation) and the projectile velocity at detonation. Fragment distributions have been recorded for statically detonated rounds and typical results are shown in Table 1-3.

Figure 1-31 shows a typical condition at impact for a wing. The HE projectile shown is of the superquick type and has detonated immediately upon contact with the wing lower surface. A hole is formed in the lower surface due to fragments and blast.

The size of the resulting damage zone (figure 1-32) depends on the extent of the fragment cone in the plane of the structure, and is a function of:

(a)   The distance between the structure and the detonation point (stand-off distance)
(b)   The fuzing delay,
(c)   The angle of the fragment cone, $\emptyset$,
(d)   Orientation of the structure relative to the flight path.

(a) STATIONARY PROJECTILE   (b) PROJECTILE WITH FORWARD VELOCITY, V_p
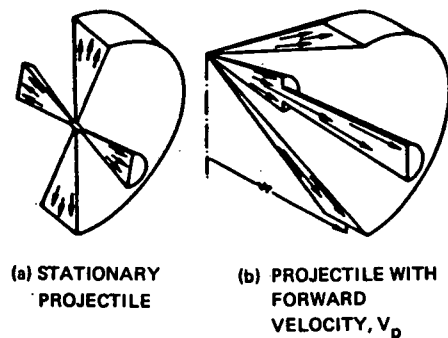
Figure 1-30. Fragment Cone Formation

Table 1-3. Static Fragmentation Data for Typical HEI Projectile

PROJECTILE SECTION	STATIC VELOCITY (ft/s)	MEAN STATIC DIRECTION (deg)	NUMBER OF FRAGMENTS	AVERAGE FRAGMENT WEIGHT (gr)	TOTAL FRAGMENT WEIGHT (gr)
FUZE	1,300	0	2/3	118/20	296
FUZE ATTACHMENT	2,200	65	30	10	300
MAIN SPRAY	2,610	93	604	1.99	1,202
BASE	1,550	140	20	32	640

FRAGMENTS

• SHOCK OVERPRESSURE
• CONFINED-GAS OVERPRESSURE
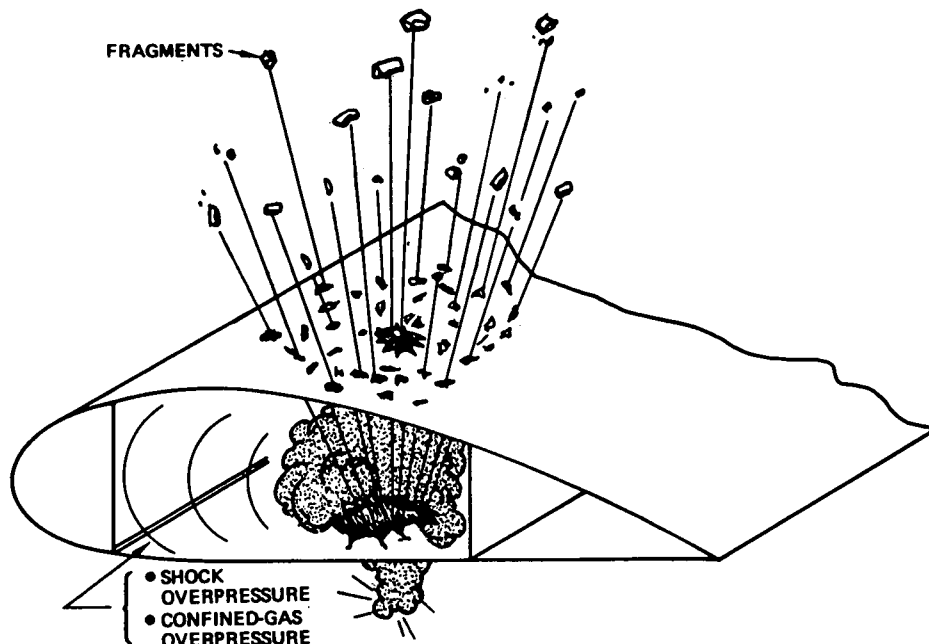
Figure 1-31. Typical Encounter with HE Projectile
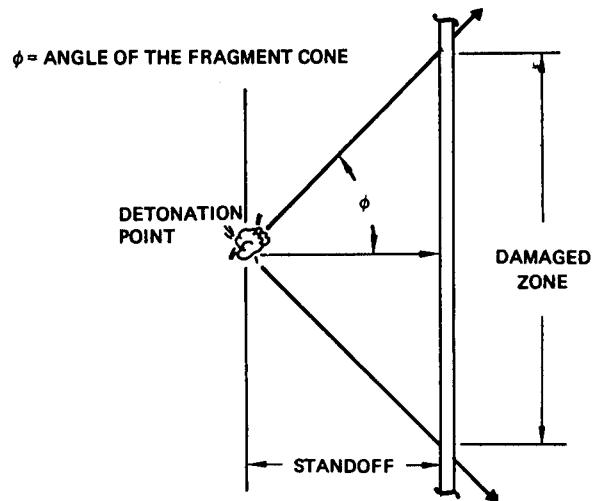
Figure 1-32. Damaged Zone Due to HE Projectile Fragment Cone

Estimating the damage caused by HE projectiles requires consideration of the effects of each of the damage components illustrated in Figure 1-33, including:

1. The typical damage size from the fragments in the cone;
2. The upper-bound on damage from an individual fragment;
3. The size and fragment density (fragments per square foot) of the fragment cone;
4. The effects of the blast.

An estimate is also required of the degree of interaction between the damage components. For small fragment cones (with high fragment densities), the individual fragment damages will overlap, producing an effective damage size equal to the fragment cone diameter. With large cones, however, the fragment density will be low and the individual damages will have little interaction. The effective total damage size will not be much larger than the largest individual damage size. There will be intermediate fragment densities (i.e., intermediate fragment cone sizes) where the individual fragment damages are at the maximum separation for which interaction can occur. This condition will produce the maximum total effective damage size. The resultant effective damage size curve reflecting this behavior is shown schematically in Figure 1-33.

Qualitative illustration of the effects discussed is given in Figure 1-34, showing damage done to honey comb skins by a superquick-fuzed HE projectile, with the exit panel located 10-inches downstream of the detonation. The entry panel was stressed in tension and the exit panel was in compression at the time of impact. In Figure 1-34(a), the front face of the entry panel shows damage induced by a narrow fragment cone. The rear face of the entry panel (Figure 1-34(b)) shows considerable damage from internal blast and fragments. In Figure 1-34(c) the size and density of the fragment cone are clearly defined, with only moderate interaction between outer fragment damages. In Figure 1-34(d), the rear face of the exit panel has severe central damage and increased interaction between outer fragment damages.
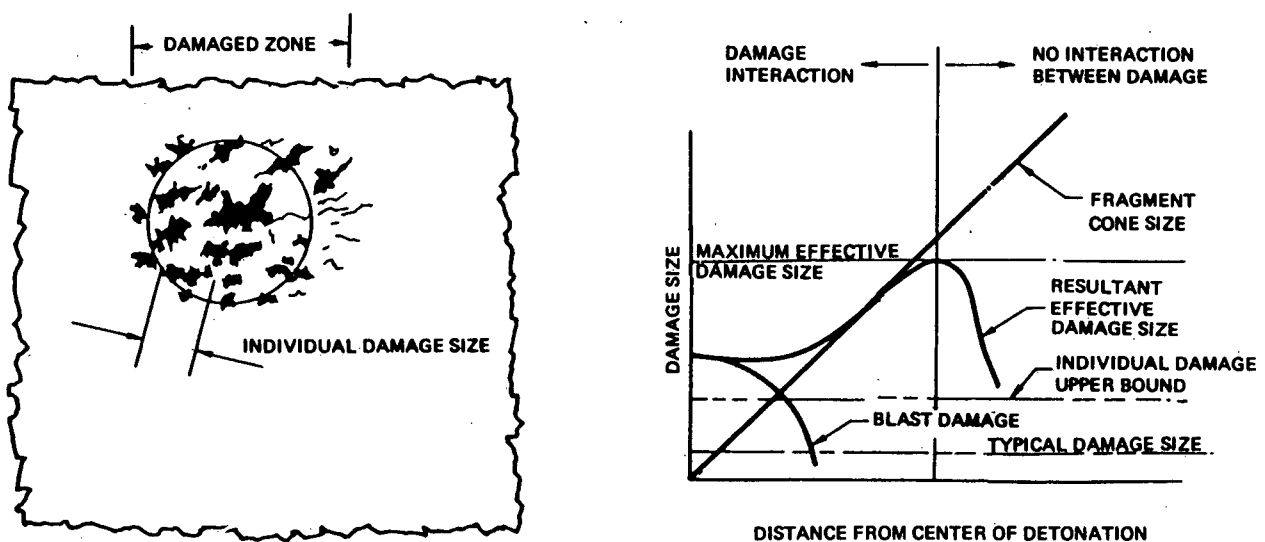
Figure 1-33. Effective Damage Size Resulting From HE Projectile Impact

(a) FRONT FACE, ENTRY PANEL

(c) FRONT FACE, EXIT PANEL

(b) REAR FACE, ENTRY PANEL

(d) REAR FACE, EXIT PANEL
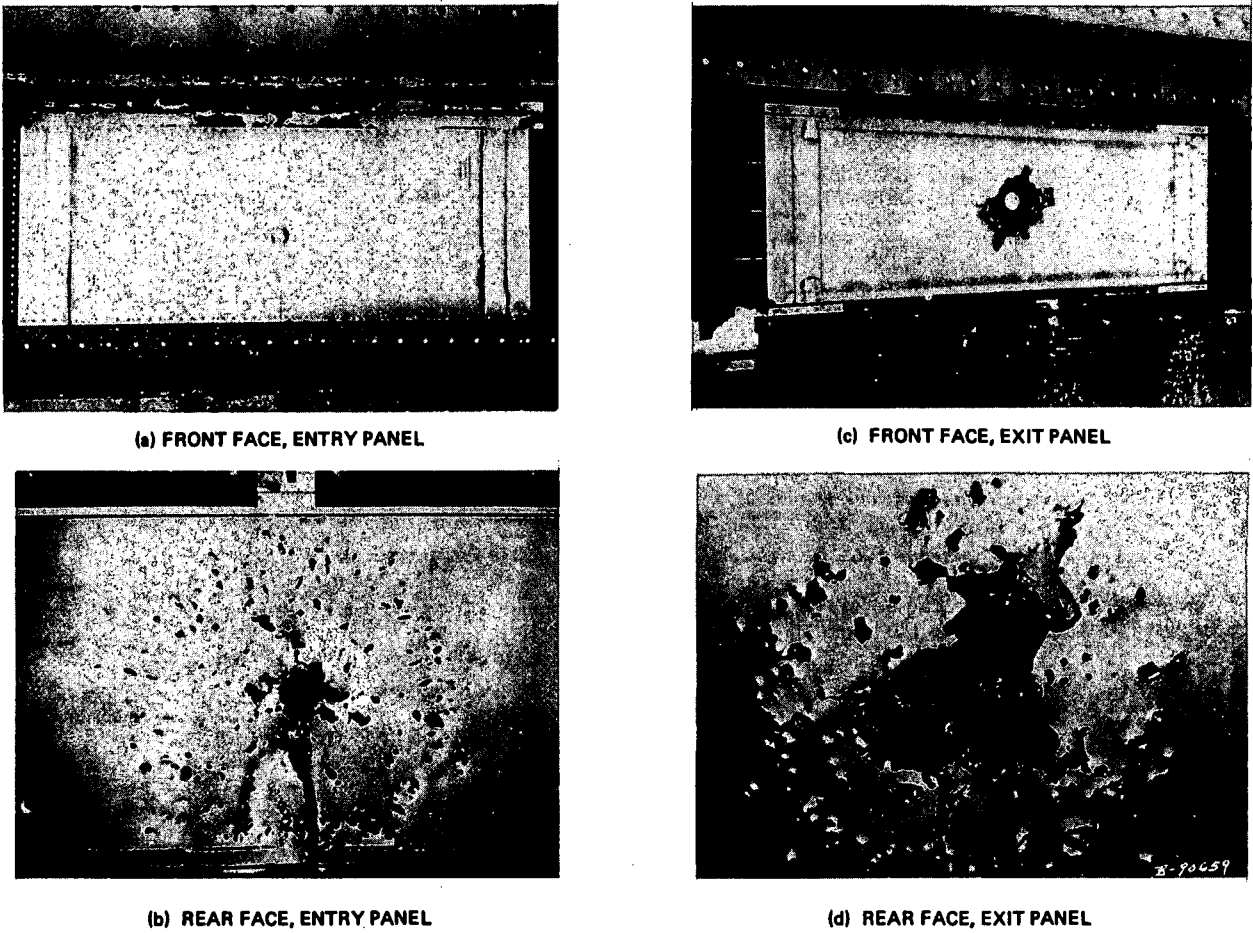
Figure 1-34. Fragment Cone Damage in Honeycomb Panels, Inflicted by Typical HE Projectile, Exit Panel 10-in Downstream of Detonation

1.1.2.3.2 Blast Effects

In addition to fragment effects, blast is a significant damage mechanism when structure is exposed to high explosive projectiles. Regardless of whether the blast is internal or external, the .structure will initially experience a transient overpressure due to the shock wave. This overpressure can cause extensive structural damage in lightweight aircraft structure. For internal blast only, the interior structure will experience a residual pressure after the shock wave has dissipated, caused by the confinement of explosive gases. This confined gas pressure can also be a significant failure mechanism.

Overpressure Due to Shock Wave

The detonation of an explosive causes a shock wave that travels radially outward from the center of detonation. The shock wave travels at the local speed of sound, characterized by its Mach number. When the shock front arrives at a location, the pressure immediately jumps from ambient to a higher value. The overpressure is called "side-on overpressure", and its magnitude depends on the type and quantity of explosive and the distance from the detonation. Figure 1-35 shows estimated peak overpressure as a function of distance, for a representative HE projectile. However, this is not a stable condition, and the overpressure immediately begins to decay, resulting in the classic pressure-time response at a point shown in Figure 1-36. This "blastwave" response is characterized by a peak positive overpressure, a time duration, a decay shape and a total impulse. All of these parameters change with distance from the detonation.

● EVALUATION FOR TYPICAL HE PROJECTILE
● ASSUMING 50% LOSS FOR FRAGMENTATION
● ASSUMED AMBIENT 14.7 lb/in²
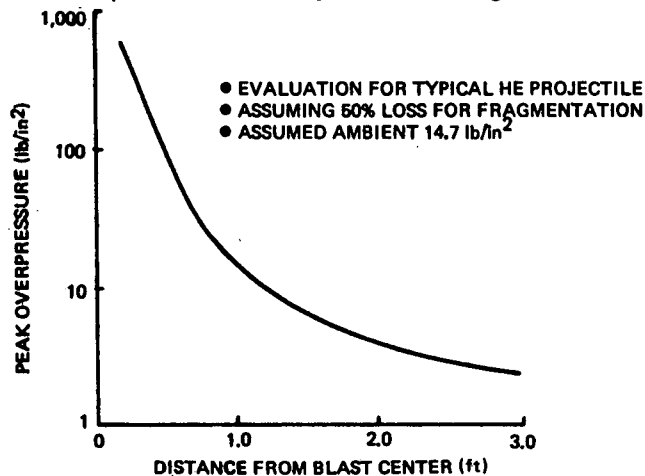
Figure 1-35. Peak Overpressure Resulting From Detonation of Typical HE Projectile

In order to simplify loading analysis, it is common practice to transform the actual pressure pulse, which has an exponential decay, into an equivalent triangular-shaped pulse having the same total impulse as the actual pulse. This can be done in two ways: 1) maintaining the peak overpressure of the actual pulse, or 2) maintaining the same time duration as the actual pulse.
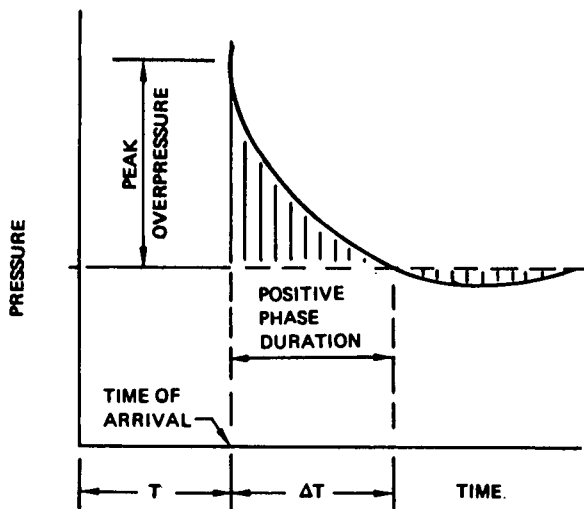
Figure 1-36. Typical Pressure-Time Response at Some Location Away From Detonation
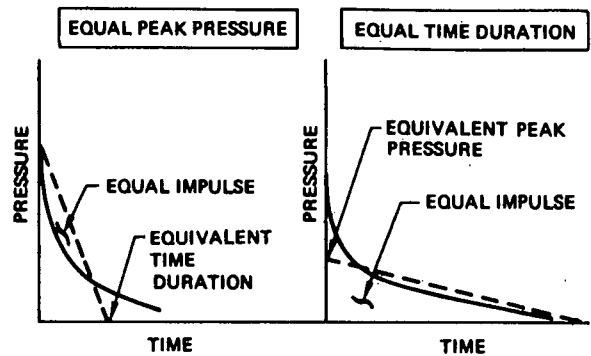
Figure 1-37. Two Methods of Developing Equivalent Triangular Pulse

Figure 1-37 shows these two ways of forming an equivalent triangular pulse. A rule of thumb often used for deciding which form is the best for a specific application is to select the triangular pulse that most nearly approximates the actual pulse pressure at time T/16, where T is the natural period of the structure (Ref. 1-5).

From the standpoint of loading analysis, however, the side-on overpressure characterized above acts only on surfaces parallel to the direction of travel of the shock. In general, the pressure loading felt by structural surfaces will be either the reflected overpressure or the Mach stem overpressure, as determined by the angle of incidence between the shock front and the surface.

Figure 1-38 shows the case of reflected overpressure at an unyielding structural surface. As the incident shock front intersects the surface the air particles stop. As a result, these particles now have a velocity relative to particles further from the surface which are still moving. In other words, particles at point 0 have a velocity relative to particles in region Y, referring to Figure 1-38. This relative velocity is directed toward Region Y, giving the effect of a new shock front moving into Region Y. This is the reflected shock. The initial conditions for the reflected shock wave are those resulting from the passage of the incident shock. Thus, the conditions in Region R, which are those felt by the structural surface, are the result of a double shock.

• REGION X—AMBIENT CONDITIONS
• REGION Y—CONDITIONS CREATED BY INCIDENT SHOCK
• REGION R—CONDITIONS CREATED BY THE REFLECTED SHOCK ENTERING REGION Y
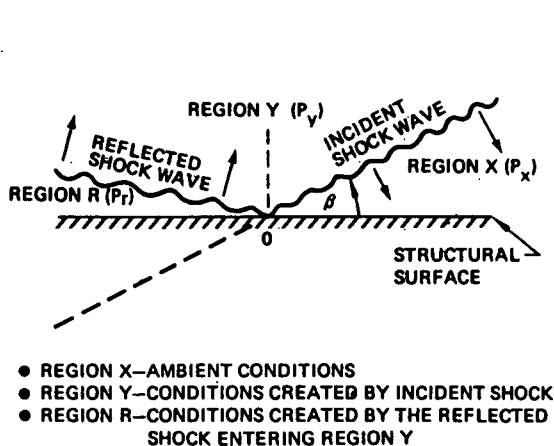
Figure 1-38. Incident and Reflected Shock Fronts at a Surface
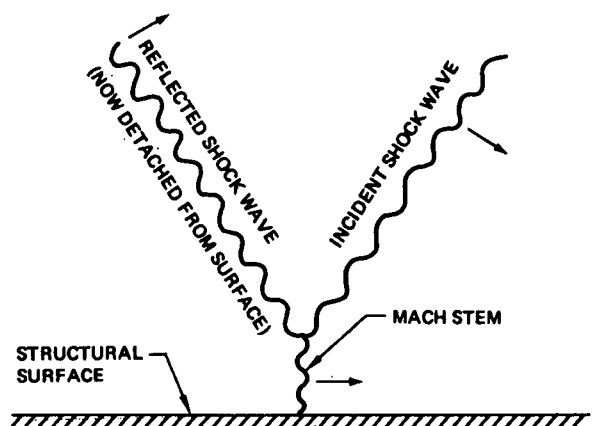
Figure 1-39. Mach Stem Formation Resulting From Oblique Impingement

However, as the angle of incidence, β, of the initial shock front is increased, a value is reached such that the incident wave does not reflect, but instead travels along the surface, forming a "Mach stem". The pressure loading behind the Mach stem is the Mach-stem overpressure, and acts directly on the structure.

Figure 1-39 shows a Mach stem situation. The critical angles of incidence for Mach stem formation depend on the Mach number of the incident shock, and are available in the literature (Reference 1-5, and others). These critical angles range from 90-degrees for acoustic shocks (M=1) to approximately 40-degrees for shocks of Mach number greater than 1.5. When β is greater than the critical value, Mach stem overpressures rather than reflected overpressures should be used in the structural analysis.

Residual Pressure Due to Confined Gas

When internal blast occurs, the expansion of the product gases is resisted by the structure. The gases may be confined within the structure unless released by the venting that results from penetration or structural failure. The result of this confinement is a quasistatic internal pressure acting on the structure. The penetration holes and vents act as orifices, resulting in exponential pressure decay. In addition, rib or bulkhead failure can result in rapid expansion of gas into an adjacent bay. The amplitude of the residual pressure depends on the enclosing volume. Figure 1-40 shows estimated residual pressures resulting from confining the blast of a typical HE round within the volumes indicated, with no venting. The damage potential of the confined gas residual pressures is enhanced by their relatively long duration.
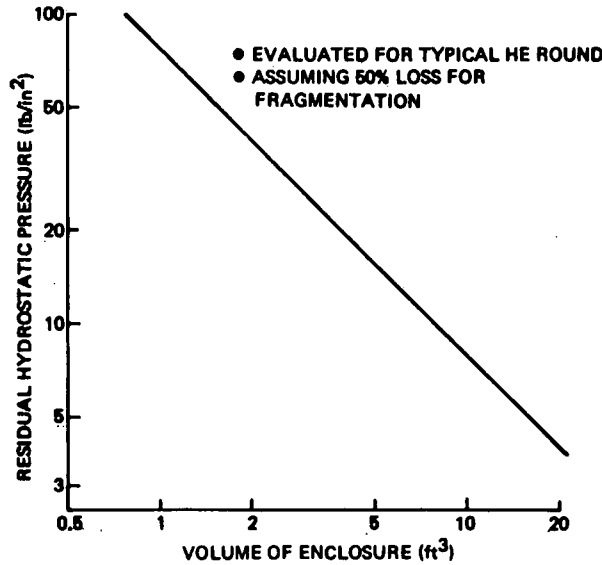
Figure 1-40. Hydrostatic Pressure From Explosions in Closed Cells

1.2 ENGINE DEBRIS PROJECTILES (Following Discussion is From Refs. 1-6 and 1-7)

Non-contained engine failures, resulting in the escape of an engine fragment from the engine case, do not occur very often, the average rate in commercial service has been less than one per million engine hours worldwide in recent years, (Ref. 1-6). Further, the probability of this once-per-million-hour event causing an aircraft accident, defined as a penetration of fuselage or damage to wings or vital components, has proved to be about one chance in 8.5. Figure 1-41 indicates the proportion of aircraft accident sources between 1954 and 1974, indicating that 97.2% of all aircraft accidents have been the result of events other than non-contained engine failures.
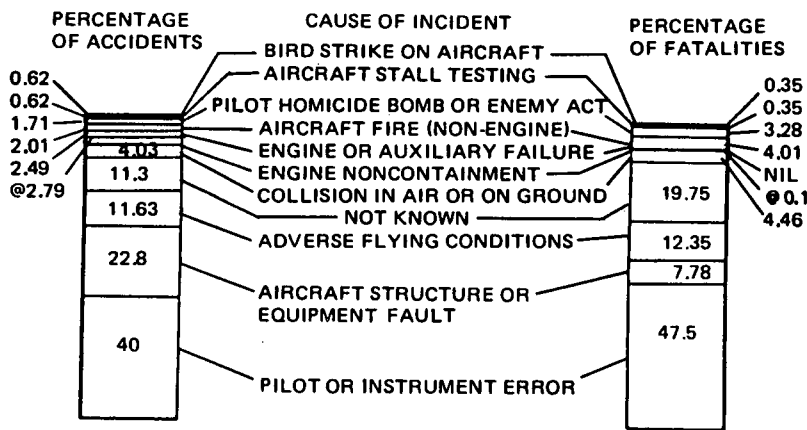
Figure 1-41. Analysis of Aircraft Accident and Fatalities—1954 to 1974

Nevertheless, these incidents do occur and must be addressed. The effects of an uncontained projectile emanating from an engine and subsequently striking an adjacent portion of the airframe, can be assessed in the same manner as for nonexploding military projectiles. There is an important distinction, however, in that the engine debris projectile is typically an irregular fragment (as opposed to a bullet), behaving more like a warhead fragment or the fragments generated from a high-explosive projectile.

1.2.1 Description of Engine Debris Projectiles

Rolls-Royce (Ref. 1-6) has made available the results of a study on non-containment incidents associated with their commercial engines, in which they recorded the weights of fragments, the direction of release, energy and size, wherever such information could be obtained. These results are summarized in the following paragraphs.

Weight of Fragment

Figure 1-42 shows the weight of the largest fragment released in each incident as a percentage of the bladed disc weight. The fragments vary from part of a blade to a complete disc. The incidents categorized as aircraft accidents are indicated, showing that complete discs are less likely to cause a problem than disc fragments, but fragments of any size are capable of causing unacceptable damage if they hit certain parts of the aircraft.
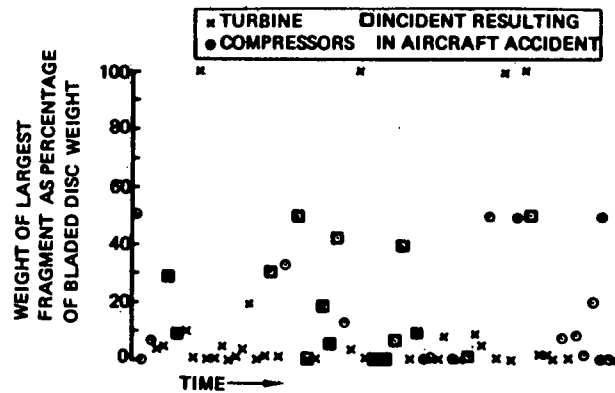
Figure 1-42. Noncontained Failure—1954 to 1974 Inclusive

Compressor and turbine non-containment are indicated on the plot and it shows that only turbine discs have been released complete, probably because a turbine disc has easier access to freedom than a compressor disc.

Figure 1-43 gives the percentage of incidents in which the weight of the largest fragment released was a given percentage of the bladed disc weight or less. It is a way of showing the reduction in the number of non-contained failures that would be achieved by providing an ability to contain an increasing weight of fragment. For example, the ability to contain a fragment weight 5% of the bladed disc weight would have prevented 56% of all non-containments. If the former figure were 10% we would have prevented 72% of the non-containments. Thereafter the gains are less spectacular.
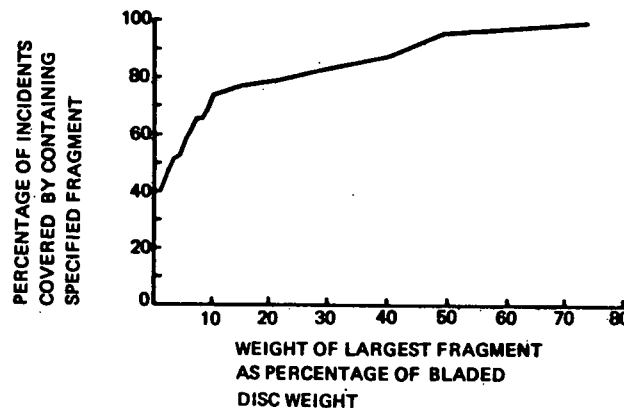
Figure 1-43. Number of Incidents Versus Fragment Weight

When a fragment strikes the inside of an engine casing and it is not contained, it is sometimes deflected on its way through the casing. Figure 1-44 illustrates the effect of such deflection upon the subsequent path of a fragment.

Since the point of penetration of the casing is at a random circumferential position, the probability of an aircraft item in line with a disc being struck by a fragment is unaffected by deflection of the fragment by the casing. But the axial deflection of the fragment is important in that it affects the axial length of the possible impact area on the aircraft.

A study of the axial deflection of debris in actual incidents produced the result shown in Figure 1-45 where axial deflection is plotted against weight of fragment. It shows that only the lighter fragments were appreciably deflected, the maximum deflection being ±33-degrees whereas the heavy fragments were not deflected more than ±5-degrees.

Thus, the situation may be as shown on Figure 1-46 where a pack of discs creates over-lapping fields of possible debris distribution so that any protection or special measures taken by the aircraft designer will require sensibly uniform application over a length slightly greater than the length of the rotor pack, tailing off to zero beyond each end of the rotor.
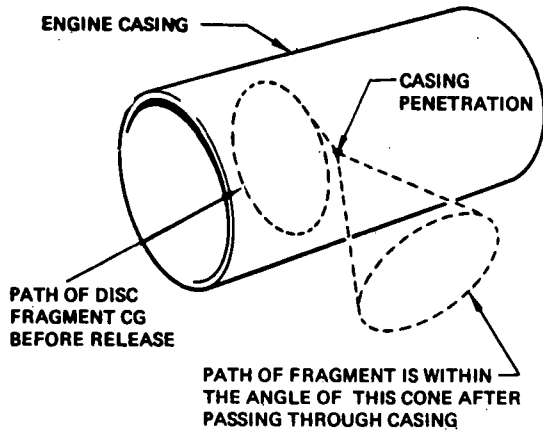
Figure 1-44. Debris Spread
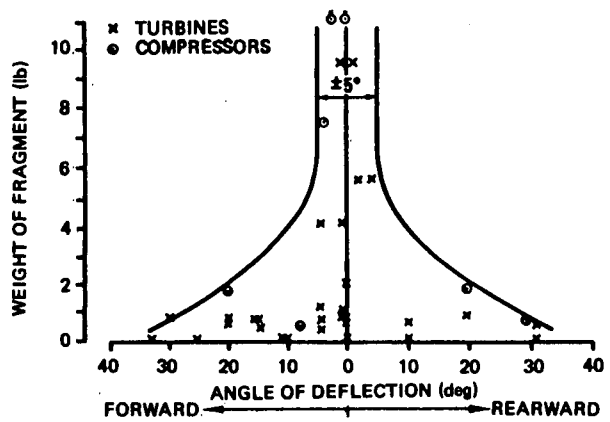
Figure 1-45. Debris Spread Versus Weight of Fragment
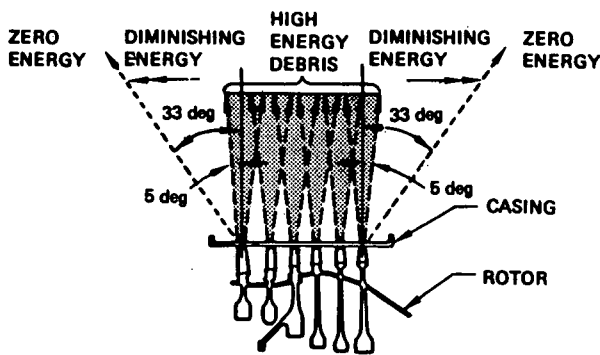
Figure 1-46. Direction and Energy of Emerging Debris
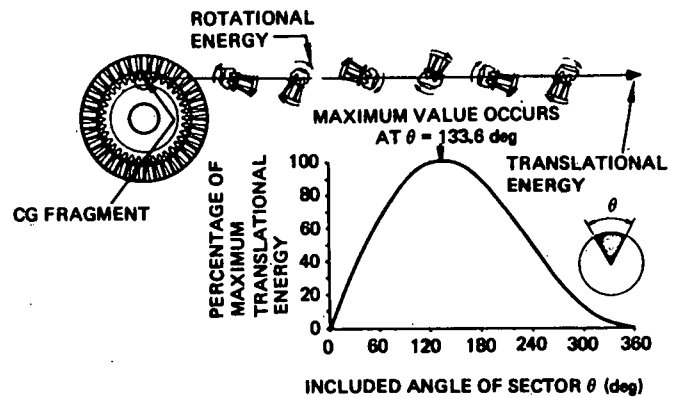
Figure 1-47. Definition of Fragment With Maximum Energy

Energy of Fragment

A fragment has two kinds of energy when it leaves an engine, see Figure 1-47. It has kinetic energy along its flight path which is tangential to the radius described by its center of gravity when it was part of the disc. It also has rotational energy about its own center of gravity. Experience shows that for practical purposes it is the former, i.e., its translational energy, that causes the real damage on impact and this is because the translational energy is in the direction of the impact and, for realistic fragments, it is invariably much greater than the rotational energy.

Figure 1-47 also shows a plot of disc sector size against its translational energy. The fragment with maximum translational energy is a disc segment subtending an angle of 133.6-degrees. An unbroken disc has no translational energy unless it picks some up as a result of friction developed in rubbing against static parts which may throw it sideways out of an engine with a relatively low velocity.

The energy with which a fragment leaves an engine is less than its initial energy because it expends some energy in penetrating the engine casing. In calculating the energy of an emerging fragment a proportion of the amount of energy the engine casing is capable of containing should be subtracted from the initial energy of the fragment.

To determine the blade containment ability of a casing, Rolls-Royce plotted blade energy against a function of blade dimensions and casing properties for all known cases of blade release, including experimental tests and service experience. The result is shown in Figure 1-48 where contained and non-contained failures are identified.
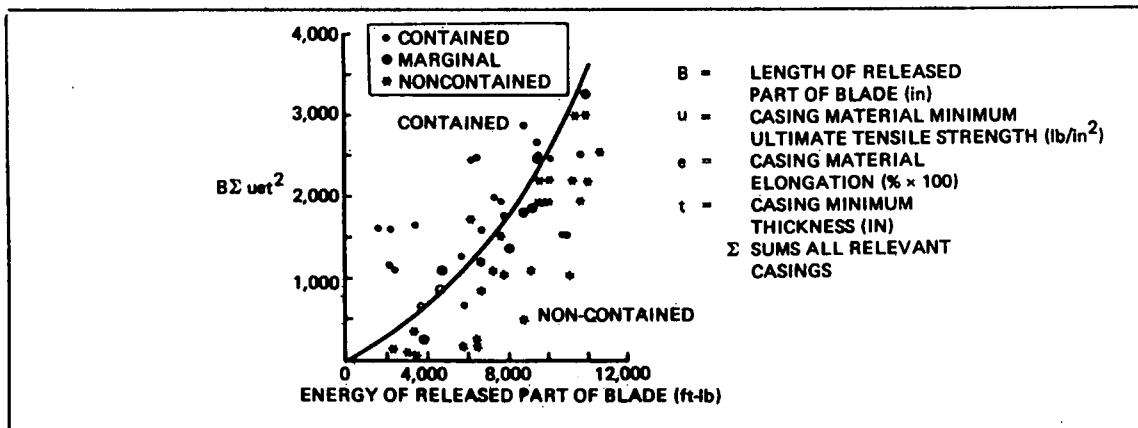
Figure 1-48. Blade Containment Criterion

Unfortunately the behavior of a casing is not quite as straightforward as to absorb an equal amount of energy regardless of the initial energy of the fragment. In containment tests a fragment with an energy level just beyond the containment capabilities of a casing lost 90% of its energy in passing through the casing. But when a portion of a rotor, comprising four blades and a piece of disc, was released from a rotor rotating inside a casing designed to contain a single released blade, the fragment passed through the casing with a near-zero loss of energy.

That some energy was lost was shown by damage and distortion to the casing and to the blades in the fragment but the loss was too small to be measured in terms of fragment velocity before and after penetration. Evidently, the casing did not develop its full containment potential when subjected to loadings far beyond its capabilities.

Further containment tests are in progress to build up more data on this problem and to establish a formula for the amount of energy destroyed in a range of fragments when they pass through a casing of known blade containment ability. Meanwhile, until more data becomes available it seems reasonable to assume that the loss of energy varies from 100% for a single blade, to zero for the 4-blade fragment tested, or any larger fragment. The 4-blade fragment weighed 6.5% of the weight of the bladed disc.

There is an additional loss of energy in fragments that are deflected on passing through the casing. The amount of this loss depends upon the degree of deflection, and from theoretical considerations and practical observations the relationship between deflection and residual energy is as shown in Figure 1-49. This relationship can be used in calculating the possible energy of deflected fragments in the forward and rearward fields covered by the possible axial spread of debris.
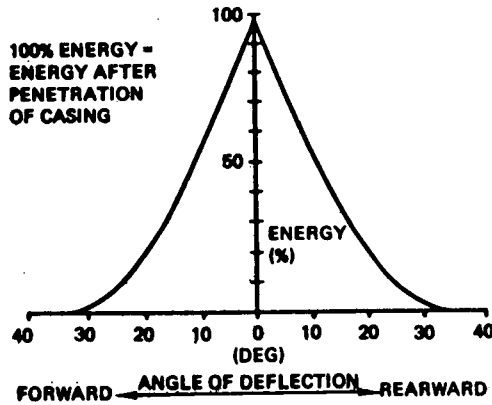
Figure 1-49. Energy After Deflection Versus Angle of Deflection
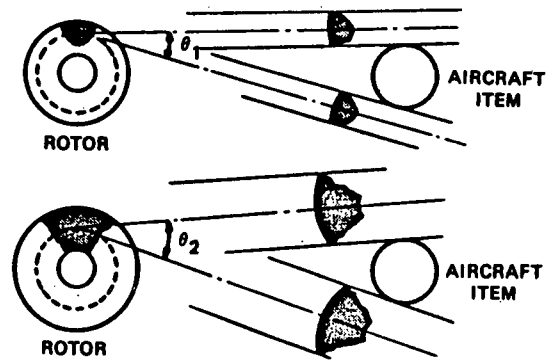
Figure 1-50. Fragment Size Effect on Probability of Strike

Size of Fragment

The maximum dimensions of a fragment thrown by an engine is important in terms of the probability of striking a given vulnerable item of the aircraft. Figure 1-50 shows that for a given aircraft layout the larger the fragment the more likely it is to strike a given object. The chances of the small fragment striking the object are $\emptyset_1$, in 360-degrees, but for the large fragment they are $\emptyset_2$ in 360-degrees and clearly the larger the fragment the greater the probability of a strike.

Figure 1-51 shows actual non-contained failures in terms of the arc of disc released against percentage of incidents. These results can be used for calculating the probability of impact of fragments of various sizes upon aircraft vulnerable items for various aircraft/engine arrangements. The results for turbines and compressors are shown separately to illustrate that compressors have tended to release larger arcs of disc rim than turbines. This is due to factors such as disc proportions.
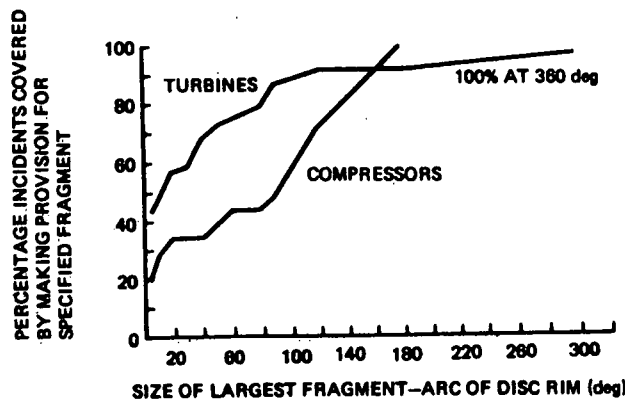
Figure 1-51. Failure Incidence in Terms of Fragment Size

1.2.2 Encounter Parameters

The important encounter parameters that must be defined for penetration and damage assessment are identical to those needed for the projectiles previously discussed: striking velocity, angle of obliquity and attitude. Particular emphasis must be placed upon attitude, however, as this can be a significant factor in the damage potential of fragments having a high ratio of length to diameter, i.e., long, flat fragments such as a portion of a turbine blade. An additional consideration is the rotational energy of the impacting fragment, as this can be a significant factor in penetration and damage potential. Encounter conditions for engine debris analysis can be predicted with greater certainty than for encounter with military projectiles because of the fixed location and known operating characteristics of the engine.

1.2.3 Typical Terminal Effects

As with all fragment impacts, engine debris fragments can penetrate the airframe causing damage to skin and substructure, and may penetrate and degrade system components. The potential exists for ignition of fuel or injury to passengers or crew.

Figure 1-52 from Reference 1-7 gives an indication of the penetrating capability of engine debris fragments, based on calculations using the empirical formula shown on the figure. Fragment energy is plotted against the weight of target material required to contain the fragment.

To emphasize the damage potential of the fragments, typical weights of heavy wing and fuselage surfaces are indicated on the diagram giving some idea of their respective energy absorbing capabilities. The resulting energies are only approximate as both the curves and the test results are only concerned with flat plates. The stiffeners of the wing and fuselage (included in the weight shown) may offer appreciably increased energy absorption due to their depth.

However, this does not alter the general inference of Figure 1-52 which is that even two or three layers of such structure is not capable of stopping the smallest of the three debris forms.
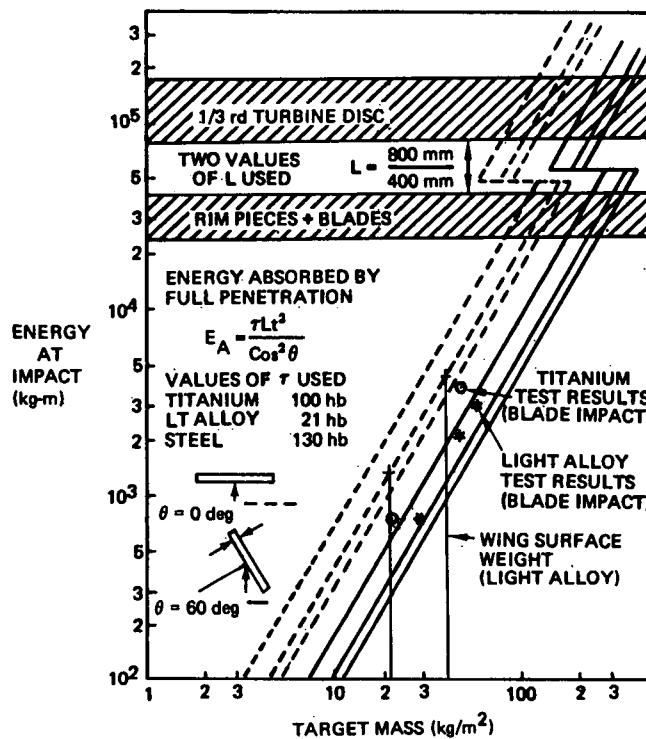
Figure 1-52. Structural Effects of Engine Burst Non-Containment-Fragment Impact Energy vs. Target Weight

1.3 REFERENCES AND BIBLIOGRAPHY

1-1. W. D. Dotseth, "Survivability Design Guide for U.S. Army Aircraft, Vol. I, Small-Arms Ballistic Protection", USAAMRDL Technical Report 71-41A.

1-2. J. G. Avery and T. R. Porter, "Survivable Combat Aircraft Structures Design Guidelines and Criteria", AFFDL-TR-74-49 and -50, April 1974.

1-3. J. G. Avery, S. J. Bradley and K. M. King, "Battle Damage Tolerant Wing Structural Development Program", Final Report, NASC Contract N00019-75-C-0178, Boeing Document D180-26069-1, 1979.

1-4. P. R. Fitzpatrick, "Model for the Prediction of Explosive Projectile Damage to Aircraft Structures", Proceedings of the JTCG/AS Aircraft Survivability Symposium, Naval Post Graduate School, Monterey, California 13-15 July 1976.

1-5. G. F. Kinney, "Explosive Shocks in Air", Macmillan Company, New York, 1962.

1-6. D. McCarthy, "Definition of Engine Debris and Some Proposals for Reducing Potential Damage to Aircraft Structure", AGARD Conference Proceedings No. 186, Jan. 1976.

1-7. T. W. Coombe, D. F. Vowles, "Structural Effects of Engine Burst Non-Containment", AGARD Conference Proceedings No. 186, Jan. 1976.

SECTION II

ANALYSIS METHODS FOR PREDICTING STRUCTURAL RESPONSE
TO PROJECTILE IMPACTS

2.0 ANALYSIS METHODS FOR PREDICTING STRUCTURAL RESPONSE TO PROJECTILE IMPACT

The purpose of this section of the Design Manual is to inform aircraft designers of the analysis methods and data available for predicting the response of metal and fiber composite structure to projectile impact. The analysis methods discussed are applicable to impacts from small arms projectiles, missile warhead fragments, and the fragmentation and blast effects of high-explosive projectiles, as described in Section I. The responses addressed include penetration capability, damage size and type, strength and stiffness degradation of damaged structure, and internal load redistribution. This section provides the tools needed to implement the impact damage tolerance design guidelines presented in Section III.

2.0.1 General Approach to Impact Damage Tolerance Analysis

Figure 2-1 is the impact damage tolerance analysis methodology which is described in detail in Section III of this Manual. The objectives of the analysis are to evaluate the structural capability of the damaged airframe and to compare this with the structural performance requirements dictated by the mission. Both the requirements and the capabilities can be expressed as load factors.
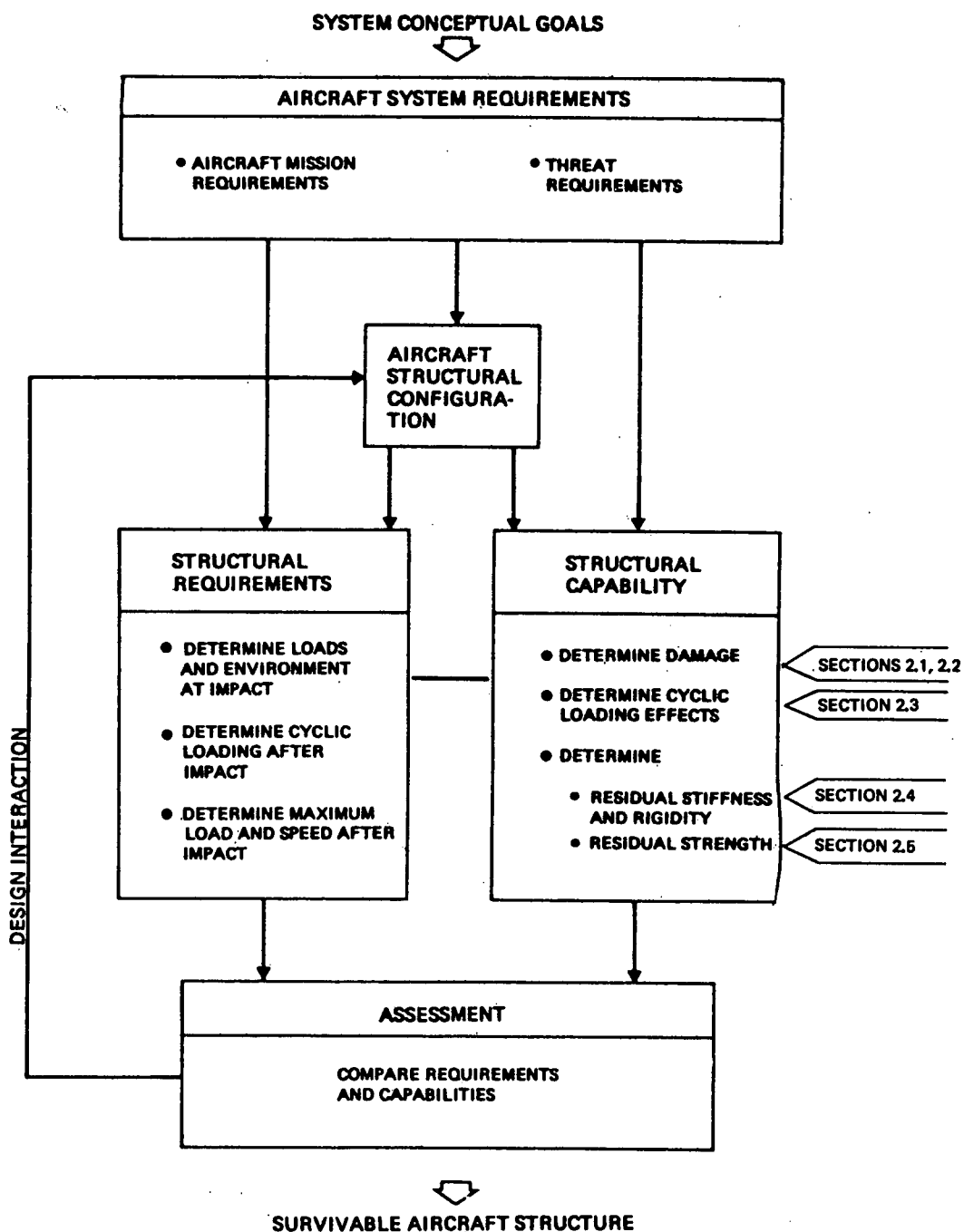
Figure 2-1. Design Methodology for Achieving Impact Damage Tolerant Structure

Structural requirements are determined from analysis of the operational flight loads and the physical environment associated with primary missions. Next the operating stress levels for critical structural elements are determined, including levels corresponding to:

o   Operating loads at the time of projectile encounter;

o   Cyclic loads after projectile impact;

o   Maximum loads after projectile impact.

These loads and the physical environment (temperature, for example) are used to establish strength requirements at impact, and the cyclic loading and residual static strength requirements of the damaged structure following impact.

Determining structural capability, however, requires predicting the size and severity of the induced damage and the resulting structural degradation. The analysis methods subsequently described in this Section are used primarily to establish the structural capability following damage, i.e., to quantify the right-hand portion of Figure 2-1, by assessing the factors discussed below.

2.0.1.1 Factors Determining the Structural Capability of Projectile Damaged Structure

The first step in projectile damage tolerance analysis is to determine the type and size of the inflicted damage. Analysis methods for predicting damage from projectiles are presented in Section 2.1 (Penetration Effects) and 2.2 (Damage Size and Type). Structural damage from projectile impact is a function of the type of projectile and engagement conditions, as well as geometry and material of the structural configuration. The damage imposed can also be influenced by the physical environment, applied loads, and compounding effects such as hydrodynamic ram pressures generated by passage of the projectile through the liquid portions of a fuel cell.

Damaged structure that does not fail at the time of impact will be subjected to cyclic loading from gust and maneuvers during continued flight. These cyclic loadings may induce fatigue that can alter the size and character of the imposed damage, thereby changing the residual strength of the structure. Methods for analyzing the effect of cyclic loads on projectile damaged airframes are presented in Section 2.3.

The stiffness of damaged structure is also altered due to reduction of net section. This stiffness degradation can cause aerodynamic instabilities and extensive load redistribution within the structure. Section 2.4 discusses analysis methods and considerations associated with the stiffness degradation of ballistic damaged structure.

The damaged airframe must have sufficient residual strength to sustain the flight loads subsequently encountered. Section 2.5 presents analysis approaches for predicting the residual strength of projectile damaged structure, including: fracture analysis methods and data for monolithic structure and stiffened (crack-arresting) structure; and a review of recommended analysis methods for multiple-load-path structure including finite element techniques applied to damaged configurations.

The final results of the structural capability assessment can be presented as a "strength- time history" (an example is shown in Figure 2-2). The initial structural capability is the design ultimate strength. When the projectile penetrates the structure, however, there is an instantaneous loss of strength which is initially influenced by dynamic effects, including dynamic load redistribution and forces associated with the contact between the projectile and the structure. The dynamic effects are soon dissipated, and if failure has not occured at impact the resulting strength capability is the static residual strength of the damaged structure. As flight continues, this strength may be altered by the effects of cyclic loading and environmental factors as described above.

Once the structural capability assessment has been completed, the final task of the design analysis is to compare capabilities with requirements. For example, Figure 2-3 shows, schematically, a comparison of stress-time (requirements) and strength-time (capability) histories for a wing lower surface. The strength capability is reduced by the impact, but does not fall below the strength requirement at the time of encounter. In this example, the strength requirements exceed the strength capabilities in the landing-approach segment of flight and structural failure occurs.

2.0.1.2 Incorporation of Probabilistic Events

Both the structural requirements and the capabilities depend on probabilistic events, as illustrated in Figure 2-4. For example, variability in damage size and severity arises from the potential range of projectile striking velocities, obliquities, and hit locations, as well as the considerable scatter noted in the measured effects of projectile impacts. The residual strength of damaged structure is subject to uncertainties in material composition, failure modes, notch-sensitivity, and constraint. The probabilistic aspects of flight loadings are well known.

Figure 2-5 repeats the survivable structures analysis methodology shown earlier as Figure 2-1, with the addition of the probabilistic parameters involved in establishing the structural requirements and the structural capabilities. Flight loadings, for example can be conveniently expressed as probability of exceedance, as shown in Figure 2-6, and this is routinely done in fatigue and fail-safe design analyses. However, loading requirements for impact damage tolerance analysis differ from fatigue and fail-safe requirements in two ways:

o   Loading requirements for impact damage tolerance can be based on probable exceedances per mission or sortie, rather than lifetimes or inspection intervals.

o   The segment of the sortie during which impact occurs must be identified, so that loading requirements at impact and subsequent to impact can be established.

As discussed earlier, structural capability is influenced by the location, size, and character of the damage. Assuming that all regions of the airframe have equal probability of being hit by the projectile, the probability of hitting a critical structural element can be established from element projected area and projectile trajectory considerations. This is a method commonly used in vulnerability assessment. However, if the projectile threat scenario and mission
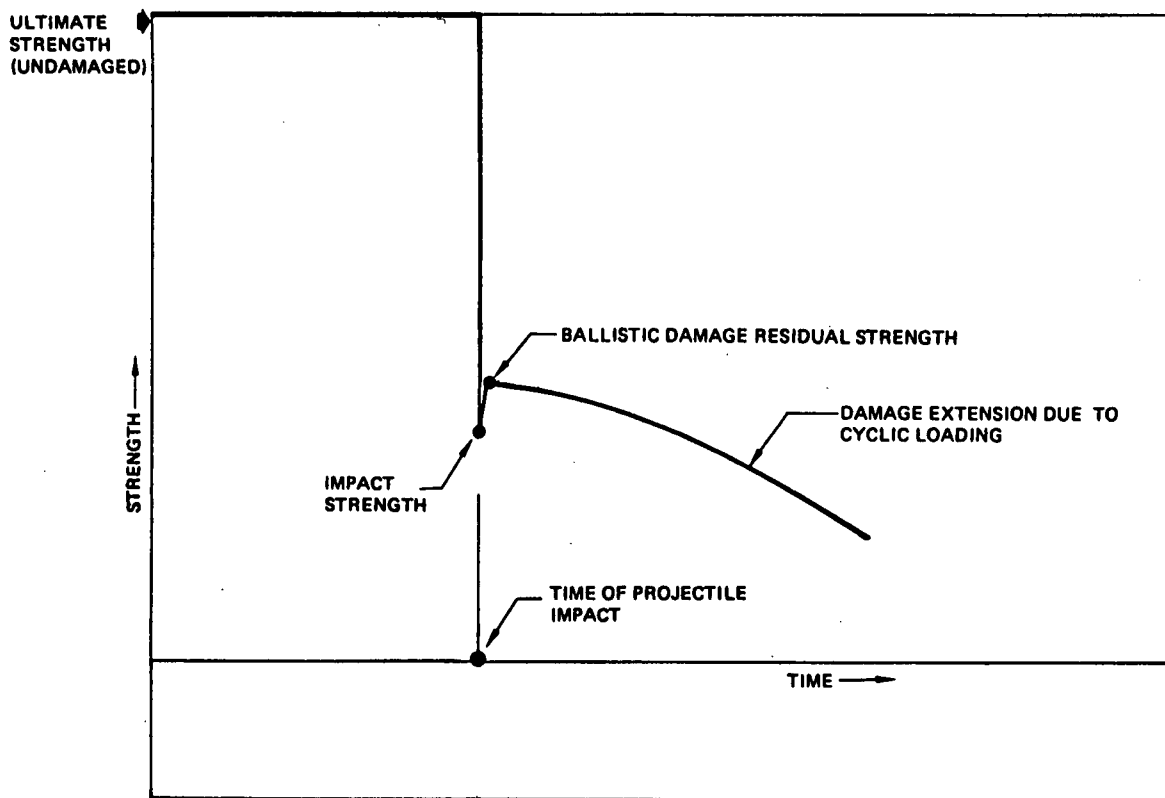
Figure 2-2. Strength-Time History for a Structural Element, Indicating Structural Capability
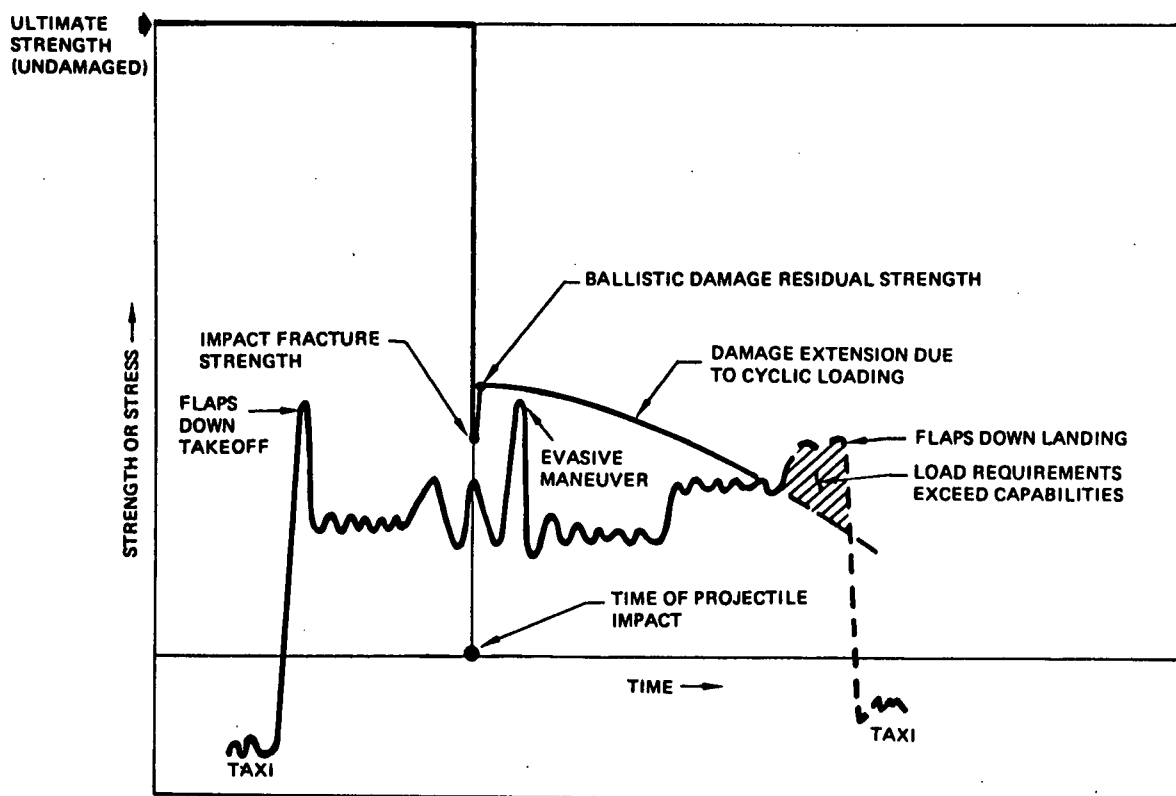
Figure 2-3. Comparison of Stress-Time and Strength-Time Histories To Assess Requirements-vs-Capabilities
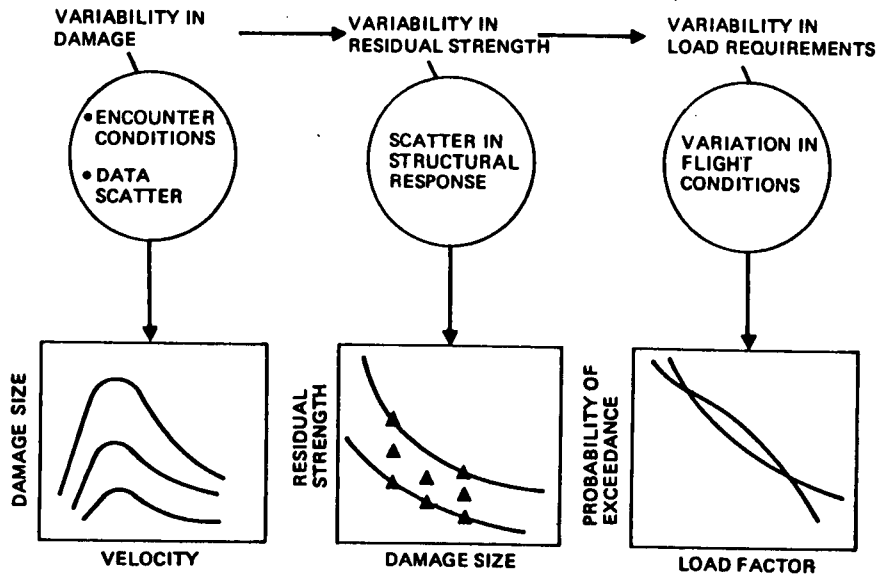
Figure 2-4 Structural Survivability Analysis Must Address Probabilistic Events
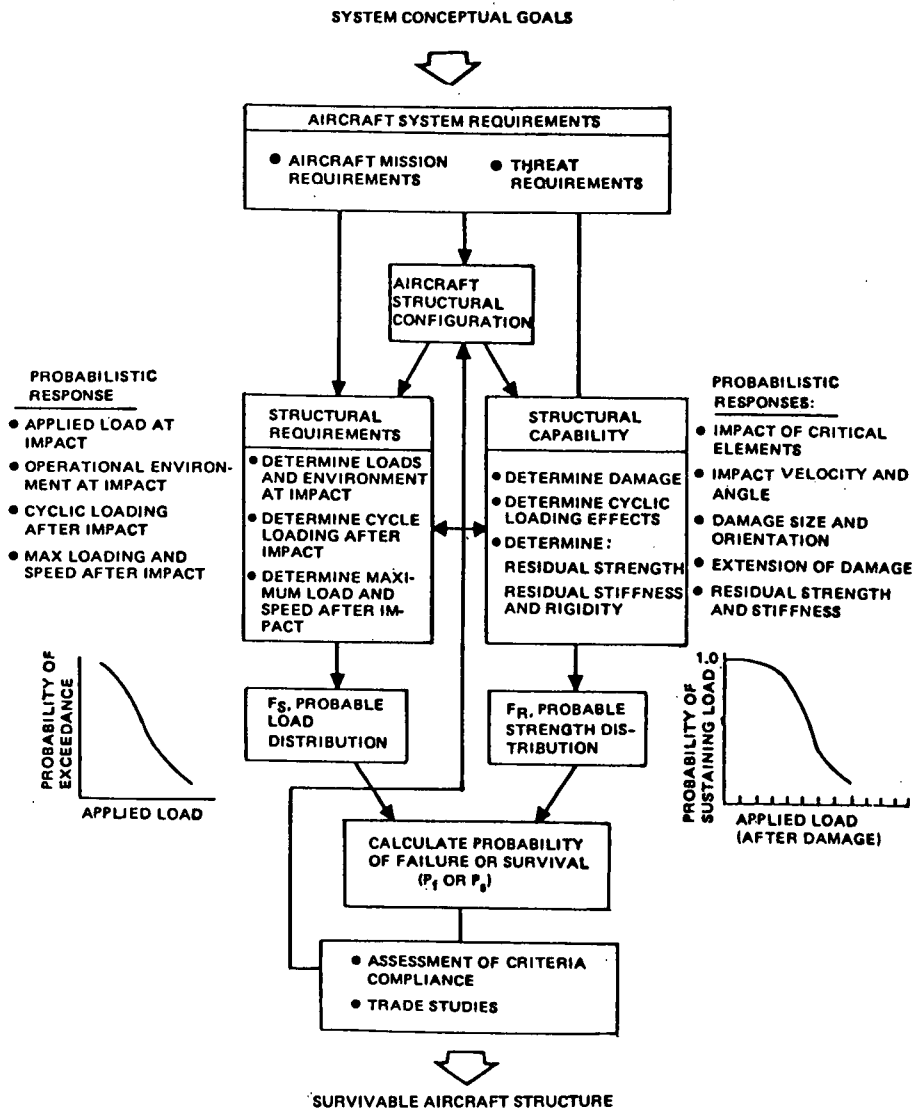
Figure 2-5. Survivable Structures Analysis Methodology in Probabilistic Format
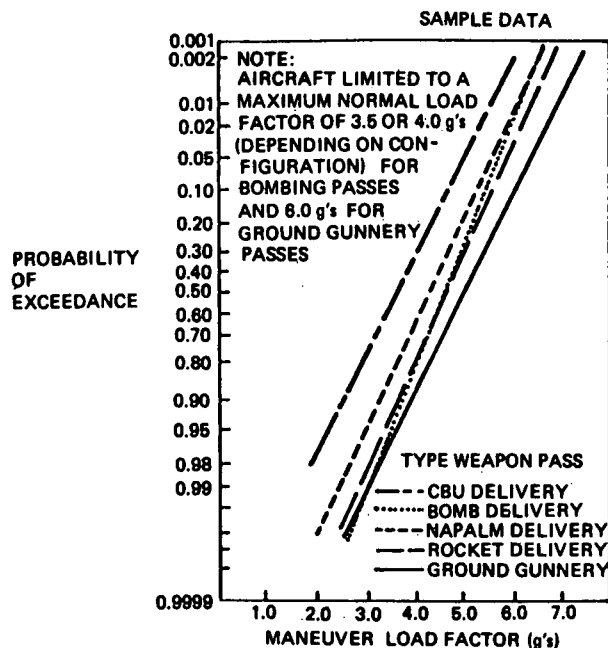
Figure 2-6 Load Factors Experienced During
Various Weapon Deliveries
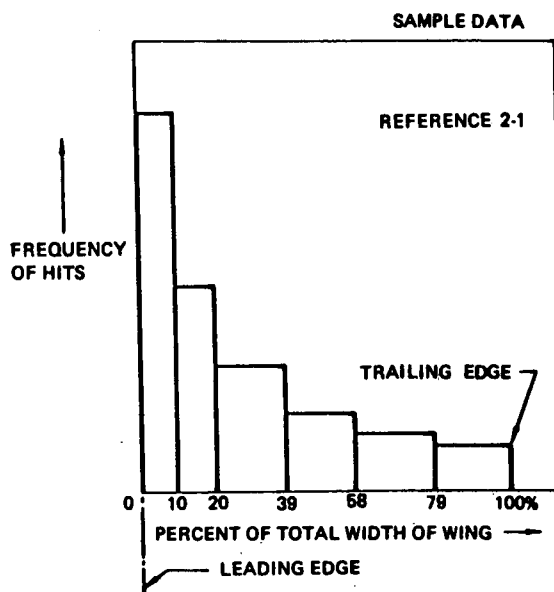
Figure 2-7 Frequency of Wing Hits as a Function
of the Chordwise Location

profile are defined, more sophisticated methods such as threat encounter models can be used to determine the most probable spatial distribution of hits on the aircraft, and the most probable engagement conditions. Figure 2-7 and 2-8 are typical results of this type of assessment for a tactical fighter performing an air-to-ground attack mission.

Damage size predictions can be made for the probable encounter conditions. Statistical distributions for ballistic damage response have not yet been adequately defined, but damage data obtained from ballistic testing is definitely amenable to statistical analysis. Figure 2-9 shows typical small arms projectile damage measurements in a notch-sensitive high-strength aluminum alloy. The systematic variation of damage size with projectile velocity is evident as indicated by the mean. The probabilistic representation shown in Figure 2-10 was developed assuming that the variations in damage size at a given velocity were random and could be represented by a normal distribution. Other distributions could be applied, of course.
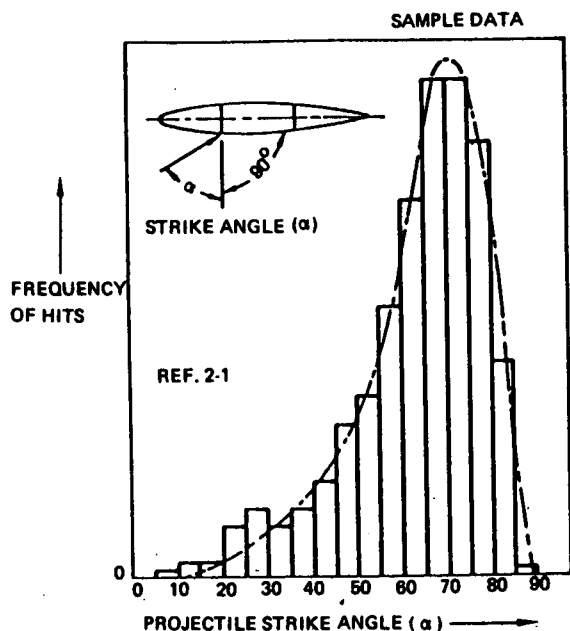
Figure 2-8. Frequency of Hits as a Function of Strike Angle
(Sample Result from Encounter Analysis)
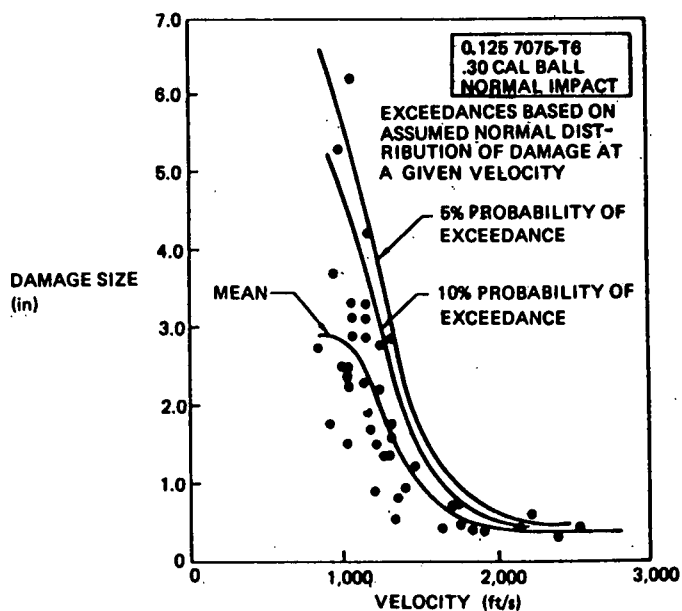
Figure 2-9 Typical Small Arms Projectile Damage Test Data
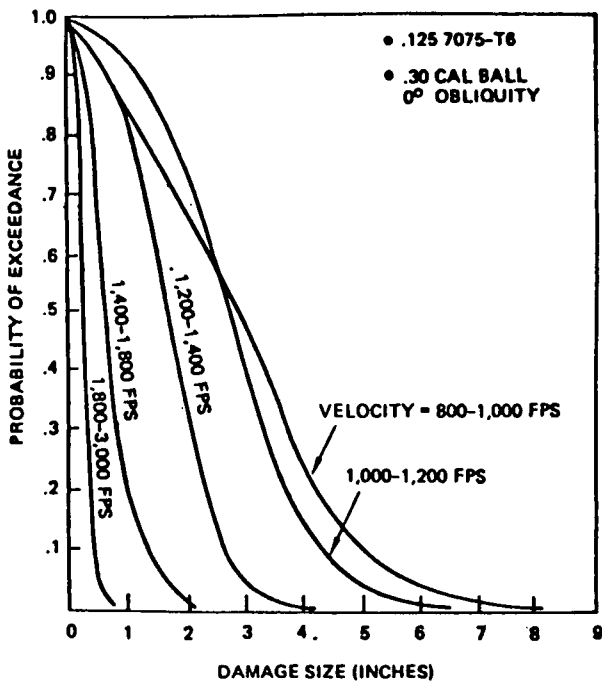
Figure 2-10 Probable Extent of Damage Resulting From Impact
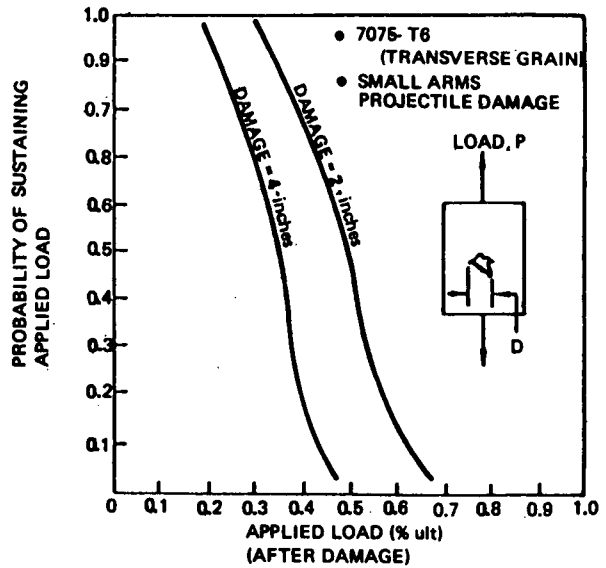
Figure 2-11 Probable Residual Strength of Projectile Damaged Tension Panel

A similar probability approach can be taken in predicting the residual strength of projectile damaged structure. For 7075-T6 tension elements containing small arms projectile damage, Figure 2-11 shows a probabilistic representation for the residual tensile strength using data from Ref. 2-2.

The final calculation of the structural capability of an element must include the combined effect of variability in both damage size and residual strength. Figure 2-12 shows the completed residual strength prediction for 7075-T6 tension elements damaged by .30 caliber bullets in the 800-1,000 feet per second velocity range.

When the approach described above is applied to the entire airframe, strength capability can be expressed, probabilistically, in terms of operational load factor as shown in Figure 2-13. A parallel assessment can be done for residual stiffness capability in terms of operational speed. Once a capability has been developed in the form shown in Figure 2-13, it can be combined with requirements which are also expressed statistically, such as the operational loading requirements shown before in Figure 2-6. The result of this final combination is the overall probability of survival for the structure operating in a specified loading environment, accounting for variability in operating loads, damage size, residual strength, and the probability of hitting critical structural elements.
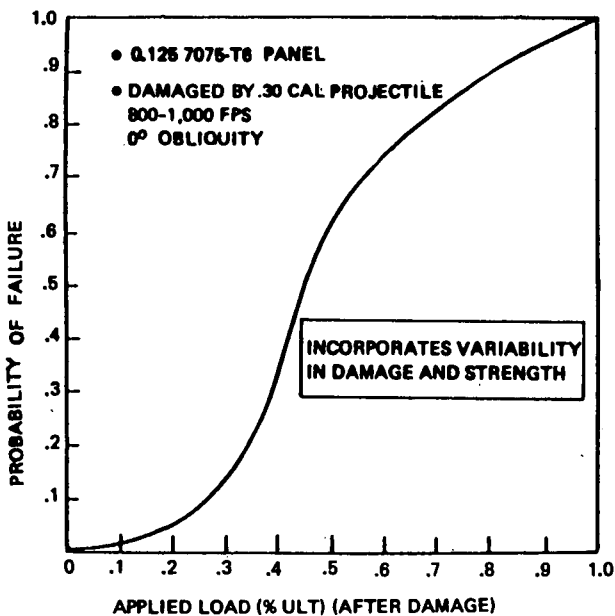
Figure 2-12 Probable Residual Strength Capability of Damaged Tensile Element
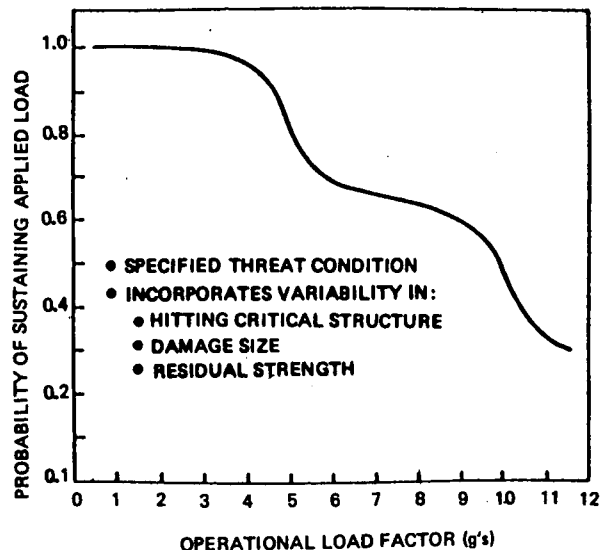
Figure 2-13 Degraded Performance Capability of Damaged Airframe

2.0.2 Overview of the State-of-the-Art in Impact Damage Tolerance Analysis Methods

A survey of the data and analysis methods available for implementing the impact damage tolerance methodology described above was conducted during the initial stages of the Design Manual preparation. All the NATO member nations were afforded the opportunity to contribute relevent work, and an AGARD Specialists Meeting on Impact Damage Tolerance was held in 1976. The proceedings from this meeting are available.*

IABG of Germany has done significant work in developing damage and residual strength prediction methods for non-exploding and exploding projectiles impacting aircraft structure. This work includes applications of finite element analysis techniques in establishing stress intensity factors for projectile impact damage, and full-scale ballistic and structural tests for verification. Much of the IABG work is summarized in References 2-1, 2-4, 2-5, and 2-6.

The RAE of Great Britain has done ballistic testing to provide data defining the effects of applied loading on the residual tensile strength of aluminum and fiber composite skin panels. This work has involved primarily high-explosive projectiles. Results of these studies were not available for inclusion in the Manual.

In the U.S., each of the military services has sponsored research programs developing design and assessment methods for structural survivability to projectile weapon threats. This research includes ballistic testing for developing and verifying damage models as well as constructing sophisticated analysis methods such as the BR-1 code for predicting the response of aircraft structure to high-explosive anti-aircraft artillery projectiles.

The Air Force Flight Dynamics Laboratory reviewed and documented the state-of-the-art of analysis methods and data as of 1974 in AFFDL-TR-74-49 and -50 (Ref. 2-7). There were many gaps in the available data and analysis methods, resulting in difficulties in integrating impact damage tolerance into the structural design process. Some of these gaps are being addressed in current programs, including damage models for composites, and analysis and simulation of the ballistic impact response of full-scale structure. Figure 2-14 is a partial roadmap of U.S. Air Force and Navy structural survivability design research conducted over the past 10-years. This AGARD Design Manual contains the significant results of this research. Key developments associated with the programs are described below.

As indicated in Figure 2-15, Air Force contract F33615-67-C-1660, performed by the Martin-Marietta Corporation, established a methodology for quantitative assessment of structural vulnerability with respect to projectile impacts. Residual strength results were obtained from finite element analysis of damaged structure and presented in probabilistic form similar to the presentation in Figure 2-13. Testing was done to define damage from high-explosive projectiles impacting stiffened panels under tension and compression loading.

* See AGARD Conference Proceedings No. 186, "Specialists Meeting on Impact Damage Tolerance of Structures," AGARD-CP-186, Jan. 1976.
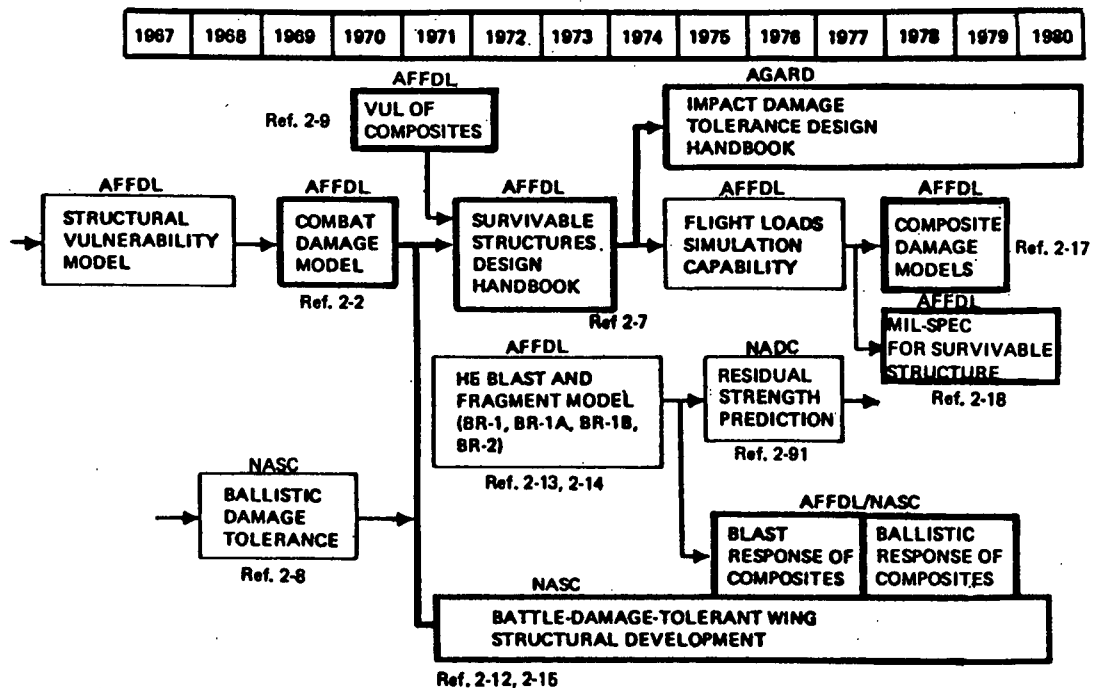
Figure 2-14: Impact Damage Tolerance Design Technology Research

- Developed methodology for quantitative vulnerability assessment of design

- Applied finite element analysis to battle damaged structure

- Developed residual strength data for HE damage

- Damage size model for nonexploding projectiles

- Fracture model for residual strength
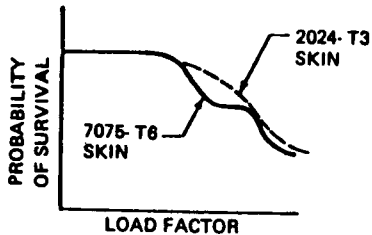
Reports: AFFDL-TR-70-115
AFFDL-TR-70-116
(Ref. 2-2)
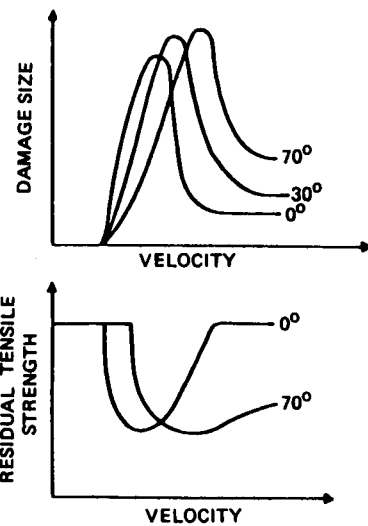
Figure 2-15. Aircraft Structural Vulnerability to Conventional Weapons (F33615-67-C 1660)

Figure 2-16 Aircraft Structural Combat Damage Model (F33615-69-C-1581)

Air Force contract F33615-69-C-1581 "Aircraft Structural Combat Damage Model" (Ref. 2-2), developed the ballistic damage and residual strength prediction models needed for implementing the methodology developed under F33615-67-C-1660. This work, performed by Boeing, included substantial ballistic impact testing of aircraft structural materials against small arms projectiles and provided computerized prediction models of damage size and residual strength as indicated in Figure 2-16.

Substantial ballistic damage and residual strength test data for metals was developed under the Navy contract "Aircraft Wing Structural Concepts with Improved Ballistic Damage Tolerance" (Ref. 2-8), performed by General Dynamics/Convair Division. The data is for small arms projectiles impacting several types of structural configurations.

Data on the ballistic damage response of advanced fiber composites began appearing in the early 1970's. Air Force contract F33615-71-C-1111 (Ref. 2-9), performed by Grumman, provided residual strength data for boron and graphite/epoxy impacted by small arms projectiles. Other composite programs sponsored by the Air Force included F33615-71-C-1414 "Advanced Development on Vulnerability/Survivability of Advanced Composite Structures" (Ref. 2-10), and F33615-70-C-1570 "Evaluation of Ballistic Damage Resistance and Failure Mechanisms of Composite Structures" (Ref. 2-11).

In 1974, Boeing incorporated the available analysis methods and data into a design handbook, AFFDL-TR-74-50, "Survivable Combat Aircraft Structures Design Guidelines and Criteria" (Ref. 2-7). This work was done under contract F33615-73-Q-3032 (see Figure 2-17). A design methodology was developed that incorporates structural survivability into the aircraft design process, and this methodology provided the basic approach applied to this Manual.

- Defined structural S/V design approach within structural integrity discipline

- Summarized data and models

Reports: AFFDL-TR-74-49
AFFDL-TR-74-50
(Ref. 2-7)

STRUCTURAL
REQUIREMENTS

MISSION | THREAT

CONFIGURATION

STRUCTURAL
REQUIREMENTS

STRUCTURAL
CAPABILITY

STRUCTURAL
ASSESSMENT
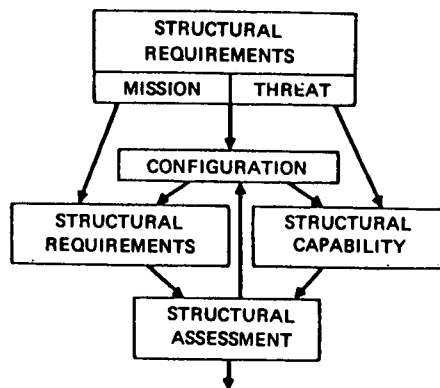
STRUCTURAL S/V DESIGN APPROACH

Figure 2-17 Survivable Combat Aircraft Structures Design Handbook (F33615-73-Q-3032)

One of the most comprehensive aircraft structural survivability programs was Navy contract N00019-75-C-0178 "Battle Damage Tolerant Wing Structure Development Program" (Ref. 2-12), sponsored by Naval Air Systems Command (NASC). This program, performed by Boeing, developed a graphite/epoxy wing-box structural design meeting stringent battle damage and weight reduction criteria. Considerable test data was generated defining the damage and residual strength response of graphite/epoxy impacted by high-explosive projectiles. Damage tolerant designs were developed using hybrid laminates combining graphite with fiberglass. A full-scale wing box was fabricated and tested under load against a high-explosive projectile impact.

A major advance in impact damage analytical capability was made under Air Force contract F33615-72-C-1045, and -3060 "Effects of Internal Blast on Combat Aircraft Structure" (Refs 2-13, 2-14), done by Northrop for AFFDL. This work, as shown in Figure 2-18, developed the BR-1 computer codes for predicting structural response to high-explosive projectiles. The BR-1 codes use advanced finite element techniques, and represent a state-of-the-art analysis method readily accepted by the structural design community. The capability of the codes was extended to fiber composite materials by Boeing, under a modification to Navy contract N00019-75-C-0178, in 1977 (Ref. 2-15).

Air Force contract F33615-76-R-3135, "Structural Flight Loads Simulation Capability" (Figure 2-19), currently being worked by the University of Dayton, will provide the Air Force Flight Dynamics Laboratory with the capability of loading full-scale structural components during ballistic testing.

An analysis method for residual strength prediction of metal skin panels impacted by high-explosive projectiles was developed by Northrop for the Naval Air Development Center (NADC), under contract N62269-76-R-0272, using the material crack growth resistance curve in terms of the J-integral and the elastic-plastic analysis of the damaged structure (Ref. 2-91). The analysis method was verified by ballistic test.

Under Air Force contract F33615-78-C-3403, "Survivable Composite Structure for Combat Aircraft" (Ref. 2-17), available test data on the ballistic response of advanced fiber composite materials was evaluated and used to construct damage and residual strength analysis models incorporating structural design and threat parameters. Deficiencies in the available data were identified.

As an additional step toward achieving survivable structure, a draft military specification for survivable combat aircraft structure is being prepared under Air Force contract AFFDL F33615-78-C-3423 "Proposed Military Specification for Survivable Aircraft Structures (Nonnuclear)," (Ref. 2-18).

Reports: AFFDL-TR-73-136
AFFDL-TR-76-73
(Ref. 2-13)

STRESS

TIME

FRAGMENT MODULE

BLAST PRESSURE PREDICTION MODULE

FINITE ELEMENT STRUCTURAL RESPONSE MODULE

● Projectile characterized by:

● Discrete base and fuse fragments

● Distributed side spray fragments

● Penetration model

● Hole size model

● Momentum transfer model

● "BLAST" code developed by NOL

● Spherical explosion source

● Normally reflected overpressure

● Residual gas pressure in confined volume

● Plate and beam elements

● Elastic/plastic dynamic response

● Large deflection capability

● Stiffness alteration due to fragment penetrations

Figure 2-18. BR-1 Computer Code for Predicting Response to Internal Blast and Fragments

● Will provide load capability for full-scale components during ballistic test (At AFFDL)

● Will provide verified analysis models

AIR FLOW NOZZLE
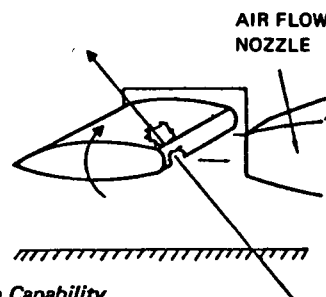
Figure 2-19. Structural Flight Loads Simulation Capability
(F33615-76-R-3135)

2.1 ANALYSIS METHODS FOR BALLISTIC PENETRATION

The need to determine whether the projectile can penetrate a structural member arises in damage analysis whenever the structural element being analyzed is shielded by adjacent structure. For example, in assessing damage done to a spar web, it is important to recognize that the attacking projectile must first penetrate the skin and that its velocity and configuration will be altered by the penetration. This alteration can influence the extent of damage inflicted to the spar web. Thus, the penetration-related questions that arise in impact damage assessment are:

1. Did the projectile penetrate the shielding element?

2. What is the post-impact condition of the projectile after penetrating the shielding element?

If the projectile does not penetrate the shielding member, then its subsequent damage capability is zero. If penetration does occur, the damage capability of the emergent projectile depends on its physical condition, residual velocity, and attitude. Ballistic penetration criteria and post-impact projectile conditions are discussed in the following subsection.

2.1.1 Ballistic Limit Assessment

There are several methods of defining projectile penetration and the corresponding threshold velocity at which penetration occurs, usually called the ballistic limit velocity. Projectile velocities greater than the ballistic limit velocity result in penetration. Some of these definitions are shown in Figure 2-20. The various definitions are not of great concern in structural assessment. Whatever the definition selected, the projectile velocity resulting in penetration 50-percent of the time, designated V_{50}, is the estimate of ballistic limit velocity most frequently used.

For a given projectile, the ballistic limit velocity depends on the material and thickness of the impacted structure, and the angle of obliquity between the structure and the projectile flight path. The probability is very high that armor-piercing projectiles and warhead fragments will penetrate typical aircraft structure under most encounter conditions.
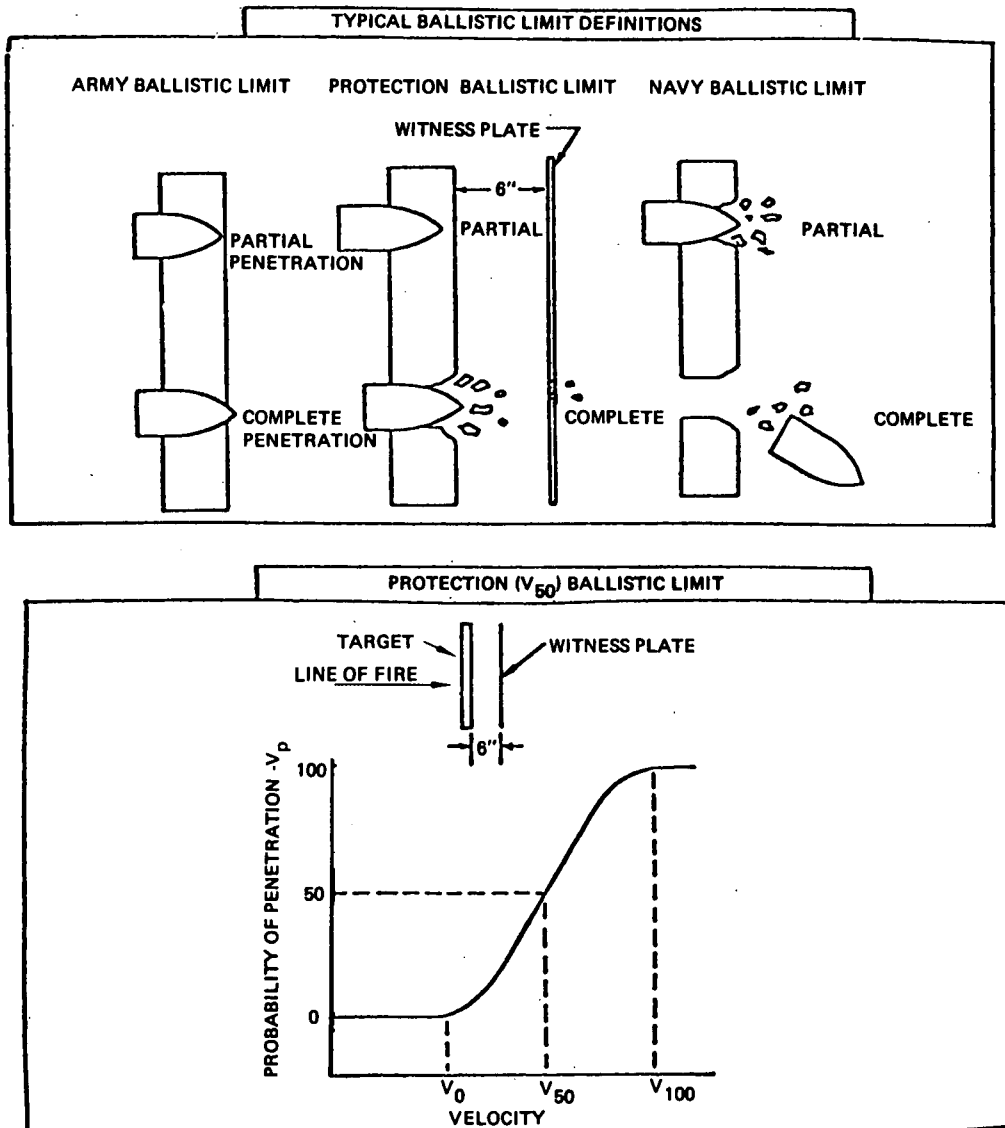
Figure 2-20 Ballistic Limit Definitions Commonly Used

2.1.1.1 Ballistic Limit Assessment for Metallic Structure

Ballistic limit prediction models are given in Reference 2-2 for several aluminum alloys, titanium, and steels impacted by small-arms projectiles, and in many other available references. Reference 2-19, for example, has penetration equations for armor-piercing projectiles impacting aircraft structural materials and Reference 2-20 gives prediction techniques for fragment projectiles which are widely used in the aircraft vulnerability community.

Because of the considerable technical literature and analysis models available for predicting ballistic limits, only an overview will be presented here. The reader should consult with vulnerability specialists for specific ballistic limit data. Figure 2-21 from Reference 2-21, shows the penetration capability of untumbled small-arms projectiles and steel fragments as a function of target sheet thickness and projectile angle of obliquity for several aircraft materials. The angle of obliquity is the angle between the projectile flight path and a normal to the impacted surface. These penetration curves, plotted on log-log coordinate scales, may be used for approximating purposes.

Figure 2-22 shows the penetration capability of certain missile warhead fragments impacting sheets of aluminum, steel, and titanium. These curves were calculated using the Joint Technical Coordinating Group - Munitions Effectiveness (JTCG/ME) penetration equations from Reference 2-22, with a fragment shape factor of 0.5687. Because of the importance of the JTCG/ME penetration equations, a brief summary of the approach is given below.

The JTCG/ME penetration equations predict ballistic limit, projectile failure, projectile residual velocity and change in obliquity following penetration. Projectile impact conditions are characterized by the three basic parameters V, θ, and ∅, representing velocity, obliquity, and yaw angle, respectively. The parameters defining the configuration of the projectile are the principal dimensions L and d (length and diameter), a nose-shape parameter, the nose angle, or the nose length divided by the projectile diameter.

The general form of the ballistic limit equation for penetrators impacting with zero obliquity (V_{50}) is:

$$(V_{50})_0 = \left[C \left(\frac{\rho_c t A_p}{W} \right)^b \right] + K$$

where

C	=	empirical constant;
ρ_c	=	density of the projectile core;
t	=	target thickness;
A_p	=	presented area of projectile;
W	=	weight of projectile;
b	=	empirical constant;
K	=	empirical constant.

The ballistic limit for oblique impacts is obtained by multiplying the above prediction by the secant of the obliquity angle. An equation of similar form is used for fragments.

356-T6 Al., 7.62-mm AP.

356-T6 Al., 12.7-mm AP.

356-T6 Al., 14-5-MM AP.

356-T6 Al., 23-mm API.
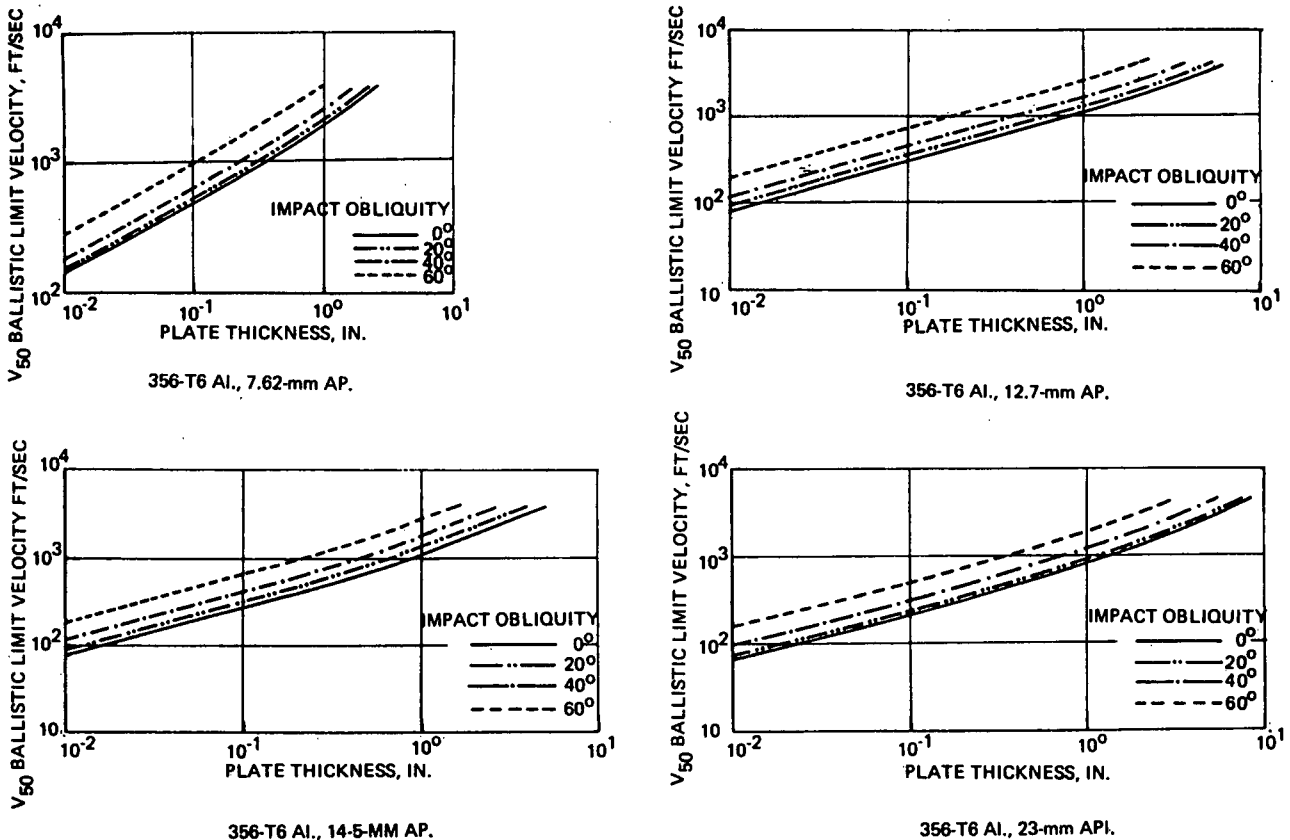
Figure 2-21 Typical V₅₀ Ballistic Limits for Aircraft Structural Materials
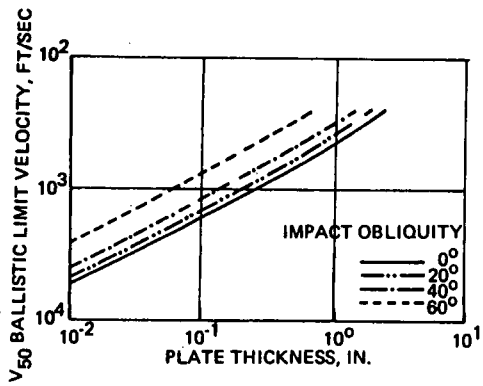
2014-T6 or 7075-T73 Al., 7.62-mm Ball.
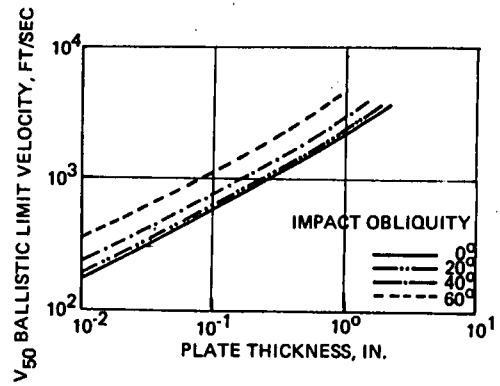
2014-T6 or 7075-T73 Al., 7.62-mm AP.
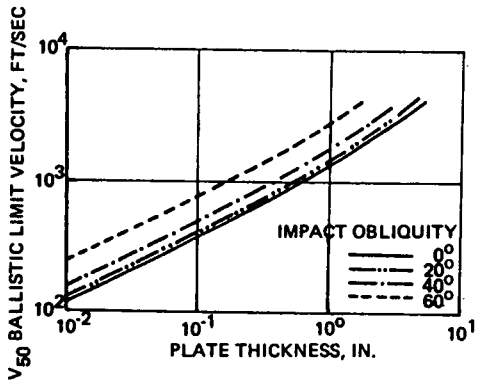
2014-T6 or 7075-T73 Al., 12.7-mm AP.
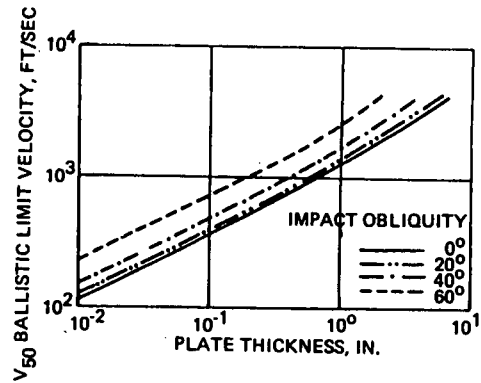
2014-T6 or 7075-T73 Al., 14.5-mm AP.
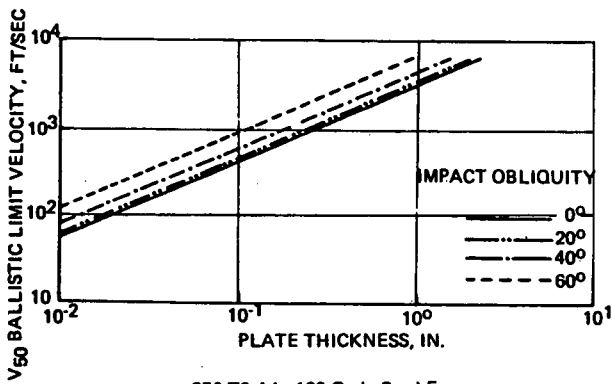
356-T6 Al., 120-Grain Steel Frag.
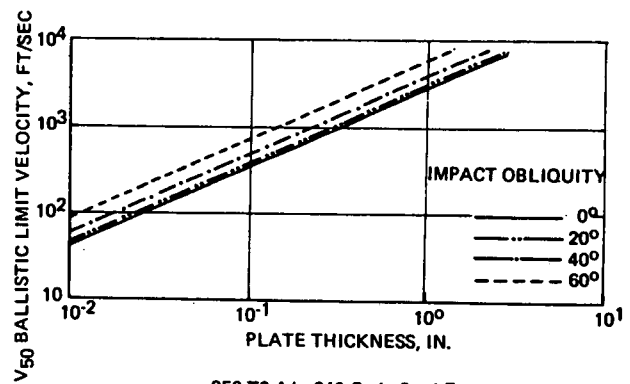
356-T6 Al., 240-Grain Steel Frag.
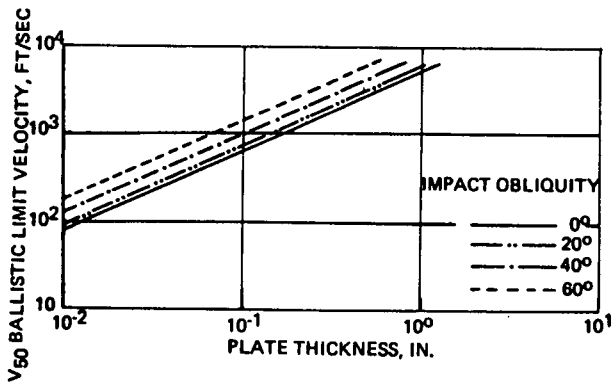
2014-T6 or 7075-T73 Al., 30-Grain Steel Frag.
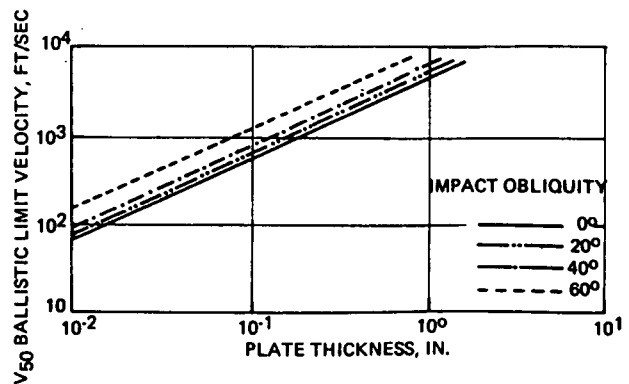
2014-T6 or 7075-T73 Al., 60-Grain Steel Frag.

Figure 2-21. Typical V_{50} Ballistic Limits for Aircraft Structural Materials (Cont)

V_{50} BALLISTIC LIMIT VELOCITY, FT/SEC

PLATE THICKNESS, IN.

IMPACT OBLIQUITY
0°
20°
40°
60°
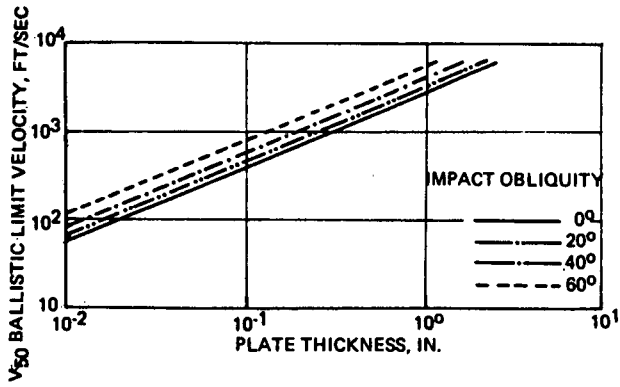
2014-T6 or 7075-T73 Al., 120-Grain Steel Frag.

V_{50} BALLISTIC LIMIT VELOCITY, FT/SEC

PLATE THICKNESS, IN.

IMPACT OBLIQUITY
0°
20°
40°
60°
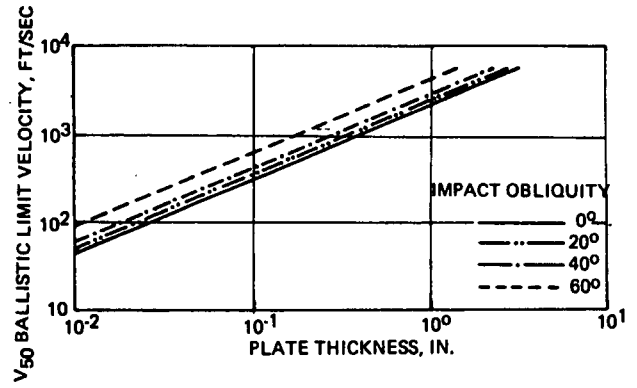
2014-T6 or 7075-T73 Al., 240-Grain Steel Frag.

V_{50} BALLISTIC LIMIT VELOCITY, FT/SEC

PLATE THICKNESS, IN.

IMPACT OBLIQUITY
0°
20°
40°
60°
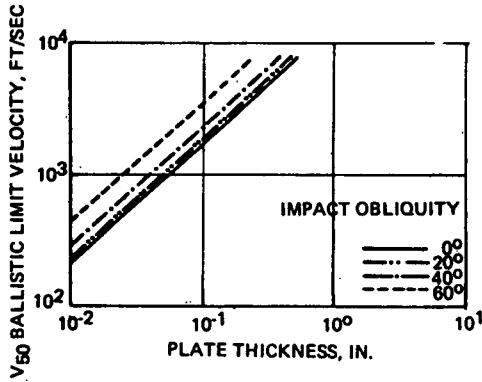
4340 Steel (360 BHN), 30-Grain Steel Frag.

V_{50} BALLISTIC LIMIT VELOCITY, FT/SEC

PLATE THICKNESS, IN.

IMPACT OBLIQUITY
0°
20°
40°
60°
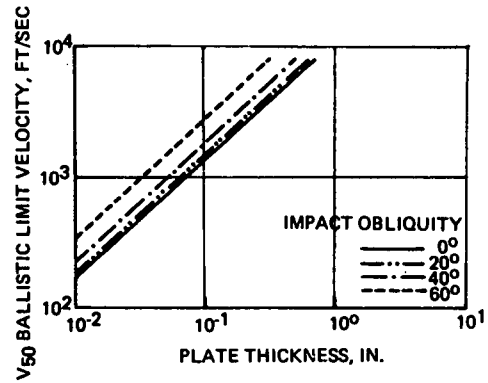
4340 Steel (360 BHN), 60-Grain Steel Frag.

V_{50} BALLISTIC LIMIT VELOCITY, FT/SEC

PLATE THICKNESS, IN.

IMPACT OBLIQUITY
0°
20°
40°
60°
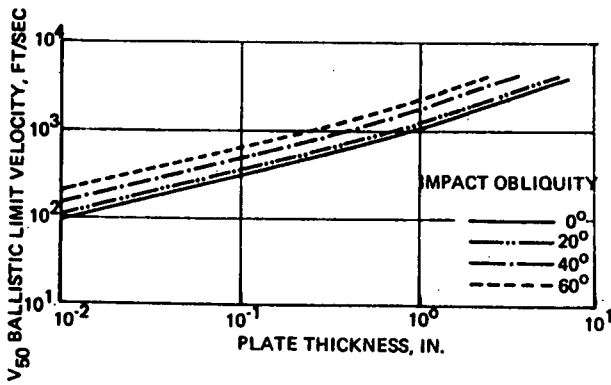
2014-T6 or 7075-T73 Al., 23-mm API

V_{50} BALLISTIC LIMIT VELOCITY, FT/SEC

PLATE THICKNESS, IN.

IMPACT OBLIQUITY
0°
20°
40°
60°

4340 Steel (360 BHN), 7.62-mm Ball.

V_{50} BALLISTIC LIMIT VELOCITY, FT/SEC

PLATE THICKNESS, IN.

IMPACT OBLIQUITY
0°
20°
40°
60°

4340 Steel (360 BHN), 7.62-mm AP.

V_{50} BALLISTIC LIMIT VELOCITY, FT/SEC

PLATE THICKNESS, IN.

IMPACT OBLIQUITY
0°
20°
40°
60°
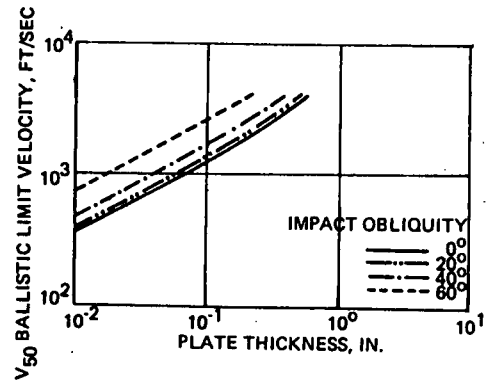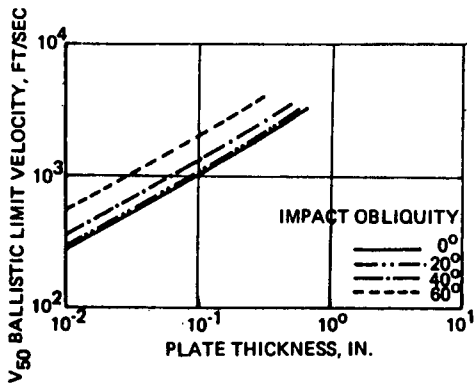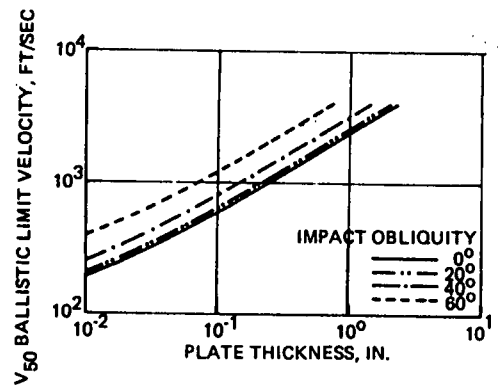
4340 Steel (360 BHN), 12.7-mm AP.

Figure 2-21 Typical V_{50}, Ballistic Limits for Aircraft Structural Materials (Cont)
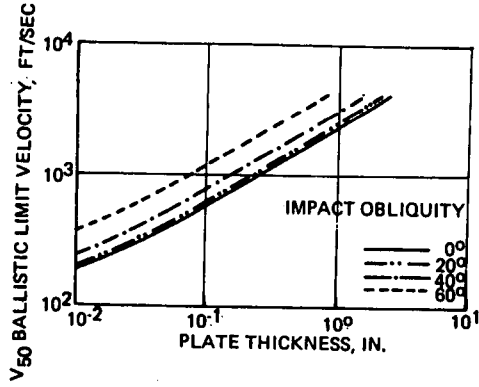
4340 Steel (360 BHN), 14.5-mm AP.
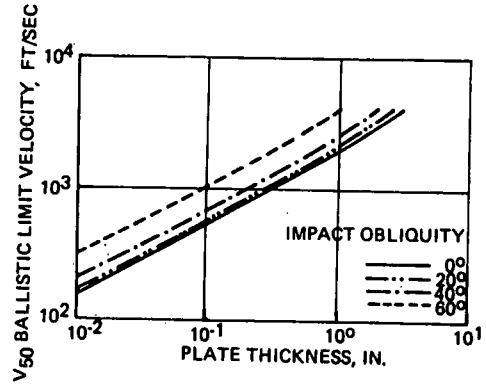
4340 Steel (360 BHN), 23-mm AP1.
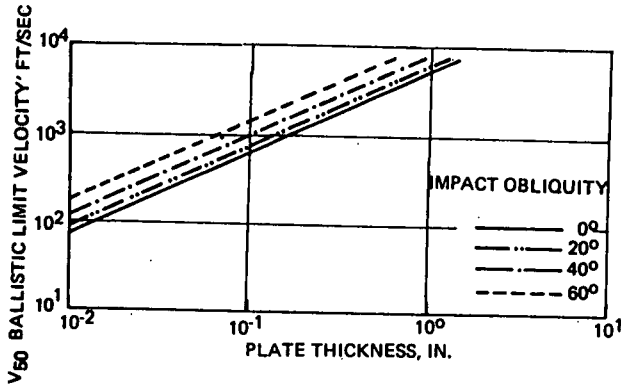
356-T6 Al., 30-Grain Steel Frag.
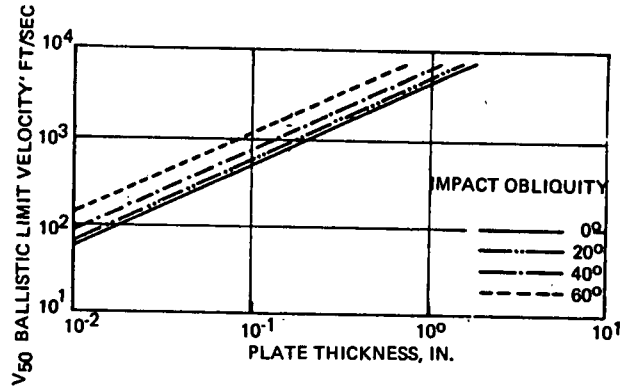
356-T6 Al., 60-Grain Steel Frag.
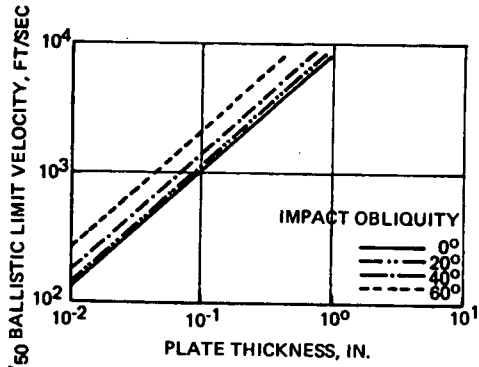
4340 Steel (360 BHN), 120-Grain Steel Frag.
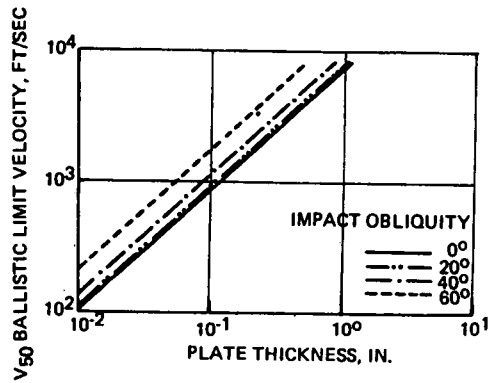
4340 Steel (360 BHN), 240-Grain Steel Frag.

Figure 2-21 Typical V_{50} Ballistic Limits for Aircraft Structural Materials (Concluded)
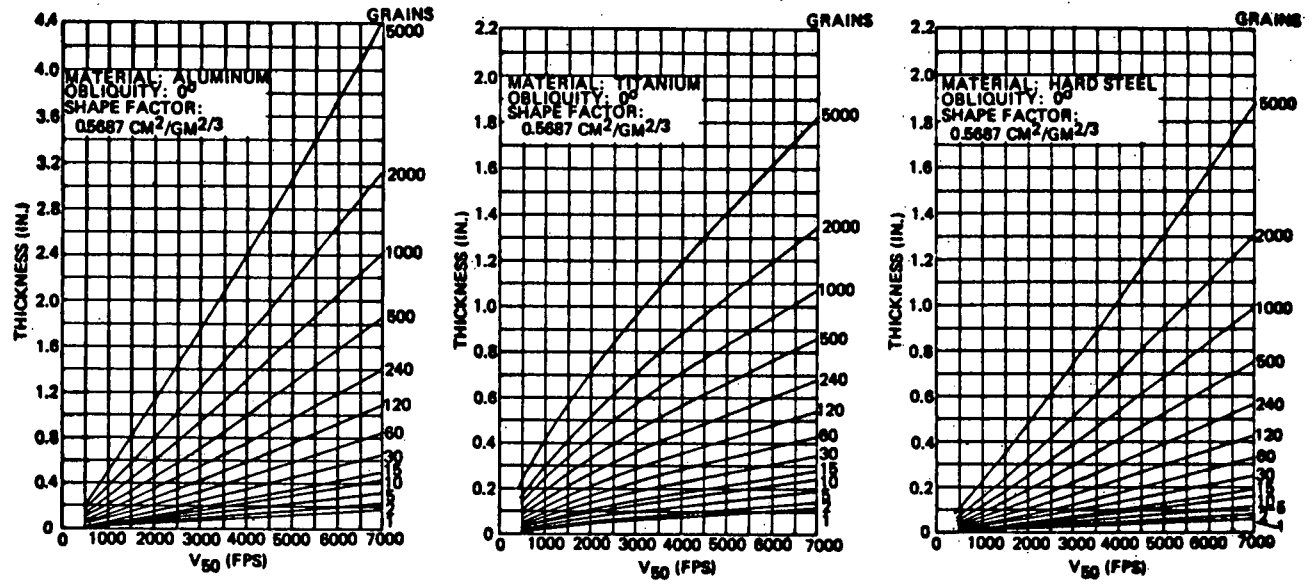
Figure 2-22. Typical Ballistic Limits for Fragments Impacting Metals

2.1.1.2 Ballistic Limit Assessment for Fiber Composite Structure

At the time of this writing there is not enough data available to formulate an adequate ballistic limit model for fiber composites. There is a test program underway in the U. S. to obtain the data needed, coordinated by AFFDL/FES for the JTCG. Some preliminary test results from that program were obtained from AFFDL and used with several graphite/epoxy ballistic limit test results available from Reference 2-12 to develop a very preliminary ballistic limit model for compact steel fragments impacting graphite/epoxy laminates (see Ref. 2-17).

Formulation of the model was based on the penetration equations presented in the "Penetration Equations Handbook" (Ref. 2-22), mentioned above, released in draft form by the JTCG/ME. The model for ballistic limit (V_{50}) is given below. Its application is limited to compact mild steel fragments impacting $0,\pm45,90$ graphite/epoxy laminates.

$$V_{50} \cos \theta = 3925 \left(\frac{\rho t A_p}{W_f} \right)^{1.58}, \qquad \text{(Eqn. 2-1)}$$

where

ρ = laminate density (lbs/in^3),
(0.056 lbs/in^3 for graphite/epoxy),

t = laminate thickness (in),

A_p = average presented area of the fragment, based on JTCG/ME recommendations as follows:

A_p = $3L^2/2$ for cubes;

= $\pi d^2/4$ for spheres;

= $d^2 \left[\frac{\sqrt{2}}{2} (L/d) + \frac{\sqrt{2}}{2} (\frac{\pi}{4}) \right]$ for cylinders;

where d equals the diameter of a sphere or cylinder, L equals the length of one side if the fragment is cubical, or the length if cylindrical;

W_f = fragment weight (lbs),

θ = angle of obliquity.

Figure 2-23 compares model predictions with the (very limited) available test data. The following example will clarify the use of the model:

Given: Fragment: 1/4-inch mild steel cube:

ρ_{stl} = .283 lbs/in^3,

θ = 0-degrees.

Laminate: Graphite/epoxy:

ρ = 0.056 lbs/in^3,

t = 0.25-inch.

EFFECTIVE PROJECTILE VELOCITY, V cos θ (ft/s)

8,000

6,000

● Penetration
O No penetration

Type of projectiles: compact mild steel fragments
Note: All unmarked data points are 0 deg obliquity

4,000

PENETRATION

3,000

NO PENETRATION

2,000

—60°

—70°

O—70°

60°—70°

1,000 —60°

60°
60° —0°
—60°

70°

70° 70°

$$V_{50} \cos \theta = 3,925 \left(\frac{\rho t A_p}{W_f}\right)^{1.58}$$

θ = Obliquity angle (deg)
ρ = Density of impacted laminate (lb/in³)
t = Laminate thickness (in)
A_p = Presented area of fragment (in²)
W_f = Weight of fragment (lb)

0

0.2   0.4   0.6   0.8   1.0   1.2

$\rho A_p t / W_f$

Figure 2-23 Preliminary Ballistic Limit Model for Graphite/Epoxy Laminates Impacted by Compact Fragments

Calculations for V_{50}:

$$W_f = \rho_{stl} L^3 = (0.283)(0.25)^3,$$
$$= 0.004422\text{-lbs};$$

$$A_p = \frac{3}{2}L^2 = \frac{3}{2}(0.25)^2 = 0.094\text{-in}^2,$$

$$V_{50} = 3925 \left(\frac{\rho t A}{W_f}p\right)^{1.58} \sec \theta,$$

$$= 3925 \left[\frac{(0.056)(0.25)(0.094)}{0.004422}\right]^{1.58}(1.0),$$

$$= 576 \text{ ft/s}.$$

2.1.2 Projectile Degradation Due to Penetration

The interaction between the projectile and the structure during penetration causes physical changes in both. The alteration of the projectile configuration is of importance in that it influences the potential for further damage following the initial impact. For most armor-piercing small arms projectiles, there are two principal degrading mechanisms:

1. Stripping the jacket from the projectile (this is a factor in incendiary functioning).

2. Breaking the penetrator. This failure mechanism has the most effect on subsequent damage and penetration capability.

Several available methods for predicting the extent of degradation are described in the following paragraphs.

Jacket Stripping. Figure 2-24, from Reference 2-2, is a regime diagram showing the condition of U.S. .30 caliber bullets after impacting aluminum panels. Regimes, in terms of projectile velocity and panel thickness, are shown for a nearly intact projectile (i.e., little detectable physical damage after impact), and projectiles with partially and fully stripped jackets. The regime diagram was developed by examining projectiles recovered after penetration. It is evident that increasing the angle of obliquity causes significant increases in the probability of jacket stripping. Figure 2-25 shows a representative collection of damaged projectiles, indicating the effect of velocity and obliquity on projectile degradation.

NEARLY INTACT BULLET **FULLY STRIPPED CORE**
PARTIALLY STRIPPED CORE **NO PENETRATION**

a) θ = 0°   b) θ = 40°   c) θ = 60°
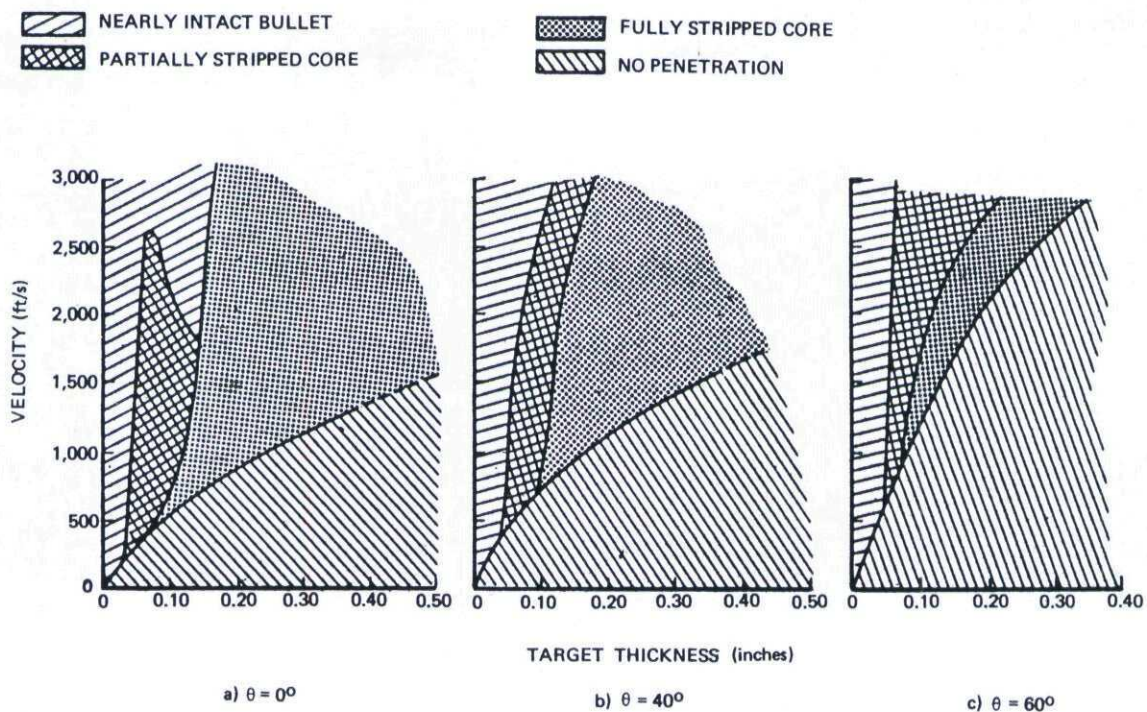
*Figure 2-24 Projectile Post-Impact Condition Regime Diagram
U.S. .30 AP Projectiles*
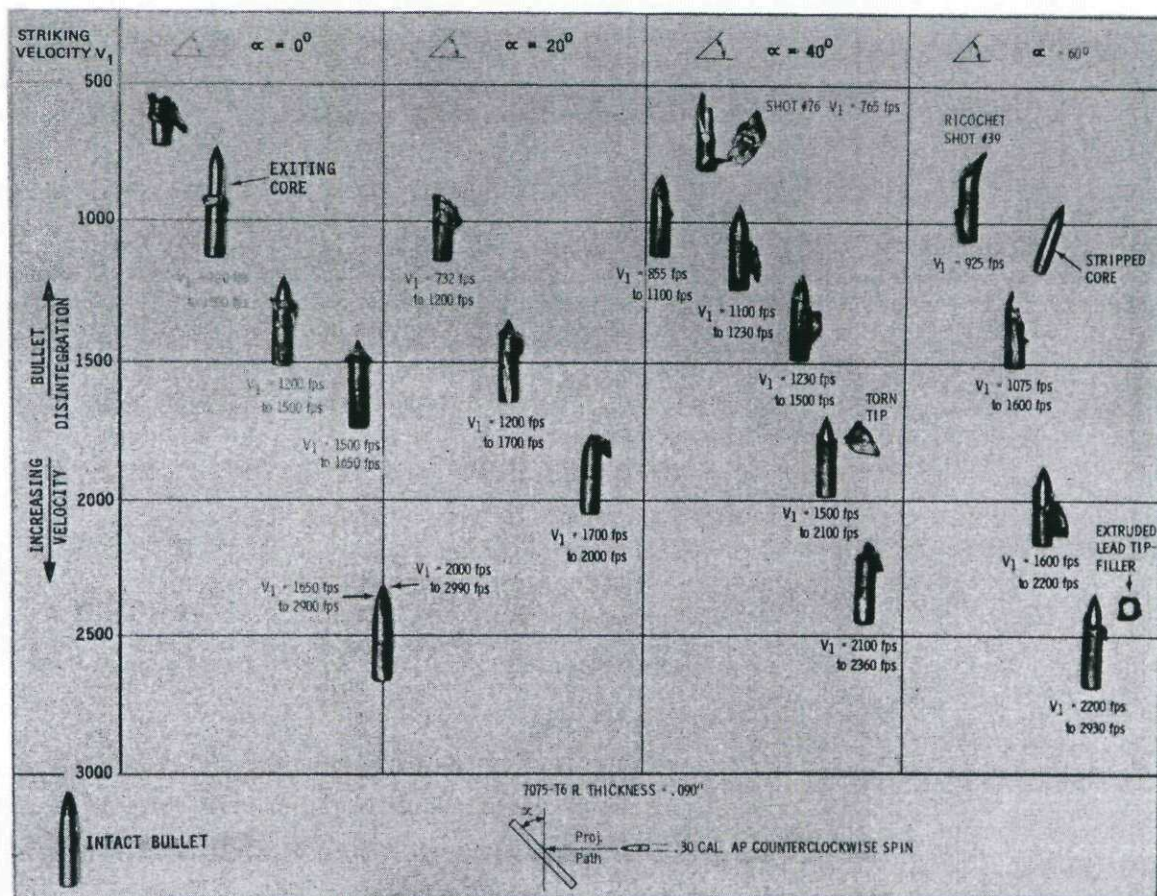
Figure 2-25.   Effect of Velocity and Obliquity on Post-Impact Condition.

44

Core-Breakage. Figure 2-26, also from Reference 2-2, shows regime diagrams defining core breakage in .30 caliber bullets impacting aluminum panels. Reference 2-22 gives core breakage results and presents analytic equations for predicting core break-up (and jacket stripping) as well as the mass loss in penetrating fragments. The user should consult the reference for detailed information.
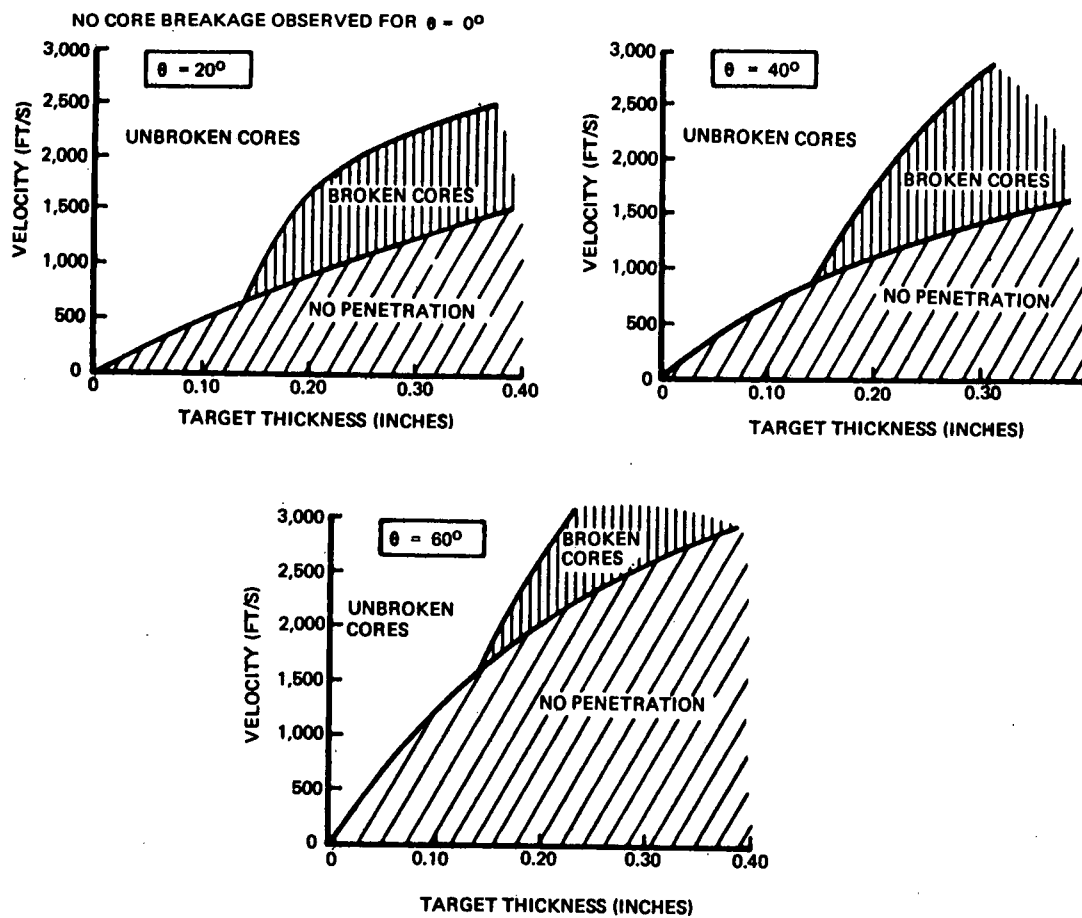
Figure 2-26. Condition of Projectile After Penetration
(7075-T6 Aluminum Targets 0.30 AP Projectiles)

2.2 ANALYSIS METHODS FOR BALLISTIC DAMAGE SIZE AND TYPE

The following paragraphs define the parameters which influence the size and character of projectile impact damage, and describe techniques for analytical prediction. Predicting damage size is the first step is assessing the structural capability of impacted structure, since damage size determines net section strength loss, stiffness loss, and the flaw size for failure analysis. The discussion is organized according to projectile type as follows:

2.2.1   Non-Exploding Projectiles;
2.2.2   High Explosive Projectiles;
2.2.3   Engine Debris Projectiles.

Within each projectile category the responses of both metallic and fiber composite structure are discussed. Section 2.2.4 discusses the effects of fluid pressure in causing damage, a phenomenon known as hydrodynamic ram.

2.2.1 Damage Caused by Non-Exploding Projectiles

There has been considerable development of analysis methods for predicting damage resulting from non-exploding projectile impacts, particularly for metal structure. Significant progress has also been made recently with regard to predicting damage in advanced fiber composites such as graphite/epoxy.

2.2.1.1 Non-Exploding Projectiles Impacting Metals

An extensive characterization of damage from nonexploding projectiles impacting metals is reported in Reference 2-2, including definition of the types of damage and the parameters that influence damage size. Analysis models were developed for predicting: (1) upper and lower limits of damage size; (2) the character of the resulting damage, e.g., holes, cracks; and (3) the probable orientation of the damage relative to the applied loading, the material grain direction, and the projectile trajectory. Some pertinent results from Reference 2-2 are summarized in Sections 2.2.1.1.1 and 2.2.1.1.2 below.

2.2.1.1.1 Non-Exploding Projectiles Impacting Metals - Discussion of Parameters Influencing Damage

Figure 2-27 illustates some of the characteristic features of projectile impact damage in metal sheet. Three components of damage can generally be identified: 1) a hole through which the projectile has passed, 2) cracks emanating from the hole, 3) spallation, i.e., material removed by transverse delamination. The region between two cracks often forms a "petal," particularly in thinner gage materials. In many cases, the petal may detach, thus increasing the size of the hole. Spallation is invariably most extensive on the exit surface of the sheet, although small regions of spallation are often present on the entry surface.

ENTRY SURFACE

EXIT SURFACE
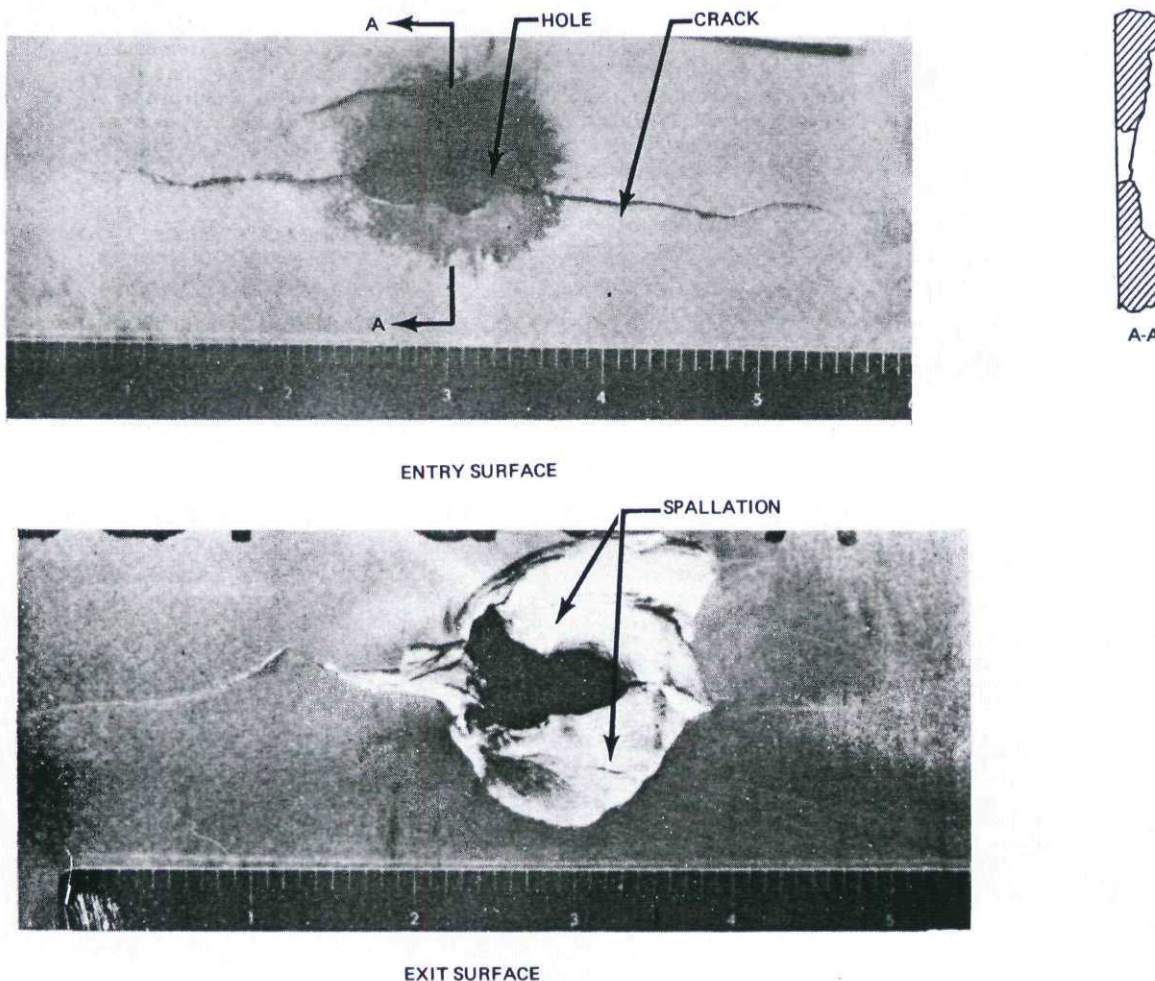
Figure 2-27. Representative Projectile Impact Damage in Metal Sheet

The size and severity of the damage depends on the relative prominance of the three components, which, in turn, depends on the material of the impacted structure, the type of projectile, and the velocity and obliquity of impact. For example, materials and conditions which augment the extent of cracking result in increased damage size, and also increase the significance of the damage as a flaw causing degradation of residual strength.

The encounter and structural parameters which are most significant in determining projectile damage size are:

1. Projectile type,
2. Projectile velocity,
3. Projectile obliquity,
4. Target sheet thickness,
5. Target sheet material,

6. Applied stress,
7. Target sheet rolling grain direction,
8. Target structural configuration,
9. Temperature.

The following paragraphs describe the manner in which these parameters influence the damage resulting from an impact. The damage referred to in the discussion is the maximum visual damage as measured in the approximate plane of the impacted sheet.

Effect of Projectile Size and Type - With projectiles that are similar in construction but of different size, it is generally found that larger projectiles produce larger damage. When similarity is not present, however, smaller projectiles may indeed produce more damage. For example, the deformability of the projectile as it penetrates can be a factor. Ball projectiles, which have a relatively soft core, often produce greater damage than armor-piercing projectiles of identical size. Similarly, projectiles with jackets tend to cause more damage than jacketless projectiles of the same size.

Evidence of the effect of projectile type (as opposed to size) on damage is shown in Figure 2-28 which compares the damage in 0.250-inch 7075-T6 aluminum sheet due to three types of 20-mm projectiles, fired under similar conditions:

1. Finnish Lahte-type armor-piercing tracer (APT) - weight 2320 grains;

2. U.S. M-53 armor-piercing incendiary (API) - 1550 grains;

3. U.S. M-55-A2 training round - 1520 grains.

The maximum damage produced by these projectiles under similar impact conditions was 1.38, 5.0 and 2.6 inches, respectively. The largest damage was produced by the M-53, which has a deformable nose cap. None of the projectiles had a complete jacket.

Impact damage from fragment penetration differs from that caused by bullets because of the difference in the geometric shapes of the projectiles, and also because of frequent differences in striking velocity. Spin-stabilized ogive projectiles can induce significant in-plane wedging forces that contribute to crack and petal formation. Fragments from missile warheads and high-explosive projectiles come in diverse sizes and shapes, so that it is difficult to generalize. However, compact (chunky) fragments, particularly cubical fragments, tend to penetrate by a shearing mechanism, thus "punching" through a metal panel. Spallation will likely occur on the exit surface, even at relatively low striking velocities. Representative damage patterns from compact fragments are shown in Figures 2-29 and 2-30, showing typical shear damage patterns, with little cracking adjacent to the perforation.
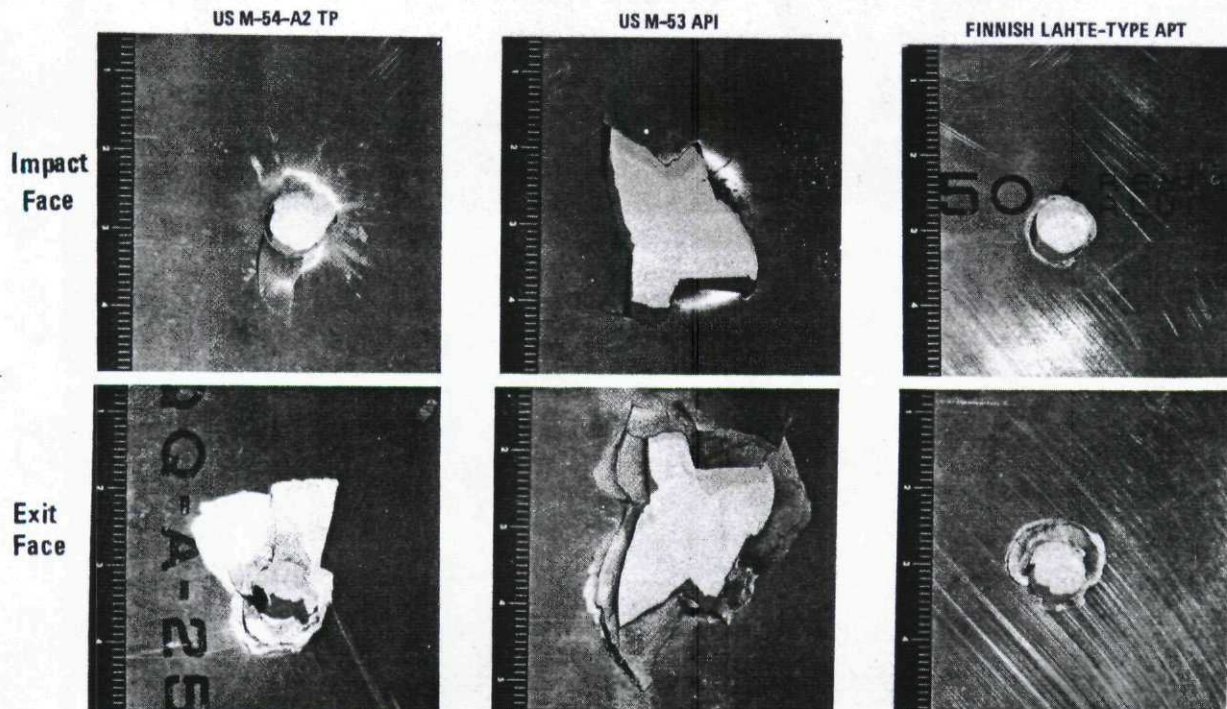
Figure 2-28. Damage in 0.25 7075-T6 Due to 20-mm Projectile Impacts (Similar Impact Conditions)

ENTRANCE

3540 ft/s   2880 ft/s   1502 ft/s   550 ft/s

EXIT
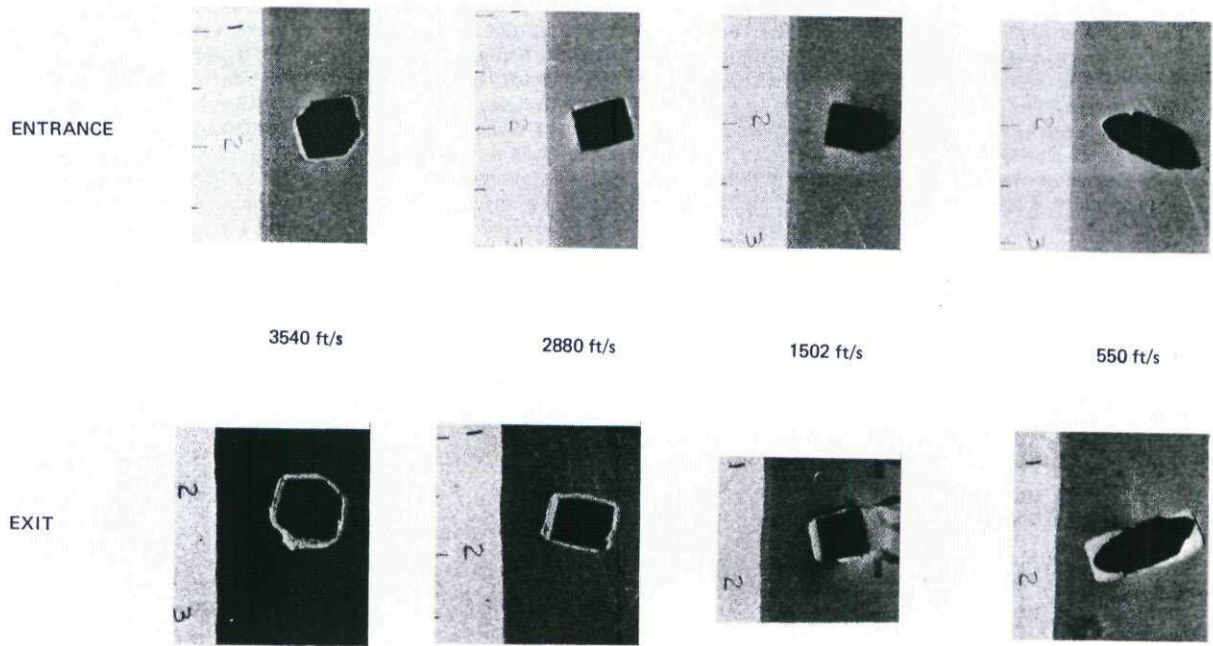
*Figure 2-29. Damage Type Variation with Velocity, Compact Fragment,
0.063 7075-T6, θ = 0 deg*

ENTRANCE   EXIT

$\theta = 0^o$ 3520 ft/s

$\theta = 60^o$ 3638 ft/s
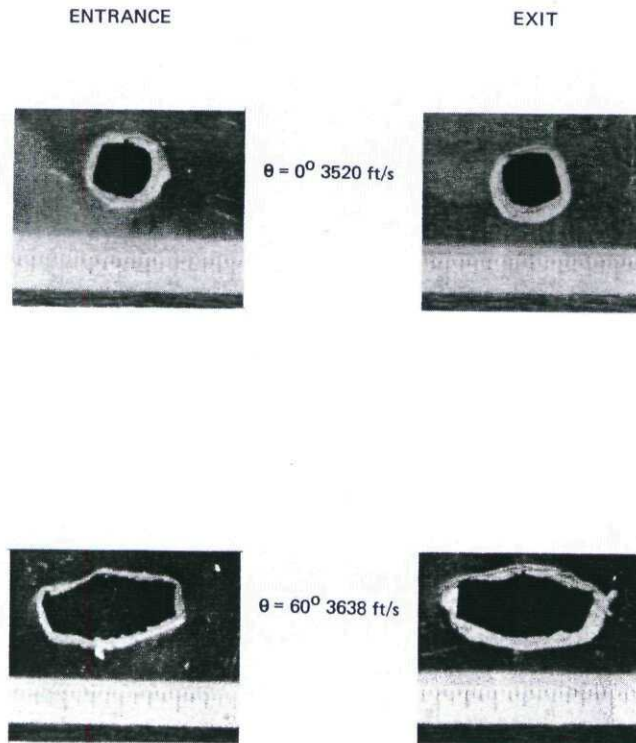
*Figure 2-30. Variation in Damage Type with Obliquity Angle, 0.125 7075-T6 Aluminum
Alloy Impacted by Compact Fragment*

Effect of Projectile Velocity. For a given target material and projectile obliquity, the variation of projectile velocity can result in the damage size variation shown in Figure 2-31 which also illustrates the concepts of incipient damage, maximum damage and high-velocity damage. The response is characterized by a maximum damage size that occurs just above the penetration (ballistic) limit. Cracking is the predominant damage component at this velocity. Further increases in projectile velocity result in lesser damage (due to less cracking), until a plateau is reached called the high-velocity damage. The high-velocity damage is a relatively smooth hole, only slightly larger than the projectile diameter. The increase in damage with reduced velocity is evident. Further velocity increases do not produce any significant change in damage size, unless velocities can be reached that result in appreciable projectile break-up. The difference between the maximum damage and the high-velocity damage depends primarily on sheet thickness. Figure 2-32 is a photograph showing these for .30-caliber AP bullets impacting 0.090-inch 7075-T6 sheet, with velocities ranging from 800 to 2500 feet per second. The behavior described is most pronounced for spin-stabilized small-arms projectiles impacting relatively notch-sensitive sheets such as 7075-T6. However, it is generally true that maximum cracking occurs when the striking velocity of the projectile is slightly above the ballistic limit velocity. Reference 2-7 presents supporting data from fragment impacts.
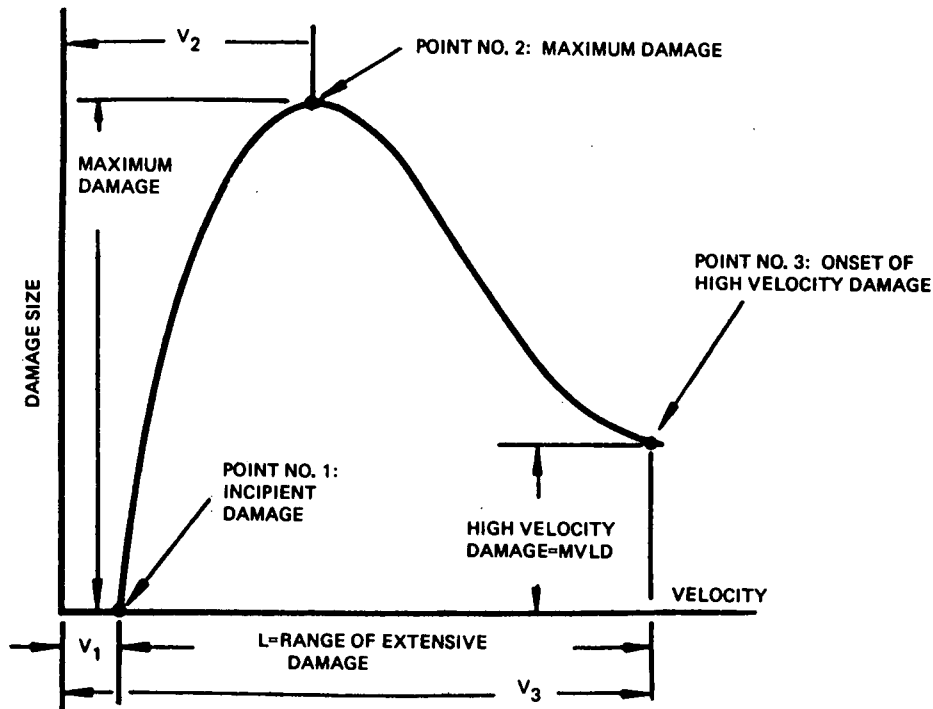
Figure 2-31. Typical Variation of Damage Size with Projectile Velocity
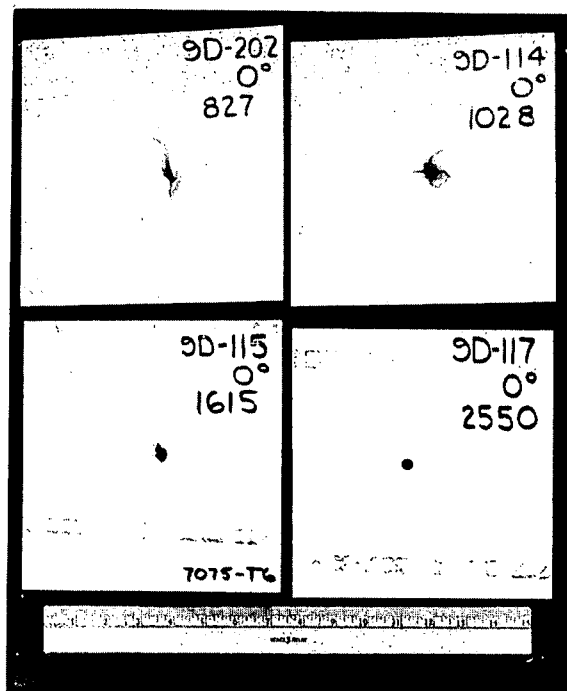
Figure 2-32. Effects of Projectile Velocity on Damage Size (.090 7075-T6, .30 Cal AP)

Effect of Projectile Obliquity. The angle of obliquity (or impact angle) has a pronounced effect on damage size. The following are generally true regarding obliquity effects:

1. When impact angles are increased and other conditions held constant, the maximum damage will also increase as long as projectile velocities are sufficient to cause penetration.

2. The projectile velocities associated with incipient damage, maximum damage, and the onset of high-velocity damage increase directly with obliquity angle increase.

Figure 2-33 illustrates these obliquity effects, and Figure 2-34 is a photograph showing 0.090-inch 7075-T6 impacted at several obliquities with velocity held constant. There is a significant reduction in damage size as the obliquity angle increases from 60- to 70-degrees because the projectile richochets off the sheet rather than penetrating.
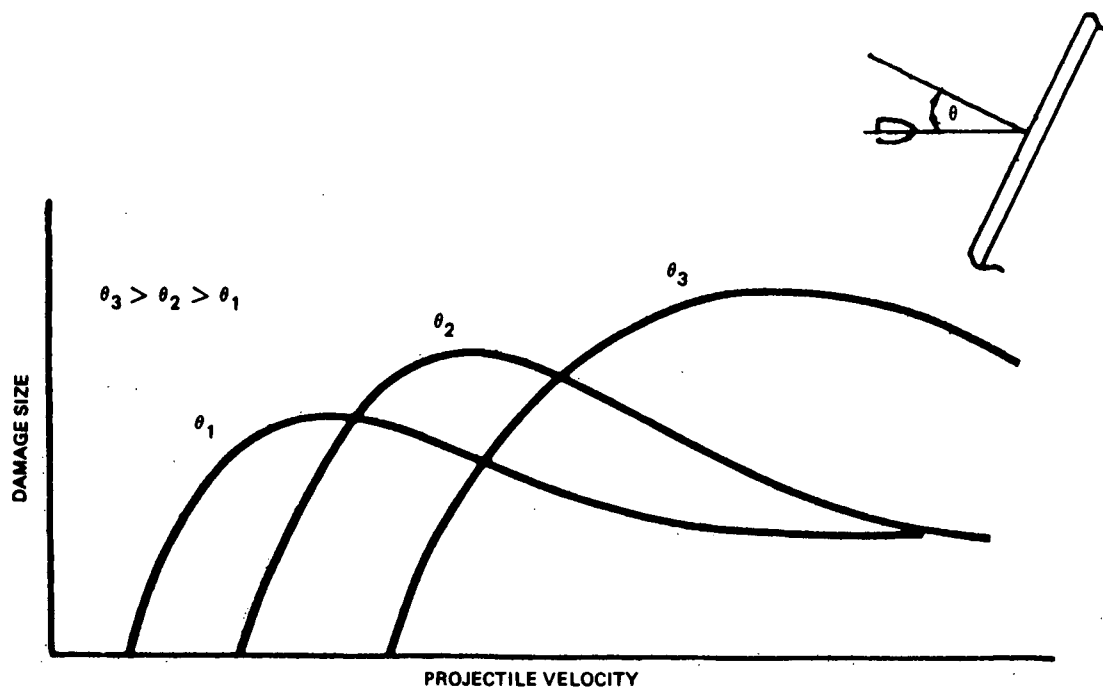
Figure 2-33. Typical Effect of Obliquity on Damage Size
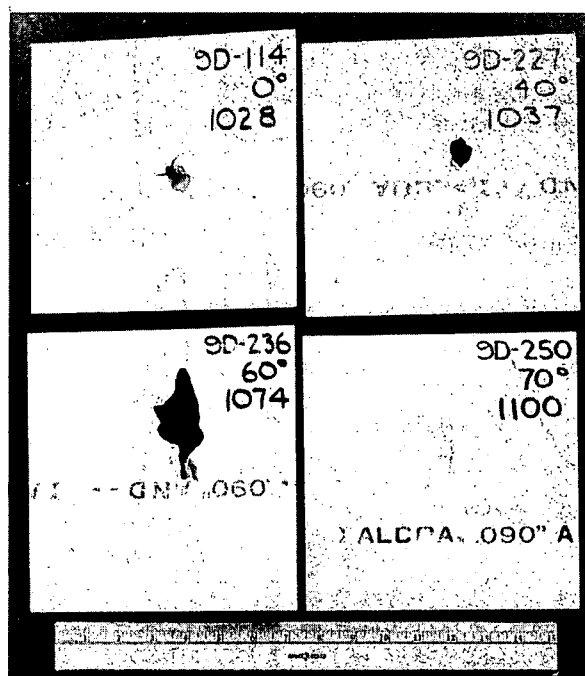
Figure 2-34. Effects of Obliquity on Damage Size (.090 7075-T6, .30 Cal AP)

Effect of Sheet Thickness. Damage size is highly dependent on the thickness of the impacted sheet. A convenient thickness parameter is the ratio of sheet thickness to projectile diameter (t/d) or other characteristic dimension. For small arms projectiles, when t/d is less than about 0.1, the hole component of damage predominates, with little cracking or spallation. As t/d is increased beyond 0.1, the damage size increases until a maximum is reached at t/d ratios of approximately 0.4. The typical response is shown in Figure 2-35(a). It should be kept in mind that since damage size also depends on projectile velocity, this figure shows the maximum damage that occurs for each given t/d ratio.

The remaining illustrations in Figure 2-35 demonstrate the effects of all the parameters discussed, namely: the effect of projectile velocity, obliquity angle and projectile type. Figure 2-35(b) illustrates the extent of scatter in damage size test results near the ballistic limit.

Effect of Sheet Material. The choice of material will have a marked effect on the resulting size and type of damage, since materials differ in their resistance to impact damage. A comparison of damages produced under identical impact conditions, changing only target material, will show large differences in damage size. It was shown that the damage sizes for 2024-T3, 2024-T81 and 7075-T6 aluminums have the ratios 1/2.2/5.1, respectively. On the same basis, the ratio for 6A1-4V titanium was found to be 1.8. These materials rank in the following order of damage resistance, with the first having the highest:

1. 2024-T3,
2. 6A1-4V,
3. 2024-T81,
4. 7075-T6.

Since damage tolerance is also dependent on material properties such as notch-sensitivity, material selection is a means of reducing structural degradation due to battle damage.

Effect of Rolling Grain Direction. Data for 7075-T6 showed that there is a higher than random probability that the lateral damage (ie., the greatest damage dimension) will align with the grain direction apparent in rolled sheet aluminum. The probability was higher yet (0.69) when the supports were also parallel to the grain direction. The probability increased to 0.83 if a tensile stress field was applied normal to the rolling grain direction at the time of projectile impact.

Effect of Applied Stress. There is evidence that the level of externally applied load existing at the time of impact can have a significant influence on the induced damage. However, this influence has not yet been quantified sufficiently for incorporation into analysis methods. The available evidence consists of the results of firing projectiles into tension panels under load. These tests have shown that there is generally a threshold stress level causing the panel to fracture immediately upon impact (Ref. 2-23, for example). This threshold stress may be lower than the static residual strength of similarly impacted unstressed panels. Section 2.5.1.4.3 discusses this effect in
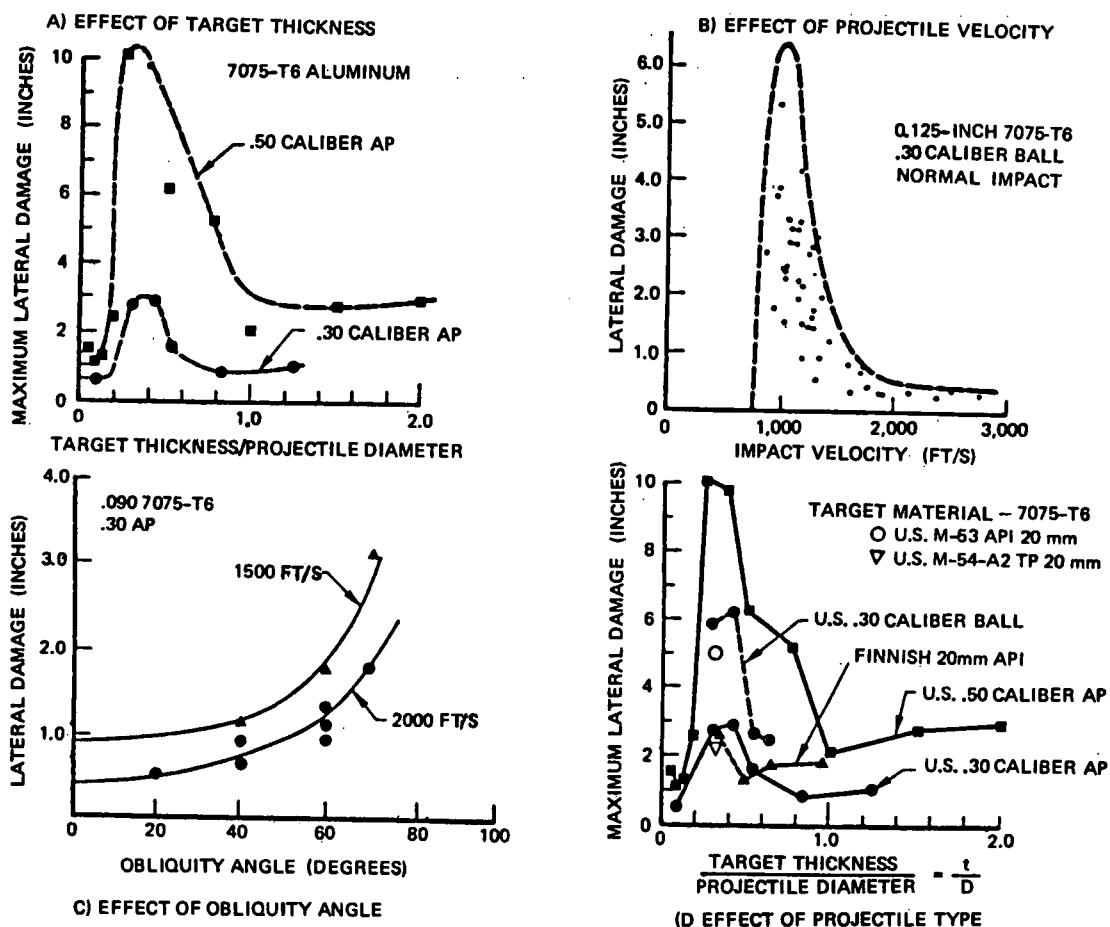
Figure 2-35 Effect of Parameters on Impact Damage in Metals

more detail, from the standpoint of residual strength analysis. From the standpoint of damage assessment, it is at least certain that applied stresses equal to or greater than the threshold level will very likely cause an increase in the induced damage size, depending on the potential for crack extension. There is currently no analysis method which relates applied stress (either tension or compression) to damage size.

Effect of Structural Configuration. Typical aircraft structure consists of skin with stiffening elements. Limited test results tend to indicate that damage size in skin is influenced by the proximity of stiffeners. The damage size in the skin is smaller for impacts near the stiffener; however, the damage can be larger if the stiffener is also impacted. There is currently no verified analysis method which addresses the effect of adjacent stiffening on damage size and type.

Effect of Temperature. Reference 2-7 reports damage-assessment testing of 2024-T3, 7075-T6, 6A1-4V and 4130 steel chilled to -65°F. The aluminum and the titanium alloys did not show increased damage size at the reduced temperature. The steel, however, showed an appreciable increase. Further definition of this effect is not currently available.

2.2.1.1.2 Non-Exploding Projectiles Impacting Metals - Damage Size Prediction

The previous section described the parameters influencing the size and character of ballistic impact damage. The following paragraphs present analysis models for predicting damage size which, in general, incorporate the parameters of major importance. The methods presented are applicable to small arms projectiles and compact fragments such as generated by some types of missile warheads and engine debris. Small arms projectiles are treated first, reflecting the most advanced analytical development. This is followed by a fairly well-developed method for predicting damage size from compact fragments. In both cases, the analysis methods predict a measure of damage which is considered most influential in causing structural degradation.

This raises a fundamental question in regard to ballistic damage assessment. Ballistic damage is complex, and decisions must be made concerning what components of damage should be measured and incorporated into analytical models. This question is probably never resolved to everyone's satisfaction. However, a purely engineering approach has been of some value, in which the appropriate damage measure is defined as a dimension parallel to the original surface of the impacted sheet that encompasses either: 1) the tip-to-tip length of a crack, or 2) the diameter defining the extent of spallation, or 3) the diameter defining the extent of combined cracking and spallation. The largest such dimension is defined as the "damage" resulting from the impact being considered. The term "lateral damage" has been used in the literature.

<u>Small Arms Projectiles Impacting Metals - Damage Size Prediction</u>. A damage size model for bullets impacting metals, LATDAM, is presented in Reference 2-2. This model has been applied in many aircraft vulnerability assessments to predict the upper and lower bounds on the damage size caused by projectile impact. The predictions given are the largest extent of the damage within the plane of the target.

The damage size, which is subject to large scatter ranges, is represented by two fourth-order polynomial equations that bound the expected damage size. Each equation is controlled by the damage and velocity coordinates of three points. These three points, shown in Figure 2-36, are:

1. The point of incipient damage (for the upper bound damage prediction) or the point of guaranteed damage (for the lower bound damage prediction);

2. The point of maximum damage; and

3. The point of onset of high-velocity lateral damage (modest velocity increases beyond this point cause little change in damage).
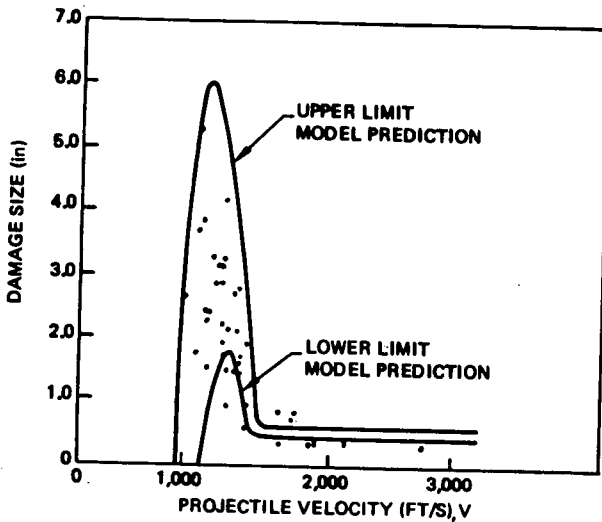
(A) TYPICAL TEST RESULTS

$$DAMAGE\ SIZE = \begin{cases} 0 \text{ for } V^* < V_1 \\ K_\theta\ NIMLD\ [\alpha_4\ v^4 + \beta_4\ v^3 + \gamma_4\ v^2 + \delta_4\ v] \\ \qquad \text{for } V_1 < V^* < V_3 \\ HVLD \text{ for } V^* > V_3 \end{cases}$$

(UPPER LIMIT)
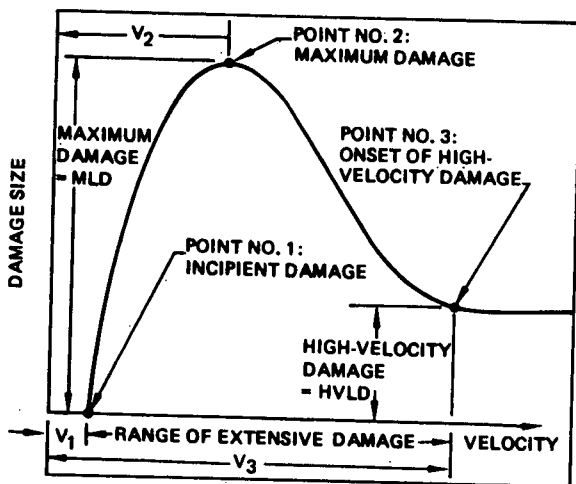
(B) DAMAGE MODELING PARAMETERS

WHERE:

$V^* = V[\cos \theta]^{0.7}$

V = PROJECTILE IMPACT VELOCITY
θ = OBLIQUITY ANGLE

$v = \dfrac{V^* - V_1}{V_3 - V_1}$

$NIMLD = C_1 d\ [\alpha_1\ (t/d)^4 + \beta_1\ (t/d)^3 + \gamma_1\ (t/d)^2 + \delta_1\ (t/d) + \epsilon_1]$

$HVLD = d[C_3 + 0.6(t/d)^2]$

d = PROJECTILE DIAMETER
t = PANEL THICKNESS

Figure 2-36. Summary of LATDAM Damage Size Model

The coordinates of these points, both velocity and damage, are functions of: (1) impact condition parameters such as velocity and angle; (2) projectile parameters including size, type and shape, and (3) structural parameters including thickness and material. All of these have been incorporated into the damage model through the use of suitable constants and functions. The basic form of the damage size equation is defined in Figure 2-36, where:

V^* = impact velocity multiplied by $(\cos\theta)^{0.7}$,

θ = impact angle (obliquity),

MLD = maximum damage = NIMLD K_θ,

NIMLD = maximum damage under normal impact; a function of t/d ratio, target material, and projectile type,

$\alpha, \beta, \gamma, \delta$ = constants that depend on the relation between the points of maximum damage and onset of high-velocity damage,

K_θ = correction factor for oblique impact; a function of impact angle, t/d, target material and projectile type.

The empirical constants needed in the damage prediction equation have been developed for U.S. .30 and .50 caliber armor piercing and ball projectiles impacting sheets of 2024-T3, 2024-T81, 7075-T6 aluminums and 6A1-4V titanium at impact angles up to 70 degrees. The damage prediction equation has also been developed for a series of simulated warhead fragments using the length to diameter radio of cylindrical fragments for projectile characterization. Extension of this model to other materials will require additional ballistic testing. However, the range of damage sizes represented by the 2024-T3 and 7075-T6 aluminum alloys should cover the sizes expected for many metals. That is, few metals will show less ballistic damage than 2024-T3, and few will show greater damage than 7075-T6.

The following paragraphs give a more detailed description of the LATDAM damage size model, including a sample damage size calculation.

Model Statement

Upper Limit:

$$LD_{UL} = \begin{cases} 0 & \text{(for } V^* < V_1) \\ K_\theta \cdot \text{NIMLD } (\alpha_4 v^4 + \beta_4 v^3 + \gamma_4 v^2 + \delta_4 v) & \\ & \text{(for } V_1 \leqslant V^* \leqslant V_3) \\ \text{HVLD} & \text{(for } V_3 < V^*) \end{cases}$$

(Eqn. 2-2a)

Lower Limit:

$$LD_{LL} = \begin{cases} 0 & \text{(for } V^* < V_1{}^*) \\ \text{NIMLD}^* (\alpha_4{}^* v^4 + \beta_4{}^* v^3 + \gamma_4{}^* v^2 + \delta^*{}_4 v) & \\ & \text{(for } V_1 \leqslant V^* \leqslant V_3) \\ \text{HVLD}^* & \text{(for } V_3 < V^*) \end{cases}$$

(Eqn. 2-2b)

Input Parameters

V = impact velocity (ft/s),

V^* = $V (\cos\theta)^{0.7}$,

θ = impact angle (degrees),

d = projectile diameter (in),

t = target thickness (in),

v = normalized impact velocity,

$= \dfrac{V (\cos\theta)^{0.7} - V_1}{V_3 - V_1}$,

NIMLD = $C_1 d(\alpha_1 (\frac{t}{d})^4 + \beta_1 (\frac{t}{d})^3 + \gamma_1 (\frac{t}{d})^2 + \delta_1 (\frac{t}{d}) + \epsilon_1)$,

HVLD = $d(C_3 + 0.6 (t/d)^2)$,

HVLD^* = 3/4 (HVLD),

NIMLD^* = $\text{HVLD}^* + 1/4 (\text{NIMLD-HVLD}^*)$,

V_1^* = $V_1 + 200$ ft/s.

Although constants are available only for U. S. projectiles, the models provide reasonably accurate damage predictions for 7.62, 12.7, and 14.5 mm projectiles when the constants for the most closely related projectile are used along with the actual projectile diameters. The validity of the model for projectiles larger than 14.5-mm has not been definitely shown. The available information indicates that only the HVLD portion is needed to predict normal impact lateral damage for solid, nonjacketed projectiles of any size.

There are several possible approaches that could be used to predict damage from oblique impacts by projectiles larger than 14.5-mm. One approach would be to apply the K_θ correction directly to the HVLD prediction. Another would be to modify the appropriate Kp constants based on projectile diameter and use the model as is. Lastly, the predictions provided by the .50 caliber projectiles could be used directly.

Damage predictions for the impact of yawed projectiles can be estimated by substituting a projection of the projectile length for the diameter d. At normal impact angles, the full projection can be used. The projection length should be reduced for oblique impact angles since the model already accounts for an increased projectile diameter caused by tumbling during oblique impact. However, there is insufficient experimental verification for confident application to yawed projectiles.

The following Tables 2-1 through 2-11 present the equations and constants required for applying the LATDAM model. Those interested in implementing the damage model should consult Ref. 2-2.

Table 2-1. Lateral Damage Model—Upper Limit

Table 2-2. Lateral Damage Model—Lower Limit

Table 2-3. Limits on K_1 and K_3

Table 2-4. Velocity Limits V_1, V_2, V_3

- Equation number: 2-6
- Basic form:

$$V_i = C_{i1} \ln(t/d) = C_{i2} \geqslant V_i' \ (\text{ft/sec})$$

$$V_1^* = V_1 + 200 \ (\text{ft/sec})$$

- Input:

  t = sheet thickness
  d = projectile diameter

• Constants: projectile and material	Velocity of incipient penetration V_1			Velocity of maximum lateral damage V_2			Velocity of onset of high-velocity lateral damage V_3		
	C_{11}	C_{12}	V_1'	C_{21}	C_{22}	V_2'	C_{31}	C_{32}	V_3'
.30-caliber armor-piercing									
2024-T3	550	800	100	600	1,340	500	500	2,500	1,800
2024-T81	650	750	100	600	1,340	500	500	2,180	1,800
7075-T6	650	750	100	725	1,580	500	1,125	3,250	1,800
6Al-4V titanium	500	1,100	100	725	2,000	600	580	3,200	2,400
.30-caliber ball									
2024-T3	650	1,250	100	725	1,800	500	500	2,180	1,800
2024-T81	650	1,250	100	725	1,800	500	500	2,180	1,800
7075-T6	650	1,350	100	725	1,640	500	870	2,500	1,800
.50-caliber ball and armor piercing									
2024-T3	650	1,080	100	725	1,800	500	500	2,180	1,500
2024-T81	650	1,080	100	725	1,800	500	500	2,180	1,500
7075-T6	650	1,080	100	725	1,580	500	870	2,500	1,500
6Al-4V titanium	500	1,100	100	725	2,320	800	580	3,200	2,000

Table 2-5. Normal Impact, Maximum Lateral Damage

- Equation number: 2-7
- Basic form:

$$
\text{NIMLD}
\begin{cases}
C_0 & t/d < \mu \\
C_1 \ d\left(\alpha_2 \lambda^4 + \beta_2 \lambda^3 + \gamma_2 \lambda^2 + \delta_2 \lambda\right) & \mu \leqslant t/d < \mu + \xi_1 \\
C_2 & \mu + \xi_1 < v
\end{cases}
$$

- Calculation form:

$$\text{NIMLD} = C_1 d\left[\lambda\left\{\delta_2^* + \lambda\left[\gamma_2^* + \lambda\left(\beta_2^* + \lambda\alpha_2^*\right)\right]\right\}\right]$$

- Inputs and constants (in order of use):

  C_0 from equation 2-14
  C_1 from equation 2-12
  C_2 from equation 2-13

  $\eta = C_2/C_1$

	Aluminum	Titanium
μ	0.15	0.10
ξ_1	0.70	0.60

K_1 = solution to equation (2-3)

$$\Delta_2 = \left(1 - K_1\right)^3; \ \Delta_1 = K_1^2\left(1 - K_1\right)^3 = K_1^2 \cdot \Delta_2$$

$$\alpha_2 = \left(\frac{3K_1 - 1}{\Delta_1}\right) + \eta\left(\frac{K_1 - 3}{\Delta_2}\right)$$

$$\beta_2 = \frac{-4K_1^2 - 4K_1 + 2}{\Delta_1} + \eta\left(\frac{-2K_1^2 + 4K_1 + 4}{\Delta_2}\right)$$

$$= \frac{2 - 4K_1(1 + K_1)}{\Delta_1} + \eta\left(\frac{4 + K_1(4 - 2K_1)}{\Delta_2}\right)$$

$$\gamma_2 = \frac{8K_1^2 - K_1 - 1}{\Delta_1} + \eta\left(\frac{K_1^3 + K_1^2 - 8K_1}{\Delta_2}\right)$$

$$= \frac{K_1(8K_1 - 1) - 1}{\Delta_1} + \eta\left(\frac{K_1\left[K_1(K_1 + 1) - 8\right]}{\Delta_2}\right)$$

$$\delta_2 = \frac{-4K_1^2 + 2K_1}{\Delta_1} + \eta\left(\frac{-2K_1^3 + 4K_1^2}{\Delta_2}\right)$$

$$= \frac{2K_1(1 - 2K_1)}{\Delta_1} + \eta\left(\frac{2K_1^2(2 - K_1)}{\Delta_2}\right)$$

$$\lambda = \frac{t/d - \mu}{\xi_1}$$

t = target thickness
d = projectile diameter

Table 2-6. Normal Impact Lateral Damage Model

- Equation number: 2-8

$\alpha_2, \beta_2, \gamma_2, \delta_2, \xi_1, \mu$ —see equation 2-7

- Basic form:

$$NIMLD = \begin{cases} C_0 \\ C_1 \cdot d \left[\alpha_1 \, (t/d)^4 + \beta_1 \, (t/d)^3 + \gamma_1 \, (t/d)^2 + \delta_1 \, (t/d) + \epsilon_1\right] \\ C_2 \end{cases}$$

$$\begin{aligned} t/d &< \mu \\ \mu &\leq t/d \leq \mu + \xi_1 \\ t/d &> \mu + \xi_1 \end{aligned}$$

$$\alpha_1 = \frac{\alpha_2}{(\xi_1)^4}$$

$$\beta_1 = \frac{\beta_2}{(\xi_1)^3} - \frac{4\mu\alpha_2}{(\xi_1)^4}$$

- Calculation form:

$$NIMLD = C_1 \cdot d \left[\epsilon_1 + (t/d)\left\{ \delta_1 + (t/d)\left[\gamma_1 + (t/d)\left(\beta_1 + \alpha_1 \cdot t/d\right)\right]\right\}\right]$$

$$\gamma_1 = \left(\frac{\gamma_2}{(\xi_1)^2}\right) - \left(\frac{3\mu\beta_2}{(\xi_1)^2}\right) + \left(\frac{6\mu^2\alpha_2}{(\xi_1)^4}\right)$$

- Input and constants:

C_0 from equation 2-14

C_1 from equation 2-12

C_2 from equation 2-13

$$\delta_1 = \frac{\delta_2}{(\xi_1)} - \frac{2\mu\gamma_2}{(\xi_1)^2} + \frac{3\mu^2\beta_2}{(\xi_1)^3} - \frac{4\mu^3\alpha_2}{(\xi_1)^4}$$

$$\epsilon_1 = -\left(\frac{\mu\delta_2}{(\xi_1)}\right) + \frac{\mu^2\gamma_2}{(\xi_1)^2} - \frac{\mu^3\beta_2}{(\xi_1)^3} + \frac{\mu^4\alpha_2}{(\xi_1)^4}$$

Table 2-6a. Constants for NIMLD Equation

Material and projectile	α_1	β_1	γ_1	δ_1	ϵ_1
.30-caliber armor-piercing $K_p = 1.0$					
2024-T3	-27.693	76.150	-74.152	29.033	-2.929
2024-T81	-30.539	83.535	-80.633	31.032	-3.107
7075-T6	-32.782	89.336	-85.697	32.578	-3.243
6Al-4V mill anneal (Ti)	-124.320	238.604	-150.958	42.869	-2.904
.30-caliber ball $K_p = 2.1$					
2024-T3	-29.838	81.720	-79.044	30.544	-3.064
2024-T81	-31.700	86.539	-83.258	31.835	-3.178
7075-T6	-32.880	89.588	-85.916	32.645	-3.249
.50-caliber armor-piercing and ball $K_p = 2.1$					
2024-T3	-29.838	81.720	-79.044	30.544	-3.064
2024-T81	-31.700	86.539	-83.258	31.835	-3.178
7075-T6	-32.880	89.588	-85.916	32.645	-3.249
6Al-4V (Ti)	-129.052	247.199	-166.205	43.972	-2.969

Material	K_m	μ	ξ_1
2024-T3	1	0.15	0.70
2024-T81	2.2	0.15	0.70
7075-T6	5.1	0.15	0.70
6Al-4V	1.80	0.10	0.50

Table 2-7. High-Velocity Lateral Damage

- Equation number: 2-9

- Basic forms:

$$HVLD = d\left[C_3 + 0.6 \, (t/d)^2\right]; \quad HVLD^* = 3/4\left(HVLD\right)$$

- Input and constants:

d = projectile diameter

t = target thickness

Material	C_3
2024	1.5
7075-T6 6Al-4V	1.75

Table 2-8. K_θ Correction—7075-T6 Aluminum

- Equation number: 2-10

- Basic form:

$$K_\theta = \begin{cases} h_1 & t/d < \xi_3 \\ \alpha_3\,(t/d)^3 + \beta_3\,(t/d)^2 + \gamma_3\,(t/d) + \delta_3 & t/d > \xi_3 \end{cases}$$

- Calculation form:

$$K_\theta = \left\{ \delta_3 + (t/d)\left[\gamma_3 + (t/d)\left(\beta_3 + (t/d)\cdot\alpha_3 \right)\right]\right\}$$

- Input and constants (in order of use):

Projectile	C_{10}	ξ_3
.30-caliber armor-piercing	0.005	0.21
.30-caliber ball	0	∞
.50-caliber armor-piercing	0.001	0.35

θ = impact angle
t = target thickness
d = projectile diameter

$h_1 = C_{10}\theta + 1.0$

$h_2 = 1.0 + 2.85\,(\theta/60)^2 - 1.90\,(\theta/60)^3$

$\xi_2 = [1.0 - 0.00429\,\theta]\,(d/.30)^{0.5}$

$K_2 = \xi_3/\xi_2$

$\tau = \dfrac{h_1 - h_2}{(1 - K_2)^3}$

$\alpha_3 = \dfrac{2\tau}{(\xi_2)^3}$

$\beta_3 = \dfrac{-3(1 + K_2)\tau}{(\xi_2)^2}$

$\gamma_3 = \dfrac{6K_2\tau}{(\xi_2)}$

$\delta_3 = h_1 - \left[(K_2)^2(3 - K_2)\tau\right]$

Table 2-9. K_θ Correction for 2024 Aluminum and 6Al-4V Titanium

- Equation number: 2-11

- Basic form:

$$K_\theta = \begin{cases} h_1 & t/d < \xi_3 \\ \alpha_3\,(t/d)^3 + \beta_3\,(t/d)^2 + \gamma_3\,(t/d) + \delta_3 & \xi_3 < t/d < \xi_2 \\ h_3 + \dfrac{(1 - h_3)\,(t/d - \xi_2)^2}{(4.5 - h_3)^2} & \xi_2 < t/d \end{cases}$$

- Calculation form:

$$K_\theta = \left\{ \delta_3 + (t/d)\left[\gamma_3 + (t/d)\left(\beta_3 + (t/d)\alpha_3 \right)\right]\right\}$$

- Inputs and constants (in order of use):

Material and projectile	C_{10}	C_{11}	C_T	ξ_3	ξ_2	K_2
2024	0.0167	0.03	1.0	0.4	0.6	0.667
6Al-4V	0.08	0.025	—	0.1	0.3	0.333
.30-caliber armor-piercing			1.0			
.50-caliber armor-piercing and ball			0.5			

$h_1 = C_{10}\theta C_T + 1.0$

$h_2 = C_{11}\theta C_T + 1.0$

$K_2 = \xi_3/\xi_2$

$\tau = \dfrac{(h_1 - h_2)}{(1 - K_2)^3}$

$\alpha_3 = \dfrac{2\tau}{(\xi_2)^3}$

$\beta_3 = \dfrac{-3(1 + K_2)\tau}{(\xi_2)^2}$

$\gamma_3 = \dfrac{6K_2\tau}{(\xi_2)}$

$\delta_3 = h_1 - \left[(K_2)^2(3 - K_2)\tau\right]$

(a) .30-CALIBER, ARMOR-PIERCING AND BALL

(b) .50-CALIBER ARMOR-PIERCING AND BALL
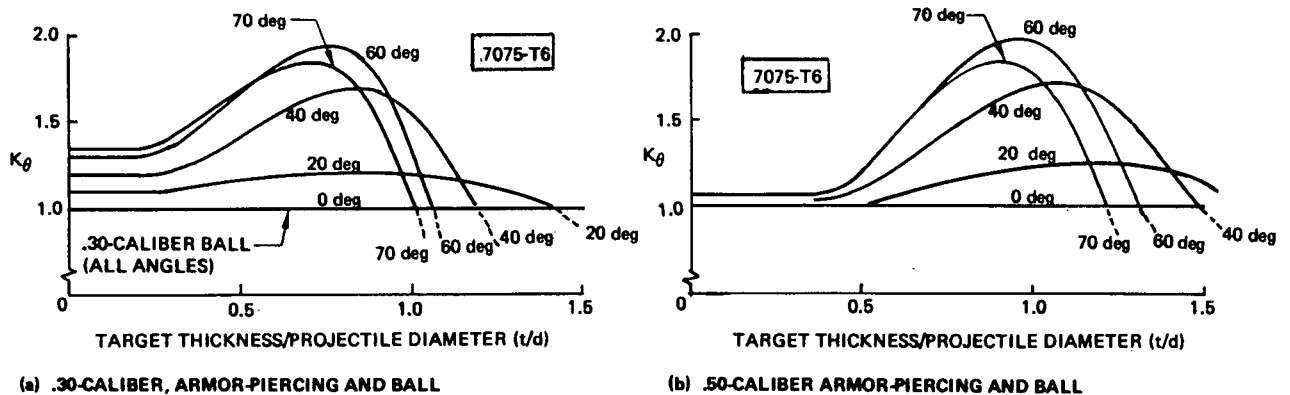
Figure 2-37. K_θ for 7075-T6 Aluminum (See Ref. 2-2 For Other Materials)

Table 2-10. NIMLD Constants C_0, C_1, C_2

- Equation numbers: 2-12, 2-13, 2-14

- Basic form:

  Thin-section NIMLD $= C_0 = 1.0 + K_m (0.40)$ (2-14)

  Principal NIMLD $= C_1 = 1.0 + 1.9 K_p K_m$ (2-12)

  Thick-section NIMLD $= C_2 = 1.0 + 0.45 K_m$ (2-13)

- Constants:

Projectile	K_p
.30-caliber armor-piercing	1.0
.30-caliber ball	2.1
.50-caliber armor-piercing	2.1
.50-caliber ball	2.1

Target material	K_m
Aluminum 2024-T3	1.0
2024-T81	2.2
7075-T6	5.1
Titanium 6Al-4V mill anneal	1.8
6Al-4V special anneal	1.85
6Al-1V-1Mo duplex anneal	2.75
8Al-1V-1Mo mill anneal	3.0

Table 2-11. Constants C_0, C_1, C_2, C_3

Material and projectile	C_0	C_1	C_2	C_3
.30-caliber armor-piercing				
2024-T3	1.4	2.9	1.45	1.5
2024-T81	1.9	5.1	2.0	1.5
7075-T6	3.0	10.6	3.3	1.75
6Al-4V mill anneal	1.7	4.4	1.8	1.75
.30-caliber ball				
2024-T3	1.4	5.0	2.0	1.5
2024-T81	1.9	9.8	3.1	1.5
7075-T6	3.0	21.5	5.8	1.75
.50-caliber armor-piercing and ball				
2024-T3	1.4	5.0	2.0	1.5
2024-T81	1.9	9.8	3.1	1.5
7075-T6	3.0	21.5	5.8	1.75
6Al-4V mill anneal	1.7	8.2	2.7	1.75

Sample Calculation

The use of the damage model is best demonstrated by the following example calculation of the damage resulting from a .30 caliber bullet impacting a wing panel. The conditions are:

Projectile: .30 caliber AP, $K_p = 1.0$ (Table 2-10),

Impact Velocity: 2080 ft/s,

Impact Angle: 59.7 degrees,

Target Material: 7075-T6 aluminum, $K_m = 5.1$ (Table 2-10),

Target Thickness: 0.090 inches.

The calculation procedure is:

1. Calculate $t/d = 0.090/0.300 = 0.30$

2. Determine K_θ from Table 2-8, noting that $t/d = 0.3$ is greater than $\xi_3 = 0.21$.

$C_{10} = 0.005$

$h_1 = 1.0 + (0.005) (59.7) = 1.299$

$h_2 = 1.0 + 2.85 \left(\frac{59.7}{60}\right)^3 - 1.9 \left(\frac{59.7}{60}\right)^3 = 1.95$

$\xi_2 = \left[1.0 - (0.00429) (59.7) \right] (30/30)^{1/2} = 0.744$

$K_2 = \frac{0.21}{0.744} = 0.282$

$\tau = \frac{1.299 - 1.950}{(1-0.282)^3} = -1.762$

$\alpha_3 = \frac{(2) (-1.762)}{(0.744)^3} = -8.561$

$\beta_3 = \frac{(3) (1 + 0.282) (-1.762)}{(0.774)^2} = 12.250$

$\gamma_3 = \frac{(6) (0.282) (-1.762)}{(0.774)} = -4.012$

$\delta_3 = 1.299 - \left[(0.282)^2 (3-0.282) (-1.762) \right] = 1.680$

$K_\theta = \delta_3 + (t/d) \left\{ \gamma_3 + (t/d) \cdot \left[\beta_3 + (t/d) \alpha_3 \right] \right\}$

$= 1.680 + (0.30) \left\{ -4.012 + (0.30) \left[12.250 + (0.30) (-8.561) \right] \right\}$

$= 1.348$

3) Calculate C_1 from Table 2-10, noting that t/d is greater than $\mu = 0.15$.

$$C_1 = 1.90 \, K_p K_m + 1 = (1.90)(1.0)(5.1) + 1 = 10.6$$

4) Calculate NIMLD from Table 2-6 using constants from Table 2-6a.

$$NIMLD = C_1 d \left[\xi_1 + (t/d) \left\{ \delta_1 + (t/d) \left[\gamma_1 + (t/d)(\beta_1 + \alpha_1 \, (t/d)) \right] \right\} \right]$$

$$= (0.300)(10.6) \left\{ -3.243 + (0.3) \left\{ 32.578 + (0.3) \left[-85.697 \right. \right. \right.$$
$$\left. \left. \left. + (0.30)(89.336 + (0.3)(-32.782)) \right] \right\} \right\}$$

$$= 3.06 \text{ inches}$$

5) Calculate HVLD from Table 2-7:

$$HVLD = d \, (C_3 + 0.6 \, (t/d)^2) = 0.300 \, (1.75 + 0.6 \, (0.300)^2)$$

$$= 0.541 \text{ inches}$$

6) Calculate V_1, V_2, and V_3 (see Table 2-4):

$$V_1 = 650 \ln (0.30) + 750 = -782 + 750 = -32 \text{ ft/s}$$

$$\text{Use} \quad V_1 = V_1 = 100 \text{ ft/s} \quad \text{(a limiting value)}$$

$$V_2 = 725 \ln (0.30) + 1580 = 707.1 \text{ ft/s}$$

$$V_3 = 1125 \ln (0.30) + 3250 = 1895.5 \text{ ft/s}$$

$$V_3 - V_1 = 1795.5 \text{ ft/s}$$

$$V^* = V \, (\cos \theta)^{0.7} - V_1 = 2080 \, (\cos 60)^{0.7} - 100 = 1180 \text{ ft/s}$$

$$v = \frac{1180}{1795.5} + 0.657$$

$$\psi = \frac{HVLD}{NIMLD-K_\theta} = 0.131$$

$$\frac{V_2 - V_1}{V_3 - V_1} = 0.338$$

7) Calculate K_3 (see Table 2-3):

Obtain solution of: $\left\{ K_3^4 \psi - 4K_3^3 \psi + 6K_3^2 \psi - 4K_3 + 1 = 0 \right\} = 0.261$

Obtain solution of: $\left\{ -2K_3 + 1 + \psi \, K_3^2 (K_3 - 2) = 0 \right\} = 0.513$

Since $0.261 < 0.338 < 0.513$

$$K_3 = 0.338$$

8) Calculate remaining constants defined in Table 2-1:

$$\Delta_3 = (0.338)^2 (1 - 0.338)^3 = 0.033$$

$$\Delta_4 = (1.0 - 0.338)^3 = 0.290$$

$$\alpha_4 = \frac{(3)(0.338) - 1}{0.033} + (0.131) \frac{0.338 - 3}{0.290} = -0.788$$

$$\beta_4 = \frac{(-4)(0.338)^2 - (4)(0.338) + 2}{0.033} + (0.131) \frac{(-2)(0.338)^2 + (4)(0.338) + 4}{0.290}$$

$$= 8.073$$

$$\gamma_4 = \frac{(8)(0.338)^2 - 0.338 - 1}{0.033} + (0.131) \frac{(0.338)^3 + (0.338)^2 - 8(0.338)}{0.290}$$

$$= -13.944$$

$$\delta_4 = \frac{-4(0.388)^2 + 2(0.338)}{0.033} + (0.131) \frac{-2(0.388) + 4(0.338)^4}{0.290}$$

$$= 6.780$$

9) Calculate the Upper Limit on Lateral Damage (see Table 2-1):

$$LD_{UL} = (3.06)(1.35)(0.657) \left[6.780 + (0.657) \left\{ -13.944 + (0.657) \left[8.073 + (0.657)(-0.778) \right] \right\} \right]$$

$$LD_{UL} = 2.39 \text{ inches}$$

10) Calculate coefficients for Lower Limit on Lateral Damage

V_1^* = 100 + 200 = 300 ft/s

$V_3-V_1^*$ = 1595.5 ft/s

V^* = 2080 (cos 59.7)$^{0.7}$ -300 = 980 ft/s

v = 980/1595.5 = 0.614

HVLD* = 3/4 (0.541) = 0.406 inches

NIMLD* = 0.406 + 1/4(3.06-0.406) = 1.070 inches

ψ = 0.406/1.070 = 0.379

K_3 = 0.289

Δ_3 = 0.030

Δ_4 = 0.359

α_4 = -7.289

β_4 = 22.246

γ_4 = -23.005

δ_4 = 8.427

11) Calculate the Lower Limit on the Lateral Damage (see Table 2-2)

$$LD_{LL} = (1.07)(0.614) \left[8.427 + \frac{(0.614)}{[22.246 + (0.614)(-7.289)]} \right] (-23.005 + (0.614)$$

= 0.658 inches

In Reference 2-2, upper- and lower-limit damage prediction curves were calculated and graphed by computer for conditions listed below. Figure 2-38 is an example of the type of graph. The conditions graphed were:

Projectiles: .30-caliber AP,
                  .30-caliber ball,
                  .50-caliber AP and ball;
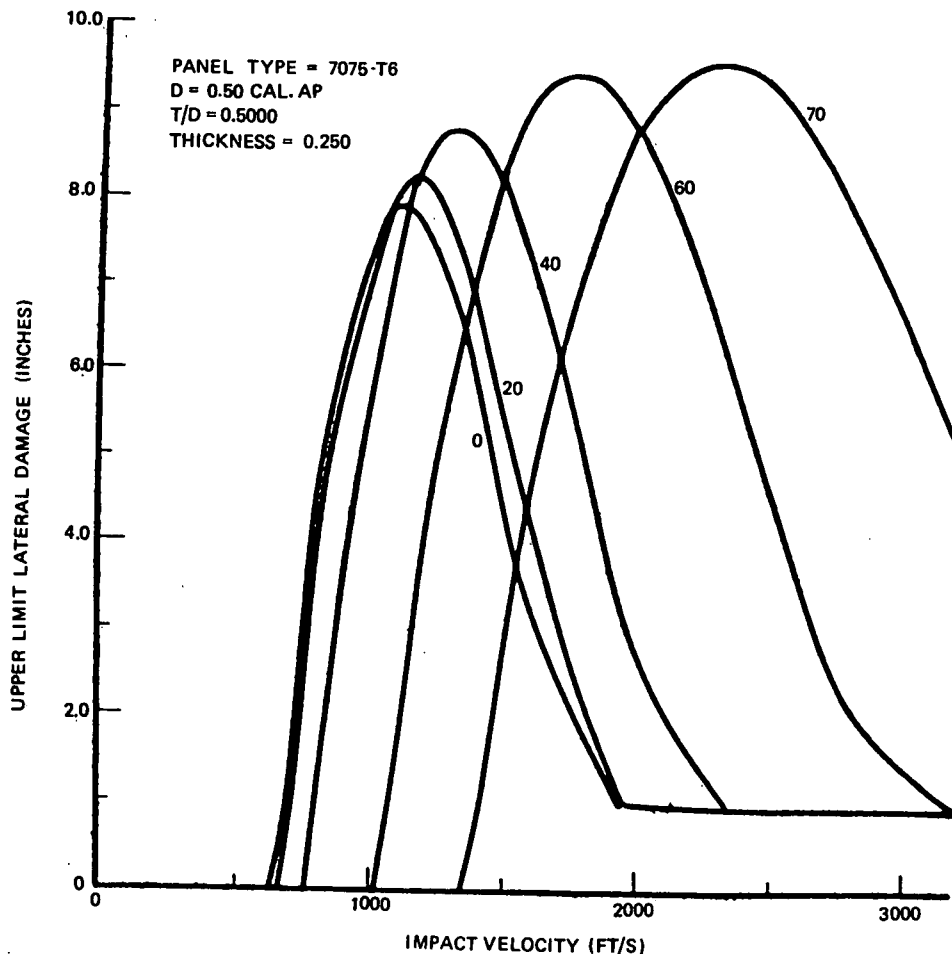
Figure 2-38. Sample Damage Prediction From LATDAM Model

Materials:	2024-T3 aluminum, 2024-T81 aluminum, 7075-T6 aluminum, 6AL-4V titanium (except .30-caliber ball);
Thickness:	0.032, 0.063, 0.090, 0.125, 0.160, 0.190, 0.250, 0.375, 0.500, 0.750, 1.000 inches;
Impact Angles:	0, 20, 40, 60, and 70 degrees.

As a convenience, the upper-limit damage-size predictions have been reformulated in terms of maximum upper-limit damage for varying panel gages over a specified velocity range. The results are presented in Figures 2-39 through 2-42. These curves provide a condensation of the prediction curves in Reference 2-2. This is made possible by transforming the velocity variation into a velocity range (0 to 3200 ft/s), and plotting the maximum damage within the range.

Test data reported in Reference 2-7 have been used to extend the damage size prediction capability of Reference 2-2 to additional structural materials and several foreign projectiles. A limited number of damage evaluation tests were conducted using the following materials:

7475-T761, 7475-T61, 2219-T87,	4130 steel (83 ksi), 4130 steel (178 ksi).

Based on analysis of the data in Reference 2-7, it appears that the maximum damage in 7475-T61, 7475-T761, 2219-T87 and 4130 (83 ksi) is approximately one-half that of 7075-T6 for identical small arms projectile impacts. On the same comparison basis, 4130 steel heat-treated to 178 ksi, shows maximum damage one and one-half times that of 7075-T6. The latter result demonstrates the effect of heat treatment on damage size in a high-strength steel. These conclusions are tentative, and further test verification is desirable.
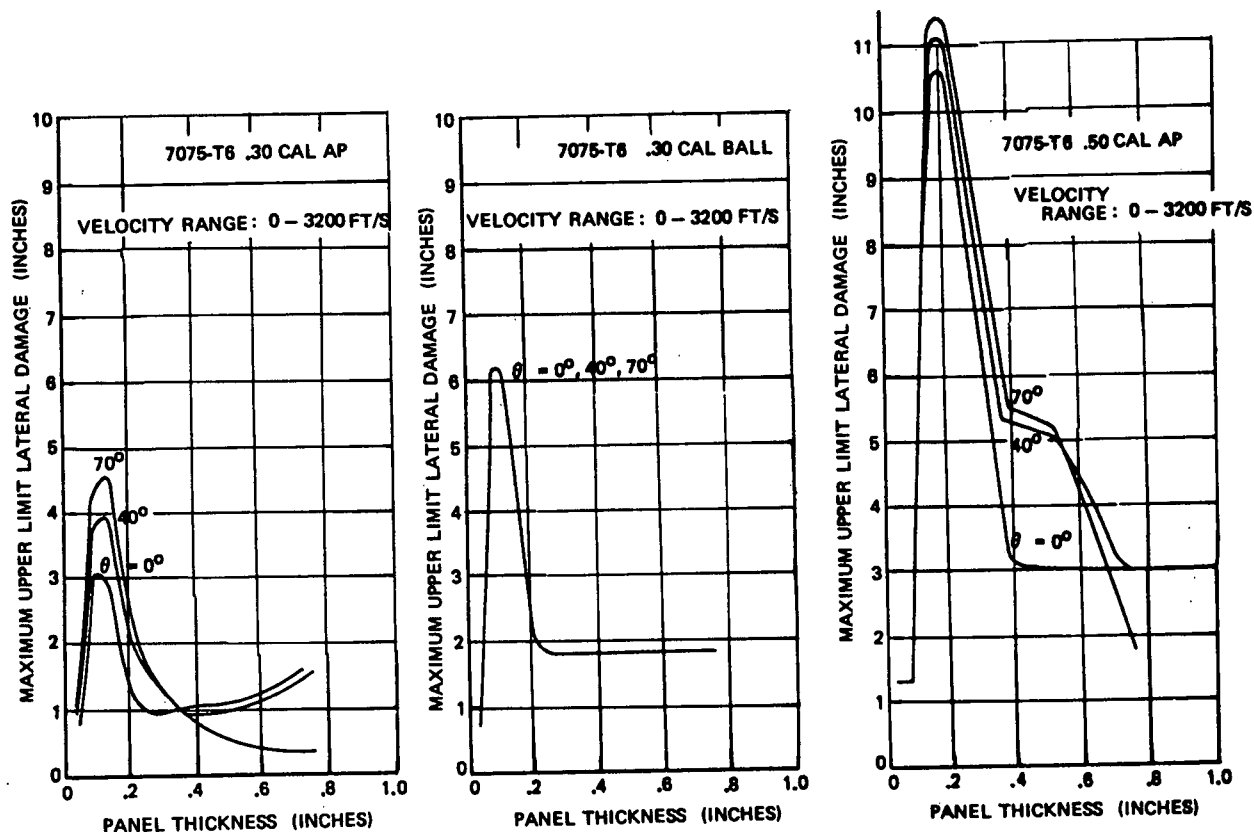
Figure 2-39. Maximum Upper Limit Lateral Damage for 7075-T6
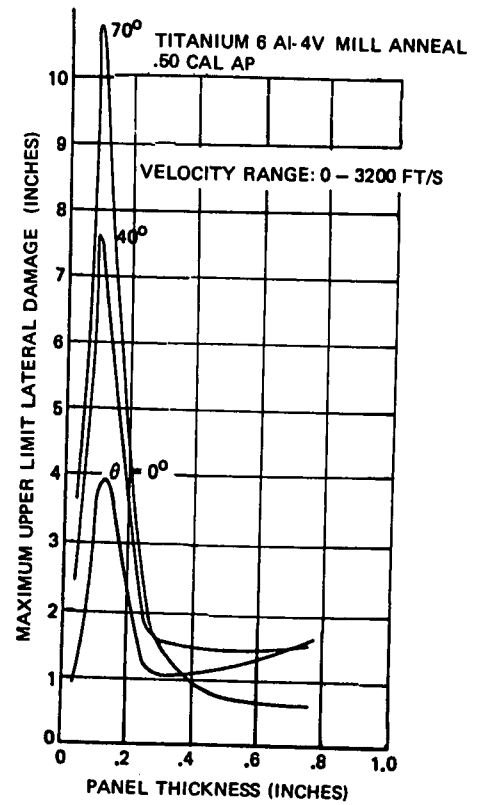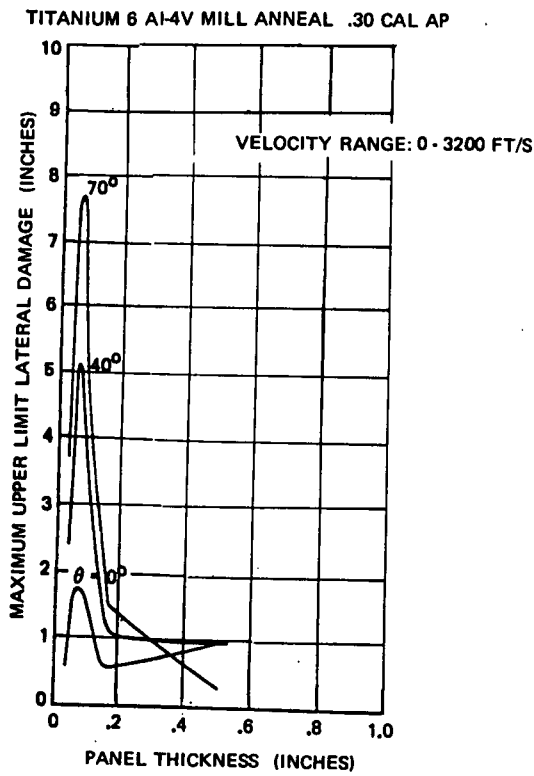
Figure 2-40. Maximum Upper Limit Lateral Damage for Titanium 6 Al-4V Mill Anneal
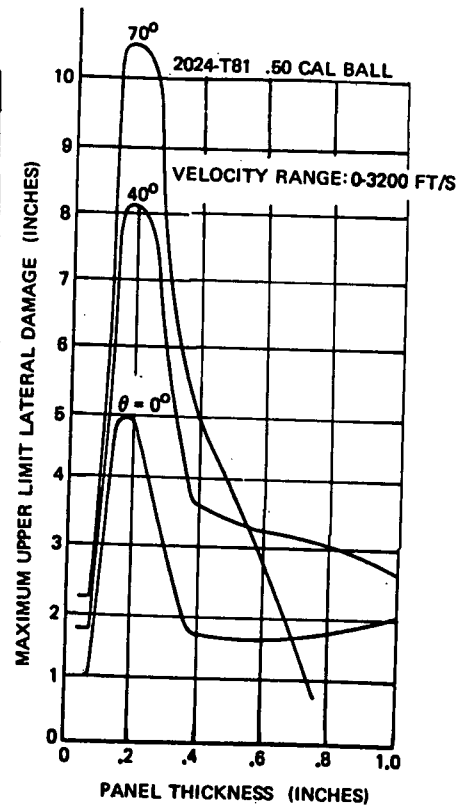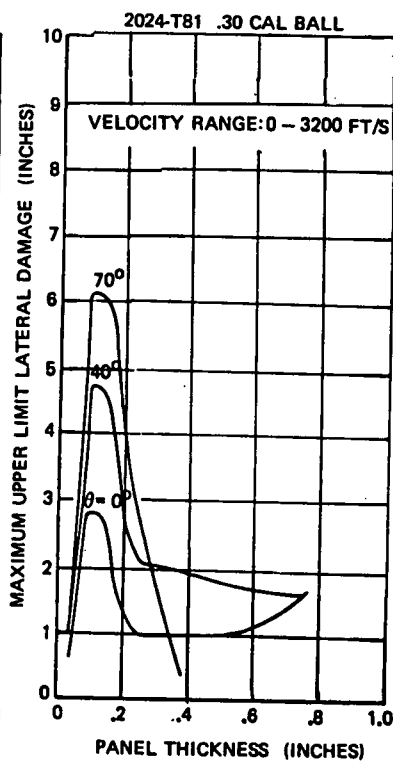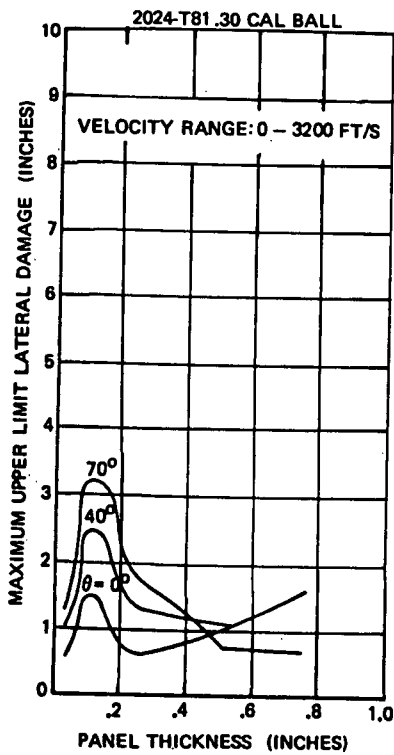
Figure 2-41. Maximum Upper Limit Lateral Damage for 2024-T81
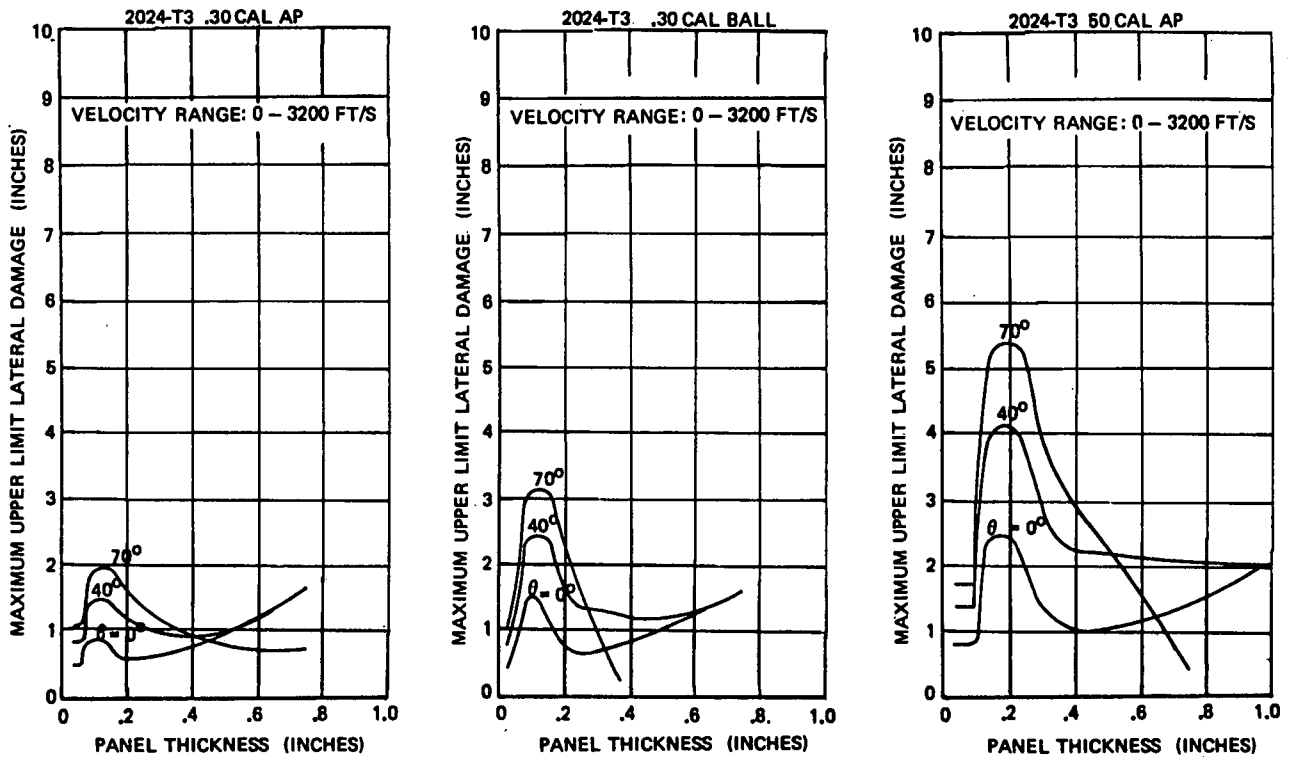
Figure 2-42. Maximum Upper Limit Lateral Damage for 2024-T3

Compact Fragments Impacting Metals - Damage Size Prediction. Photographs of typical damages from compact fragments were shown previously in Figures 2-29 and 2-30. Compact fragments are those having a length to diameter ratio of approximately unity. Damage prediction techniques for fragments impacting metal are not as well developed as the prediction techniques for small arms projectiles. This is partially due to the diversity of fragment sizes and shapes, ranging from cubes to continuous rods. Although the dimensions of preformed or controlled fragments are relatively precise, fragments generated by natural fragmentation have somewhat random shapes.

An analysis model was developed in Reference 2-7 for predicting damage size in aluminum due to singly impacting, high-velocity compact fragments, and verified by ballistic test data available in 1973. In total, the fragment damage data available encompassed two materials (7075-T6, 2024-T3), sheet gages from 0.032 to 0.375 inches, three fragment types (cubes, cylinders, spheres), angles of obliquity from 0 to 80 degrees, and velocities up to 6,000 feet per second. The model is described below, and should be applicable to low-density fragment impacts from missile warheads, particularly surface-to-air missiles. High-density impacts induce interactions between adjacent damages, and there is currently no general method available for quantifying the resulting damage.

As explained in Reference 2-7, examination of the fragment damage data indicated that the lateral damage is essentially independent of projectile velocity in the high-velocity range (2,000 to 6,000 ft/s). This behavior is similar to that established for small arms projectiles in Reference 2-2. The data also indicated that material effects were not pronounced in this range, as the damage sizes for 2024-T3 and 7075-T6 were nearly the same. These observations led to the development of a fragment damage model for aluminum alloys similar in form to the high-velocity damage model for small arms projectiles given in Reference 2-2. The final expression is:

$$LD = \frac{L_p}{\cos\theta} \left[1.16 + 0.6 \left(\frac{t}{L_p} \right)^2 \right] , \qquad \text{(Eqn. 2-15)}$$

where:

LD = lateral damage size (inches),

L_p = the maximum projected frontal dimension of the fragment (inches),

θ = obliquity angle, measured between the flight path and a normal to the target surface,

t = target thickness (inches).

The parameter L_p depends on both the size and shape of the fragment. For example, L_p equals the diameter when the fragment is spherical; when the fragment is a cube, L_p equals $\sqrt{3}$ times the length of a side. For a cylinder having a length-to-diameter ratio of unity, L_p equals $\sqrt{2}$ times the diameter. Figure 2-43 shows the L_p equations for several common shapes.

Approximately 60 data points were available for establishing the validity of the model predictions, as shown in Figure 2-44. The correlation is considered to be good, considering the several sources of data and the extent of scatter usually found in damage-size test data.

PROJECTILE	CONFIGURATION	MAXIMUM PRESENTED LENGTH, L_p	PROJECTILE	IDEALIZED SHAPE	MAXIMUM PRESENTED LENGTH, L_p
CUBE		$L_p = \sqrt{3}L$	SPHERE		$L_p = d$
ROD		$L_p = \sqrt{a^2 + b^2 + c^2}$	CYLINDER		for L/d = 1: $L_p = \sqrt{2}\,d$ for L/d ≠ 1 $L_p = \sqrt{d^2 + L^2}$
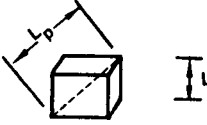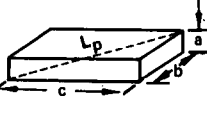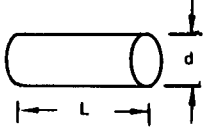
Figure 2-43. Presented Lengths for Common Projectiles.

□ STEEL CUBES, 2600–5200 ft/s;
$\theta = 0, 30, 60°$;
0.063–0.250 7075-T6

■ STEEL CUBES, 2300–5045 ft/s;
$\theta = 0, 30, 60°$
0.063–0.250 2024-T3

● STEEL SPHERES, 3000–6000 ft/s;
$\theta = 0, 45, 50, 60, 70, 80°$
0.125 2024-T3

△ STEEL CYLINDERS (LENGTH/DIAMETER = 1)

LATERAL DAMAGE PREDICTION:

$$LD = \frac{L_p}{\cos\theta}\left[1.16 + 0.6\left(\frac{L}{L_p}\right)^2\right]$$
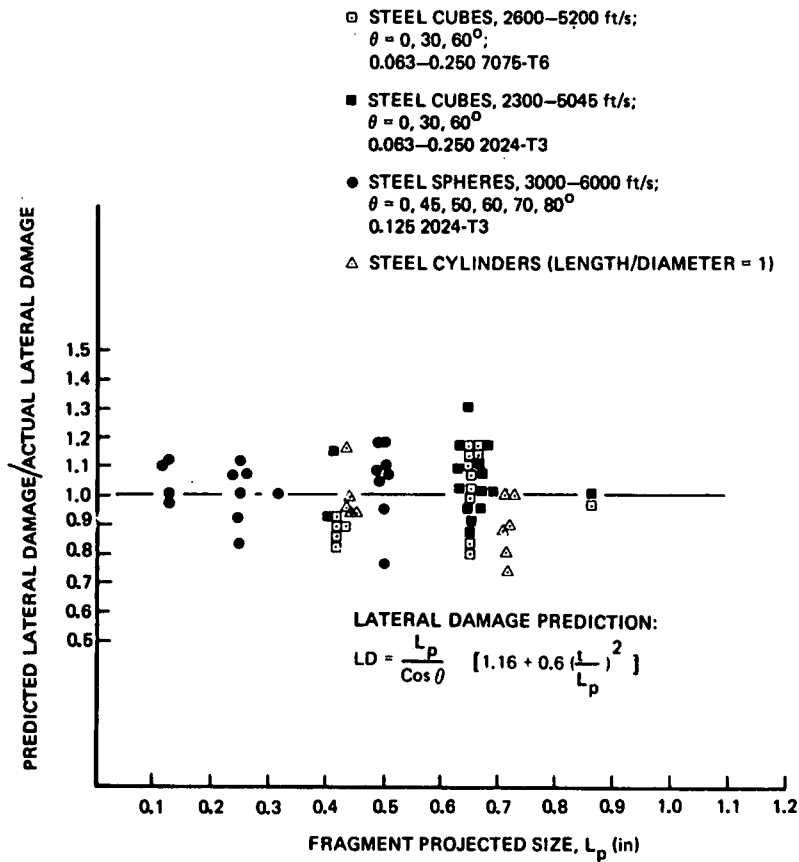
Figure 2-44. Verification of Damage Size Predictions for Compact Fragments Impacting Aluminum

2.2.1.1.3 Non-Exploding Penetrators Impacting Metals - Damage Type Prediction.

Reference 2-2 presents a model for estimating the type of damage resulting from various impact/target conditions. Damage type refers to whether the damage is a clean hole, a hole surrounded by a spalled area, a petalled hole, a crack, or a gouge. The model is presented in the form of the regime diagram shown in Figure 2-45, which correlates damage type with projectile impact velocity and target thickness (or t/d ratio). The input parameters are:

Impact velocity,	Target material,
Obliquity angle,	Projectile size and type.
Target thickness,	

The damage type model is limited to .30 caliber AP projectiles impacting 7075-T6 aluminum. Only two obliquity angles are presented; interpolation techniques can be used for other angles. The normalized sheet thickness, t/d, can be used to extend this diagram to other fully-jacketed AP projectiles.

2.2.1.1.4 Non-Exploding Penetrators Impacting Metals - Damage Orientation Prediction.
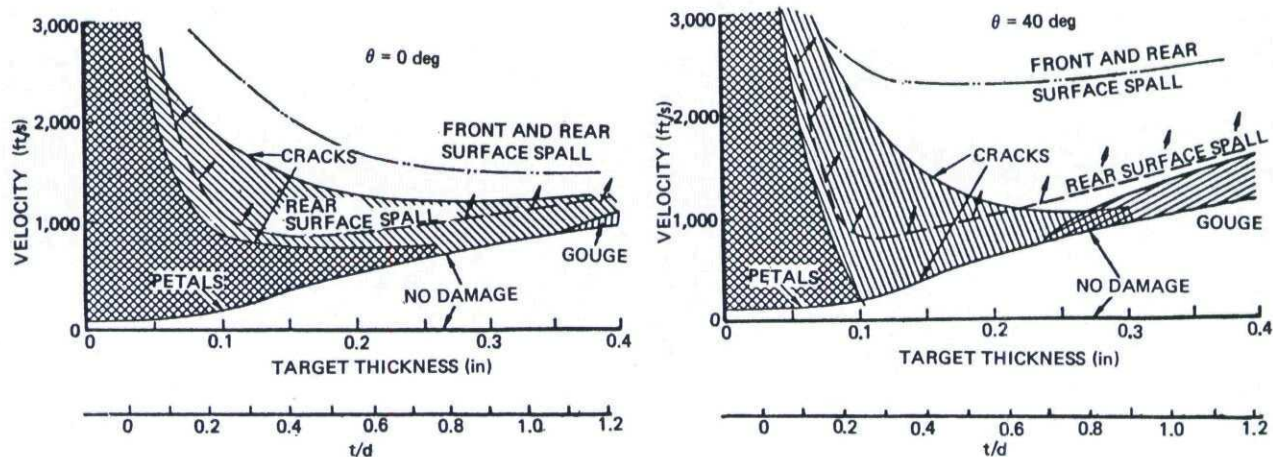
Figure 2-45. Damage Type Regime Diagrams (Small-Arms Projectiles Impacting 7075-T6)

A technique for estimating the probable orientation of the largest damage dimension is given in Reference 2-2. This technique is represented in the data presented in Tables 2-12, 2-13, and 2-14. The tables give probabilities for the largest damage direction to be oriented:

1. Within ±30 degrees of a direction, Q, defined below;
2. Within ±30 degrees of a normal to the Q-direction;
3. Within ±15 degrees of a line 45-degrees from the Q-direction.

The directions, Q, selected for the assessment were:

1. Maximum damage parallel to support direction;
2. Maximum damage parallel to flight path;
3. Maximum damage normal to applied stress.

The tables were formulated from the results of small arms and cylindrical projectiles impacting 7075-T6 aluminum alloy. The tables are used by locating similar impact combinations within the tables. Most combinations of applied stress direction, material grain direction, and support direction will be found, except for the case where all three are parallel. No test data were available for this condition. In addition, the oblique impact tests consisted of flightpaths that were, (1) parallel to the support direction; (2) normal to the applied stress direction (when stressed), and (3) either parallel or normal to the grain directions.

The pertinent data from Table 2-12 shows a 0.52 probability for the largest damage to be parallel to the flight path. The influence of stress field, shown by the data of item D in Table 2-12, indicates a 0.44 probability of the damage being normal to the stress field. However, the combination of parallel grain and support directions provide a 0.67 probability for the damage to parallel the grain (see item A-2 of Table 2-13), perpendicular to the direction indicated by the stress. It is believed that for these impact conditions, the effect of stress and support conditions will counteract each other and the relative flight path will be more influential. Thus, the most likely orientation of the maximum damage will be about 65-degrees from the grain. The probability associated with this should be 0.52.

66

Table 2-12. Probable Lateral Damage Orientation - 7075-T6 Aluminum

CONDITIONS & DATA SOURCE	PROBABILITY OF MAXIMUM LATERAL DAMAGE ORIENTATION				NUMBER OF TESTS
	WITHIN ±30° OF DIRECTION Q	+15° OF 45° FROM DIRECTION Q	+30° OF ⊥ TO DIRECTION Q	NO ORIENTATION PREFERENCE	
A) UNSTRESSED TARGETS - NORMAL IMPACT					
1. GRAIN ⊥ TO Q					
α	.155	.232	.525	.088	181
γ	.282	.487	.205	.026	39
δ	.333	.111	.556	-	18
AVERAGE	.189	.265	.475	.071	238
2. GRAIN ∥ TO Q					
α	.375	.500	.125	-	8
β	.833	.125	-	.042	24
δ	.667	.242	.030	.061	33
AVERAGE	.692	.231	.031	.046	65
3. TOTAL - NEGLECTING GRAIN DIRECTION					
α	.164	.243	.508	.085	189
β	.833	.125	-	.042	24
γ	.282	.487	.205	.026	39
δ	.549	.196	.216	.039	51
AVERAGE	.297	.257	.380	.066	303
B) UNSTRESSED TARGETS - OBLIQUE IMPACT - IMPACT ∥ TO Q					
1. GRAIN ⊥ TO Q					
α	.469	.257	.263	.011	179
γ	.400	.360	.240	-	25
δ	.348	.043	.347	.261	23
AVERAGE	.449	.247	.269	.035	227
2. GRAIN ∥ to Q					
δ	.676	.162	-	.162	37
3. TOTAL - NEGLECTING GRAIN DIRECTION					
α	.469	.257	.263	.011	179
γ	.400	.360	.240	-	25
δ	.550	.117	.133	.200	60
AVERAGE	.481	.235	.231	.053	264

CONDITIONS & DATA SOURCE	PROBABILITY OF MAXIMUM LATERAL DAMAGE ORIENTATION				NUMBER OF TESTS
	WITHIN ±30° OF DIRECTION Q	+15° OF 45° FROM DIRECTION Q	+30° OF ⊥ TO DIRECTION Q	NO ORIENTATION PREFERENCE	
C) STRESSED TARGETS - NORMAL IMPACT - STRESS ⊥ TO Q					
1. GRAIN ∥ TO Q					
β	.863	.100	.012	.025	80
δ	.774	.132	.019	.075	53
AVERAGE	.827	.113	.015	.045	133
2. GRAIN ⊥ TO Q					
β	.300	.400	.300	-	10
γ	.448	.482	.069	-	29
δ	.553	.143	.286	.018	56
AVERAGE	.495	.274	.221	.010	95
3. TOTAL - NEGLECTING GRAIN DIRECTION					
β	.800	.133	.045	.022	90
γ	.448	.483	.069	-	29
δ	.660	.138	.158	.044	109
AVERAGE	.688	.180	.102	.030	228
D) STRESSED TARGET - OBLIQUE IMPACT, IMPACT ∥ TO Q, STRESS ⊥ TO Q					
1. GRAIN ∥ TO Q					
δ	.865	.054	-	.081	37
2. GRAIN ⊥ TO Q					
γ	.438	.281	.281	-	32
3. TOTAL - NEGLECTING GRAIN DIRECTION					
AVERAGE	.667	.159	.130	.043	69
A-B TOTAL - IMPACT INTO UNSTRESSED TARGETS					
AVERAGE	.383	.247	.310	.060	567
A-C TOTAL - NORMAL IMPACT					
AVERAGE	.465	.225	.260	.050	531

(CONT)

CONDITIONS & DATA SOURCE	PROBABILITY OF MAXIMUM LATERAL DAMAGE ORIENTATION				NUMBER OF TESTS
	WITHIN ±30° OF DIRECTION Q	±15° OF 45° FROM DIRECTION Q	+30° OF ⊥ TO DIRECTION Q	NO ORIENTATION PREFERENCE	
C-D TOTAL - IMPACT INTO STRESSED TARGETS					
	.683	.176	.108	.033	297
B-D TOTAL - OBLIQUE IMPACT					
	.520	.218	.211	.051	333
A-B-C-D GRAND TOTAL					
α	.312	.250	.389	.049	368
β	.807	.132	.035	.026	114
γ	.384	.408	.200	.008	125
δ	.642	.132	.140	.086	257
AVERAGE	.486	.222	.241	.051	864

α = PHASE II, SERIES A - 8" X 8" TARGET
β = PHASE II, SERIES C - 12" X 36" TARGET } ALL GRIPPED ACROSS NARROW END
γ = REFERENCE (2-8)- 15.9" X 31.9" TARGET
δ = REFERENCE (2-55)- 18" X 36" TARGET

DIRECTION Q IS:
1. PARALLEL TO SUPPORTS OR GRIPS
2. PARALLEL TO RELATIVE FLIGHT PATH
3. NORMAL TO STRESS DIRECTION

Table 2-13. Probable Damage-To-Grain Orientation   7075-T6 Aluminum

Table A & B

CONDITIONS & DATA SOURCE	PROBABILITY OF MAXIMUM LATERAL DAMAGE ORIENTATION				NUMBER OF TESTS
	WITHIN ±30° OF GRAIN DIRECTION	+15° OF 45° FROM GRAIN DIRECTION	+30° OF ⊥ TO GRAIN DIRECTION	NO ORIENTATION PREFERENCE	
A) UNSTRESSED TARGETS - NORMAL IMPACT					
1. GRAIN ⊥ TO SUPPORTS					
α	.525	.232	.154	.088	181
γ	.205	.487	.282	.026	39
δ	.556	.111	.333	-	18
AVERAGE	.475	.265	.189	.071	238
2. GRAIN ∥ TO SUPPORTS					
α	.375	.500	.125	-	8
β	.833	.125	-	.042	24
δ	.667	.242	.030	.061	33
AVERAGE	.692	.231	.031	.046	65
3. TOTAL - NEGLECTING SUPPORT DIRECTION					
α	.508	.243	.164	.085	189
β	.833	.125	.042	.042	24
γ	.205	.487	.282	.026	39
δ	.549	.196	.216	.039	51
AVERAGE	.522	.257	.154	.067	303
B) UNSTRESSED TARGETS - OBLIQUE IMPACT - IMPACT ∥ TO Q					
1. GRAIN ⊥ TO SUPPORTS - IMPACT ACROSS GRAIN					
α	.263	.257	.469	.011	179
γ	.240	.360	.400	-	25
δ	.348	.043	.347	.261	23
AVERAGE	.270	.247	.448	.035	227
2. GRAIN ∥ TO SUPPORTS - IMPACT ALONG GRAIN					
δ	.676	.162	-	.162	37
3. TOTAL - NEGLECTING SUPPORT AND IMPACT DIRECTION					
α	.263	.257	.469	.011	179
γ	.240	.360	.400	-	25
δ	.550	.117	.133	.200	60
AVERAGE	.326	.235	.386	.053	264

Table C & D

CONDITIONS & DATA SOURCE	PROBABILITY OF MAXIMUM LATERAL DAMAGE ORIENTATION				NUMBER OF TESTS
	WITHIN ±30° OF GRAIN DIRECTION	+15° OF 45° FROM GRAIN DIRECTION	+30° OF ⊥ TO GRAIN DIRECTION	NO ORIENTATION PREFERENCE	
C) STRESSED TARGETS - NORMAL IMPACT					
1. STRESS ⊥ TO GRAIN					
β	.863	.100	.012	.025	80
δ	.774	.132	.019	.075	53
AVERAGE	.827	.113	.015	.045	133
2. STRESS ∥ TO GRAIN					
β	.300	.400	.300	-	10
γ	.069	.482	.448	-	29
δ	.286	.143	.554	.018	56
AVERAGE	.221	.274	.495	.010	95
3. TOTAL - NEGLECTING GRAIN DIRECTION					
β	.800	.133	.045	.022	90
γ	.069	.483	.448	-	29
δ	.523	.138	.293	.046	109
AVERAGE	.575	.180	.215	.030	228
D) STRESSED TARGETS - OBLIQUE IMPACT					
1. STRESS ⊥ TO GRAIN, IMPACT ALONG GRAIN					
δ	.865	.054	-	.081	37
2. STRESS ∥ TO GRAIN, IMPACT ACROSS GRAIN					
γ	.281	.281	.438	-	32
3. TOTAL - NEGLECTING GRAIN DIRECTION					
AVERAGE	.595	.159	.203	.043	69
A-B TOTAL - IMPACT INTO UNSTRESSED TARGETS					
AVERAGE	.431	.247	.262	.060	567
A-C TOTAL - NORMAL IMPACT					
AVERAGE	.545	.225	.180	.050	531

Grand Total Table

CONDITIONS & DATA SOURCE	PROBABILITY OF MAXIMUM LATERAL DAMAGE ORIENTATION				NUMBER OF TESTS
	WITHIN ±30° OF GRAIN DIRECTION	+15° OF 45° FROM GRAIN DIRECTION	+30° OF ⊥ TO GRAIN DIRECTION	NO ORIENTATION PREFERENCE	
C-D TOTAL - IMPACT INTO STRESSED TARGETS	.580	.176	.211	.033	297
B-D TOTAL - OBLIQUE IMPACT	.382	.218	.349	.051	333
A-B-C-D GRAND TOTAL					
α	.394	.250	.307	.049	368
β	.807	.132	.035	.026	114
γ	.200	.408	.384	.008	125
δ	.599	.132	.183	.086	267
AVERAGE	.482	.222	.245	.051	864

α = PHASE II, SERIES A - 8" X 8" TARGET
β = PHASE II, SERIES C - 12" X 36" TARGET } ALL GRIPPED ACROSS NARROW END
γ = REFERENCE (2-8) - 15.9" X 31.9" TARGET
δ = REFERENCE (2-55) - 18" X 36" TARGET

Table 2-14. Material Effects on Damage Orientation Phase II - Series A Targets

DAMAGE ORIENTATION	PROBABILITY FOR DAMAGE ORIENTATION									
	ALL MATERIALS NORMAL IMPACT			7075-T6 ONLY NORMAL IMPACT			OTHER THAN 7075-T6 NORMAL IMPACT *	7075-T6 OBLIQUE IMPACT
	A	B	C	A	B	C	A	D
+30° OF GRAIN DIRECTION	.449	.375	.447	.525	.375	.519	.320	.263
+15° FROM 45° TO GRAIN DIRECTION	.247	.500	.253	.232	.500	.243	.276	.257
+30° FROM NORMAL TO GRAIN DIRECTION	.203	.125	.201	.155	.125	.153	.276	.128
NO DIRECTION PREFERENCE	.101	-	.099	.088	-	.085	.128	.011
NUMBER OF TESTS	276	8	284	181	8	189	95	179

A - GRAIN DIRECTION NORMAL TO SUPPORTS
B - GRAIN DIRECTION PARALLEL TO SUPPORTS
C - WEIGHTED AVERAGE OF A AND B
D - GRAIN DIRECTION NORMAL TO SUPPORTS, IMPACT CROSS-GRAIN

ALL TARGETS WERE 8" X 8"

* INCLUDES DATA FROM 2024-T3 ALUMINUM AND 6A1-4V M.A. TITANIUM

2.2.1.2 Non-Exploding Projectiles Impacting Fiber Composites

There have been a number of programs (Ref. 2-9 through 2-12, 2-17, and 2-24 through 2-30) investigating the response of laminated fiber composite structure to projectile impact. These studies have shown that the unique characteristics of composite materials can have a significant influence on damage response, and that damage models developed for metal structure are not applicable. Some of the properties of composite structure that influence projectile damage are (1) orthotropic strength and stiffness characteristics, (2) the low ductility of certain fibers such as graphite/epoxy, and (3) low interlaminar strength. The following sections discuss characteristic damage responses observed in fiber composites, and existing analysis methods for damage size prediction.

2.2.1.2.1 Non-Exploding Projectiles Impacting Fiber Composites – Discussion of Parameters Influencing Damage

The results of examining graphite/epoxy laminates damaged by small arms projectiles and fragments are reported in Reference 2-12. The damage modes illustrated in Figure 2-46 were noted from this examination. They include:

- Perforation,
- Delamination,
- Peeling,
- Fiber buckling,
- Gouging.

Figures 2-47 and 2-48 show representative entrance and exit damages in thin graphite/epoxy and boron/epoxy laminates impacted by fragments and small arms projectiles. The relatively smooth perforation, conforming closely to the shape of the projectile, is characteristic of penetrator damage in thin laminates. The exit surface may often show peeling and splitting.
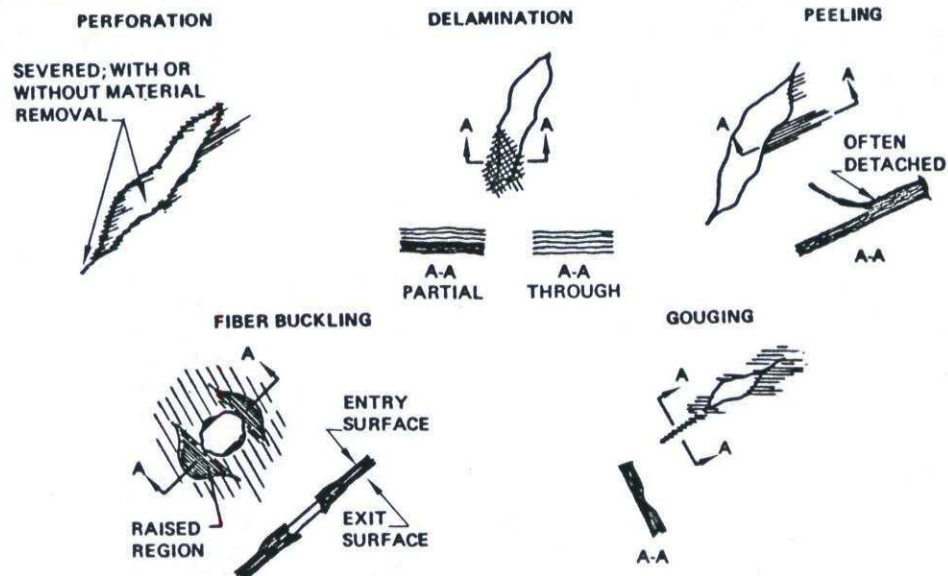
Figure 2-46. Typical Ballistic Damage in Fiber Composites

ENTRY DAMAGE

EXIT DAMAGE
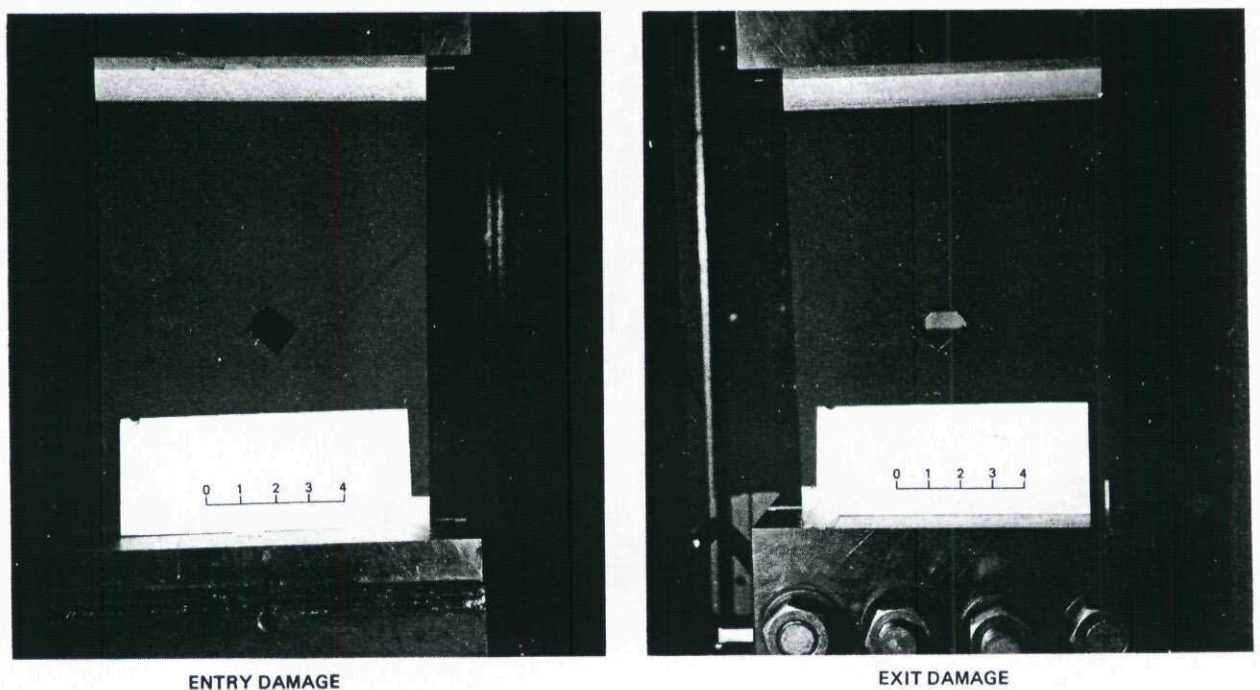
Figure 2-47. Typical Damage in Thin Graphite/Epoxy Laminate Impacted by Fragment
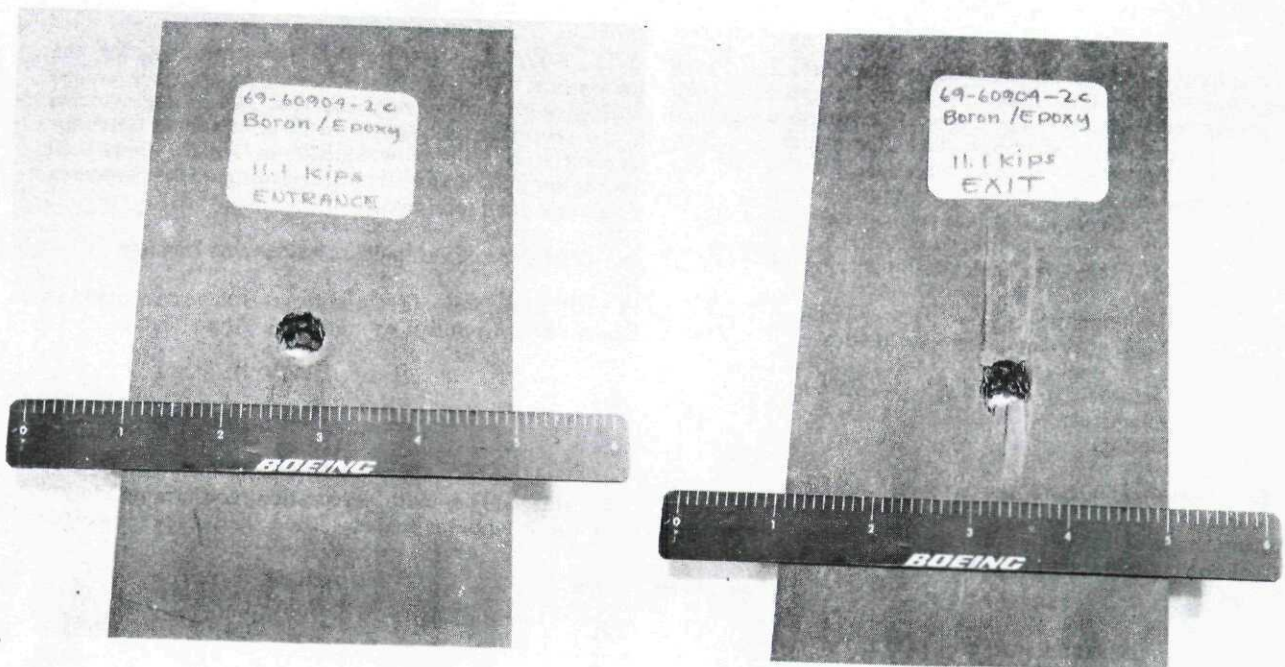
Figure 2-48. Typical Small Arms Projectile Penetration Damage in Boron/Epoxy Sandwich

Delamination in composites results from their relatively low interlaminar strengths, which is largely dependent on the resin, and can be especially significant in reducing the compression strength of impacted laminates. Delamination caused by the penetration of a small arms projectile is shown in Figure 2-49 where the internal delaminations around the perforation were revealed by ultrasonic inspection. The white areas appearing in the scan are delaminations. Holes, removed surface plies, and intact laminate are dark. The figure shows a delaminated area around both the 0-degree obliquity impact damage and the 80-degree obliquity damage. However, the 80-degree impact caused far more delamination than the impact at 0-degree obliquity.
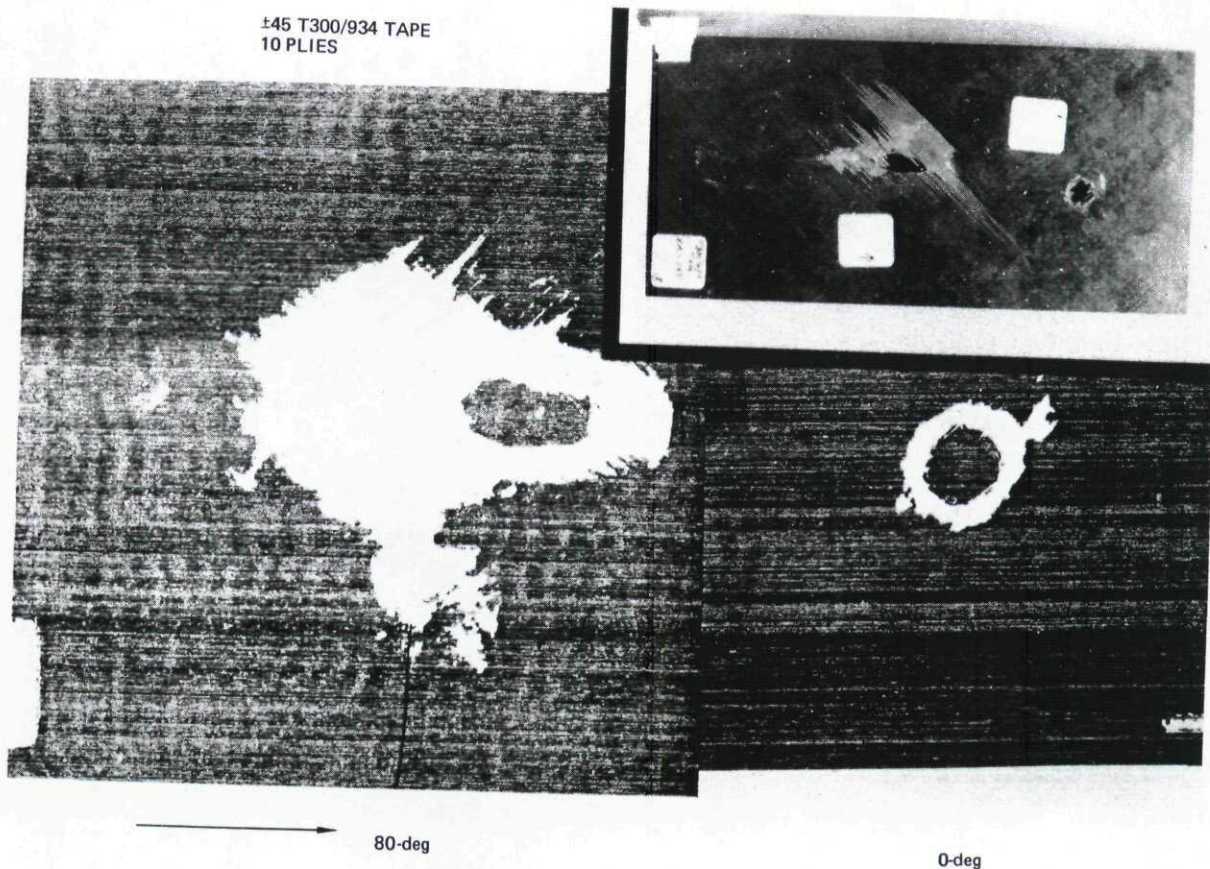
Figure 2-49. Ultrasonic C-Scan of Ballistic Damaged Graphite/Epoxy Panel

Internal delamination may exist even though there is no externally visible damage, as shown for low-velocity, non-penetrating, projectile impacts in Reference 2-31. These test results were obtained by impacting 0.146-in graphite/epoxy laminates with a 5/8-in diameter spherical head indentor at impact energy levels ranging from 5 in-lb to 74 in-lb. Figure 2-51 shows ultrasonic scans defining the extent of internal delamination. Internal delamination is pronounced at impact energies as low as 15 in-lb, but no external damage was visible until impact energies reached 35 in-lb. Even at 55 in-lbs, the external damage was limited to a small, smooth dent approximately ¼-inch in diameter (as shown in Figure 2-50) yet the extent of internal delamination was 1¼-inch in diameter (as shown in Figure 2-51). Figures 2-52 and 2-53 show the internal delamination revealed by sectioning 55 and 15 in-lb impacted specimens, respectively. The results of static tension and compression tests show that the barely visible 55-in-lb damage caused strength reductions of twenty-five and sixty percent respectively.
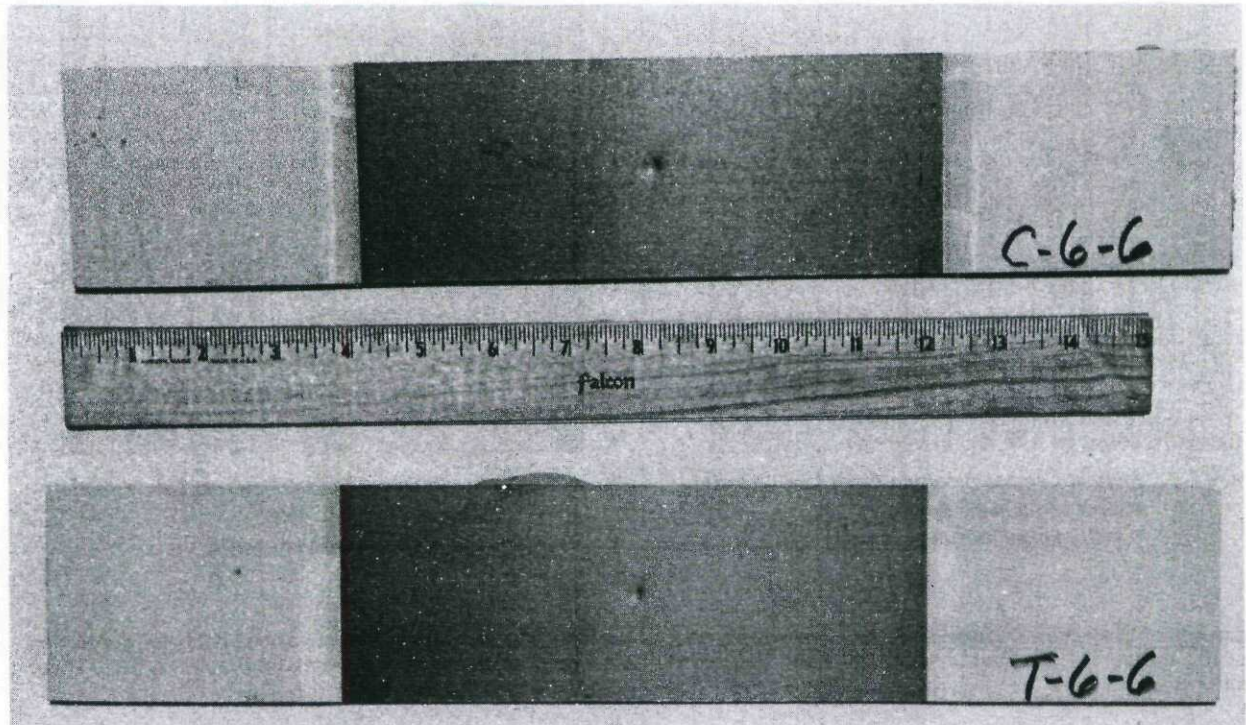
Figure 2-50. External Damage Resulting from Low Velocity Impact of 55 in-lbs Energy
(5/8 Dia Spherical Indentor)
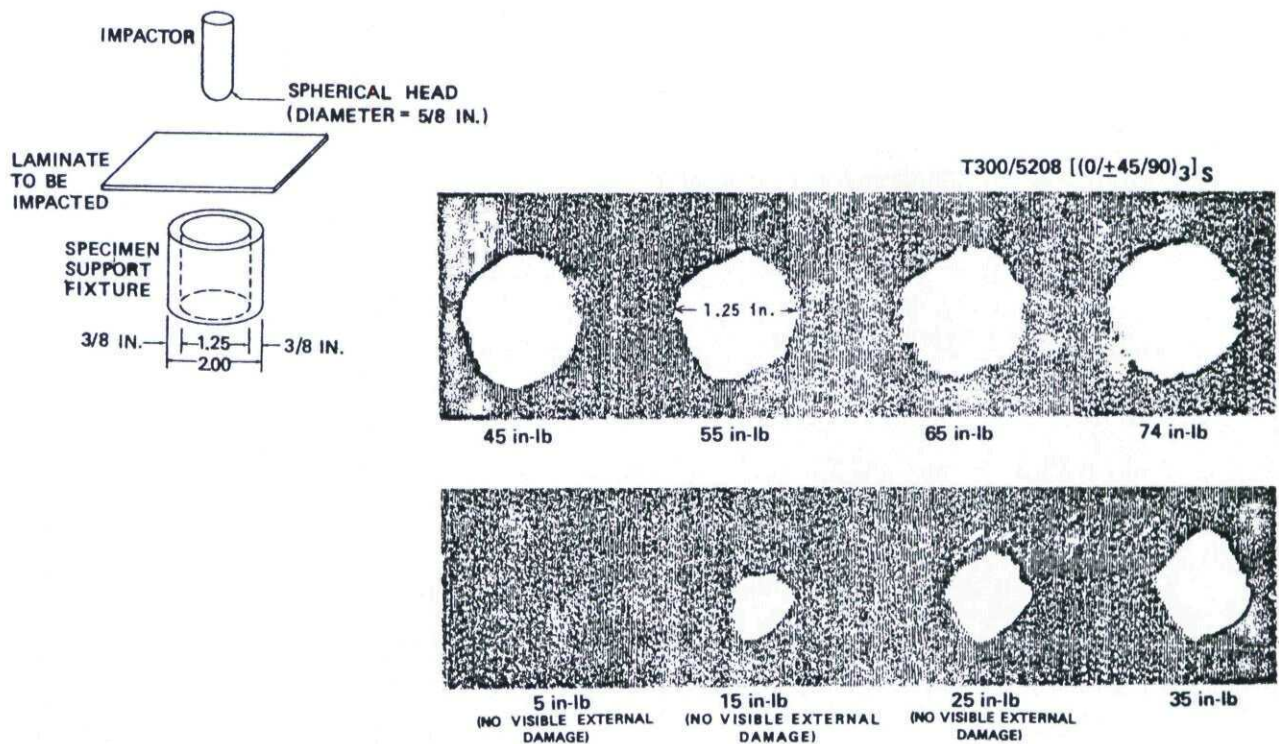
Figure 2-51. Ultrasonic Scans Showing Delamination Caused by Low Velocity Impacts

72
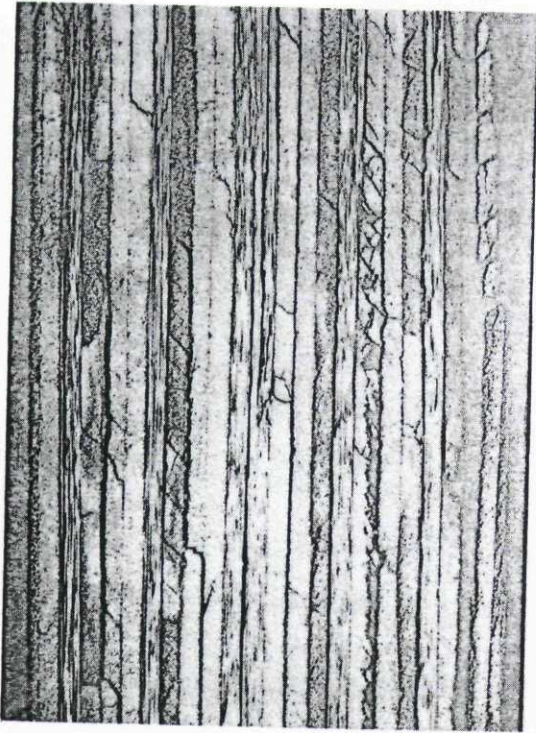
Figure 2-52. Internal Damage Resulting From Low Velocity
Impact of 55 in-lbs Energy
(0.146—in.graphite/epoxy laminate)
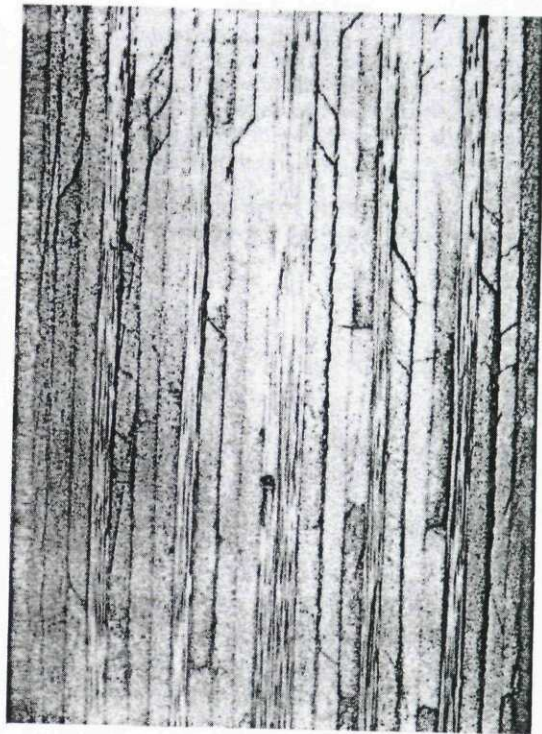
Figure 2-53. Internal Damage Resulting From Low Velocity
Impact of 15 in-lbs Energy
(0.146—in.graphite/epoxy panel)

Measures of Projectile Damage in Fiber Composites. As a prelude to developing quantitative damage prediction models, measures of visual damage in fiber composites have been defined as indicated in Figure 2-54. These measures are:

1. Maximum Perforation - The maximum dimension of thru-the-thickness material separation. This dimension corresponds approximately to a "see-through" capability.

2. Maximum Perforation Plus Deep Delamination - This dimension includes the Maximum Perforation defined above plus any adjacent region that is delaminated deep into the thickness. This measure defines laminate that is most likely ineffective from a structural standpoint.

3. Maximum Transverse Perforation - The maximum perforation width transverse to the Maximum Perforation.

4. Maximum Extent of Visible Damage - The maximum extent of visual ballistic impact damage including surface peeling.

① MAXIMUM PERFORATION
② MAXIMUM PERFORATION PLUS DEEP DELAMINATION
③ MAXIMUM TRANSVERSE PERFORATION
④ MAXIMUM EXTENT OF VISIBLE DAMAGE
(Includes peeling of surface ply(s))
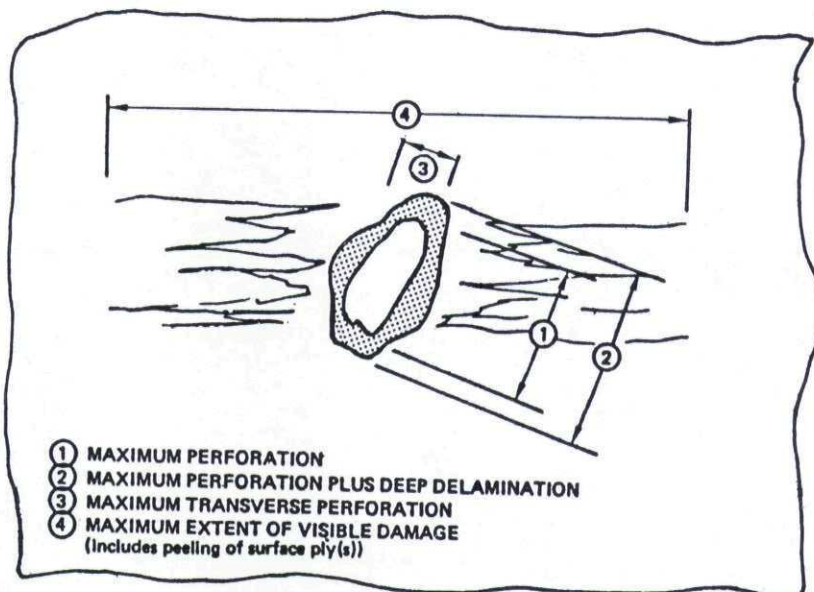
Figure 2-54. Representative Measures of Ballistic Damage in Composite Materials

Effect of Laminate Configuration on Damage. Several design parameters are associated with laminate configuration, including the fiber/resin system, the ply orientations, the thickness of the laminate, and the practice of combining several types of fibers to form a hybrid laminate. The effect of these parameters on the extent and character of ballistic damage is an important question that remains unanswered in many aspects. Some data is available, however, leading to the results described in following paragraphs.

Effect of Fiber/Resin System. Fiber composite laminates can be constructed from various fibers and resins. For example, T300 (Narmco) and AS (Hercules) are commonly used graphite fibers. Glass fibers and, more recently, Kevlar, have frequent application. Representative 350°F resins include 5208 and 934 epoxies. For high temperature applications, polymide rather than epoxy is a more appropriate resin. T300/934, T300/5208 and AS/3501 are representative graphite/epoxy systems for aircraft.

There are no comprehensive evaluations available that isolate and quantify the relative response of the different fiber/resin systems to ballistic impact damage. However, ballistic tests are reported in Reference 2-12 comparing the ballistic damage characteristics of several graphite/epoxy and Kevlar/epoxy systems. Steel cubes or 0.50 caliber armor piercing bullets were fired into 0.05-inch panels at angles of obliquity of 0- and 80-degrees. The comparisons are shown in Figure 2-55. The "maximum perforation plus through delamination" is the most significant damage measure for structural degradation, and it is apparent that there is little difference between the three graphite/epoxy systems. The Kevlar/epoxy laminates consistently showed less damage than the graphite/epoxy.
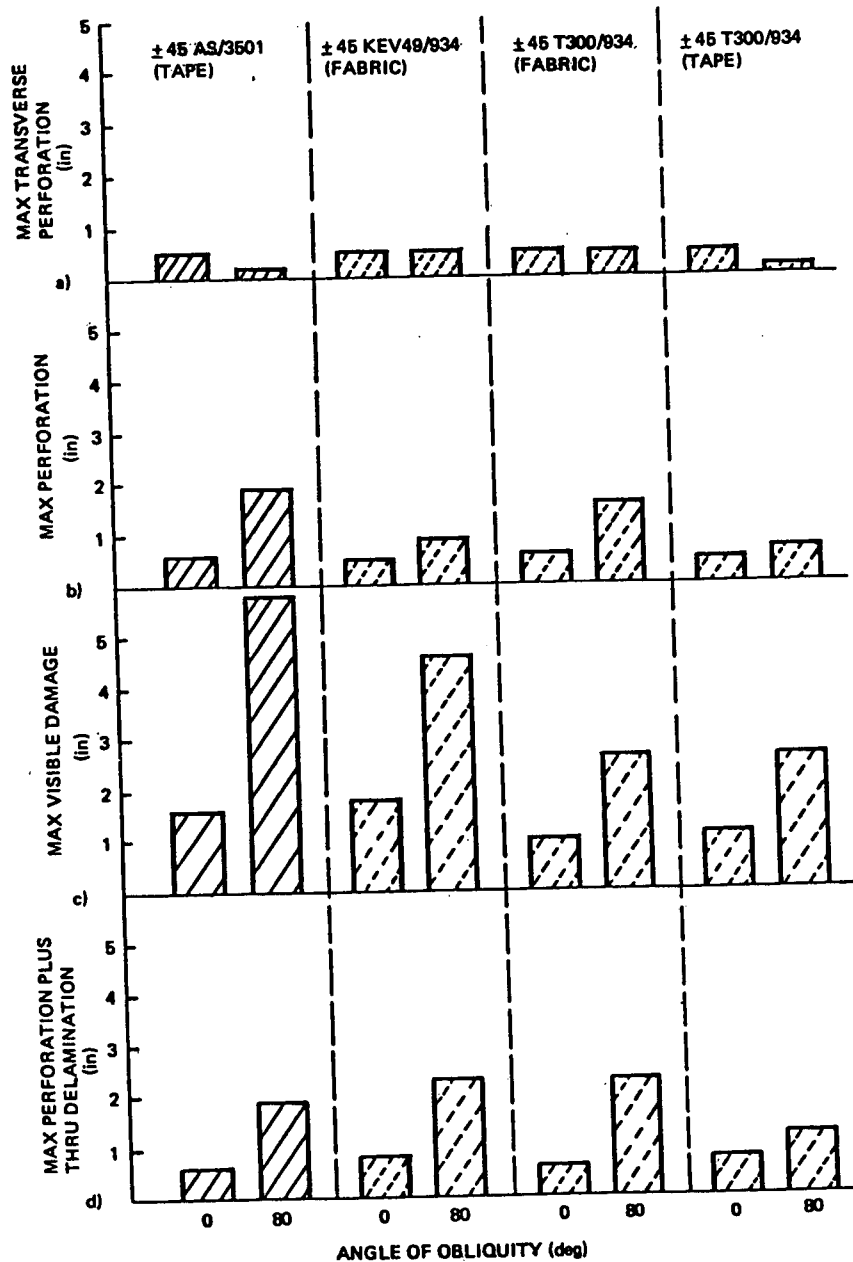
Figure 2-55. Comparison of Visual Damage in Several Composite Laminates (Penetrated by .50 Caliber Armor-Piercing Projectiles)

74

Effect of Tape or Fabric Construction. Composite laminates can be constructed using either preimpregnated tape or fabric. The tape typically consists of unidirectional fibers, and desired ply orientations are obtained by aligning the tape during layup. Fabric typically consists of a 0/90 woven configuration.

The limited data available for comparing the relative ballistic damage resistance of tape and fabric indicates that graphite/epoxy laminates constructed from tape exhibit greater visual damage than corresponding laminates made from fabric. However, in most applications the differences between the ballistic damage response of tape and fabric would not be structurally significant because the greater damage was primarily a surface effect due to the greater tendency of the tape laminate to peel. This is illustrated by comparing Figures 2-56 and 2-57.

Effect of Laminate Thickness. Laminate thickness has a significant effect on damage caused by penetrators. Damage size in thin composite laminates tends to conform to the projected size of the projectile on the plane of the impacted laminate (i.e., the minimum damage size allowing passage of the projectile through the panel). This is not true with thicker laminates, because the damage to the exit face can be extensively increased by delamination, frequently resulting in rear surface spallation.

In tests to determine the effect of laminate thickness on damage size (Ref. 2-12), damage was induced by firing steel rods into 0.25 and 0.50-inch 0/+45/90 AS/3501 laminates. The 0.50-inch laminate showed far greater damage than the 0.25-inch laminate. Exit damage was much greater than entry for both thicknesses.

Effect of Impact Conditions on Damage. Ballistic impact conditions including projectile type, velocity, and angle of obliquity have a significant effect on the size and character of impact damage in laminated composites, as in metals. In many situations the influence of the impact conditions depends on the laminate configuration. For example, the variation of damage size with projectile impact velocity is more pronounced in thick laminates than in thin laminates. The following discussion is based on evaluations of available data. In most cases, the data is not adequate to fully define the effects of impact conditions on damage except as qualitative trends applicable only to the conditions tested.

Effect of Projectile Size and Type. Projectile damage in fiber composites tends to conform to the contour of the projectile more closely than experienced in most aircraft quality metals, which often exhibit considerable cracking emanating from the primary perforation. In composites, damage is more confined to a region of perforation plus a region of delamination around the penetration area. The latter increases in size with increasing laminate thickness as described above.
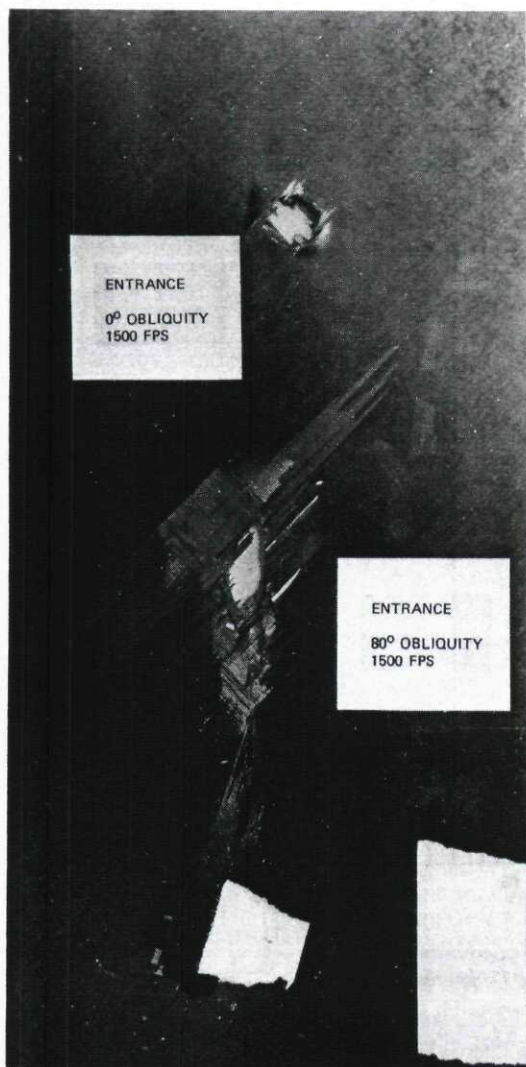
Figure 2-56. Typical Projectile Impact Damage in Graphite/Epoxy Tape Laminate
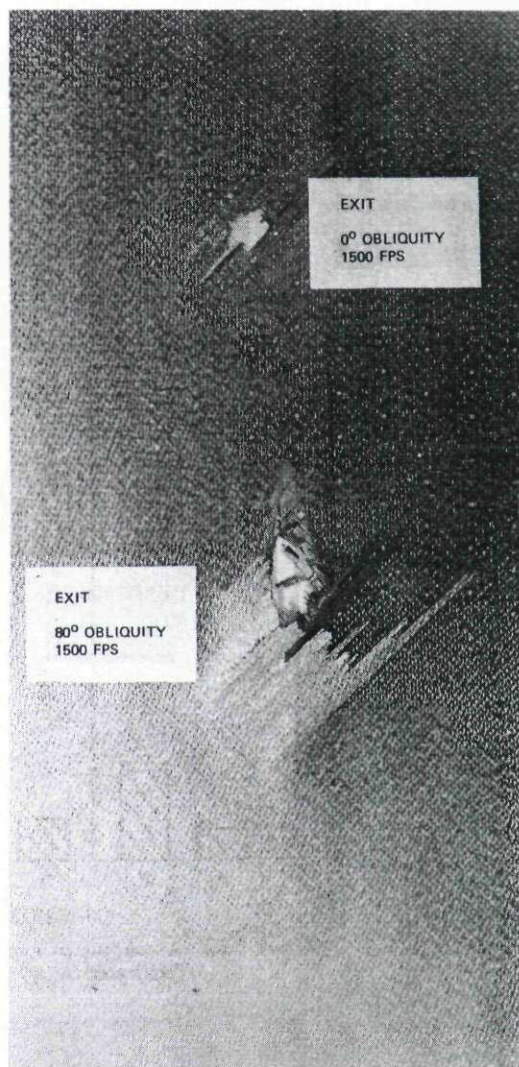
Figure 2-57. Typical Projectile Impact Damage in Graphite/Epoxy Fabric Laminate

In assessing the influence of projectile size on damage, it is useful to represent the projectile by its maximum presented length, termed L_p. As a result of an evaluation of available ballistic testing of thin graphite/epoxy and boron/epoxy laminates, the maximum perforation plus deep delamination on both entry and exit faces was found to be slightly larger than L_p, and it was proposed in Reference 2-27 to add some constant β to L_p to give a prediction of the damage induced by any projectile. The value which best fit the test data was 0.2-inch. For thin laminates impacted at 0-degree obliquity, then, maximum perforation plus deep delamination is related to projectile presented length by:

$$LD = L_p + 0.2\text{-inch} \qquad \text{(Thin laminates of graphite/epoxy or boron/epoxy, normal obliquity).}$$

Thicker laminates exhibit increased maximum perforation plus deep delamination on the exit face. Experience with metals (Ref. 2-7) has shown that damage size can vary as a function of the ratio of panel thickness to projectile size, and this has proved to be true of exit damage in composites also. Figure 2-59 shows this effect for $0/\pm45/90$ AS/3501 graphite/epoxy.
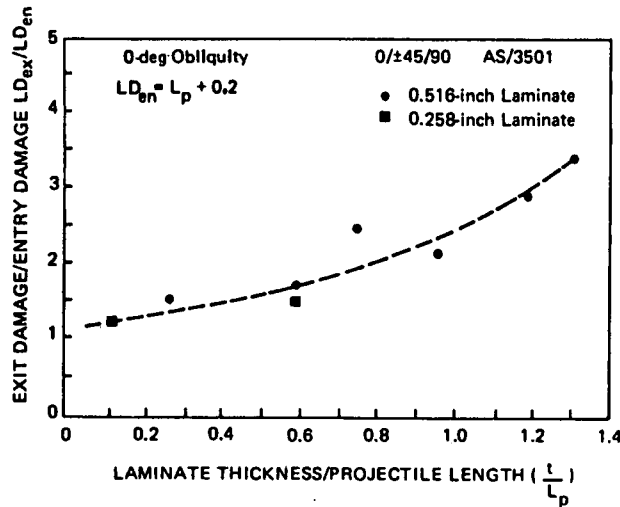
Figure 2-59. Effect of Laminate Thickness and Projectile Size on Exit Damage

Effect of Projectile Obliquity. Considerable test data is available (Ref. 2-27) showing that damage size in thin fiber composite laminates varies inversely with the cosine of the angle of obliquity. This type of variation is shown in Figure 2-60. The line represents the projectile maximum presented length L_p divided by the cosine of the angle of obliquity, θ. The actual damage (maximum perforation plus deep delamination) plots somewhat above this line, and can be predicted reasonably well using the constant β identified for normal impacts. The damage can then be described as:

$$LD = \frac{L_p}{\cos\theta} + 0.2$$

Figure 2-61 shows a similar comparison for a thick graphite/epoxy laminate.
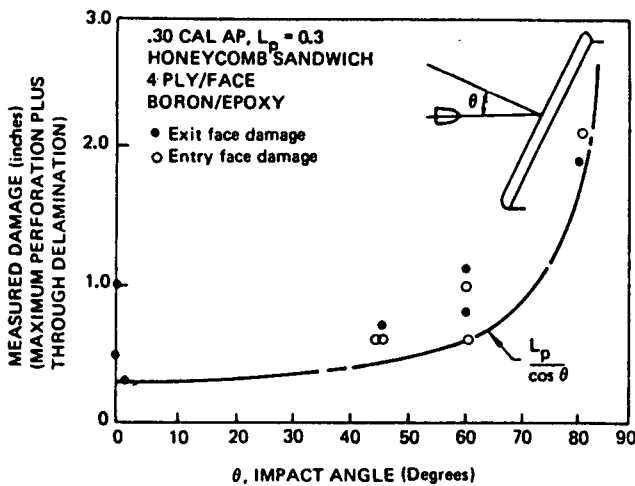
Figure 2-60. Effect of Projectile Obliquity on Penetration Damage in Thin Laminates
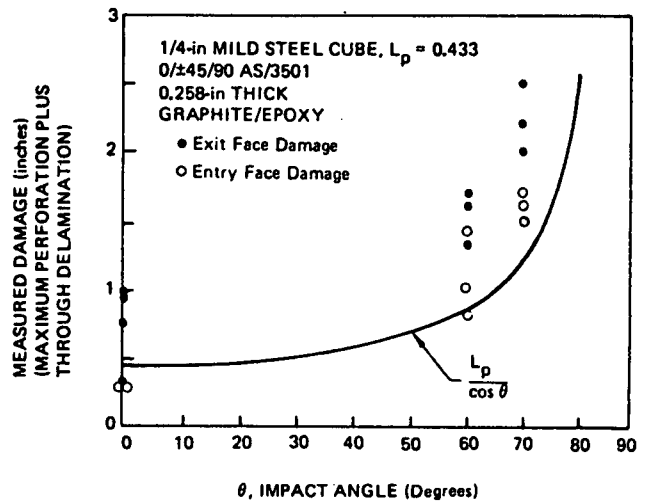
Figure 2-61. Effect of Projectile Obliquity on Penetration Damage in Thick Laminates

Effect of Projectile Velocity. Considerable testing with small arms projectiles and fragments fired into thin (less than 0.2-inch) fiber composite laminates has shown that visual damage size is relatively insensitive to projectile velocity. Figure 2-62 is representative of the results obtained in thin laminates. These data were obtained for impact conditions well above the ballistic limit.

Testing of graphite/epoxy was recently conducted (Ref. 2-12) to determine if damage size becomes more sensitive to projectile velocity as the ballistic limit (V_{BL}) is approached. Mild steel cubes were fired into laminates ranging in thickness from 0.25-inches to 1.0-inches, at velocities between 500 and 5,000 feet per second. The results, shown in the right-hand portion of Figure 2-62, show that while the damage size increases rapidly with increasing velocity for velocities such that $0.7 < (V/V_{BL}) < 1.3$ (approximately), it remains relatively constant for higher V/V_{BL} ratios. This is in contrast to metals, where the maximum damage occurs at velocities near the ballistic limit and diminishes before leveling at high velocities (Ref. 2-2).
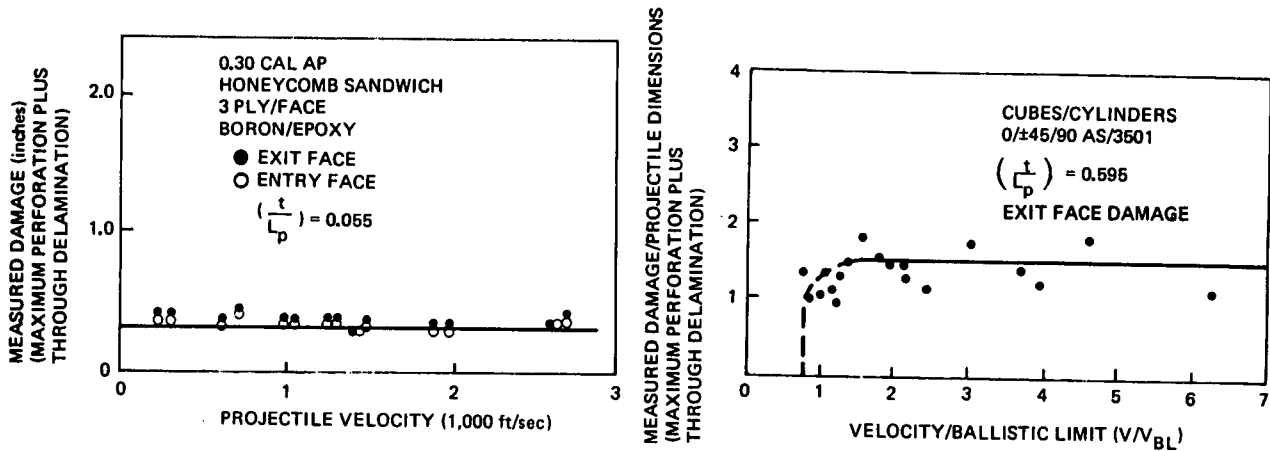
Figure 2-62. Effect of Projectile Velocity on Penetration Damage

2.2.1.2.2 Non-Exploding Penetrators Impacting Graphite/Epoxy – Damage Size Prediction

As discussed in Section 2.2.1.2, penetrator damage in thin graphite/epoxy or boron/epoxy laminates tends to conform to the contour of the projectile. This behavior has been used to develop a damage size prediction model that correlates well with experimental results, and provides an equivalent flaw size for residual strength predictions. The damage model, published in Reference 2-17, is quite comprehensive and was developed from a substantial quantity of test data reported in Reference 2-12. Parameters used in developing damage models for metals, and early damage models for thin composites were used where applicable in developing the present model. The result is a prediction of mean damage having a fairly high degree of confidence for many laminate configurations and impact conditions.

The basis for the model is an early damage prediction method for thin laminates presented by Avery/Porter in Ref. 2-17. They determined that both entry and exit damage size in thin laminates is best described as maximum perforation plus deep delamination, and that this damage can be closely represented by the presented length of the projectile in the plane of the impacted laminate plus a constant, β, as illustrated in Figure 2-63. They found that β = 0.2-inch gave the best correlation with test data. Later test data showed that this relationship provides a fairly good prediction of entry damage in all thicknesses of laminated graphite/epoxy. The resulting model is:

$$LD_{en} = \frac{L_p}{\cos\theta} + 0.2\text{-inch} \qquad \text{(All Laminate Thicknesses)} \qquad \text{(Eqn. 2-16)}$$

When test data for thicker laminates ranging from 0.25 to 1.0-inches was obtained, it became obvious that while entry damage still followed Equation 2-16, exit damage was much larger. In metals, the parameter t/L_p (thickness/projectile size) had been used (Ref. 2-2) in damage prediction, and as previously discussed, this parameter is applicable for correlating damage in graphite/epoxy also. For metals, the damage model has the form:

$$LD = \frac{L_p}{\cos\theta} f(\frac{t}{L_p}) \qquad \text{(Metals)}$$

For graphite/epoxy, the form is:

$$LD_{ex} = LD_{en} f(\frac{t}{L_p}) \qquad \text{(All Laminate Thicknesses)}$$

Where:

LD_{ex} = Maximum exit damage size (maximum perforation plus deep delamination);

LD_{en} = Maximum entry damage size;

L_p = Maximum presented length of the projectile (see Figure 2-43) (inches).

t = Laminate thickness (inch)

The available ballistic impact data was analyzed to evaluate the necessary parameters, and a least-squares curve fit was made to determine $f (t/L_p)$, as indicated in Figure 2-64. The damage measure used was maximum perforation plus deep delamination normalized by $(L_p/\cos\theta) + 0.2$. To assure that velocity effects were isolated, only data for impacts well above ballistic limits were included in the analysis.

The resulting expression for exit damage prediction is:

$$LD_{ex} = (LD_{en}) \ (0.95 + 0.57 \frac{t}{L_p} + 0.63 \ (\frac{t}{L_p})^2 + 0.14 \ (\frac{t}{L_p})^3) \qquad \text{(Eqn. 2-17)}$$

This equation has considerable verification for values of t/L_p less than 0.8, although data is limited above that ratio. For values of t/L_p less than 0.2, Equation 2-16 can be used for both entry and exit damage.

This damage model does not include a parameter representing the influence of projectile velocity on damage size. As was shown in Figure 2-62, damage size remains constant for velocities above approximately 1.3 V_{BL}, where V_{BL} is the ballistic limit. Below 1.3 V_{BL}, damage size diminishes rapidly to zero; however, no equation has been developed to predict damage size in this region due to lack of data. (See Section 2.2.1.2.1.)
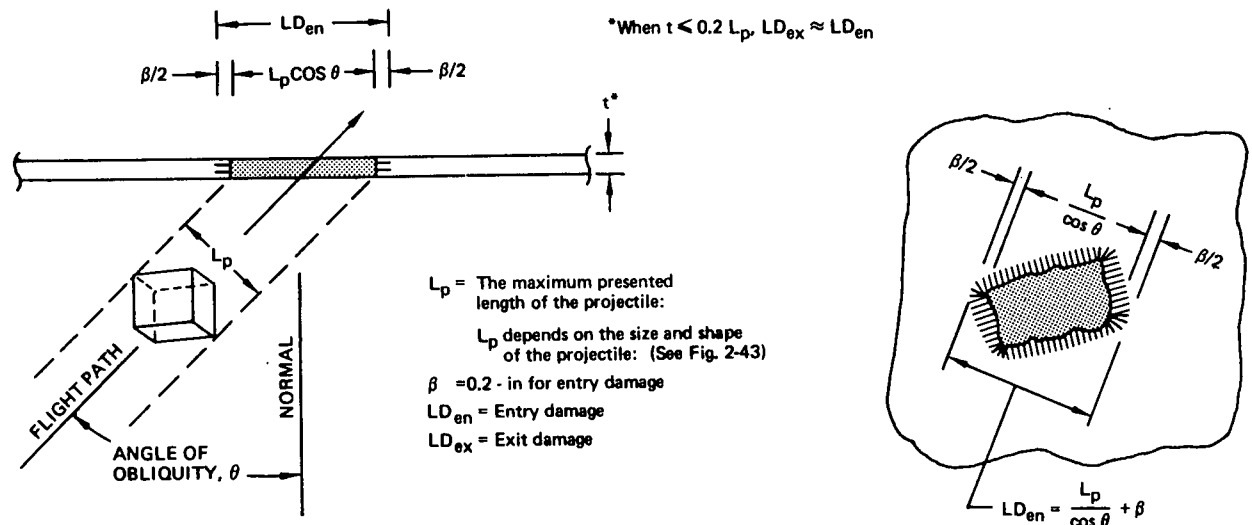
Figure 2-63. Model for Predicting Entry Damage in Graphite/Epoxy
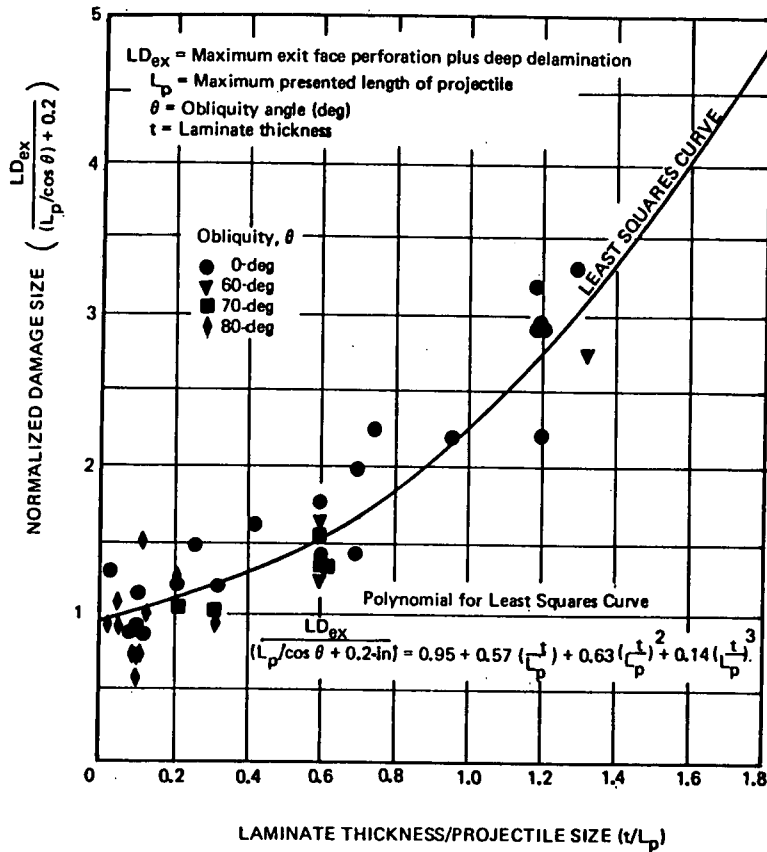
Figure 2-64. Damage Size Model for Graphite/Epoxy

The following example shows how the damage prediction model is used:

Given: Fragment: 1/4-inch mild steel cube (L = 0.25-in)

$V = 1.3 \, V_{BL}$ (V_{BL} = Ballistic Limit Velocity)

$\theta = 45\text{-degrees}$

Laminate: Graphite/Epoxy

$t = 0.25\text{-inch}$

Calculations for LD_{en} and LD_{ex}:

$L_p = \sqrt{3}L = \sqrt{3}(0.25) = 0.433\text{-in}$

$\cos \theta = \cos 45 = 0.707$

$LD_{en} = \dfrac{L_p}{\cos\theta} + 0.2 = \dfrac{0.433}{0.707} + 0.2 = 0.812$

$\dfrac{t}{L_p} = \dfrac{0.25}{0.433} = 0.577$

$LD_{ex} = LD_{en} \left(0.95 + 0.57 \left(\dfrac{t}{L_p}\right) + 0.63 \left(\dfrac{t}{L_p}\right)^2 + 0.14 \left(\dfrac{t}{L_p}\right)^3\right)$

$= 0.812 \quad (0.95 + 0.57 \,(0.577) + 0.63 \,(0.332) + 0.14 \,(0.192))$

$= 0.812 \quad (0.95 + 0.329 + 0.209 + 0.027)$

$= 1.23\text{-in.}$

2.2.2 Damage from High Explosive (HE) Projectiles

High explosive (HE) projectiles are fired from anti-aircraft artillery (AAA) or from guns mounted in aircraft (air-to-air). The projectiles have a contact-activated fuze which may contain a mechanism providing a brief delay before detonation is initiated. Those HE projectiles which do not have a delay mechanism are termed "superquick" or "instantaneous". The detonation of a superquick fused projectile is actually started outside the impacted structure. Delay fuzed projectiles usually detonate within the structure.

The structural damage done by HE projectiles (20- to 30-mm, for example) is the result of multiple fragment penetrations and internal blast pressures, acting separately and in combination. The fragments are created as the metal casing surrounding the explosive bursts due to the intense pressures generated by the detonation. Fragment damage degrades structural strength and stiffness, and blast pressures added to the existing flight loads can cause excessive deformations and element failures.

The nature and extent of structural damage from HE projectile fragments and blast pressure depend upon these variables:
- o Material type and thickness;
- o Projectile size and delay characteristics;
- o Striking velocity and obliquity;
- o Distance from detonation to impacted structure (standoff);
- o Internal volume of structural cell and extent of venting.

The significance of each of these variables will become clear in the paragraphs below. Qualitative descriptions of HE projectile damage in metallic and fiber composite structure are presented followed by a discussion of damage prediction analysis techniques for blast and fragments given in Sections 2.2.2.1 and 2.2.2.2, respectively.

Characteristics of HE Projectile Damage in Metallic Structure. Qualitative illustration of damage in metallic structure due to HE projectile impacts is presented in Figures 2-65, 2-66, and 2-67. Figure 2-65 shows typical entry damage in 7075-T6 stiffened skin panels. Impact into a stiffener generally causes severence, and considerable damage can be done to adjacent stiffeners as seen in Figure 2-65(c), depending upon the spacing between stiffeners.

Figures 2-66 and 2-67 show typical damage from the dispersed fragment cone resulting from the stand-off distance between the detonation point and the surface impacted. The panels shown were located 10-inches downstream of the detonation. The skin/stiffener panels were 0.050-inches thick, and the integrally stiffened panel shown in Figure 2-66(d) was 0.060-inches thick.

In Figure 2-66(a) the size and density of the fragment cone are clearly defined, as are the typical damages from the fragments and the large central damage. Only moderate interaction between these damages is evident. This panel was fabricated from 6Al-4V annealed titanium. Figures (b), (c) and (d) show increased interaction between the several damage components, including the probable influence of blast. The panel in (b) is 2024-T3, and the panels in (c) and (d) were 7075-T6. All panels were stressed in tension or compression at the time of impact. Figure 2-67 shows typical damage in honeycomb panels.
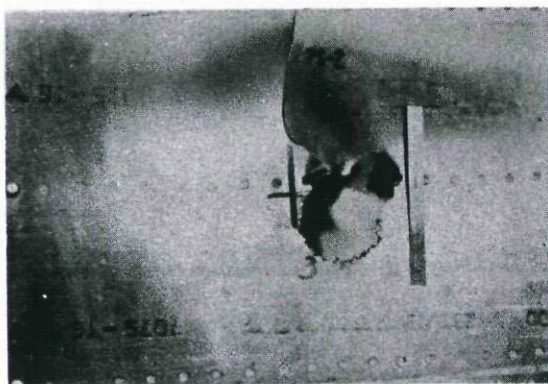
(a) IMPACT INTO STIFFENER, FRONT FACE OF
ENTRY PANEL, 7075-T6
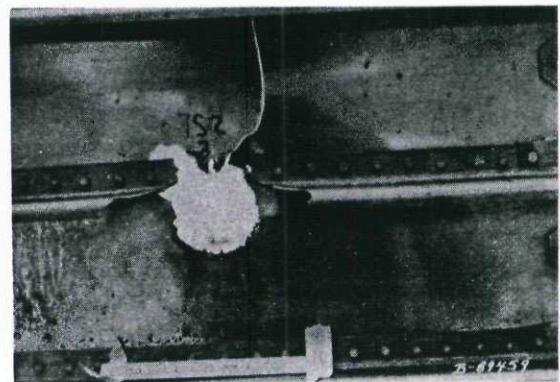
(b) IMPACT INTO STIFFENER, REAR FACE OF
ENTRY PANEL, 7075-T6
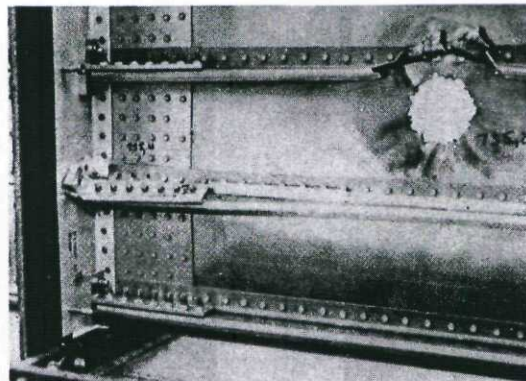
(c) IMPACT ADJACENT TO STIFFENER, 7075-T6

Figure 2-65. Typical Entry Damage From HE Projectile, Instantaneous Fuze, Zero Obliquity
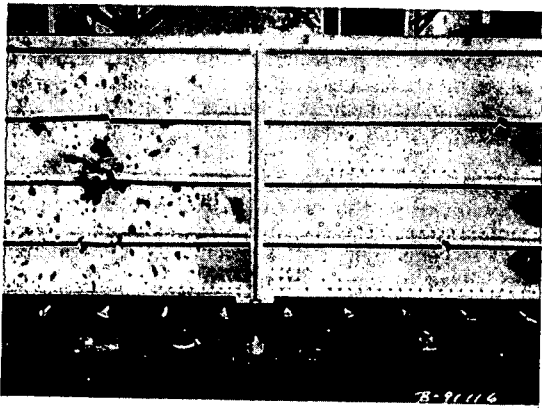
(a) 6Al-4V ANNEALED
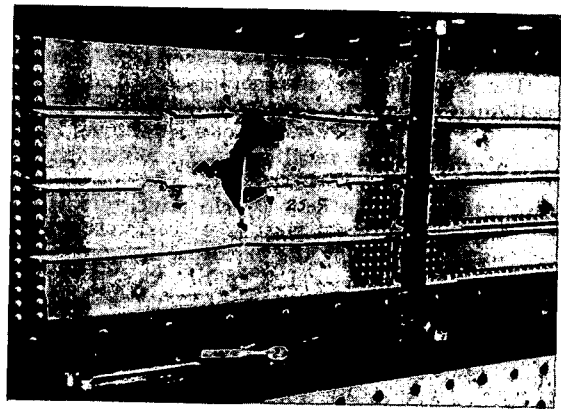
(b) 2024-T3
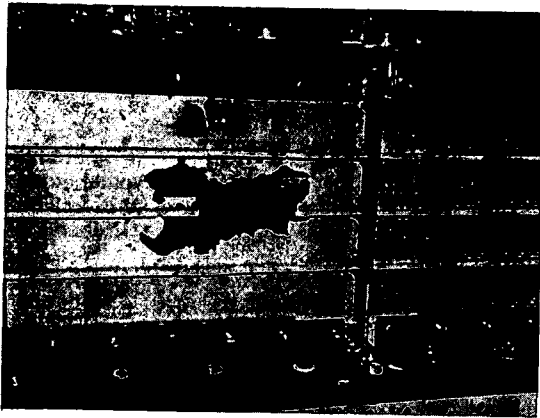
(c) 7075-T6
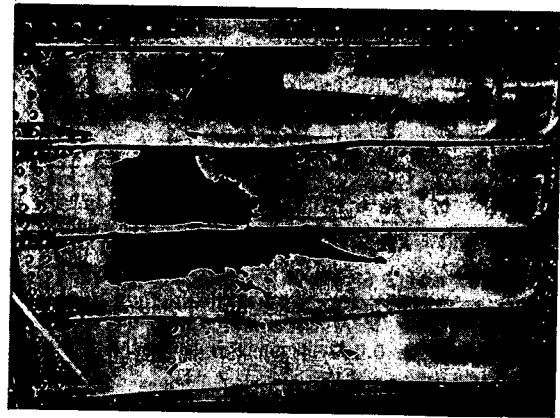
(d) 7075-T6, INTEGRALLY STIFFENED

Figure 2-66. Fragment Cone Damage From HE Projectile Impact, 10-inches Stand-off
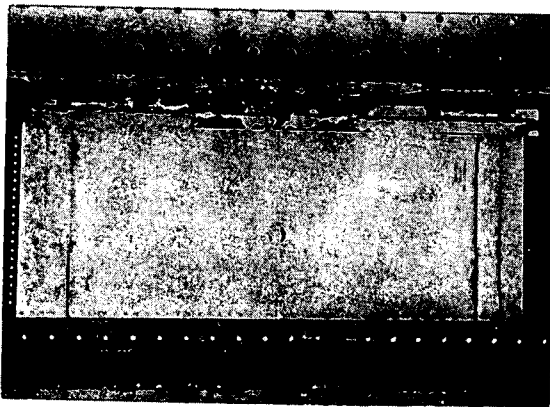
(a) FRONT FACE, ENTRY PANEL
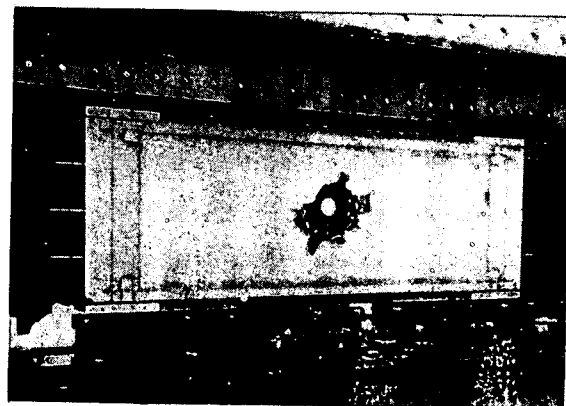
(b) REAR FACE, ENTRY PANEL

(c) FRONT FACE, EXIT PANEL

(d) REAR FACE, EXIT PANEL

Figure 2-67. Fragment Cone Damage in Honeycomb Panels From HE Projectile Impact, 10-inches Standoff

Characteristics of HE Projectile Damage in Fiber Composite Structure. Reference 2-12 reports extensive investigation of HE projectile impact damage in advanced fiber composite aircraft structure, including ballistic testing with HE projectiles, blast testing, and the development of analytical methods for predicting the effects of internal blast and fragments. Significant characteristics of HE projectile damage in composites determined from this and other programs are summarized below.

For all the graphite/epoxy configurations tested using superquick projectiles, it was found that damage to the entry face tends to be induced mainly by the fragment spray, and the area of removed material is generally bounded by the fragment cone intersection. The extent of exit face damage was controlled by the thickness and strength of the panel. As a function of stand-off, high local blast pressures combined with fragment penetration can destroy relatively large portions of the exit face.

Typical damage caused by HEI projectile fragments in a thin graphite/epoxy laminate is shown in Figure 2-68. The panel was a 0.066-in T300/934 (tape) laminate impacted with a superquick round while held by simple supports without an enclosing structure. The effect of the angle of obliquity of the fragments can be seen by the elongated individual damages near the edge of the fragment impact zone. From the data available, there is some evidence that entry face damage is inversely proportional to projectile velocity (see Figure 2-69). This is due to the narrowing of the fragment cone with increasing velocity, resulting in a smaller area removed on the entry face.
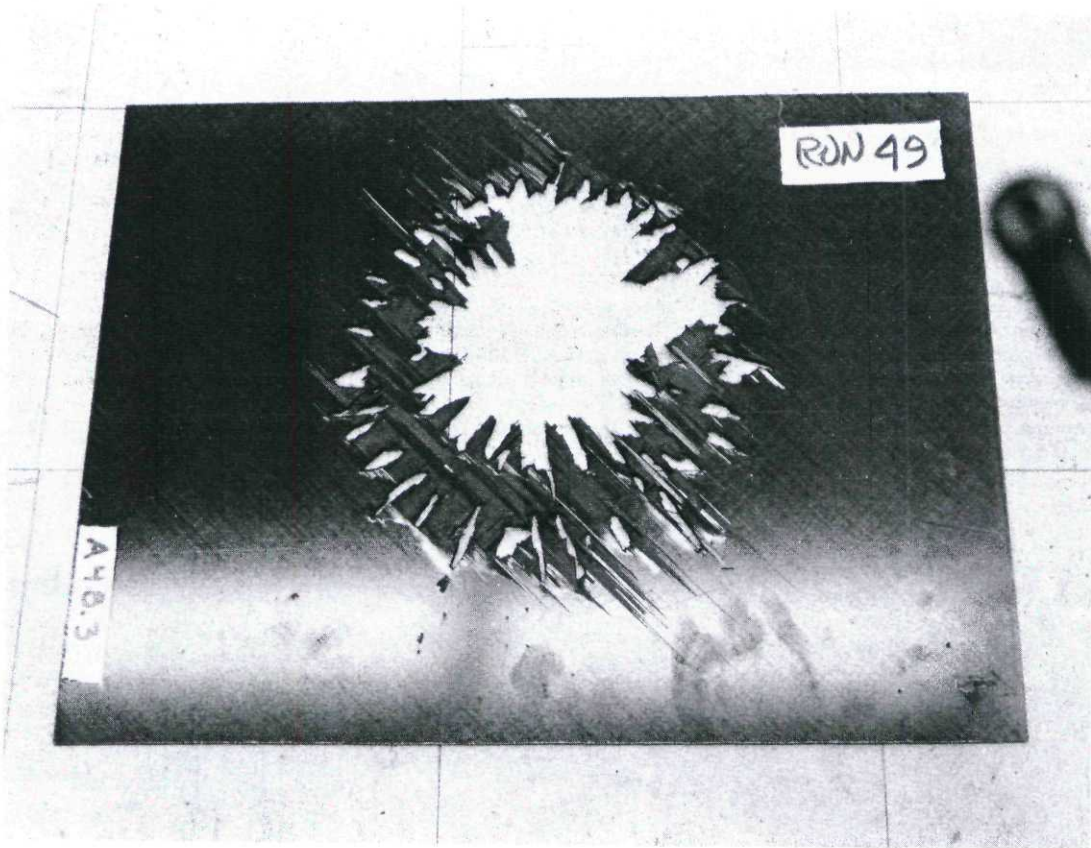
Figure 2-68. HEI Projectile Impact Into 0.066-in Graphite/Epoxy Laminate (Fabricated from Tape)
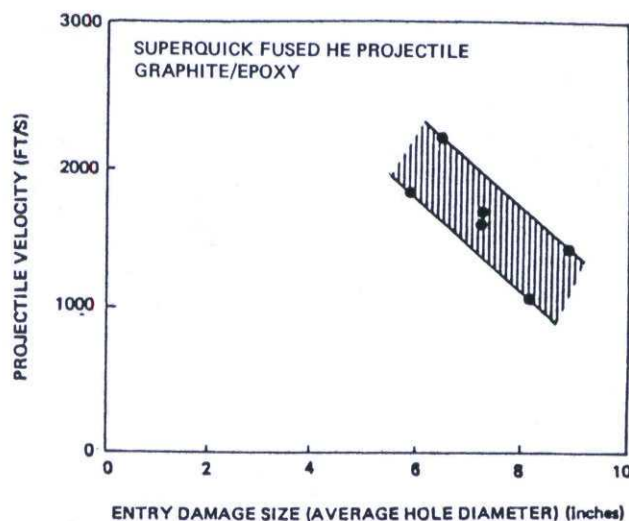
Figure 2-69. Effects of Velocity on Entry Damage Size

A comparison of the damage characteristics of tape and fabric laminates can be made from Figure 2-70, showing a 0.070-inch T300/934 panel fabricated from preimpregnated fabric impacted in a manner similar to the laminate fabricated from tape shown in Figure 2-69. The fabric constructed laminate experienced less delamination, but the penetration damage was nearly identical.

Ballistic testing has been done (Ref. 2-12) on wing-box segments having 0.125-inch thick graphite/glass hybrid laminate skins. A schematic of the impact condition and the resulting damage is shown in Figure 2-71 for a superquick fuzed HE projectile impacting a 15-inch by 30-inch double-cell box at 30-degree obliquity. For comparison with thin-skin damage response, HEI projectiles were fired into two wing box cells having skins constructed of 50-plies of 0/+45/90 AS/3501 graphite/epoxy. As shown in Figures 2-72 and 2-73, there was still significant fragment damage, but there were no skin detachment failures. The two test boxes shown were exposed to identical impact conditions, but one box was impacted by a superquick and the other a delay fuzed round. There are significant differences in the type of damage resulting from each type of fuze, as seen in the photographs.

As shown in Figure 2-74, the ultimate strain capability of graphite/epoxy is much lower than that of high-strength aluminum alloy, resulting in less ability to absorb the energy of blast loadings without rupture. The interlaminar shear strength is also lower, and internal delaminations due to blast loadings can be a significant degrading mechanism. Blast induced damage processes for composites include:

1. Deformation failure;
2. Delamination;
3. Failure at attachments;
4. Penetration.

Panel deformation failure refers to fiber and/or resin failure due to exceeding ultimate strain during bending or membrane response. Delamination means separation between plies. Delamination under blast loading may occur with (or be caused by) degradation of the matrix, resembling a "crumbling" action. Internal delaminations may be undetectable except by non-destructive inspection or cross-sectioning techniques. Extensive delamination, however, may cause a pronounced thickening and softening of the panel. External delaminations appear as plies stripped from the surface, and is generally referred to as peeling.

Failure at attachments may occur as a result of panel deformation similar to the failure modes experienced in metal structures. This results from edge fixity and cross-section reduction at attachment holes. However, bolted attachments in composites exposed to internal blast exhibit a "skin detachment" failure mode. In this failure mode, the composite skin fails in bearing at the bolt, causing enlargement of the bolt hole and subsequent separation of the skin from the substructure. Penetration, in the context of blast damage, refers to "blowing a hole" in a composite panel by a concentrated blast wave. Tests illustrating these damage processes are reported in Reference 2-12, using both bare explosive charges and HEI projectiles.
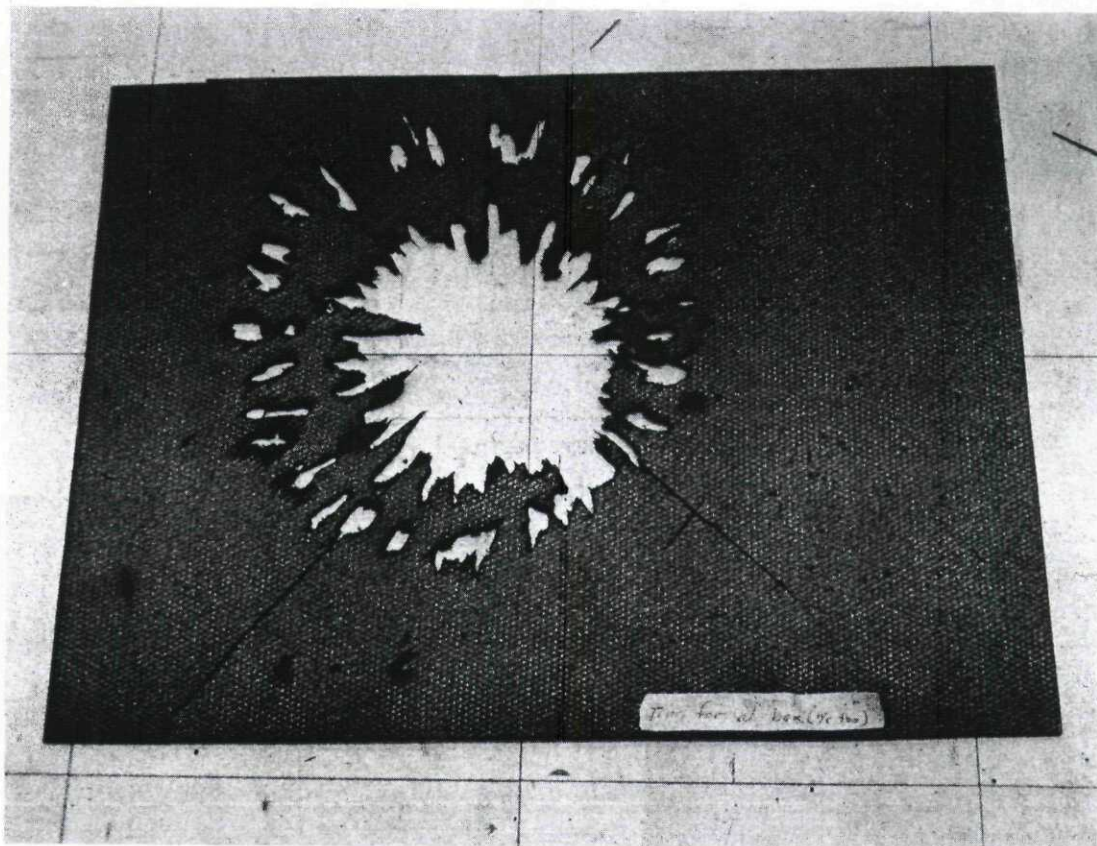
Figure 2-70. HEI Projectile Impact Into 0.07-in Graphite/Epoxy Laminate (Fabricated from Fabric)

83

ENTRY

SPAR CHORD NOT DAMAGED

IMPACT POINT

50% OF ONE SPAR CAP REMOVED (25% OF TOTAL CAP AREA)
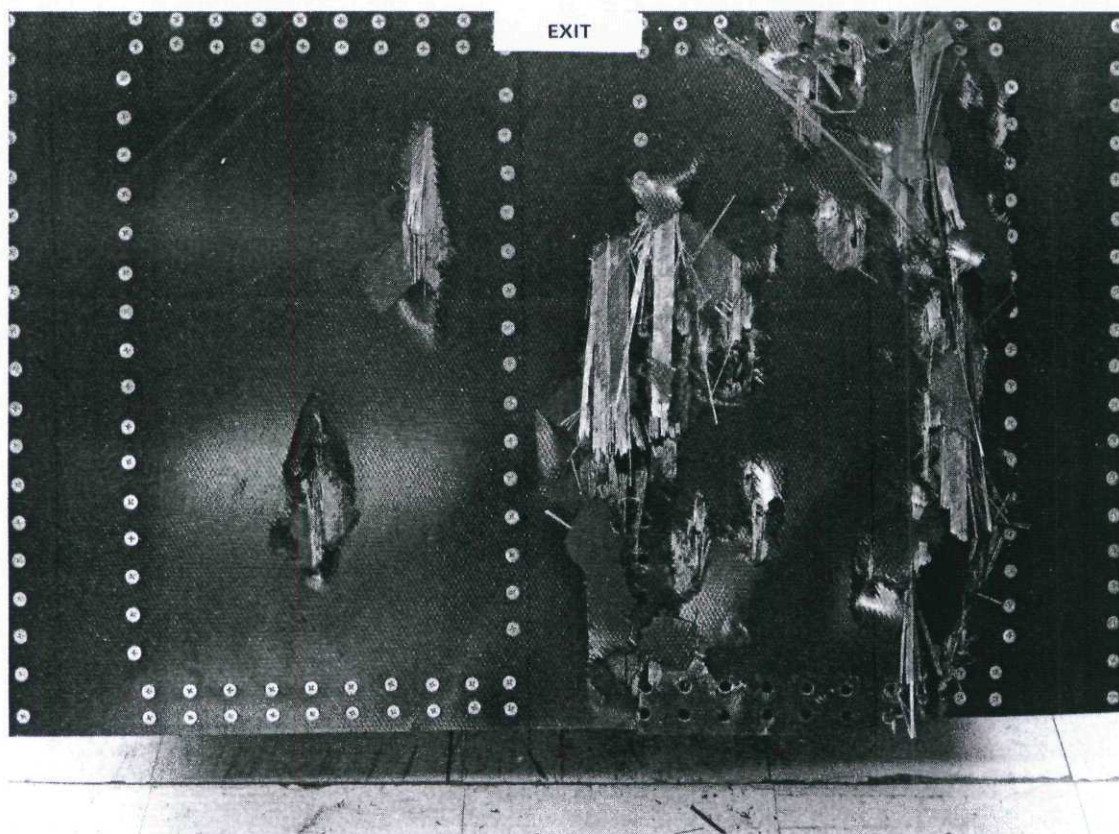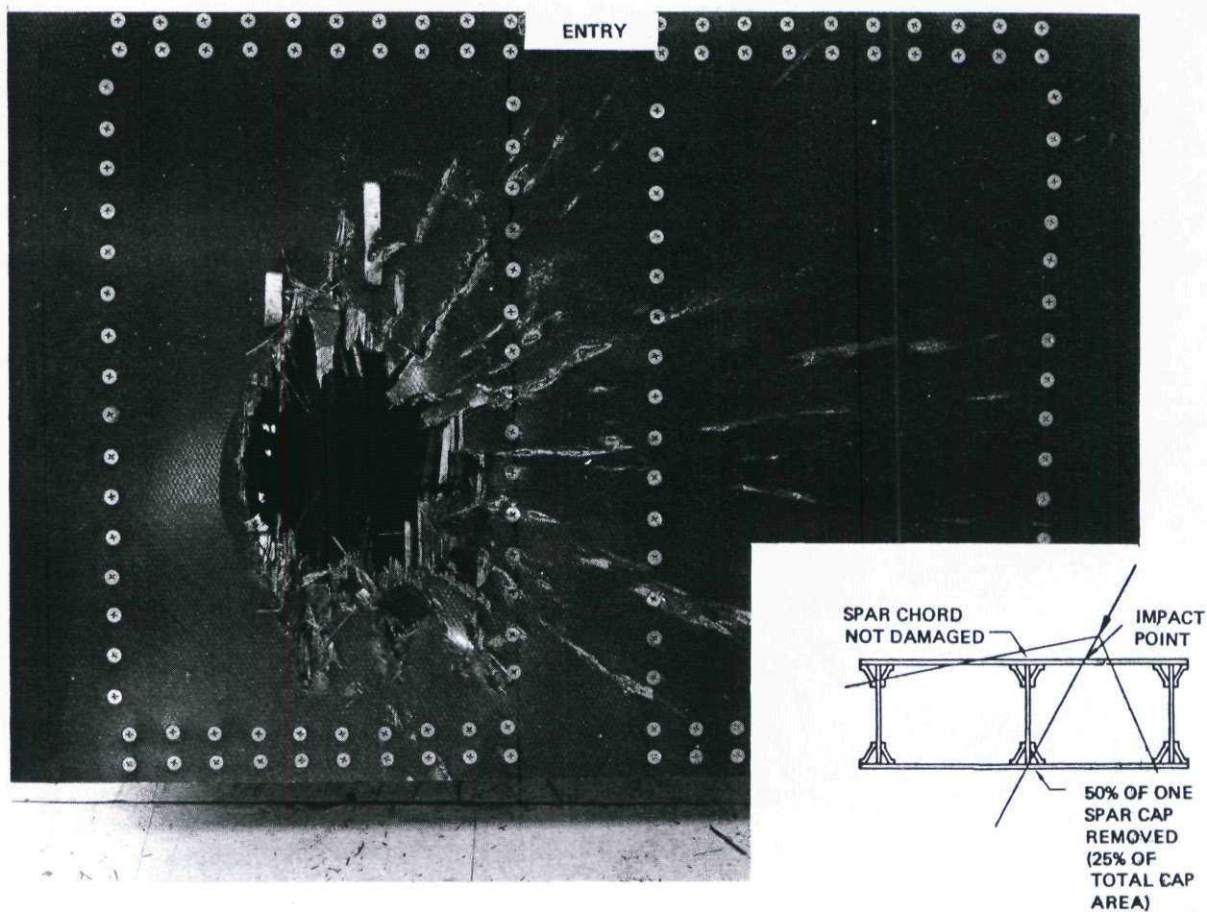
EXIT

*Figure 2-71. Damage From HEI Projectile Aimed at Exit Spar Cap
(30-deg Obliquity) (Two-Cell Graphite/Epoxy Box Structure)*

84

SUPER QUICK
FUSE

DELAYED
FUSE

15-Inches
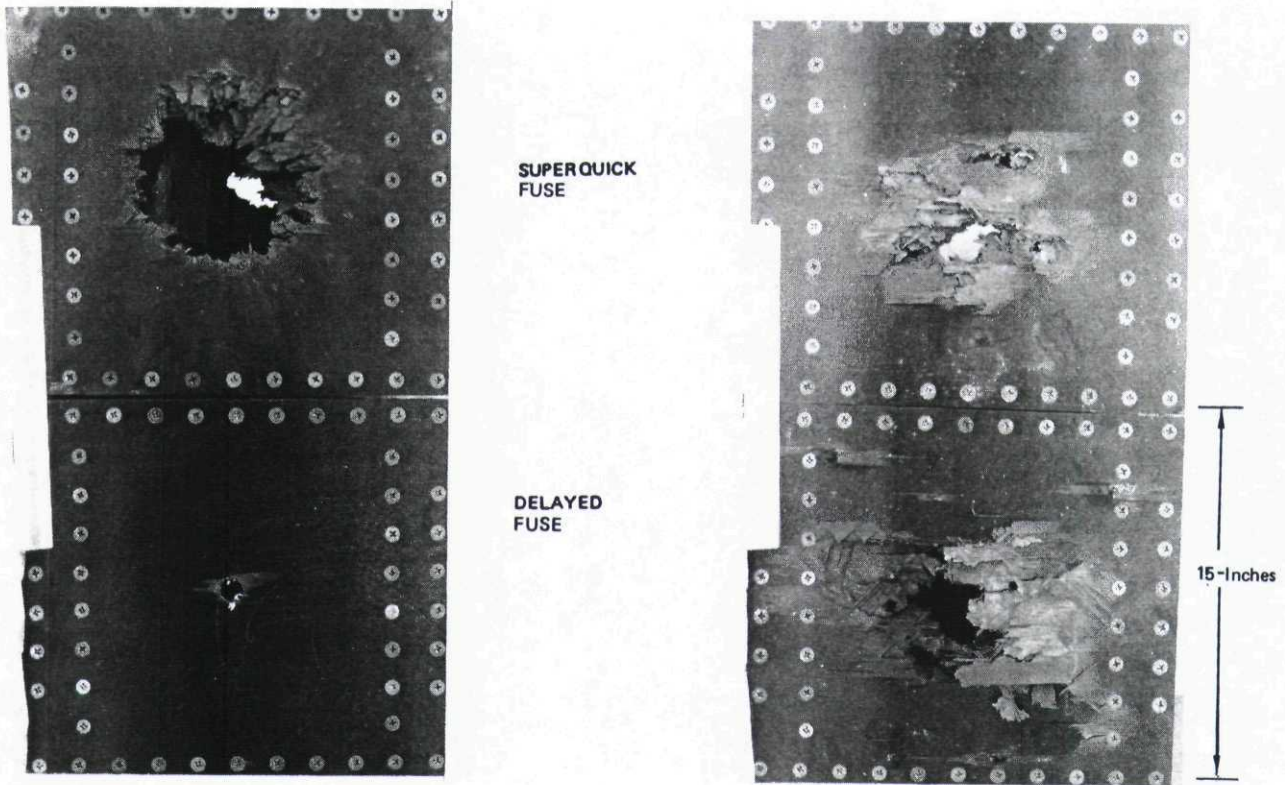
Figure 2-72. HEI Projectile Impact Into Thick-Skinned
Box Structure (Entrance Face)

Figure 2-73. HEI Projectile Impact Into Thick-Skinned
Box Structure (Exit Face)
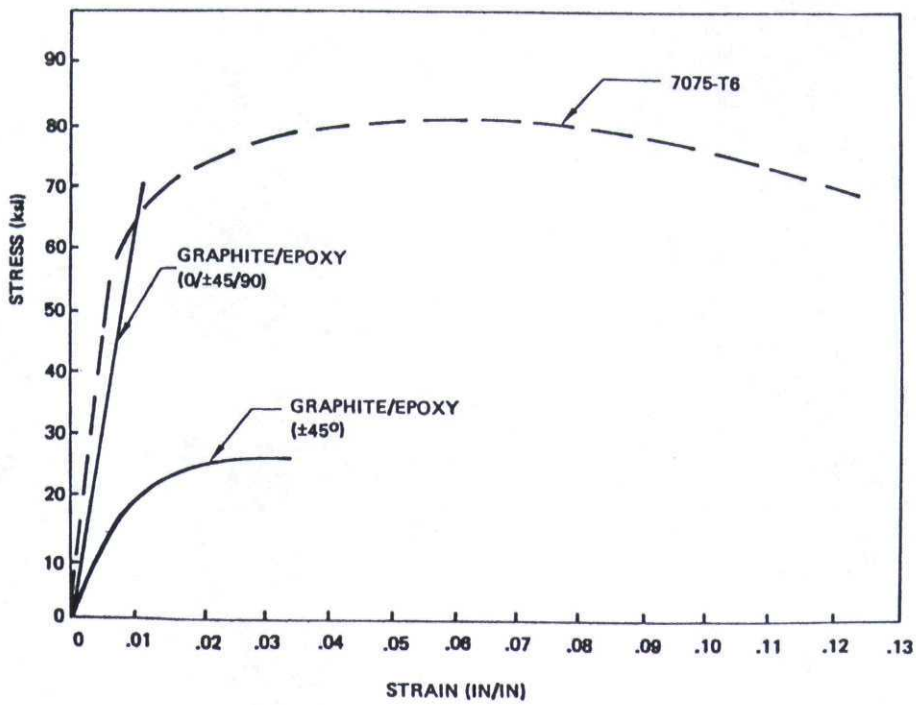
Figure 2-74. Ultimate Strain Capability of Graphite/Epoxy
Compared with Aluminum Alloy

2.2.2.1 Prediction of Damage Caused by Fragments from HE Projectiles

The spray of fragments from the detonation of a moving HE projectile forms cones with their axes along the projectile flight path. In order to predict the damage resulting from these fragment impacts it is necessary to determine the extent of the fragment spray on the structure, the number and sizes of the fragments and their impact locations, the damage size inflicted by each fragment, and the spacing and resulting interactions of the fragment damages. Section 2.2.2.1.1 discusses some of the analytical aspects of predicting fragment distributions. Following that discussion, Section 2.2.2.1.2 describes one of the most comprehensive of the available analysis methods for predicting fragment damage from HE projectile detonations; namely, the BR-2 computer code (Ref. 2-14).

2.2.2.1.1 Characteristics of the Fragment Distributions From HE Projectiles

Figure 2-75 shows a typical HE projectile, identifying major segments of the case (e.g., base, sidespray, fuze attachment, and fuze). When the projectile detonates, these segments are the sources of fragments which can be represented with reasonable accuracy as emanating within distinct radial cones. This representation is as a convenience in formulating models for fragment generation.

Characteristic velocities and cone angles for the fragments from each of the major case segments can be determined from static firings. Table 2-16 presents representative static firing information for an HE projectile, including the number of fragments, their weights, size, velocity and cone angle. Data of this type can be used to develop fragmentation models such as shown in Figure 2-76. This fragmentation model is used in the BR-2 code described later in Section 2.2.2.1.2. Note that the point of origin is not the same for all fragment cones emanating from the projectile. This should be considered when assessing the distance between structure and detonation point for the fragment cones.
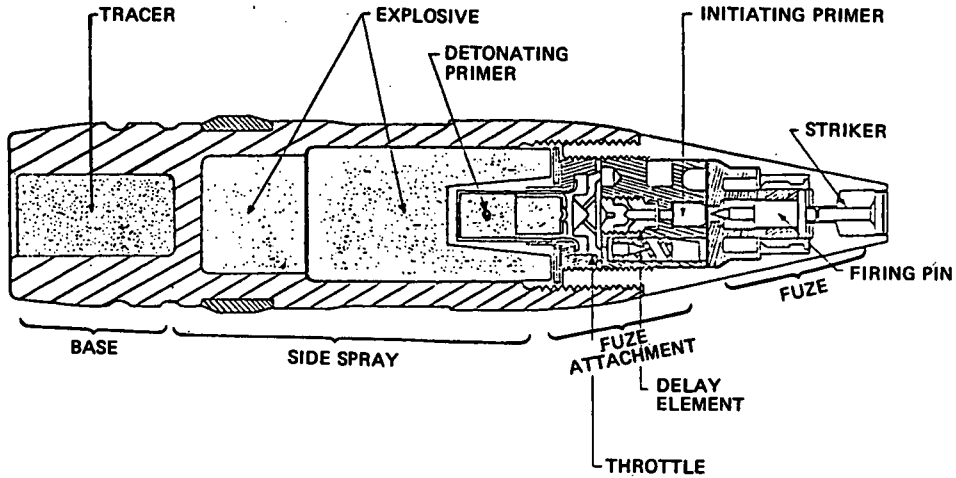
Figure 2-75. Cross-section of a Typical HE Projectile
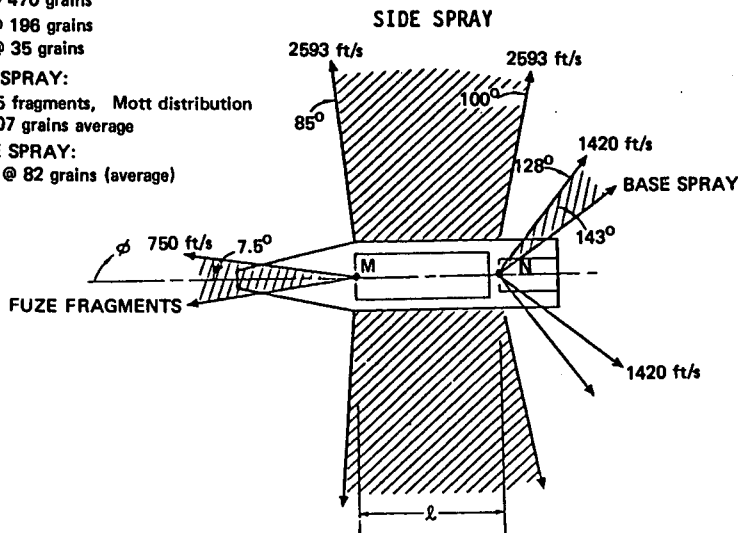
Figure 2-76. Typical Model for HE Projectile Fragmentation (Static Firing)

Table 2-16. Fragment Distribution Data Obtained from Static Detonation of HE Projectile

Projectile Segment Contributing Fragments		Static Velocity	ϕ, Cone Angle			Number of Fragments	Average Fragment Weight	Average Presented Length (Lp)
			ϕ_i(Inner)	ϕ_0(Outer)	ϕ Mean			
		(ft/s)	(deg)	(deg)	(deg)		(grains)	(inch)
	FUZE	1300	—	7.5	0	2 3	118 20	1.13 .62
	FUZE ATTACHMENT	2200	57.5	72.5	65	30	10	.50
	SIDE-SPRAY	2610	85.5	100.5	93	604	2	.29
	BASE	1550	132.5	147.5	140	20	32	.73

The intersection of the fragment cones with the structure results in damage zones defined by conic sections as shown in Figure 2-77. The extent of the damage zone, as indicated in Figure 2-78, depends on:

o   The angle of the fragment cone, which depends on projectile velocity;
o   The distance between the structure and the detonation point (standoff distance);
o   The orientation of the structural surface relative to the projectile flight path (defined by the obliquity angle, θ).

In formulating fragment distribution models, it is necessary to assume that the fragments are uniformly spaced around the circumference of the conic circle because of insufficient data. This appears to be a reasonable assumption, judging from the fragment pattern shown in Figure 2-79.
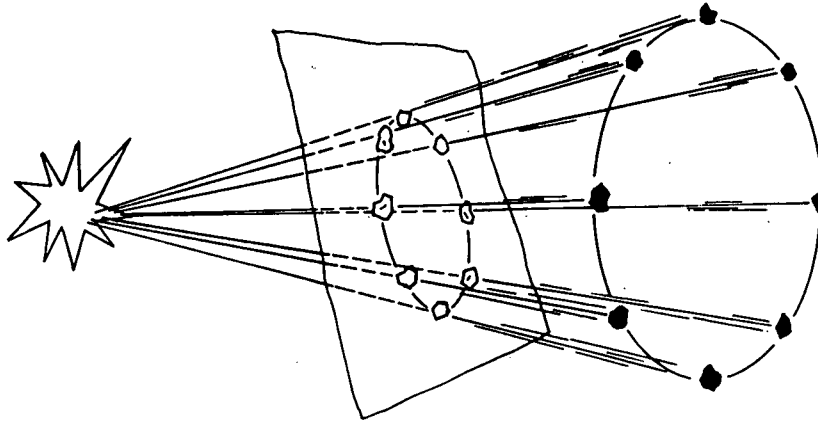
Figure 2-77. Boundaries of the Fragment Damage Zones on a Plane Surface are Conic Sections

Edge of Structural Plane

R = The distance between the structure and the detonation point measured along the projectile flightpath (slant-range standoff)

r = The distance between the structure and the detonation point measured normal to the structural (normal standoff)

θ = The angle made between the projectile flightpath and a line normal to the structure (obliquity)

ϕ = The angle made between the fragment flightpath and the projectile flightpath (cone angle)

Figure 2-78. Parameters Determining Extent of Fragment Damage Zone
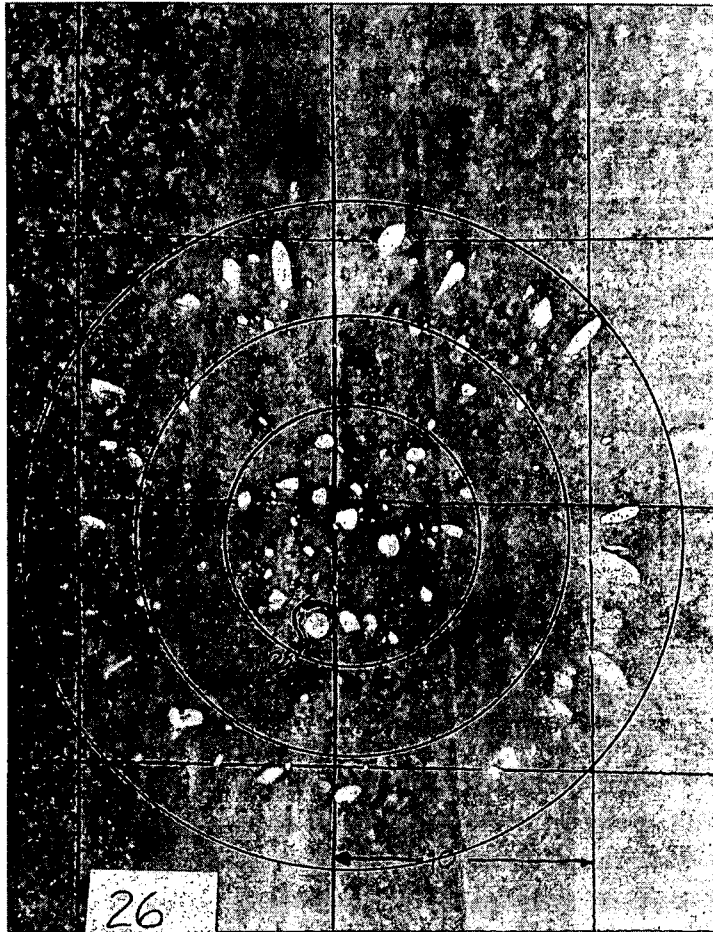
*Figure 2-79.   Fragment Pattern From HEI Projectile,
10-inch Stand-off (0-Degree Obliquity)*

The factors described above indicate the influence of key parameters in determining the distribution of fragment damages on the structure. This distribution has a pronounced influence on the resulting strength degradation, and can best be characterized by an "effective" damage size as indicated in Figure 2-80. This is discussed in more detail in Section 2.5.

The next six figures, 2-81 through 2-86, give a step-by-step procedure using graphical and manual calculational methods to estimate the fragment damage distribution on structure impacted by HE projectiles. Equations or instructions for graphical constructions are given on each figure, presented in the order required for application.

The procedure presented in the figures may be summarized as follows:

1. (Figure 2-81) The projectile velocity is added to the static firing velocity of the fragment cones. This gives the fragment cone angles measured from the projectile flight path, and the velocities of the fragments. Fragment cone angles and velocities have been computed for a typical HE projectile listed in Table 2-17, and are given in Figure 2-82. (Eqn. 2-18, Eqn. 2-19)

2. (Figure 2-83) The obliquity angle, θ, the cone angle, $\emptyset$ (from Step 1), and the normal standoff distance, r, are used to calculate the lengths of the major and minor axes of the conical fragment damage zone. (Eqn. 2-20, Eqn. 2-21)

3. (Figure 2-84) Given the orientation of the projectile flight path relative to the intersected structural plane, the point on the structure defined by the intersection of a perpendicular from the detonation point, and the major and minor axes from Step 2, the location and orientation of the fragment damage zone can be defined graphically, including the location of the center of the conical section. (Eqn. 2-22)

4. (Figure 2-85) (X_n, Y_n), the coordinates of the nth fragment on the perimeter of the conic section can be calculated if the total number of fragments is known and a uniform circumferential spacing is assumed. The X_n value is then used in the ellipse equation from Step 2 to solve for Y_n. (Eqn. 2-23)

5. (Figure 2-86) The (X_n, Y_n) coordinates of the nth fragment are used to calculate the obliquity angle of nth the fragment relative to the structure, θ_{fn}. The fragment velocity found in Step 1 is now used with each θ_{fn} to predict the size of the damage caused by the fragment impact, as described in Section 2.2.

The procedure above can be used for any cone angle or cone sub-angle. Where there are a large number of fragments, it may be best to divide the region defined by the inner and outer cone angles into several sub-cone angles. In this case, a normal distribution of fragments between the inner and outer angles could be assumed if no data were available, with the mean of the distribution located at the radius of the mean cone angle.

	Static detonation		Dynamic detonation	
	Velocity, V_S (ft/s)	Cone angle, ϕ_S (deg)	Velocity, V_R (ft/s)	Cone angle, ϕ_R (deg)
Projectile	0	0	2,000	NA
Fuze	1,300	0	3,300	0
Fuze attachment	2,200	65	3,544	39
Side spray	2,610	93	3,204	54
Base	1,550	140	1,286	51

VECTOR DIAGRAM FOR SIDE SPRAY CONE ANGLE

(Eqn. 2-18)
$$V_F = \left[V_p^2 + 2V_pV_s\cos\phi_s + V_s^2\right]^{\frac{1}{2}}$$

(Eqn. 2-19)
$$\phi_R = \arccos\left[\frac{V_p + V_s\cos\phi_s}{V_F}\right]$$

Where:
V_p = Projectile velocity
V_s = Fragment static velocity
V_F = Resultant fragment velocity
ϕ_s = Fragment static cone angle
ϕ_R = Fragment resultant cone angle

ϕ_R = 54-DEGREES

V_F = 3,204 ft/s

ϕ_s = 93 DEGREES

V_s = 2,610 ft/s

V_p = 2000 ft/s

SIDE SPRAY RESULTANT VELOCITY

2,000 Ft/s

Figure 2-81. Example Calculation for Side Spray Fragment Cone Angle

DAMAGE INTERACTION — NO INTERACTION BETWEEN DAMAGE

FRAGMENT CONE SIZE

MAXIMUM EFFECTIVE DAMAGE SIZE

RESULTANT EFFECTIVE DAMAGE SIZE

INDIVIDUAL DAMAGE UPPER BOUND

BLAST DAMAGE

TYPICAL DAMAGE SIZE

DISTANCE FROM CENTER OF DETONATION

DAMAGE SIZE

• THE EFFECTIVE DAMAGE SIZE, TD_{eff} DETERMINES RESIDUAL TENSILE STRENGTH OF THE PANEL

DETONATION

(A) INDIVIDUAL IMPACTS NOT DISTINGUISHABLE

(B) INDIVIDUAL DAMAGES TEND TO INTERCONNECT

(C) NO INTERCONNECTION OF INDIVIDUAL DAMAGES

TD_{eff}

Figure 2-80. Variation of Fragment Impact Density With Standoff Distance

PROJECTILE	FUZE				FUZE ATTACHMENT						SIDE SPRAY						BASE					
V_P	Φ_M	V_M	Φ_o	V_o	Φ_I	V_I	Φ_M	V_M	Φ_o	V_o	Φ_I	V_I	Φ_M	V_M	Φ_o	V_o	Φ_I	V_I	Φ_M	V_M	Φ_o	V_o
0	0	1300	8	1300	58	2200	65	2200	73	2200	86	2610	93	2610	101	2610	133	1550	140	1550	148	1550
200	0	1500	7	1499	53	2314	60	2292	68	2268	81	2633	89	2607	96	2581	127	1423	135	1403	143	1385
400	0	1700	6	1697	50	2438	56	2397	63	2351	77	2871	84	2620	92	2567	120	1313	128	1270	137	1232
600	0	1900	5	1896	46	2573	53	2513	59	2448	73	2724	80	2647	87	2569	111	1227	121	1157	130	1093
800	0	2100	5	2096	43	2715	49	2640	55	2557	69	2789	76	2690	83	2587	102	1169	111	1069	121	975
1000	0	2300	4	2295	40	2864	46	2775	52	2676	65	2867	72	2746	78	2619	92	1144	101	1014	110	888
1200	0	2500	4	2495	38	3019	43	2917	48	2805	62	2957	68	2815	74	2667	82	1153	89	996	97	840
1400	0	2700	4	2694	36	3180	41	3066	46	2941	58	3057	64	2896	70	2728	73	1196	78	1019	84	838
1600	0	2900	3	2894	34	3344	38	3221	43	3085	55	3187	61	2989	66	2802	64	1269	68	1078	71	883
1800	0	3100	3	3094	32	3512	36	3380	40	3234	52	3285	57	3092	63	2888	57	1368	58	1179	59	968
2000	0	3300	3	3293	30	3684	34	3544	38	3389	50	3410	54	3204	59	2985	50	1488	51	1286	50	1083
2200	0	3500	3	3493	29	3858	33	3711	36	3548	47	3543	52	3324	56	3092	45	1623	45	1421	43	1221
2400	0	3700	3	3693	27	4034	31	3881	34	3712	45	3682	49	3452	53	3208	40	1771	39	1569	37	1374
2600	0	3900	2	3893	26	4213	29	4054	33	3878	43	3826	47	3586	50	3331	36	1928	35	1729	33	1538
2800	0	4100	2	4092	25	4393	28	4229	31	4048	41	3975	44	3727	48	3462	33	2092	32	1896	29	1709
3000	0	4300	2	4292	24	4575	27	4407	30	4220	39	4128	42	3872	45	3600	30	2263	29	2068	26	1887
3200	0	4500	2	4492	23	4759	26	4586	29	4395	37	4285	40	4022	43	3743	28	2437	26	2246	24	2068
3400	0	4700	2	4692	22	4943	25	4767	27	4571	36	4446	39	4177	41	3891	26	2616	25	2427	22	2252
3600	0	4900	2	4892	21	5129	24	4949	26	4750	34	4609	37	4335	39	4043	24	2797	22	2610	20	2439
3800	0	5100	2	5092	20	5316	23	5133	25	4930	33	4776	35	4496	38	4200	23	2981	21	2796	18	2628
4000	0	5300	2	5292	20	5504	22	5318	24	5112	32	4945	34	4660	36	4360	21	3166	20	2984	17	2819
4200	0	5500	2	5492	19	5693	21	5504	23	5295	31	5116	33	4827	35	4523	20	3354	18	3173	16	3010

Figure 2-82. Effect of Projectile Velocity on Fragment Flight Paths

Ellipse Equation

$$\frac{x^2}{a^2} + \frac{y^2}{b^2} = 1$$

(2-20) $a = \frac{r}{2}[\tan(\theta + \phi) - \tan(\theta - \phi)]$

(2-21) $b = a\left[\dfrac{\cos^2\phi - \sin^2\theta}{\cos^2\phi}\right]^{\frac{1}{2}}$

Figure 2-83. Calculation of the Major and Minor Axes of the Conic Section Defining the Fragment Damage Zone

Major axis of ellipse oriented along a line defined by the perpendicular intercept $\overline{N}$ and the flight path intercept, I.

C = Center of Ellipse
I = Projectile Flight Path Intercept
$\overline{N}$ = Perpendicular Intercept From Detonation Point

(Eqn. 2-22)

$h = a + r \tan(\theta - \phi)$
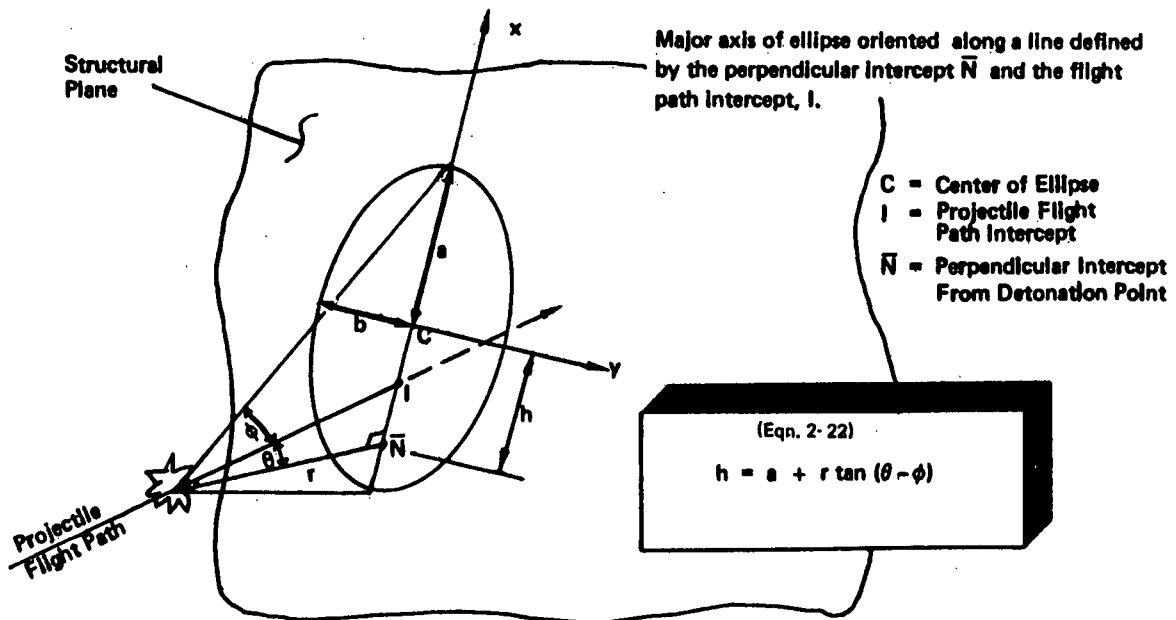
Figure 2-84. Graphical Procedure for Orienting the Major Axis of the Fragment Damage Zone

91

r = Normal standoff   Edge of Structural Plane

N = Total number of fragments (assumed to
     be uniformly distributed)

$\gamma = \dfrac{2\pi}{N}$ = Angular fragment spacing

n = The nth fragment

ϕ = Fragment cone angle

θ = Projectile obliquity

C = Center of Ellipse

X_n = Location of nth fragment
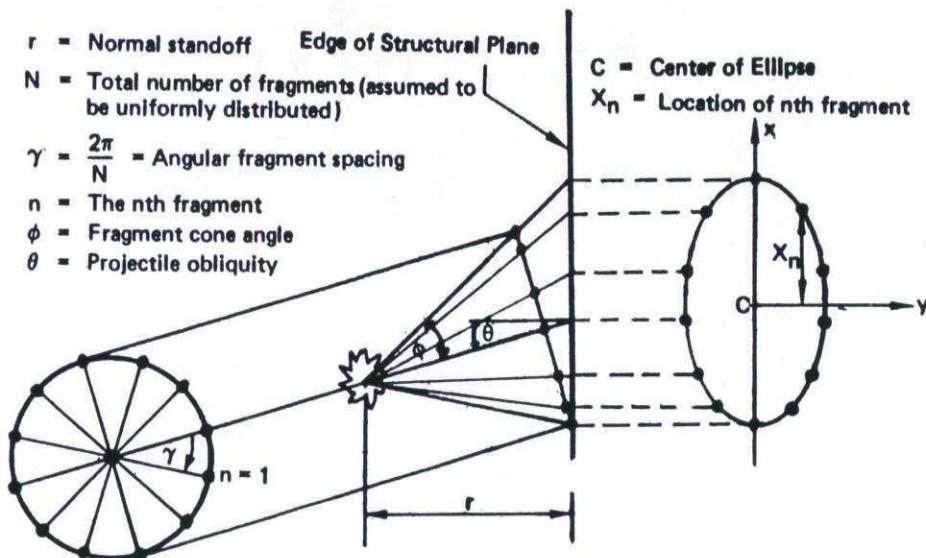
(Eqn. 2-23)

$$X_n = \frac{r \tan\phi \sin n\gamma}{\cos^2\theta\,(1 - \tan\phi \tan\theta \sin n\gamma)} + r\tan\theta - \frac{r\sin\theta\cos\theta}{\cos^2\phi - \sin^2\theta}$$

Use X_n in the ellipse equation to solve for
the Y_n coordinate of the nth fragment

Figure 2-85. Fragment Impact Coordinates Can be Determined Assuming
Uniform Distribution Around Fragment Cone

(Eqn. 2-24)

$$\theta_{fn} = \arccos\left[\frac{r}{[(h+X_n)^2 + Y_n^2 + r^2]^{1/2}}\right]$$
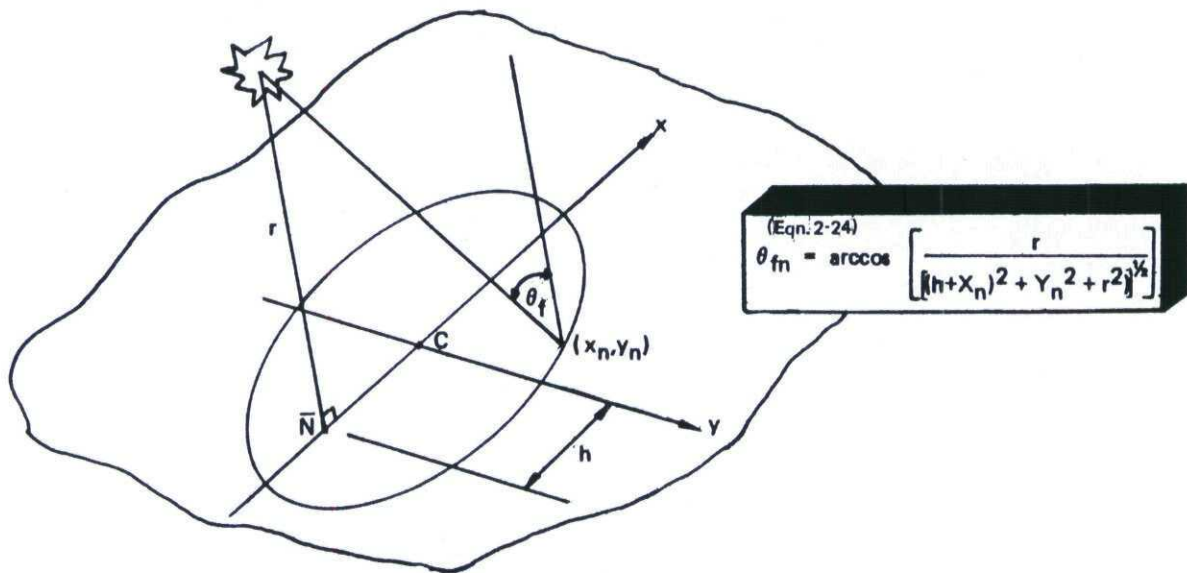
Figure 2-86. Obliquity Angle of Fragment is Calculated from Fragment Impact Coordinates

2.2.2.1.2 The BR-2 Computer Code for Predicting Fragment Damage (Extractions from Refs. 2-13 amd 2-14)

The BR-2 computer code, Reference 2-14, developed by Northrop for AFFDL/FES in 1975, is an analysis tool for predicting the area removed by fragments from HE projectiles impacting metallic structure. BR-2 was developed from the fragmentation subroutine of the BR-1 computer code which predicts structural deformation due to blast pressure loadings and fragment impacts. (See section 2.2.2.2.3 for a description of BR-1). The two codes together are designed to assess the effects of HE projectile detonations.

Figure 2-87 is a flow diagram showing the calculational steps contained in BR-2. The structure is modeled using rectangular or triangular elements, each containing additional interior grid points that are used for fragment pattern development. HE projectile characteristics are stored within the code in the form of static firing data as indicated in Table 2-18. The side-spray is represented by a Mott size distribution rather than by discrete fragments. Fuse attachment and base fragments are discrete.

Projectile velocity, flight path and detonation coordinates are program inputs. The code then calculates the resultant velocities and angles of the fragment cones. The obliquity angle, distance from detonation center, and threshold penetration criteria are calculated for the centroid of each finite element. BR-2 then determines whether any of the grid points associated with a given finite element are within the hit zone for each fragmentation source, and if so, whether penetration occurs.

Penetration criteria are based on Thor-type equations, with constants stored for aluminum, titanium and steel. The area of material removed by a fragment perforation is the projected area (i.e., the "footprint") of the impacting fragment at the target surface for velocities less than 1,000 feet per second, with an adjustment applied for velocities greater than 1,000 feet per second. The percentage of the total area of each finite element removed by fragment impacts is calculated. The primary use of this information is in adjusting the stiffness of the finite elements in subsequent structural response analysis.

Figure 2-87. Flow Chart of the BR-2 Computer Code

Table 2-17. Fragmentation Data for Typical HE Projectile

PROJECTILE SECTION	STATIC VELOCITY* (ft/s)	MEAN STATIC DIRECTION (deg)	NUMBER OF FRAGMENTS	AVERAGE FRAGMENT WEIGHT (GRAINS)	TOTAL FRAGMENT WEIGHT Σ (GRAINS)
FUZE	1,300	0	2/3	118/20	296
FUZE ATTACHMENT	2,200	65	30	10	300
SIDE SPRAY ▲	2,610	93	604	1.99	1,202
BASE	1,550	140	20	32	640
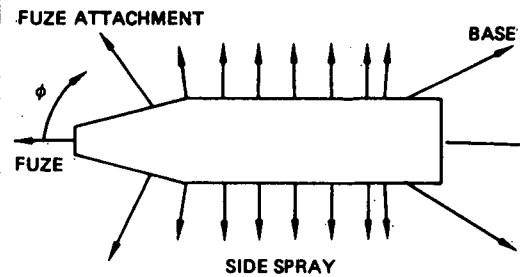
REF: AFFDL-TR-73-136
    "EFFECTS OF INTERNAL BLAST ON
     COMBAT AIRCRAFT STRUCTURES"

▲ MOTT SIZE DISTRIBUTION
* ASSUMED TO BE CONSTANT

FUZE ATTACHMENT   BASE

ϕ FUZE   SIDE SPRAY

The code incorporates many of the principles described in the previous section. The concepts and equations used in BR-2 warrant the detailed description below, as they define a cohesive approach to HE fragment damage prediction that is complementary to the information provided in 2.2.2.1.1. The topics addressed are:

a. Fragmentation from side spray of projectile;
b. Fragmentation from fuze, fuze attachment, and base;
c. Dynamic fragment velocity and direction;
d. Mott size distribution for side spray fragmentation;
e. Minimum perforation velocity;
f. Penetration dynamics;
g. Total surface area removed by Mott size distribution penetration;
h. Impulse loading from fragmentation - penetration fragments;
i. Impulse loading from fragmentation - non penetrating fragments;
j. Mott size distribution fragmentation on individual target elements;
k. Establishment of percent hit of a target element from side spray;
l. Stiffness and mass change of perforated elements.

The nomenclature used in this discussion is defined below.

A_p	Presented area of fragment of projectile,
C, C_2	Empirical constants,
E_c	Elastic modulus of a core material,
j	Empirical constant,
Q_4	Dimensionless parameter,
T	Target thickness,
V	Impact velocity,
V_r	Residual velocity after impact,
V_{50}	The ballistic limit (at any obliquity),
$(V_{50})n$	The ballistic limit at normal incidence,
$a, b, c,$	Empirical constants,
d	The diameter of a projectile,
d_c	The diameter of the core of a projectile,
g	Gravitational constant,
k, m	Empirical constants,
α	An empirical constant,
β	An angle parameter,
θ	The obliquity of impact,
θ_r	The obliquity after impact,
θ_{r_0}	An obliquity parameter,
λ_r^0	Ratio of applied bending moments to moment required for failure,
ρ	Density of the target element,
ρ_c	Density of the projectile core,
α_c	Strength of the projectile core.

Fragmentation from Side Spray of Projectile. Fragmentation is assumed to spray out from the side of the projectile as well as from the nose and the base. The side spray emanates from an assumed line source of length   and is contained within the spray angles $\emptyset_{front}$ and $\emptyset_{back}$. The criterion that a particular target point (X_T, Y_T, Z_T) is hit by this spray is determined as follows:
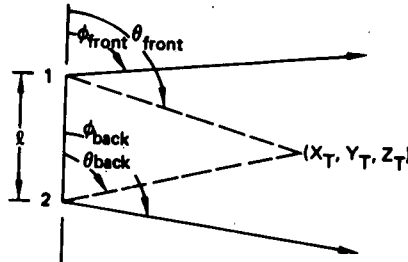
Figure 2-88 Fragment Side-Spray Pattern

The hit criterion is, as seen from Figure 2-88, is:

$$\theta_{front} \geq \emptyset_{front} \quad \text{and} \quad \theta_{back} \leq \emptyset_{back} \qquad \text{(Eqn. 2-25)}$$

Now the nature of the spray is such that $\emptyset_{front} < \emptyset_{back}$ for all of the HE projectiles of interest. Identifying the two end points as 1 and 2, then:

$$\emptyset_1 = \min(\emptyset_{front}, \emptyset_{back}) \qquad \text{(Eqn. 2-26)}$$

$$\emptyset_2 = \max(\emptyset_{front}, \emptyset_{back}) \qquad \text{(Eqn. 2-27)}$$

and the hit criterion will be

$$\theta_1 \geq \emptyset_1 \quad \text{and} \quad \theta_2 \leq \emptyset_2 \qquad \text{(Eqn. 2-28)}$$

where $\theta_1 > \theta_2$ as guaranteed in the discussion below.

Using the center of the explosive charge (X_P, Y_P, Z_P) and the directional cosines of the axis of the projectile (D_X, D_Y, D_Z), the points 1 and 2 are given by:

$$
\begin{aligned}
X_1 &= X_P + (\ell/2)D_X \\
Y_1 &= Y_P + (\ell/2)D_Y \\
Z_1 &= Z_P + (\ell/2)D_Z \\
\end{aligned}
\qquad \text{(Eqn. 2-29)}
$$

$$
\begin{aligned}
X_2 &= X_P - (\ell/2)D_X \\
Y_2 &= Y_P - (\ell/2)D_Y \\
Z_2 &= Z_P - (\ell/2)D_Z \\
\end{aligned}
\qquad \text{(Eqn. 2-30)}
$$

Then, using the dot product of two unit vectors, one obtains:

$$\theta_1 = \cos^{-1}\left(\frac{D_X(X_T-X_1) + D_Y(Y_T-Y_1) + D_Z(Z_T-Z_1)}{\left[(X_T-X_1)^2 + (Y_T-Y_1)^2 + (Z_T-Z_1)^2\right]^{1/2}}\right) \qquad \text{(Eqn. 2-31)}$$

$$\theta_2 = \cos^{-1}\left(\frac{D_X(X_T-X_2) + D_Y(Y_T-Y_2) + D_Z(Z_T-Z_2)}{\left[(X_T-X_2)^2 + (Y_T-Y_2)^2 + (Z_T-Z_2)^2\right]^{1/2}}\right) \qquad \text{(Eqn. 2-32)}$$

Both θ_1 and θ_2 will be limited to values between zero and π. Also:

$$D_X^2 + D_Y^2 + D_Z^2 = 1$$

must hold. If, and only if, $\theta_1 < \theta_2$, then use $\theta_1 = \pi - \theta_1$ and $\theta_2 = \pi - \theta_2$.

The total smear area of the fragment spray at distance R is determined from Figure 2-89.
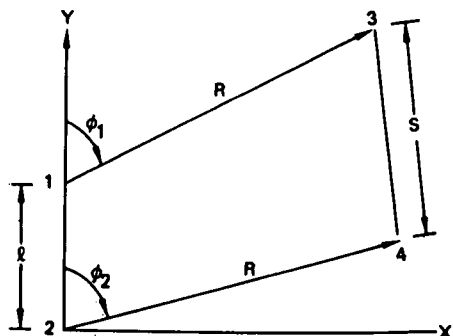
Figure 2-89. Side-Spray Geometry

The coordinates of points 3 and 4 in Figure 2-89 are:

$$X_3 = R \sin \phi_1$$
$$Y_3 = \ell + R \cos \phi_1$$
$$X_4 = R \sin \phi_2$$
$$Y_4 = R \cos \phi_2$$

The length S is obtained from:

$$S = \sqrt{\Delta X^2 + \Delta Y^2}$$

$$S = \left[R^2 (\sin \phi_1 - \sin \phi_2)^2 + (\ell + R(\cos \phi_1 - \cos \phi_2))^2 \right]^{\frac{1}{2}}$$

or

$$S = R \left[(\sin \phi_1 - \sin \phi_2)^2 + (\ell/R + \cos \phi_1 - \cos \phi_2)^2 \right]^{\frac{1}{2}} \qquad \text{(Eqn. 2-33)}$$

The smear area is then approximately:

$$A_{SMEAR} = \pi R S (\sin \phi_1 + \sin \phi_2) \qquad \text{(Eqn. 2-34)}$$

where the radius R is approximated as the distance between the target point and the center of the projectile. Thus:

$$R = \left[(X_T - X_P)^2 + (Y_T - Y_P)^2 + (Z_T - Z_P)^2 \right]^{\frac{1}{2}} \qquad \text{(Eqn. 2-35)}$$

Fragmentation from Fuze, Fuze Attachment and Base. In addition to the side spray which emanates from the side of the projectile, there are also fragments emanating from:

a.   the projectile fuze;
b.   the projectile fuze attachment;
c.   the base of the projectile.

Fragment Velocity and Direction. Table 2-17 gave the velocity and mean direction of the fragments for a static detonation of the projectile. If the projectile is moving with a velocity relative to the target at the time of detonation, the velocity and direction of the fragments must be altered to account for the dynamic consideration. Only the case of the projectile motion (relative to the target) in the direction of the projectile axis will be considered. For forward motion of the projectile (relative to the target), the forward velocity of the fragments increases in magnitude and the cone angle is reduced. In general,

$$V_D = (V_o^2 + V_P^2 + 2 V_o V_P \cos \phi_s)^{\frac{1}{2}} \qquad \text{(Eqn. 2-36)}$$

and

$$\phi_D = \arccos \left[\frac{V_P + V_o \cos \phi_s}{V_D} \right], \qquad \text{(Eqn. 2-37)}$$

where

$$V_D = \text{the dynamic velocity (ft/s)};$$

$$V_o = \text{the fragment static velocity (ft/s)};$$

$$V_P = \text{the projectile velocity at time of detonation, relative to the target (ft/s)};$$

$$\phi_D = \text{the fragment dynamic direction (degrees)};$$

$$\phi_s = \text{the fragment static direction (degrees)}.$$

Mott Size Distribution for Side Spray Fragmentation. The Mott size distribution equation is of the form:

$$N(m) = N_o \, e^{-\left(\frac{2m}{\overline{m}}\right)^{\frac{1}{2}}} \qquad \text{(Eqn. 2-38)}$$

where:

$$N_o = \text{total number of fragments};$$

$$\overline{m} = \text{average fragment weight};$$

$$N = \text{number of fragments with weight greater or equal to m}.$$

Typical numerical values of N_0 and $\bar{m}$ for a side spray are listed in Table 2-17.

The Mott size distribution equation can also be written as:

$$\log N = \log N_0 - \left(\frac{2m}{\bar{m}}\right)^{\frac{1}{2}} \log e \ . \tag{Eqn. 2-39}$$

Solving equation (2-39) for m, one obtains:

$$m = \frac{\bar{m}}{2}\left[\frac{\log N_0 - \log N}{\log e}\right]^2 = \frac{\bar{m}}{2}\left[\log_e \frac{N_0}{N}\right]^2 \ . \tag{Eqn. 2-40}$$

Minimum Perforation Velocity. The criterion for fragment penetration is assumed to be governed by the empirical equation:

$$V_c = 10^{C_1} (t \, A_f)^{C_2} m_f^{C_3} (\sec \theta)^{C_4}; \tag{Eqn. 2-41}$$

where:

V_c = minimum fragment velocity for penetration (ft/sec);

t = the target plate thickness (in.);

A_f = average presented area of fragment (in^2);

m_f = fragment weight (grains);

θ = the obliquity angle (degrees).

The average presented area of the fragment can be related to fragment weight by the empirical formula:

$$A_f = K^{-2/3} m_f^{2/3} \tag{Eqn. 2-42}$$

where K is a fragment shape factor and is approximately equal to 700 for the projectile described in Table 2-17. Defining:

$$C_5 = (2/3)C_2 + C_3 ; \tag{Eqn. 2-43}$$

then

$$V_c = 10^{C_1} (t \, K^{-2/3})^{C_2} (\sec \theta)^{C_4} m^{C_5} \ . \tag{Eqn. 2-44}$$

The constants C_1, C_2, C_3, C_4, and C_5 for typical target materials are in Table 2-18.

Table 2-18. Minimum Perforation Velocity Constants

Target material	C_1	C_2	C_3	C_4	C_5	C_7*
1. Aluminum alloy	6.185	0.903	-0.941	1.098	-0.339	0.025
2. Titanium alloy	7.552	1.325	-1.314	1.643	-0.431	0.05
3. Steel	6.601	0.906	-0.963	1.286	-0.359	0.08

*Constant used in ricochet calculations.

Penetration Dynamics. Since the velocity of the fragments hitting the target is specified by V_D, the minimum perforation velocity equation, Equation (Eqn. 2-44), can be used to compute a critical mass m_c which satisfies this equation with $V_c = V_D$. In particular,

$$m_c = \left[\frac{V_D}{10^{C_1}(t \, K^{-2/3})^{C_2}(\sec \theta)^{C_4}}\right]^{\frac{1}{C_5}} \tag{Eqn. 2-45}$$

C_5 is always negative; therefore, for a given velocity, m_c represents a minimum for the fragment weight that will perforate the target (i.e., any fragment lighter than this critical weight will not perforate the target; it will either imbed into the target or ricochet).

From the Table 2-17 data and the values of m_c for each of the projectile sections, the number of fragments and their weight which penetrate the target are determined. For other than the main (side) spray, this determination is quite explicit. For the side spray where the fragment size distribution is according to the Mott size distribution, the determination is as follows:

If:

$$m_c < \frac{\bar{m}}{2}\left[\frac{\log N_0 - \log (N_0 - 1)}{\log e}\right]^2 \tag{Eqn. 2-46}$$

then there is total penetration. If:

$$m_c > \frac{\overline{m}}{2}\left[\frac{\log N_o - \log(1)}{\log e}\right]^2 = \frac{\overline{m}}{2}\left[\frac{\log N_o}{\log e}\right]^2 \qquad \text{(Eqn. 2-47)}$$

then there is no penetration. (Caution: m_c varies from element to element as each element has its own t and θ.)

If there is neither 100% penetration nor 0% penetration, then for the side spray:

$$N_c = N_o e^{-\left(\frac{2m_c}{\overline{m}}\right)^{0.5}} \qquad \text{(Eqn. 2-48)}$$

The ratio of N_c/N_o is the ratio of the total number of fragments penetrating the target element to the fragments hitting the target elements. (For 100% penetration, use $N_c = N_o$.)

If N_c is the total number of fragments penetrating, according to the Mott size distribution the total mass penetrating is:

$$M_{T,P} = \begin{array}{l}\text{Total Mass}\\\text{Penetrating}\end{array} = \int^{N=N_c} m(N)\ dN = \frac{\overline{m}}{2}\int^{N_c}\left[\frac{\log N_o - \log N}{\log e}\right]^2 dN$$

$$= \frac{\overline{m}}{2}\left[(\ln N_o)^2 N_c - 2\ln N_o(N_c \ln N_c - N_c) + N_c(\ln N_c)^2 - 2N_c \ln N_c + 2N_c\right] \qquad \text{(Eqn. 2-49)}$$

In this notation, ln is the natural log, i.e., $\log_e$.

For the total mass penetrating a target, it is necessary to know the total area made by the holes of all penetrating fragments. The average presented area of a fragment in terms of its mass is given by the empirical formula given previously:

$$A_f = K^{-2/3} m^{2/3} \qquad \text{(Eqn. 2-50)}$$

where

A_f = average presented area of fragment (in^2);
K = fragment shape factor;
m = fragment weight (grains).

The hole size (Figure 2-90) produced in the target, A_H, in terms of surface area in the target, is given by the empirical formula:

$$A_H = A_f \sec\theta \quad \text{if } V_D \leqslant 1000 \text{ ft/s} \qquad \text{(Eqn. 2-51)}$$

$$A_H = A_f\left[1 + k(V_D - 1000)\right]^2 \sec\theta \quad \text{if } V_D > 1000 \text{ ft/s} \qquad \text{(Eqn. 2-52)}$$

where k is a material constant given in Table 2-19 and V_D is in units of ft/s.

Table 2-19. Material Constants for Determining Target Hole Size

Material	k
Aluminum	.00036
Titanium	.00032
Steel	.00030

From the above equations, the hole size in the target in terms of the fragment mass is:

$$A_H = K^{-2/3} Q\, m_f^{2/3} \qquad \text{(Eqn. 2-53)}$$

where

$$Q = \sec\theta \quad \text{if } V_D \leqslant 1000 \text{ ft/s} \qquad \text{(Eqn. 2-54)}$$

$$Q = \left[1 + k(V_D - 1000)\right]^2 \sec\theta \quad \text{if } V_D > 1000 \text{ ft/s}$$
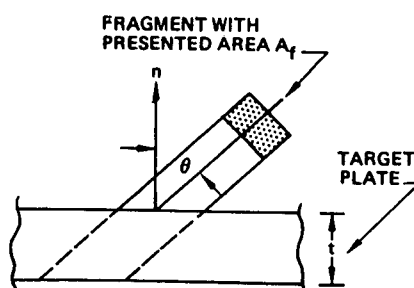
Figure 2-90. Hole Produced in Target
$(V_D < 1000 \text{ ft/s})$

Total Surface Area Removed by Mott Size Distribution Penetration. The total surface area removed from a target being hit by a Mott size distribution is given by

$$A_{H,T} = \int^{N_C} A_H \, dN = \int^{N_C} K^{-2/3} Q \, m_f^{2/3} \, dN$$

$$= K^{-2/3} Q \int^{N_C} \left\{ \frac{\bar{m}}{2} \left[\ln N_0 - \ln N \right]^2 \right\}^{2/3} dN$$

$$A_{H,T} = K^{-2/3} Q \left(\frac{\bar{m}}{2} \right)^{2/3} \int^{N_C} \left[\ln \frac{N_0}{N} \right]^{4/3} dN \equiv K^{-2/3} Q \left(\frac{\bar{m}}{2} \right)^{2/3} I_1$$

(Eqn. 2-55)

The evaluation of the integral for $A_{T,H}$ is performed by numerical integration; unity must be used as the lower limit of integration.

Impulse Loading from Fragment Impacts - Penetrating Fragments. When a fragment penetrates the target, material of weight m_s is removed from the target where:

$$m_s = \rho_s A_s t_s$$

(Eqn. 2-56)

The momentum transferred to the plate is approximately (neglecting the change in direction of the fragment):

$$I_P = m_f \left(V_D - \left[V_D^2 - V_C^2 \right]^{\frac{1}{2}} \right)$$

(Eqn. 2-57)

The direction of this transferred momentum is in the same direction as the velocity vector $\vec{V}_D$ (neglecting the change in direction of the fragment due to penetration).

For a Mott size distribution of the fragmentation, the total impulse imparted is:

$$I_{P,T} = \int_1^{N_C} I_P \, dN = \int_1^{N_C} m_f \left\{ V_D - \left(V_D^2 - V_C^2 \right)^{\frac{1}{2}} \right\} dN$$

or

$$I_{P,T} = \int_1^{N_C} m_f \, dN - V_D \int_1^{N_C} \left[1 - \left(\frac{V_C}{V_D} \right)^2 \right]^{\frac{1}{2}} m_f \, dN$$

(Eqn. 2-58)

Using equations (Eqn. 2-44) as shown and with $m = m_C$ (i.e., $V_C = V_D$):

$$I_{P,T} = V_D \int_1^{N_C} m_f \, dN - V_D \int_1^{N_C} \left[1 - \left(\frac{m_f}{m_c} \right)^{2C_5} \right]^{\frac{1}{2}} m_f \, dN$$

(Eqn. 2-59)

Using equation (Eqn. 2-40) in the above equation:

$$I_{P,T} = V_D \int_1^{N_C} m_f \, dN - \frac{\bar{m}}{2} V_D \int_1^{N_C} \left[1 - \left(\frac{\log_e \frac{N_0}{N_c}}{\log_e \frac{N_0}{N}} \right)^{-4C_5} \right]^{\frac{1}{2}} \left[\log_e \frac{N_0}{N} \right]^2 dN$$

$$\equiv V_D \left[M_{T,P} - \frac{\bar{m}}{2} I_2 \right]$$

(Eqn. 2-60)

The evaluation of the integral I_2 is carried out by numerical integration.

Impulse Loading from Fragment Impacts - Non-Penetrating Fragments. If the fragment does not penetrate, it will either ricochet off the target or imbed into the target. For aluminum plates and fragment velocities greater than or equal to 2000 ft/s, no ricochets will occur for $\theta \leq 50°$. The fragments will imbed into the target and the impulse transferred (in the direction of the velocity vector V_D) is:

$$I_I = m_f V_D \quad (m_f \text{ in units of mass})$$

(Eqn. 2-61)

For a Mott size distribution of the fragmentation, the total impulse imparted is (with $\bar{m}$ and $M_{T,P}$ in units of mass):

$$I_{I,T} = V_D \int_{N_C}^{N_0} m_f \, dN = V_D \left(\bar{m} N_0 - M_{T,P} \right)$$

(Eqn. 2-62)

For aluminum with $V_D < 2000$ ft/s or $\theta > 50°$ or for titanium or steel, the non-penetrating fragments will ricochet. The ricochet mechanics are as follows:
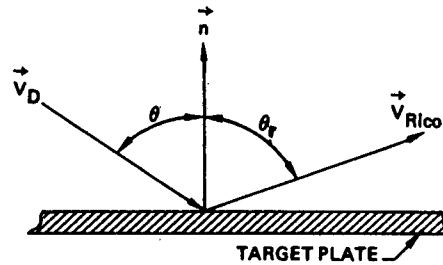
Figure 2-91. Ricochet Geometry

The ricochet angle is given by the empirical equation:

$$\sin\theta_r = 1 - e^{-(C_7\theta)}$$

(Eqn. 2-63)

Where the constant C_7 is given in Table 2-18 and θ is in degrees.

The ricochet velocity is given by :

$$V_{Rico} = V_D \sin\theta \sin^2\theta_r$$

(Eqn. 2-64)

The impulse transferred into the target plate is then:

$$I = \Delta(m_f V)$$

(Eqn. 2-65)

Resolving the impulse into two directions, the normal component is:

$$I_n = m_f(\Delta V_n) = m_f(V_D \cos\theta + V_{Rico} \cos\theta_r)$$

(Eqn. 2-66)

and is in the direction opposite to the normal shown in Figure 2-91. The tangential component is:

$$I_t = m_f(\Delta V_t) = m_f(V_D \sin\theta - V_{Rico} \sin\theta_r)$$

(Eqn. 2-67)

As an approximation, the tangential component of the impulse is neglected for the case of ricochet. If the target plate is steel, this is an excellent approximation. For a steel target, the ratio of I_t/I_n is 0.15, 0.05 and 0.01 for an obliquity angle θ of 20-, 50- and 80-degrees respectively. For an aluminum target, the ratio of I_t/I_n is 0.32, 0.53 and 0.64 for an obliquity angle of 20-, 50- and 80-degrees, respectively (for aluminum, for θ 50-degrees, there usually will be no ricochet and this approximation is not made.) For a titanium target the ratios of I_t/I_n are intermediate to those for steel and aluminum. In addition to considering the ratio of I_t/I_n, a given amount of normal impulse loading is usually always a more severe loading on the structure than the same amount of tangential impulse.

Thus the impulse imparted for a fragment that ricochets off the target is:

$$I_R = m_f V_D \left[(\cos\theta + \sin\theta \sin^2\theta_r \cos\theta_r)\right]$$

(Eqn. 2-68)

or using $\sin\theta_r = 1 - e^{-C_7\theta}$, i.e., (Eqn. 2-63) then:

$$I_R = m_f V_D \left\{\cos\theta + \sin\theta\left[1 - e^{-C_7\theta}\right]^2 \left[1 - (1 - e^{-C_7\theta})^2\right]^{1/2}\right\}$$

(Eqn. 2-69)

For a Mott size distribution of the fragmentation, the total impulse imparted is:

$$I_{R,T} = \int_{N_c}^{N_o} I_R \, dN = V_D \left\{\cos\theta + \sin\theta \, (1 - e^{-C_7\theta})^2 \right. \times$$

$$\left. \left[1 - (1 - e^{-C_7\theta})^2\right]^{1/2}\right\} \left\{\overline{m} N_o - M_{T,P}\right\}$$

(Eqn. 2-70)

The direction of the ricochet impulse is normal to the target plate.

Mott Size Distribution for Fragment Impacts on Individual Target Elements. The previously determined total quantities $A_{H,T}$, $I_{P,T}$, $I_{t,T}$, and $I_{R,T}$ are in terms of a single angle θ and for a single target material. These terms are to be computed for each element hit by fragmentation for the purpose of establishing the surface area removed and the impulse imparted to each element. If the target element is at an obliquity angle θ relative to the fragmentation spray, the effective smear area for that target element is multiplied by the factor $\cos\theta$. Thus for a target element that is 100% hit by the fragmentation, the ratio of the quantities to that element to the total quantities are:

$$\frac{A_{H,N}}{A_{H,T}} = \frac{A_N \cos\theta}{A_{SMEAR}}$$

(Eqn. 2-71)

or

$$A_{H,N} = \frac{A_N \cos\theta}{A_{SMEAR}} A_{H,T}$$

(Eqn. 2-72)

where

A_N = surface area of element N;

$A_{N,H}$ = surface area removed from element N.

Likewise:

$$I_{X,N} = \frac{A_N \cos \theta}{A_{SMEAR}} I_{X,T} \qquad X = P, I, or R$$

(Eqn. 2-73)

where:

$I_{,XN}$ = impulse imparted to element N (from perforation fragments, imbeding fragments or ricocheting fragments).

The above equations are also applicable to fragmentation from other sections of the projectile by defining A_{SMEAR} as the total area hit by all fragments from the particular section of the projectile.

Establishment of Percent Hit of a Target Element from Side Spray. With regard to rectangular elements, each panel element is evenly divided into a 3 X 3 grid (Figure 2-92). Each of these grid points is given the hit criteria test for each fragment source.

Figure 2-92. Grid for Establishing Percent of Hit on Panel Element
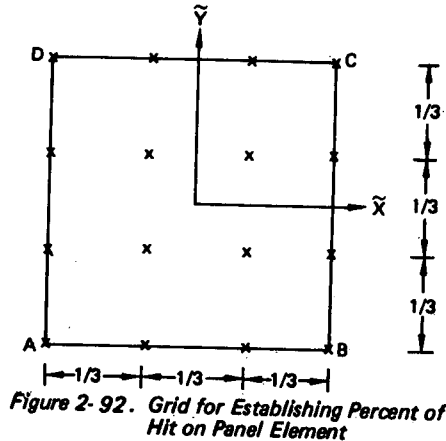
Define:

$$h(\tilde{x},\tilde{y}) = \begin{cases} 1. & \text{if hit criteria are satisfied;} \\ 0. & \text{if hit criteria are satisfied.} \end{cases}$$

(Eqn. 2-74)

The percent hit of the element in fractional form is then given by:

$$H = H_A + H_B + H_C + H_D$$

(Eqn. 2-75)

where

$$H_A = \left[1/4\, h(-1/2,-1/2) + 1/2h(-1/6,-1/2) + 1/2h(-1/2,-1/6) + h(-1/6,-1/6) \right]/9;$$

(Eqn. 2-76)

$$H_B = \left[1/2h(1/6,-1/2) + 1/4h(1/2,-1/2) + h(1/6,-1/6) + 1/2h(1/2,1/6) \right]/9;$$

(Eqn. 2-77)

$$H_C = \left[h(1/6,1/6) + 1/2h(1/2,1/6) + 1/2h(1/6,1/2) + 1/4h(1/2,1/2) \right]/9;$$

(Eqn. 2-78)

$$H_D = \left[1/2(-1/2,1/6) + h(-1/6,1/6) + 1/4h(-1/2,1/2) + 1/2h(-1/6,1/2) \right]/9.$$

(Eqn. 2-79)

H_A, H_B, H_C and H_D represent the distributions of the percent hit of the entire element to the corners A, B, C and D, respectively.

Stiffness and Mass Change of Perforated Elements. The elements that are perforated undergo both a change in their stiffness and mass. It is assumed in the BR-1 code, Reference 2-13, that only the plate elements are perforated. The amount that an element is perforated is measured in terms of the amount of surface area removed from the element as given by equation (Eqn. 2-72).

Let:

A_{TNI} = surface area removed from element n by fragments from projectile section I (I = 1, 2, 3, 4).

(Eqn. 2-80)

Then define k_n as:

$$k_n = (1 - A_{TN1})(1 - A_{TN2})(1 - A_{TN3})(1 - A_{TN4})$$

(Eqn. 2-81)

The term k_n is the ratio of the elements surface area after all fragments have struck to the original surface area of the element. Equation (Eqn. 2-81) is of the product form since once some of the surface area has been removed by fragmentation from one of the projectile sections, the surface area then available for perforation has been accordingly reduced. If an element is not perforated by fragments from a projectile section, A_{TN1} is set to zero in the BR-1 code.

For expediency of running the code and minimization of code size, it is assumed that all perforation (from all of the four potential sources) occurs at the same time. The selected time is the time that the element is first perforated by fragments from any of the four projectile sections. Actually, it is anticipated that many of the elements in most cases are hit by fragments from only one of the projectile's sections.

The stiffness of any plate element can be corrected to allow for the perforation of the element by multiplying $\{c\}$ (see equation Eqn. 2-82) of the element by k_n. This also properly corrects the pressure loading on the element since the total pressure loading, $\{f\}$, is dependent on the surface area of the element. The last two terms on the right hand side of equation (Eqn. 2-82) resulted from an integration of the element's strain energy over the element's (mid-plane) surface area. With the assumption that the perforations are located randomly over the element's surface and the individual perforation holes are small relative to the total surface area of the element, the effective strain energy in the perforated element can be estimated by multiplying the strain energy as evaluated for the non-perforated element by the factor k_n. As the element's stiffness comes into the equations of motion through the strain energy terms and the strain energy includes both the membrane and bending strain energy, both the membrane and bending stiffness are thus taken into account.

Consider now the effect of mass change due to perforation. The BR-1 code mass matrix is based on the mass lumped to the node points. It is desirable to make an "adjustment" to the inverted mass matrix for computer operating expediency. The lumped mass matrix, as well as the inverse lumped mass matrix, is of diagonal format of its submatrices. Each of these submatrices corresponds to the mass lumped to each node. Each of these submatrices is of size 6 X 6. The upper left 3 X 3 corner of the mass matrix will always be a 3 X 3 diagonal of the form

$$[UL] = \begin{bmatrix} m & 0 & 0 \\ 0 & m & 0 \\ 0 & 0 & m \end{bmatrix}$$

(Eqn. 2-82)

3 X 3

This part of the mass matrix will not be altered by the post and pre-multiplication of the transformation matrix $[J]$ due to the "orthogonality" of the $[J]$ matrix; it also will not be altered by the offset transformation matrix (see Appendix F of Reference 2-13). The lower 3 X 3 matrix (of these 6 X 6 submatrices) corresponds to the rotary inertia mass at the node and the remaining two 3 X 3 matrices, which are non-null only if there is an offset at the node, is a cross-term involving rotation and deflection of the node. It is generally the case that the rotary inertia energy of a system is of secondary significance to the translation kinetic energy. Thus, as a way to expediently incorporate mass change in the code due to perforation, for a node point without offsets, it is apparent that by multiplying the inverse (6 X 6) mass matrix by a quantity that properly corrects only m (which is the lumped mass for the node) the primary part of the kinetic energy which is due to translation is properly taken into account and secondary kinetic energy due to rotary inertia is at least approximately taken into account. For a node point with offset(s), all terms in the mass matrix involving offset distances are proportional to the translational mass quantity m. Thus again using the principle of rotational kinetic energy (defined now as explicitly excluding offset) being of secondary significance the (6 X 6) mass matrix is approximately proportional to m and the (6 X 6) mass matrix (or its inverse) can with good approximation be corrected for perforation by a quantity that properly corrects only m.

The "quantity", Kr, to correct the inverse (6 X 6) mass matrix is given as follows: (It is used as a multiplication factor on the (6 X 6) inverse mass matrix.)

$$K_r = \frac{m}{\sum_r k_n m_n}$$

(Eqn. 2-83)

where r defines the node, r is the summation over all elements i.e. trying into the node r, k_n is given by equation (Eqn. 2-81) and is automatically unity for beam elements, and m is the total lumped mass for the node. Though each element has its "own" time associated with k_n, the BR-1 code will use a single time for each node which will be approximated by the average time at which the perforated elements of that node are perforated by the source that first perforates an element of that node.

In the above discussion of mass adjustment for perforation, it is assumed that the perforations are randomly located over the surface of each element.

2.2.2.2 Predicting Damage Caused by Blast from HE Projectiles

There are two components of blast pressure generated by HE projectiles: a shock overpressure and a confined gas pressure that occurs when gases produced by the detonation are confined within enclosed cells. Figure 2-93 shows an idealization of the shock and confined gas overpressure components. The parameters affecting the intensity of these pressure loadings are described in Table 2-20. Damage occurs when these transient pressure loadings combined with existing flight loads exceed the strength capability of structural elements, resulting in rupture, attachment failures, and buckling failures.

Regardless of whether the detonation is initiated internally (delay-fuzed projectile) or externally (superquick-fuzed projectile or missile warhead), the structure will initially experience a dynamic overpressure, often referred to as a shock wave. This pressure loading is of very short duration, typically lasting one hundred microseconds or less. However, the peak pressure can be very high, and extensive damage can result. The confined gas pressure typically has a lower peak value than the shock overpressure, but it has a much longer duration and may continue to act against interior structure after the shock wave has dissipated. As a result, confined gas pressure can be a significant failure mechanism in cellular structure.

The following paragraphs describe the dynamic pressure loadings induced by blast and some of the general features of structural response to these loadings, and several analysis methods available for blast damage assessment and design. Available analysis techniques for predicting blast damage in structure are less precise than those available for projectile penetration damage. In fact, predicting blast damage per se is an intractable problem. This is partly due to the fact that blast damage is more dependent upon configuration than projectile damage, and partly due to the fact that very little parametric empirical data is available.
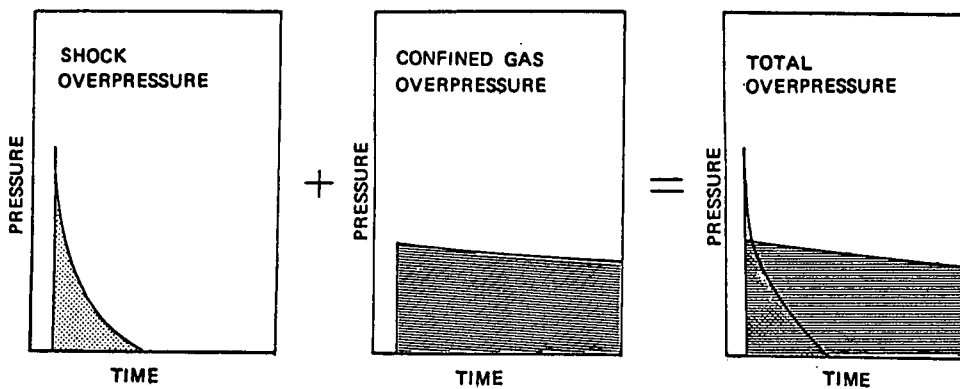
Figure 2-93. Overpressure from Confined Detonation—Resultant of Two Pressure Components

Table 2-20. Parameters Affecting the Components of Blast Pressure Loadings

COMPONENT OF BLAST PRESSURE	CONTROLLING PARAMETERS
SHOCK OVERPRESSURE:	
INCIDENT SHOCK OVERPRESSURE P	EXPLOSIVE CHARACTERISTICS: • CASE WEIGHT • EXPLOSIVE COMPOSITION • EXPLOSIVE WEIGHT • CASE CONSTRUCTION • DECAY CHARACTERISTICS DISTANCE FROM DETONATION CENTER
REFLECTED SHOCK OVERPRESSURE, P_R	INCIDENT OVERPRESSURE, P ANGLE OF INCIDENCE, β NATURAL FREQUENCY OF STRUCTURE TIME DURATION OF OVERPRESSURE
CONFINED GAS PRESSURE, P_S	EXPLOSIVE CHARACTERISTICS VOLUME OF ENCLOSURE EXTENT OF VENTING

2.2.2.2.1 Dynamic Pressure Loadings Induced by HE Projectiles

The character of the shock overpressure and confined gas pressure pulses resulting from the detonation of HE projectiles is described in this subsection. These are transient pressure loadings, of course, consisting of a nearly instantaneous increase of pressure to a peak value followed by a rapid decay of pressure. The structure responds in a dynamic manner. It will be evident from the discussion of the response of structural members to transient pressure pulses (Sections 2.2.2.2.2 and 2.2.2.2.3) that the time duration of the pressure pulse, the peak pressure, and the total impulse are significant parameters for analysis.

2.2.2.2.1.1 Shock Overpressure

The shock overpressure or shock wave is the classic "blast wave" shown in Figure 2-94, consisting of a peak overpressure that immediately begins to decay. This wave propagates outward from the center of detonation travelling at the local speed of sound, i.e., the sonic velocity corresponding to the peak overpressure, which is always greater than the sonic velocity of the medium at ambient conditions. The pressure pulse is characterized by a peak positive overpressure, a time duration, a decay shape and a total impulse. Values of these parameters depend on the strength and shape of the explosive charge as well as the distance from detonation. For certain situations, most notably spherical and point charges, tabulated values of these parameters may be found in the literature (Ref. 2-34, for example), typically presented as TNT equivalents. These are generally unsatisfactory for describing explosions generated by high-exploding projectiles, however, because of asymmetric effects caused by the construction of the projectile case and the velocity of the projectile, plus the general unreliability of explosive pulse characterization within distances near the center of detonation. Further experimental work will be required before this deficiency can be corrected.

The overpressure pulse described above represents the pressure response of a point within the medium, i.e., in free-air. It is not direction-dependent, and is sometimes called "side-on" overpressure. When the shock wave strikes an element of structure, however, the pressure loading initially acting on the structure will be either the reflected overpressure or the Mach stem overpressure, depending on the angle of incidence between the shock front and the surface. For nearly head-on incidence, the incoming shock wave is reflected from the surface of the structure, as shown in Figure 2-95, and the superposition of the incident and reflected waves causes a pressure amplification on the surface. This amplified pressure is the reflected overpressure. However, as the angle of incidence,β, of the initial shock front is increased, a value is reached such that the incident wave does not reflect, but instead travels along the surface, forming a "Mach stem" as shown in Figure 2-96. The pressure loading behind the Mach stem is the Mach-stem overpressure, and acts directly on the structure.
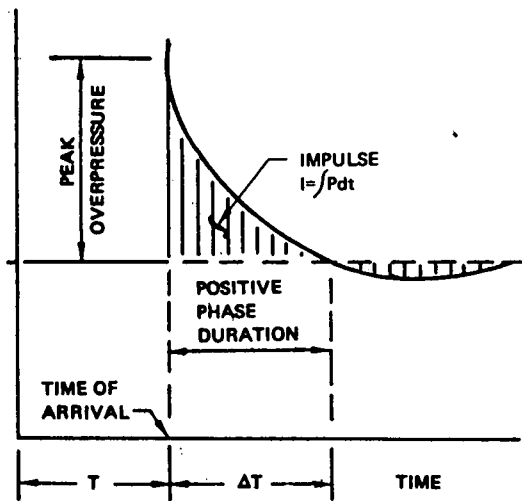
Figure 2-94. Typical Pressure-Time Response at Some Location Away From Detonation
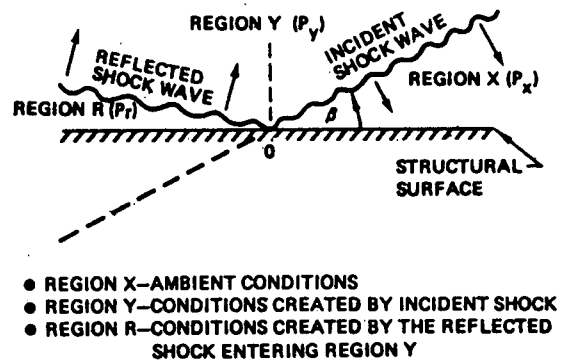
Figure 2-95. Incident and Reflected Shock Fronts at a Surface

- REGION X—AMBIENT CONDITIONS
- REGION Y—CONDITIONS CREATED BY INCIDENT SHOCK
- REGION R—CONDITIONS CREATED BY THE REFLECTED SHOCK ENTERING REGION Y
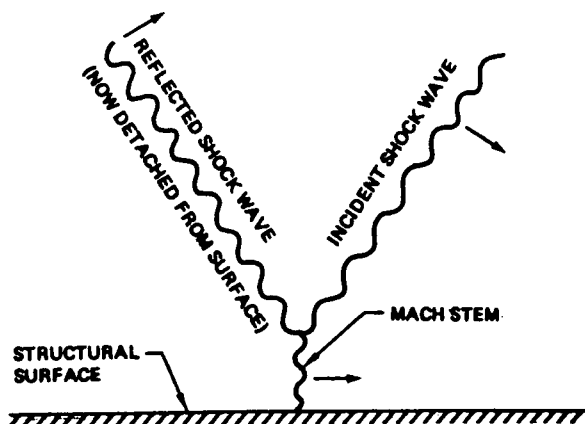
Figure 2-96. Mach Stem Formation Resulting From Oblique Incidence of Shock Front
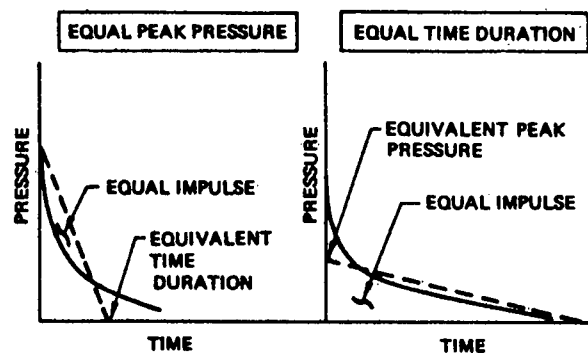
Figure 2-97. Two Methods of Developing Equivalent Triangular Pulse

In order to simplify structural analysis, it is common practice to transform the actual pressure pulse, which has an exponential decay, into an equivalent triangular-shaped pulse having the same total impulse as the actual pulse. Figure 2-97 shows two methods for doing the transformation.

Numerical Values of Shock Overpressure, Normal Incidence. Figures 2-98 and 2-99, present shock overpressure pulse characteristics for a typical HE projectile and for one pound of TNT, both detonated at sea level and at altitudes of 10,000, 20,000, 30,000, and 60,000 feet. The figures give the following information:
1. Pulse time duration (positive phase);
2. Peak incident overpressure, i.e., the peak "side-on" overpressure;
3. Peak reflected overpressure of equivalent triangular pulse, based on normal (non-oblique) incidence.

These values are plotted as functions of distance from detonation. The numerical data was obtained from operation of the computer code BLAST, described in Reference 2-32. BLAST is the most comprehensive analysis tool currently available for predicting pressure pulses from HE projectile detonations. The projectile characteristics that were input to the BLAST code were obtained from Ref. 2-14. This information included charge weight, explosive number, L/D ratio, and case/charge weight ratio.

Numerical Values of Shock Overpressure, Oblique Incidence. The data in Figures 2-98 and 2-99 is for normal (non-oblique) incidence of the shock front (β =0, Figure 2-95), as oblique incidence is not treated in the BLAST computer code. The validity of available methods for assessing the effects of obliquity is uncertain. For qualitative assessments, Figure 2-100 presents reflection coefficients for oblique incidence, giving η, the ratio of peak reflected overpressure at the angle of incidence β to the peak reflected overpressure at normal incidence. The data is presented for detonation altitudes from sea level to 60,000 feet. In developing this data, the BLAST code was used to establish the ratio of incident nonoblique overpressure to relected overpressure as a function of altitude. The ratio of reflected overpressure to incident pressure for oblique incidence was obtained from Reference 2-33. This figure from that reference appears in modified form as Figure 2-101.

The parameter η, appearing in Figure 2-100, was then calculated from the relationship:

$$\eta = \frac{P_{R\beta}}{P_{RO}} = \frac{P_{R\beta}}{P_i}\left(\frac{P_i}{P_{RO}}\right) \qquad \text{(Eqn 2-84)}$$

where,

$P_{R\beta}$ = reflected overpressure from oblique incident shock wave;

P_{RO} = reflected overpressure from nonoblique incident shock wave;

$\dfrac{P_{R\beta}}{P_i}$ = ratio of reflected overpressure to incident overpressure, oblique incident shock wave (obtained from Figure 2-101);

$\dfrac{P_{RO}}{P_i}$ = ratio of reflected overpressure to incident overpressure, nonoblique incident shock wave (obtained from NOL BLAST code, Ref. 2-32).

η can be used to compute the peak pressure of the equivalent triangular pulse for oblique incidence, once the corresponding value for nonoblique incidence has been obtained from Figure 2-98 or 2-99. This is done from:

$$P_{\Delta\beta} = \eta P_{\Delta o} \qquad \text{(Eqn 2-85)}$$

where,

$P_{\Delta\beta}$ = peak pressure of equivalent triangular pulse, oblique incidence;

η = reflection coefficient from Figure 2-100;

$P_{\Delta o}$ = peak pressure of equivalent triangular pulse, nonoblique incidence, from Figure 2-98 or 2-99.

This relationship is based on the following:

$$P_{\Delta o} = \frac{2}{t_d} I_{RO} \qquad \text{(Eqn 2-86)}$$

$$P_{\Delta\beta} = \frac{2}{t_d} I_{R\beta} \qquad \text{(Eqn 2-87)}$$

where I_{RO} and I_R are the impulses corresponding to the normal incidence and oblique incidence reflections. The time duration of the pulse, t_d, is assumed to be independent of angle of incidence. It follows that:

$$\frac{P_{\Delta\beta}}{P_{\Delta o}} = \frac{I_R}{I_{RO}} = \frac{P_{R\beta}}{P_{RO}} = \eta \qquad \text{(Eqn 2-88)}$$

$$P_{\Delta\beta} = \eta P_{\Delta o}$$

P_Δ = PEAK OVERPRESSURE (EQUIVALENT TRIANGULAR PULSE)
P_i = PEAK INCIDENT OVERPRESSURE
t = TIME DURATION

ALTITUDE: 20,000 FEET

BASED ON TOTAL REFLECTED IMPULSE FOR NON-OBLIQUE (NORMAL INCIDENCE) REFLECTIONS

TIME DURATION (MS)

OVERPRESSURE (PSI)

DISTANCE FROM DETONATION (FT)

ALTITUDE: 10,000 FEET

BASED ON TOTAL REFLECTED IMPULSE FOR NON-OBLIQUE (NORMAL INCIDENCE) REFLECTIONS

TIME DURATION (MS)

OVERPRESSURE (PSI)

DISTANCE FROM DETONATION (FT)

SEA LEVEL

BASED ON TOTAL REFLECTED IMPULSE FOR NON-OBLIQUE (NORMAL INCIDENCE) REFLECTIONS

TIME DURATION (MS)

OVERPRESSURE (PSI)

DISTANCE FROM DETONATION (FT)

Figure 2-98. Blast Pressure Pulse Characteristics for Typical HE Projectile

106

P_Δ = PEAK OVERPRESSURE (EQUIVALENT TRIANGULAR PULSE)
P_i = PEAK INCIDENT OVERPRESSURE
t = TIME DURATION
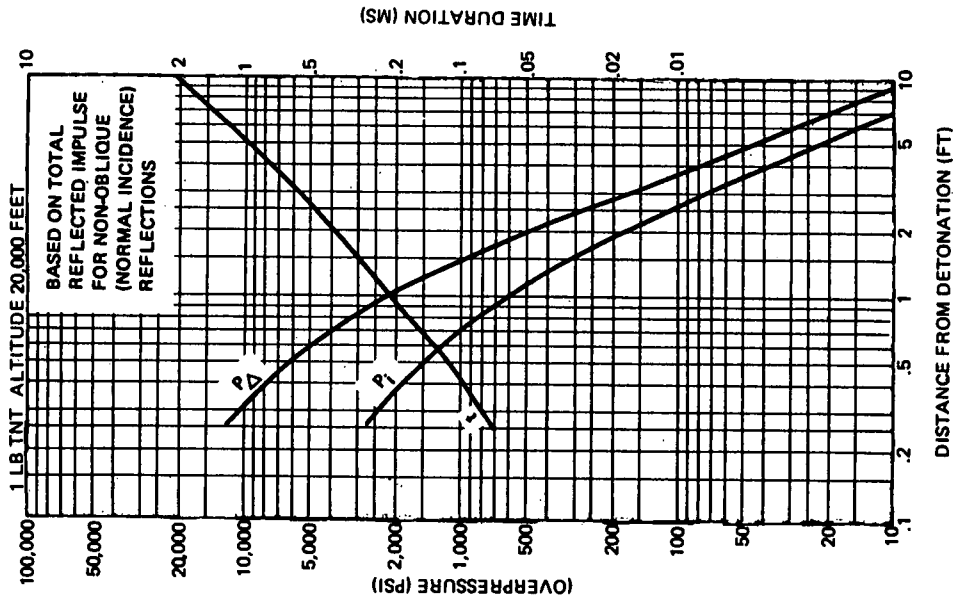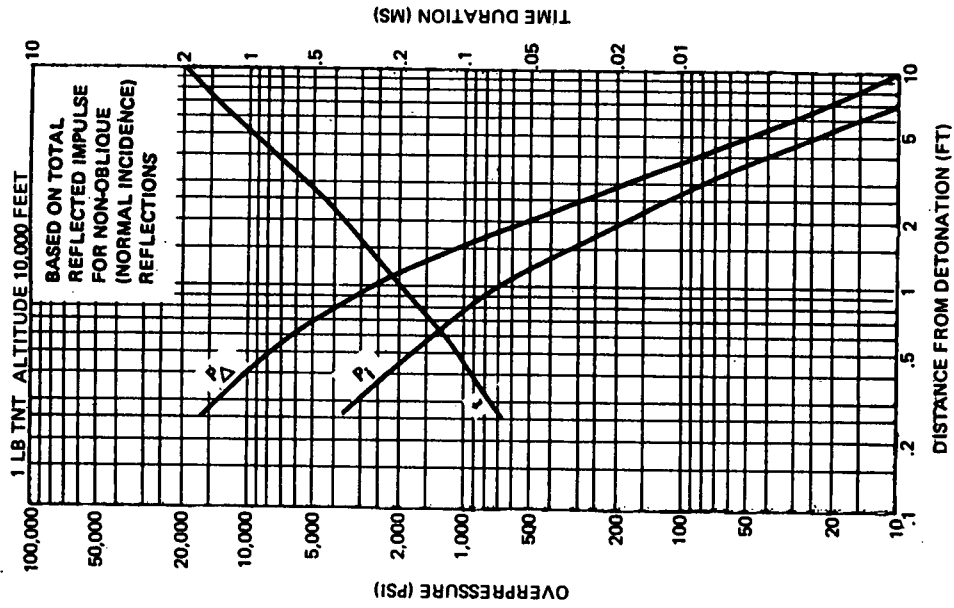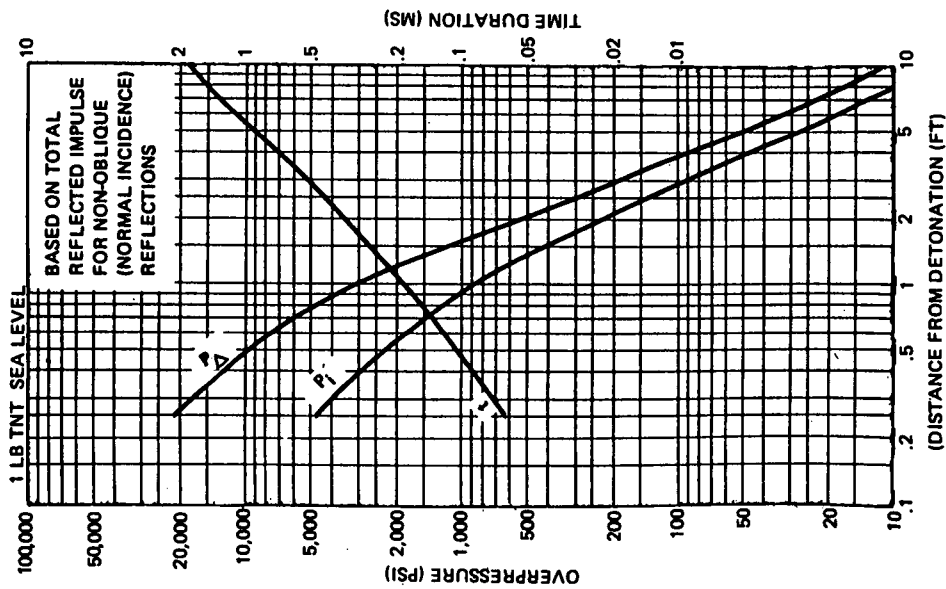
Figure 2-99. Blast Pressure Pulse Characteristics—1-lb TNT
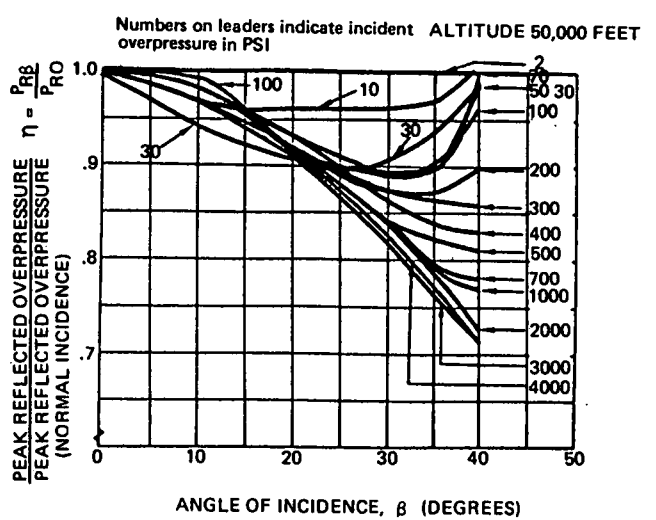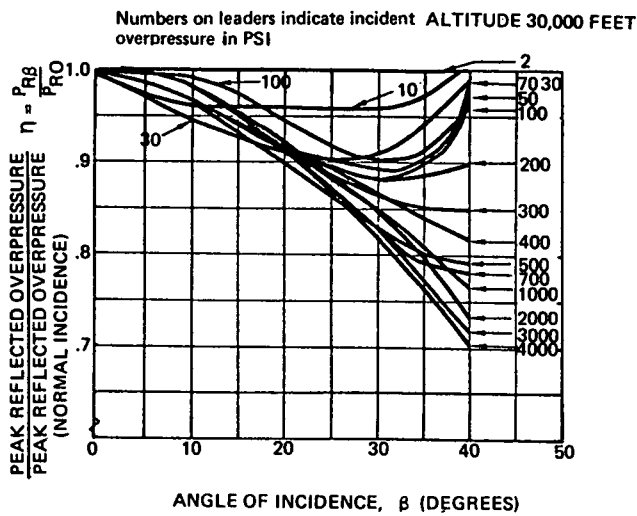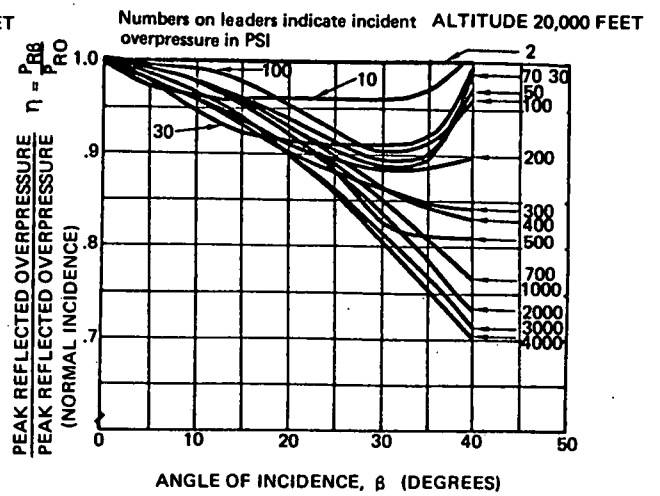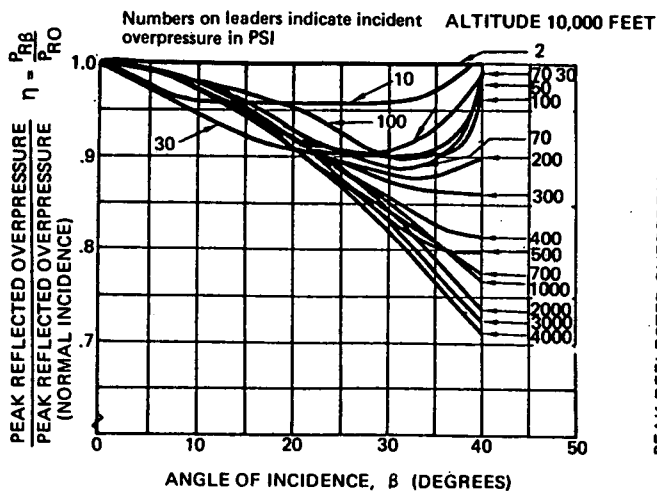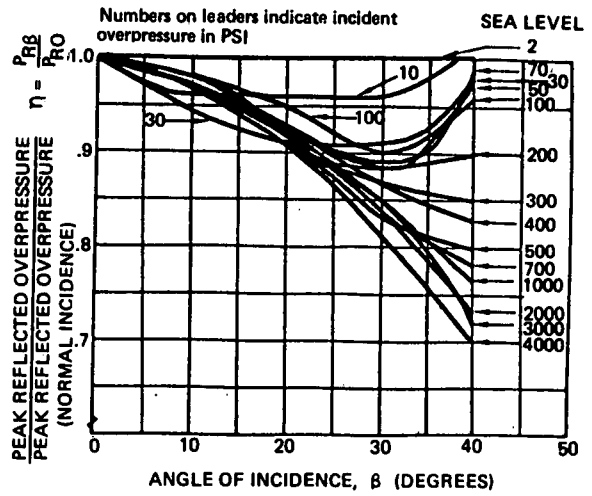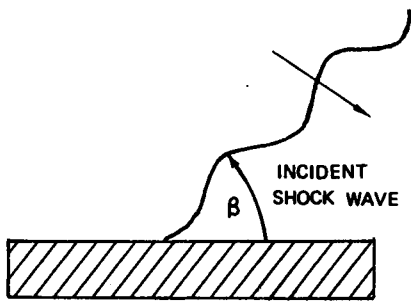
Figure 2-100. Reflection Coefficients for Oblique Shock Waves
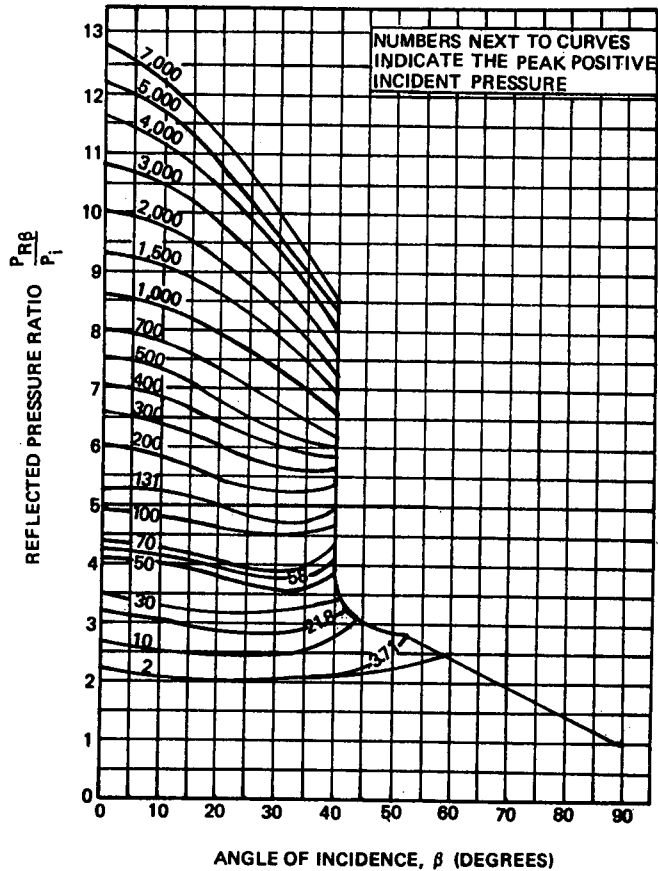
Figure 2-101. Reflected Pressure Coefficient Versus Angle of Incidence

2.2.2.2.1.2 Confined Gas Pressure

Expansion of the hot gases generated by an internal explosion may be restricted by the enclosing structure, creating an internal pressure loading. The gases are confined until released by the venting available through fragment perforations, existing vents to adjacent cells such as lightening holes in webs, or the failure of internal structure resulting in the availability of additional volume for expansion. The penetration holes and vents act as orifices, resulting in exponential decay of the internal pressure as the confined gases exit through the orifices.

As a first approximation, confined gas pressures can be represented as an instantaneous pressure rise followed by pressure decay at a rate controlled by the availability of venting. Prediction of the amplitude of confined gas overpressures and the rate of pressure decay due to venting are presented in Figures 2-102 and 2-103, generated using BLAST (Ref. 2-32) computer code and explosive characteristics from Ref. 2-14. These curves can be used to establish the pressure-time history for confined gas overpressures resulting from internal detonations of a typical HE projectile.

Figure 2-102 gives peak confined gas overpressure within unvented enclosures of variable volume, assuming no venting and no heat transfer through the walls of the enclosure. Figure 2-103 shows the decay of the confined gas overpressure that results from venting of the enclosure. The degree of venting is represented by the vented surface area, A, and the time-histories are developed for various values of the ratio of vent area to enclosed volume.

- ADIABATIC CONDITIONS
- DATA GENERATED BY BLAST COMPUTER CODE (REF. 2-32)
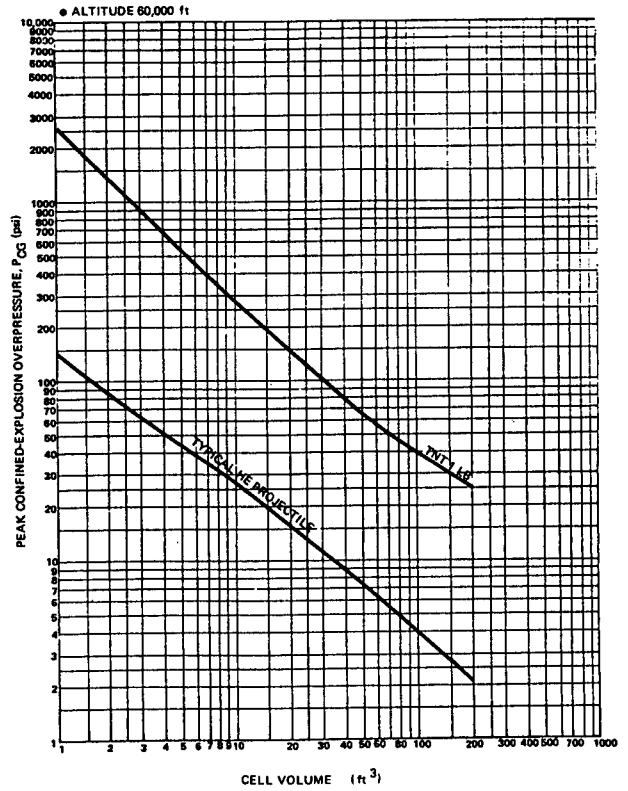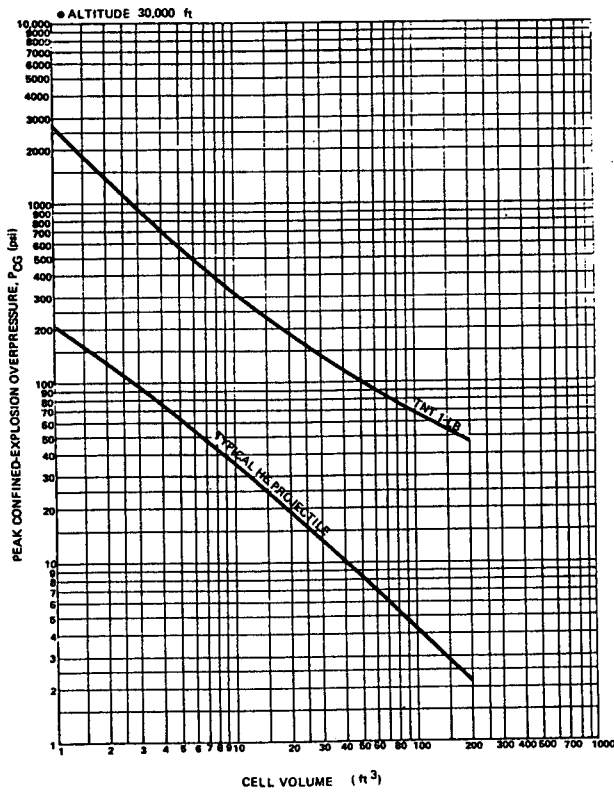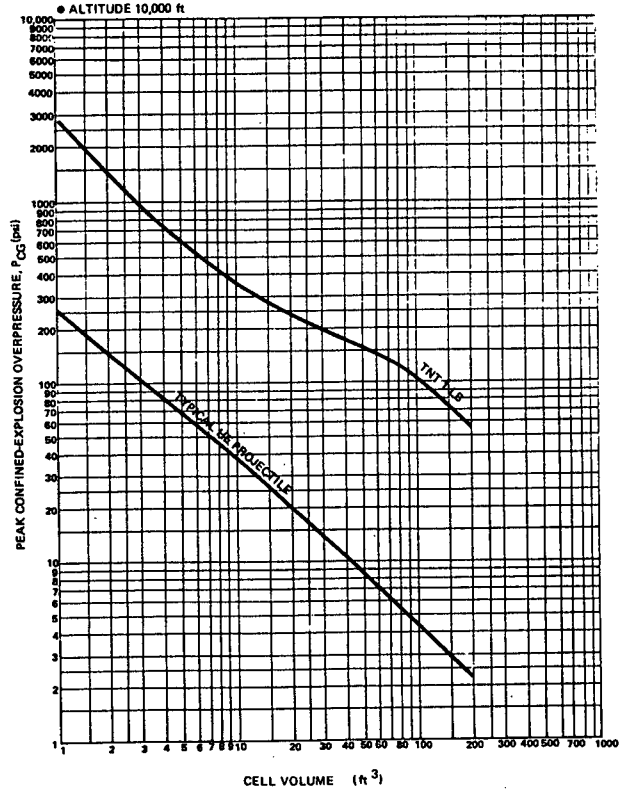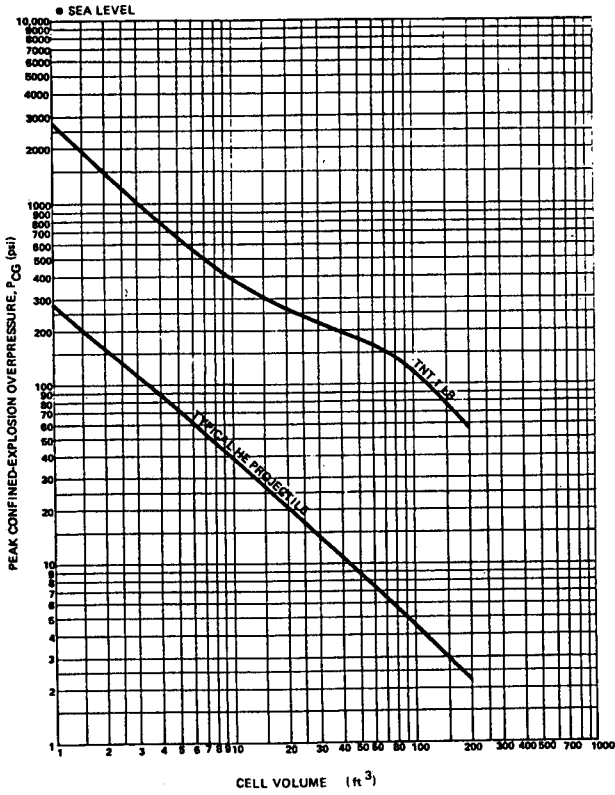
Figure 2-102. Peak Pressure Generated by Confined Explosion (No Venting)

110
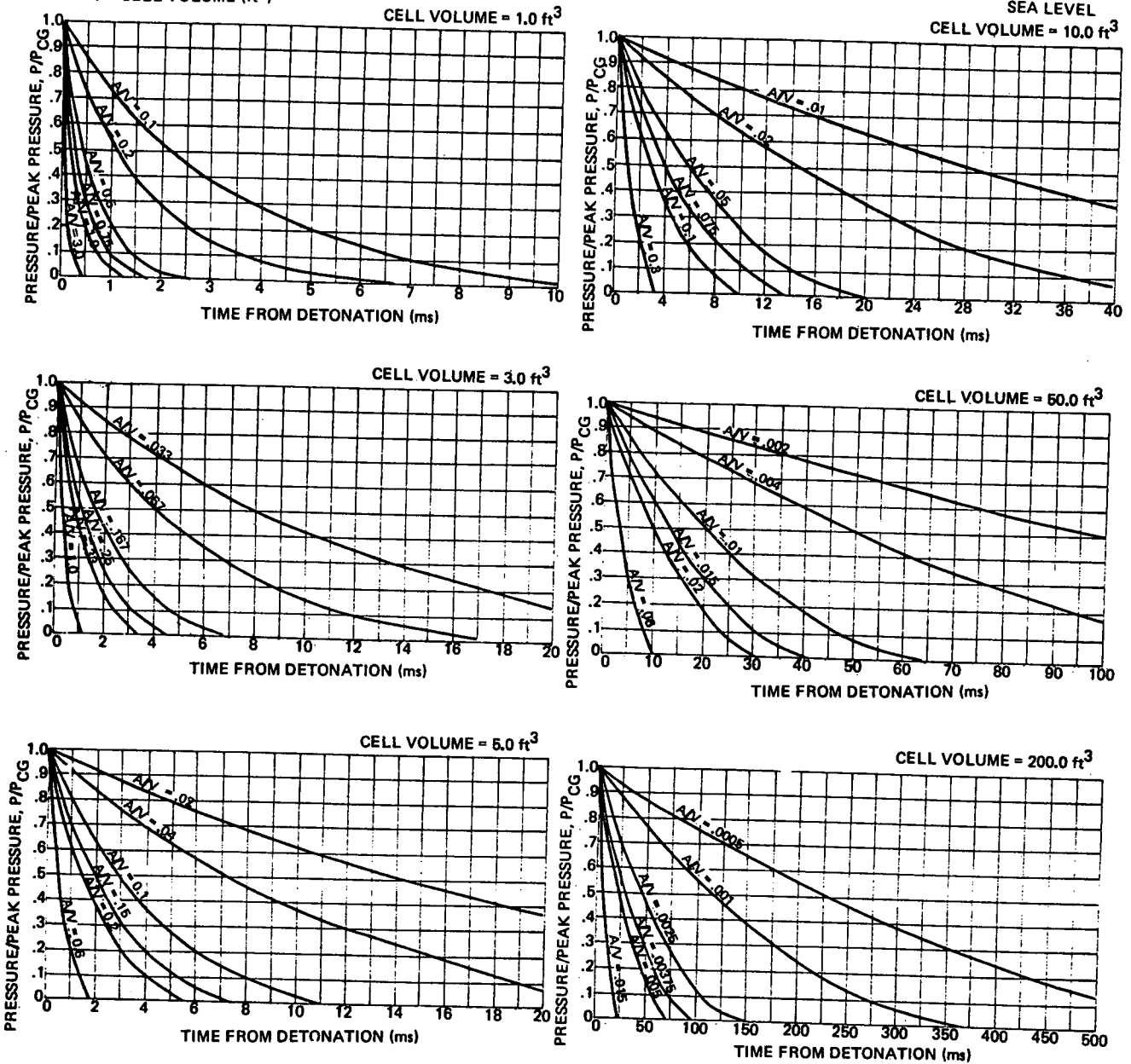
Figure 2-103. *Confined Gas Pressure—Time Histories for Internal Detonations in Vented Enclosure, Typical HE Projectile*

2.2.2.2.2 Fundamental Aspects of the Response of Structure to Blast Pressure Loadings

This subsection discusses, in general, the dynamic behavior of structure which is subjected to transient pressure loadings of the type described in 2.2.2.2.1. Some understanding of this behavior will be of value in comprehending the deformation analysis methods presented in 2.2.2.2.3.

Structural Response to Transient Pressures. The deformation of a structure exposed to transient pressure loadings depends on the amplitude/time characteristics of the loading and the mass distribution and stiffness properties of the structure. Some general information on the response of the structure to loadings of this type can be obtained by studying the response of the one-dimensional linear elastic system idealized in Figure 2-104. This system has a characteristic natural frequency, ω, and a corresponding natural period of free vibration, T.

Figure 2-105 shows a typical blast pressure pulse, which is to be applied to the linear oscillator. The pulse is defined by a force (P_m) per unit mass, a time duration (t), a decay function ($\emptyset$), and an impulse (I). The resulting displacement of the oscillator can be written as (Ref. 2-35):

$$x = \frac{P_m}{\omega^2} \, f, \tag{2-89}$$

where,

$$f = \frac{\omega^2}{P_m} \, (X_0 + A)\cos\omega t + (\frac{\dot{X}_0}{\omega} + B)\sin\omega t$$

$$A = \frac{-P_m}{\omega} \int \phi(t) \sin\omega \, tdt$$

$$B = \frac{P_m}{\omega} \int \phi(t) \cos\omega \, tdt$$

If a <u>static</u> force P_S is applied to the oscillator, the displacement is:

$$X_s = \frac{P_s}{\omega^2} \tag{2-90}$$

Taking the maximum dynamic displacement from (2-89) and dividing by the expression for static displacement (2-90) gives:

$$\frac{X_m}{X_s} = \frac{P_m}{P_s} \, f_{max} \tag{2-91}$$

From (2-91), the ratio of dynamic (P_m) and static (P_s) loads which cause the same maximum displacement is:

$$\frac{P_m}{P_s} = f_{max}^{-1} \tag{2-92}$$

Similarly, it can be readily shown that if a purely impulsive load is applied to the oscillator (i.e., an ideal pressure pulse has impulse I_0, but zero time duration) the maximum displacement is:

$$X_m = \frac{I_0}{\omega} \tag{2-93}$$

This corresponds to the displacement caused by a static load of magnitude:

$$P_s = I_0\omega \tag{2-94}$$

For any applied pressure pulse, the impulse can be written as:

$$I = P_m \, q \tag{2-95}$$

where,

$$q = \int \emptyset(t)dt$$

Combining 2-94 and 2-95 gives:

$$\frac{I}{I_0} = \frac{P_m}{P_s} \, \omega q$$
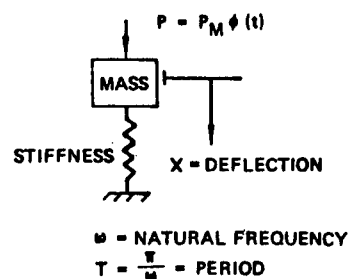
Figure 2-104. One-Degree-of-Freedom Linear Elastic Structure
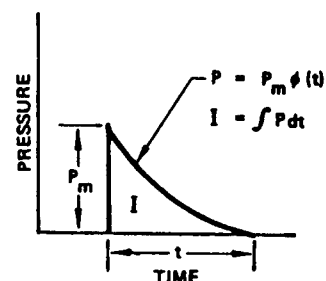
Figure 2-105. Typical Blast Pressure Pulse

The two equations (2-92 and 2-96) give the peak amplitude/impulse combinations which produce the same maximum displacement of a linear oscillator. These relations can be used to illustrate some basic aspects of dynamic structural response by constructing pressure-impulse diagrams defining the displacement of the oscillator to different types of transient loading pulses. Figure 2-106, from Reference 2-35, shows a pressure-impulse (PI) diagram for the linear elastic oscillator responding to triangular pressure pulses of varying peak pressures and time durations. Points along the curve represent different pulse durations, and these durations can be compared with the natural period of the oscillator. Point A, for example, corresponds to a pulse duration of approximately 1/5 of the natural period of free vibration, while Point C corresponds to a duration of nearly twice the natural period. The figure indicates that:

1. For very short-duration loadings, say durations less than 1/5 of the natural period, response depends only on the impulse of the pulse and is independent of the peak pressure.

2. For longer pulse durations, say twice the natural period of the oscillator, response becomes insensitive to impulse, depending primarily on peak pressure.

3. For intermediate durations, response depends on both peak pressure and impulse.

These general observations hold for any type of pressure/time history, but structural response is also influenced by the shape of the pressure/time curve as determined by the decay function. This can be seen from Figure 2-107 which shows the PI diagrams for rectangular, triangular, and exponential pulses. Figure 2-108 presents a PI diagram for a rigid-plastic structural system, an idealization appropriate when elastic deformations are negligible relative to plastic deformations. These PI curves are similar in shape to those of the elastic system, but have shifted outward from the origin, indicating the greater capacity for absorbing energy due to the plasticity. This generality of PI relationships has resulted in their use as damage criteria by a number of investigators (References 2-36 and 2-37).

In most applications involving HE projectiles the shock overpressures from either internal or external blast will be of a very short or intermediate category, and the residual confined gas pressure from internal blasts can be regarded as a step function loading.
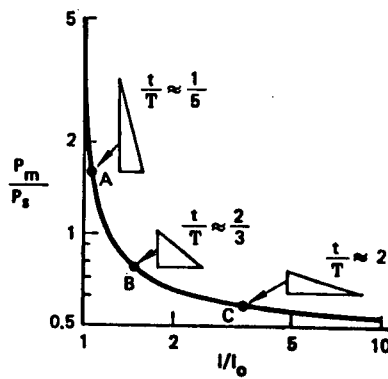
Figure 2-106. Pressure-Impulse Diagram for Triangular Pulse
Causing the Same Maximum Deflection
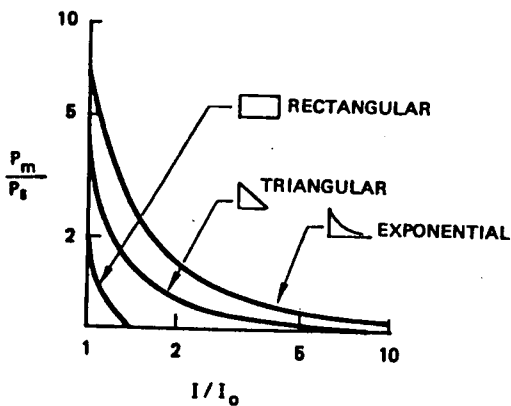
Figure 2-107. Effect of Pulse Shape,
Elastic Structure
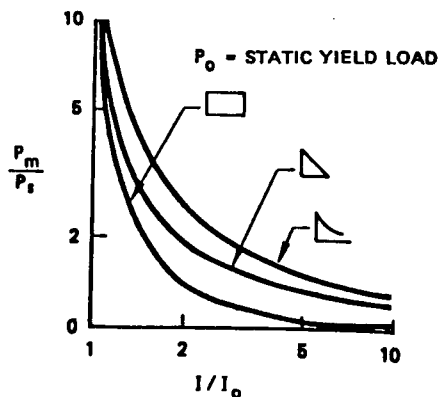
Figure 2-108. Effect of Pulse Shape,
Rigid-Plastic Structure

2.2.2.2.3 Analysis Methods for Predicting Structural Response

A general approach for predicting the damage done to structural elements by blast pressure is shown in Figure 2-109. This approach includes assessing the stresses or deformations induced by both shock overpressure and confined gas pressure, and superimposing these with the stresses or deformations due to applied flight loads. The resulting condition is then compared with design allowables to determine if a failure has occurred.

Some of the analytical methods available for predicting structural response to blast loadings include:

1. Finite Element Analysis
2. Finite Difference Analysis
3. Dynamic Plate Analysis
4. Equivalent Static Load Analysis
5. Critical Impulse Failure Criteria
6. Empirical Failure Criteria for Components

Finite element analysis, specifically the BR-1 series of codes and also general purpose codes with dynamic capability such as MARC and NASTRAN, is the most accurate approach available, particularly for assessing multi-element structure. However, this accuracy is achieved at the expense of time and resources. Dynamic analysis using finite element and finite difference codes is costly in terms of computer time, because of the small time steps required to maintain stability. Because of this, less expensive (and hence, less accurate) approaches are required for many applications, particularly for trade studies and other conceptual and preliminary design applications. These less-accurate approaches are usually based on the response of a simple structural element such as a plate or beam. Methods 3, 4, 5, and 6 below fall into this category.

2.2.2.2.3.1 Finite Element Analysis for Predicting Structural Response to Blast

The BR-1 and BR-1A computer codes (Ref. 2-13, 2-14) were developed by Northrop and released to the technical community in 1974. The BR-1FC computer code is a modification of the BR-1 code extending the capability to fiber composite structure, developed by Boeing in 1978 (Ref. 2-15). The codes are designed to predict the stresses and deflections in aircraft structure caused by HE projectile detonations.

The BR-1, BR1-A and BR-1FC computer codes provide the most comprehensive analysis approach now available for predicting the blast response of metallic and fiber composite structural configurations, and correlation with test data has been good. They are all dynamic response codes using elastic-plastic stress/strain laws. The BR-1A is a modification of the BR-1 which includes triangular plate elements. All use library routines to compute the blast pressure and fragment dispersion on each element as a function of time for several high-explosive projectiles. In addition, BR-1FC uses the method developed by Sandhu to calculate stresses and strains in each layer of a laminated fiber composite plate, providing the laminated orthotropic elastic-plastic capability lacking in the other two. The following is a summary of the BR-1 code family.

Description of BR-1 Input. The BRI code is designed to predict transient response of skin-rib-stiffener type aircraft structure subjected to impulsive forces or pressure. The user has the option of either selecting the force as direct input data or letting the code compute the pressure by specifying the size and type of an explosive. The structural elements included in the program are regular axial, torsional, and bending load carrying beams; offset beams, isotropic rectangular and triangular plates with both in-plane and bending load carrying capabilities. In addition, the BR-1FC accepts laminated orthotropic plate elements.

The BR-1 code accepts structural data in the form of (1) joint coordinates, (2) structural elements as identified by terminal joints and their physical and dimensional data, and (3) constraints at given joint locations. If the user chooses the option of providing predetermined external force data, he can input each impulsive force or pressure at each corresponding time. On the other hand, if the user wishes to use the blast pressure prediction subroutine, he must select an explosive and let the program compute the external force.

Description of BR-1 Output. The BR-1 code prints out all the input data in an edited format. Data includes structural information, control codes to the program, bar data, plate data, joint data, constraint data, fragmentation data, convergence of the eigenvalue and the stable time increment, blast data, load data and initial stress data. The computed data are printed out in the following order:

1. Deflections at all node points (Printed as each time step is completed);
2. Stress-strain data for panels (Printed after completion of all time steps);
3. Stress-strain data for bars.

The types and configurations of finite elements in the BR-1 code, the number of Gaussian stations per finite element, the number of points for which stresses are computed at each Gaussian station, the total number of points (per finite element) for which stresses are computed are all presented in Table 2-21.

For failure assessment, stresses are computed at all Gaussian stations and at various locations through the thickness of the plate elements and the beam element as indicated in Figure 2-110. At each point for which stresses are computed an automated check is made to determine if failure has occurred. If failure has occurred, a statement of the structural failure is made in the printout and the stresses at points for which stresses are printed are thereafter listed as zero. The location and identification of points within beam and plate elements at which the test for failure is made are shown in Figures 2-111 and 2-112. The program checks for failures in the longitudinal, transverse and shear directions of each layer at each station point. A longitudinal failure is indicated whenever the strain in the fiber direction exceeds the largest strain input on the longitudinal tension or compression stress-strain curve, depending on the sign of the strain. Transverse and shear failures are similarly defined as the exceedance of the largest strain on the transverse and shear stress-strain curves.

Three different failure criterion may be used to halt the program before the specified number of time steps have elapsed. These are point failure, station failure and node failure. Table 2-22 gives a description of each.
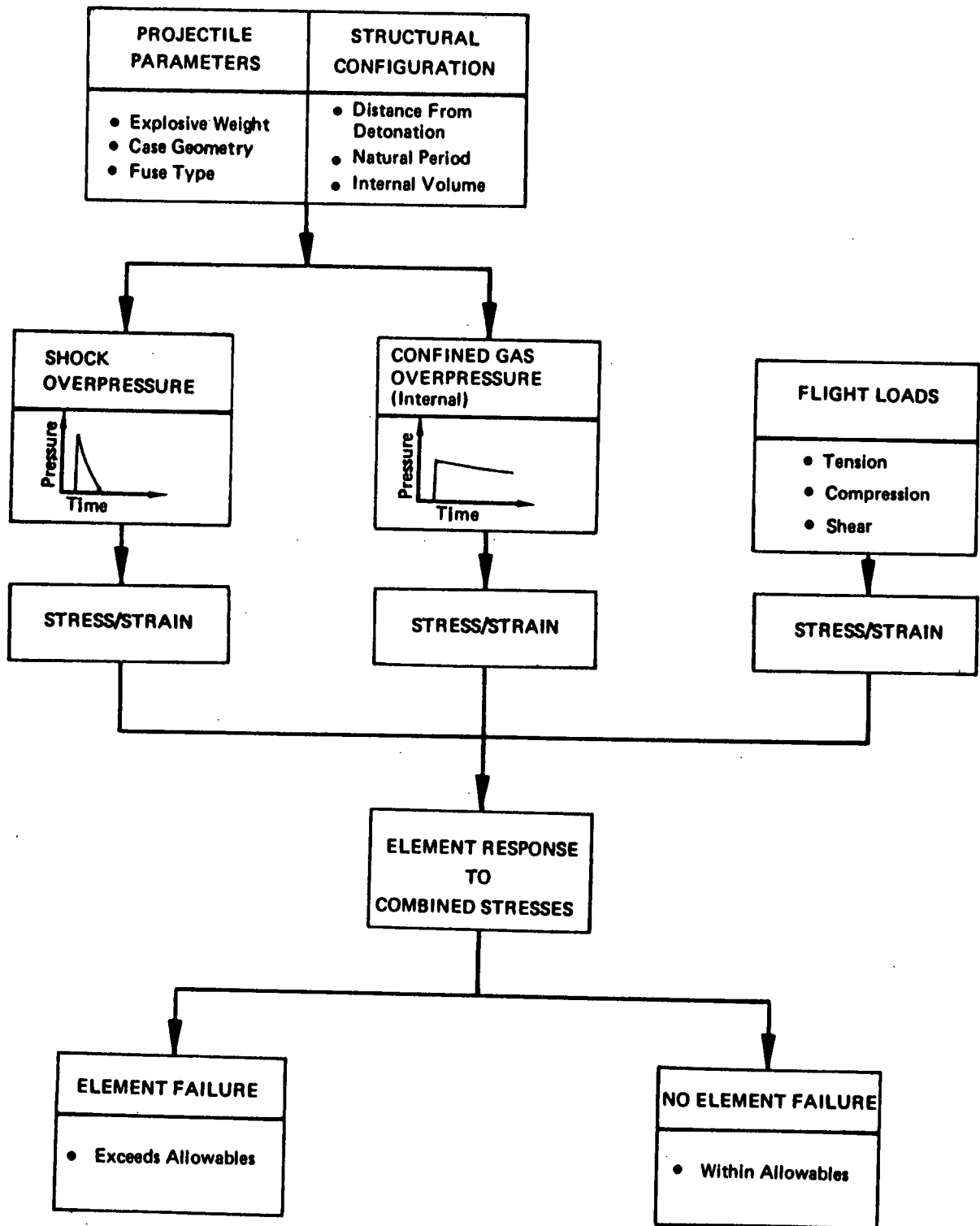
Figure 2-109. General Approach to Predicting Structural Response to Blast

Table 2-21: Points Where Stress are Computed and Failure May Be Predicted

Finite element	Cross section	Number of Gaussian stations per finite element	Number of points at a Gaussian station	Number of points for which stresses are computed per finite-element
Isotropic plate	Rectangular	9	4	36
Orthotropic plate	Rectangular	9	1	18-144[a]
Beam	Rectangular	3	8	24
Beam	I-section	3	10	30
Beam	Tee-section	3	7	21

a Depends on number of layers

PLATE ELEMENT   BEAM, RECTANGULAR CROSS-SECTION   BEAM, I CROSS-SECTION   BEAM, TEE CROSS-SECTION
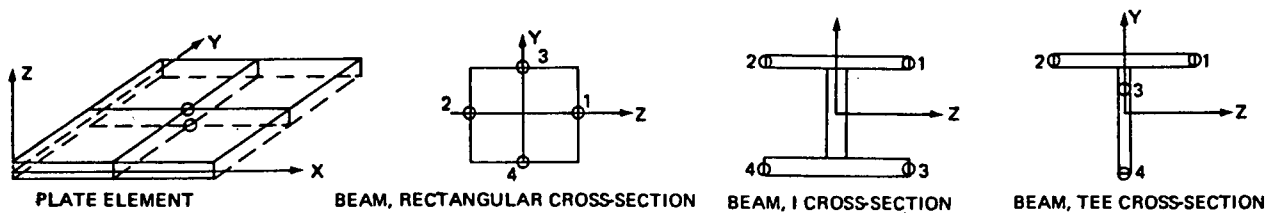
NOTE: ONE ADDITIONAL POINT WHICH IS NOT AN EXTREME FIBER POINT IS SELECTED FOR THE TEE CROSS SECTION SO EACH BEAM ELEMENT HAS PRINTED DATA FOR FOUR POINTS.

Figure 2-110. Location of Points for Which Stresses and Strains are Printed Out

Table 2-22. Description of Types of Failure

Type of structure	Types of failure		
	Number 1 (point failure)	Number 2 (station failure)	Number 3 (node failure)
Beam elements only	Any point of the structure fails.	For any beam element, all cross-section points at any (x) station fail.	All beam elements tieing into any one node have at least one station failure.
Plate elements only	Any point of the structure fails.	For any plate element, all cross-section points at any of the nine stations fail.	All plate elements tieing into any one node have at least three station failures.
Beam and plate elements	Any point of the structure fails.	All cross-section points at any (x) station of any beam element or any (x, y) station for any plate element fail.	All beam and plate elements tieing into any one node have in the beam elements at least one station failure and in the plate elements at least three station failures.

116

THE X, Y, Z DIRECTIONS OF THE MEMBER COORDINATE SYSTEMS ARE SHOWN
ON THE FIGURES.
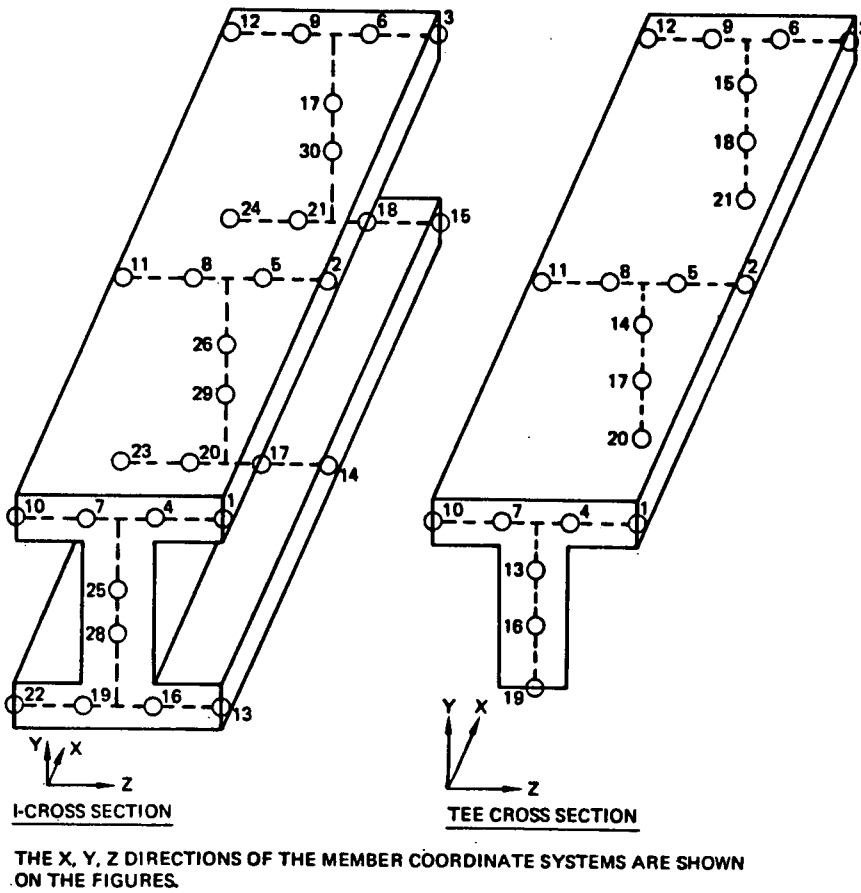
Figure 2-111. Beam Finite Elements With Tee and I-Cross Sections

The x, y, z directions of the member coordinate systems
are shown on the figures.
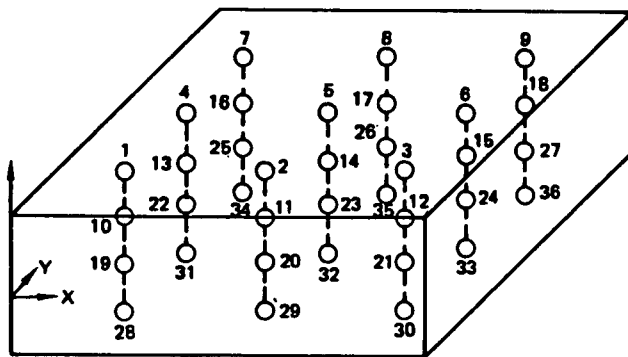
ISOTROPIC RECTANGULAR PLATE ELEMENT

POINTS No. 1 THROUGH 9
IN TOP SURFACE;

POINTS NO. 28 THROUGH 36
IN BOTTOM SURFACE
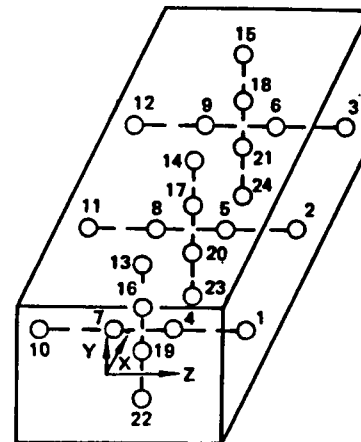
BEAM ELEMENT WITH RECTAN-
GULAR CROSS SECTIONS

POINTS NO. 13, 14, AND 15
IN TOP SURFACE;
POINTS NO. 22, 23, AND 24
IN BOTTOM SURFACE;
POINTS NO. 1, 2, AND 3
IN ONE SIDE SURFACE;
POINTS NO. 10, 11, AND 13
IN THE OTHER SIDE SURFACE

Figure 2-112. Plate and Beam Finite Elements with Rectangular Cross Sections

Structural Response Theory (Extracted From Ref. 2-13). The scheme used to determine the transient structural response in the BR-1 code is similar to the method presented by Wu and Witmer (Reference 2-38). While Wu and Witmer limit their development to "one-dimensional" planar analysis and infinitesimal strains, the BR-1 analysis uses a "two-dimensional" (structure and structural deformations defined in terms of two independent spatial variables) theory of structures in three-dimensional space, and also considers finite strains. Both theories consider the nonlinear geometric aspect of large deflections and nonlinear material properties.

The BR-1 response equations are obtained by considering the structure to be modeled by finite elements. In particular, the finite elements are restricted to flat finite plate elements and straight finite beam elements. These finite elements are assumed to have displacement patterns through their thickness according to the Bernoulli-Euler hypothesis, and it is this restriction which renders the geometrically three-dimensional finite elements as "two-dimensional" mathematical elements. Element node points are defined at the corners of the plate elements and at the end points of the beam element.

The theory used is known as the assumed displacement finite element method since the displacement pattern over the surface (or length) of the finite element is prescribed in terms of the displacements at the node points of the element. The total structure is modeled by an assemblage of these finite elements connected to each other only at their node points.

Each element faithfully retains the material properties of the structural continuum and the geometry is faithfully preserved by the model within the limitations of the finite element method. The approximation in the theory lies principally in the continuity conditions between elements and the displacements of the finite elements.

Using the Principle of Virtual Work together with D'Alembert's Principle, the dynamic equations of equilibrium are obtained. In particular, the dynamic equations of equilibrium which give rise to the transient response are the form:

$$[M]\{\overset{*}{q}\} = \{C\}$$

where:

$$\{C\} = \{F\} - \{P\} - [H]\{q*\}$$

(Eqn. 2-97)

$\{F\}$ consists of the external and body forces. $\{P\}$ and $[H]\{q*\}$ consist of the nodal forces resulting from the internal stresses within the structure. $\{q*\}$ is the matrix of generalized displacements at the nodes. The lumped mass approach is used in developing $[M]$.

The constitutive equations for the BR-1 code were developed for isotropic materials and incorporate the von Mises yield condition, the Prandtl-Reuss normal flow rule, and isotropic work hardening. Furthermore, the constitutive equations are developed for finite strains and are based on the approximation that the terms of the order of the strain squared are of infinitesimal (negligible) magnitude relative to unity. Such an approximateion is deemed acceptable when the strains are limited to less than ten percent.

The strain-displacement equations that were used in the development of the BR-1 code were chosen to avoid the limitation that deflections be small compared to the plate surface dimensions. The equations are deemed suitable for strains up to approximately ten percent and rotations up to approximately twenty percent.

The integration of equation (2-97) is carried out numerically in the BR-1 code with the use of the central-finite-difference method to obtain displacement increments at the end of each time increment. From the incremental displacements and the strain-displacement equations, incremental strains are computed. The incremental strains are used in combination with the constitutive relations (and strain rate considerations, when appropriate) to determine incremental stresses. The total displacements, strains, and stresses are then updated by the BR-1 code at the end of each time increment.

Finite strain is included in the BR-1 response theory. This means that strain is not assumed to be infinitesimal relative to unity. However, the theory does assume that the product of strains is negligible compared to unity which is deemed acceptable when strains are limited to the order of 10-percent. With finite strain the Kirchhoff stress required in the strain energy term can be properly obtained. Furthermore, the von Mises yield criterion can be written in the true invariant form with stress definition based on the deformed cross-sectional areas.

The same finite strain approach (without the BR-1 simplification that the finite strains be moderate, i.e., less than 10 percent) has been successfully backed up by experimental verification with straining into the failure region under the condition of uniaxial tension, (Reference 2-39).

In developing the BR-1 code, considerable attention was directed to establishing a time increment that would result in a numerically stable solution. Leech (Reference 2-98) has presented the criterion that would be applicable in determining the maximum time increment for the time integration in the BR-1 code. An iterative technique was developed in the BR-1 code to automate the utilization of this criterion.

Blast Pressure Loading (Partially Extracted From Ref. 2-13). The BLAST code (Reference 2-32) was developed by the Naval Ordnance Laboratory to describe the overpressures resulting from the detonation of an HE projectile internal to an aircraft structure. The BLAST code is used as a subroutine in the BR-1 codes to determine the transient pressure (or impulse) resulting from the internal detonations. The BLAST subroutine of the BR-1 code analytically divides the internal explosion into two damaging mechanisms - the shock wave and the confined explosion gas pressure. For the shock, the code generates the incident and normally reflected pressure-time history and impulse for the positive phase duration at specified distances. State-of-the-art explosion theory and experimental data were used to develop the shock calculation model.

The code reduces the shock calculation for all cases to the reference data from a free field, bare spherical 1-lb TNT explosion at sea level ambient conditions. The pressure-time history during the positive phase duration is given by the empirical equation (Reference 2-32).

$$\Delta P/\Delta P_i = (1-t/t_d)\, e^{-t/t_d}\left[1 + \frac{(228/R-0.95)}{(0.5 + t/t_d)}\right]$$

(Eqn. 2-98)

where:

ΔP = instantaneous incident overpressure;

ΔP_i = peak incident shock overpressure;

t = time measured from shock arrival;

t_d = positive phase duration;

R = distance from explosion, cm (the minimum R for calculations is 65).

The code has provisions for converting the incident overpressure to normally reflected pressure which is applied to panel element surfaces.

The confined gas overpressure that is computed in the BLAST code accounts for the chemical reaction of the explosive with the surrounding air until the final gas temperature is reached. The code uses the final temperature and amount of gas in the structural volume to determine the final pressure. The BLAST code has the capability of calculating the variation of the overpressure with time for venting due to holes in the entry and exit walls, but this feature of the BLAST code is not incorporated into the BR-1 code because venting effects are not important in the transient response of the order of 1 millisecond which is characteristic of the problem that the BR-1 code is expected to solve.

BR-1FC Modification for Fiber Composites. The existing BR-1A code used isotropic, elastic-plastic plates providing good characterization of most metal structure. Blast response analysis of composites, however, requires the laminated orthotropic elastic-plastic capability provided by the BR-1FC modification, as indicated in Figure 2-113. The BR-1FC (Fiber Composite), developed by Boeing (Ref. 2-15) replaces the isotropic elastic-plastic stress-strain relations with nonlinear orthotropic laminated plate equations of the type developed by Sandhu in Reference 2-41. In the Sandhu method, stresses and strains are computed in each layer of the laminate (Figure 2-114) at a given load level and are used to determine the moduli in the layer coordinate system. These moduli are then used to calculate the laminate stiffnesses for use in determining incremental stresses and strains due to the next load increment.

A spline fit method was used to interpolate between input points in the stress-strain curves to determine stresses and moduli. A layer is defined as having failed in a given direction (fiber direction, transverse to fiber direction or shear) when the strain in that direction is greater than the maximum value input for its stress-strain curve. The BR-1FC program requires inputting tension and compression stress-strain curves in the fiber direction and transverse to the fiber direction, and a shear stress-strain curve to define the stress-strain behavior of a laminate.

Correlation of BR-1FC Predictions with Test Data. Panel deflections and failure observations from blast tests of graphite/epoxy and aluminum panels were used to verify the predictions of the BR-1 and BR-1FC codes. Figure 2-115 shows the BR-1FC finite element model of the graphite/epoxy test panels and the aluminum supporting beams. The test setup for the bare charge tests consisted of a charge suspended in the center of a spherical blast chamber, with the test panel positioned at the desired standoff distance and supported by an aluminum angle frame mounted on support beams. C-4 explosive charges were sized to provide approximately the explosive capability of a typical HEI projectile. The 13-inch by 13-inch test panels were bolted to the angle frame on one-inch centers. Panel displacement was measured by photographing the rear surface of the panel in silhouette with a high-rate framing camera.

The test conditions and measured deflections are summarized in Table 2-23. Photographs of the damaged test panels are shown in Figure 2-116, including aluminum panels tested for comparison. BR1-4 panels, which were 0.098-inch 0/90 T300/934, showed considerable delamination and cracking between fibers, although no fractured fibers were seen. The BR1-7 and BR1-8 panels were thinner and of balanced layup (0.062-inch $0_2/\pm 45/90$ T300/934 and .077-inch $0/\pm 45_2/90$ T300/934, respectively). These showed much more extensive damage, with massive regions of delamination and many broken fibers. The BR1-7-3 panel was blown out of the test frame.

The aluminum panels (BR1-6 and BR1-9) showed less damage than the graphite/epoxy panels, although they exhibited permanent deformation which the composite panels did not. The BR1-6 panels (0.063-inch 7075-T6) had approximately 0.4-in of permanent set. Corresponding values for the BR1-9 panels (.040-inch 7075-T6) were: 9-1 = 0.85-in; 9-2 = 0.5-in; 9-3 = 1.1-in.

FINITE ELEMENT MODEL OF STRUCTURE

EXPLOSION

BR-1A — Isotropic elastic-plastic capability

BR-1FC — Adds orthotropic laminated plate capability
Uses Sandhu method for nonlinear stress-strain response
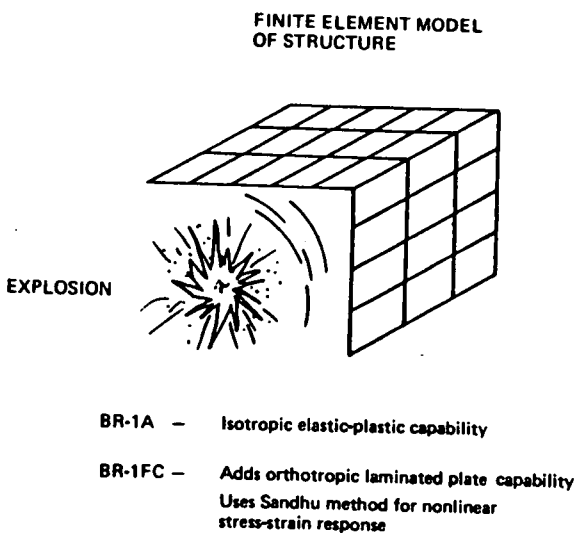
Figure 2-113. BR-1 Modification for Fiber Composite Analysis Capability

LAYER 4 LAYER 3 LAYER 2 LAYER 1

LAYER AXES

LAYER
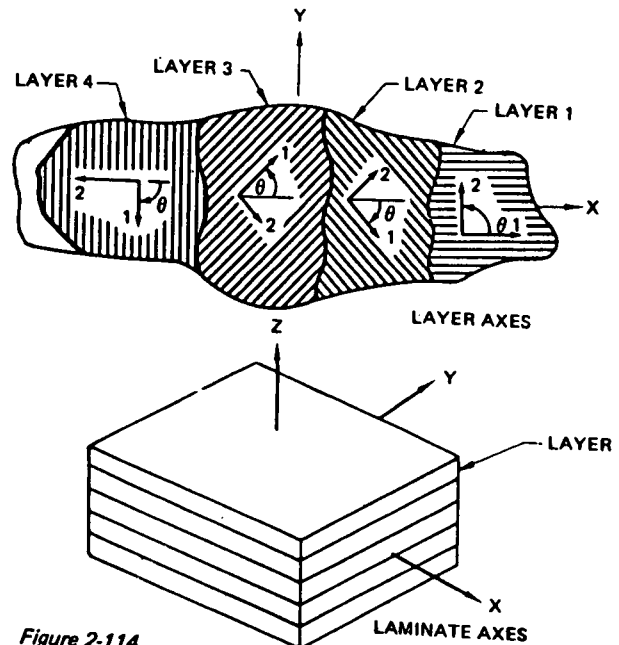
LAMINATE AXES

Figure 2-114. Laminate and Layer Coordinate Orientations Used in BR-1FC

Y
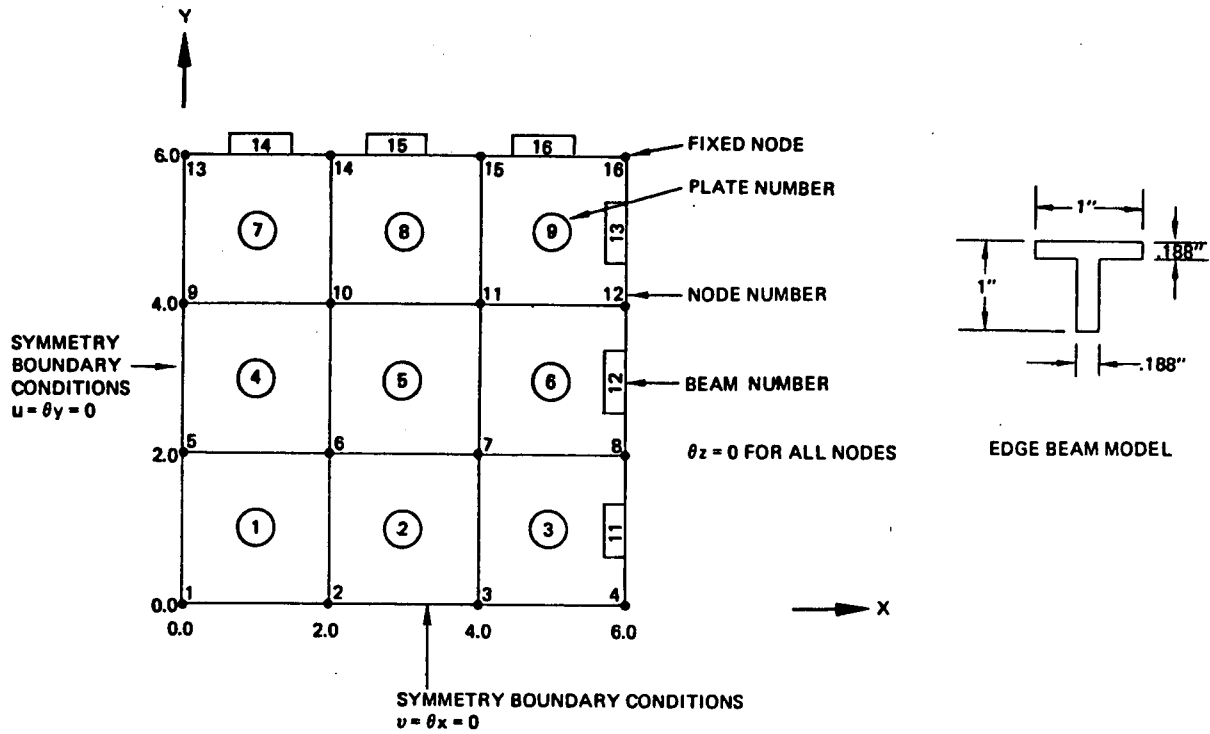
Figure 2 - 115. BR-1 Finite-Element Model of Blast Panel

Table 2-23. Blast Test Results of Graphite - Epoxy and 7075-T6 Panels

Panel	Laminate	Thickness (in)	Standoff distance (in)	Peak reflected overpressure (lb/in^2)		Maximum deflection measured (in)
				Gage 1 (center)	Gage 2 (3.5 in off center)	
BR1-1-1	(±45)	0.143				
-2	(±45)	0.143				
-3	(±45)	0.143				
BR-1-2-1	(0/+45/90)	0.119				
-2	(0/+45/90)	0.119	6	3,081	—	0.82A
-3	(0/+45/90)	0.119	6	4,216	1,969	0.62
BR1-3-1	(0/+45/0/90)	0.145	6	2,410	2,107	0.23
-2	(0/+45/0/90)	0.145	6	—	—	0.80A
-3	(0/+45/0/90)	0.145				
BR1-4-1	(0/90)	0.098	6	1,960	3,610	1.20A
-2	(0/90)	0.098				
-3	(0/90)	0.098	6	—	810	0.46B
BR1-5-1	7075-T6	0.100				
-2	7075-T6	0.100				
-3	7075-T6	0.100	6	2,984	—	0.2
BR1-6-1	7075-T6	0.063	6	2,722	1,994	0.66
-2	7075-T6	0.063	6	3,458	1,941	1.09A
-3	7075-T6	0.063				
BR1-7-1	$(0_2/+45/90)$	0.062	6	—	1,395	0.68B
-2	$(0_2/+45/90)$	0.062	10	1,105	—	
-3	$(0_2/+45/90)$	0.062	6	—	3,124	1.97B
BR1-8-1	$(0/+45_2/90)$	0.077	6	—	3,160	0.91B
-2	$(0/+45_2/90)$	0.077	10	—	603	
-3	$(0/+45_2/90)$	0.077	6	4,400	4,300	1.18A
BR1-9-1	7075-T6	0.040	6	—	1,582	1.48A
-2	7075-T6	0.040	10	771	623	0.88
-3	7075-T6	0.040	10	—	1,710	1.30

A = passed peak deflection
B = panel fractured

120

BR1-4-3
0.098-inch, 0/90 (6-inch Stand-off)

BR1-7-2
0.062-inch, $0_2/\pm 45/90$ (10-inch Stand-off)

BR1-4-1
0.098-inch, 0/90 (6-inch Stand-off)
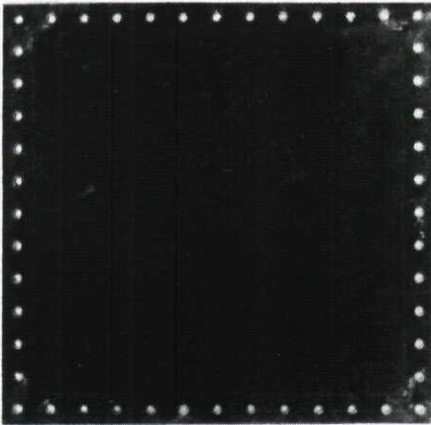
BR1-7-1
0.062-inch, $0_2/\pm 45/90$ (6-inch Stand-off)
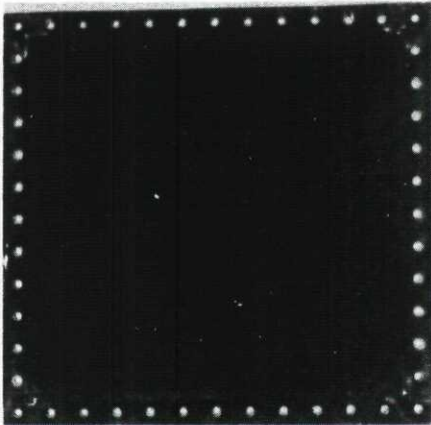
BR1-2-3
0.119-inch, $0/\pm 45/90$ (6-inch Stand-off)

BR1-3-2
0.145-inch, $0/\pm 45/0/90$ (6-inch Stand-off)

BR1-2-2
0.119-inch $0/\pm 45/90$ (6-inch Stand-off)

BR1-3-1
0.145-inch, $0/\pm 45/0/90$ (6-inch Stand-off)

Figure 2-116. Photographs of Graphite/Epoxy Panels After Blast Exposure
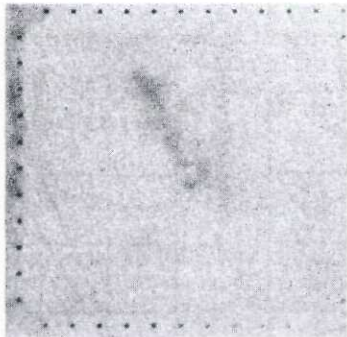
BR1-6-1 0.063-in. 7075-T6 (6-in. Stand-off)
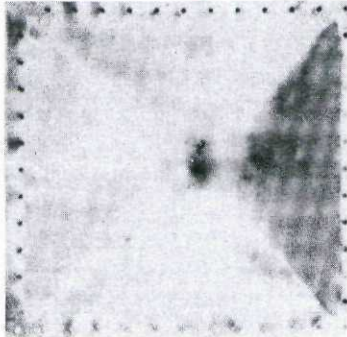
BR1-9-1 0.040-in. 7075-T6 (6-in. Stand-off)

BR1-9-3 0.040-in. 7075-T6 (10-in. Stand-off)

BR1-8-3 0.077-in. 0/±45₂/90 (6-in. Stand-off)

BR1-6-2 0.063-in. 7075-T6 (6-in. Stand-off)

BR1-9-2 0.040-in. 7075-T6 (10-in. Standoff)
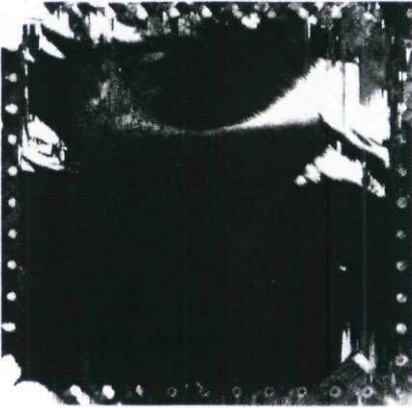
0.062-inch $0_2/\pm45/90$ (6-inch Stand-off)

BR1-8-2
0.077-inch $0/\pm45_2/90$ (10-inch Stand-off)

BR1-8-1
0.077-inch $0/\pm45_2/90$ (6-inch Stand-off)

Figure 2-116. (Concluded) Photographs of Graphite/Epoxy Panels After Blast Exposure

Figures 2-117 to 2-120 show measured and predicted panel deflections including failure points, and Table 2-24 summarizes failure results compared with BR-1FC predicted failures. Considering the variables involved in this type of testing, BR-1FC predictions show good agreement with the test results.
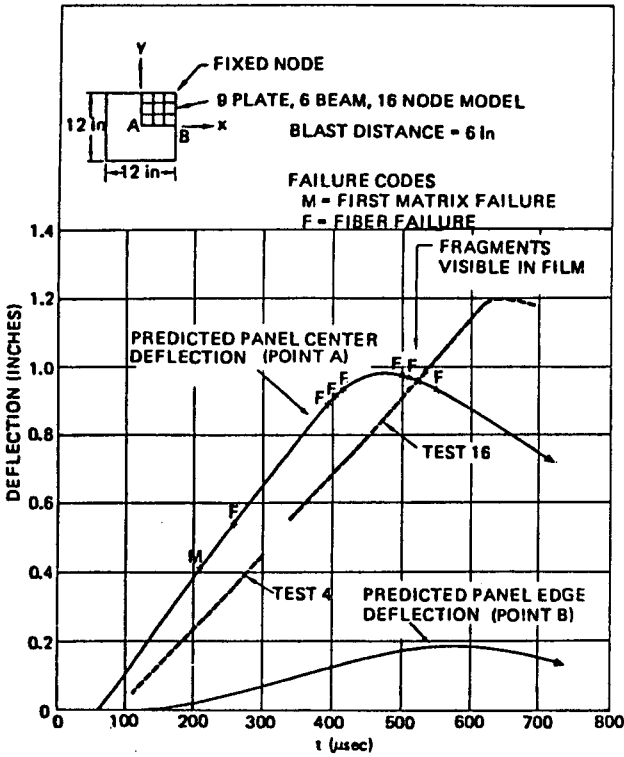
Figure 2-117. Panel BR1-4, 0/90, 0.10-in
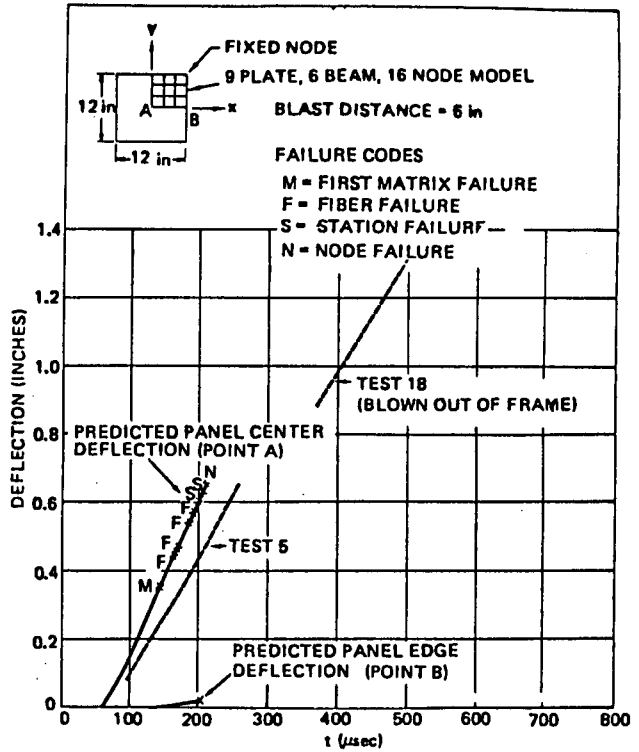
Figure 2-118. Panel BR1-7, 0₂/+45/90, 0.062-in
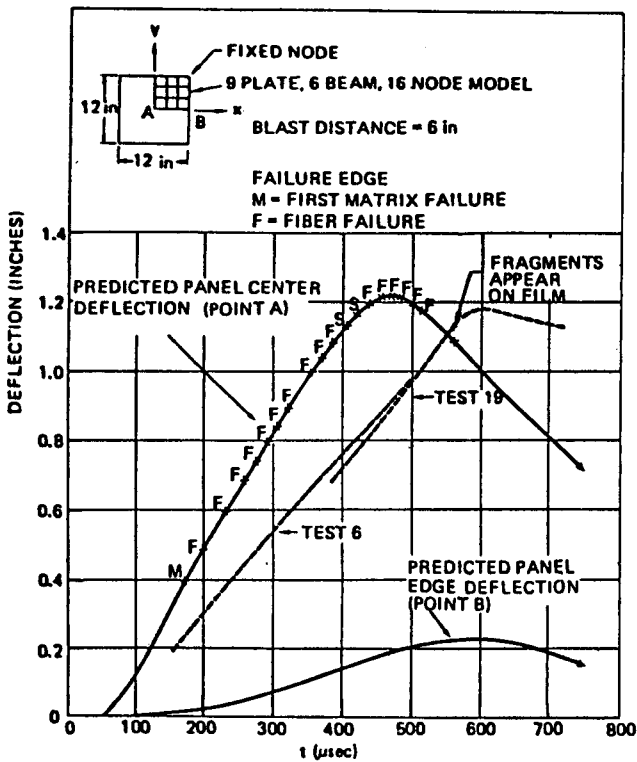
Figure 2-119. Panel BR1-8, 0/±45₂/90, 0.077-in
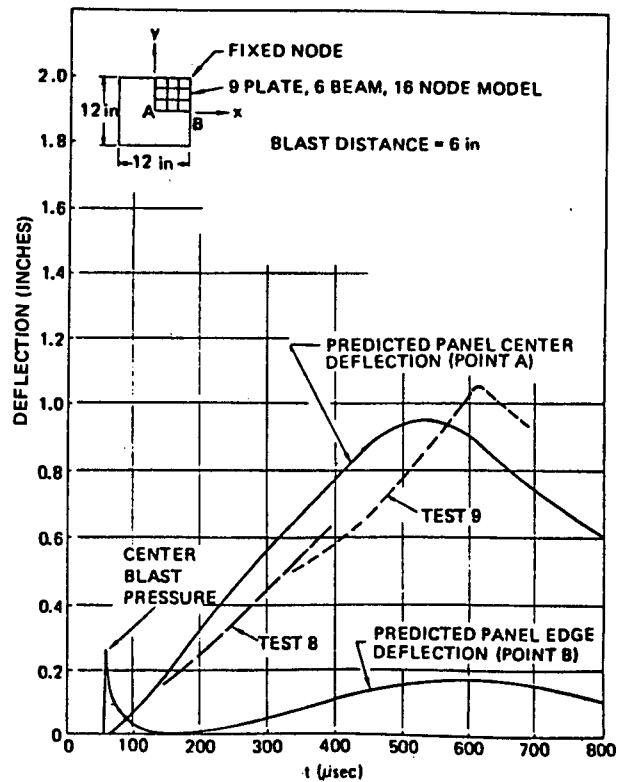
Figure 2-120. Panel BR1-6, 7075-T6, 0.063-in

Table 2-24. Correlation of Blast Panel Failures with Predictions

Panel	Test result	BR-1FC prediction
BR1-2-	No visible damage	Small number of matrix failures predicted
BR1-3-	No visible damage	No failures predicted
BR1-4-1,2	Cracks, some fibers broken	Many matrix failures, small number of fiber failure
BR1-7-1,3	Blown out of frame	Many station failures, node failure
BR1-8-1,3	Many fibers broken	Many fiber failures, 2 station failures

Matrix failure = Transverse or shear failure in a layer
Fiber failure = Fiber fracture in a layer
Station failure = Inability of laminate to carry load at
one of the nine stations in the plate
Node failure = At least three station failures in all elements
connecting to a node

Application of BR-1FC to Full-Scale Structural Configuration. The BR1 code family is ideally suited to assessing the damage and residual strength capability of full-scale structure. The BR-1FC code was used in a further step in the verification of the codes. A section of the three-spar wing test box described in Ref. 2-12 was modeled using the BR-1FC and BR-2 (fragment damage) codes. This graphite/epoxy box, shown in Figure 2-121, was tested by loading to 40-percent limit bending load and shooting with a HEI projectile. The ultimate strength of the damaged box was determined following the shot.

The section of the box modeled with BR-1FC is shown in Figure 2-122. The box design consists of ±45 graphite fabric skin with spar chords of 0-degree graphite tape encapsulated in ±45 fabric. Glass fabric stiffeners are used between spars to support the skin and feed the blast pressure loads into the ribs. The BR-1FC model of the box consists of 72 nodes, 60 plates and 36 beams. Only the exit skin was modeled, since the damage to the entrance skin is almost entirely due to fragment effects. Figure 2-123 shows the predicted nodal deflections.
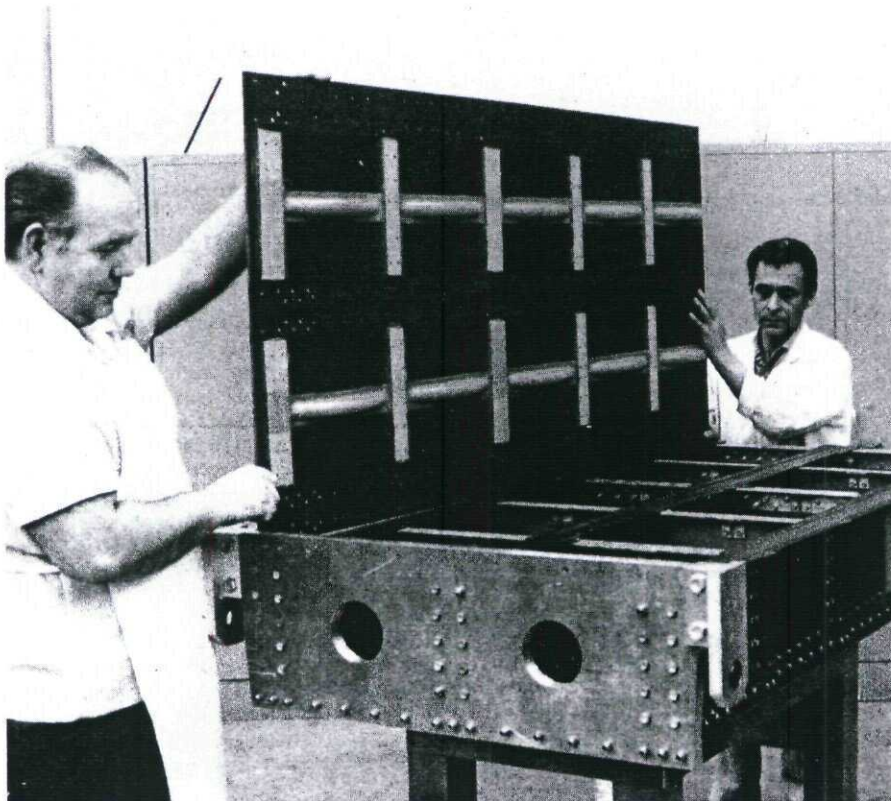
Figure 2-121. Full-Scale Graphite/Epoxy Wing-Box Component Assembly
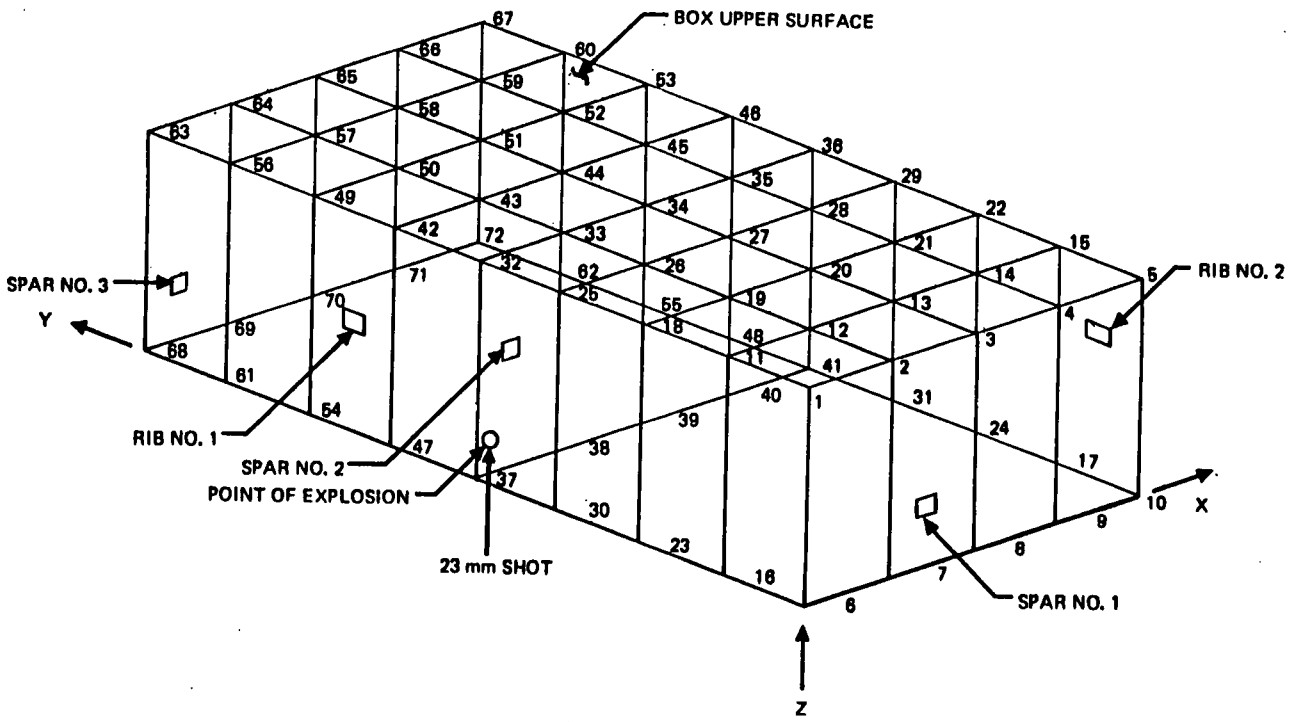
Figure 2-122. Model of Full-Scale Wing-Box Test Component
(One Rib Bay Modeled)
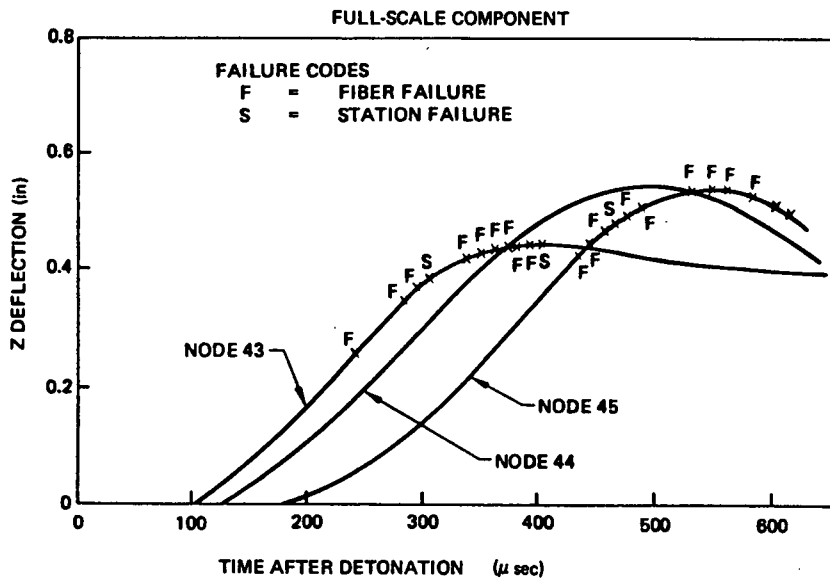
Figure 2-123. Nodal Deflection Predictions

2.2.2.2.3.2 Finite Difference Analysis

Typical of the finite-difference analysis methods for blast response are those developed by MIT beginning in the early 1960's. These programs and their derivatives (References 2-38, 2-52, 2-66, 2-96) have been used extensively for predicting the response of beams, rings, plates, and shells to blast, and there is considerable experimental verification. The technique is a straightforward application of finite-difference methods, and is available to all users.

These computer codes provide for material behavior through the specification of one of several "STRESS" subroutines. The three subroutines most commonly used are:

1. The elastic, perfectly plastic model (EL-PP);
2. The elastic, strain-hardening model (EL-SH);
3. The elastic, strain-hardening, strain-rate-dependent model (EL-SH-SR).

The (EL-SH-SR) material code uses a power law dependency of flow stress on strain rate. In all cases, provision for unloading exists. For biaxial stress states, the von Mises yield criterion is used along with the associated flow rule for plane stress. In application, the panel to be analyzed is divided conceptually into a number of layers in the thickness direction. This division into layers allows a stress gradient in the thickness direction. The stresses in each layer are considered constant, and are obtained from the strains at mid-thickness. Internal forces are calculated by a through-the-thickness summation rather than the usual integration.

Although the finite-difference programs provide a very useful tool for analyzing structural response to blast, they have two limitations:

1. Finite-difference techniques generally are unsuitable for analyzing complex, built-up structure such as frequently found in aircraft application. Finite element analysis is more appropriate for this application.

2. Finite-difference techniques are inconvenient for parametric and configuration studies, in that considerable labor is required to alter loadings, boundary conditions, and structure.

2.2.2.2.3.3 Dynamic Plate Analysis

Important contributions to the understanding of the response of structure to transient pressure loadings of large amplitude have been made using dynamic plate models such as developed by Haskell, Massmann, Ankeney (Refs. 2-54, 2-70, and 2-33) and others. These models address the dynamic response of a single structural element, namely a plate with tractable boundary conditions such as simply supported or clamped edges. The advantage of this approach is that it can provide good analytic simulation of certain structural configurations, particularly skin panels, and this can often be done in terms of explicit mathematical equations containing the significant design parameters. In other words, many good results may be obtained rapidly and inexpensively.

Certain requirements must usually be met, however, in order to achieve useful analytical validity, including:

a. Bending and membrane response;
b. Preferably finite deflection capability;
c. Appropriate material response characterization extending into the plastic deformation regime (for metals). Elastic-perfectly plastic or elastic-linear plastic response may be appropriate. In many materials the elastic deformation may be negligible and rigid-plastic response can be applied.

An approach which greatly enhances the credibility of dynamic plate analytical models is to correlate them with more comprehensive analysis methods such as the finite element techniques (BR-1, MARC, for example). Following this correlation (even calibration), the simple model can be used to good advantage in lieu of the more expensive approach, provided the simulation capability of the plate representation is not exceeded.

Massmann (Ref. 2-70) has shown good correlation between the predictions of a dynamic plate analysis and the MARC finite element computer code. The plate analysis applies elastic-perfectly plastic material behavior, and the dynamic response of the plate is represented by a one-dimensional spring-mass system incorporating two non-linear springs. The stiffness of one of the springs simulates elastic-perfectly plastic plate bending, and the stiffness of the other spring describes elastic-perfectly plastic membrane response of a thin plate undergoing large deflections. For square plates with clamped edges, loaded by a transient pressure pulse applied uniformly to the surface of the plate, predicted maximum deflections were within 10-percent of predictions obtained using MARC finite element analysis.

The dynamic plate model eveloped by Haskell is well-documented in Ref. 2-54, including verification of strain predictions by testing instrumented panels, using explosive charges.

2.2.2.2.3.4 Equivalent Static Load Method of Analysis

The equivalent static load method consists of analytically converting the dynamic overpressure loading into a static load that will cause the same deflection of the structural element. This conversion typically involves simulating the dynamic response of the element by a one-dimensional spring-mass system having the same natural frequency as the element, as indicated previously in Section 2.2.2.2.2. Once determined, the equivalent static load is used to calculate stresses using routine stress analysis methods. The equivalent static load method is widely used in dynamic structural analysis because it provides a useful correlation between static and dynamic capability.

For first-cut approximations, the two overpressure components of an internal detonation, shock and confined gas, can be separately converted into equivalent static pressures, and their sum used as the total equivalent static pressure acting on the structure. The equivalent load method can be summarized as follows:

a. Determine fundamental natural period of free vibration of the structural element being analyzed;
b. Determine equivalent triangular pressure pulse corresponding to reflected shock overpressure. The equivalent triangular pressure pulse has the same impulse as the actual pressure pulse;
c. Determine equivalent static pressure loading for shock overpressure;

d. Determine equivalent triangular pressure pulse corresponding to confined gas pressure;
e. Determine equivalent static pressure loading for confined gas pressure;
f. Add the results of c) and e), forming the resultant equivalent static pressure loading;
g. Calculate corresponding stresses.

Calculation Steps for Equivalent Load Method

1. The first step in developing the equivalent loading is to determine the natural period, T, of the structural element. Many closed form analytic solutions for the natural modes of vibration of plates are available.

    The expressions for natural period of vibration from Reference 2-42 have been evaluated for aluminum plates and $0/\pm45/90$ and ±45 graphite/epoxy laminates. Results are given in Figures 2-124 through 2-135. The corresponding equations and terminology are shown in Figure 2-136, with elastic properties for some selected laminates given in Table 2-25. Table 2-26 gives constants required for the natural period calculations.

2. The next step is to determine the pulse duration and the equivalent triangular pulse pressure corresponding to the reflected shock overpressure. The pulse duration is a function of explosive type and quantity, and the distance between the center of detonation and the structural element. The equivalent triangular pressure, however, is also a function of the angle of incidence of the shock front, β, defined as the angle between a tangent to the shock front and the structural plane.

    Figures 2-98 through 2-112, shown previously, present curves for several threats and detonation altitudes giving the pressure pulse time duration, t_d, the incident overpressure, P_i, and P_Δ the peak pressure of the equivalent triangular pulse for a normal shock impingement ($\beta = 0$), plotted as functions of distance from detonation. If the shock angle of incidence β is zero, then P_Δ can be used directly. If β is not equal to zero, P_Δ must be adjusted. This is done as follows:

    a. Find P_Δ and P_i on Figures 2-98 or 2-99.

    b. Go to Figure 2-100 and find the reflection coefficient, η, corresponding to the angle of incidence, β, and the incident pressure, P_i.

    c. The adjusted P_Δ is given by:

    $$P_{\Delta\beta} = \eta \, P_{\Delta o}$$

    The adjusted shock overpressure can now be used with t_d in Step 4.

3. The third step is to determine the equivalent triangular pulse for the confined gas pressure. The peak confined gas pressure and the time duration of the pulse varies with explosive quantity, altitude, cell size, the amount of venting area relative to the cell size. The venting area includes openings inherent in the structure plus any cell wall area removed by projectile detonation and fragmentation.

    The confined gas peak pressure, P_{CG}, for a totally confined explosion, can be read from the curves in Figure 2-102. The pulse duration is found from Figure 2-103, by reading the time required for the pressure in the cell to return to ambient. This pulse duration depends on the ratio of vent area to cell volume for the given cell size.

4. The last two steps resulted in values for the peak overpressure and time duration of the equivalent triangular pulses for the shock overpressure and confined gas overpressure. Step one resulted in a value for the natural period of vibration of the structural element. These values can now be used in Figure 2-137 to determine the equivalent static pressure loading. The curve is used separately for shock and confined gas, then the equivalent static loads are added to get the total equivalent static load acting on the structure.

    For many cases of practical interest, the confined gas pressure is of long duration relative to the natural period of the structure. The result is that the structure perceives the residual gases as a "step" pressure loading. The ratio P_{static}/P_Δ will be large (ie. greater than 1) for these long duration pulses.

    When using Figure 2-137, it is useful to note that fiber composite laminates containing 0-degree fibers have essentially elastic deformation to failure, so a ductility ratio of unity applies for these laminates.

127

Figure 2-125. *Natural Periods, Graphite/Epoxy, 0/±45/90, Clamped*

Figure 2-124. *Natural Periods, Graphite/Epoxy, 0/±45/90, Simply Supported*

All Edges Clamped

Graphite/Epoxy 0/±45/90

$E_x = 6.8 \times 10^6$ psi $\mu_{xy} = .31$
$E_y = 6.8 \times 10^6$ psi $\mu_{yx} = .31$
$G_{xy} = 2.6 \times 10^6$ psi
$W = .057$ lb/in^3

LAMINATE THICKNESS (inches)

Panel Width, B (inches)

NATURAL PERIOD (FUNDAMENTAL MODE) (seconds)

All Edges Simply Supported

Graphite/Epoxy 0/±45/90

$E_x = 6.8 \times 10^6$ psi $\mu_{xy} = .31$
$E_y = 6.8 \times 10^6$ psi $\mu_{yx} = .31$
$G_{xy} = 2.6 \times 10^6$ psi
$W = .057$ lb/in^3

LAMINATE THICKNESS (inches)

Panel Width, B (inches)

NATURAL PERIOD (FUNDAMENTAL MODE) (seconds)

B/A

128

Figure 2-127. Natural Periods, Graphite/Epoxy, $O_2/\pm45/90$, Clamped

Figure 2-126. Natural Periods, Graphite/Epoxy, $O_2/\pm45/90$, Simply Supported

129
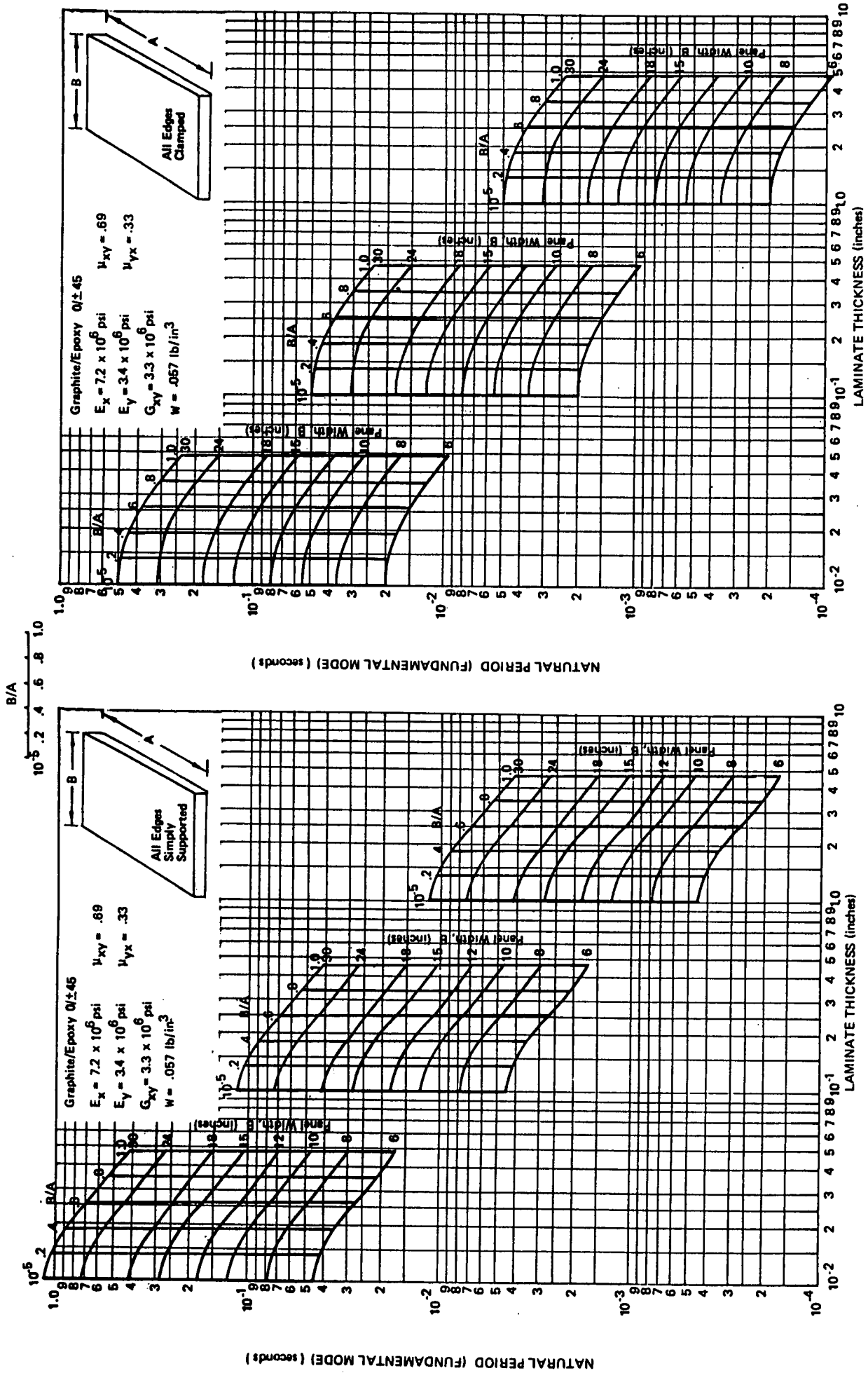
Figure 2-129. Natural Periods, Graphite/Epoxy, 0/±45, Clamped

Figure 2-128. Natural Periods, Graphite/Epoxy, 0/±45, Simply Supported

130
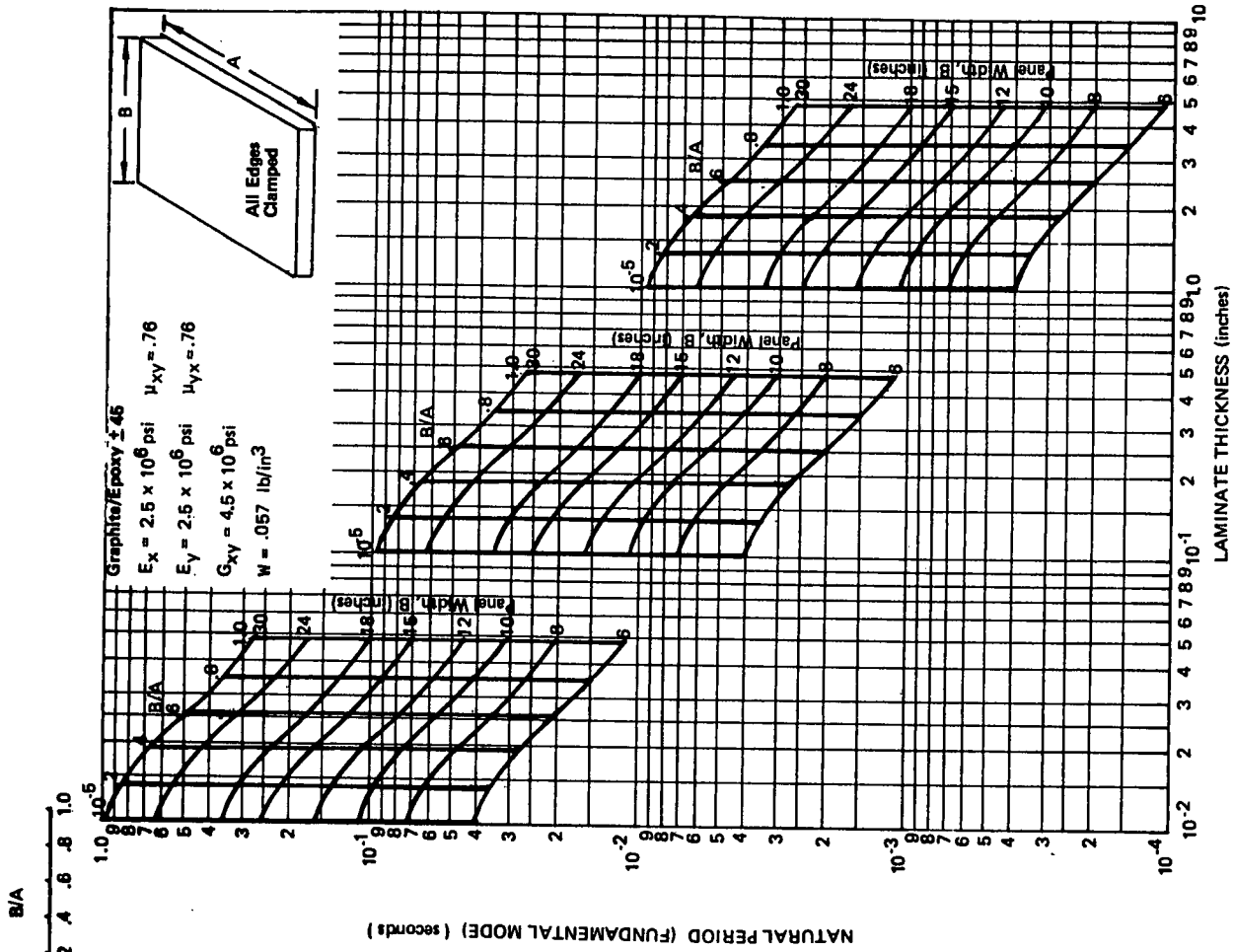
Figure 2-131. Natural Periods, Graphite/Epoxy, ±45, Clamped
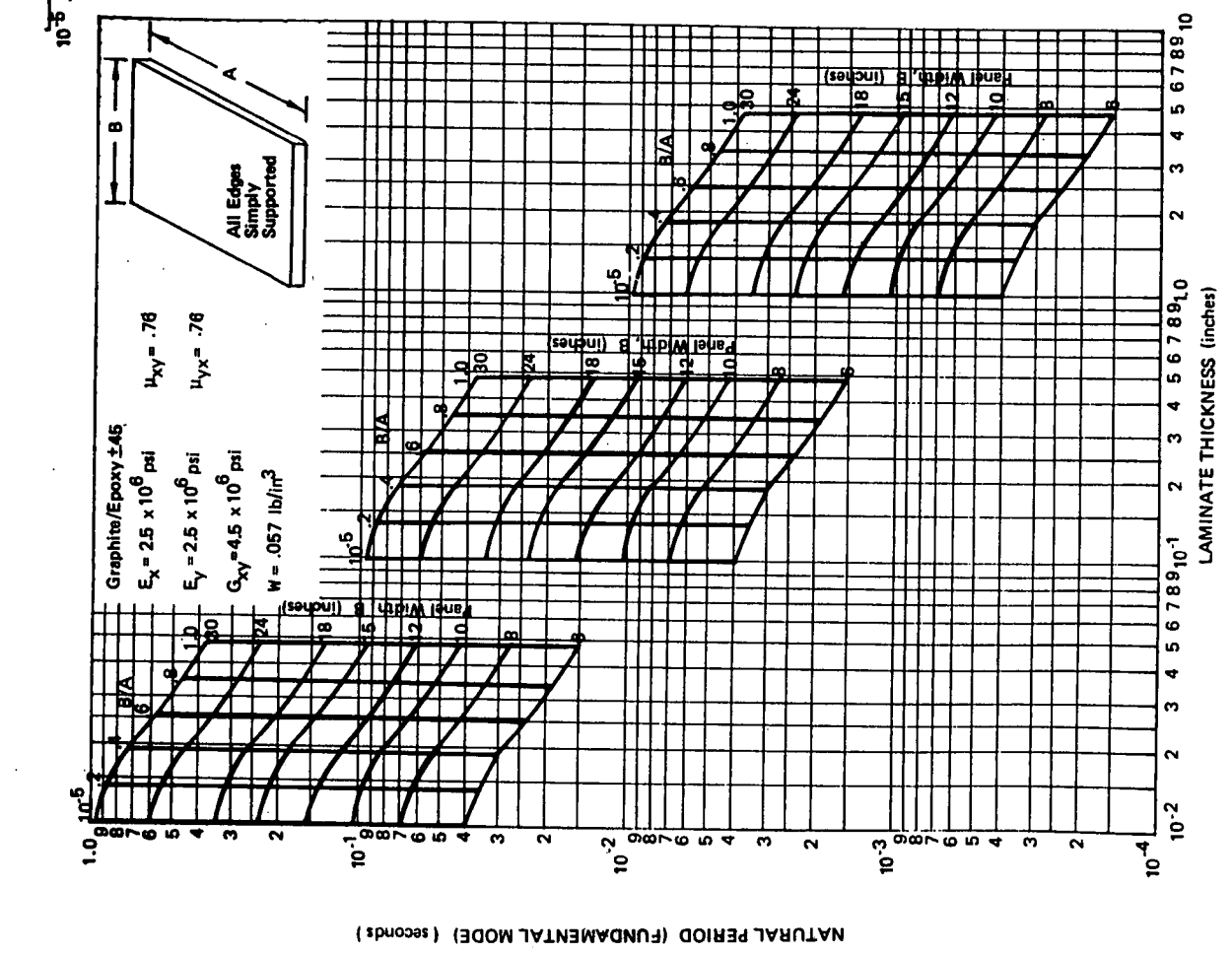
Figure 2-130. Natural Periods, Graphite/Epoxy, ±45, Simply Supported

Figure 2.133. Natural Periods, 7075-T6 Aluminum, Clamped

Figure 2-132. Natural Periods, 7075-T6, Aluminum, Simply Supported

132

Figure 2-135. Natural Periods, 6 AL-4V Titanium, Clamped
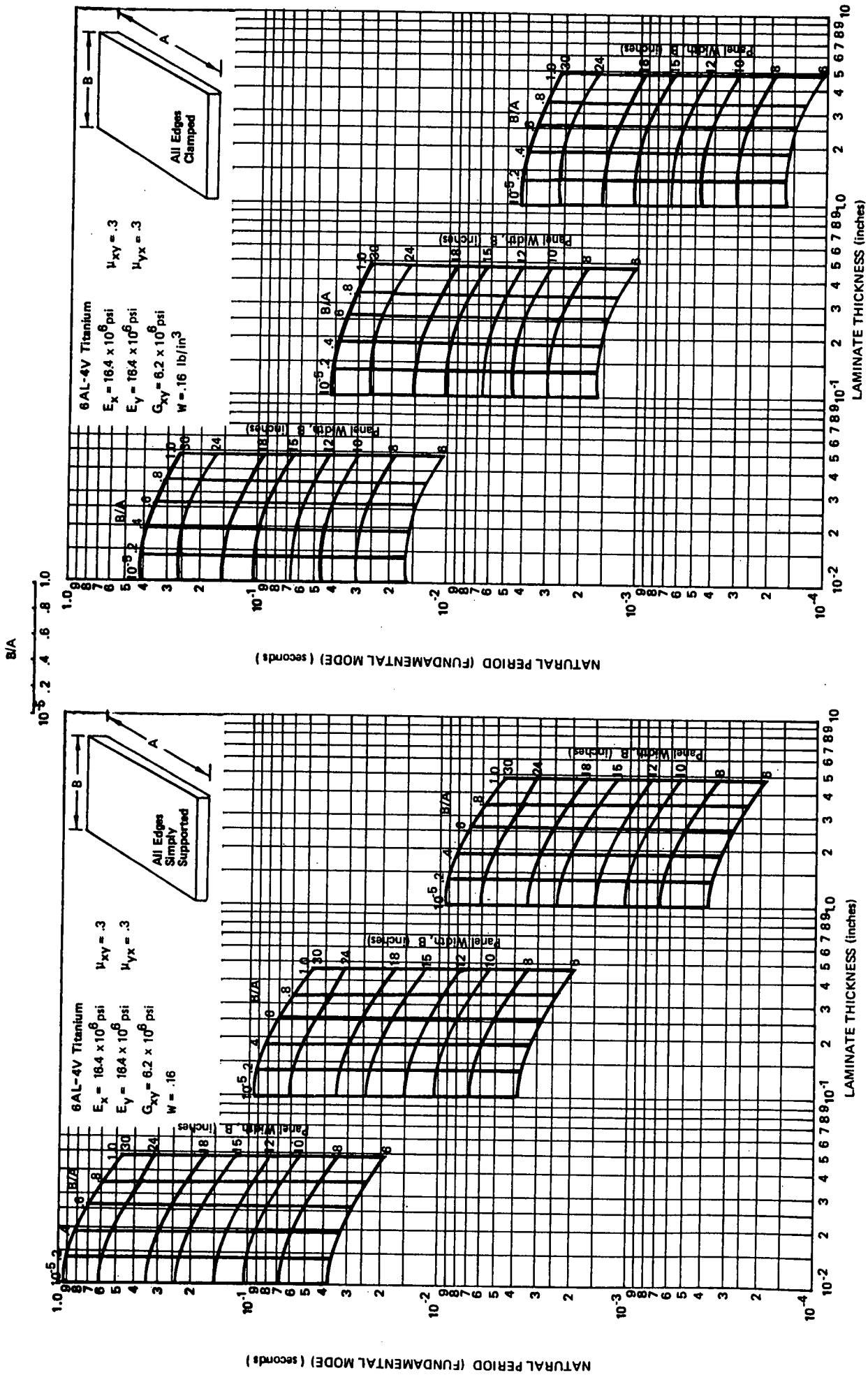
Figure 2-134. Natural Periods, 6 AL-4V Titanium, Simply Supported

$$T = 2\pi b^2 \sqrt{\rho} \left[D_{11} a_1{}^4 (\frac{b}{a})^4 + 2(D_{12} + 2D_{66}) a_2 (\frac{b}{a})^2 + a_3{}^4 D_{22} \right]^{-\frac{1}{2}}$$

where:

T	= Natural Period of Fundamental Mode (sec)
a,b	= Dimensions of Plate (inches)
ρ	= Plate Density (lb. sec^2/in^3)
	= $\rho_0 h$
ρ_0	= Material Mass Density (ρ_0 = 147.5(10)$^{-6}$ for GR/EP) $\frac{lb. sec^2}{in^4}$
h	= Panel Thicknes (inches)
a_1, a_2, a_3	= Constants Deternined by Edge Support Conditions (see Table 2-26)

$$D_{11} = \frac{E_x h^3}{12(1-\mu_{xy}\mu_{yx})} \quad ; \quad D_{12} = \frac{\mu_{xy} E_y h^3}{12(1-\mu_{xy}\mu_{yx})}$$

$$D_{22} = \frac{E_y h^3}{12(1-\mu_{xy}\mu_{yx})} \quad ; \quad D_{66} = \frac{G_{xy}}{12} h^3$$

E_x, E_y, G_{xy} = Elastic Modulii (psi)

μ_{xy}, μ_{yx} = Poisson's Ratios
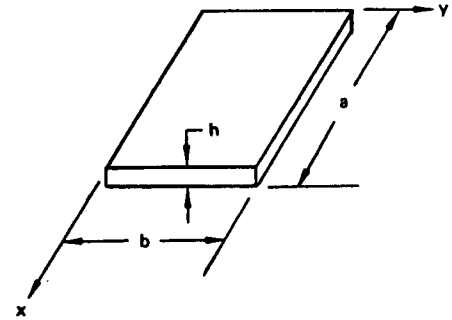
Figure 2-136. Natural Period of Specially Orthotropic Rectangular Plates

Table 2-25. Elastic Properties of Selected Graphite/Epoxy Laminates

LAY-UP	PERCENTAGE 0	±45	90	Ex (psi)	Ey (psi)	Gxy (psi)	μ_{xy}	μ_{yx}
0/± 45/90	25	50	25	$6.8(10)^6$	$6.8(10)^6$	$2.6(10)^6$	0.31	0.31
0_2/± 45/90	40	40	20	$8.7(10)^6$	$6.0(10)^6$	$2.2(10)^6$	0.30	0.21
0/± 45	33	67	0	$7.2(10)^6$	$3.4(10)^6$	$3.3(10)^6$	0.69	0.33
± 45	0	100	0	$2.5(10)^6$	$2.5(10)^6$	$4.5(10)^6$	0.76	0.76

Table 2-26. Coefficients for Natural Period Equations (Ref. 2-42)

BOUNDARY CONDITIONS	a_1	a_2	a_3	m	n
	4.730 4.730 $(m+.5)\pi$ $(m+.5)\pi$	151.3 $12.30 a_3(a_3-2.)$ $12.30 a_3(a_1-2.)$ $\frac{(a_1 a_3 (a_1-2.)^*}{(a_3-2.))}$	4.730 $(n+.5)\pi$ 4.730 $(n+.5)\pi$	1 1 2,3,4... 2,3,4...	1 2,3,4 1 2,3,4
	4.730 $(m+.5)\pi$	$12.30 a_3(a_3-1.)$ $\frac{a_1 a_3(a_1-2.)^*}{(a_3-1.))}$	$(n+.25)\pi$ $(n+.25)\pi$	1 2,3,4...	1,2,3... 2,3,4...
	4.730 $(m+.5)\pi$	$12.30 n^2\pi^2$ $n^2\pi^2 a_1(a_1-2.)$	$n\pi$ $n\pi$	1 2,3,4...	1,2,3... 1,2,3...
	$(m+.25)\pi$	$\frac{(a_1 a_3(a_1-1.)^*}{(a_1-1.))}$	$(n+.25)\pi$	1,2,3...	1,2,3...
	$(m+.25)\pi$	$n^2\pi^2 a_1 (a_1-1.)$	$n\pi$	1,2,3...	1,2,3...
	$m\pi$	$m^2 n^2 \pi^4$	$n\pi$	1,2,3...	1,2,3...

Ref: "Theory of Laminated Plates," Progress in Material Science Series, Vol. IV, Technomic Publishing Co., 1970

$$\text{DUCTILITY RATIO} = \frac{\text{TOTAL DEFORMATION}}{\text{LIMITING PLASTIC DEFORMATION}}$$
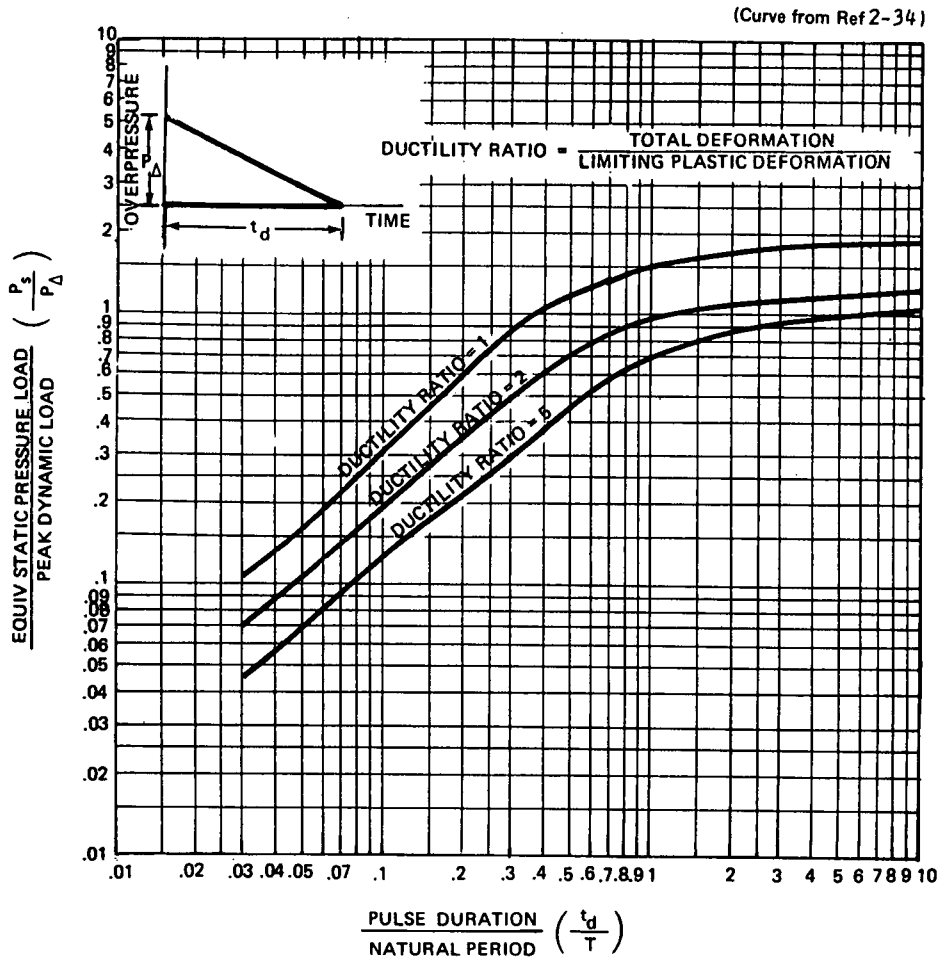
Figure 2-137. Equivalent Static Pressure Developed By a Triangular Pressure Pulse

2.2.2.2.3.5 Critical Impulse Failure Criteria

An interesting dynamic failure criterion is presented in Reference 2-36 and further described in Reference 2-33. This criterion essentialy states that structural failure under transient loadings can be correlated to a critical impulse applied for a critical time duration where the latter is assumed to be one-quarter of the natural period of free vibration of the structure. The critical impulse can be expressed as:

$$I_c = (\rho/E)^{\frac{1}{2}} t \, \sigma_y \qquad\qquad \text{(Eqn. 2-99)}$$

where

E = elastic modulus;

ρ = mass density of the material;

t = thickness;

σ_y = "dynamic" yield strength.

In applying this method to skin panels supported by transverse and longitudinal members, for example, one first calculates the critical impulse and natural period of the panel. Incident pressure pulses having a duration of one-quarter of the natural period or more, having an impulse at least equal to I_c, will cause rupture of the panel at the attachments.

2.2.2.2.3.6 Empirical Failure Criteria for Components

Failure criteria have been developed by detonating explosive charges within or near parked aircraft. The result of this testing, much of which was conducted at the U.S. Army Ballistic Research Laboratory, is a visual assessment and judgement of lethality. In other words, an engineering estimate is made of whether or not the resulting damage would have killed a flying aircraft. An example of this type of criteria is shown in Figure 2-138. This figure, from Reference 2-7, shows estimated kill thresholds for typical wing and fuselage structure resulting from internal detonations of bare charges of TNT. The correlating parameters depend primarily on skin gage and volume or cross-section.
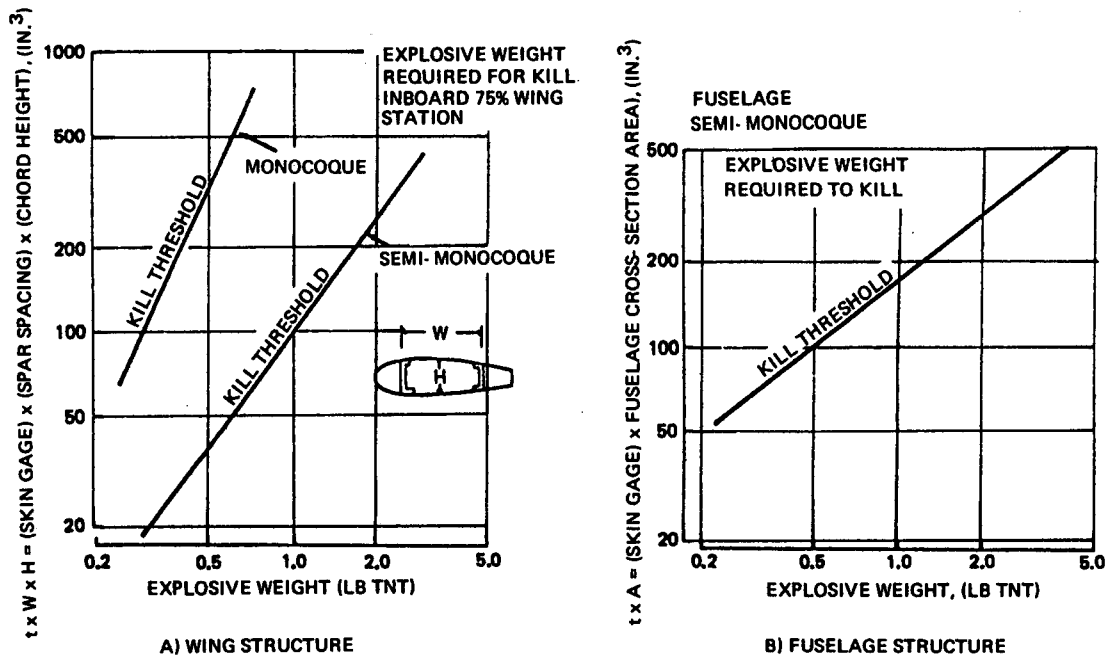
Figure 2-138. Internal Blast Threshold Kill Levels

2.2.3 Damage From Engine Debris Projectiles

Non-contained engine failures do not occur very often, the average rate in commercial service has been less than one per million engine hours worldwide in recent years (Reference 2-43). Further, the probability of this once-per-million-hour event causing an aircraft accident, defined as a penetration of fuselage or damage to wings or vital components, has proved to be about one chance in 8.5. Figure 2-139 indicates the proportion of aircraft accident sources between 1954 and 1974, indicating that 97.2% of all aircraft accidents have been the result of events other than non-contained engine failures.

Nevertheless, these incidents do occur and must be addressed. The effects of uncontained projectile emanating from an engine and subsequently striking an adjacent portion of the airframe, can be assessed in the same manner as for nonexploding military projectiles. There is an important distinction, however, in that the engine debris projectile is typically an irregular fragment (as opposed to a bullet), behaving more like a warhead fragment or the fragments generated from a high-explosive projectile.

2.2.3.1 Description of Engine Debris Projectiles (Extracted From Refs. 2-43 and 2-44)

Rolls-Royce (Reference 2-43) has made available the results of a study on non-containment incidents associated with their commercial engines, in which they recorded the weights of fragments, the direction of release, energy and size, wherever such information could be obtained. These results are summarized in the following paragraphs.

Weight of Fragment. Figure 2-140 shows the weight of the largest fragment released in each incident as a percentage of the bladed disc weight. The fragments vary from part of a blade to a complete disc. The incidents categorized as aircraft accidents are indicated, showing that complete discs are less likely to cause a problem than disc fragments, but fragments of any size are capable of causing unacceptable damage if they hit certain parts of the aircraft.

Compressor and turbine non-containment are indicated on the plot and it shows that only turbine discs have been released complete, probably because a turbine disc has easier access to freedom than a compressor disc.

Figure 2-141 gives the percentage of incidents in which the weight of the largest fragment released was a given percentage of the bladed disc weight or less. It is a way of showing the reduction in the number of non-contained failures that would be achieved by providing an ability to contain an increasing weight of fragment. For example, the ability to contain a fragment weight 5% of the bladed disc weight would have prevented 56% of all non-containments. If the former figure were 10% we would have prevented 72% of the non-containments. Thereafter the gains are less spectacular.
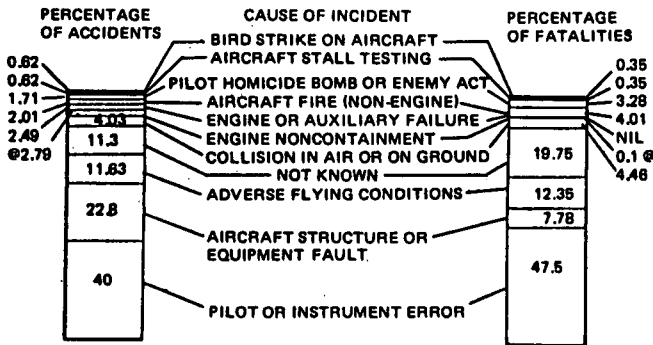
Figure 2-139. Analysis of Aircraft Accident and Fatalities — 1954 to 1974

Figure 2-140. Noncontained Failures — 1954 to 1974 Inclusive
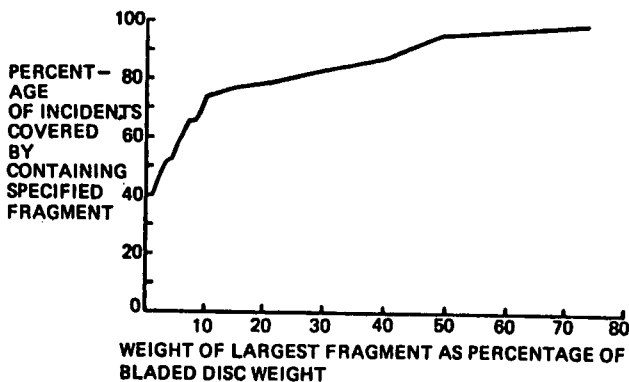
Figure 2-141. Number of Incidents Versus Fragment Weight

When a fragment strikes the inside of an engine casing and it is not contained, it is sometimes deflected on its way through the casing. Figure 2-142 illustrates the effect of such deflection upon the subsequent path of a fragment. Since the point of penetration of the casing is at a random circumferential position, the probability of an aircraft item in line with a disc being struck by a fragment is unaffected by deflection of the fragment by the casing. But the axial deflection of the fragment is important in that it affects the axial length of the possible impact area on the aircraft.

A study of the axial deflection of debris in actual incidents produced the result shown in Figure 2-143 where axial deflection is plotted against weight of fragment. It shows that only the lighter fragments were appreciably deflected, the maximum deflection being +33 degrees whereas the heavy fragments were not deflected more than +5 degrees.

Thus, the situation may be as shown on Figure 2-144 where a pack of discs creates overlapping fields of possible debris distribution so that any protection or special measures taken by the aircraft designer will require sensibly uniform application over a length slightly greater than the length of the rotor pack, tailing off to zero beyond each end of the rotor as shown in the figure.

Energy of Engine Debris Fragments A fragment has two kinds of energy when it leaves an engine, see Figure 2-145. It has kinetic energy along its flight path which is tangential to the radius described by its center of gravity when it was part of the disc. It also has rotational energy about its own center of gravity. Experience shows that for practical purposes it is the former, i.e., its translational energy, that causes the real damage on impact and this is because the translational energy is in the direction of the impact and, for realistic fragments, it is invariably much greater than the rotational energy.

Figure 2-145 also shows a plot of disc sector size against its translational energy. The fragment with maximum translational energy is a disc segment subtending an angle of 133.6 degrees. An unbroken disc has no translational energy unless it picks some up as a result of friction developed in rubbing against static parts which may throw it sideways out of an engine with a relatively low velocity.

The energy with which a fragment leaves an engine is less than its initial energy because it expends some energy in penetrating the engine casing. In calculating the energy of an emerging fragment a proportion of the amount of energy the engine casing is capable of containing should be subtracted from the initial energy of the fragment.

Figure 2-142. Debris Spread
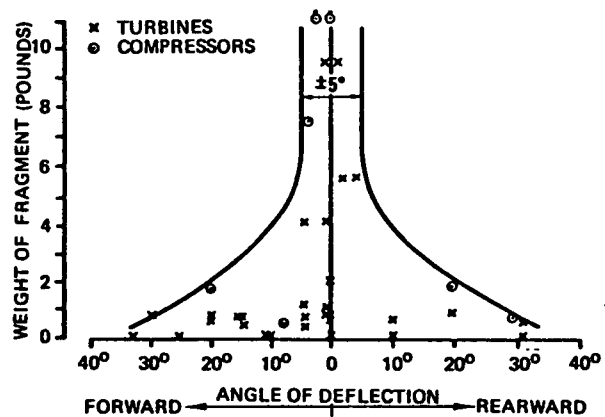
Figure 2-143. Debris Spread Versus weight of Fragment
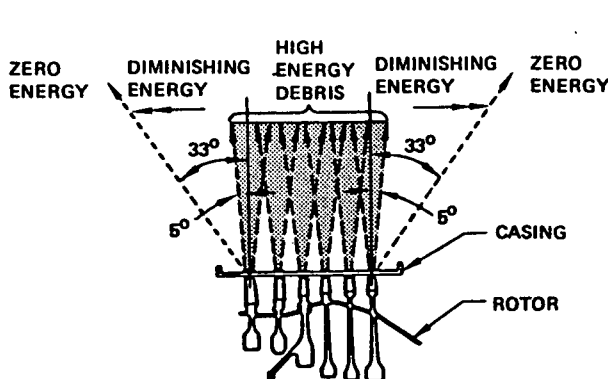
Figure 2-144. Direction and Energy of Emerging Debris
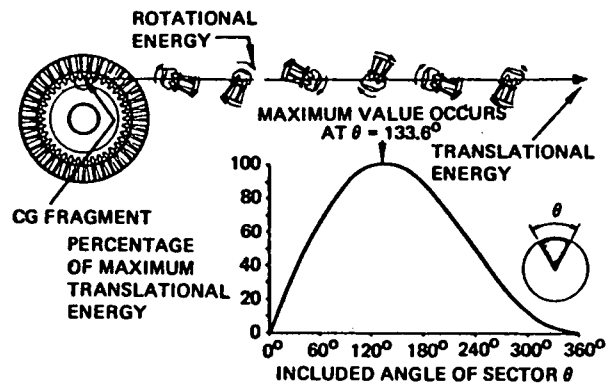
Figure 2-145. Definition of Fragment With Maximum Energy

To determine the blade containment ability of a casing, Rolls-Royce plotted blade energy against a function of blade dimensions and casing properties for all known cases of blade release including experimental tests and service experience. The result is shown in Figure 2-146 where contained and non-contained failures are identified.

Unfortunately, the behavior of a casing is not quite as straightforward as to absorb an equal amount of energy regardless of the initial energy of the fragment. In containment tests a fragment with an energy level just beyond the containment capabilities of a casing lost 90% of its energy in passing through the casing. But when a portion of a rotor, comprising four blades and a piece of disc, was released from a rotor rotating inside a casing designed to contain a single released blade, the fragment passed through the casing with a near-zero loss of energy.

That some energy was lost was shown by damage and distortion to the casing and to the blades in the fragment but the loss was too small to be measured in terms of fragment velocity before and after penetration. Evidently, the casing did not develop its full containment potential when subjected to loadings far beyond its capabilities.

Further containment tests are in progress to build-up more data on this problem and to establish a formula for the amount of energy destroyed in a range of fragments when they pass through a casing of known blade containment ability. Meanwhile, until more data becomes available it seems reasonable to assume that the loss of energy varies from 100% for a single blade, to zero for the 4-blade fragment tested, or any larger fragment. The 4-blade fragment weighted 6.5% of the weight of the bladed disc.

There is an additional loss of energy in fragments that are deflected on passing through the casing. The amount of this loss depends upon the degree of deflection, and from theoretical considerations and practical observations the relationship between deflection and residual energy is as shown in Figure 2-147. This relationship can be used on calculating the possible energy of deflected fragments in the forward and rearward fields covered by the possible axial spread of debris.

Size of Engine Debris Fragments The maximum dimensions of a fragment thrown by an engine is important in terms of the probability of striking a given vulnerable item of the aircraft. Figure 2-148 shows that for a given aircraft layout the larger the fragment the more likely it is to strike a given object. The chances of the small fragment striking the object are θ_1 in 360 degrees, but for the large fragment they are θ_2 in 360 degrees and clearly the larger the fragment the greater the probability of a strike.

Figure 2-149 shows actual non-contained failures in terms of the arc of disc released against percentage of incidents. These results can be used for calculating the probability of impact of fragments of various sizes upon aircraft vulnerable items of various aircraft/engine arrangements. The results for turbines and compressors are shown separately to illustrate that compressors have tended to release larger arcs of disc rim than turbines. This is due to factors such as disc proportions.
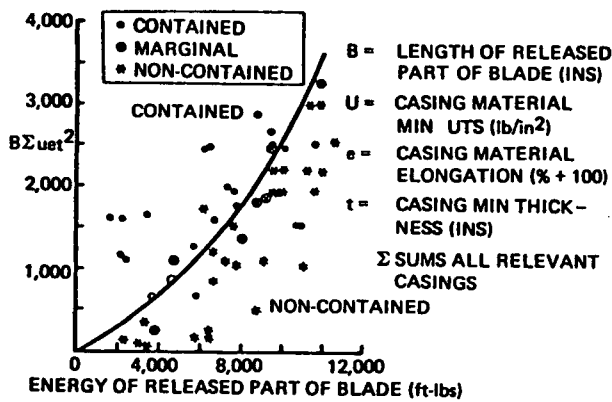
Figure 2-146. Blade Containment Criterion
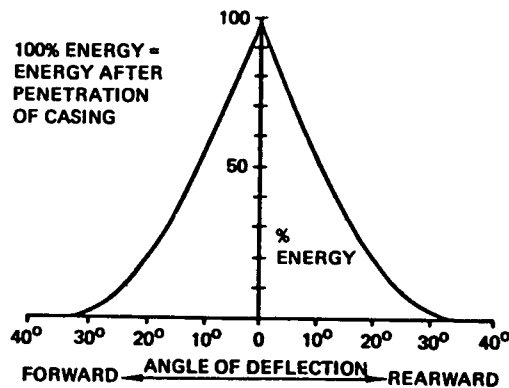
Figure 2-147. Energy After Deflection Versus Angle of Deflection Deflection
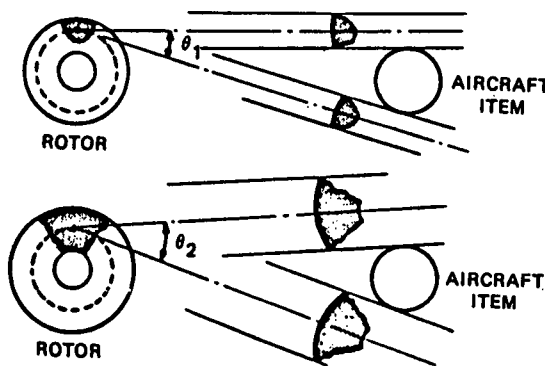
Figure 2-148. Fragment Size Effect on Probability of Strike
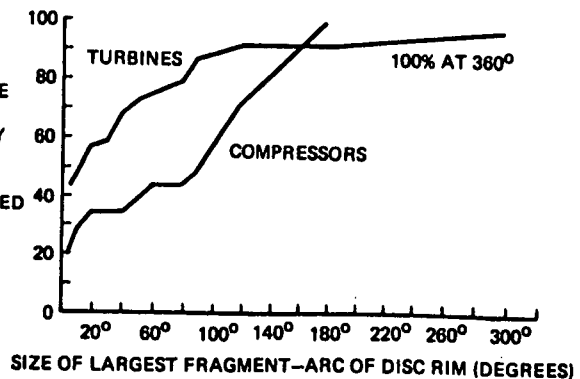
Figure 2-149. Size of Fragment Related to Percentage of Incidents

2.2.3.2 Encounter Parameters

The important encounter parameters that must be defined for penetration and damage assessment are identical to those needed for the military projectiles previously discussed: striking velocity, angle of obliquity and attitude.

Particular emphasis must be placed upon attitude, however, as this can be a significant factor in the damage potential of fragments having a high ratio of length to diameter, i.e., long, flat fragments such as a portion of a turbine blade. An additional consideration is the rotational energy of the impacting fragment, as this can be a significant factor in penetration and damage potential.

Encounter conditions for engine debris analysis can be predicted with greater certainty than for encounter with military projectiles because of the fixed location and known operating characteristics of the engine.

2.2.3.3 Typical Terminal Effects

As with all fragment impacts, engine debris fragments can penetate the airframe causing damage to skin and substructure, and may penetrate and degrade system components. The potential exists for ignition of fuel or injury to passengers or crew.

Figure 2-150 from Reference 2-44, gives an indication of the penetrating capability of engine debris fragments, based on calculations using the empirical formula shown on the figure. Fragment energy is plotted against the weight of target material required to contain the fragment.

To emphasize the damage potential of the fragments, typical weights of heavy wing and fuselage surfaces are indicated on the diagram giving some idea of their respective energy absorbing capabilities. The resulting energies are only approximate as both the curves and the test results are only concerned with flat plates. The stiffeners of the wing and fuselage (included in the weight shown) may offer appreciably increased energy absorption due to their depth.

However, this does not alter the general inference of Figure 2-150 which is that even two or three layers of such structure is not capable of stopping the smallest of the three debris forms.
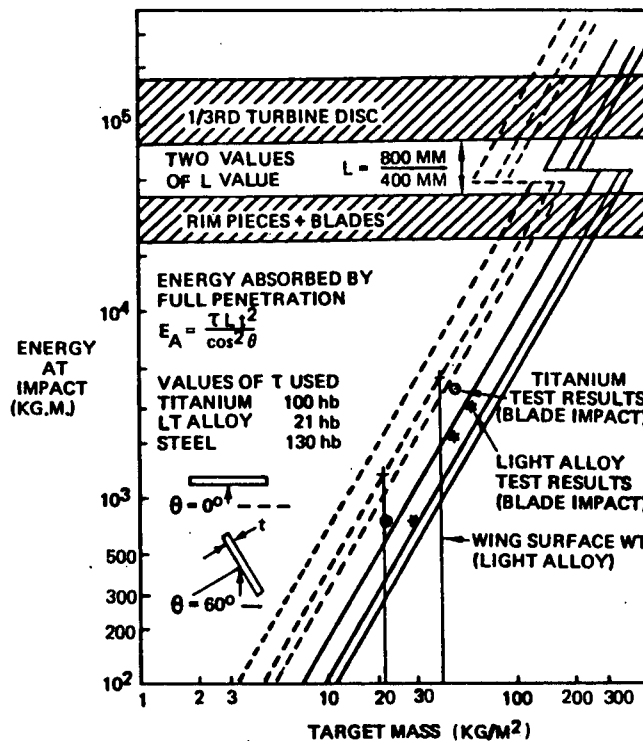
Figure 2-150. Structural Effects of Engine Burst Non-Containment

2.2.4 Hydrodynamic Ram Damage

Hydrodynamic ram is a phenomenon that may cause extensive structural failure of aircraft fuel cells when they are subjected to ballistic impact. During impact and penetration of the fuel cell, intense pressure waves are generated within the liquid by the projectile. The response of the fuel cell to this pressure loading varies according to its construction. For example, the walls of an integral fuel cell are formed by the aircraft skin, which is usually constructed of high-strength, metal designed to withstand normal flight loads. This type of structure can fail catastrophically in response to hydrodynamic ram pressure loading due to fracturing of the walls of the cell. Self-sealing fuel cells can also be defeated due to hydrodynamic ram by gross tearing of the material or by misalignment of the wound edges, thereby defeating the self-sealing process. Both of these effects become increasingly severe as fuel cells become smaller, or projectile kinetic energies increase.

Fuel-cell failure can lead to numerous modes of aircraft kill. One particularly effective mode is fuel starvation from the failure of a cell which contains a large proportion of the total fuel. Other possible kill modes are explosion and fire, ignited by an incendiary projectile or by secondary ignition sources within the aircraft. In addition, the hydrodynamic ram pressure pulse can directly damage critical components, such as pumps and valves within the cell, or it can indirectly damage components that lie outside of and adjacent to the cell walls.

At present there are no analysis models that can predict the extent of hydrodynamic ram damage under general conditions. Damage size cannot be predicted in the manner defined in the previous sections for air-backed panels. However, development programs are underway to acquire this capability.

Lundstrom of NWC has developed an analysis method to predict hydrodynamic ram pressures generated by small arms ammunition. Reference 2-45 describes the analysis, and a computer code is available. The analysis method is based on the conversion of projectile kinetic energy to pressure field energy and includes the effects of reflections from the tank walls. In addition, pressure prediction analysis methods are reported in Reference 2-45. The remainder of this section discusses hydrodynamic ram from a qualitative standpoint, with a description of hydrodynamic ram phenomenology, followed by a summary of available analyses.

2.2.4.1 Hydrodynamic Ram Loadings and Response

Figure 2-151 is a schematic representation of the events leading to hydrodynamic ram structural damage. Figure 2-152 is a failure-mode diagram corresponding to these events. A detailed description of ram phenomenology is given in Section 2.2.4.2.

Figure 2-153 shows typical pressure measurements at various distances downstream from the entry wall. The projectile was a 3/8-inch steel sphere impacting at 4,800 feet per second. Figure 2-154 shows the variation of damage size in the entry wall with projectile velocity. The entry wall was a monolithic panel, and the projectile was a 3/8-inch fragment simulator. The step-function response in damage size is typical for entry walls. At low velocity, the damage is a simple puncture with a diameter slightly greater than the projectile. Above a certain velocity this minimal damage suddenly jumps to spectacular proportions. The response of the exit wall to projectile velocity is quite different. As shown in Figure 2-155, the damage increases linearly with increasing velocity.

The effect of tank length is shown in Figure 2-156. An overkill condition occurred until the length of the tank was greater than 12 inches. Beyond this length, the damage decreased in a fairly linear manner with increasing length.

ENTRY WALL PENETRATION   TRAVERSE AND TUMBLE

CAVITY

FLUID SHOCK   DRAG PRESSURE PULSE

EXIT WALL PENETRATION   CAVITY OSCILLATION AND DECAY   DAMAGED TANK
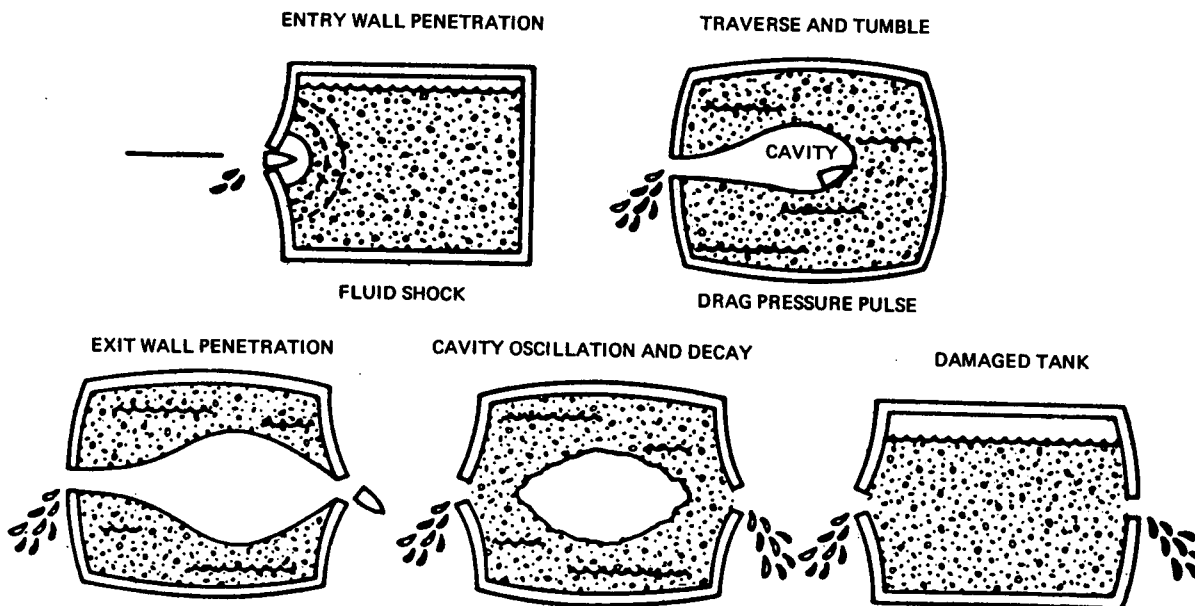
Figure 2-151. Schematic of Typical Hydrodynamic Ram Events
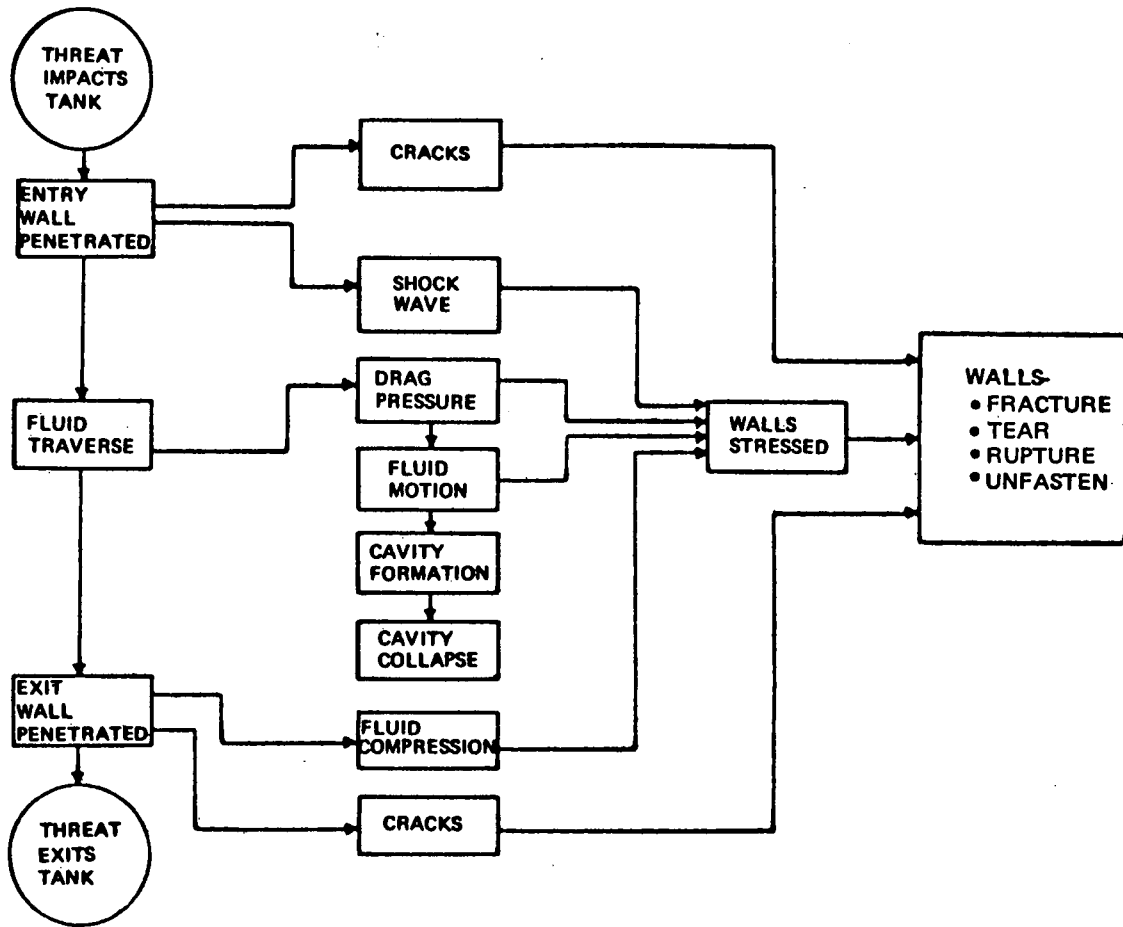
Figure 2-152. Hydrodynamic Ram Failure Mode Diagram
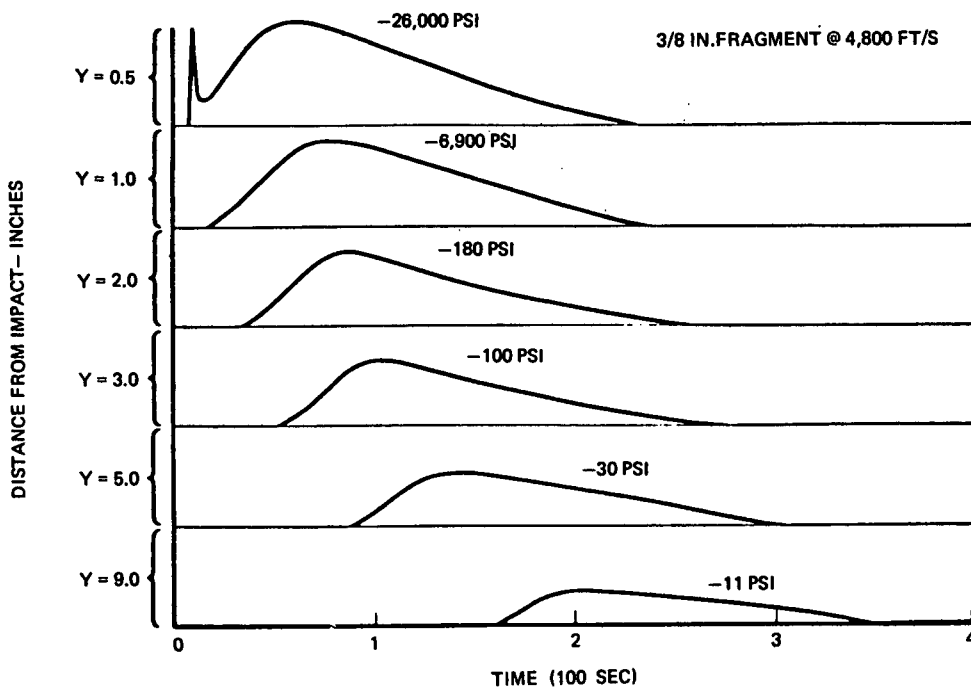
Figure 2-153. Typical Entry Wall Loading
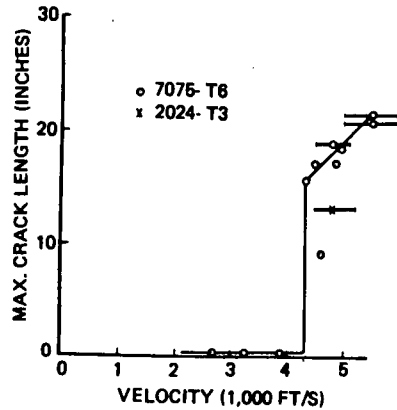
Figure 2-154. Entry Wall Damage — Fragment Simulator
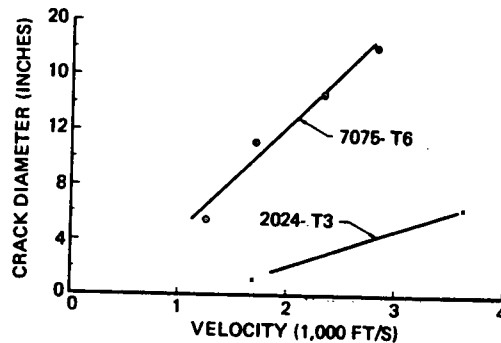
Figure 2-155. Exit Wall Damage - Effect of Velocity - Fragment Simulator
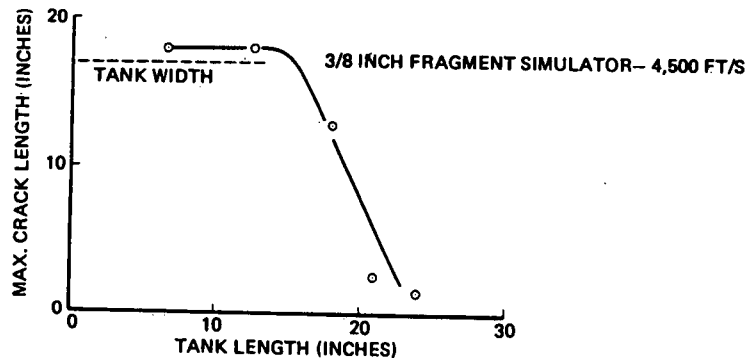
Figure 2-156. Effect of Tank Length

2.2.4.2 Hydrodynamic Ram Phenomenology

Since design models are not yet available for predicting hydrodynamic ram damage extent in structure, it is relevant to describe in some detail what is known about the physics of hydrodynamic ram. Although this discussion does not answer design questions, it should enable the designer and analyst alike to better understand the direction of hydrodynamic ram research and analysis.

2.2.4.2.1 Shock Waves

The sudden impact and penetration of the projectile generates a shock front in the fluid about the impact point. The shock front propagates away from the impact point in a somewhat hemispherical shape and its strength diminishes rapidly as it travels (observations indicate that the peak pressure at the front decays more rapidly transversely, i.e., along the wall, than in the fluid). This event is termed the "shock phase". It is a short-duration effect resulting in the application of an impulsive pressure load to the penetrator-damaged entry wall. This impulsive load can cause extensive entry wall damage.

2.2.4.2.2 Drag Pressure

As the penetrator travels in the fluid, its velocity is reduced by fluid drag pressures, often augmented by the tumbling of the projectile. The fluid acquires a radial velocity at the projectile/fluid interface, typically forming a "cavity" as shown in Figure 2-157. The dissipating kinetic energy of the projectile appears as a transient pressure pulse in the fluid, as indicated in Figure 2-158. This "fluid drag" phase is of longer duration than the shock phase, and less localized, creating a complex pressure field within the fluid, including reflections from the tank walls. Extensive structural damage can be done by the drag-induced pressures, particularly at exit walls which may become prestressed by the fluid pressure prior to the arrival of the projectile. Figure 2-159 shows typical drag-phase hydrodynamic ram damage in thin gage aluminum web structure, and Figure 2-160 shows hydrodynamic ram damage in graphite/epoxy wing structure induced by an HEI superquick projectile.

143
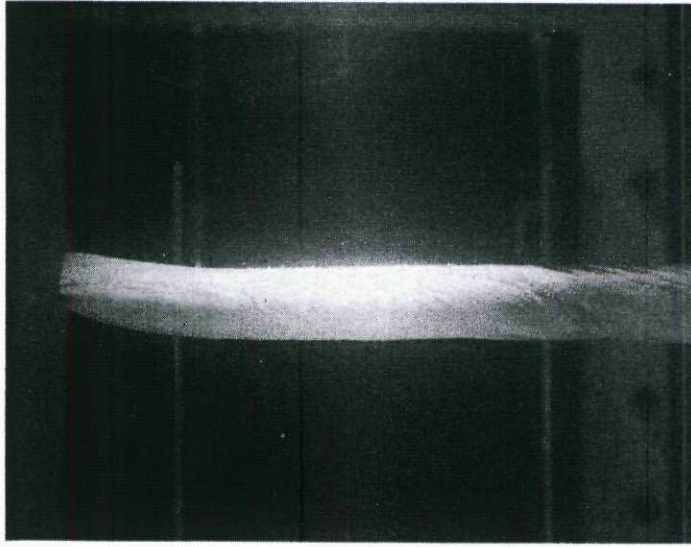
*Figure 2-157. Photograph of Cavity Formation Behind Tumbling
14.5-mm API in Water-Filled Tank*

TIME (MSEC)

(t = 0 is adjusted to beginning of pulse.)
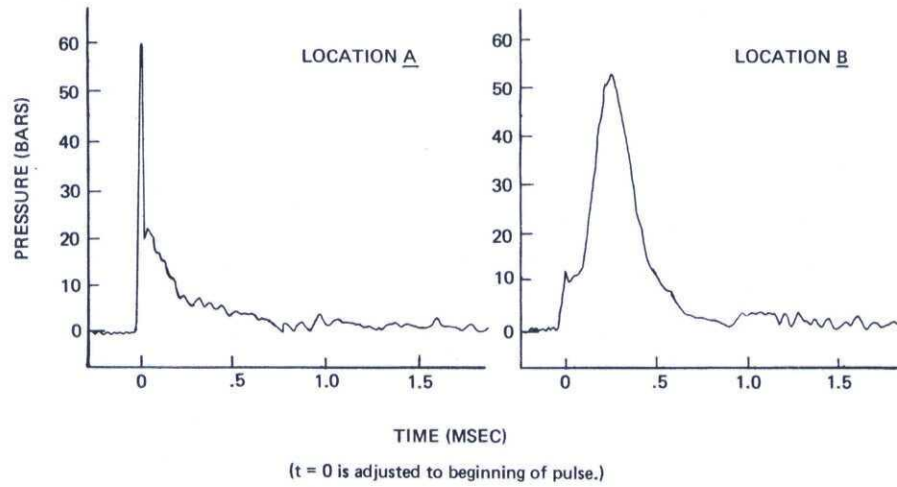
Figure 2-158. Typical Drag-Phase Pressure Pulses
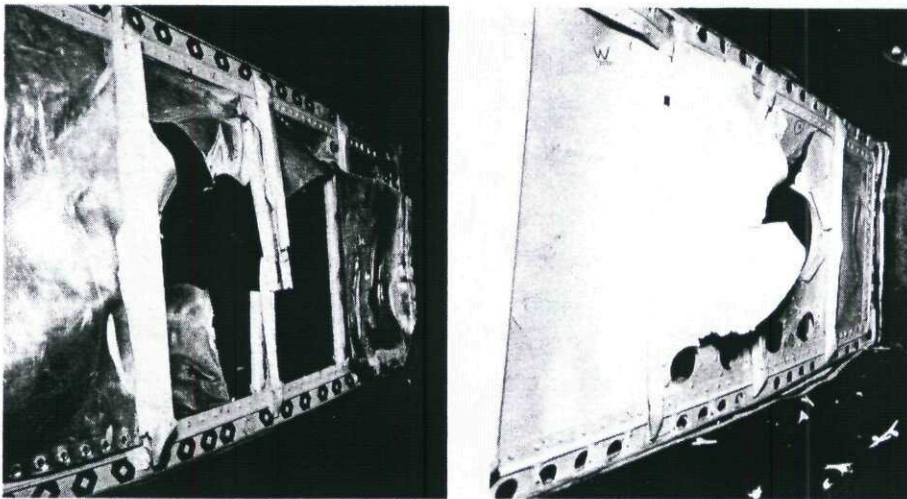
Figure 2-159. Hydraulic Ram Damage in Wing Structure

Figure 2-160. Hydraulic Ram Entry Damage in Graphite-Glass/Epoxy Wing-Box Structure

2.2.4.2.3 Fluid/Structure Interaction

The pressure waves described above travel through the fluid and ultimately impinges on fluid/structural interfaces, namely the tank walls. This situation is shown schematically in Figure 2-161, showing an oblique planar wave for ease of graphical presentation. The incident wave generated by a source within the fluid has travelled through Region I, and the fluid in Region I has acquired corresponding pressure increases and particle velocity. The fluid in Region II, ahead of the incident wave front is undisturbed.

Region III demonstrates the area of fluid/structure interaction. The incident wave has impinged on the wall, and a reflected wave has been generated at the wall surface and is travelling back through the fluid initially set in motion by the incident wave. Thus, the pressure at the wall results from the effects of superimposing an incident and reflected pressure wave. Neglecting cavitation effects, the component of the fluid velocity normal to the wall surface must equal the normal component of the wall velocity. Thus, the motion of the fluid and the wall are "coupled," so that the pressure "felt" by the wall depends on wall motion as well as incident conditions.

Region I: Far field fluid
            pressure behind
            incident wave

Region II: Undisturbed fluid
            ahead of incident
            wave

Region III: Pressure at wall determined
            by superimposed waves and
            wall motion
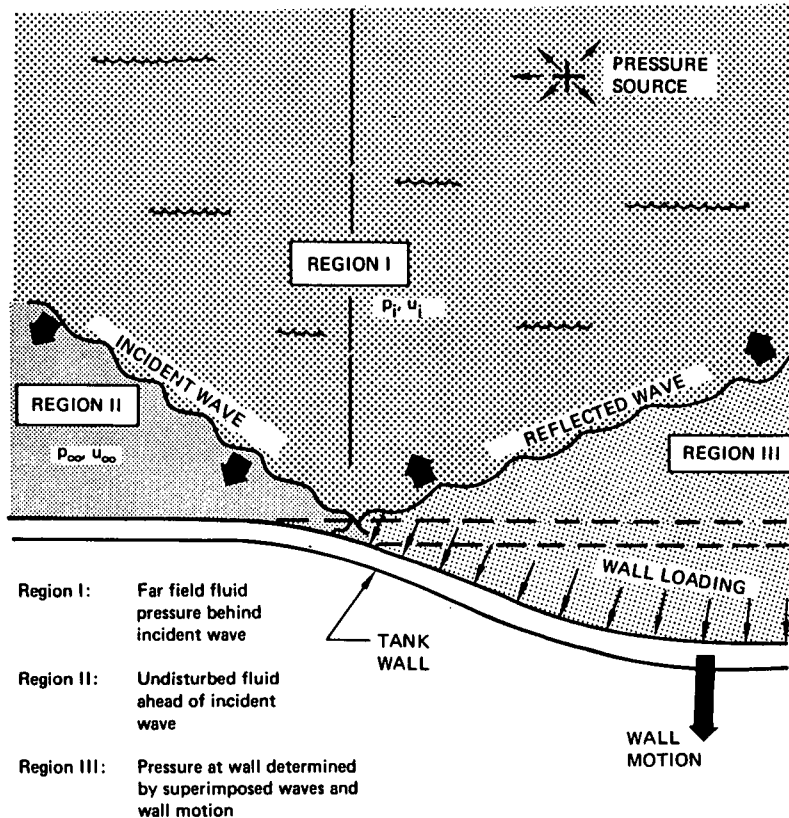
Figure 2-161. Interaction Between Tank Wall and Fluid Pressure Pulse

2.2.4.2.4 Structural Response and Failure

From the structural standpoint, hydrodynamic ram generates high-intensity, transient internal pressure loads on the fuel tank walls, which are typically skin panels, spar webs, and rib webs for integral tanks. Figure 2-162 shows a typical projectile impact into a wing cell containing fuel, using a multi-rib wing-box configuration as an example. It is assumed that the tank is completely full. The projectile has entered from above, penetrating the upper surface, traversing the liquid fuel and emerging from the lower wing cover.

The entire cell will experience ram generated incident pressures, and these will be most intense near the trajectory of the projectile. The effective pressure loads depend on the time-duration of the pressure application relative to the natural period of the structural deformation modes, and the ratio of elastic-to-plastic response. As mentioned previously, the effective pressure loadings from typical threat encounters are sufficient to cause massive structural failure by deformation and rupture in certain configurations.

It is convenient to address the structural response of the entry wall, the exit wall, and the side walls:

1. **Entry wall (the upper wing skin in the example in Figure 2-162)**
   Prior to impact, the entry wall is stressed by operational loading conditions, which may include internal pressure. The projectile penetrates the wall, imposing a ballistic damage. The shock pressure generated in the fluid loads the damaged wall immediately, supplemented by drag-phase pressure loadings as the projectile loses kinetic energy in the fluid. The combined effects of the ram pressures, the operational loads, and the damage can induce failure by several potential mechanisms:

   a. Compression (instability) failure can occur due to a combination of compression end-loads (flight loadings) and the transverse loadings induced by ram.

   b. Tension failure can occur in response to ram-induced membrane and bending stresses combined with flight-induced stresses, leading to rupture. In particular, membrane stresses combined with transverse pressure represent a severe loading condition for fracture failure initiating from the ballistic damage, because the transverse pressure increases the stress-intensity at the damage. The severity of this effect increases as the curvature of the wall increases during deformation.

2. **Exit Wall (the lower wing skin in the example in Figure 2-162)**
   The exit wall is also stressed by operational loads prior to impact, but it is additionally stressed by ram pressures before penetration. Analysis has indicated (Ref. 2-53) that these ram-induced pre-penetration stresses can be large, and the effects of pre-load at impact are certainly of significance. The exit wall must be regarded as a pre-stressed, pre-deformed surface at the time of projectile impact. Of course, it is possible that the exit wall is never penetrated, because of trajectory alteration within the fluid.

   With the added emphasis on pre-impact stress/deformation, exit wall failure modes are qualitatively similar to those of the entry wall. Quantitatively, however, the exit wall is less influenced by the shock phase ram-pressures and more influenced by the drag-phase pressures, particularly with tumbling projectiles.

3. **Side Walls (the rib and spar webs in the example in Figure 2-162)**
   Side walls are primarily exposed to the drag-phase pressures, which can be very intense for walls near the trajectory. Side walls are not penetrated, so they do not contain ballistic damage. Primary failure mechanisms are excessive deformation and rupture.

ENTRY WALL	EXIT WALL	SIDE WALLS
● Ballistic damage	● Ram pressure loading	● Ram pressure loading
● Shock and drag pressure loading	● Ballistic damage	
	● Continued ram loading	
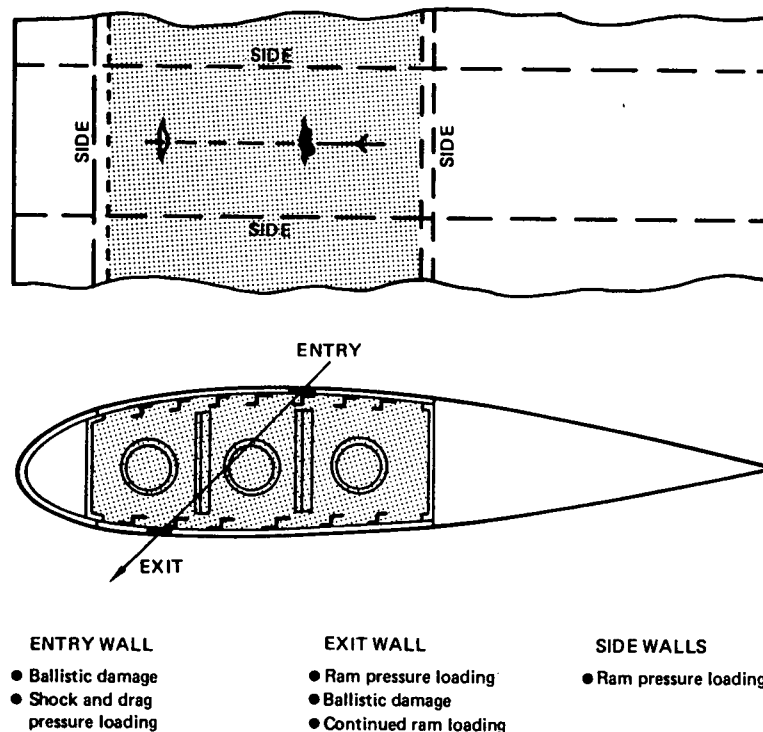
Figure 2-162. Hydrodynamic Ram Damage Mechanisms for Typical Integral Tank

2.2.4.3 Status of Hydrodynamic Ram Analysis

This section describes the analysis methodologies required to predict damage from hydrodynamic ram. The elements of the required analysis are shown in Figure 2-163, borrowed from Reference 2-45, consisting of:

1. Trajectory analysis,
2. Fluid (source) pressure analysis,
3. Fluid/structure interaction,
4. Structural response and failure.

The trajectory analysis tracks the location and dynamics of the projectile traveling in the fluid. The fluid pressure analysis defines the pressure-time history at selected points within the fluid. The fluid/structure interaction relates the pressure acting on the structure to the incident source pressure and the motion of the structure, and defines the resulting deflection, and stress/strain history of the wall. Structural response and failure criteria predict wall failure in terms of the deflections, stresses, and imposed ballistic damage. The following paragraphs summarize certain key developments pertaining to the overall analysis of hydrodynamic ram structural damage and some of these are detailed in the following subsections. The Naval Weapons Center (NWC) developed the basic trajectory analysis and drag-phase source pressure prediction theory (Ref. 2-45), which was published in 1971. This was followed by their release of the NWC Hydraulic Ram Program Version One (HRP-V1), a computer code which uses the developed theory to predict drag-phase pressures generated by a penetrator, and accounts for the influence of projectile tumbling. The NWC Hydraulic Ram Program (Version One) does not predict pressures acting on the fluid/structure interfaces. The method of images used to establish reflected pressure pulses provides good prediction of reflection effects at points within the fluid away from the wall, but the wall itself can only be rigid, transmissive, or a free-surface.

Dr. Ball of the Naval Post-Graduate School applied BR-1 (Ref. 2-13) to predict structural response to hydrodynamic ram pressures, by modifying the code to accommodate the "piston theory" approach for fluid/structure coupling. The modified code, designated BR-1HR, accepts source pressure-time histories from the NWC HRP-V1. The HRP-V1 code is run first to develop the incident pressures at the wall, which are then manually input to BR-1HR, which develops wall pressures at the nodes of the finite element model. Wall deflections predicted by BR-1HR have been much less than observed experimentally, and it is generally agreed that piston theory is an inadequate representation of fluid/structure coupling.

NWC returned to the problem of fluid/structure coupling and developed the variable image methodology (Ref. 2-46). This method alleviates some of the planar assumptions associated with piston theory, and provides a more accurate and versatile fluid/structure coupling model. Variable image coupling was combined with a small deflection, linear elastic, dynamic plate structural model, to formulate the UHRSR computer code (Ref. 2-47).
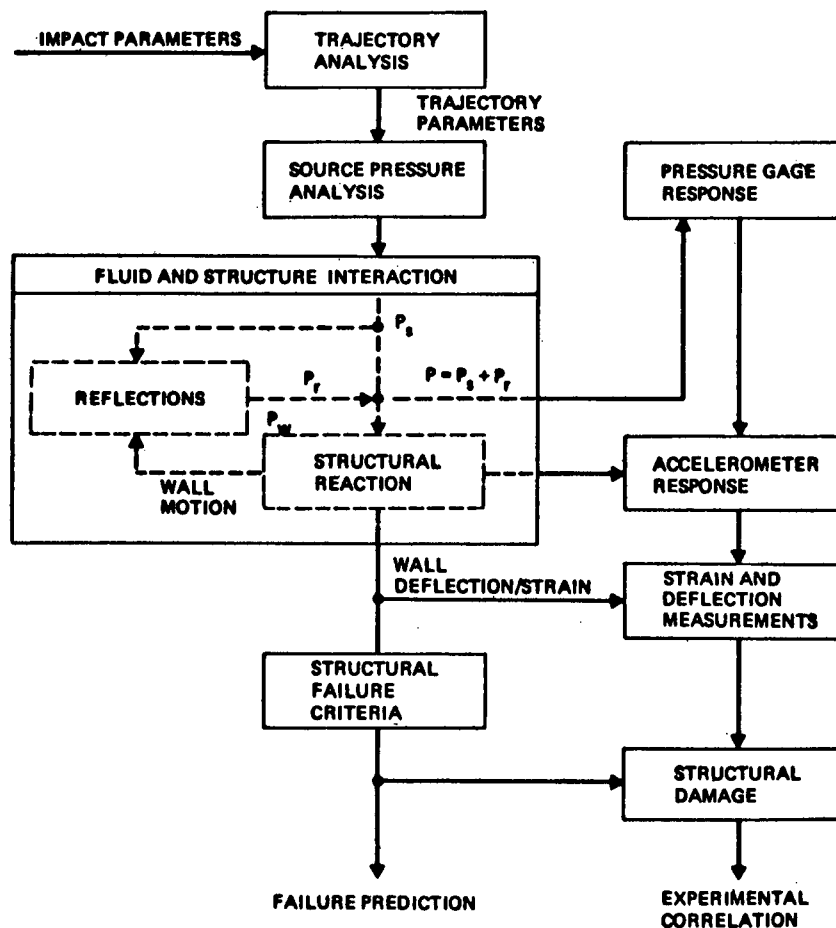
Figure 2-163. Methodology for Hydrodynamic Ram Analysis (Ref. 2-45)

2.2.4.3.1 Trajectory and Fluid Pressure Analysis

Drag phase pressures are caused by deceleration of the projectile as it traverses the fluid. E. A. Lundstrom (Ref. 2-45) applied the classical hydrodynamic theory of a travelling object in a perfect fluid to predict drag-phase pressures. Hydrodynamic ram pressures are calculated from Bernoulli's equation, using the potential function for a line of pressure sources along the trajectory of the projectile. The strength of the sources is calculated from the kinetic energy loss of the projectile in travelling incremental distances along the trajectory.

Certain aspects of the problem, such as projectile tumbling, jacket-stripping, and cavity dynamics, required empirical definition. Extensive testing was done at the Naval Weapons Center (NWC) to quantify these effects and incorporate the results into the fluid pressure prediction analysis. The final methodology was developed into a computer code for rectangular fluid-filled tanks impacted by single penetrators. Figure 2-164 shows the primary elements of the code, hereafter referred to as the NWC hydrodynamic ram program or the HRP-V1 code. The code includes both trajectory analysis to determine the strength of the moving sources, and the solution of the Bernoullis equation to obtain fluid pressures and velocities throughout the tank. A mirror image of the line of sources is used. A brief summary of the NWC hydrodynamic ram program is given below, and a complete development is available in Reference 2-48.
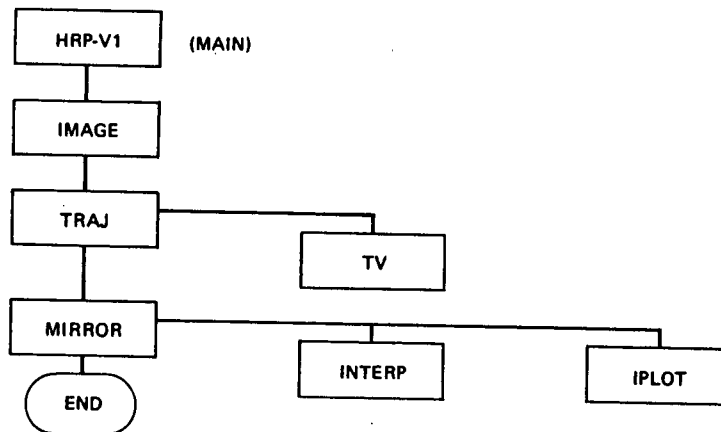
Figure 2-164. NWC Hydraulic Ram Program Version One (HRP-V1)

Three primary parameters which must be determined in order to calculate fluid pressure caused by a projectile traveling a tank of fluid are velocity, rate of kinetic energy loss, and time of arrival of the projectile as a function of distance along the trajectory. The projectile velocity is determined by Newton's second law:

$$m \frac{dV}{dt} = -D$$ (Eqn. 2-100)

where

  m = projectile mass,
  V = projectile velocity,
  D = drag,
  t = time.

Drag is a function of the projectile velocity, the fluid density, and the size and orientation of the projectile. The time at which the projectile starts to tumble and at which it becomes fully tumbled must be known. Substituting a function for drag into Equation 2-100 gives:

$$\frac{dV}{dx_b} = -\beta V_b$$ (Eqn. 2-101)

where β is called the velocity decay coefficient. Because of the tumbling action of the projectile an empirical function was developed for β. Then, Equation 2-101 was integrated to give:

$$V_b = V_o e^{-\beta_1 x_b}$$ (Eqn. 2-102)

where

  V_b = velocity at x_b,

  V_o = initial velocity,

  x_b = position of the projectile along the trajectory.

The rate of kinetic energy loss due to the velocity decay is:

$$\frac{dE}{dx_b} = m \beta_1 V_b^2,$$ (Eqn. 2-103)

where

  E = kinetic energy,
  m = mass of the projectile.

The stripping of the projectile jacket causes a change in kinetic energy. An approximation for the energy deposition due to stripping is used. The total energy deposition is:

$$\frac{dE}{dx_b} = m_c \, \beta c \; V_b^2 + \alpha \, \frac{E_{js}}{\beta_j} \, e^{-\beta_j(x_b - x_s)}$$ (Eqn. 2-104)

where

m_c = mass of the core,

E_{js} = $\frac{1}{2} m_j V_s^2$,

V_s = velocity of the projectile at the stripping location,

m_s = mass of the jacket,

α = obtained empirically to be 1/3

The flow field is described by a potential function which satisfies the wave equation:

$$\nabla^2 \emptyset = \frac{1}{c^2} \frac{\partial^2 \emptyset}{\partial t^2}$$ (Eqn. 2-105)

where $\emptyset$ is the potential function and c is the speed of sound in the fluid. The effect of the projectile and cavity on the fluid is approximated by a line of sources along the projectile path. This source is a function of the distance along the trajectory and the retarded time, $\tau = t - r/c$ where r is the distance between the source point and the present position of the projectile. The strength of the source is developed by a conservation of energy equation. Although the effect of the cavity is contained in these calculations, the absence of fluid in the cavity is not accounted for, which results in the theory being invalid during cavity collapse. Therefore, all negative pressures resulting from the theory should be set to zero. Because the effect of the walls was not included on the cavity size calculations, as the cavity approaches maximum size the source strength becomes increasingly erratic. Using the conservation of energy method by combining the work done by difference between ambient pressure and cavity pressure and the energy deposited in the fluid by the projectile, the total differential energy is calculated. Due to the mathematical difficulty of the boundary conditions of the walls, they are approximated by mirror images of the line sources (Ref. 2-48).

At this point, with some mathematical exercises, all the terms of Bernoulli's equation are known, so that pressure can be calculated from:

$$p - P_o = \xi \, \frac{\partial \emptyset}{\partial t} - \frac{1}{2} \xi \, u^2$$ (Eqn. 2-106)

where:

ξ = source strength,

$\emptyset$ = potential function,

P_o = ambient pressure,

u = fluid velocity.

The fluid pressures generated by the projectile are governed by Bernoulli's equation, but the limitations of the theory should be remembered. Since the effects of the projectile are modeled by a line of sources, the pressure will approach infinity at the projectile. Because of the absence of fluid in the cavity, the negative pressures generated by the theory should be set to zero. This gives the assumption of bulk cavitation in the cavity.

The subroutines used by the HRP-V1 code, diagrammed in Figure 2-164, are described in Figure 2-165. NWC, NPGS, UDRI and Boeing have all made comparisons of HRP-V1 pressure predictions with test data. All are generally in agreement that the results correlate well. The following are results from a Boeing comparison study done in 1977 (Ref. 2-49).

Test data on hydrodynamic ram pressures generated by small arms projectiles was available from previous Boeing test programs (Ref. 2-50). Figure 2-166 shows the hydrodynamic ram test tank in the Impact Mechanics Laboratory. High-speed motion pictures were made with two 10,000 frames/second Hycam cameras with time-calibrated film. Pressures were measured with acceleration-compensated quartz transducers. Pressure signals were conditioned with charge amplifiers and displayed on oscilloscopes using a fast-rise preamplifier. Velocities were computed by elapsed time through a two foot segment measured from the entry diaphragm.

Figure 2-167 shows the correlation of the predicted peak pressures with the experimental results. The errors were evaluated and the root mean square (rms) found, and this evaluation demonstrated good correlation. Naval Weapons Center did a rms analysis of peak pressures and impulse, showing a similar correlation (Ref. 2-51). Figure 2-168 shows comparison plots of pressure vs. time curves for several tests. In some of the figures a time shift can be seen. This is probably due to uncertainties in predicting tumbling behavior. From this evaluation, it appeared that the program can predict pressures which correlate well with experimental data.

149

ROUTINE	DESCRIPTION

HRP–V1

<u>MAIN</u>   Calls the subroutines necessary to generate hydraulic ram induced pressure-time curves at user specified points within a body of fluid.

IMAGE

<u>SUBROUTINE</u> Computes the coordinates of the projectile entrance/exit points in the three-dimensional image volumes with respect to the actual volume where lower front corner is at 0,0,0.

TRAJ

<u>SUBROUTINE</u> Computes the following quantities as a function of bullet distances along trajectory; time of bullet arrival; bullet velocity; maximum cavity radius; time of cavity collapse; drag parameter as a function of time

TV

<u>SUBROUTINE</u> (Called by TRAJ)
Computes the value of the velocity decay parameters, then integrates the equations of motion to obtain bullet velocity as a function of time.

MIRROR

<u>SUBROUTINE</u>   Computes: Total pressure at a user-specified point as a function of time; pressure due to the time derivative of the velocity potential; total fluid velocity as a function of time; and x, y and z components of fluid velocity.

INTERP

<u>SUBROUTINE</u> (Called by MIRROR) Interpolates the following quantities between discrete points along the bullet trajectory: distance and velocity of bullet as a function of retarded time; radius of attached cavity as a function of retarded time.

IPLOT

<u>SUBROUTINE</u> (Called by MIRROR)   Generates graphic presentation of the total pressure versus time at each point in the fluid body specified by the user.

Figure 2-165. Description of Routines in NWC Hydraulic Ram Program Version One (HRP-V1)
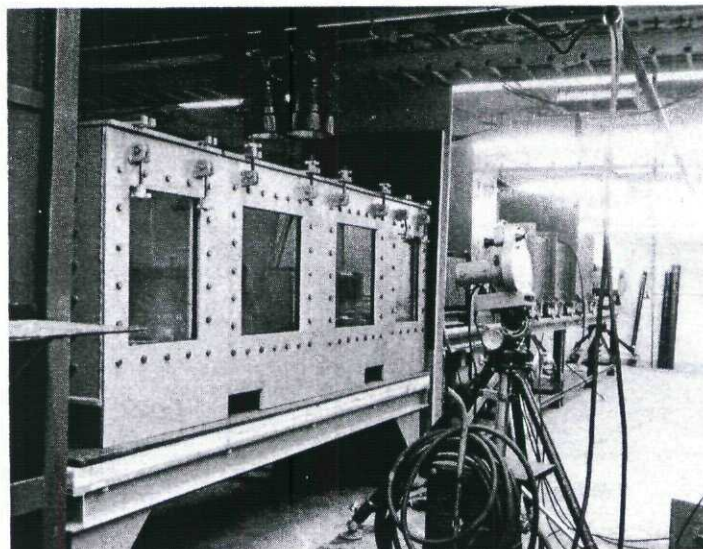
Figure 2-166. Hydraulic Ram Test Tank, Boeing Impact Mechanics Laboratory

MEASURED
PRESSURE (psi)

PREDICTED PRESSURE (psi)

○ 14.5 API, 3295 FPS
□ .50 AP, 1750 FPS, JET FUEL
△ 14.5 API, 2750 FPS
▽ .50 AP, 2750 FPS
(Numbers refer to transducer)
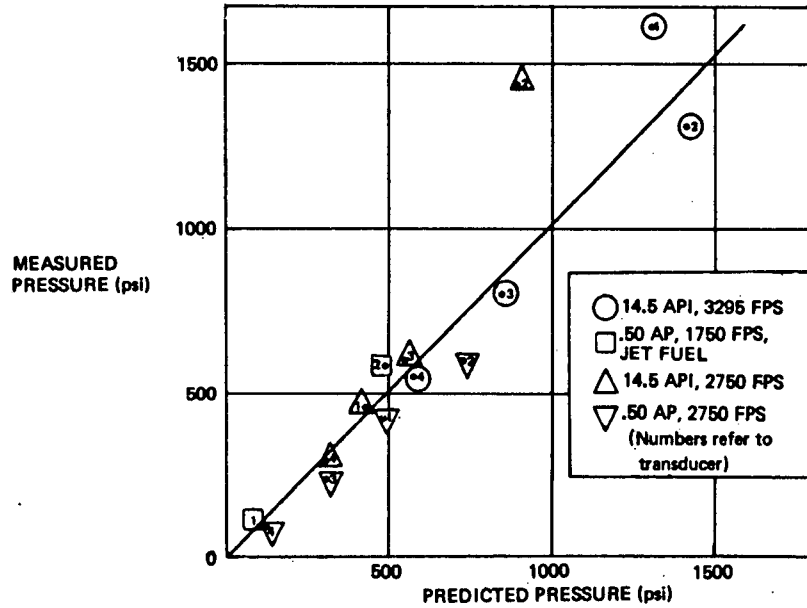
Figure 2-167. Correlation of NWC Hydraulic Ram Program Peak Pressure Prediction With Boeing Test Data

14.5 mm API BULLET
3295 ft/sec
WATER
NORMAL OBLIQUITY
TEST 2307

NO. 4

NO. 3

END OF DATA
NO. 2

--- EXPERIMENTAL
— PREDICTED

NO. 1

END OF DATA

PRESSURE (psi)

TIME (μsec)

.50 CAL AP BULLET
1750 ft/sec
JET FUEL
NORMAL OBLIQUITY
TEST 23

NO. 3

--- EXPERIMENTAL
— PREDICTED

NO. 2

PRESSURE (psi)

TIME (μsec)

14.5 mm API BULLET
2750 ft/sec
WATER NORMAL
OBLIQUITY
TEST 2270

NO. 4

NO. 3

NO. 2

--- EXPERIMENTAL
— PREDICTED

NO. 1

PRESSURE (psi)

TIME (μsec)

.50 CAL AP BULLET
2750 ft/sec
WATER
NORMAL OBLIQUITY
TEST 2272

NO. 4

NO. 3

NO. 2

--- EXPERIMENTAL
— PREDICTED

NO. 1

END OF DATA

PRESSURE (psi)

TIME (μsec)

Figure 2-168. Results of Boeing Study to Compare NWC HRP-V1 Code Predictions With Available Boeing Data on Hydraulic Ram Pressures

2.2.4.3.2 Fluid/Structure Coupling

The fluid pressures and velocities obtained from solutions of the wave equation and Bernoullis' equation as described above satisfy boundary conditions at the projectile and cavity surfaces only, and not at the tank walls. The two boundary conditions at a wall/fluid interface are (ignoring cavitation):

1. The fluid pressure equals the pressure acting on the wall,

2. The component of fluid velocity normal to the wall surface equals the normal component of the wall velocity.

In order to predict wall loading due to hydrodynamic ram, solutions to the wave equation satisfying these conditions are needed, and it is clear from the nature of the boundary conditions that the fluid and wall motions are coupled. Lundstrom, in Reference 2-45, applied Kirchoff's general solution of the wave equation to outline an approach for obtaining wall pressures. However, because of anticipated computational labor, attention has been directed toward less complex coupling models, notably piston theory. Piston theory assumes that the reflected wave is a plane wave propagating parallel to the wall normal. For such a wave, the relationship between the fluid pressure and velocity behind the wave is:

$$p_r = -\rho c\, u_{rn},$$

(Eqn. 2-107)

where ρ is the fluid mass density and c is the sonic velocity. At the wall, the pressure is the sum of the incident pressure (p_i), and the reflected pressure:

$$
\begin{aligned}
p &= p_i + p_r \\
&= p_i - \rho c\, u_{rn}
\end{aligned}
$$

(Eqn. 2-108)

If the second boundary condition above is written as:

$$u_n = u_{in} + u_{rn} = \dot{w}_n,$$

(Eqn. 2-109)

so that:

$$u_{rn} = \dot{w}_n - u_{in},$$

(Eqn. 2-110)

then:

$$p = p_i + \rho c\, (u_{in} - \dot{w}_n).$$

(Eqn. 2-111)

The incident fluid pressure and normal velocity (u_{in}) are considered to be known from the solution for sources within the fluid volume. A structural response model is now required to complete the solution, by providing the link between applied pressure and wall velocity.

If the incident wave is also planar and traveling parallel to the wall surface normal, Equation 2-111 becomes:

$$p = 2p_i - \rho c\dot{w}_n .$$

(Eqn. 2-112)

2.2.4.3.3 Structural Response Analysis

The next step in the analytical development is to introduce a structural model to predict wall motion, stresses, and failure resulting from the transient hydrodynamic ram pressures. The structural model must satisfy a dynamic equation of equilibrium which includes the fluid/structure coupling terms as a minimum requirement. In addition, in order to adequately treat the problem, the structural model needs large deflection, elastic/plastic capability, and analytical sophistication to represent the boundary conditions of multi-element aircraft structure. In the course of hydrodynamic ram analytical development, a number of structural models have been used, ranging from one-dimensional harmonic oscillators to the BR-1 series of finite-element computer codes. Experience with these models has resulted in increased knowledge and further definition of development requirements and goals.

The general nature of hydrodynamic ram structural response can be illustrated most conveniently from a simple harmonic oscillator structural model. The one-dimensional equation of dynamic equilibrium is:

$$M\ddot{w} + Kw = F(t)$$

(Eqn. 2-113)

where M is the mass, K is the stiffness, F(t) is the externally applied force resulting from the ram pressure at the wall, and w is the deflection. Analytical expressions for the wall pressure loading come from consideration of fluid/structural coupling as described in the previous section. The piston theory coupling can be written as:

$$p(t) = p_i + \rho c u_{in} - \rho c\dot{w}$$

(Eqn. 2-114)

Substituting into (2-113) and placing all of the wall-motion dependent functions on the left side of the equation gives the following form of the dynamic equation of equilibrium for the oscillator:

$$M\ddot{w} + \rho cA\dot{w} + Kw = p_i A + \rho cA u_{in}$$

(Eqn. 2-115)

where A is the appropriate surface area.

The dynamic equation of equilibrium defines the forces acting on the oscillator. These include an inertial force involving structural mass and acceleration, a stiffness term expressing the capability of the structure to resist external forces by developing internal loads during deflection, and the forces associated with the fluid/structure interaction, which depend on the incident pressure and the velocity of the structure.

In principal, this incorporation of the fluid/structure coupling relations into the dynamic equation(s) of equilibrium is applicable to any structural response formulation. Appropriate dynamic structural response models can be found in References 2-47, 2-52, and 2-15. The latter is the BR-1FC blast response computer code described previously in Section 2.2.2.2.3.1. This code has the requisite orthotropic as well as isotropic large deflection, elastic-plastic capability for measuring the response of structures to transient pressure loadings. To date this code has not been used with hydrodynamic ram pressure prediction codes, but is the best structural response model available for this purpose.

Section 2.2.2.2.3 of this Manual also describes several additional methods for assessing the response of structure to transient pressure loadings. These methods are presented in the context of application to transient pressures induced by explosive detonation, but they are also applicable for the case of hydrodynamic ram, provided the proper fluid/structure algorithms are incorporated.

2.3 EFFECTS OF CYCLIC LOADING ON PROJECTILE IMPACT DAMAGE

The cyclic loading induced during flight can influence the severity of existing impact damage by initiating fatigue-cracks at the damage site, subsequent crack sharpening or blunting, and crack growth. There can be significant time-dependent changes in the residual strength of the structure due to these alterations in the size and character of the impact damage.

Projectiles produce a wide variety of damage types, including cracks, holes, tears, large deformations, even totally severed structural elements. The response of the damaged structure when exposed to cyclic loads reflects this wide variety of structural damage. For example, the cyclic loading can result in immediate growth when the projectile damage is a crack. There may be, however, a time (number of cycles) devoted to crack nucleation.

The following subsections describe several important aspects of the fatigue response of impact damaged structure in terms of crack initiation and extension, and suggest an approach which basically consists of assuming immediate fatigue crack initiation at the damage site, and then applying conventional crack growth analysis.

2.3.1 Fatigue Crack Initiation

A certain amount of flight time (number of cycles) may be required before fatigue cracks initiate in the vicinity of projectile damage. This interval is defined as the initiation phase. Two types of fatigue crack initiation may occur in impact damaged structure:

a.   Fatigue crack initiation at some point on the periphery of the damage;

b.   Fatigue crack initiation in undamaged structure adjacent to damage structure.

2.3.1.1 Crack Initiation From Ballistic Damage

It has been demonstrated that when ballistic-damaged metal panels are cyclic loaded, fatigue cracks can initiate at the edge of the damage. Forman (Reference 2-55) showed through test and analysis that there may be a minimum number of cycles required to initiate these cracks. However, there is no analytical technique available to predict the cycles required.

Therefore, it is recommended that immediate crack initiation be assumed for establishing subsequent damage growth. This means assuming zero initiation time, and represents an upper bound for ballistic-damage severity from a fatigue-crack initiation standpoint.

2.3.1.2 Crack Initiation in Adjacent Undamaged Structure

Projectile penetration of multiple-element structure creates a configuration consisting of severed, damaged, and undamaged elements. Because of the load redistribution throughout the structure, the remaining unfailed elements may experience significant increases in loading. Fatigue damage (crack initiation, element failures) in these remaining structural elements can seriously degrade their performance, significantly reducing the residual strength capability. Analysis of these elements requires determination of the load redistribution and the fatigue performance of the elements when subjected to these new loadings.

2.3.2 Fatigue Crack Growth

Fatigue crack growth is the progressive extension of the crack due to cyclic loadings. The term "fatigue crack" will be used with the understanding that it is not strictly correct for laminated fiber composite materials such as graphite/epoxy. The direction of growth is generally normal to the maximum principal stress direction in metal structure. With composite materials, however, fiber orientation influences the growth direction.

Fatigue crack growth data are presented as the change of crack length with applied load cycles. This parameter is called the crack growth rate (inches/cycle). Integration of the estimated growth rate from an initial to a terminal crack size will define the required number of cycles (time) for the crack to extend to the terminal size. The terminal size used in the analysis could correspond to the critical crack length, as defined by fracture mechanics. The analysis of fatigue crack growth in metals has been developed in some detail, and similar techniques are under development for fiber composites.

Fatigue crack growth is influenced by a number of variables. These include:

a.   Load
     Temperature
     Minimum stress
     Direction
     Spectrum
     Frequency

c.   Environment
     Maximum
     Temperature
     Atmospheric
     Pressure

b.   Geometry
     Crack size
     Crack configuration
     Structural size and configuration

d.   Material Properties
     Material type - metal, composite
     Alloy and chemistry
     Heat treat and processing
     Microstructure and grain direction

The analysis methods for predicting fatigue crack growth must consider all these variables. Load and geometry are basic factors that must be defined for the specific structure analyzed. Environmental and metallurgical factors are included in the crack-growth data used for the analysis.

2.3.2.1 Crack Growth Analysis for Metallic Structure

If zero crack initiation time is assumed for projectile damage, as recommended in 2.3.1.1, the prediction of damage extension rates under cyclic loading can be done using the same analysis methods appropriate for conventional crack growth. Many methods have been proposed in recent years for correlating fatigue-crack growth-rate data in terms of the loading and geometric variables, and definitive description of any method is beyond the scope of this Manual. The stress intensity factor (i.e., the fracture mechanics approach) is summarized below. This method has gained the widest acceptance and is adaptable to a wide variety of structural configurations. The approach assumes that the fatigue-crack growth rate is governed by the crack-tip stress field as given by linear-elastic fracture mechanics theory. In this analysis the crack-tip stress field is directly related to the stress intensity factor, K, and this factor is related to growth rate by:

$$\frac{\Delta 2a}{\Delta N} = F(K),$$

<div align="right">(Eqn. 2-116)</div>

where; $\frac{\Delta 2a}{\Delta N}$ = fatigue-crack growth rate (inches/cycle);

$F(K)$ = a functional relationship determined by test.

The stress intensity factor is a function of the panel geometry, crack length, and applied stresses. Solutions for the stress intensity factor for various geometries and loadings are presented in Section 2.4. Additional information may be found in References 2-56 and 2-57, among many.

The influence of material properties and environment is included in the functional relationship. Test data must be used to define this information for each condition. Fatigue crack growth-rate curves defining this relationship for a number of cases are presented in Figures 2-169 through 2-171, for several structural materials. The growth rate is a function of maximum stress intensity factor; that is, the stress intensity factor corresponding to the maximum value of applied stress in the load cycle. In cases where sufficient data was available an estimated upper bound on fatigue-crack growth rate was included.
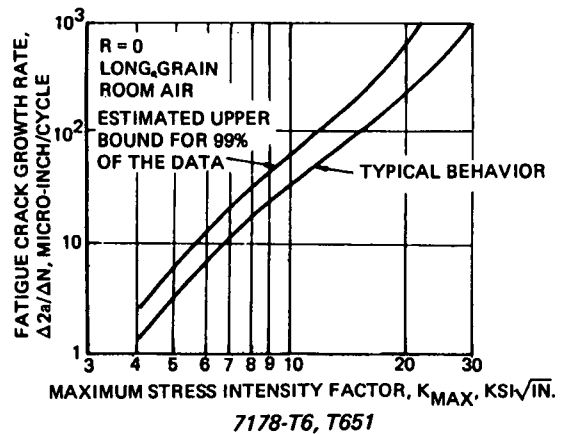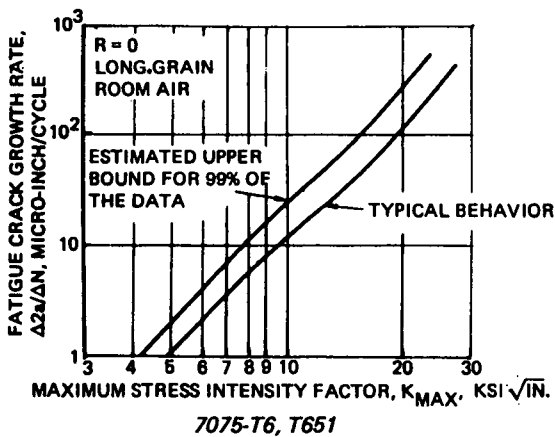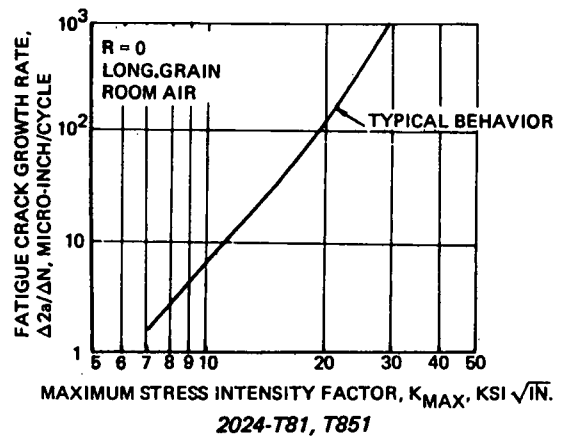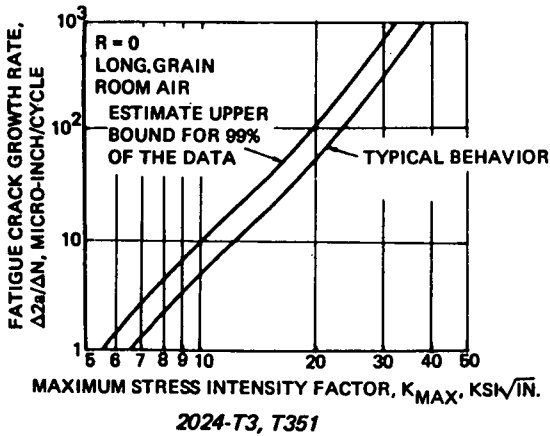
Figure 2-169. Estimated Fatigue Crack Growth Behavior
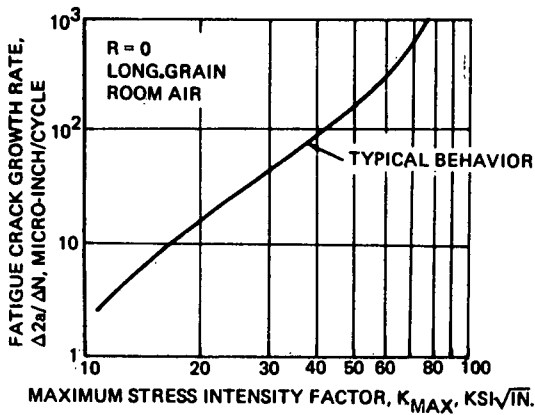
Figure 2-170. Estimated Fatigue Crack Growth Behavior
for Ti 6Al-4V Condition I (Mill Anneal)
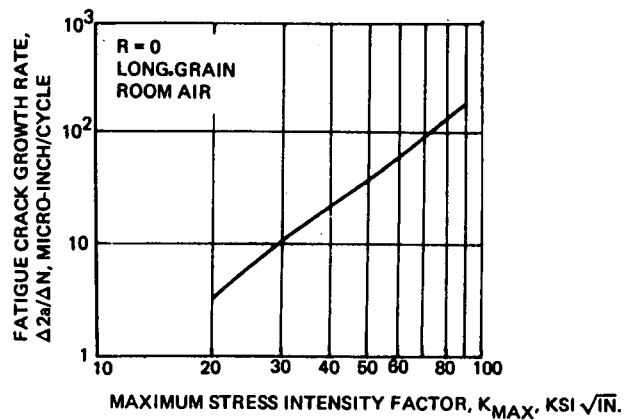
Figure 2-171. Estimated Typical Fatigue Crack Growth
Behavior for 4330 M, H_tT. 180-200

The crack growth in a particular structural element is estimated by integrating the appropriate crack growth-rate data for the spectra of loadings and environments imposed on the structure. This is done using an iterative technique. Satisfactory estimations can be made quickly by hand for many cases. However, computerized analysis methods, such as described in Reference 2-58, provide the capability for evaluating a more complex loading environment. The computer techniques also permit efficient investigation of several variations of the problem. In many cases, only limited or perhaps no applicable fatigue crack growth data are available. In these cases, estimates must be made. The effects of some variables that influence growth are discussed in the following paragraphs to help in making these estimates.

The crack-growth-rate versus stress-intensity-factor curves are based on the maximum stress intensity factor in the load cycle (corresponding to the maximum stress). Each curve is defined for a stress ratio $R = 0$, where

$$R = \sigma_{min}/\sigma_{max}$$
$$= K_{min}/K_{max}$$

(Eqn. 2-117)

The majority of the available test data in the literature are for this condition. When data for the required values of R are not available, Figure 2-172 can be used to estimate the crack growth behavior. In the case of reversed loading ($\sigma_{min} < 0$ and R negative), using the solutions for $R = 0$ will give good results. This is equivalent to neglecting the negative stress part of the cycle.

Physical environment has a significant influence on fatigue crack growth rate. Generally, the influence of moisture or high humidity is the most important. Experience from the behavior of commercial aircraft has shown that in-service crack growth is often representative of the high-humidity or "wet" condition. Crack growth rates for the wet conditions can be several times that experienced in the laboratory air environment. Data from Reference 2-59 showing the influence of moisture on fatigue crack growth in two aluminum alloys are presented in Figure 2-173. As seen in the figure, the growth rate is accelerated in the 7075-T6 material by the environment. A similar result is shown in Figure 2-174 for titanium alloy 6Al-4V.
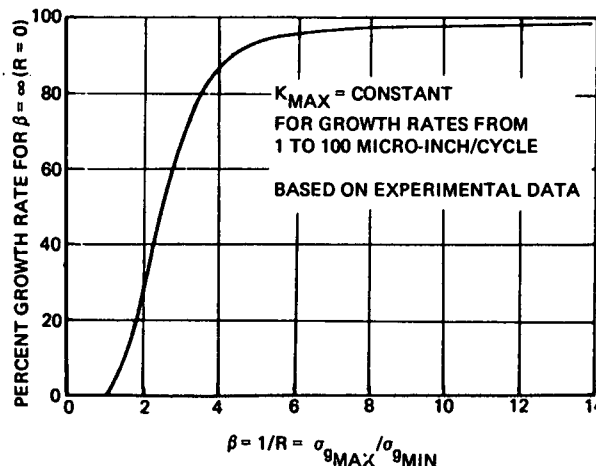
Figure 2-172. Influence of Stress Ratio (β) on the Fatigue Crack Growth Rate
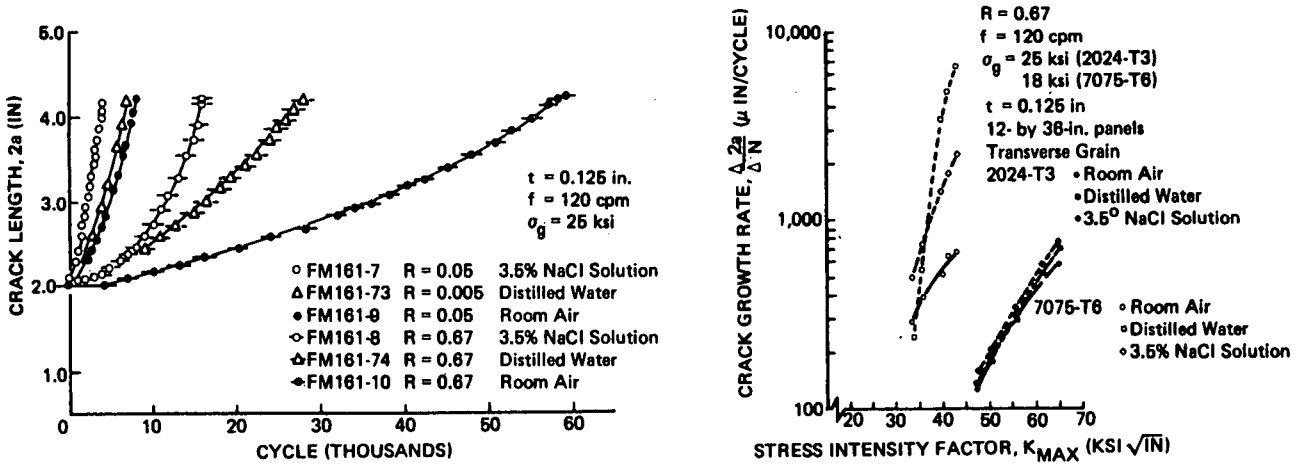
Figure 2-173. Influence of Environment on Fatigue Crack Growth
in 7075—T6 and 2024-T3
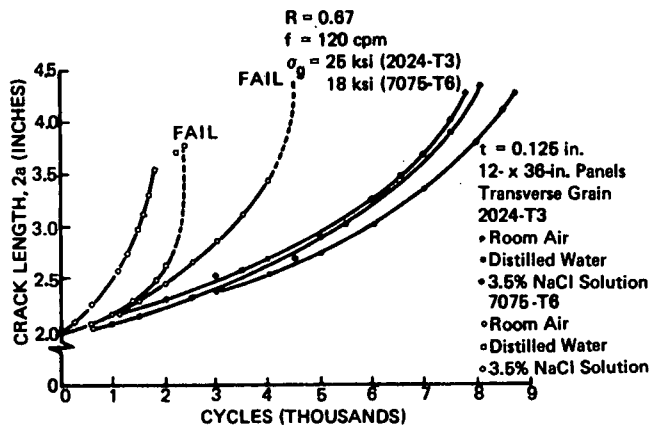
Figure 2-174. Influence of Environment on Fatigue Crack Growth
in Ti 6Al—4V Mill Anneal

Cyclic frequency generally is not considered to be a major variable in fatigue crack growth analysis. Test data supporting this conclusion are shown in Figure 2-175 for 7075-T6 aluminum alloy (Reference 2-60). Exceptions are encountered in the case of long cycle times within a reactive environment. For most crack-growth estimates conducted in support of impact damage analyses, cyclic loading frequency need not be considered.

The influence of temperature on fatigue crack growth is generally small. Aluminum alloys, however, do show an increase in growth rate with increasing temperature. Other materials, such as titanium alloys and steels, have variable performance with temperature. The temperature influence on cyclic load damage extension for these materials, however, can generally be neglected for the normal range of operating temperatures on aircraft.

The data presented in this section were generated with constant amplitude loading; that is, the load applied to the test specimen was repetitive in size and shape. In aircraft structure, however, the loading has randomly sequenced variable amplitudes with a changing mean stress. Estimating fatigue crack growth under these loading conditions requires an estimate of the cycle loading spectrum, and method of estimating the growth with variable load cycles.

The loading spectrum should be developed to reflect the usage and configuration applicable to the aircraft evaluated. These requirements may come from procurement specifications or from an evaluation of the aircraft and mission. A discussion of these loading variables is presented in Section III.

It has been shown (Reference 2-61) that fatigue crack growth can be correlated on a cycle-by-cycle basis corresponding to the individual load increases (that is, the portion of the cycle with a positive slope) see Figure 2-176. It is suggested that the spectrum loading be analyzed using the individual load increases rather than the complete cycle in the developed spectrum. The crack growth is then estimated progressively in sequence with the load spectrum.

Load-cycle sequence has been shown (Reference 2-62) to influence fatigue-crack growth behavior. This is in part due to the fatigue-crack growth for a given cycle being a function of previous loading history. It is suggested that the interaction effects be neglected and the constant amplitude data be used directly for projectile damage tolerance analysis.
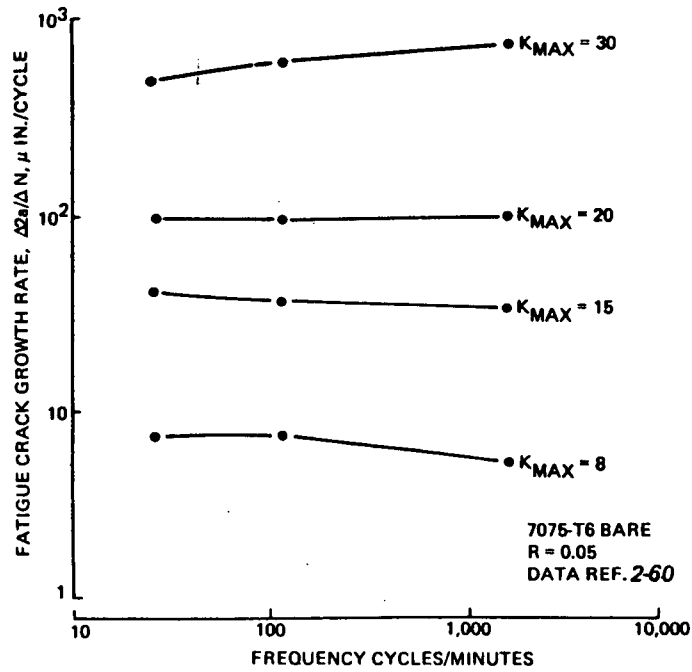
2-175. Influence of Cyclic Frequency on Fatigue Crack Growth Rate
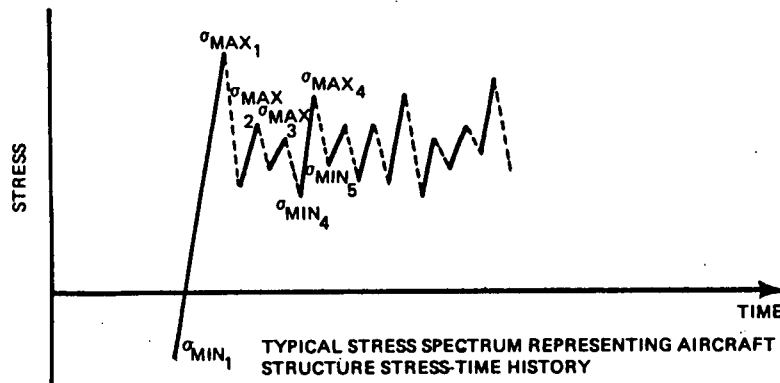
For Fatigue Crack Growth Analysis Consider Only the Load Increases—These Are Shown By the Solid-Dark Lines. Neglect the Load Decreases

For Example: The Growth for Cycle 4 Is Given by Using σ_{MAX_4} and σ_{MIN_4} to Calculate K_{MAX_4} (a Function of σ_{MAX_4} and Crack Length) and $R_4 = \sigma_{MIN_4}/\sigma_{MAX_4}$

Figure 2-176. Spectrum Load Fatigue Crack Growth Analysis Method

2.3.2.2 Damage Extension Analysis for Fiber Composite Structure

Composite materials such as glass-reinforced plastic, boron/epoxy, boron-polyimide, and graphite/epoxy, consist of a brittle, high-modulus fiber imbedded within a low-strength matrix. The matrix is generally more sensitive to fatigue damage than the fibers. When exposed to cyclic loading, the interaction of matrix and fibers causes varying responses. For example, the direction of crack propagation is dependent on the fiber orientation as well as the loading direction. Undirectional fiber-composite materials experience damage propagation between the fibers in a direction which is generally parallel to the loading direction.

Cyclic loading of ballistic-damaged, crossplied, advanced composite materials often does not produce any discernible damage extension. Consequently, the residual strength of ballistic-damaged fiber-composite structure may not change with cyclic loading. In fact, in some cases an increase in strength can occur. This increase has been shown for some layups of boron/epoxy, glass/epoxy, and steel-wire-reinforced aluminum. The data available are not sufficient to allow a quantitative assessment of behavior. However, it does illustrate the complex behavior of composite structure and the care that must be exercised when evaluating its behavior.

2.4 STIFFNESS DEGRADATION OF IMPACT DAMAGED STRUCTURE

Stiffness reduction in impact damaged structural elements can be important from two standpoints. The first is the alteration of load distribution within the structure, potentially causing overloading and failure of undamaged elements. The second area of potential concern is the residual stiffness of major structural components, since stiffness degradation may lead to instability and control inadequacy. These two topics are discussed in the following sections. However, there are few verified analysis methods for predicting stiffness degradation associated with ballistic damage. Both of these stiffness degradation effects, but particularly the latter, become increasingly significant as the extents of the inflicted damage becomes larger. Stiffness degradation may well be a problem for HE projectile impacts, but it is generally insignificant with small arms.

2.4.1 Stiffness Degradation of Damaged Structural Elements

Stiffness reduction due to loss of area and deformation of the elements can cause significant redistribution of the internal loading in multiple-element structure. Analysis of structure containing damaged elements requires evaluation of their stiffness alteration. Finite-element structural analysis techniques, for example, require a definition of the stiffness of each individual element in the structural model. Section 2.2.2.1.2 describes a technique for altering the stiffness of perforated elements.

Stiffness degradation of axially loaded panels due to projectile damage was studied previously by Martin-Marietta under Air Force contract F33615-67-C-1660. From this study the following expression was developed for constant cross-section, tension-loaded panels as shown in Figure 2-177.

$$\frac{\delta_2}{\delta_1} = 1 - \frac{TLD}{a\,\tan\alpha} - \frac{b}{a\,\tan\alpha}\;\log_e\left[1 - \frac{TLD}{b}\right]$$

(Eqn. 2-118)

where

$\dfrac{\delta_2}{\delta_1}$ = change in compliance (deflection of element after damage divided by defection before damage)

This expression assumes an ineffective area around the damage and constant stress on the remaining cross section. The value of α for use in this expression was approximately 20-degrees, as determined by test. For finite-element structural modeling it is suggested that this expression be used for partially damaged plate elements.

Similarly, for shear elements, the following expression was suggested:

$$\frac{\delta_2}{\delta_1} = \frac{1}{1 - \dfrac{0.785\,(TLD)^2}{ab}}$$

(Eqn. 2-119)

Rod elements (or those axial-loaded structural elements for which the cross-section is small relative to the length) generally will not suffer significant stiffness changes prior to element failure. Therefore, for finite-element evaluations, the stiffness of those that are not severed (but are partially damaged) would be equal to the undamaged value.

Beam elements (elements carrying bending) can experience significant changes in bending stiffness due to partial damage. When developing a finite-element structural model it may be necessary to include this stiffness change if bending elements are included in the idealization.

2.4.2 Stiffness Degradation of Damaged Structural Components

Aircraft structure that is damaged by large caliber HE projectiles, can experience significant changes in stiffness at the component level. For example, severe skin damage (panel detachment or rupture) in a wing can reduce the torsional stiffness below the flutter requirements of the operating envelope. Severance of a wing spar could have a similar effect. Empennage structure, because of the generally low flutter margins, also could be similarly vulnerable.

It is beyond the scope of this Manual to present flutter analysis techniques for damaged structure. The relationship between projectile damage and wing flutter requirements was considered in Reference 2-63, using finite-element techniques for developing the stiffness matrix of the damaged configuration. That study will provide guidance for assessing flutter capability.
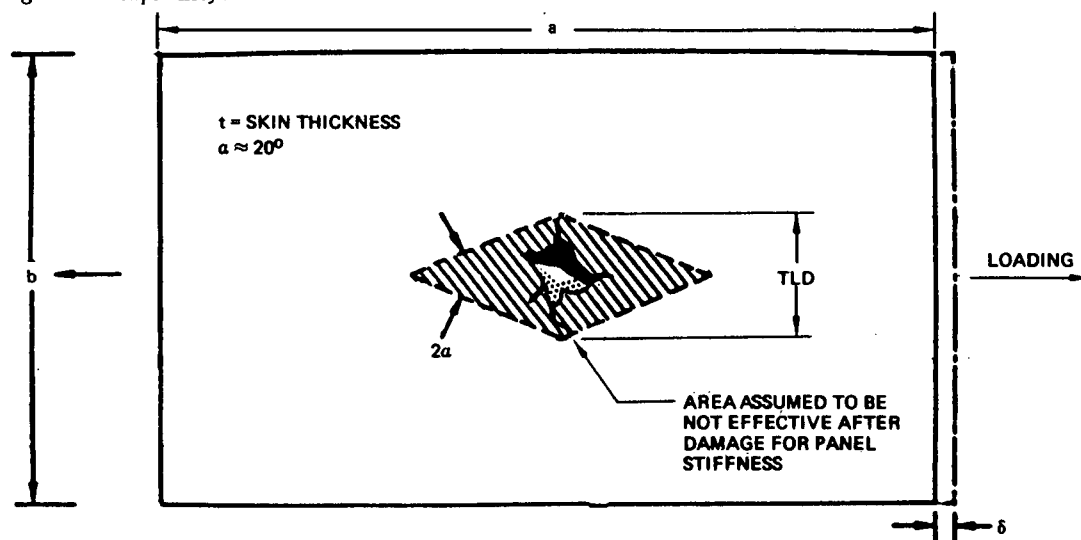
Figure 2-177. Effective Damage for Panel Stiffness Calculation

2.5 STRENGTH DEGRADATION OF IMPACT DAMAGED STRUCTURE

Projectile damage destroys a portion of the load-carrying capability of the structure, alters the distribution of internal loads, and introduces a flaw which may cause failure by locally disturbing the stress field. The latter effect is most significant with regard to the relatively small damage induced by small arms projectiles and dispersed warhead or engine debris fragments. High-explosive projectiles can often create damage of sufficient size to substantially degrade structural performance by all three effects. Estimating the residual strength of structure damaged by projectile impact is a major step in predicting structural capability.

Predicting residual strength loss due to the destruction of load-carrying material is straightforward provided the damage has been accurately determined. Thus, this aspect of the problem reduces to the problem of predicting damage, using methods discussed in Section 2.2. The same comment applies to establishing the effects of internal load redistribution. Once the damage is known, finite-element or other analysis methods can be used to determine redistribution.

Unique problems do arise, however, with regard to assessing the effects of the flaw introduction aspect of projectile damage. These problems center around estimating the effective flaw size represented by the ballistic damage. Historically, investigation in this area was initially directed at determining the effects of ballistic damage in monolithic metallic tension members. This priority was established because tensile failure due to unstable crack growth emanating from a ballistic damage is the most probable mechanism for causing structural failure due to projectile impact in metallic structure. Consequently, most of the analytical development available for presenting in this section pertains to tensile failure, or more precisely, fracture of tensile elements containing flaws induced by projectile penetration.

In the early 1970's, attention was directed toward establishing the response of advanced fiber composite materials (graphite/epoxy, for example) to projectile impact. Because of the high notch-sensitivity of many graphite/epoxy laminate configurations, and the past experience with metallic structure cited above, the initial consideration was tensile failure of damaged structure. Quite recently, the effect of delamination in degrading compression strength has been identified as a serious problem. But again, the analysis methods for composites presented herein reflect the early concern for tensile failure.

The analysis methods presented in this section for evaluating strength capability have been somewhat arbitrarily organized according to structural complexity: 1) analysis of monolithic panels, 2) analysis of multiple load-path panels, and 3) analysis of multi-element structure. The application of conventional and modified fracture mechanics analysis to ballistic damaged panels is discussed under the first category (2.5.1). The extension of these approaches to the requirements of panels having discrete stiffening members is discussed under the second category (2.5.2). Finally, the analysis of damaged components using finite element methods is discussed under the last category (2.5.3).

2.5.1 Analysis of Monolithic Panels Containing Impact Damage

This section addresses analysis methods for predicting the effect of projectile damage on the residual tensile strength of single structural elements. The topics presented include fracture mechanics analysis as applied to projectile damaged panels, the significance of the dynamic loading effects induced by impact and blast, and the influence of combined stress conditions. The methods apply directly to monolithic components, but are distinct from the strength-prediction methods presented later for multi-element structure which include consideration of the interaction between elements.

Some fundamental aspects of the residual strength behavior of tensile panels are shown schematically in Figure 2-178, identifying two limiting cases denoted as "notch-insensitive" and "notch sensitive". In ductile materials, or when the type of damage results in low stress concentration, residual strength is determined by the net cross-sectional area of the member. This represents notch-insensitive behavior, and is the least-severe condition (greatest residual strength). Predicting residual strength resulting from notch-insensitive behavior is straightforward once the size of the projectile damage has been determined.

The most severe strength reduction occurs when sharp-edged cracks exist in brittle materials. Failure in this case is characterized by unstable, rapid crack growth, and the residual strength may be much lower than net area strength. This is termed notch-sensitive behavior, and is associated with fatigue-crack damage in metals. Linear elastic fracture mechanics analysis is commonly used for assessing the notch-sensitive response of aircraft structure containing sharp-edged flaws.

The residual strength of ballistic-damaged tension members does not usually fit either of these categories, but is rather often located in-between, referred to as transition behavior. The transition behavior of ballistic-damaged members is due to the initial bluntness of the flaw created by ballistic penetration. Two distinct analysis approaches, each involving linear elastic fracture mechanics (LEFM), have been applied to predicting residual strength resulting from ballistic impact. The first approach is a direct application of conventional LEFM, endeavoring to characterize the geometric nature of the ballistic flaw so that failure can be predicted using K_c (critical stress intensity factor) determined from fracture toughness tests of specimens containing sharp-edged cracks. The second approach is a modified application of LEFM, making use of an empirically determined "effective" critical stress intensity factor, Λ_c, peculiar to ballistic flaws and found from tensile tests of panels containing ballistic damage.

There is an additional consideration which is unique to projectile damage tolerance assessment: the apparent strength of the structure is influenced by the dynamic loadings and rate effects induced by the impact. Because of this, structural elements may not be able to carry as great an applied load during impact as immediately after impact. "Impact fracture" is the term used to describe the fracture of a stressed panel at impact. This type of fracture occurs when local cracks initiated by the impact immediately propagate across the panel. The impact fracture failure mechanism is distinct from residual strength failure, in that residual strength failures occur when surviving (but damaged) panels are subjected to increased loadings. Figure 2-179 depicts this distinction. From the available data, a threshold level termed "impact fracture strength" can be defined, and this strength in some materials is significantly lower than the corresponding static residual strength.

ULTIMATE TENSILE STRENGTH (F_{tu})

σ_c
GROSS
FAILURE
STRESS

NOTCH INSENSITIVE MODE
$$\sigma_c = F_{tu}\left(\frac{b-TLD}{b}\right)$$

TRANSITION

NOTCH SENSITIVE MODE
$$\sigma_c \sim (TLD)^{-\frac{1}{2}}$$

TRANSVERSE LATERAL DAMAGE SIZE (TLD)

PANEL WIDTH
(b)

σ

b

TLD
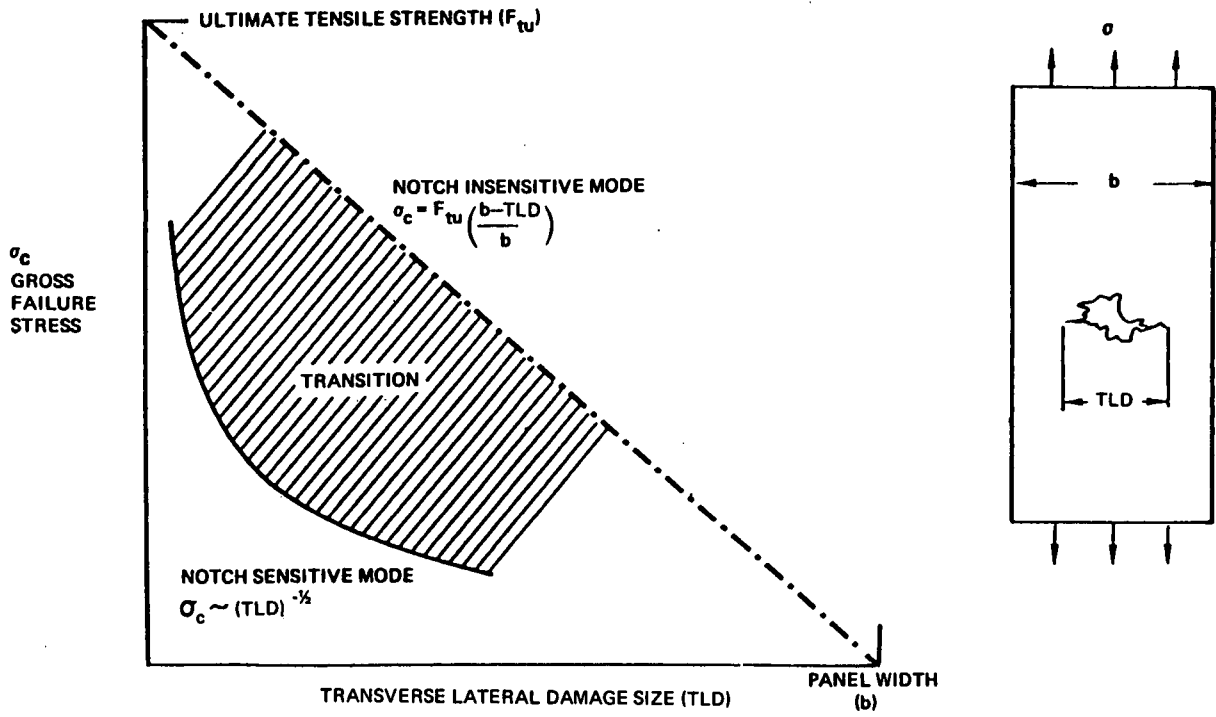
Figure 2-178. Variation in Fracture Response With Failure Mode

APPLIED LOAD
AT IMPACT

PANEL SURVIVES IMPACT

PANEL FAILS AT IMPACT

SAFE-LOAD

IMPACT
FAILURE

INCREASE APPLIED
LOAD UNTIL
DAMAGED
PANEL FAILS

RESIDUAL
STRENGTH

APPLIED GROSS STRESS

THRESHOLD FOR APPLIED
LOAD INFLUENCE

DAMAGE
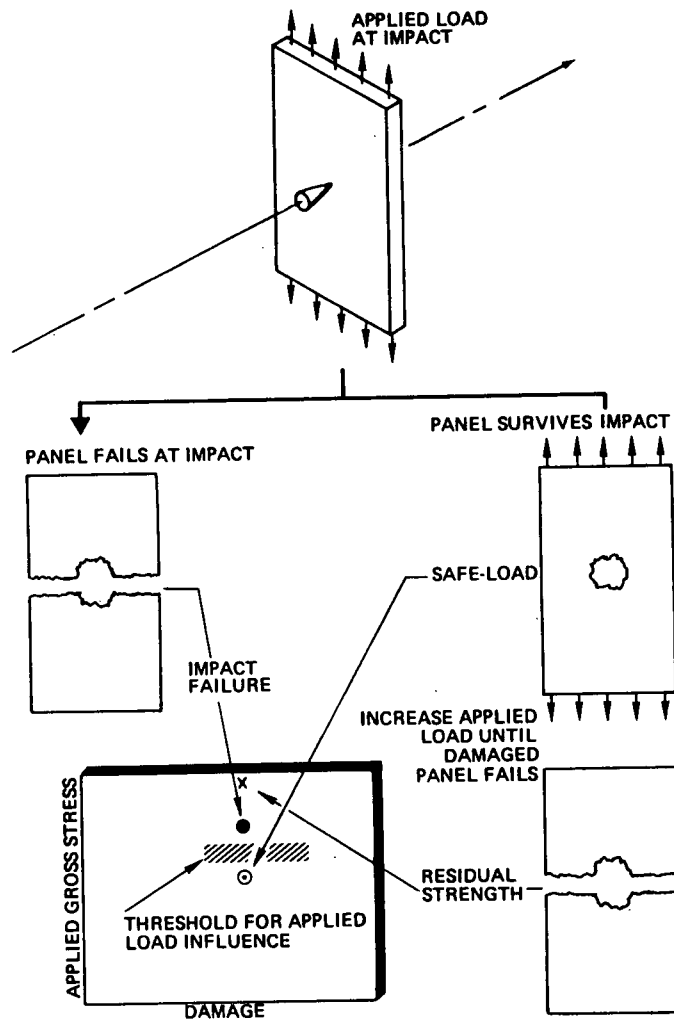
*Figure 2-179. Strength Degradation of Tensile
Panels Due to Ballistic Impact*

Since the effects of combined stress conditions are also significant in the assessment of strength degradation, particularly when blast or hydrodynamic ram pressures are imposed on damaged structure, the discussion that follows is organized into four categories:

2.5.1.1 Conventional Fracture Mechanics Applied to Ballistic Damage;

2.5.1.2 Modified Fracture Mechanics Applied to Ballistic Damage;

2.5.1.3 Dynamic Effects Associated With Strength Degradation

2.5.1.4 Combined Stress Effects

2.5.1.1 Conventional Fracture Mechanics Applied to Ballistic Damaged Panels

In the context of this discussion, conventional fracture mechanics means developing fracture criteria using a critical stress intensity factor for plane stress determined from fracture toughness tests of panels containing a sharp-edged central crack. Since projectile damage is generally not a sharp-edged crack, appropriate expressions for the stress intensity factor associated with the damage pattern must be established. In principal this is not a particularly difficult task, as demonstrated by the successful results of several investigations discussed below. Application, however, requires the capability to predict the damage patterns resulting from diverse impact conditions. This latter requirement is difficult to meet, leading to the modified fracture mechanics approach described in 2.5.1.2.

Equations for the stress field near a sharp-edged crack tip as given by linear elastic fracture mechanics (LEFM) theory are shown in Figure 2-180(a). Based on this theory, any cracked structure that satisfies the basic assumptions of isotropic, linear elasticity has the same stress distribution near the crack tip, and the amplitude of the stress is directly proportional to the stress intensity factor, K. Fracture criteria are based on the assumption that a material-dependent value of the stress intensity factor exists, termed K_C (the critical stress intensity factor), at which the cracked panel will fail. The critical stress intensity factor is determined by test, and treated as a material property subject to certain geometric limitations.

The stress intensity factor (K) depends on the applied stress condition and the geometry of the structural element. For the case of an infinite panel containing a sharp-edged crack, and subjected to gross tensile stress as indicated in Figure 2-180(b), the stress intensity factor is:

$$K = \sigma \sqrt{\pi a},$$

<div align="right">(Eqn. 2-120)</div>

where:

σ = gross tensile stress;

a = half crack length.

$$\sigma_x = \frac{K}{\sqrt{2\pi r}} \cos\frac{\theta}{2}\left[1 - \sin\frac{\theta}{2}\sin\frac{3\theta}{2}\right]$$

$$\sigma_y = \frac{K}{\sqrt{2\pi r}} \cos\frac{\theta}{2}\left[1 + \sin\frac{\theta}{2}\sin\frac{3\theta}{2}\right]$$

$$\tau_{xy} = \frac{K}{\sqrt{2\pi r}} \sin\frac{\theta}{2} \cos\frac{\theta}{2}\cos\frac{3\theta}{2}$$

where K is the stress intensity factor and r << a

(a) CRACK TIP STRESS FIELD GIVEN BY LINEAR ELASTIC ANALYSIS

(b) INFINITE PANEL CONTAINING A SHARP-EDGED THROUGH CRACK
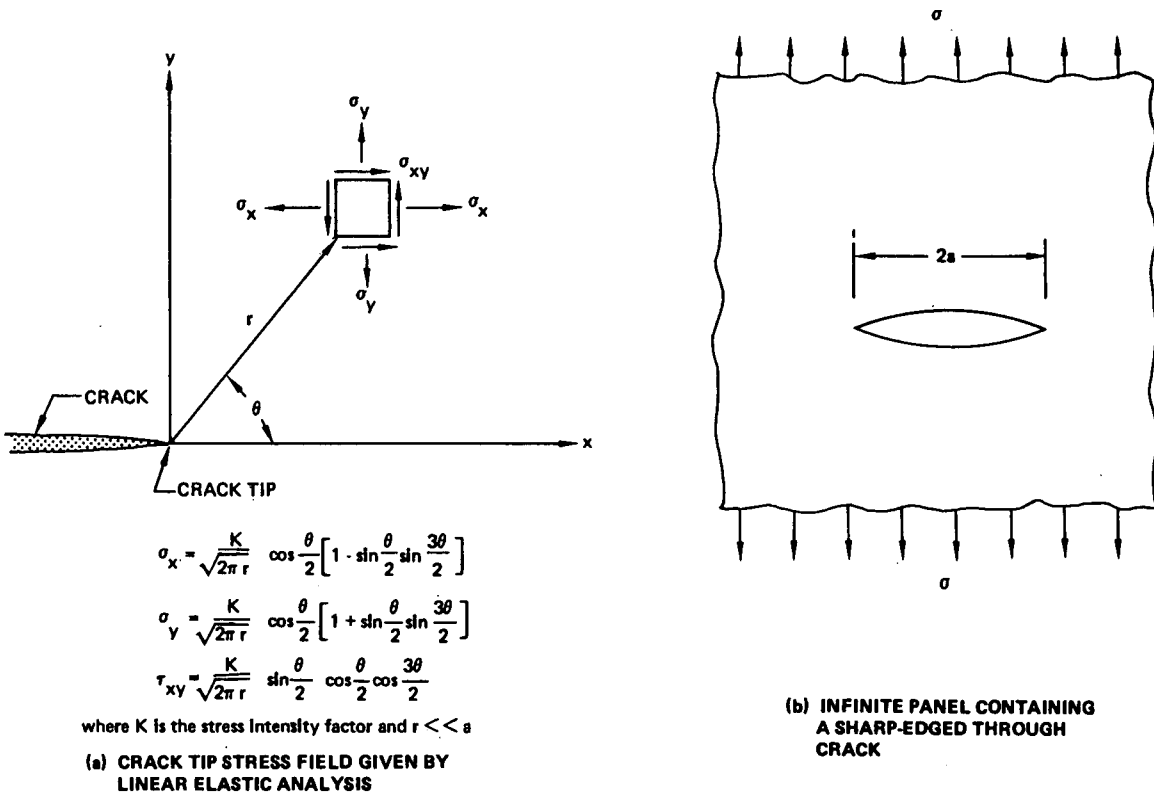
Figure 2-180. Stress Field and Geometry for Fracture Mechanics Application

In many important applications, however, the panel to be analyzed is not of infinite extent and the flaw is not a simple sharp-edged crack. For these applications, corrections are generally available and may be applied to the basic equation above, providing the more general relationship:

$$K = \sigma \sqrt{\pi a} \; \alpha \left(\frac{a}{w}\right) F$$

(Eqn. 2-121)

where

$\alpha\left(\frac{a}{w}\right)$ = a function providing correction for finite geometry

F = a function providing correction for the deviation of the flaw shape from a simple sharp-edged crack.

The crack length, 2a, must often be corrected for slow crack-growth that may occur prior to final fracture, and the development of a plastic zone at the tips. This underscores the fact that measurable physical damage cannot always be used directly in damage tolerance analysis, and this is particularly true with regard to ballistic damage. In fact, translating the ballistic damage into an effective crack length is the fundamental problem of residual strength prediction.

Relationships for calculating the stress intensity factor for various geometric configurations are available in the fracture mechanics literature, References 2-56, 2-57, and 2-64, for example. Values of the critical stress intensity factors are available for most aircraft materials. However, there are several important factors that must be considered when applying fracture mechanics analysis to projectile impact damage. References 2-2, 2-4, 2-8, 2-16, 2-65 and others discuss various aspects of the application. The most significant of these factors are the effect of damage geometry since ballistic damage seldom corresponds exactly to a sharp-edged crack, and the effect of damage spacing which may become significant in the case of multiple impacts from HE projectiles or missile warheads. Additional factors include the effects of plasticity, panel thickness, temperature, and the influence of a reactive environment. The latter factors are of significance regardless of the source of the damage, and are discussed herein primarily for completeness.

2.5.1.1.1 Effect of Damage Geometry

Ballistic impact damage ranges from cracks to smooth holes depending on the material and geometry of the impacted structure and the projectile impact conditions, as described in Section 2.2. Because of this, characterizing the flaw shape is an important step when applying conventional fracture mechanics analysis to impact damage. Relevant characterization is reported in Reference 2-65 describing an investigation to establish effective flaw sizes for aluminum and titanium panels impacted by small-arms projectiles. Residual strength tests were conducted of damaged panels and the results were analyzed using linear elastic fracture mechanics. Following, in part, the terminology from Reference 2-65, the following measures of ballistic damage will be useful:

H_o = maximum transverse extent of through-hole;

S_o = maximum transverse extent of spall;

L_o = maximum transverse extent of cracking;

TLD = maximum extent of structurally significant transverse damage without regard to type (but limited to the three types above).

The term "transverse," as used above, means normal to the applied tensile load.

Figure 2-181 summarizes the results of work reported in the reference. The fracture mechanics equations shown in the figure incorporate specific finite width and plasticity zone corrections. The user may, of course, elect to reformulate the equations using alternate forms of the corrections. Four types of ballistic damage in metals were considered:

1. **Crack-like damage in thin aluminum alloy sheets.** This type of damage was induced by high-obliquity impacts, with the obliquity plane in the longitudinal direction of the sheet. In this case, the damage looks and behaves like a crack. The half-crack length is taken as one-half the total transverse damage, augmented by plasticity zone corrections. Good correlation between analytic predictions and test results were obtained for 0.25-inch 2024-T851, 7178-T651, 7075-T7351, and 7075-T651 aluminum alloys.

2. **Smooth, round holes in thin aluminum sheet.** This type of damage has little back or front surface spallation, and no visible cracks on either face. High velocity armor-piercing bullets at nearly zero obliquity may produce damage of this form. It was found that the residual strength of 0.25-inch 2024-T851 containing smooth, round holes from .50 caliber AP impacts, could be predicted by net area, similar to the behavior of drilled holes in a ductile alloy.

3. **Ragged hole with cracks in thin sheet.** This type of ballistic damage is frequently generated in thin sheets, and consists of through-cracks extending in several directions from an irregularly shaped hole. The cracks change direction as they radiate from the hole. The term "petalling" is sometimes used to describe this damage pattern. Good correlation was obtained with test results for 0.114-inch 6Al-4V titanium by applying a correction fator dependant upon the minimum tip angle at the farthest damage extent, as indicated in Figure 2-181.

4. **Through-hole with surrounding spall in thick plate.** Damage of this type occurs when thick aluminum plates (3/8-inch and thicker, for example) are penetrated by armor-piercing projectiles or fragments. The back surface spall surrounding the hole may be extensive, and may or may not contain visible cracks. Good correlation for 0.50-inch and 0.75-inch 7075-T651 plate (impacted by .50 caliber AP bullets) was obtained using Bowie's (Ref. 2-67) analysis for a circular hole with edge cracks. The length of the edge cracks is not known, a priori, and must be determined in a way that provides test correlation.

Crack-Like Damage in Thin Aluminum Sheets

Critical Stress:

$$\sigma_c = K_c \left[W \tan \left(\frac{\pi a}{W} \right) \right]^{-\frac{1}{2}}$$

Equivalent Crack Half-Length:

$$a = \frac{TLD}{2} + \frac{\sigma_c^2}{2\pi \sigma_y^2} \tan \frac{\pi TLD}{2W}$$
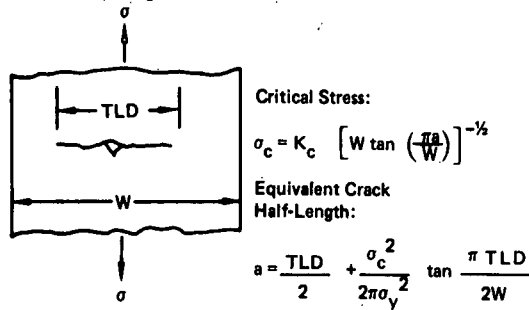
Smooth, Round-Hole Damage in Thin Aluminum Sheets
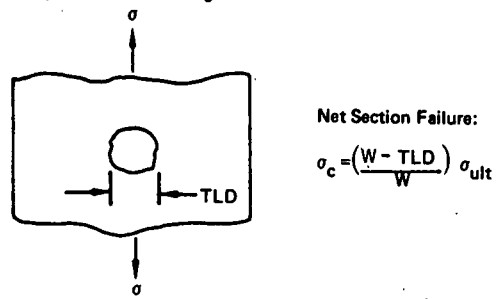
Net Section Failure:

$$\sigma_c = \left(\frac{W - TLD}{W} \right) \sigma_{ult}$$

Ragged Hole With Cracks in Thin Sheet

Critical Stress:

$$\sigma_c = \frac{K_c}{\left(1 - \frac{\psi m}{2\pi}\right)} \left[W \tan \left(\frac{\pi a}{W} \right) \right]^{-\frac{1}{2}}$$

Equivalent Crack Half-Length:

$$a = \frac{TLD}{2} + \frac{\sigma_c^2}{2\pi \sigma_y^2} \tan \left(\frac{\pi TLD}{2W} \right)$$

Through Hole With Surrounding Spall in Thick Plate

Critical Stress:

$$\sigma_c = \frac{K_c}{F} \left[\left(W - H_o \right) \tan \left(\frac{\pi a}{W - H_o} \right) \right]^{-\frac{1}{2}}$$

See Table 2-27 for F

Equivalent Crack Half-Length:

$$a = 0.15 \left(\frac{TLD}{2} - \frac{H_o}{2} \right)$$

(For ¾-in Plate)

$$= 0.30 \left(\frac{TLD}{2} - \frac{H_o}{2} \right)$$
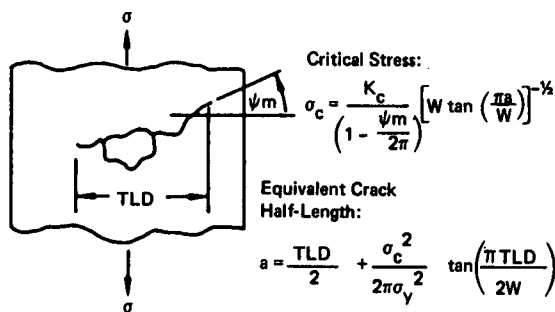
(For ½-in Plate)
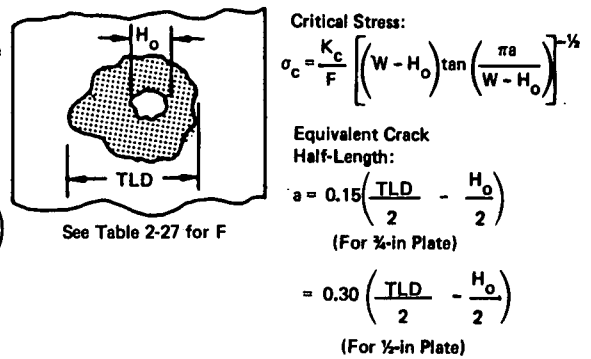
Figure 2-181. Residual Tensile Strength Predictions for Several Types of Projectile Damage (REF(2-65))

Table 2-27. Factor for Through-Hole With Surrounding Spall (Using Bowie's Analysis, Ref. 2-67)

$\frac{2a}{H_o}$	F
0.00	3.39
0.10	2.73
0.20	2.41
0.30	2.15
0.40	1.96
0.50	1.83
0.60	1.71
0.80	1.58
1.00	1.45
1.50	1.29
2.00	1.21
3.00	1.14
5.00	1.07
10.00	1.03
∞	1.00

Elliptical and Rectangular Damage Shapes (Extracted From Ref. 2-14)

Many ballistic impact damages, particularly those resulting from HE projectile fragments, appear to be elliptical or rectangular, with cracks emanating from the elliptical or rectangular hole. Reference 2-68 reports some analytical characterization of the stress intensity factors for these types of flaws, and these results are presented in the following paragraphs.

The stress intensity factor for an elliptic hole with edge cracks may be presented in the form

$$K = \sigma \sqrt{\frac{\pi D}{2}} \, F_e$$

(Eqn 2-122)

Values of F_e for the configuration and notation of Figure 2-182 is presented in Figure 2-183 and Table 2-28. The stress intensity factor for a rectangular hole with edge cracks may be presented in the form:

$$K = \sigma \sqrt{\frac{\pi D}{2}} \, F_r \quad ;$$

(Eqn. 2-123)

with F_r for the rectangular flaw in Figure 2-182 corresponding to F_e for the elliptic flaw in Equation (1). Values of F_r are shown in Figure 2-184.

A nondimensional crack length can be defined such that:

$$\lambda = \frac{D}{2c} \quad ;$$

(Eqn. 2-124)

and the parameter s can be introduced (Ref. 2-69):

$$s = \frac{(D/2)-c}{D/2} \cdot$$

(Eqn. 2-125)

Upon subsituting Equation (Eqn. 2-124) into Equation (Eqn. 2-125), one obtains:

$$s = \frac{\lambda - 1}{\lambda}$$

(Eqn. 2-126)

The parameters F_e and F_r as a function of s and λ are given in Table 2-29. Table 2-29 was developed with the use of curves in Reference 2-69.

For values of s greater than 0.4 (see Table 2-29), the flaw shape and dimensions have little effect on F_e and F_r which are approximately unity. Furthermore, for this condition, the stress intensity factor, in effect, depends only on the crack length plus hole length (i.e., the total damage) and not the ratio of crack length to hole length. As s decreases below 0.4, for all practical purposes the crack-flaw interaction parameters in Table 2-29 decrease monotonically with decreasing s. In situations with D/2 → c (i.e., λ → 1), the crack lengths are quite small relative to the flaw length and F_e and F_r approach zero. Thus, the effect of the crack diminishes as s approaches zero in the sense that the computed stress intensity factor becomes quite small.
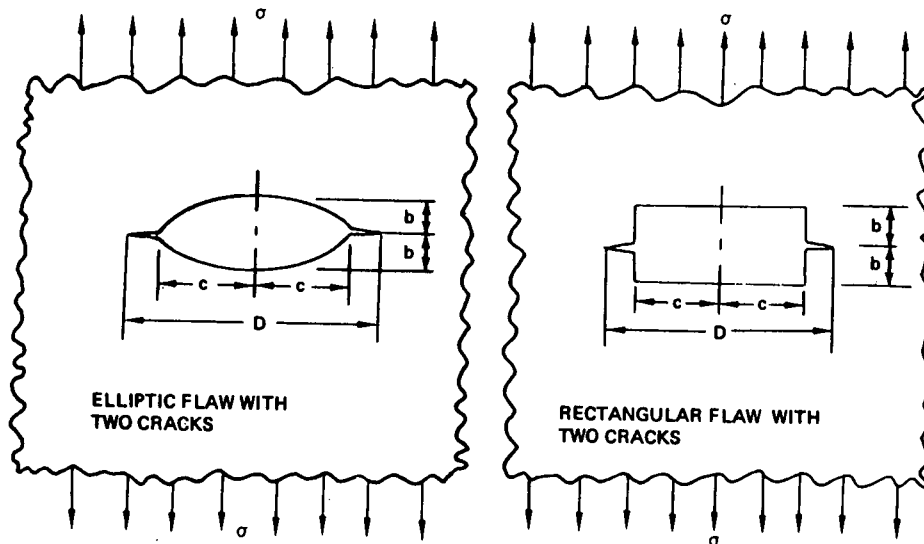
Figure 2-182. Goemetric Definition of Elliptical and Rectangle Holes with Two Edge Cracks
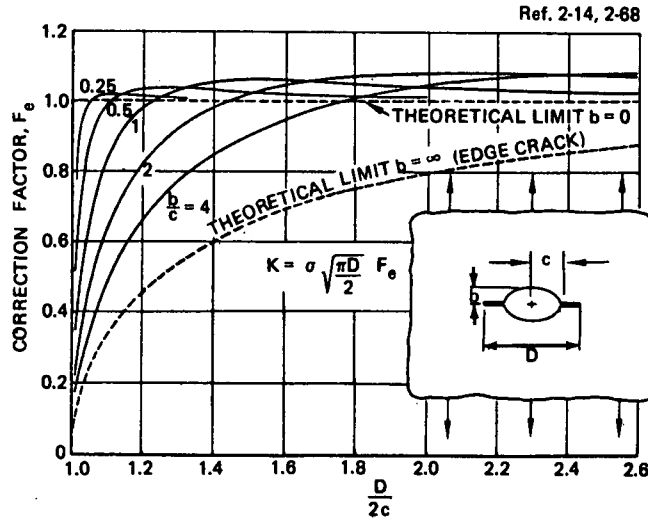
Figure 2-183. Stress Intensity Correction Factors for Cracks Emanating from an Elliptical Hole in an Infinite Plate Subjected to Uniaxial Stress

Table 2-28. Correction Factors for an Elliptical Hole with Edge Cracks (Infinite Plate Subjected to Uniaxial Stress)
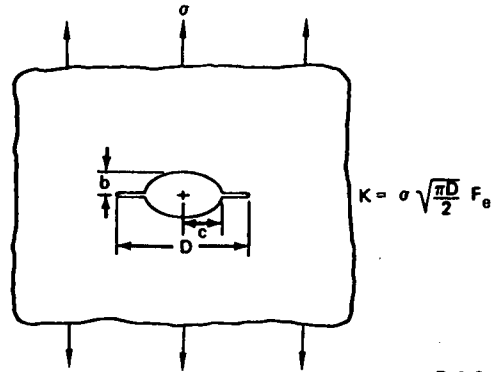
Ref. 2-14, 2-68

$\frac{D}{2c}$	$F_e\left(\frac{b}{c}=0.25\right)$	$F_e\left(\frac{b}{c}=0.5\right)$	$F_e\left(\frac{b}{c}=1\right)$	$F_e\left(\frac{b}{c}=2\right)$	$F_e\left(\frac{b}{c}=4\right)$
1.02	0.9050	0.6757	0.4514	0.3068	0.2114
1.03	0.9597	0.7742	—	—	—
1.04	0.9865	0.8398	0.6082	0.4297	—
1.05	0.0013	0.8861	—	—	0.3137
1.06	1.0098	0.9206	0.7104	0.5164	—
1.08	1.0179	0.9664	0.7843	0.5843	0.4463
1.10	1.0206	0.9925	0.8400	0.6401	0.5027
1.15	1.0202	1.0258	0.9322	0.7475	0.5901
1.20	1.0176	1.0357	0.9851	0.8241	—
1.25	—	—	—	—	0.7248
1.30	—	1.0366	1.0358	0.9255	—
1.40	—	1.0317	1.0536	0.9866	0.8494
1.50	—	—	1.0582	1.0246	—
1.55	—	—	—	—	0.9279
1.60	—	—	1.0571	1.0483	—
1.80	—	—	1.0495	1.0714	1.0063
2.00	—	—	1.0409	1.0777	—
2.10	—	—	—	—	1.0551
2.20	—	—	1.0336	1.0766	—
2.40	—	—	1.0251	1.0722	1.0788

Refs. 2-14

CORRECTION FACTOR, F_r

$\frac{b}{c} = 0.125$

$\frac{b}{c} = 0.25$

$\frac{b}{c} = 0.5$

$\frac{b}{c} = 1$

$\frac{b}{c} = 2$

$K = \sigma \sqrt{\frac{\pi D}{2}} \, F_r$

D/2c
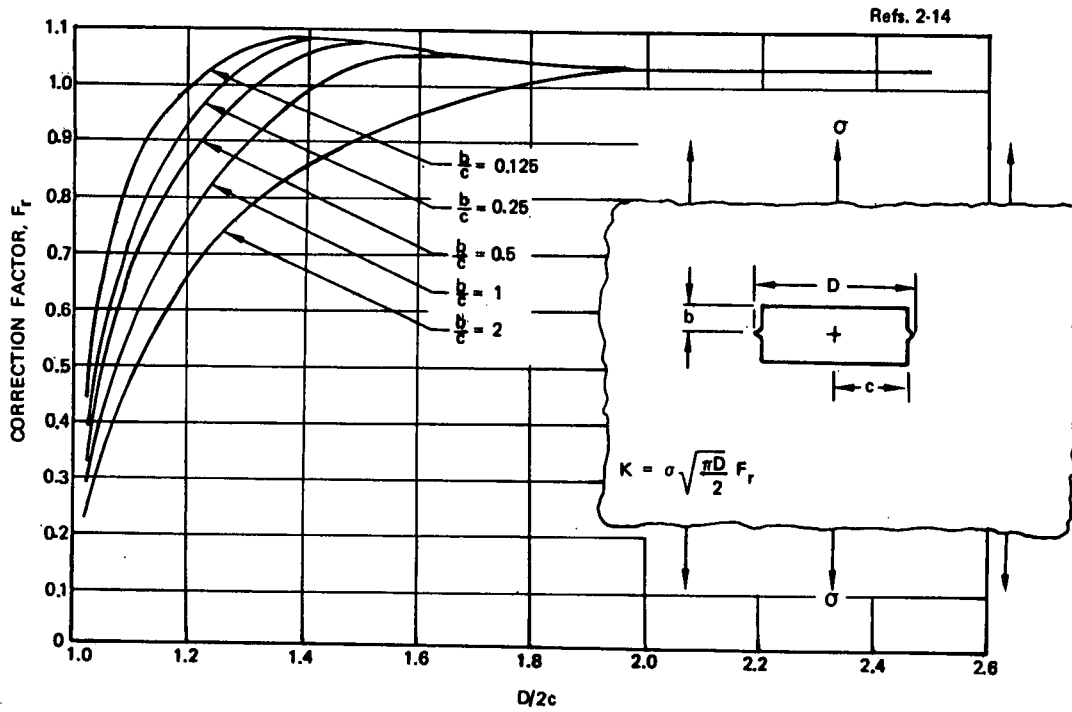
Figure 2-184. Correction Factors for a Rectanglar Hole with Edge Cracks (Infinite Plate Subjected to Uniaxial Stress)

Table 2-29. Crack-Flaw Interaction Parameters For Elliptic And Rectangular Flaws

s	λ	b/c 4.0 F_e	F_r	2.0 F_e	F_r	1.0 F_e	F_r	0.5 F_e	F_r	0.25 F_e	F_r	0.125 F_e	F_r
1.0		1.00	N.A.[1]	1.00	1.00	1.00	1.00	1.00	1.00	1.00	1.00	N.A.[1]	1.00
0.6	2.5	1.09	N.A.	1.09	1.01	1.05	1.01	0.93	1.01	0.93	1.01	N.A.	1.01
0.5	2.0	1.06	N.A.	1.10	1.01	1.06	1.01	0.99	1.01	0.99	1.01	N.A.	1.01
0.4	1.60	0.99	N.A.	1.01	0.95	1.05	1.02	1.00	1.03	1.00	1.03	N.A.	1.03
0.3	1.43	0.87	N.A.	0.98	0.86	1.04	0.99	1.00	1.04	1.00	1.05	N.A.	1.06
0.2	1.25	0.72	N.A.	0.87	0.71	1.02	0.82	1.00	0.92	1.00	0.98	N.A.	1.01
0.1	1.11	0.52	N.A.	0.65	0.49	0.86	0.60	1.00	0.70	1.02	0.76	N.A.	0.87
0.08	1.09	0.46	N.A.	0.59	0.44	0.80	0.54	0.95	0.62	1.02	0.69	N.A.	0.80
0.06	1.063	0.40	N.A.	0.52	0.38	0.72	0.47	0.91	0.54	0.98	0.61	N.A.	0.71
0.04	1.042	0.33	N.A.	0.44	0.31	0.61	0.38	0.84	0.44	0.93	0.51	N.A.	0.60
0.02	1.02	0.23	N.A.	0.31	0.22	0.45	0.27	0.66	0.31	0.87	0.37	N.A.	0.42

(1) N.A. means not available

Ref. 2-14, 2-69

2.5.1.1.2 Effect Of Damage Spacing - Multiple Impact Damage

This section addresses the residual strength of structure containing closely spaced multiple impact damages. The discussion is applicable to damage from HE projectile fragments or from warhead fragments impacting in close proximity. Because of this proximity, the damages may interact with each other, either by direct physical intersection or by the superposition of the local stress fields about adjacent damages. When this occurs, the damages can no longer be treated as isolated flaws as described in the previous section.

The method described here for assessing the residual strength of multiple impact damaged structure was developed in association with the BR-2 computer code (Reference 2-14). It employs a linear elastic fracture mechanics methodology applicable to isotropic metallic structure, but could possibly be applicable to fiber composites with quasi-isotropic symmetric lay-ups. There is very little substantiating test data available for either metals or composites.

Figure 2-185 illustrates the multiple damage phenomena and the concept of an effective damage size. The figure shows fragment impacts generated by detonation of an HE projectile, but the concept is applicable to any threat. In (a), because of the very high areal density of the impacting fragments, individual fragment damages do not occur.

The effective damage controlling structural degradation is essentially a single sharp-edged hole. In (b), individual damages are apparent and, significantly, they are spaced quite closely so that their separate stress concentration fields can superimpose. The effective damage size in this case depends on the size and spacing of the damages. In (c), at a still greater stand-off distance, individual damages are still evident, but they are widely separated. Interaction between damages will be negligable, and the effective damage size will be largely determined by the largest single damage size, as with the case of single penetrations.

In order to quantitatively establish the effective damage size resulting from a fragment pattern, the effect of superimposing the local stress fields associated with adjacent damages must be determined, as indicated in Figure 2-186 for the case of two collinear damages. In this case, the local stress fields are additive, causing a higher stress at the interior edges of each damage. The initial failure mode anticipated would be a transverse fracture initiating at these inner edges, causing the two cracks to merge. Subsequent panel failure would depend on the capability of the panel to contain the merged crack at the stress levels induced by the flight envelope.

The significance of stress field superposition depends on the size of the individual damages and their spacing and arrangement relative to each other. The result of superposition is not always an increase in local stress; in some cases a reduction may result from the shielding of a damage by surrounding damages.
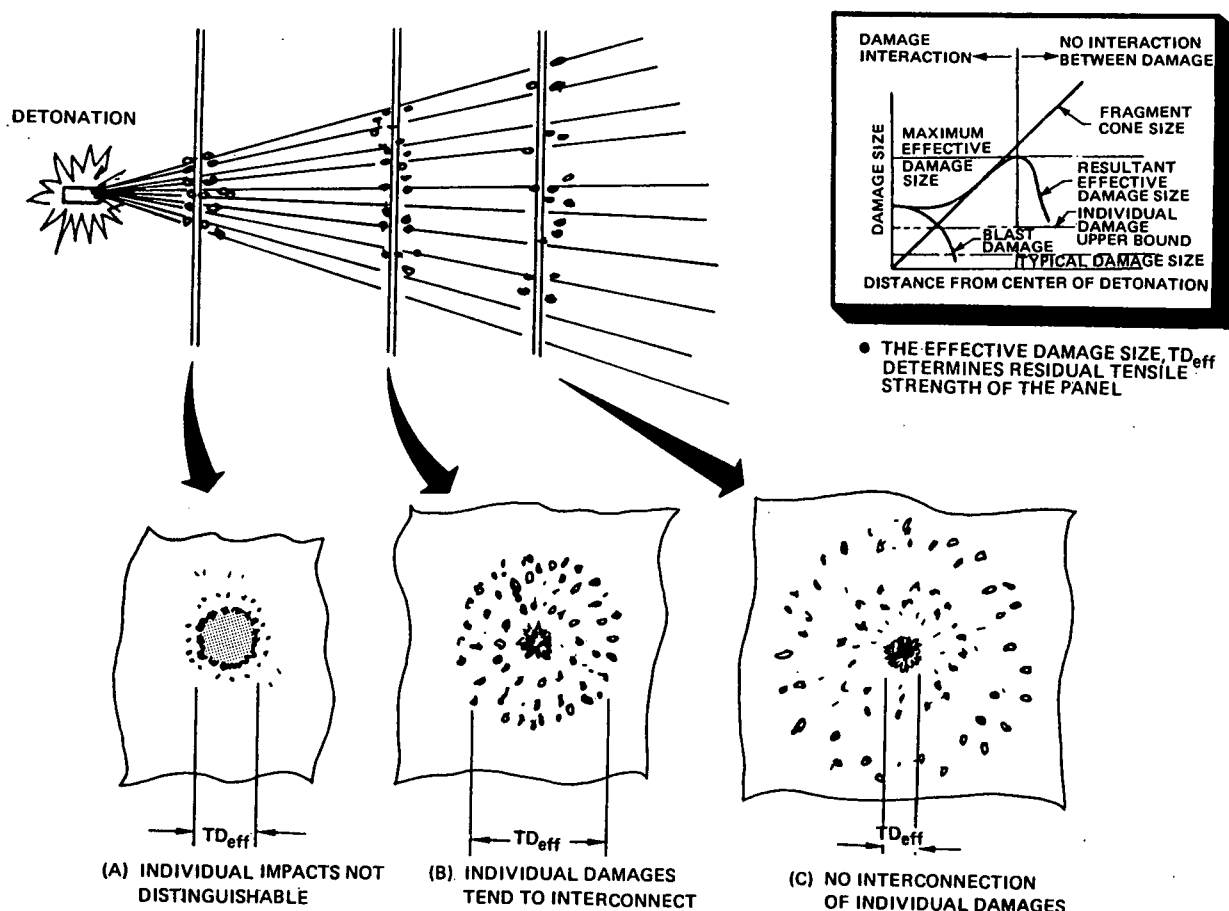
Figure 2-185.   Variation of Fragment Impact Density With Standoff Distance
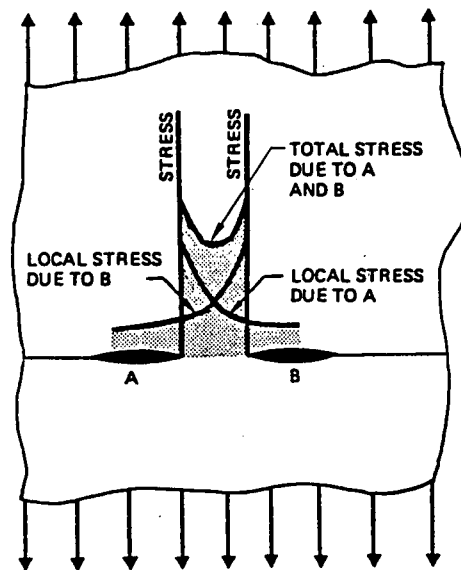
Figure 2-186. Closely Spaced Damages Showing Resultant
Superposition of Local Stress Fields

Reference 2-14 presents analytical predictions of damage interaction effects for isotropic, homogenous materials (e.g., metals), based on linear elastic fracture mechanics analysis described in Refs. 2-111, 2-112. This is, of course, the same approach described in the previous section for application to single damages. For the case of multiple damages it is convenient to define the ratio:

$$\eta = \frac{K}{K_o}$$

<div align="right">(Eqn. 2-127)</div>

where

K = The stress intensity factor at the tips of cracks comprising the multiple damage pattern;

K_o = the corresponding stress intensity factor for a single crack;

= $\sigma_c \sqrt{\frac{\pi}{2} D}$., for the case of uniform tension loading.

Values of η for various damage patterns are available in Reference 2-14, and several of these damage patterns plus others are presented on the following pages (Figures 2-187 to 2-196). Application of these results in predicting residual strength following multiple impacts entails the following steps:

1. Define the impact locations and impact conditions of the multiple penetrators, based on threat characteristics and engagement conditions.

2. Determine the probable effective sizes of the individual damages using suitable damage size models.

3. Examine the damage pattern, and estimate local failure regions leading to damage merging, based on the information presented in Figures 2-187 to 2-196 and suitable values of the critical stress intensity factor for the materials considered.

4. Assess overall panel failure, based on the most probable overall failure mode.

The analysis described above is not a simple one if a complex damage pattern in involved. Results are very configuration dependant, and computer-aided analysis supported by testing may well be required to generate design information of broad application. The following detailed discussion of Figures 2-187 through 2-196, extracted from Ref. 2-14, is provided to develop a qualitative understanding of the interactions of crack-induced stress fields.

It is convenient to refer to a normalized opening mode stress-intensity factor

$$K_o = \frac{K}{\sigma_c \sqrt{\frac{\pi}{2} D}}$$

<div align="right">(Eqn. 2-128)</div>

with D being the crack length. In the case of a single through-crack (or if the crack interaction effect is negligible), K_o equals unity. In the case of multiple cracks, K_o is a measure of the effect of the crack interactions on stress-intensity factor, and K_o may be greater than, less than, or equal to unity.

With regard to a pair of collinear, equal length cracks in a tensile stress field normal to the cracks (Figure 2-187), the effect of the interaction is to raise K_o above unity at all the crack tips. Furthermore, when each of a pair of equal cracks is parallel to the other, and the applied tensile stress is perpendicular to the cracks (Figure 2-188), the effect of the interaction is to decrease K_o below unity. The decrease of K_o below unity is a result of one crack successfully shielding the other crack from the applied tensile stress field.

Figure 2-188. *Stress Intensity Factor for Two Equal Parallel Cracks*

Figure 2-190. *Stress Intensity Factor at Inner and Outer Edges of Equal Collinear and Parallel Cracks*

Figure 2-187. *Stress Intensity Factor at Inner and Outer Edges of Two Equal Collinear Cracks*
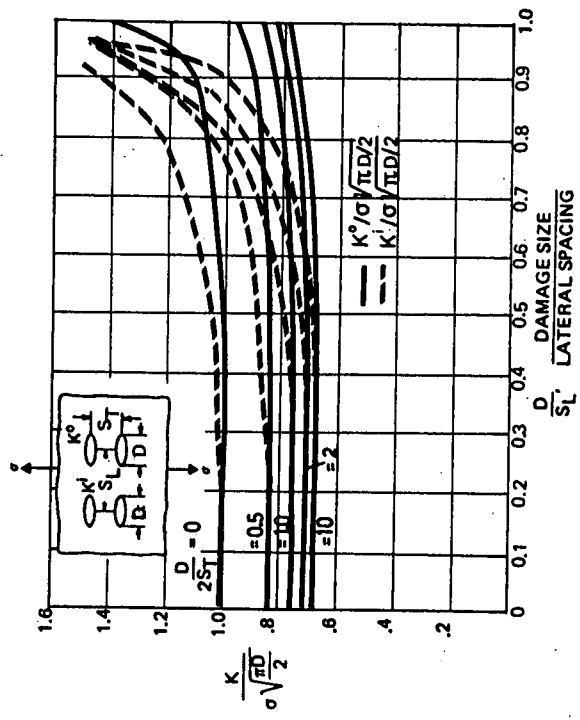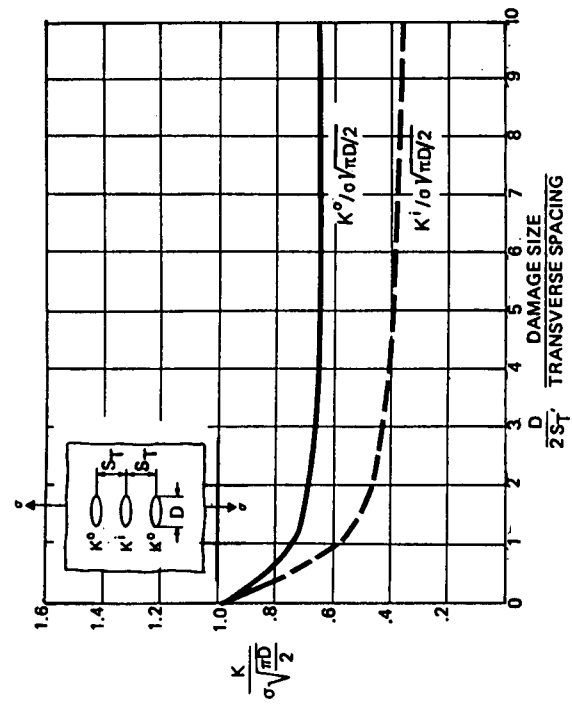
Figure 2-189. *Stress Intensity Factor at Inner and Outer Edges of Three Equal Parallel Cracks*

172

Figure 2-192. Stress Intensity Factor of the Crack Beneath the Collinear Cracks (All Cracks Equal Length)

Figure 2-194. Stress Intensity Factor at the Edges of the Central Crack (All Cracks Equal Length)

Figure 2-191. Stress Intensity Factor at the Inner and Outer Edges of the Collinear Cracks (All Cracks Equal Length)

Figure 2-193. Stress Intensity Factor at the Inner and Outer Edge of the Four Peripheral Cracks (All Cracks Equal Length)

$\dfrac{D}{2S_T} =$

2.0
0.5
1.0

0.5

1.0

2.0

$\dfrac{K}{\sigma\sqrt{\frac{\pi D}{2}}}$

$K^o/\sigma\sqrt{\frac{\pi D}{2}}$

$K^i/\sigma\sqrt{\frac{\pi D}{2}}$

$\dfrac{D}{S_L},\quad \dfrac{\text{DAMAGE SIZE}}{\text{LATERAL SPACING}}$
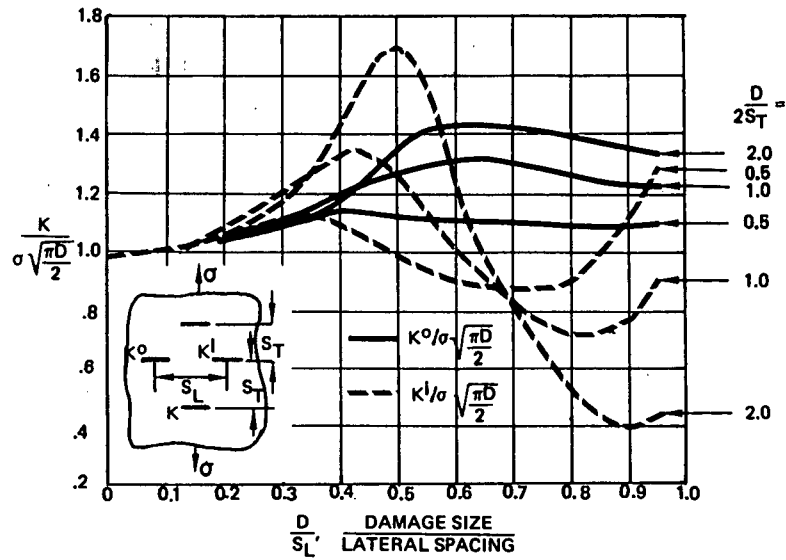
Figure 2-195. Stress Intensity Factor at the Inner and Outer Edge of the Collinear Cracks (All Cracks Equal Length)

$\dfrac{D}{2S_T} =$

0.5

1.0

2.0

$\dfrac{K}{\sigma\sqrt{\frac{\pi D}{2}}}$

$\dfrac{D}{S_L},\quad \dfrac{\text{DAMAGE SIZE}}{\text{LATERAL SPACING}}$
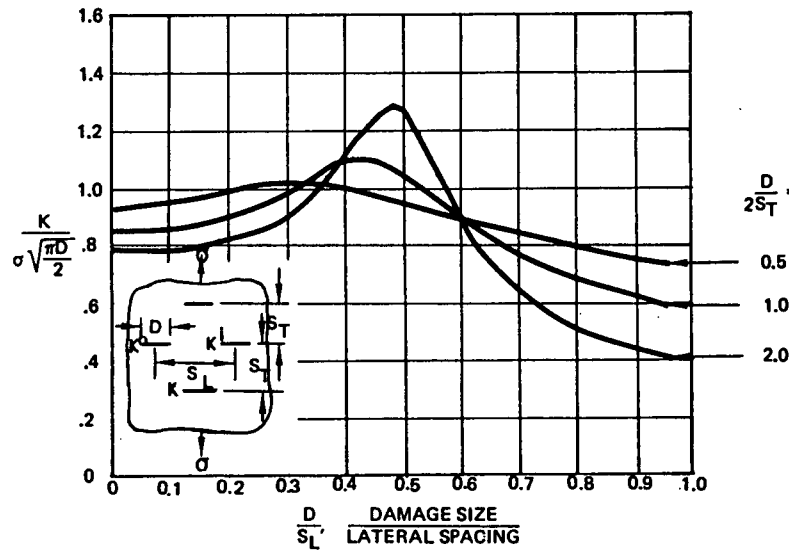
Figure 2-196. Stress Intensity Factor for the Upper and Lower Cracks

In contrast to the two equal parallel cracks in Figure 187 is the case with three equal parallel cracks in Figure 189. As a result of the interaction of the central crack with the other two cracks, the stress intensity factor at the outer cracks is somewhat reduced from the values in Figure 187. Furthermore, the outer cracks shield the inner crack, which has a stress intensity factor (Figure 189) substantially below that of an outer crack.

The single crack, the pair of collinear cracks, and the pair of parallel cracks may be taken as the starting point of an investigation of the effect of the interaction of multiple cracks having more complex geometrical patterns. When a pair of collinear cracks is superimposed on a pair of parallel cracks (Figure 2-190), the net effect of the interaction depends on the length of the crack as well as the spacings between the cracks. For the geometry in Figure 2-190, K_o will be less than unity if the parallel cracks have a greater effect on the interaction than the collinear cracks have. Shielding is effective (i.e., $K_o > 1$) if the parallel spacing parameter $D/2S_T$ is greater than 0.5, even in cases for which the collinear spacing parameter D/S_L is as large as 3/4 (where D is the crack length transverse to the stress field).

The line of centers of parallel cracks of equal length does not have to be parallel to the applied stress in order to produce effective shielding (i.e., $K_o > 1$). The normalized stress intensity factors at the inner and outer edges of a pair of collinear cracks that interact with each other and a crack that is parallel to each of them are shown in Figure 2-191. For some combinations of D/S_L and $D/2S_T$ the shielding by the lower crack results in K_o less than unity. However, for other combinations of D/S_L and $D/2S_T$ the shielding is not effective (i.e., $K_o < 1$).

The effect of the shielding by the collinear cracks on the single crack beneath them is shown in Figure 2-192. As a result of the interaction, K_o at the crack edges of the lower crack may be greater than, equal to, or less than unity.

The pattern of the five cracks in Figures 2-193 and 2-194 differs from the pattern of three cracks only because of the additional pair of collinear cracks. It appears that the added shielding resulting from the additional pair of collinear cracks lowers the stress intensity factor at the outer cracks for all combinations of D/S_L and $D/2S_T$. However, the regular pattern of the additional shielding raises the stress intensity factor at the edges of the central crack of the five cracks for many combinations of D/S_L and $D/2S_T$.

In contrast to the three-crack pattern is the four-crack pattern of Figures 2-195 and 2-196. The additional crack is parallel to the other cracks and results in a diamond pattern. The introduction of the fourth crack increases the stress intensity factor at the edges of the collinear cracks for many combinations of D/S_L and $D/2S_T$. However, the introduction of the fourth crack tends to reduce the stress intensity factor at the edges of the other non-collinear crack.

The multiple crack patterns in Figures 2-187 through 2-196 are much too regular to simulate the flaws that can be induced by the detonation of a high explosive projectile in a structural compartment. However, some of the analytic results that are exhibited may be generalized for application when there are many penetrations of the structure. For example, when there is a high density of damages in a plate, it may be hypothesized that the outer cracks successfully shield the cracks in the interior (i.e., K_0 will be less than unity for the cracks throughout the interior of the damaged zone).

When fragment penetrations occur following an internal blast of a high explosive projectile, there is uncertainty as to the exact location of the largest fragment penetrations, especially from the side spray. However, it is clear that if the shielding of the interior flaws is effective, the most severe strength degradation will occur if the largest cracks occur on the periphery of the penetration zone and are oriented in such a way as to promote the onset of fracture. Therefore, in analyses for predicting the onset of fracture when there is a densely penetrated zone, one may assume that the most damaging flaws and cracks are located on the periphery of the predicted penetration zone with the cracks oriented in such directions that will induce an early fracture.

Because of the projectile velocity and/or the target plate properties such as thickness, there may be situations when there is a sparsely penetrated zone rather than a densely penetrated zone. When there is sparse penetration, Figures 2-187 through 2-196 may be used without extrapolations for predicting the interaction effect on the stress intensity factors.

2.5.1.1.3 Additional Factors Influencing Tensile Fracture

Although damage geometry and spacing are the most unique factors, there are other important factors which must be considered in any application of fracture mechanics. For example, testing has shown that material chemistry variations within the allowable composition limits produce significant variations in fracture thoughness. In addition, fracture toughness values vary with the grain (rolling) direction. The degree and direction of variation is dependent on the material and heat treatment considered. The differences resulting from grain directions can be as large as two to one for many structural materials, with the short transverse direction (i.e., through the thickness) generally experiencing the low values. When evaluating structural performance, care should be exercised to obtain data for the same crack and load orientations. Additional factors influencing fracture toughness, including plasticity, thickness, temperature, and reactive environment, are summarized below.

Effects of Plasticity

The assumptions of linear elastic behavior are not strictly true in many cases due to the plasticity near the crack tip. For the critical case of brittle behavior, the plastic zone is small and the inaccuracies of the analysis due to plasticity are assumed to remain constant for a given material and thickness, thereby allowing the use of the analysis method in these terms. In cases where the plastic zone at the crack tip is a significant fraction of the crack length, however, the plasticity will alter the crack-length/stress relationships presented. This situation may exist for small cracks or for materials that exhibit large plasticity. In these cases additional empirical data is required for predicting failure stress levels.

Effect of Panel Thickness

Panel thickness has a significant influence on fracture behavior. In thin-gage panels the crack tip is in plane stress, while plane-strain conditions exist in thicker panels due to the increased constraint. The thin panels fracture by shear, resulting in an inclined fracture face. Thick panels fail by plane-strain cleavage (opening mode), resulting in a flat fracture surface. The opening mode (cleavage) critical stress intensity factor is termed K_{IC} or "the plane-strain fracture toughness". Due to the increased plasticity (less constraint), the plane stress fracture toughness, K_C, result in higher toughness for thin-gage materials. With intermediate panel thicknesses there is a transition where the fracture surface will be partially flat. This effect of thickness is illustrated in Figure 2-197. Figure 2-198 presents fracture toughness values from References 2-71, -72, -73 for several structural materials as a function of thickness.
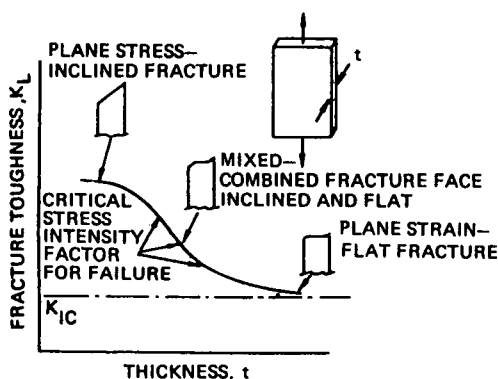
Figure 2-197. Typical Fracture Toughness Variation with Thickness
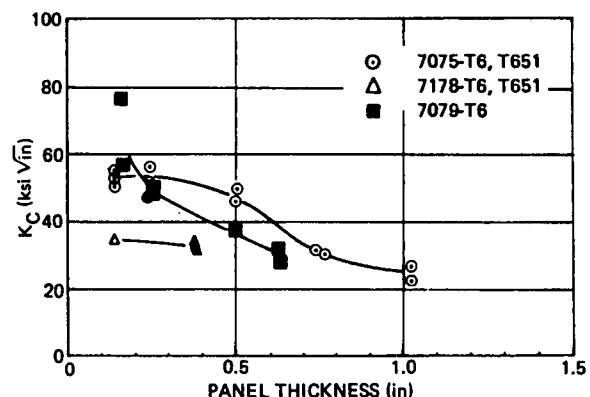
Figure 2-198. Variation of Fracture Toughness With Thickness

Effect of Temperature

The influence of temperature has a notorious history in the performance of cracked structures. A classic example of this is the temperature-augmented fracture of the Liberty Ship hulls of World War II. Aircraft structure in service operates in a wide range of environments. These environments must be considered in the residual strength analysis to ensure realistic performance estimates.

Generally, fracture toughness will decrease with decreasing temperature. An example of extreme temperature-sensitive fracture response produced by unusual processing is shown in Figure 2-199. Available data (References 2-71 through 2-78) for fracture toughness (K_C) as a function of temperature for several structural materials are presented in Figures 2-200 and 2-201. The data shown are not allowables, but they do define trends for the materials considered. This information can be used in residual strength predictions for damaged structure. It is anticipated that impact-fracture behavior will follow the same trend.
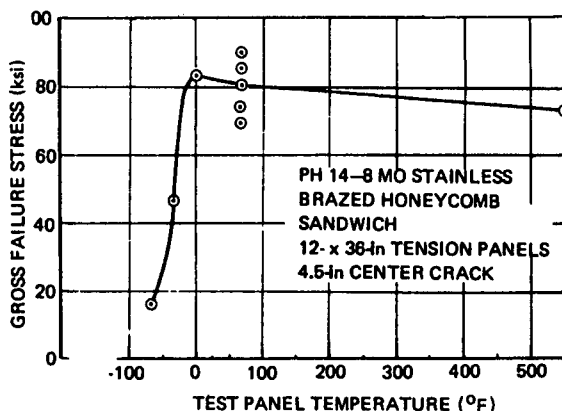
Figure 2-199. Temperature Sensitive Fracture Response
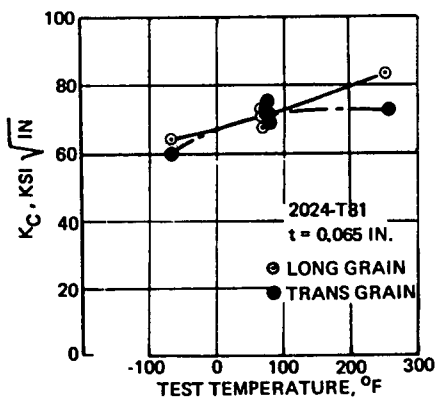
Thin 2024-T81 vs Test Temperature
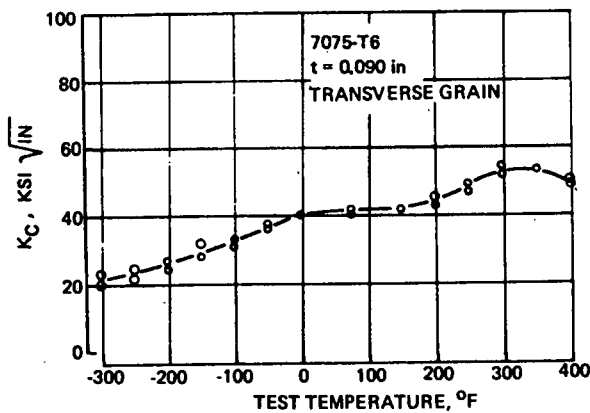
7075-T6 vs Temperature
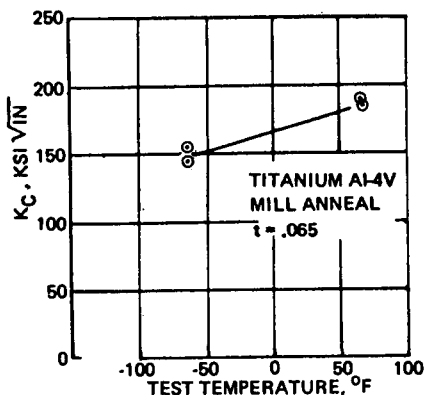
Titanium 6 Al-4 V Mill Anneal vs Temperature
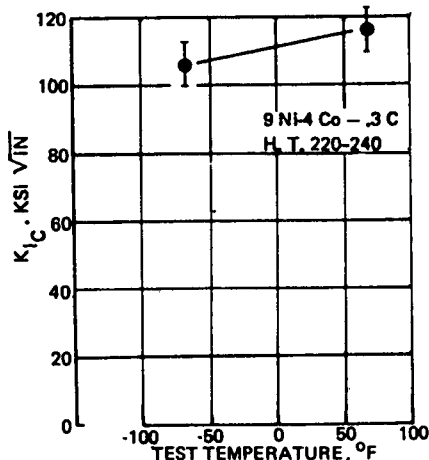
9 Ni-4 C_0 — .3C H.T. 220-240 vs Temperature

Figure 2-200. Fracture Toughness Variation With Temperature
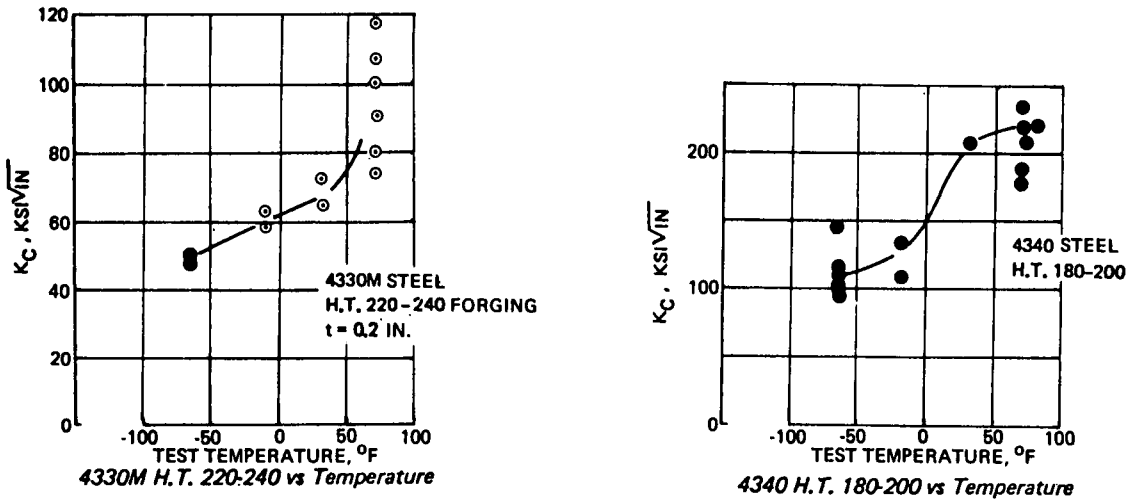
Figure 2-201. Fracture Toughness Variation With
Temperature

Effect of Reactive Environment

Possible reactive environments applicable to aircraft structure include high humidity, water, salt solution, cleaning solvents, fuel and hydraulic fluids. Structural materials that have cracks and are exposed to reactive environments have demonstrated quite different behavior than that for basic undamaged materials. An example of this is titanium alloy 8Al-1Mo-1V. Smooth specimens have shown a high resistance to stress corrosion in salt water. However, specimens with a crack have failed in salt water at loads significantly below the failure load in air. These failures result from the combination of stress and environment at the crack tip causing the crack to extend with time. Titanium alloys and high-strength steels are subject to this behavior for certain conditions. An example of extreme stress corrosion cracking behavior is shown by the data presented in Figure 2-202.

The data for stress corrosion cracking is usually presented as shown in Figure 2-203 for titanium 6Al-4V. The data from Reference 2-77 define the time to failure for given initial values of stress intensity factor. As can be seen there is a threshold value for stress corrosion cracking (KISCC). Test data for several steels from Reference 2-78 are presented in Figure 2-204 for a simulated sea water environment. Aluminum alloys generally are more resistant to stress corrosion cracking behavior. These data were obtained in the short transverse loading direction for a salt water spray environment. Figure 2-205 presents some results from Reference 2-79 where the growth rate is related to the stress intensity factor K.
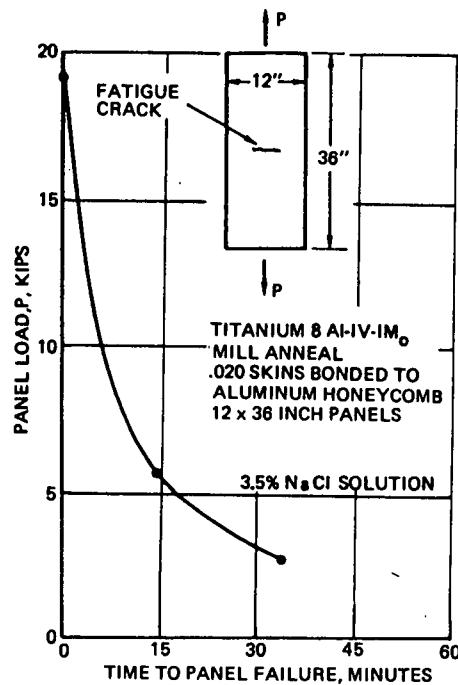
Figure 2-202. Titanium 8 Al-1V-1MO in 3.5% NaCl Sustained
Load Behavior
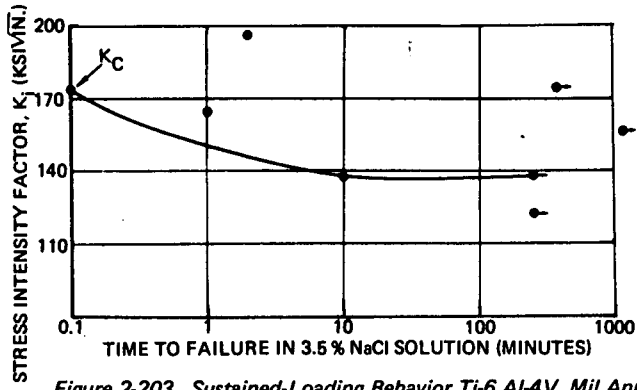
Figure 2-203. Sustained-Loading Behavior Ti-6 Al-4V, Mil Annealed,
0.125-Inch Thick
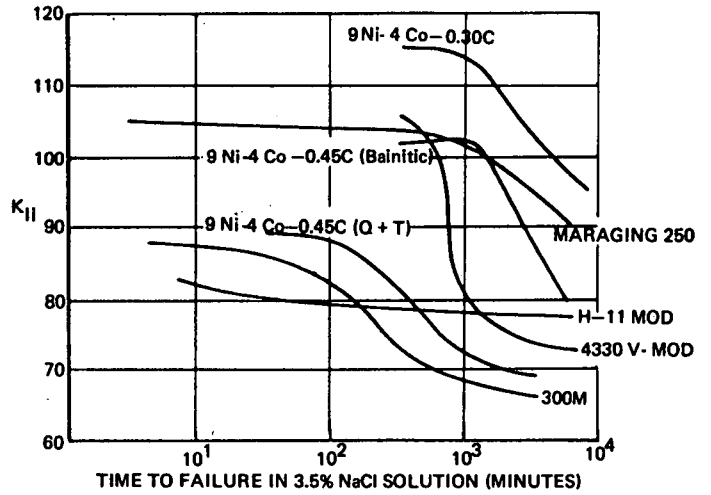
Figure 2-204. Sustained Loading Behavior for Several Steels
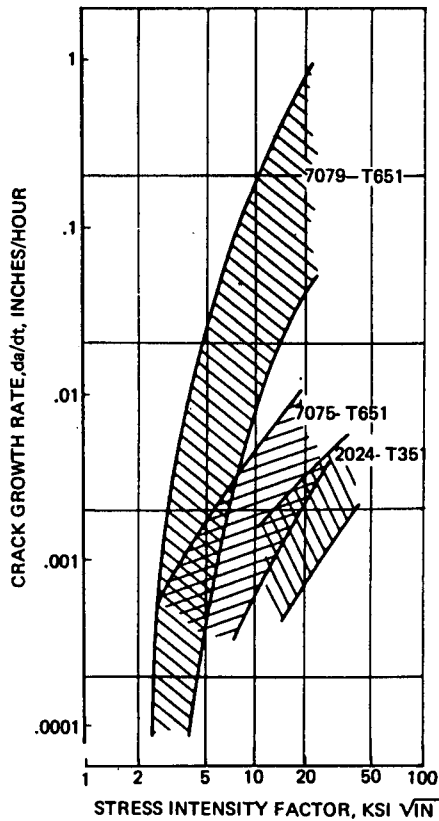
Figure 2-205. Sustain Load Stress Corrosion Cracking Behavior
of Several Aluminum Alloys

2.5.1.2 Modified Fracture Mechanics Approach

This section presents several residual strength methods which are modifications of the conventional fracture mechanics approach described in Section 2.5.1.1. These methods have proved useful in predicting the residual tensile strength of metallic and fiber composite structure containing projectile damage. The first modified approach discussed (2.5.1.2.1) makes use of an effective critical stress intensity factor for projectile damage. This parameter is determined empirically, and is used in lieu of the critical stress intensity factor K_C. The second topic presented (2.5.1.2.2) addresses additional analysis methods for predicting the residual tensile strength of projectile damaged fiber composite panels. These methods are included in this section because they are, indeed, modifications of conventional linear elastic fracture mechanics analysis.

2.5.1.2.1 Effective Critical Stress Intensity Factor For Projectile Damage

As mentioned in the previous sections, ballistic damage is physically dissimilar to sharp-edged cracks, and the geometry of ballistic damage is complex and difficult to predict by available analysis methods. As described in 2.5.1.1.1, the successful application of conventional fracture mechanics analysis to ballistic-induced damage consisted of:

1. Determining a value of K_C for the material by conventional fracture toughness tests using sharp-edged cracks;

2. Determining measures of damage that, when used as effective crack lengths, provide accurate prediction of the critical fracture of the ballistic damaged panel.

The advantage of this approach is that it makes use of available fracture toughness data, i.e., values of K_C are generally available, or are routinely determined as part of the structural development of an aircraft. The disadvantage is the difficulty of determining stress intensity factor relationships for complex ballistic damage shapes, and then developing the further analysis capability needed to relate the ballistic damage geometry to the projectile impact conditions and the structural configuration. This latter capability is important, since the final analytical objective entails predicting residual strength given the projectile impact conditions and the structural configuration.

In view of this, a more direct approach was taken in the work reported in References 2-2 and 2-8, by adopting a simple measure of damage as the effective crack-length, treating all ballistic damages as central cracks, and empirically determining an effective critical stress intensity factor from tensile tests of ballistic damaged panels. The measure of damage used in this approach (Ref. 2-2) is the transverse lateral damage, i.e., the maximum extent of structurally significant damage (holes, cracks, spall) transverse to the applied tensile stress. The effective critical stress intensity factor, called Λ_C herein and in Reference 2-2, is defined as:

$$\Lambda_C = \sigma_C \sqrt{\tfrac{\pi}{2} \ TLD}$$

(Eqn. 2-129)

σ_C = gross stress at failure

TLD = maximum transverse damage, as shown in Figure 2-206.
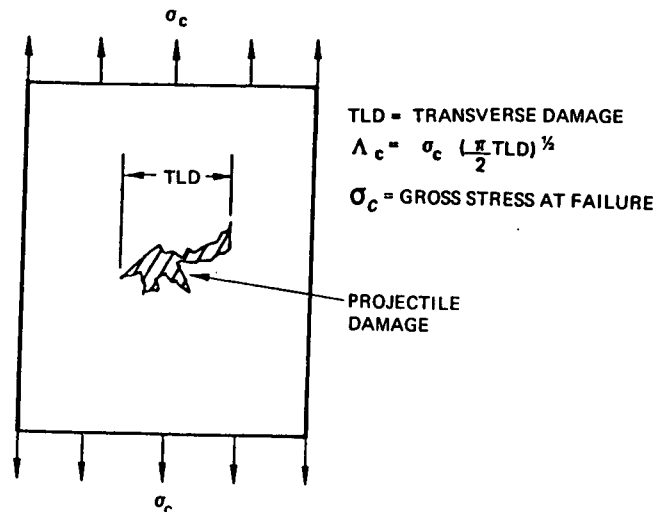
Figure 2-206. Critical Stress Intensity Factor for Projectile Damage

Values of Λc For Metallic Structure

Numerical values of Λ_C must be determined experimentally from tension tests of damaged panels. The experimentally determined critical stress and the initial transverse damage size are used in Eq. 2-129 to calculate Λ_C. Reference 2-2 presents a detailed analysis of Λ_C determinations for 2024-T81, 7075-T6, and 6Al-4V. The average values of Λ_C obtained are summarized in Table 2-30. It is felt that these values of Λ_C are representative of the materials tested, and may be used for more accurate predictions of residual strength than may be obtained from lower-bound predictions using the fatigue-crack stress intensity factor, K_C. The test data is presented in Tables 2-31 and 2-32, consisting of over 80 fracture tests including a wide range of panel thicknesses. The predominant projectile used in these tests was .50 caliber AP impacting at velocities between 1200 and 1600 feet per second.

Table 2-30. Values of Λ_c for Several Metals

MATERIAL	Λ_c (ksi $\sqrt{in.}$)	STANDARD DEVIATION (ksi$\sqrt{in.}$)	STANDARD ERROR OF THE MEAN (ksi$\sqrt{in.}$)	NUMBER OF TESTS
2024-T81 (TRANSVERSE GRAIN)	53.5	8.3	4.2	4
7075-T6 (TRANSVERSE GRAIN)	65.6	12.6	2.8	20
7075-T6 (LONGITUDINAL GRAIN)	91.9	14.9	2.7	31
6 Al-4V (TRANSVERSE GRAIN)	162.0	25.5	5.3	23

Table 2-31. Experimental Data, Residual Static Fracture

TARGET MATERIAL	TOTAL NO. OF TESTS	TARGET THICKNESS (INCHES) (AND NUMBER OF TESTS AT THICKNESS)											BALLISTIC THREAT				TARGET RESPONSE	
													PROJECTILE TYPE				MEAN IMPACT VELOCITY (FPS)	MEAN TLD / W	MEAN σ_c / σ_y
		.032	.063	.090	.114	.125	.160	.190	.250	.375	.500	.750	.30 CAL AP	.50 CAL AP	.50 CAL BALL	20 MM		
7075-T6 TRANSVERSE GRAIN	20	3	1	2		2		(1) 3	5	2	2			15	3	2	1353	0.204	0.537
7075-T6 LONGITUDINAL GRAIN	31			1		2		(1) 4	(2) 7	1	(2) 8	(2) 8		27	4		1543	0.191	0.757
2024-T81 TRANSVERSE GRAIN	4						1		3					4			1292	0.200	0.479
2024-T81 LONGITUDINAL GRAIN	1							1						1			1270	0.303	0.533
2024-T3 TRANSVERSE GRAIN	1							1						1			1500	0.158	0.895
6Al-4V TRANSVERSE GRAIN	23	2		5	(3) 8	4			4				1	19		3	1559	0.204	0.759
6Al-4V LONGITUDINAL GRAIN	1	1												1			632	0.093	0.800

(2) SOURCE: REFERENCE (2-55)
(3) SOURCE: REFERENCE (2-8)
(1) SOURCE: REFERENCE (2-65)

Table 2-32. Calculations for Residual Static Fracture Model

TEST NO.	TARGET MATERIAL	TARGET THICKNESS (IN)	TARGET WIDTH X LENGTH (IN)	PROJECTILE TYPE	IMPACT VELOCITY (fps)	IMPACT ANGLE (DEGREES)	TLD (IN)	TLD/W	σ_c (KSI)	Λ_c (KSI √IN)
REF. 2-2	7075-T6 TRANSVERSE GRAIN	0.032	12 X 36	.50 AP	576	0	3.50	0.291	20.0	46.9
		0.032	12 X 36	.50 AP	1310	0	1.53	0.128	37.8	58.6
		0.032	12 X 36	.50 AP	1105	60	1.44	0.120	41.0	61.7
		0.063	12 X 36	.50 AP	1875	0	1.05	0.087	48.9	62.9
		0.090	12 X 36	.50 AP	1216	0	2.16	0.180	41.2	76.0
		0.090	12 X 36	.50 AP	1017	60	2.70	0.225	29.4	60.6
		0.125	12 X 36	.50 AP	1248	0	4.10	0.342	23.8	60.5
		0.125	12 X 36	.50 AP	1369	0	2.30	0.192	34.0	64.6
		0.250	12 X 36	.50 AP	1410	0	3.70	0.308	25.0	60.3
		0.250	12 X 36	.50 AP	1644	0	1.90	0.159	37.5	64.6
		0.250	12 X 36	20 mm	1370	0	1.58	0.132	49.4	77.8
		0.250	12 X 36	20 mm	346	0	1.80	0.150	35.3	59.4
		0.250	12 X 36	.50 AP	1985	0	0.84	0.070	51.9	59.6
		0.375	9 X 36	.50 AP	1650	0	2.40	0.267	52.0+	101.0+
		0.375	9 X 36	.50 AP	1580	0	3.55	0.395	29.6	70.0
		0.500	7 X 36	.50 AP	2040	0	1.60	0.229	45.0	71.3
		0.500	7 X 36	.50 AP	1840	0	1.73	0.247	51.0+	84.0+
REF. 2-55	7075-T6 TRANSVERSE GRAIN	0.190	18 X 36	.50 BALL	1111	0	4.80	0.267	23.7	65.2
		0.190	18 X 26	.50 BALL	1127	0	2.60	0.144	30.7	62.6
		0.190	18 X 36	.50 BALL	1250	0	2.70	0.150	21.5	44.3
REF. 2-2 REF. 2-55 REF. 2-8	7075-T6 LONGITUDINAL GRAIN	0.090	12 X 36	.50 AP	1120	20	1.46	0.122	52.0	78.8
		0.125	12 X 36		870	0	1.52	0.127	58.6	90.5
		0.125	12 X 36		1082	0	2.35	0.195	43.3	83.2
		0.375	9 X 36	.50 AP	1370	0	1.50	0.167	56.6	86.9
		0.190	18 X 36	.50 BALL	677	0	3.45	0.192	29.3	68.3
		0.190	18 X 36	.50 BALL	1175	0	2.85	0.159	45.0	95.2
		0.190	18 X 36	.50 BALL	1105	0	1.70	0.094	41.5	67.9
		0.190	18 X 36	.50 BALL	1265	0	3.35	0.186	28.5	65.5
		0.250	12 X 32	.50 AP	1265	0	1.87	0.157	53.8	92.0
		0.250	12 X 32	.50 AP	1351	0	1.45	0.122	60.7	91.9
		0.250	12 X 32	.50 AP	1320	0	2.24	0.188	49.8	93.4
		0.250	12 X 32	.50 AP	1381	0	2.42	0.204	45.4	78.7
		0.250	12 X 32	.50 AP	1266	0	1.91	0.161	62.3	107.9
		0.250	16 X 32	.50 AP	1333	60	2.85	0.179	48.2	102.2
		0.250	16 X 32	.50 AP	1408	60	3.58	0.225	40.1	95.0
		0.500	12 X 32	.50 AP	1787	0	1.79	0.150	58.1	97.3
		0.500	12 X 32	.50 AP	1810	0	1.58	0.133	64.8	102.0
		0.500	8 X 32	.50 AP	1821	0	1.70	0.213	60.7	99.2
		0.500	12 X 32	.50 AP	1779	0	1.47	0.124	56.5	86.0
		0.500	12 X 32	.50 AP	1817	40	1.86	0.156	51.5	88.0
		0.500	12 x 32	.50 AP	1804	40	1.92	0.162	47.8	83.0
		0.500	12 X 32	.50 AP	1801	40	2.14	0.180	38.5	70.6
		0.500	12 X 32	.50 AP	1819	40	1.95	0.164	41.4	72.6
		0.750	8 X 32	.50 AP	1936	0	2.17	0.271	64.3	118.5
		0.750	8 X 32	.50 AP	1976	0	2.12	0.265	62.8	114.3
		0.750	8 X 32	.50 AP	1941	0	2.25	0.281	57.6	108.2
		0.750	8 X 32	.50 AP	1920	0	1.91	0.239	51.7	89.6
		0.750	8 X 32	.50 AP	1920	15	2.19	0.274	62.0	115.0
	7075-T6 LONGITUDINAL GRAIN	0.750	8 X 32	.50 AP	1916	15	2.31	0.289	63.0	120.0
		0.750	8 X 32	.50 AP	1937	15	2.14	0.268	55.7	102.0
		0.750	8 X 32	.50 AP	1912	15	2.32	0.290	44.5	85.0
REF. 2-2	2024-T81 TRANSVERSE GRAIN	0.160	12 X 36	.50 AP	1285	0	1.30	0.108	41.8	59.7
		0.250	12 X 36	.50 AP	1080	0	2.75	0.229	27.5	57.3
		0.250	12 X 36	.50 AP	1364	0	3.15	0.263	20.4	45.3
		0.250	12 X 36	.50 AP	1438	0	3.15	0.263	23.4	52.0
	2024-T81 LONGITUDINAL GRAIN	0.250	12 x 36	.50 AP	1270	0	3.64	0.303	31.4	75.1
	2024-T3 TRANSVERSE GRAIN	0.250	12 x 36	.50 AP	1500	0	1.90	0.1583	45.0	77.5
	6AL-4V TRANSVERSE GRAIN	0.032	12 X 36	.50 AP	1680	60	1.40	0.1167	96.2	142.8
		0.032		.30 AP	1489	60	2.67	0.223	63.1	129.5
		0.090		.50 AP	727	0	2.68	0.223	90.6	186.0
		0.090		.50 AP	1165	0	5.95	0.496	49.5	151.4
		0.090		.50 AP	888	0	3.90	0.325	82.5	204.0
		0.090		.50 AP	1225	0	2.40	0.200	100.3	195.0
		0.090		20 MM	1211	0	1.15	0.096	106.4+	143.2+
		0.125		.50 AP	1152	60	4.70	0.391	62.8	171.0
		0.125		.50 AP	1339	60	1.62	0.135	117.2	187.0
		0.125		.50 AP	1358	60	1.88	0.157	112.4	193.5
		0.125	12 X 36	.50 AP	1100	0	2.10	0.175	117.2+	213.0
		0.250	8 X 36	.50 AP	2350	0	1.15	0.144	95.6	128.8
		0.250	8 X 36	.50 AP	1940	0	1.77	0.222	95.6	159.5
		0.250	8 X 36	20 MM	434	0	1.20	0.150	95.8+	131.6+
		0.250	8 X 36	20 MM	207	0	1.75	0.219	99.4	165.0
REF. 2-65		0.114	9 X 9	.50 AP	2200	0	0.92	0.102	108.3	130.0
		0.114	9 X 9	.50 AP	2200	0	1.43	0.159	105.2	158.0
		0.114	9 X 9	.50 AP	2200	0	2.48	0.276	81.4	161.0
		0.114	9 X 9	.50 AP	2200	0	1.15	0.128	102.5	138.0
		0.114	9 X 9	.50 AP	2200	0	2.50	0.278	74.6	147.9
	6A1-4V TRANSVERSE GRAIN	0.114	9 X 9	.50 AP	2200	0	1.55	0.172	98.5	153.9
		0.114	9 X 9	.50 AP	2200	0	1.51	0.168	109.3	168.0
		0.114	9 X 9	.50 AP	2200	0	1.33	0.148	116.0	168.0

Values of Λc for Fiber Composite Structure

A survey of available test data on the residual tensile strength of ballistic damaged graphite/epoxy and boron/epoxy laminates was completed in 1974 (Ref. 2-27). Following the approach just described for metals, the relationship shown below was investigated for application to advanced fiber composites containing ballistic damage:

$$\frac{\sigma_c}{F_{tu}} = \frac{\Lambda_c/F_{tu}}{\sqrt{\frac{\pi}{2} TLD}},$$

(Eqn. 2-130)

where:

σ_c =   gross tension stress causing fracture;

F_{tu} =   ultimate tensile strength of laminate (undamaged);

Λ_c =   critical stress intensity factor for ballistic impact damage;

TLD   =   the length of the effective ballistic damage transverse to the applied tension stress.

It was found that this relationship provided good correlation of residual strength test results obtained from thin laminates of the 0, ±45, 90 layup family, as indicated in Figures 2-207 to 2-210. The measure of effective damage that best correlated the test data was:

.⌐D   = LD_{en}

where:

LD_{en} =   Predicted mean entry damage from the model given in Section 2.2.1.2.2
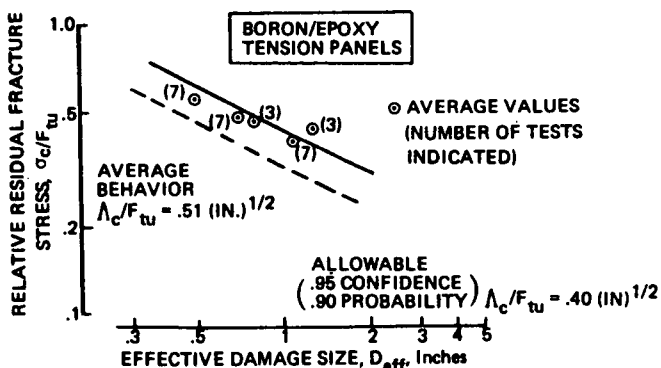
Figure 2-207. Residual Strength Data for Boron/Epoxy Panels Containing Projectile Damage
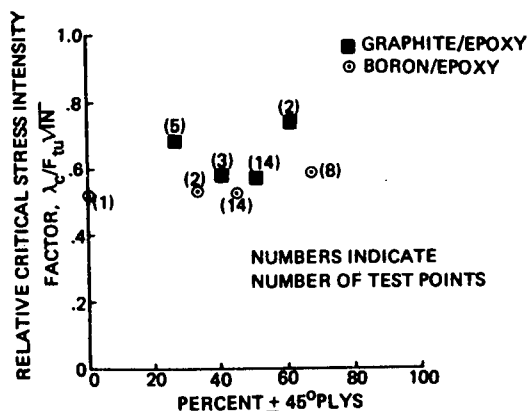
Figure 2-208. Influence of Ply Orientation on Residual Tensile Strength of Composite Panels
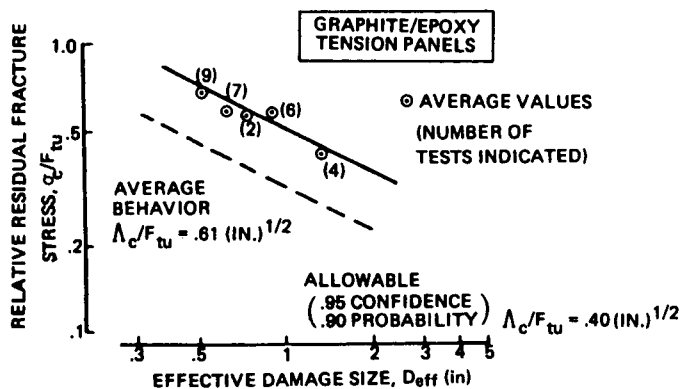
Figure 2-209. Residual Strength Data for Graphite/Epoxy Panels Containing Projectile Damage
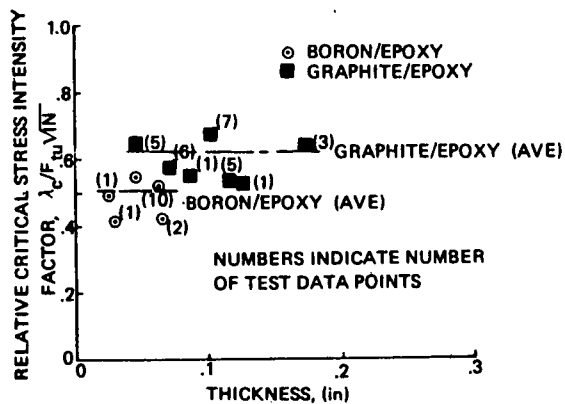
Figure 2-210. Influence of Panel Thickness on Residual Tensile Strength of Composite Panels

Average values of Λ_c/F_{tu} were found for each material. In addition, statistical data was generated for each material to establish allowable values as presented below:

MATERIAL	$\Lambda_c/F_{tu}\sqrt{in}$ AVERAGE	STANDARD DEVIATION	.90 CONFIDENCE .90 PROBABILITY
Graphite/Epoxy	0.574	0.098	0.393
Boron/Epoxy	0.509	0.059	0.401

A very significant result was determined concerning the numerical value of Λ_c for graphite and boron/epoxy laminates, and this has been further substantiated by subsequent data. Most test data involving the 0,±45,90 layup family (with 0-degree fibers in the tensile direction) can be correlated well using a constant value for the ratio Λ_c/F_{tu}. The value selected for best overall correlation was:

$$\frac{\Lambda_c}{F_{tu}} = 0.5 \quad \text{(Approximately)}.$$

(Eqn. 2-131)

This results in the following expression for residual tensile strength:

$$\frac{\Lambda_c}{F_{tu}} = \frac{0.5}{\sqrt{\frac{\pi}{2}TLD}} = \frac{0.40}{\sqrt{TLD}}$$

(Eqn. 2-132)

The above relationship provides a simple and useful method for predicting the residual tension strength of ballistic damaged laminates that are controlled by 0-degree fibers in the tensile direction.

Application of Λ_c in Residual Strength Assessment

Once values of Λ_c have been established which reflect the impact conditions and structural materials of interest, they are used in lieu of K_c in residual strength assessment. The transverse effective damage is used as the crack length, and this may be obtained from the damage prediction analysis methods presented in this Manual. The success of this approach depends in part on the degree of scatter in experimental values of Λ_c. This scatter has been found to be small enough that Λ_c can be regarded as a pseudo-material property within the range of ballistic conditions investigated. (Ref. 2-2)

Several programs (References 2-2, 2-12, 2-55, 2-4, 2-65 and 2-67) have investigated the correlation between Λ_c and K_c. Experimental values of K_c were determined in References 2-7 and 2-55 from specimens also used for ballistic strength testing, providing a direct comparison of K_c and Λ_c. The results from Reference 2-55 are shown in Figure 2-211 for both transverse- and longitudinal-grain 0.190-inch 7075-T6. Although the residual strength behavior of the ballistic damaged panels is much closer to notch-sensitive than notch-insensitive response, all the data points are clearly in the transition region.
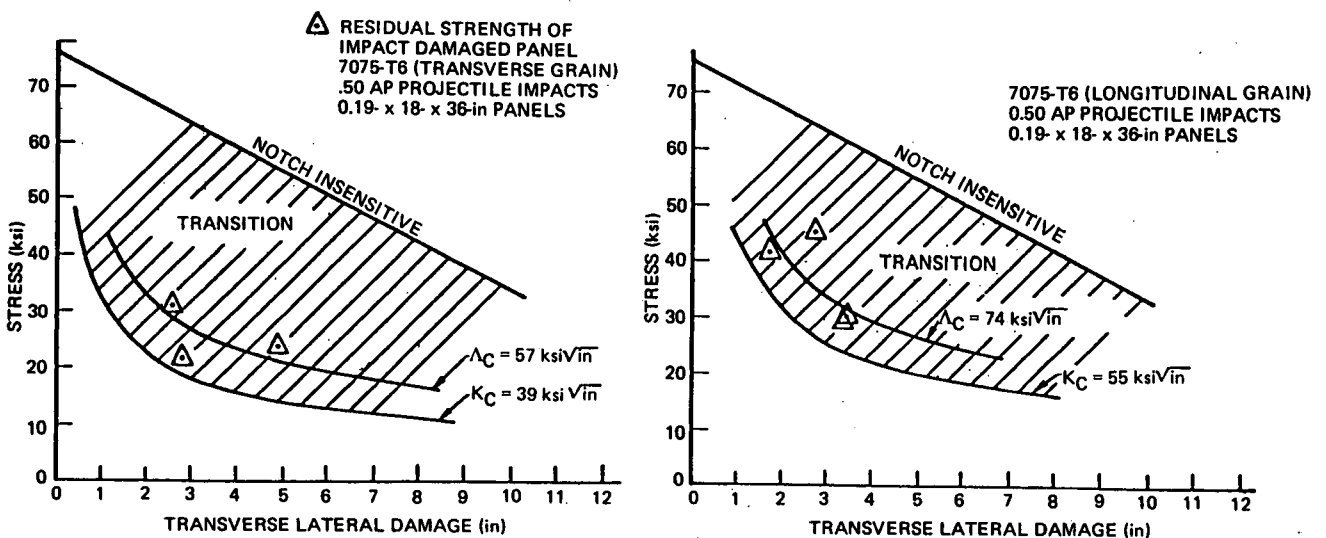
Figure 2-211. Comparison of Ballistic Damage (Λ_c) and Fatigue Damage (K_c) Residual Strength

It is believed that this behavior is typical and that the relative magnitude of Λ_c depends primarily upon the extent of cracking inflicted by the impact. In general, the tendency to crack decreases as thickness increases beyond a t/d ratio of approximately 1:3. Consequently, it would be expected that the fracture response of impact damaged sheets will appear to be more notch-insensitive as thickness is increased. The available experimental data confirm this expectation, as may be seen from Figures 2-212 and 2-213 for 7075-T6. These figures compare Λ_c with values of K_c obtained from References 2-72 and 2-73. The values of Λ_c were computed from References 2-2, 2-23, 2-65, 2-8 and 2-55.

Figures 2-212 and 2-213 can also be used to demonstrate the probable effects of fatigue cycling on the residual strength of ballistic damaged panels, since, Λ_c defines the strength with projectile damage while K_c defines the strength with a fatigue-sharpened notch. As shown by the data, for thicker gages the value of K_c is much lower than Λ_c. Cyclic loading can produce a significant reduction in strength by changing the character of the damage without a significant increase in damage size. This may occur quickly (with few cyclic load applications) making it appropriate to use K_c rather than Λ_c for residual strength evaluations at times other than immediately after threat exposure, to assure conservatism. The reader should also refer to 2.5.1.3.1 at this point, as it is shown there that dynamic effects induced by the existence of applied tensile stress at the time of impact also cause an apparent reduction in Λ_c.
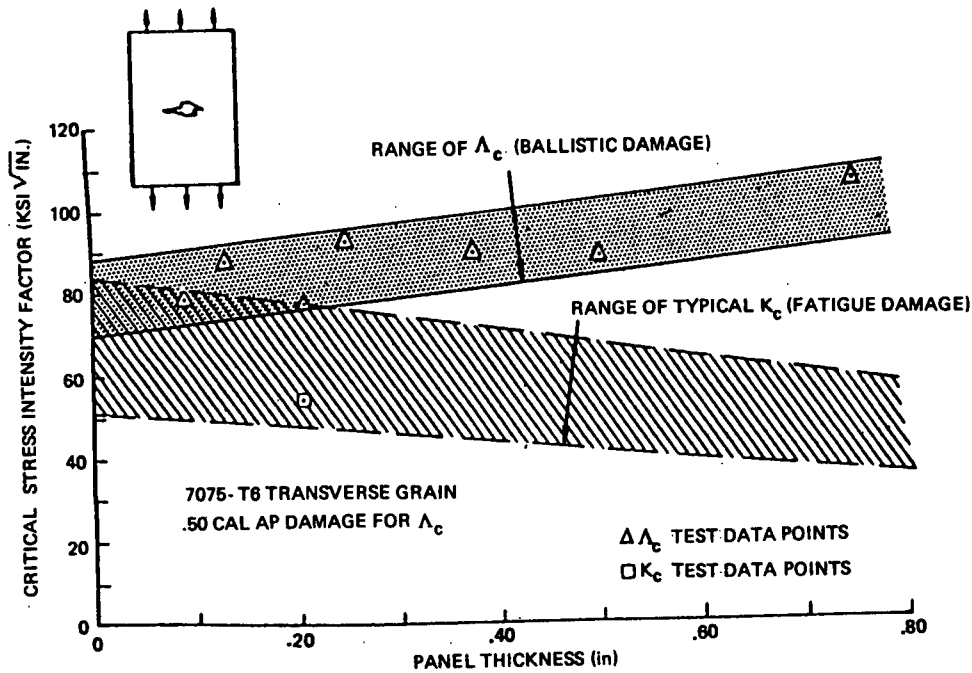
Figure 2-212. Comparison of Λ_c and K_c for Long Transverse Grain 7075-T6
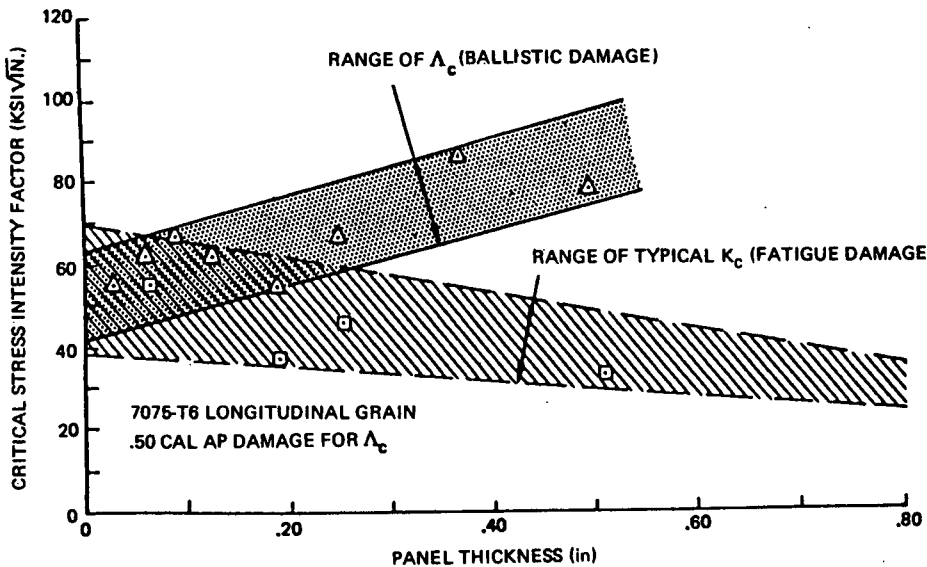
Figure 2-213. Comparison of Λ_c and K_c for Longitudinal Grain 7075-T6

2.5.1.2.2 Additional Residual Strength Prediction Techniques for Fiber Composites

Reference 2-17 describes several analysis methods for predicting the residual tensile strength of ballistic damaged advanced fiber composites, chiefly graphite/epoxy. These methods are, in most cases, modified versions of linear elastic fracture mechanics. None of the methods are completely verified by test, reflecting the overall uncertainties with regard to predicting failure in these materials, regardless of the source of damage.

Method #1. This method was developed by K. King (Ref. 2-12), using experimental data from several sources, including laminates damaged by ballistic projectiles, sawcuts, and drilled holes. The approach is fully documented in Ref. 2-12 and applies to composite laminates containing 0-degree fibers that control the laminate strength and stiffness in the tensile direction. There are many applications of this type of laminate in aircraft design, including the $0,\pm45,90$ family, and ±45 graphite hybridized with 0-degree fiberglass or Kevlar.

The prediction can be expressed in the following way:

$$\frac{1-R}{R} = 0.397 \ (\frac{E_o}{G})^{2/3} \ (TD_{eff})^{2/3}$$

(Eqn. 2-133)

where,

R   =   Critical stress ratio

   = $\frac{\sigma_c}{F_{tu}}$, with

   σ_c =   gross tension stress causing fracture

   F_{tu} =   ultimate tensile strength of laminate (undamaged)

E_o =   Modulus of elasticity of a uniaxial laminate of the 0-degree material

G   =   Shear modulus of elasticity of the hybrid laminate

TD_{eff} =   The length of the effective ballistic damage transverse to the applied tension stress field (inches), i.e., length of a sharp-edged crack causing equivalent structural degradation,

   TD_{eff} = LD_{en} for all laminate thicknesses **(Eqn. 2-16, page 77)**

This model was formulated from residual strength testing of laminates having a wide range of fiber/resin systems and layup configurations. The formulation incorporates the following assumptions:

a.   The model applies only to laminates whose tensile strength and stiffness is controlled by 0-degree fibers;

b.   The stress distribution in the vicinity of the damage is parabolic, with ultimate stress at the damage tip when fracture initiates at the critical gross stress.

c.   The region of stress concentration extends away from the damage tip to a lateral distance determined by the parameters σ_c/F_{tu}, G, and $1/E_o$.

The relationship may also be written as:

$$\frac{\sigma_c}{F_{tu}} = \frac{1}{1 + (0.397) \ (\frac{E_o}{G})^{2/3} \ (TD_{eff})^{2/3}}$$

(Eqn. 2-134)

As seen above, the method predicts that the ratio of fracture stress to ultimate strength depends on E_o/G, and the damage size. In an all-graphite laminate of the $0,\pm45,90$ family, the ratio E_o/G depends only on the percentage of ±45 fibers, since E_o is determined by the fiber/resin system (typically, E_o is about $17(10)^6$ psi for graphite/epoxy).

Figure 2-214 shows predicted values of σ_c/F_{tu} for several $0,\pm45,90$ laminates, using Method 1. Available test data is also shown, obtained from Ref. 2-12, for $0/\pm45/90$, $0_2/\pm45$, and $0_2/\pm45/90$ laminates. The correlation is very good. Predictions for residual tensile strength using the Avery/Porter method are also shown, represented by the relationship $K_c/F_{tu} \approx 0.5$. The two methods converge for the quasi-isotropic laminates plotted, but differ substantially for the 0/90 laminate.

Figure 2-215 was extracted from the Advanced Composites Design Guide, AFML, Nov. 1971, and may be used to estimate E_o, G, and F_{tu} of graphite/epoxy laminates in cases where specific test data is not available.
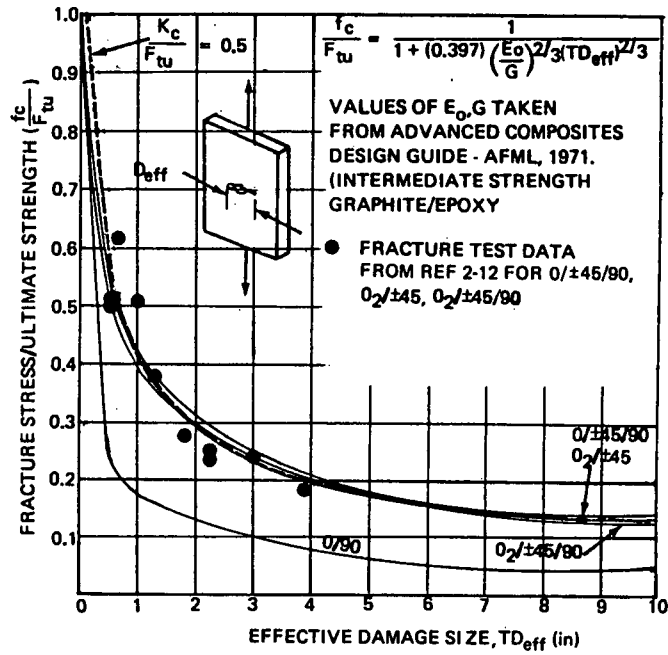
Figure 2-214.   Residual Tensile Strength of Graphite/Epoxy

ULTIMATE TENSILE STRENGTH F_x^{tu}

EXTENSIONAL MODULUS E_x

SHEAR MODULUS G_{xy}
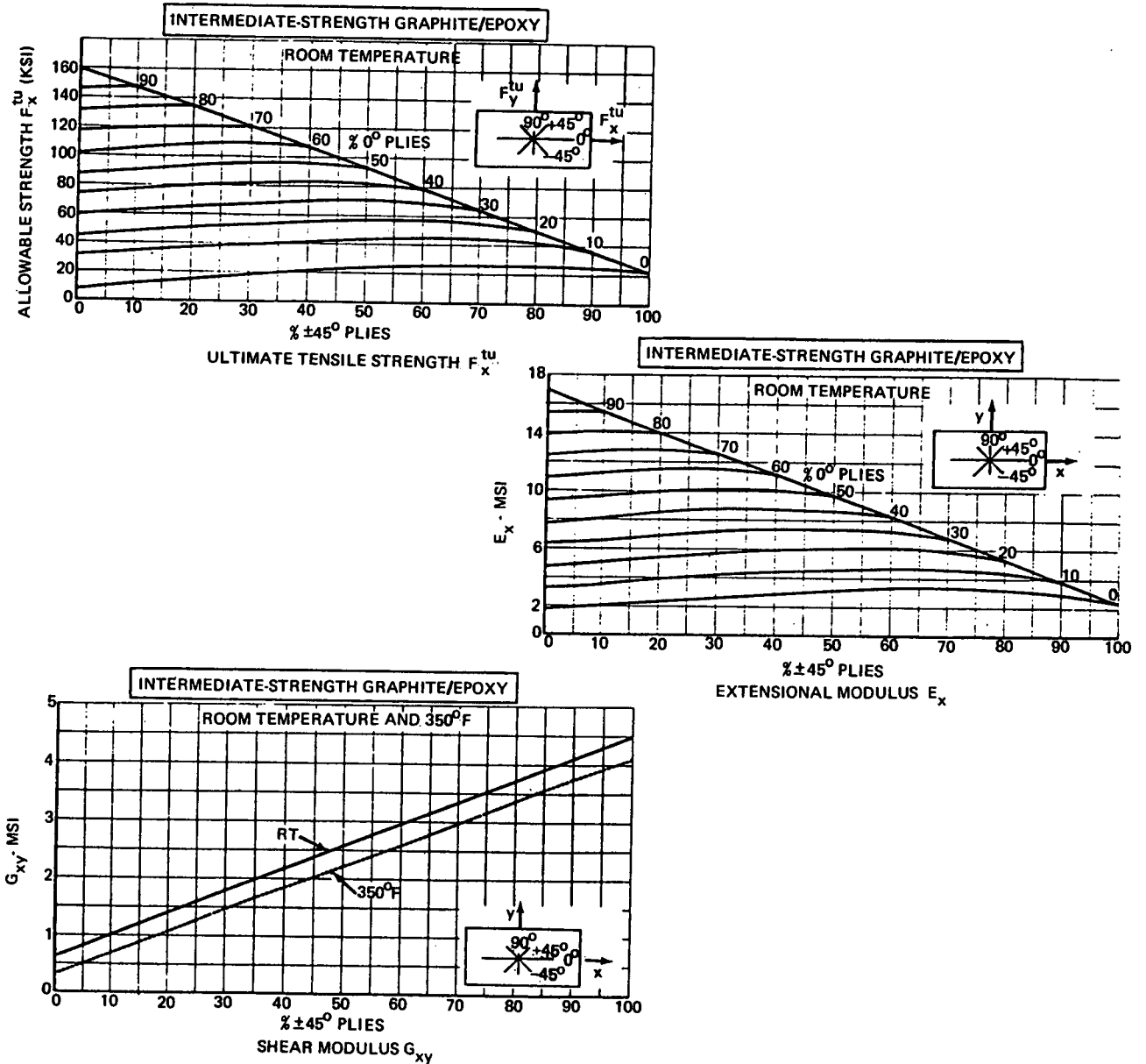
Figure 2-215. Representativive Material Properties for Graphite/Epoxy
(Advanced Composites Design Guide, AFML, Nov. 1971)

Method #2. Waddoups, et al, (Ref. 2-104) proposed that there is an inherent flaw (or intense energy region) associated with a particular composite laminate that can be used in the prediction of the fracture stress. This inherent flaw was assumed to control the static strength of the undamaged laminate and was analogous to the crack tip plastic zone in metals. The inherent flaw size (a_0) was assumed to exist at the edge of holes and was used to correlate fracture strength with hole size. This resulted in the following expressions for fracture.

For slits (through center cracks):

$$K_c = f_c \left[\pi (a + a_0) \right]^{1/2}$$

(Eqn. 2-135)

For holes:

$$K_c = f_c \left[\pi a_0 \right]^{1/2} F(a_0/R)$$

(Eqn. 2-136)

For unnotched strength:

$$K_c = f_c \left[\pi a_0 \right]^{1/2}$$

(Eqn. 2-137)

where:

a_0 = one-half inherent flaw length;

f_c = fracture stress;

K_c = critical stress intensity factor;

a = one-half slit length (for through center cracks);

R = hole radius;

$F(a_0/R)$ = Bowie function for cracks emanating from a hole.

Method #3. Another view of fracture in composites was presented by Whitney and Nuismer (Ref. 2-105). In this development, fracture is assumed to occur when the stress at some characteristic distance d_0 ahead of the notch is equal to the ultimate tensile strength of the laminate. This analysis is applied to both holes and cracks and makes use of the "exact" linear elastic stress distribution around the discontinuity. This results in the following expressions for fracture.

For slits:

(Eqn. 2-138)

$$K_Q = F_{tu} \left[\pi a \, (1 - \xi_1^2) \right]^{1/2}$$

$$\xi_1 = \frac{a}{a + d_0}$$

(Eqn. 2-139)

For holes:

$$\frac{\sigma_c}{F_{tu}} = \frac{2}{2 + \xi_2^2 + 3 \xi_2^4} \; ; \; \text{where} \; \xi_2 = \frac{R}{R + d_0}$$

(Eqn. 2-140)

For unnotched strength:

$$\sigma_c = F_{tu}$$

where:

K_Q = the apparent critical stress intensity factor;

F_{tu} = ultimate tensile strength;

a = half crack length;

d_0 = characteristic distance;

σ_c = critical fracture stress;

R = hole radius.

Whitney and Nuismer also presented a fracture criterion where failure is initiated when the average stress ahead of the notch over some characteristic distance a_0 is equal to the unnotched laminate strength. This analysis yields the following results when developed for through cracks and holes:

For slits:

$$K_Q = F_{tu} \left[\pi a_0 \xi_3 \right]^{1/2}$$

(Eqn. 2-141)

$$\xi_3 = \frac{a}{2a + a_0}$$

(Eqn. 2-142)

For holes:

$$\frac{\sigma_c}{F_{tu}} = \frac{2(1-\xi_4)}{(2-\xi_4^2-\xi_4^4)}$$

(Eqn. 2-143)

$$\xi_4 = \frac{R}{R+a_o}$$

For unnotched strength:

$$\sigma_c = F_{tu}$$

Comparing the data developed in Reference 2-7 for holes and slits over a range of damage sizes gives the results shown in Figure 2-216. As shown in the figure for damage sizes greater than one inch, analysis predicts a difference in fracture stress due to flaw shape (hole vs. slit). Available test data for panels containing holes and slits confirm this result.
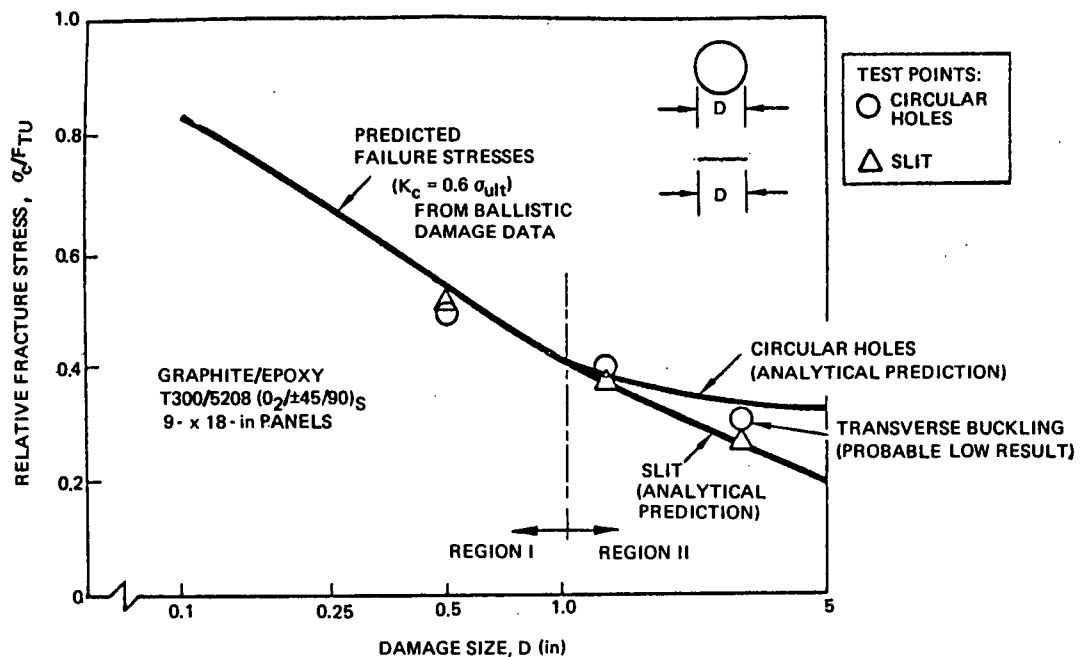
Figure 2-216. Effect of Flaw Shape on Fracture Response of Graphite/Epoxy Laminates

Method #4. This method developed by Konish (Ref. 2-109) includes experimentally determining the critical stress intensity factor (K^o_Q) for a uniaxial laminate. The critical stress intensity factor for each layer in the laminate is then calculated as follows.

$$(K_{I_F})_i = K^o_{Q_i}/\xi_{I_i} \qquad i = \text{layer number}$$

(Eqn. 2-109)

where:

$$\begin{bmatrix} \xi_1 \\ \xi_2 \\ \xi_{12} \end{bmatrix}_i = [T_{ij}]_i \ [Q_{ij}]_i \ [\beta_{ij}] \quad \begin{cases} \sqrt{\beta_{22}/\beta_{11}} \\ 1 \\ 0 \end{cases}$$

(Eqn. 2-110)

$[T_{ij}]_i$ is the transformation matrix relating layer stresses in principal coordinates to layer stresses in global coordinates, $[Q_{ij}]_i$ is the stiffness matrix of each ply in the global coordinate system, and $[\beta_{ij}]_i$ is the laminate compliance matrix relating laminate strains to laminate stresses. It should be noted that the above equation is for a laminate with a crack in the global y-direction and must be transformed by 90 degrees to obtain the K_{I_F} of a laminate loaded in the x-direction.

Figure 2-217 shows a comparison of predicted K_c values with test results for several graphite/epoxy and graphite/glass hybrid laminates. Correlation is poor for this data.
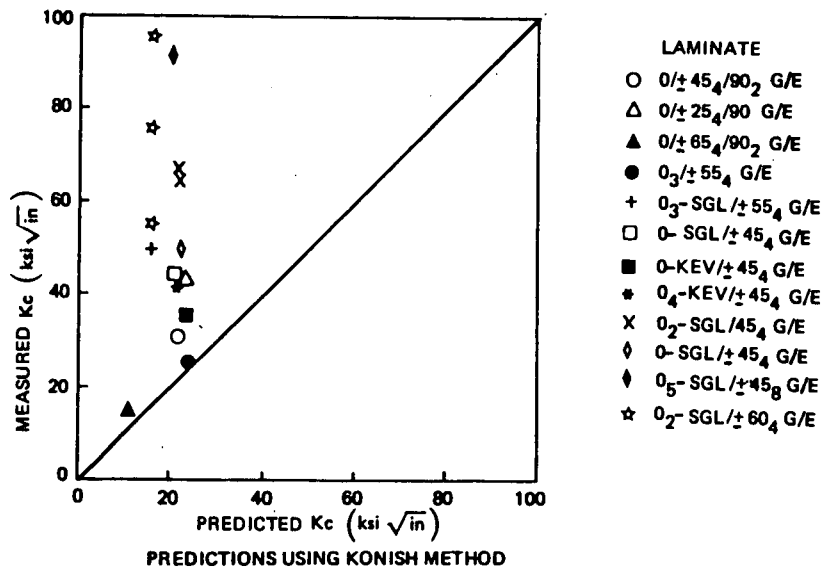
Figure 2-217. Correlation of, Test Results With Predictions from Residual Tensile Strength
Analysis Method 4

Method #5. A fundamental approach toward predicting fracture in composites has been developed by Cruse (Ref. 2-110). This method consists of computing the strain energy release rate of the laminate (G_Q) as the weighted sum of all the layer strain energy release rates, G_i.

$$G_Q = \sum_{i=1}^{n} G_i \, t_i/T, \quad (n = \text{number of plies})$$ (Eqn. 2-146)

where:

$$G_i = C_i K^2_{Q_i}$$

$$C_i = \sqrt{\frac{\beta_{11_i} \, \beta_{22_i}}{2}} \sqrt{\sqrt{\frac{\beta_{11_i}}{\beta_{22_i}}} + \frac{2\,\beta_{12_i} + \beta_{33_i}}{2\,\beta_{22_i}}}$$ (Eqn. 2-147)

t_i = the thickness of the ith ply;

T = the laminate thickness;

K_{Q_i} = the experimentally determined critical stress intensity factor of laminates of each ply orientation; for example, K_Q's determined from fracture tests of 0-deg laminates, 90-deg laminates, and ±45-deg laminates.

β_{ij} is the transformed compliance matrix of each layer. The fracture toughness of the laminate is then:

$$K_Q = \sqrt{G_Q/C}$$

where C, and C_i in equation 2-147 are similar except that laminate compliances are used in place of layer compliances.

Figure 2-218 shows a comparison of predicted critical stress intensity values with test results for several graphite/epoxy and graphite/glass hybrid laminates. Correlation is good for most of the laminates tested.
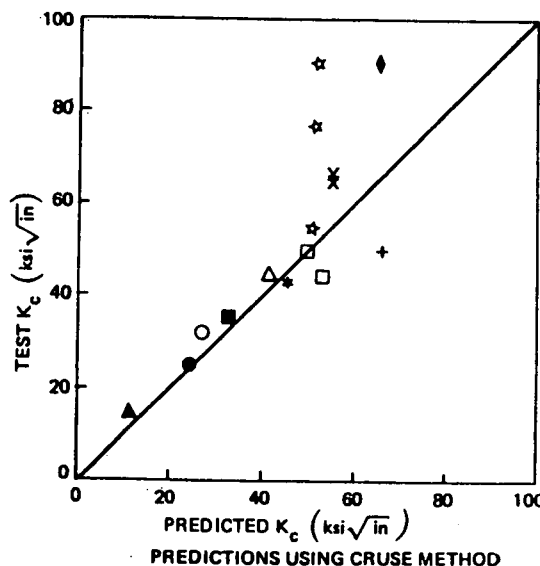
Figure 2-218. Correlation of Test Results With Predictions from
Residual Tensile Strength Analysis 5

2.5.1.3 Dynamic Effects Associated With Strength Degradation

There are two phenomena loosely catagorized as "dynamic" effects which can have a significant influence on the strength degradation caused by projectile impact. The first phenomena influences the strength of the panel at the time of impact, and is associated with the dynamic effects of the impact combined with the applied stresses existing in the panel. These applied stresses are, of course, due to the operational flight loads. The second dynamic effect arises when transient pressure loadings due to hydrodynamic ram or blast impinge on panels containing damage. The transient loadings introduce a dynamic stress field in the vicinity of the damage, requiring the consideration of dynamic stress intensity factors when assessing residual tensile strength.

2.5.1.3.1 Effect of Applied Tensile Load

Available experimental data (Ref. 2-2) shows that metallic panels, under tensile load applied prior to the impact, frequently fail at impact, even though the applied stress levels are below those required for residual strength failure. This behavior is clearly shown in Figure 2-219, which shows test results for 7075-T6 aluminum impacted by small arms projectiles. In this figure, it can be seen that impact fractures occurred at stress levels significantly below those required for the residual static fracture of similar panels which were first damaged without applied load. This is an effect of obvious significance, since it implies that failure predictions based upon residual strength data will tend to overestimate the strength of stressed panels.
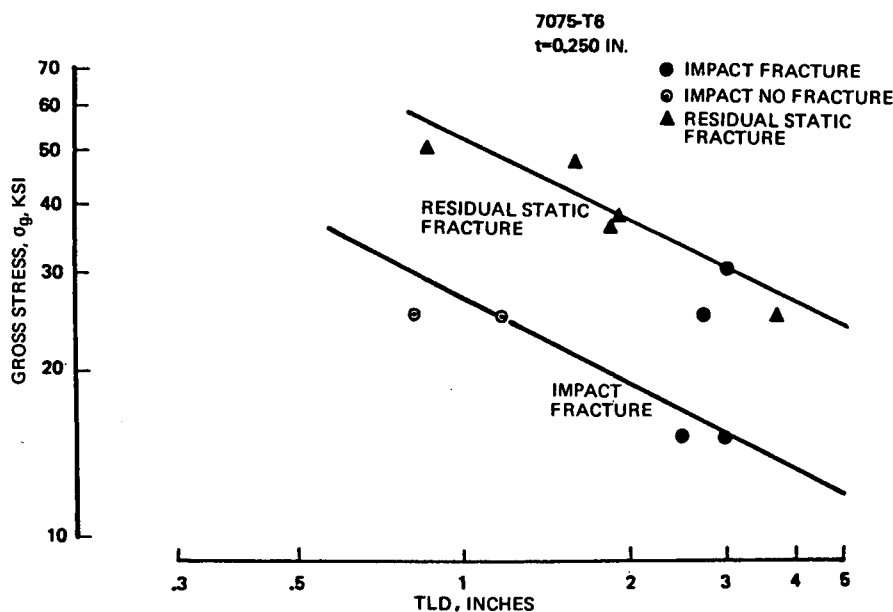
Figure 2-219. Typical Impact Fracture and Residual Strength Data

Test data is very limited. At present, the controlling parameters and their influence upon impact-fracture behavior are not fully understood. One reason for this is that the applied loads in the vicinity of the damage are complex, due to the dynamic interaction between the impacting projectile and the structural member. In addition to the applied static load, the damage area may experience dynamic stresses caused by:

o   Local bending or "denting"
o   Gross dynamic bending and twisting
o   In-plane "wedging" forces from projectile penetration.

In addition to the loading considerations mentioned above, the following factors are thought to influence impact-fracture.

1. The dynamic conditions of a running or suddenly appearing crack produce a dynamic increase in the crack tip stress field.

2. The dynamic conditions at the crack tip can result in a more brittle material response.

3. The dynamic stress conditions will be cyclic, which can result in fatigue damage extension.

Impact Fracture Analysis Methods

A limited amount of test data are available for characterizing impact fracture of 7075-T6, 2024-T81, 6A1-4V titanium and some fiber composite materials. The most comprehensive set of test data is for 7075-T6 as reported in References 2-2. Data for other materials are limited, and additional testing is required to verify prediction methods and to establish design allowables.

In Reference 2-2 and others, the possibility of predicting impact fracture in a manner analogous to that used for residual static strength was examined. The static fracture behavior (residual strength) of ballistic damaged metal panels has been characterized by Λ_c (see Section 2.5.1.2.1), the effective critical stress intensity factor for ballistic damage. A similar characterization for impact fracture is given by the formula:

$$\Lambda_c' = \sigma_c' \sqrt{\frac{\pi}{2} \text{ TLD}}$$

σ_c' = threshold applied stress for impact fracture

Λ_c' = threshold stress intensity factor for impact fracture

TLD = damage transverse to the applied stress

The table below (from Ref. 2-2) compares Λ_c and Λ_c' for transverse grain 7075-T6 panels impacted by .50 caliber AP projectiles. These are very rough estimates from incomplete data. However, the estimated values of Λ_c' are appreciably below the Λ_c values.

7075-T6 ALUMINUM ROLLING GRAIN TRANSVERSE TO APPLIED LOAD		
Thickness (in.)	Estimated Impact Fracture Λ_c' (ksi/$\sqrt{\text{in}}$)	Estimated Static Fracture Λ_c (ksi $\sqrt{\text{in}}$)
0.090	48.9	68.3
0.125	42.6	62.5
0.250	34.0	66.6
0.375	51.4	87.0

(Ref. 2-2)

Additional comments on the observed impact fracture response of several aluminum alloys and some preliminary results for advanced composites are presented below.

Longitudinal Grain 7075-T6. Review of the limited available data indicates that the estimated lower bound for Λ_c' falls within the range of typical K_c values. The results of this review are presented in Figure 2-220. The typical K_c values were established from available test data. Based on the data presented, it would be reasonable to use K_c as a lower bound for threshold impact fracture for longitudinal grain 7075-T6 in thicknesses up to 0.750 inches. Further, it is noted that the experimental lower bounds on Λ_c' tend to lie in the upper portion of the K_c envelope as the panel thickness in increased. This indicates that using K_c for a lower bound may cause an unnecessarily severe penalty for thicker sections; i.e., the impact failure predictions may prove to be too conservative. To avoid this conservatism, the data indicates that it would be reasonable to use "typical" or actual K_c values for thin sections to predict a lower bound for threshold impact fracture for panel thickness up to 0.75 inches. As seen in the figure, Λ_c' for longitudinal-grain 7075-T6 ranges between 55 and 75 ksi $\sqrt{\text{in}}$., with no appreciable thickness effect evident.

Transverse Grain 7075-T6. Reference 2-2 provides considerable impact-fracture data for transverse-grain 7075-T6, and several data points are reported in Ref. 2-55. Evaluations of Λ_c' are compared with a K_c data envelope in Figure 2-221. The Λ_c' estimates fall within the K_c envelope, as with the case of longitudinal-grain 7075-T6; however, the Λ_c' data tends to fall in the lower region of the envelope. The range of Λ_c' for transverse-grain 7075-T6 is between 33 and 50 ksi $\sqrt{\text{in}}$., as compared with 55 to 75 ksi $\sqrt{\text{in}}$. for the lower-bound range of Λ_c' for the longitudinal-grain configuration.
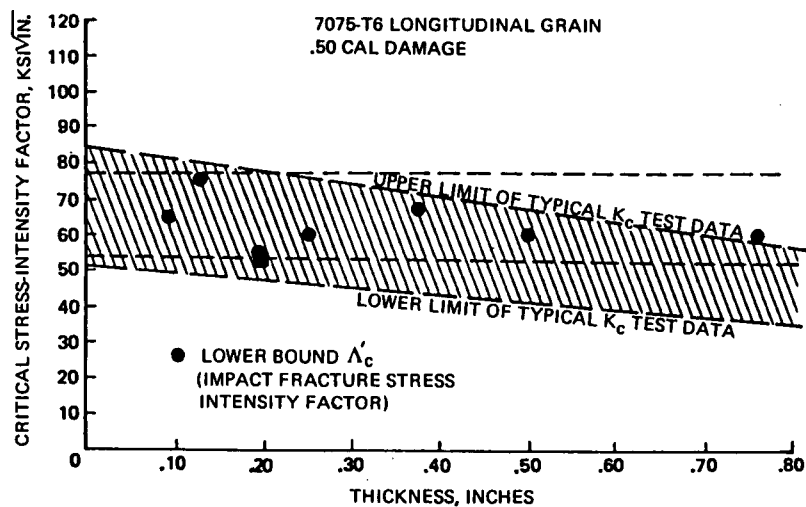
Figure 2-220. Impact Fracture Toughness Λ_c' and K_c of Longitudinal Grain 7075-T6
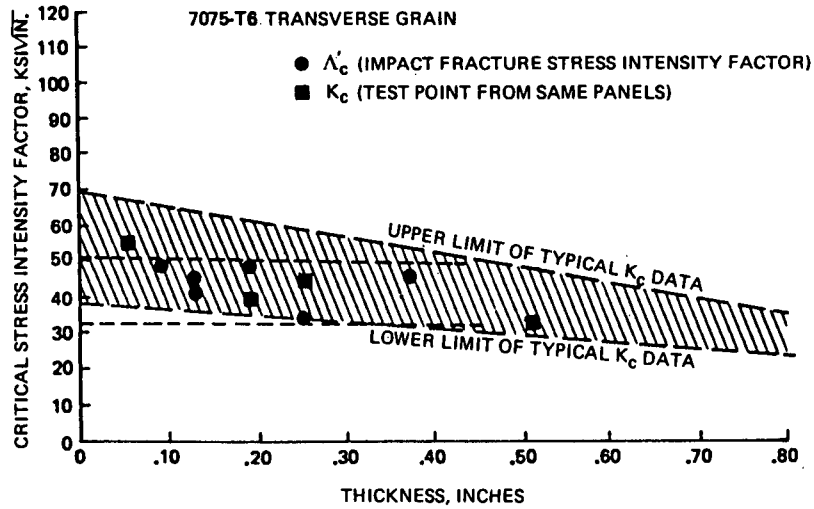
Figure 2-221. Impact Fracture Toughness Λ'_c and K_c of Transverse Grain 7075-T6

2024-T81 Aluminum. In Reference 2-2, a number of transverse-grain 2024-T81 panels were tested for impact fracture. The results were for thicknesses of 0.160 and 0.250 inches. The average Λ'_c for these data is 41 ksi $\sqrt{in}$.

6Al-4V MIL Anneal Titanium. Considerable transverse-grain 6Al-4V impact-fracture data is reported in Reference 2-2. In general, impact fracture did not occur in this material and it appears that the residual static strength predictions may be used.

Fiber Composite Materials. Experimental work with certain layups of fiber composite laminates has shown, as with metals, that the impact-fracture strength can be below the residual static strength. This is illustrated by some available impact-fracture and residual strength data shown in Figure 2-222. Test data for stressed boron/epoxy panels impacted with .50-caliber AP projectiles are shown, indicating the bracketing of the impact-fracture threshold. The residual strength of the ballistic-damaged panels and saw-cut notched panels are shown for comparison.

Using the available data for boron/epoxy and graphite/epoxy given in References 2-11, 2-12, 2-99 through 2-101 and 2-16, an analysis using the Λ'_c approach as described for metals was developed. It was found that the impact fracture toughness (Λ'_c) could be established by using the effective damage size (TD_{eff}) due to the projectile impact. The effective damage size is defined as the equivalent idealized flaw causing structural degradation. This is normally set equal to the predicted penetrater damage size, thus assuming that the maximum damage is oriented transverse to the stress field. As shown for residual strength, normalizing the test data to ultimate strength can be used to correlate materials having diverse layups and strength levels.

The numerical results of this assessment of test results are summarized in Table 2-33. The test data covers a range layup configurations and ultimate strength values. As seen in the table, there was some variation in Λ'_c/F_{tu} with different fiber systems and loadings. It should be noted that the impact-fracture toughness (Λ'_c) was not a constant percentage of ballistic-damage residual fracture toughness (Λ_c) for these test results, but demonstrated some variation with fiber/matrix types.
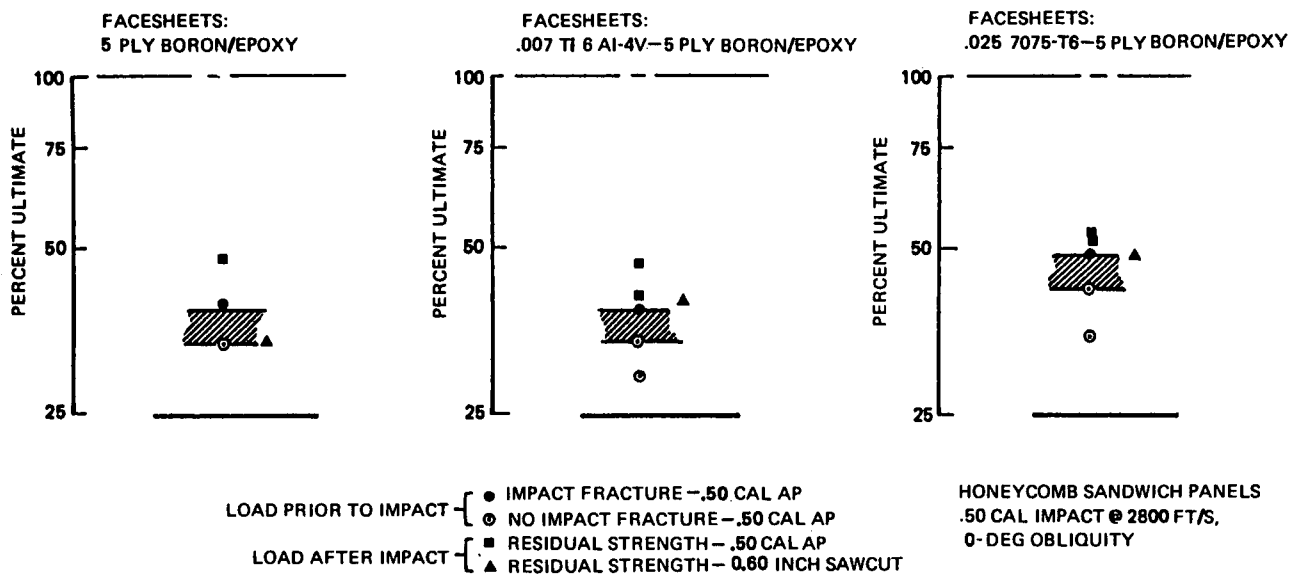
Figure 2-222. Strength of Boron-Epoxy Sandwich Panels Impacted by .50 Caliber Bullet

Table 2-33. Impact Fracture Data for Composite Panels

Material	Λ'_c/F_{tu} [1]	Λ_c/F_{tu} [2]	
Graphite/Epoxy			
T300/934	1.11 [3]	1.11	[1] $\Lambda'_c = \sigma'_c \sqrt{\frac{\pi}{2} TD_{eff}}$
T50-S/5206	0.54	0.61	
AS/3501	1.01 [3]	1.01	TD_{eff} = damage size
HT-S fiber	0.38	0.61	σ'_c = threshhold stress for impact fracture
HM-S fiber	>0.19 <0.31	0.53	
			[2] $\Lambda_c = \sigma_c \sqrt{\frac{\pi}{2} TD_{eff}}$
Boron/Epoxy			
Tension	0.41	0.51	σ_c = static residual fracture stress after impact damage
Beams, bending	0.48	0.53	
			[3] Test results are reported in Reference 2-12. These results indicated that the impact fracture threshold stress was not below the static residual fracture stress.
Hybrids			
$0_1 SGL/\pm 45_4$ AS/3501	1.07 [3]	1.07	
$0_2 SGL/\pm 60_4$ AS/3501	1.24 [3]	1.24	
$0_2 SGL/\pm 45_2$ T300/934	1.07 [3]	1.07	

2.5.1.3.2 Dynamic Stress Intensity Factors (From Reference 2-14)

When stresses are suddenly applied to a plate containing a crack and maintained at constant value for some arbitrary length of time, the stress-intensity factor is a variable function of time. In the case of suddenly applied extensional (i.e., membrane) loading there is a peak (Reference 2-81) in the opening mode membrane stress-intensity factor at the nondimensional time, $\tau = 2.9$, where:

$$\tau = 2c_2 t/D \qquad \text{(Eqn. 2-149)}$$

where:

D = Damage size

t = Actual time (seconds).

c_2 is the distortional wave speed given by:

$$c_2 = \sqrt{\frac{G}{\rho}} \qquad \text{(Eqn. 2-150)}$$

where G = Shear modulus

ρ = Mass density (e.g., slugs/ft^3)

Thus, the time required to obtain the peak in the membrane stress-intensity factor is

$$\bar{t} = 2.9D/2c_2 \qquad \text{(Eqn. 2-151)}$$

In the case of the suddenly applied bending moment (Ref. 2-82), the dynamic bending stress-intensity factor approaches the static stress-intensity factor without experiencing a peak. When $\tau = 2.9$, and with Poisson's ratio = 0.3, the dynamic bending stress-intensity factor is 65-percent of the static value if $2h/D = 0.5$, and is 73-percent of the static value if $2h/D$ is unity. Ratios of the dynamic to the static bending stress-intensity factors are not available for other 2 h/D ratios.

As a consequence of this, and the discussions presented in and in Sections 2.5.1.1.1 and 2.5.1.4, it is recommended that the peak dynamic stress-intensity factor be computed from

$$K = \sigma_m \left(\frac{\pi D}{2}\right)^{1/2} F_c(\lambda) + 0.5\sigma_b \left(\frac{D}{2} \frac{\lambda-1}{\lambda}\right)^{1/2} F_c(\lambda) G(\lambda) F_{d,b} \qquad \text{(Eqn. 2-152)}$$

where

$$F_{d,b} = \begin{cases} 1.0 \text{ if } 2h/D \geqslant 1 \text{ and } \tau = 2.9 \\ 0.73 \text{ if } 0.5 < 2h/D < 1 \text{ and } \tau = 2.9 \\ 0.65 \text{ if } 2h/D \leqslant 0.5 \text{ and } \tau = 2.9 \end{cases} \qquad \text{(Eqn. 2-153)}$$

if the peak dynamic stresses σ_m and σ_b are maintained for the nondimensional time $\tau = 2.9$. However, if the duration of the application of the stresses σ_m and σ_b is such that τ exceeds 2.9, it is recommended that $F_{d,b} = 1$ be used in Equation (2-152) in order not to underestimate the effect of the bending on the stress-intensity factor.

In Equation $(2-152)$, F_c $(\lambda)G(\lambda)$ accounts for the interaction between the crack and flaw. For a pair of cracks from the ends of an elliptic flaw, replace F_c with F_e from Figure 2-183 or Table 2-28. For a pair of cracks from the ends of an axis of a rectangular flaw, replace F_c with F_r from Figure 2-184. Until new experimental data becomes available for the fragment penetrations of high explosive projectiles, let the crack length be 0.03 inch in the computation of λ.

Insofar as σ_m and σ_b in Equation $(2-152)$ are concerned, as stated previously, let σ_m and σ_b be the peak values that are maintained continuously for at least $\bar{t} \geq 2.9$ $D/2c_2$ (see Equation 2-151). An alternate approach is to use time averaged stresses that are maintained continuously for $\bar{t} \geq 2.9$ $D/2c_2$. Fracture is predicted to occur if K from Equation $(2-152)$ is greater than K_c. Otherwise, the absence of fracture is predicted.

The concept of time-average stresses in Equation $(2-152)$ is based on heuristic reasoning, in order to arrive subsequently at predictions of fracture. Test data from carefully controlled tests are needed to assess the accuracy of fracture predictions based on the use of peak and/or average stresses in Equation $(2-152)$.

2.5.1.4 Effect of Combined Stress (From Reference 2-14)

In panels subjected to internal pressures from the detonation of high explosive projectiles or from hydrodynamic ram, there will generally be combined bending and membrane stresses. Crack propagation or catastrophic failure will be due to the combined state of stresses, and, the failure criterion should take into consideration the interaction between stress-intensity factors due to the membrane response and the bending response.

For an infinite plate with a crack of length D that is subjected to an in-plane extensional (i.e., membrane) stress σ_m that is oriented normal to the crack, the opening mode stress intensity factor is:

$$K_m = \sigma_m \sqrt{\frac{\pi}{2} D} \qquad \text{(Eqn. 2-154)}$$

If the membrane stress σ_m is replaced by a bending moment per unit length, M_b, such that the axis of the bending moment is parallel to the crack, the opening mode stress-intensity factor is (Ref. 2-80):

$$K_b = \sigma_b \sqrt{\frac{\pi}{2} D} \qquad \text{(Eqn. 2-155)}$$

with $\sigma_b = 6M_b/h^2$ $\qquad$ (Eqn. 2-156)

If the aforementioned crack were replaced by a radial crack of length D emanating from each end of a diameter of the circular flaw of radius R, then

$$K_b = \sigma_b \sqrt{\frac{\pi}{2} D} \ F(D/2R) \qquad \text{(Eqn. 2-157)}$$

where $F(D/2R)$ is a monotonically decreasing function given in Table 1 of the Roberts and Rich paper (Ref. 2-80). Equation $(2-157)$ reduces to Equation $(2-155)$ when R = 0.

Using the notation from Section 2.5.1.1.1, an alternate form for K_b can be developed, namely:

$$K_b = \sigma_b \sqrt{\frac{D}{2} \frac{\lambda-1}{\lambda}} \ F(\lambda-1) \qquad \text{(Eqn. 2-158)}$$

In the case of cracks emanating from rectangular or elliptic flaws rather than circular flaws, there are no equations available for determining K_b because of the lack of the analytic function $F(\lambda-1)$ in Equation $(2-158)$. Until exact analytic solutions become available for K_b in cases of cracks from the axes of elliptic and rectangular flaws, it is recommended that Equation $(2-159)$ be used elliptic flaws and Equation $(2-160)$ be used for rectangular flaws. Thus, for an elliptic flaw,

$$K_b = \sigma_b \sqrt{\frac{D}{2} \frac{\lambda-1}{\lambda}} \ F_e(\lambda) G(\lambda) \qquad \text{(Eqn. 2-159)}$$

where $F_e(\lambda)$ can be obtained from Figure 2-183 or Table 2-28 from Section 2.5.1.1.1. $G(\lambda)$ is obtained from Figure 2-223. Appendix C of Reference 2-14 includes additional information on $G(\lambda)$. For a rectangular flaw:

$$K_b = \sigma_b \sqrt{\frac{D}{2} \frac{\lambda-1}{\lambda}} \ F_r(\lambda) G(\lambda) \qquad \text{(Eqn. 2-160)}$$

with F_r to be obtained from Figure 2-184 of Section 2.5.1.1.1.

For circular flaws with cracks, K_b from Equation $(2-157)$ will equal K_b from Equation $(2-150)$ because of the definition of $G(\lambda)$. With the use of $G(\lambda)$ in Equations $(2-159)$ and $(2-160)$, the error in K_b for elliptic or rectangular flaws is unknown; however, it is believed that the error in K_b will not be of major significance. Moreover, it is believed that in many practical problems, membrane effects will predominate over bending effects and consequently the errors introduced by the use of Equations $(2-159)$ and $(2-160)$ will be of secondary importance in fracture predictions.
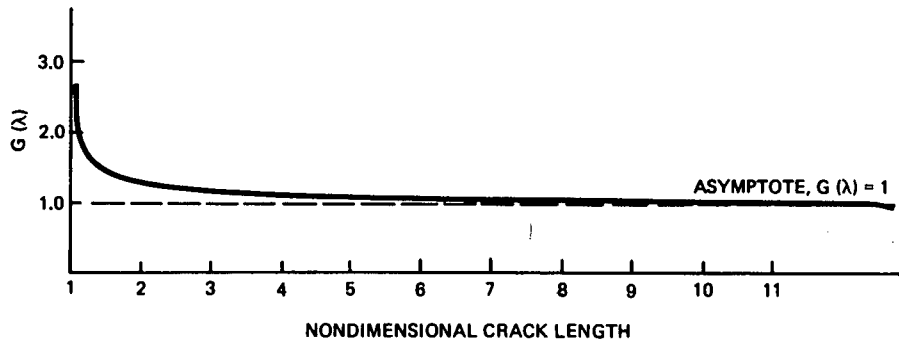
Figure 2-223. Values of G (λ) For Eqn. 2-159

From elementary stress analysis, based on linear theory, the total extensional stress on the outer fibers of a plate under combined membrane and bending loads is

$$\sigma = \sigma_m + \sigma_b \qquad \text{(Eqn. 2-161)}$$

If σ_0 is the extensional stress on the outer fiber and σ_i is the extensional stress on the inner fiber at a plate cross section, then

$$\sigma_m = (\sigma_0 + \sigma_i)/2 \qquad \text{(Eqn. 2-162)}$$

and

$$\sigma_b = \sigma_0 - \sigma_i/2 \qquad \text{(Eqn. 2-163)}$$

Analogous to the concept of superimposing a bending and membrane stress to obtain a total extensional stress, one may superimpose an opening mode bending stress-intensity factor, K_b, with an opening mode membrane stress-intensity factor, K_m, to obtain a total opening mode stress-intensity factor, namely,

$$K' = K_m + K_b \qquad \text{(Eqn. 2-164)}$$

In general, the opening mode stress-intensity factor is computed and compared with the fracture toughness K_c in order to predict the presence or absence of fracture for a particular problem. When comparisons with K_c are to be made for fracture predictions, it is recomended that K' from Equation (2-164) be replaced with:

$$K = K_m + \frac{1}{2} K_b \qquad \text{(Eqn. 2-165)}$$

The reason for introducing 1/2 before K_b in Equation (2-165) is based on experimental data and the recommendation in Reference 2-113 that for a quick estimate of crack growth rates in plates under cylindrical bending, one may use the extensional (i.e., membrane, data by merely replacing $K_{(m)}$ by $K_b/2$.

2.5.2 Analysis of Multiple Load Path Panels Containing Impact Damage

Many structural configurations cannot be represented as monolithic panels in assessing strength degradation from impact damage. The wings of transport aircraft, for example, often consist of skin with riveted stiffeners. The stiffeners can provide damage-containment or crack-arrestment capability that is not considered in the element residual strength analysis procedures presented in Section 2.5.1. Since the crack-arrestment capability can significantly improve the residual strength of damaged structure, the stiffening must be included in the analysis. This section discusses the response of stiffened panels to projectile damage, and available analytical techniques for residual strength prediction.

Figure 2-224 shows several typical damage configurations involving skin and stiffeners. In Figure 2-224(a), the damage is confined to the skin between the stiffening elements. This would be typical of a small-arms impact into the skin between stiffeners, or an entry damage from a delay fuzed HE projectile. In (b) the damage is confined to the skin but reaches into two skin bays. This damage configuration, often used in fatigue-damage analysis, is probably not typical for projectile impact damage. When the skin damage extends into more than one bay, the intermediate stiffener normally would be damaged. This is illustrated in (c) where both the skin and stiffener are damaged with the skin damage extending into two bays. Damage of this type will generally be the critical case for projectile impact damage tolerance analysis.

HE projectiles have the capability to damage several skin bays, and sever all the intermediate stiffening elements. For the particular case investigated, the threat and structural parameters such as stiffener spacing must be used to establish the extent of damage.

A) DAMAGE BETWEEN STIFFENERS

B) DAMAGE ACROSS A STIFFENER
—STIFFENER INTACT

C) DAMAGE ACROSS A STIFFENER — STIFFENER FAILED

Figure 2-224. Typical Damage Configurations Involving Stiffeners and Skin

2.5.2.1 Analytical Approach

The following discussion of the tensile failure of damaged stiffened structure is drawn from H. Vlieger (Ref. 2-88, 2-107 and 2-108). In a cracked stiffened panel, the stiffener tends to decrease the stress at the crack tip by permitting the transfer of load from sheet to stiffener. In this connection, two dimensionless parameters are significant: the tip stress reduction factor and the stiffener load concentration factor. The tip stress reduction factor, Y, is defined as the ratio of stress intensity factors for sheets with and without stiffeners.

$$Y = \frac{K_{stiffened}}{K_{unstiffened}} < 1. \qquad \text{(Eqn. 2-166)}$$

The stiffener load concentration factor is defined as the ratio of the maximum stiffener load and the load in the stiffener at the end of the panel, remote from the damage:

$$C = \left[\frac{F_{max}}{F}\right]_{stiffener} > 1. \qquad \text{(Eqn. 2-167)}$$

The values of both Y and C depend on the relative stiffness of sheet and stiffener and on the ratio of crack length and stiffener pitch.

Two basic cases of stiffened panel failure will be considered. The residual strength diagram for the stiffener critical case is shown in Figure 2-225 and the skin critical case is shown in Figure 2-226. For the stiffener critical case consider a simple panel with two stiffeners, containing a central crack. When this panel contains a crack that is small at the onset of instability, the stress condition at the crack tip will hardly be influenced by the stiffeners, and

Figure 2-225. Residual Strength Diagram for Stiffened Panel

Figure 2-226. Panel Configuration with Heavy Stiffeners. "Skin-Critical" Case

the gross stress causing unstable crack propagation will be the same as that of an unstiffened sheet. When the unstably growing crack approaches the stiffener, the load concentration in the stiffener will be so high that the stiffener fails without stopping the crack.

When the panel contains a crack extending almost from one stiffener to the other, the stiffener will be extremely effective in reducing the stress intensity at the crack tips, resulting in a higher value of the gross stress at crack growth initiation compared with the unstiffened sheet. With increasing panel load, the crack tip will get closer to the stiffener and due to the inherent increase of stiffener effectiveness, the crack growth will remain stable. Fracture of the panel will occur at the stress level indicated by $\bar{\sigma}$ due to the fact that at this level the maximum stress in the stiffener has reached the ultimate strength of the stiffener material.

When the crack is of an intermediate size (2a), there will be unstable crack growth at a stress slightly above the fracture strength of the unstiffened sheet, but this will be stopped under the stiffeners. After crack arrest the panel load can be further increased. During the application of this final load increment, the tip stress is also raised and some additional stable crack growth may occur before the ultimate stiffener load is reached, again at the stress level.

For the simple example in Figure 2-225, the foregoing considerations imply a predicted residual strength curve of the shape indicated by the heavy line. This curve contains a horizontal part determined by the stiffener strength and the tip stress reduction at panel failure after crack arrest. For initial crack lengths smaller than the stiffener pitch, this flat part constitutes a lower bound of the residual strength. It intersects the residual strength curve of the unstiffened panel at a crack length $\overline{2a}$. Assuming that the effect of the stiffener on the stress condition at the crack tip will be negligible for this crack length, this value of $\overline{2a}$ will constitute a lower limit of crack lengths for which crack arrest will occur. For this reason, $\overline{2a}$ is called the "threshold crack length." This value of $\overline{2a}$ divides the range of crack lengths considered here into an interval containing short crack lengths for which panel behavior is not affected by the presence of stiffeners and an interval of long cracks that, after some unstable growth, are stopped under the stiffeners.

For heavy stiffening ratios, skin failure may be the critical event as shown in Figure 2-226. Due to a low stiffener load concentration, the stiffener failure curve and fracture of stiffened panel curve do not intersect. In Figure 2-226 a crack size of 2a will show stable growth at point B and become unstable at point C. Crack arrest occurs at D from where further slow growth can occur if the load is raised. Finally at point E the crack will again become unstable, resulting in panel fracture.

The "threshold crack length," $\overline{2a}$, for the skin failure case is determined by projecting point E horizontally until it intersects the unstiffened panel fracture curve. This horizontal line, $\overline{\sigma}$, constitutes a lower bound of the residual strength. This value of $\overline{2a}$ divides the range of crack lengths considered into an interval containing short crack lengths for which panel behavior is not affected by the presence of the stiffeners and an interval of long cracks that, after some unstable growth, are arrested. It should be clear from the above discussion that it is not essential for crack arrest that the crack runs into a fastener hole. Crack arrest is basically a result of the reduction of crack tip stress intensity due to load transmittal to the stiffener. The criterion for crack arrest has to involve the two alternatives of stiffener failure and skin failure, depending upon the relative stiffness of sheet and stiffener. The above discussion assumes that the fastener loads do not exceed fastener capability.

So far, only the panel configuration with two stiffeners and a central crack has been considered. However, similar considerations are valid for cracked panels with more stiffeners and other locations of the crack with respect to intact and broken stiffeners.

For this methodology, the residual strength of a stiffened panel is determined from the residual strength of the unstiffened sheet by accounting for the sheet-stiffener interaction in the cracked region. The residual strength characteristics of the relevant material are sometimes not available but can be determined by a small number of tests. The interaction of sheet and stiffener is expressed by the values of Y and C.

To construct the residual strength diagrams in Figure 2-225 and 2-226, the unstiffened panel fracture curve, Y and C are needed. Basically, the stiffened panel fracture curve can be obtained by raising all points of the unstiffened panel fracture curve by a factor, 1/Y. The stiffener failure curve can be obtained by dividing the ultimate tensile stress of the stiffener by C. The stiffener curve is usually modified by a constant correction factor to account for load eccentricity and notch effects.

The finite element method or an analytical method proposed by Vlieger (Ref. 2-88), can be used to calculate Y and C. The analytical method has an advantage over the finite element method in that the effect of different panel parameters on the residual strength of a certain panel configuration can easily be assessed so that the stiffened panel can be optimized for battle damage. The finite element method has an advantage in that it is relatively easy to incorporate such effects as stiffener eccentricity, hole deformation and yielding.

The analytical method proposed by Vlieger for calculating Y and C consists of dividing the stiffened panel into its composite parts, the skin and the stiffener. In the area of the crack some load from the skin will be transmitted to the stiffener. This load transmission takes place through the fasteners, which implies that the skin will exert forces on the stiffener and the stiffener will exert forces in the opposite direction on the skin.

The problem is reduced now to that of an unstiffened plate loaded by a uniform stress and fastener forces, $F_1...F_n$. This case can be considered as a composition of three separate cases: 1) a uniformly loaded cracked sheet, 2) a sheet without a crack, loaded with forces, $F_1...F_n$, and 3) a cracked sheet with forces on the crack edges given by the function, p(x). The forces, p(x), represent the load distribution exerted on the edges of the slit to provide the necessary stress-free crack edges. The stress conditions at the crack tip in these three cases have to be determined. In terms of stress intensity factors it can be seen that for case 1) $K = \sigma \sqrt{\pi a}$ and for case 2) $K = 0$. The stress intensity factor for case (3) is a fairly complicated expression and the integral has to be solved numerically. To determine Y and C the fasteners forces have to be known. Compatibility requires equal displacement at the corresponding fastener locations of sheet and stiffener. These compatibility requirements deliver a set of n (n = number of fasteners) independent algebraic equations from which the fastener forces can be solved. After the fastener forces have been determined, the calculation of C and L are easily completed. Additional problems and refinements in adapting the methodology to a particular type of material and panel configuration are covered in Ref. 2-88.

In the analytical method adhesive bonded and integral stiffeners can be treated by assuming uniformly distributed fasteners forces, $F_1...F_n$, along the stiffeners. It should be noted that the criterion of stiffener failure is not relevant in case of integral stiffeners, since the crack can run right through the stiffeners. In that case there will only be a skin crack propagation criterion, but this will still be different from the case of mechanically fastened stiffeners. In the case of adhesively bonded stiffeners the criterion of fastener failure will be important. Load transmittal from skin to stiffener in the cracked area will set up high shear stresses in the bond. This may lead to decohesion and consequently, a decrease of the effectivity of the stiffener to take load from the skin. Decohesion will alter the residual strength diagram as in the case of fastener failure.

Arrest of unstable crack growth at the next stiffener is governed by three criteria: 1) stiffener failure, 2) fastener failure or bond failure, and 3) skin crack propagation. If any of these three criteria are met, total failure will occur. Application of the above methodology has shown good correlation with test results for metal stiffened panels.

2.5.2.2 Finite Element Analysis of Damaged Multiple Load Path Panels

Finite element methods have been developed (2-89, for example) for predicting the stress intensity factor for cracks and stress concentration factors for stiffeners. A finite element analysis is effective in applications where complicated boundary conditions and geometry rule out an exact solution for the crack tip stress intensity factor. Skin panels are idealized using constant strain triangular membrane elements, typical stiffeners as rod elements and fasteners as shear spring elements. A special element, known as a cracked (or singular) element is used at the crack tip. This element has special properties which allow the stress at the crack tip to approach infinity, hence an accurate idealization of the structure can be realized without using a very fine mesh of elements at the crack tip.

Once the internal loads and deflections have been obtained from the finite element solution, the stress intensity factor may be calculated using the following equation:

$$K_I = \frac{Ev}{4}\left[\frac{2\pi}{r}\right]^{\frac{1}{2}}$$

where: K_I is the Mode I stress intensity factor, "v" is the crack opening displacement along the crack surface at a radial (in this case, along the crack) distance "r" from the crack tip, and E is the elastic modulus of the material.

Each displacement (v_1, v_2, v_3...) along the crack is substituted in the above equation with corresponding radial distance (r_1, r_2, r_3...) and the values of the stress intensity factor (K_1, K_2, K_3....) are determined. These values are then plotted versus the radial distances. A least square straight line fit of the data is then performed and by extrapolating for the value of K_I at r = 0, the stress intensity factor at the crack tip can be found. Figure 2-227 shows the procedure. It should be noted that the stress (stress concentration factor) carried by each stiffener is determined directly by the finite element program.

a) CRACK-TIP DISPLACEMENTS

b) EXTRAPOLATION OF RADIAL STRESS INTENSITY FACTORS TO FIND CRACK-TIP STRESS INTENSITY FACTOR
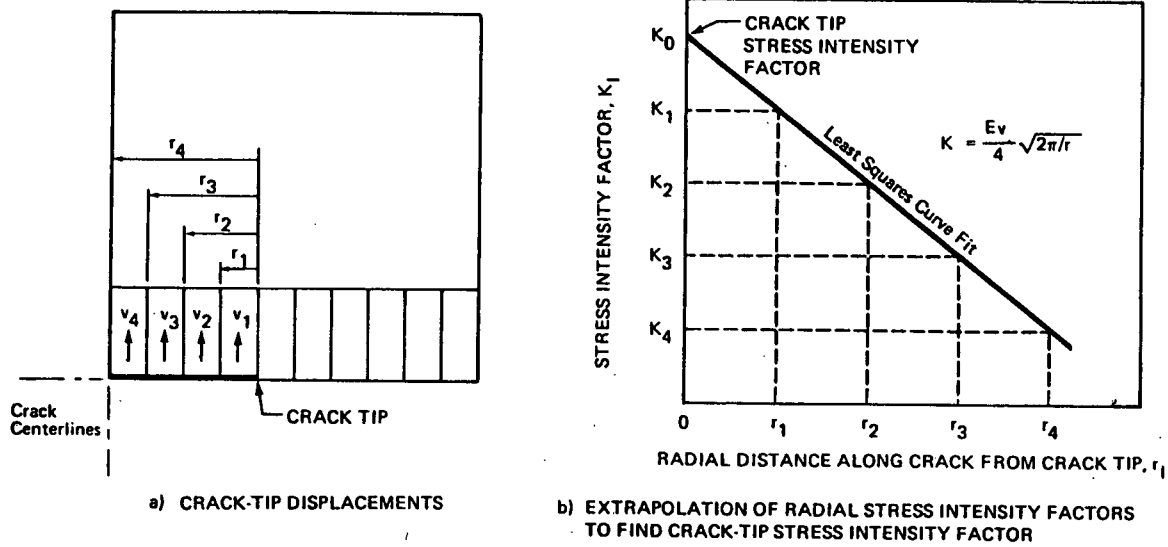
Figure 2-227. Finite Element Method for Determining Crack-Tip Stress Intensity Factors in a Damaged Stiffened Skin

The stress intensity and stress concentration factors can be found in this manner for any built-up structure, and stress intensity and stress concentration correction factor curves, such as those shown in Figures 2-228 and 2-229, can be constructed.

To use these curves, the stress intensity factor, K, at the crack tip is calculated using:

$$K = \sigma \sqrt{\pi a}\, Y_{SR}\, Y_\sigma$$

where:

K = the stress intensity factor
σ = the applied skin stress
a = half the damage size (shown as L on Figure 2-228)
Y_{SR}, Y_σ = the correction factors for the bay width and remote stress influence on the stress intensity factor (from curve, see Figure 2-228).

The stress in the stiffener, σ', is calculated using:

$$\sigma' = \sigma\, C_s\, C_\sigma$$

where:

σ' = the stress in the stiffener
σ = the applied stiffener stress
C_s, C_σ = the correction factors for the bay width and remote stress influence on the stiffener stresses (from curve, see Figure 2-229).

The residual strength of the structure can be determined by comparing the computed stress intensity or stress concentration factor with known critical values.
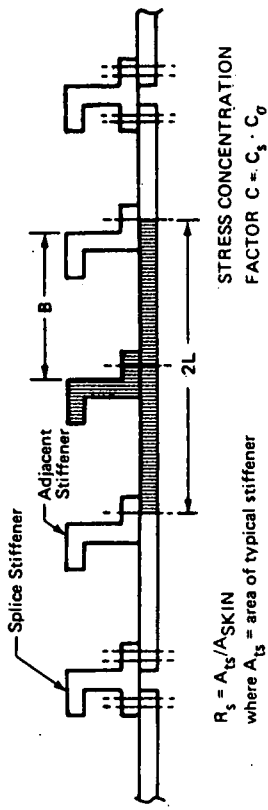
Splice Stiffener

Adjacent Stiffener

B

2L

$R_s = A_{ts}/A_{SKIN}$
where A_{ts} = area of typical stiffener

STRESS CONCENTRATION FACTOR $C = C_s \cdot C_\sigma$

a) Influence of Stiffening

C_s — 1.8, 1.6, 1.4, 1.2, 1.0

BAY WIDTH, B (inches) — 5, 6, 7, 8, 9, 10

Adjacent Stiffener
Splice Stiffener

$1.0 < R_{sp} < 3.0$

$R_s = 0.4$
0.7
1.0
$R_s = 0.4$
1.0

b) Influence of Remote Stress

C_σ — 1.1, 1.0, 0.9, 0.8

APPLIED REMOTE STRESS, σ(ksi) — 20, 24, 28, 32, 36, 40

2024 and 7178 Aluminum

$R_s =$
0.4
1.0 } 7178, 2024
$0.4 < R_s < 1.0$; 7178
$R_s = 1.0$
0.7
0.4 } 2024
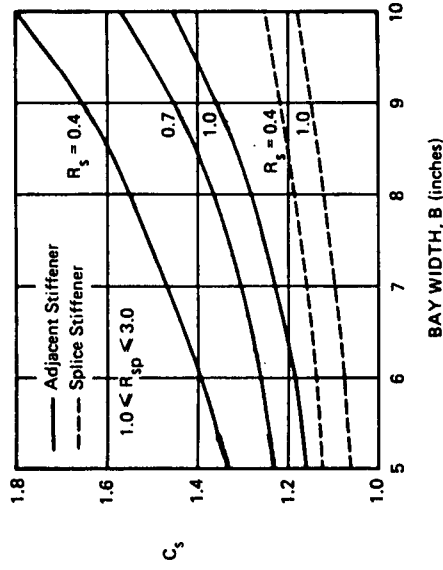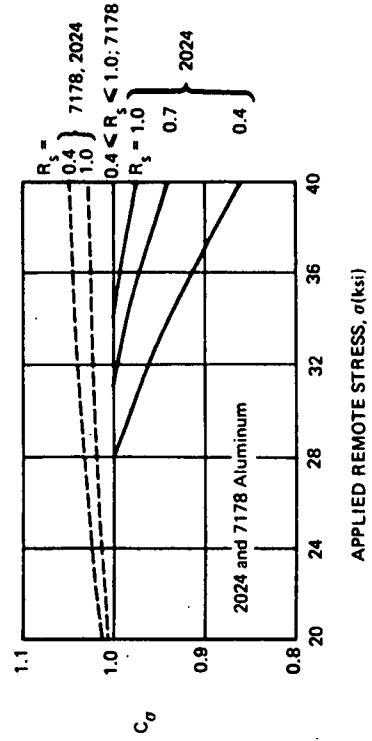
Figure 2-229. Stress Concentration Factors for Intact Stiffeners in a Panel With a Two-Bay Crack (Broken Central Stiffener)

B

2L
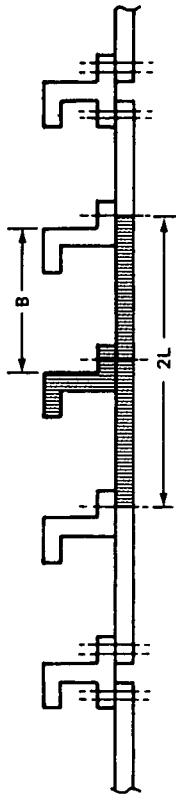
$R_s = A_{ts}/A_{SKIN}$
where A_{ts} = area of typical stiffener

$K = (\sigma\sqrt{\pi L}) Y_s$
$Y_s = Y_{SR} \cdot Y_\sigma$

a) Influence of Stiffening

Y_{SR} — 1.0, 0.9, 0.8, 0.7, 0.6

BAY WIDTH, B (inches) — 5, 6, 7, 8, 9, 10

$1.0 < R_{sp} < 3.0$

$R_s = 0.4$
$R_s = 0.2$

b) Influence of Remote Stress

Y_σ — 1.4, 1.2, 1.0, 0.8

APPLIED REMOTE STRESS, σ(ksi) — 20, 24, 28, 32, 36, 40

$0.4 < R_s < 1.0$
$1.0 < R_{sp} < 3.0$

2024 and 7178 Aluminum
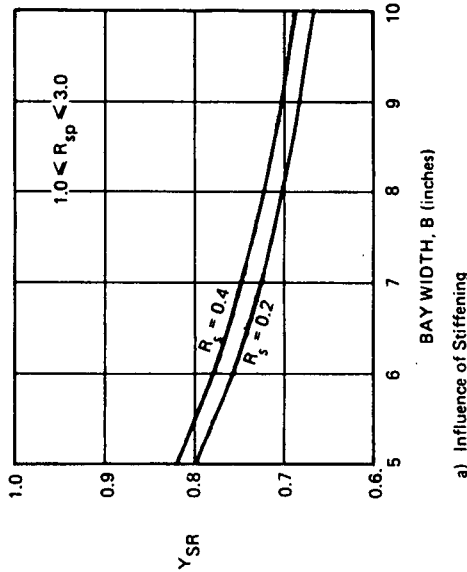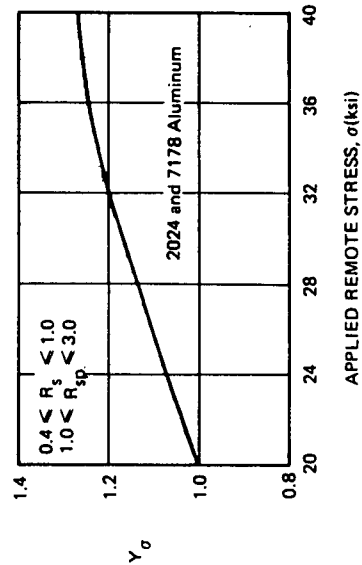
Figure 2-228. Stress Intensity Factors for a Two-Bay Skin Crack Centered Over a Broken Typical Stiffener

2.5.2.3 Engineering Analysis Method (Porter, 1974)

An alternate analysis method has been developed (Reference 2-7) from empirical data, by T. R. Porter. This method is useful because of its compatibility with the monolithic panel analysis presented earlier, and its simplicity. Figure 2-230 illustrates the technique. The "plateau" strength (σ_c Stiffened) is related to the unstiffened critical fracture stress for a full-bay crack (σ_c Unstiffened) by the ratio termed C_{Exp}.

The value of C_{Exp} is determined from the relationship shown in Figure 2-231 where C_{Exp} is related to stiffener area, skin gage, stiffener spacing, and yield strengths. It should be noted that the value of $_c$ (Unstiffened) is determined from fatigue-cracked (notch-sensitive) data even for evaluating ballistic-damaged panels. In stiffened panels containing small ballistic damages where the critical stress given by Λ_c (or Λ'_c) is greater than σ_c Unstiffened, the panel strength evaluated by Λ_c (or Λ'_c) would apply. This is illustrated in the figure.
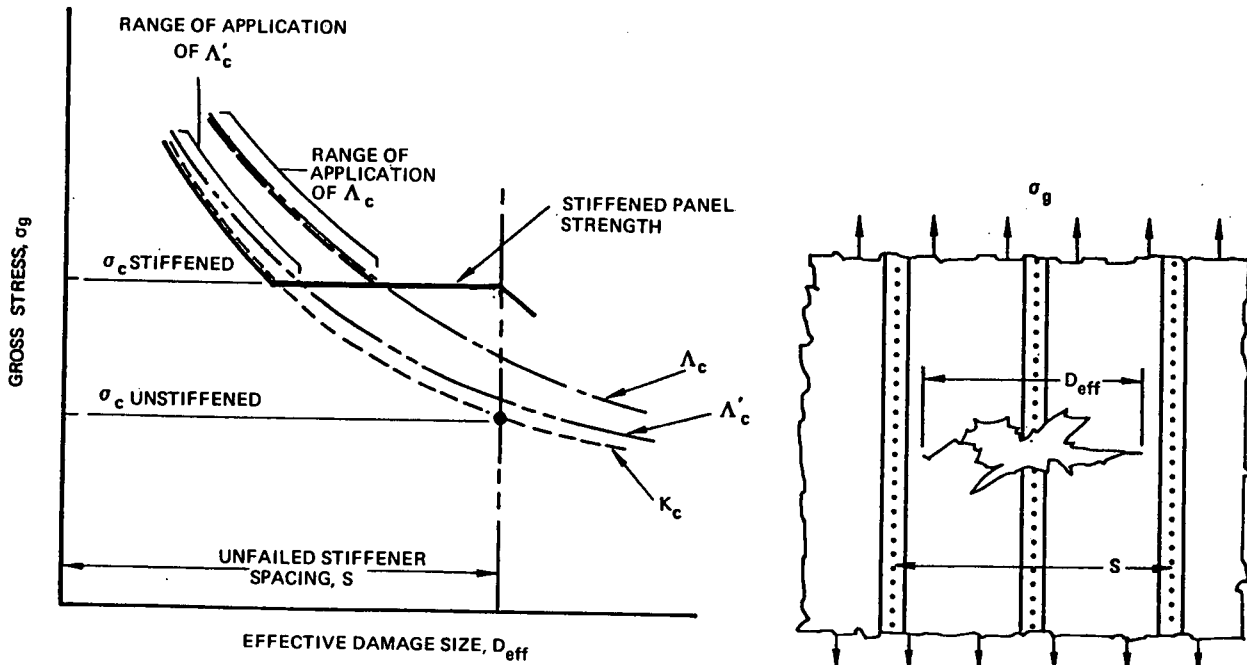
Figure 2-230. Residual Strength Assessment of Projectile Damaged Stiffened Panel

$$C_{EXP} = \frac{\text{FAILURE STRESS OF UNSTIFFENED PANEL}}{\text{FAILURE STRESS OF STIFFENED PANEL}}$$

$$R_{F_{ty}} = \frac{A_{STIFFENER}}{(t_{SKIN})(STIFFENER\ SPACING)} \times \frac{F_{ty}STIFFENER}{F_{ty}SKIN}$$

TEST DATA FOR RIVETED STIFFENERS
SKIN MATERIALS:
2024-T3, 7075-T6, 7079-T6
STIFFENER MATERIALS:
2024-T3, 7075-T6, 7079-T6, 430
301 FH, 6-4 D.A.
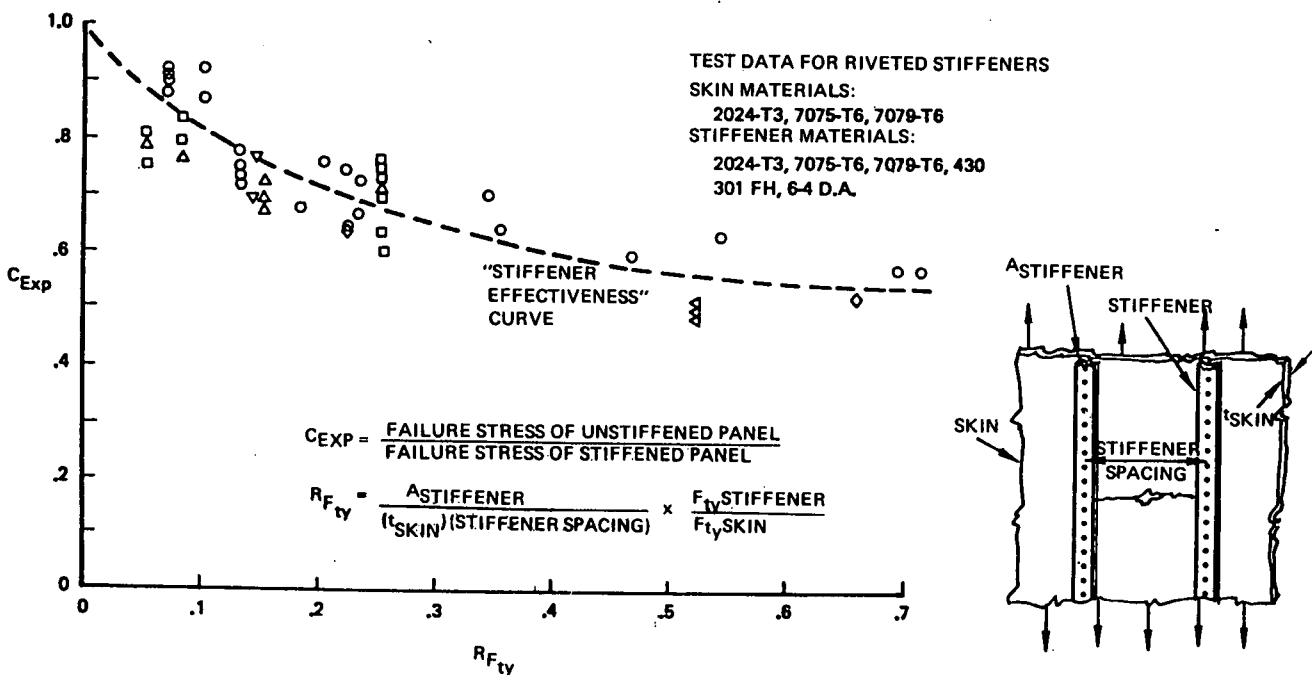
Figure 2-231. Empirical Determination of the Residual Strength of Stiffened Panel

2.5.3 Analysis of Multi-Element Structure Containing Impact Damage

The methods presented previously for predicting the structural capability of damaged elements and crack-arresting structure can be applied directly to many areas of the aircraft. However, the infliction of damage in highly redundant aircraft structural elements can cause a complex redistribution of internal loads among the elements. The availability of alternate load paths results in enhanced residual strength capability even though element failures occur.

2.5.3.1 Finite Analysis Techniques for Damaged Structure

A powerful tool for the residual strength analysis of damaged structural components (a wing or wing segment, for example), is the general purpose finite-element structural analysis computer program. These programs are commonly used in structural design analysis. Their application to damaged or altered structure is a logical extension, and has been demonstrated in several investigations (References 2-12, 2-63). Every major airframe manufacturer has finite-element program suitable for this purpose.

The operational theory of finite-element structural-analysis computer programs will not be discussed in detail here, as it is well known and well documented (Reference 2-84, for example). The basic approach is to develop a model or "structural idealization" of the component, using discrete structural elements such as plates, beams and rods. The discrete elements are connected at node points that have been established from a three-dimensional grid layout of the structural component. The elements and their properties are selected so that they duplicate the stiffness properties of the actual structure between node points.

Loads, calculated so that they provide reactions equivalent to the flight-loading conditions of the actual structural component, are applied at the node points. The matrix manipulation routines included in the computer program then develop the overall structural response of the component, by formulating the component stiffness matrix from the collection of element stiffness matrices. The output of the computer program is typically the deflections at the node points and the stresses in the elements. In essence, the computer program provides the stresses in the model elements, and these can be translated to stresses in the actual structure elements by the analyst.

The utility of these techniques for impact damage tolerance analysis lies in the fact that impact damage can be incorporated into the model by altering the stiffness properties of the damaged elements. This alteration must be made using damage models of the type discussed in Section 2.2, that relate damage size to threat, and of the type discussed in Section 2.4 that relate stiffness degradation to damage.

Using the altered element stiffness properties, the finite-element computer program can then reanalyze the structure and develop the redistribution of element stresses caused by the damage. The strength capability of the damaged structural component for any desired flight loading condition can then be determined by comparing the redistributed element stresses with structural failure criteria, including those defined in Sections 2.5.1 and 2.5.2 for damaged elements and crack-arresting structure.

Figures 2-232 to 2-234 show key aspects of the application of finite-element structural analysis to damaged structure. Figure 2-232 is a wing plan view showing the section to be analyzed for survivability to typical HE projectile impact. Figure 2-233 is the nodal diagram for the wing section. Considerable engineering judgment must be applied in preparing a nodal diagram that will ensure realistic results. Figure 2-234 is the element diagram, indicating the various elements selected for the idealization. Typical element selection might include:

1. Upper and lower skin plates -- Stiffened plates carrying shear and axial load. Stiffeners are included as part of the plate properties.

2. Spar and rib web plates -- Spar webs may be modeled as plates capable of carrying shear only.

3. Spar and rib stiffeners -- These elements may be modeled as beams carrying axial load.

4. Spar chords -- All spar chords are modeled as beam elements carrying both axial and bending load.

Figure 2-235 shows the loads applied at the nodes for a particular flight-loading condition. For example, these loads may be selected to represent flight conditions at limit load factor, or any load factor of interest.

The modeling developed at this point is that of the damaged structure. The program should now be run so that element stresses and deflections for the undamaged case are available for comparison with the damaged cases. Following this, elements are altered as shown in Figure 2-236, in accordance with a damage model, and the reanalysis was completed for comparison with element failure criteria.
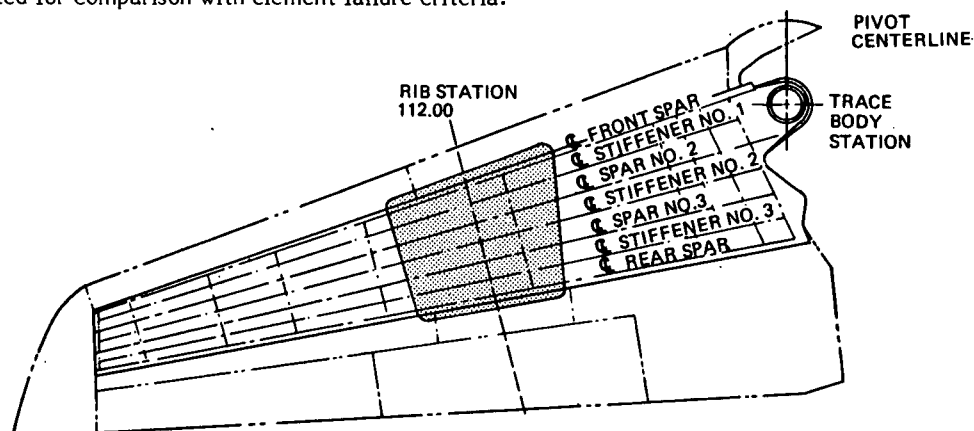
Figure 2-232. Wing Plan View
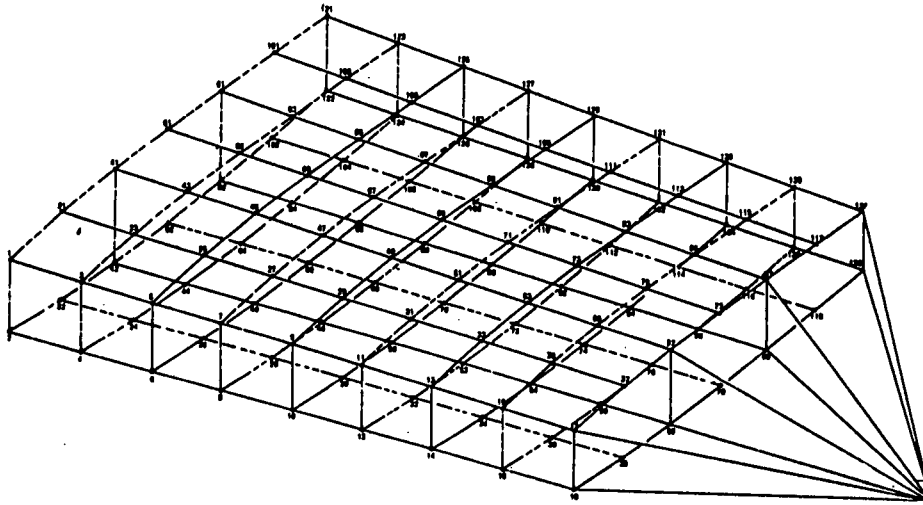
Figure 2-233. Wing Nodal Diagram
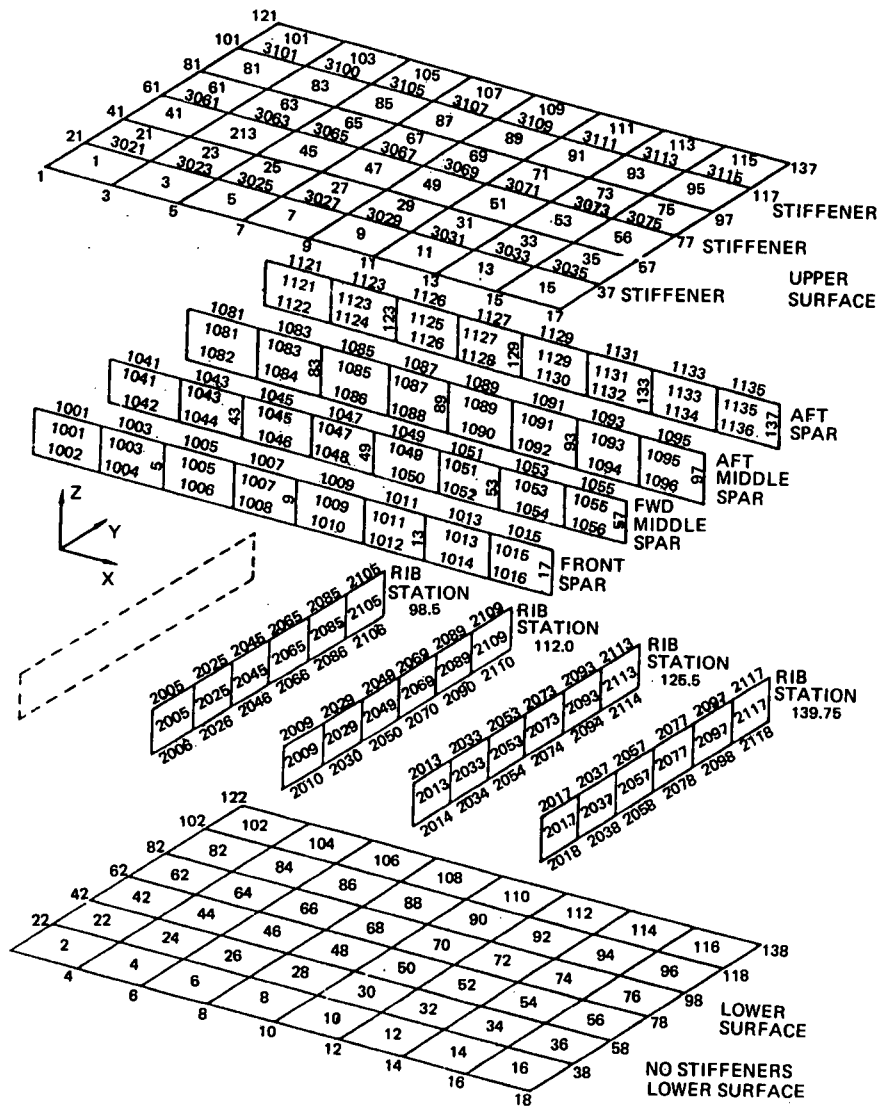
Figure 2-234. Wing Element Diagram
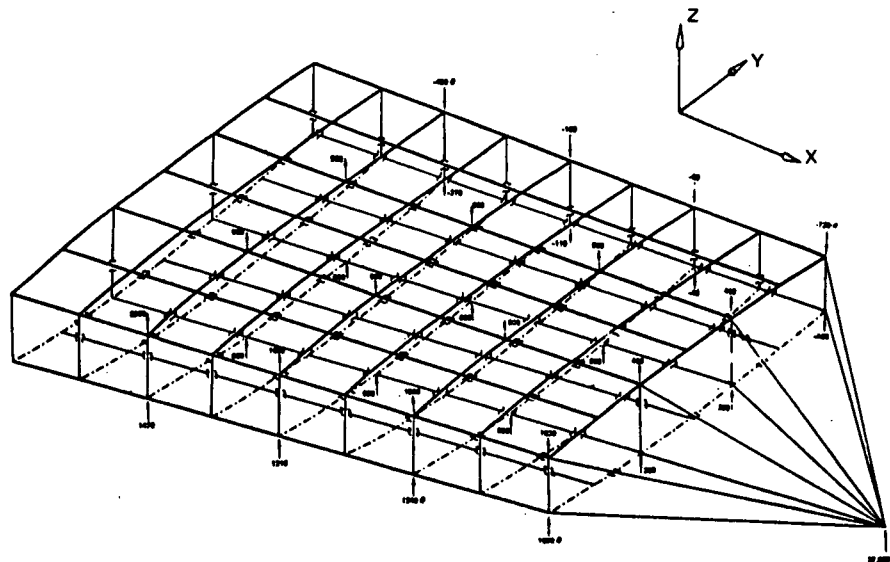
Figure 2-235. Wing Loads Diagram

XX — NODE NUMBERS
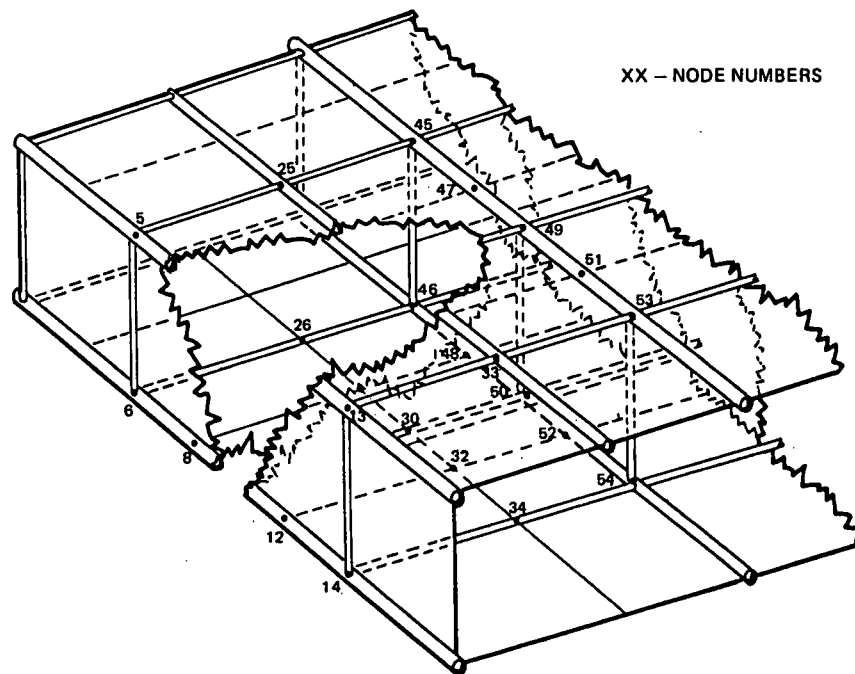
Figure 2-236. Schematic of Damaged Wing

2.5.3.2 Application of Finite-Element Techniques to Damaged Structure

Dr. Pao C. Huang, in Reference 2-114, has introduced a "Patching Technique" for the development of a finite element model representing a battle-damaged aircraft. This technique is summarized here and the applications of preprocessors PING and BING to the automatic generation of input data for NASTRAN analyses are also briefly described. Finally, the importance of modeling technique is addressed.

Finite Element Program - NASTRAN. NASTRAN, a general purpose finite element program for structural analysis developed by NASA, can be used as an example of a program for which data generation can be an overwhelming task. NASTRAN is versatile and applies to a large class of static and dynamic problems as follows:

a. Static response to concentrated and distributed loads, thermal expansion, and enforced deformation;

b. Dynamic response to transient loads and random excitation;

c. Determination of real and complex eigenvalues for use in vibration analysis and stability analysis.

However, preparing NASTRAN input for a complicated problem is a large effort in itself. It includes a layout of a grid mesh; calculations of grid point locations; generation of element properties and their connections to grid points; preparation of input sheets; and, finally, punching of input cards. All this work is time consuming and requires the effort of a team of specialists. Furthermore, possible occurrences of human errors together with unavoidable redesign cycles make the analysis formidable.

To remedy these difficulties, special input generation programs have been developed to automatically generate finite element models and their associated NASTRAN input for air vehicle structures.

Preprocessors for NASTRAN. A Planform Input Generator (PING) (Reference 2-115) which can rapidly develop a finite element model for an arbitrary wing planform of an air vehicle, and a Body Input Generator (BING) (Reference 2-116) which performs the same function for any type of shell body are currently operational. Utilizing these two preprocessors, a complete vehicle such as shown in Figure 2-237 can be easily and quickly generated for rigorous structural analyses. These two preprocessors contain many useful features which can be utilized to facilitate the development of a model to truly simulate a real missile.

The efficiency of PING is demonstrated in Figure 2-238 where a finite element model of a double wedge, solid, sweptback wing is shown as an example. This finite element model has 277 grid points, 260 plate elements, and 1400 degrees of freedom. PING was employed in the development of this mode . It only took five manhours and a few seconds of computer time to produce 1137 input cards for NASTRAN analysis.

Without PING it would take at least 360 manhours to produce the same number of cards manually. The capability of developing a finite element model rapidly and economically is an essential requirement for such complicated work as the vulnerability study of battle damaged structures.
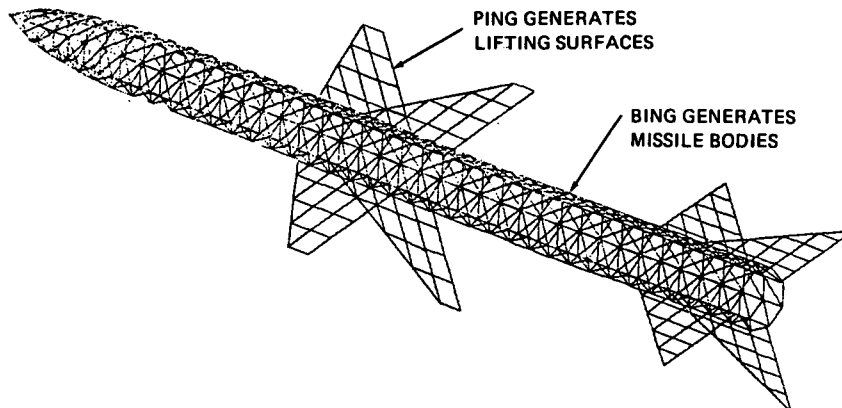
Figure 2-237.   A Complete Finite Element Model For Structural Analysis

DATA GENERATION	NASTRAN		PING/NASTRAN	
BASIC PLANFORM INFORMATION I OVERALL DIMENSIONS II MESH LAYOUT III AERO DATA	277 GRID POINTS 260 ELEMENTS		6 GRID POINTS	
	TIME (MAN HOUR)	NO. OF CARDS	TIME (MAN HOUR)	NO. OF CARDS
COMPUTATION	280	0	3	0
WRITE-UPS IN PROGRAM FORMATS	40	0	1	0
CARD PUNCHING	24	1137	.5	29
VERIFICATION AND CORRECTION (10%EST.)	16	114	.5	3
INPUT CARDS REQ'D. FOR NASTRAN		1137		1137
CARDS MANUALLY PUNCHED		1251		32
TOTAL TIME REQUIRED	360		5	

Figure 2-238.   Efficiency of Ping/Nastran

Figures 2-239 to 2-240 show some of the sample finite element models developed by PING and BING. Figure 2-239 demonstrates the useful feature of a mixed mesh which can be used to reduce the degrees of freedom in less important areas. Figure 2-240 shows a model of a curved delta wing. Figure 2-241 illustrates how patches with a circular or ellipitical hole can be used with a finer mesh around the hole for more detailed stress distribution. Figure 2-242 shows a wing with an elliptical hole which can be developed in two stages. First, a wing model without hole is developed and the elements around the hole are removed; then a patch with the hole can be developed to fit in the opening. Figure 2-243 shows a complicated but realistic missile body generated by BING. It has a nose cone and a cylindrical shell with an engine housing. Figure 2-244 shows a finite element model of a BQM 34A wing. This built-up wing has three spars connecting two curved panels. Again, a mixed mesh is used in the wing panels to reduce the degrees of freedom without sacrificing the accuracy in the important wing root area.

Using the preprocessors and NASTRAN, reliable analytical results can now be obtained easily and rapidly. Figure 2-245 shows the good correlation of the theoretical and experimental data. The latter were provided by the Naval Research Laboratory from a complete vibration test of the actual missile. The theoretical results were obtained by NASTRAN on a finite element model developed by PING and BING. It only took 40 manhours to complete the vibration model and 1200 seconds of CDC 6500 computer time to obtain the first six vibration modes. With these powerful analytical tools, elaborate structural analysis certainly becomes practical in the development of a complicated air vehicle system.

REQUIRED INPUTS CARDS

	NASTRAN	PING
NODES	277 GRID CARDS	17 CARDS
ELEMENTS	230 CQUAD2 30 CTRIA2 230 PQUAD2 30 PTRIA2	

[1385 DEGREES OF FREEDOM]
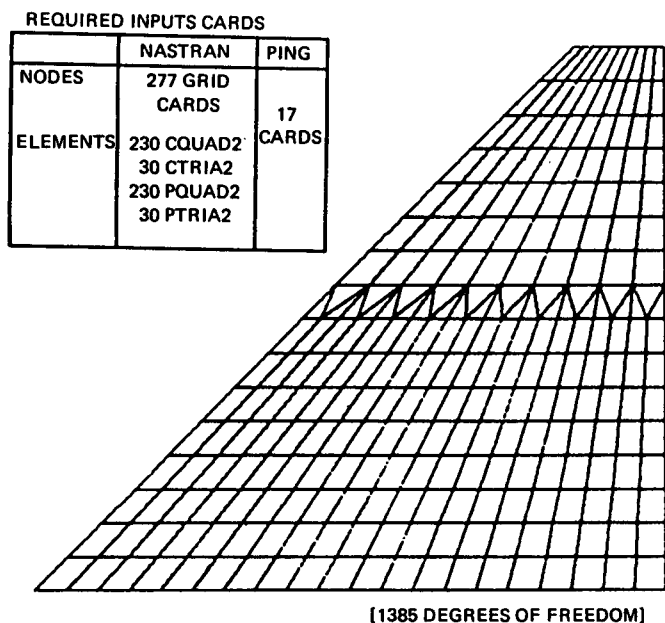
Figure 2-239. Sparrow III Solid Wing Plan Form
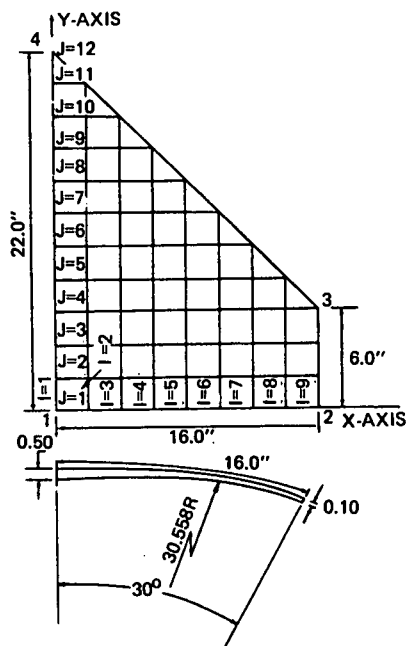
Figure 2-240. Planned Finite Element Model of a Cyclindrical Wing
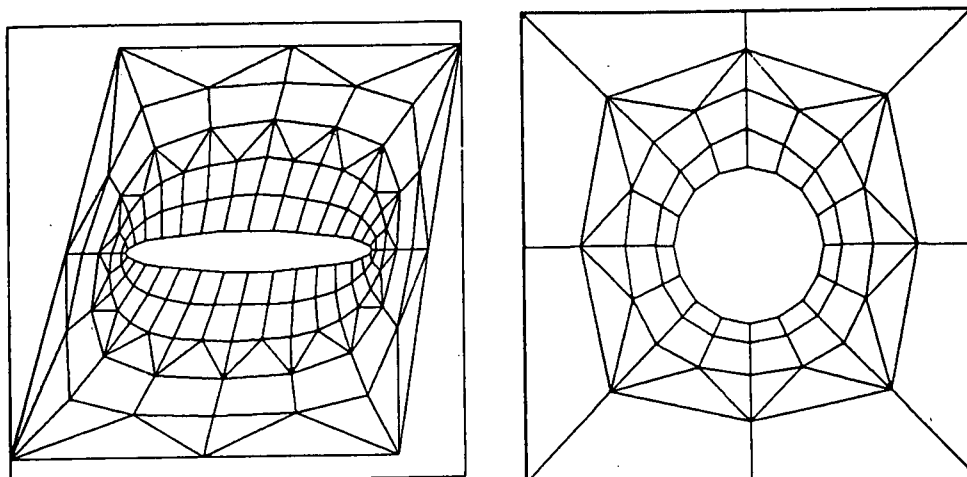
Figure 2-241. Sample Patches Developed by Ping
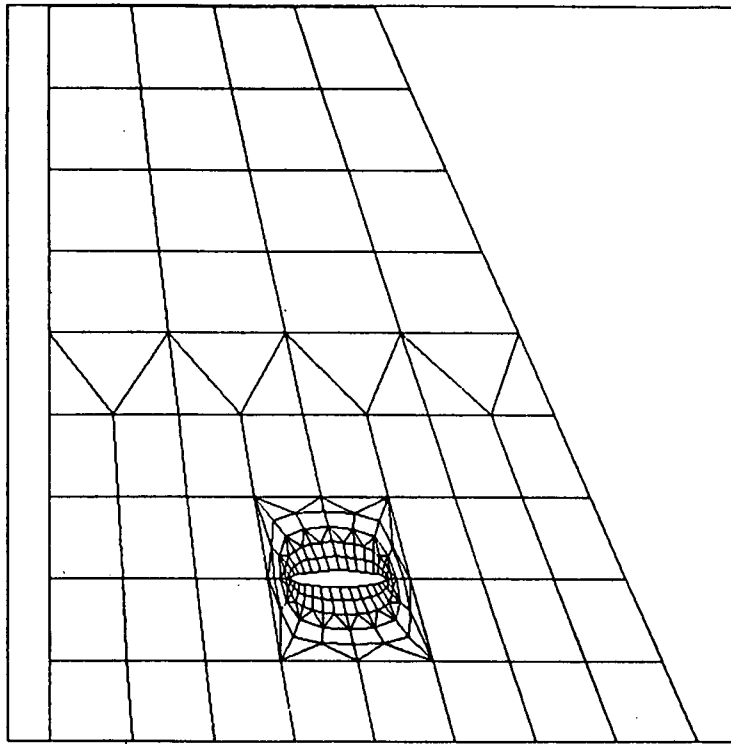
Figure 2-242. Wing with Elliptical Hole
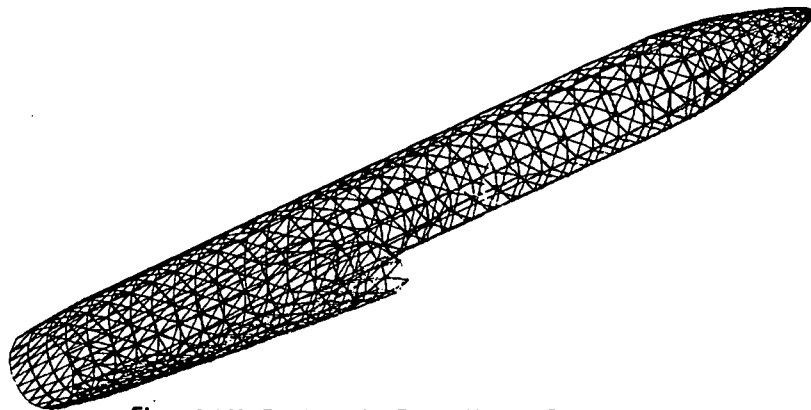
Figure 2-243. Fuselage with Engine Housing Developed by Bing
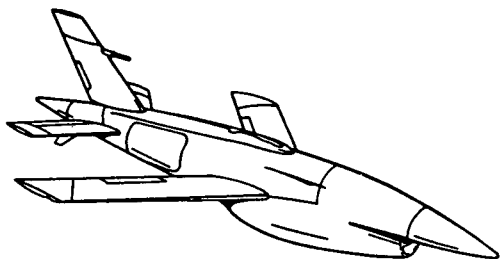
BQM 34A WING
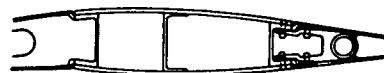
ACTUAL CROSS SECTION

FINITE ELEMENT MODEL DEVELOPED BY PING

FINITE ELEMENT MODEL CROSS SECTION

Figure 2-244. Finite Element Model of Built-up Wing Developed by Ping
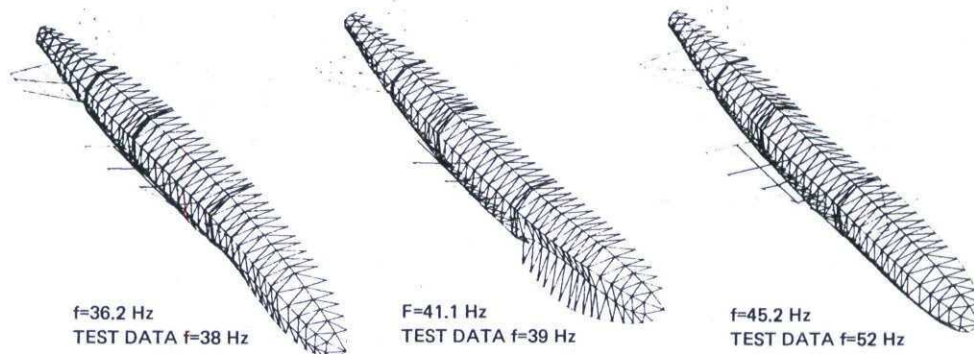
Figure 2-245. Comparison of the Theoretical and Experimental Data of a Vibration Model Developed by Ping and Bing

Patching Technique. On a demanding task such as the vulnerability study of battle damaged structures, precise stress data around the damaged area will be required to determine the possibility of crack propagation which may lead to catastrophic failure. Finite element analysis techniques will be of great value in furnishing detailed information for such a study. Therefore, an elaborate finite element model must be developed to accurately represent the damaged structure. Using PING, this task can be easily achieved. Figure 2-246 shows the procedure for the development of a damaged wing structure. First, a finite element model of the undamaged wing must be generated and the plate elements around the damage removed. Then patches of damaged components having smaller plate elements can be generated to fit the cutout. Finally, these patches are inserted into the proper locations to complete the finite element model for the damaged wing. This modeling procedure is designated as the "Patching Technique". The common gridpoints on the cutout boundaries are not joined by compatibility conditions but by using a common gridpoint number, therefore, no constraint equations are required. This feature not only eliminates many input data cards, but also yields a much better finite element model.

FINITE ELEMENT MODEL OF WING
ROOT SECTION GENERATED BY PING

PATCH OF DAMAGED COMPONENTS
GENERATED BY PING TO
FIT THE CUT-OUT

PLATE ELEMENTS AROUND
DAMAGED AREA REMOVED

COMPLETED FINITE ELEMENT MODEL
FOR A DAMAGED WING
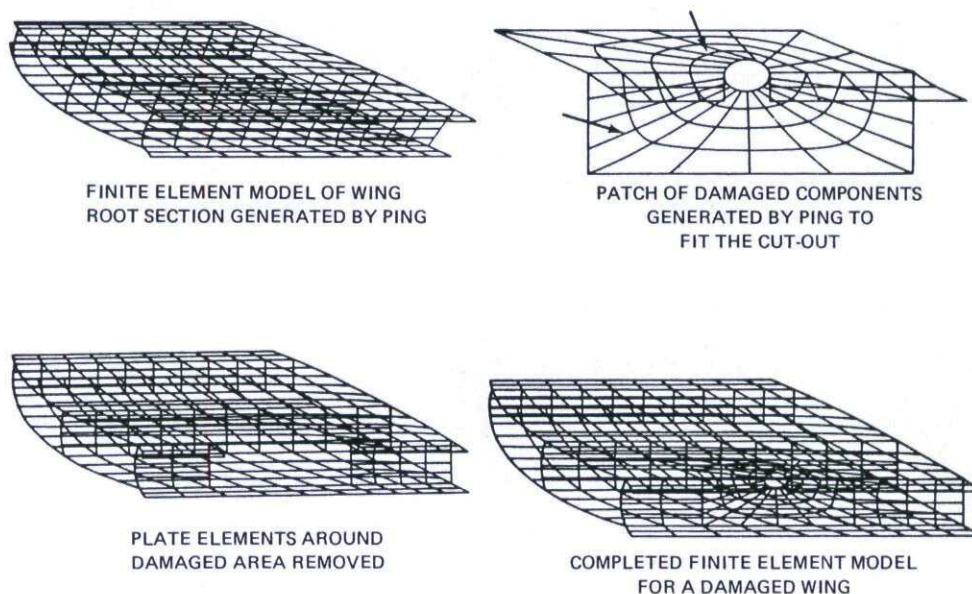
Figure 2-246. Development of Finite Element Model for a Damaged Wing with Ping

Analyses of Battle Damaged Structures. A damaged BQM 34 wing was analyzed by NASTRAN under 1g loading. The finite element model of the undamaged wing had 846 grid points, 849 plate elements, and 4602 degrees of freedom. This model not only took into account the curvatures of the skin panels, but also the varying skin thickness. Five PING runs and approximately 64 manhours were taken to complete this job. The damaged wing had a slot 1.5 inches wide in the upper skin panel and extended five inches diagonally inward from the front spar to a point where the middle spar cap was completely cut. In addition, all three spars were damaged to different degrees. Using the patching technique, the finite element model for this damaged version was quickly generated by removing elements and adding patches. The final model is shown in Figure 2-247. The NASTRAN analyses showed significantly higher stresses in the root area of the damaged wing than those in the corresponding region of the undamaged wing. However, the most critical point was found at the slot tip with a peak stress of 10,000 psi as indicated in the plot of iso-stress-lines. The actual damaged wing was tested to destruction, which occurred at a 3g loading. A crack was first formed at the tip of the slot then propagated toward the wing root at the rear spar. This was adequately predicted in the stress contour plot whereby a peak stress of 30,000 psi was obtained at 3g level; a value which was thought to be the strength of the material at that state.

BQM 34A DRONE

ISO-STRESS-LINES FOR DAMAGE COVER
OF THE BQM 34 A WING

1.G LOADING

2,500 PSI
3,000 PSI
3,500 PSI
4,000 PSI
5,000 PSI
6,000 PSI

10,000 PSI

FINITE ELEMENT MODEL OF DAMAGED BQM 34A WING

BQM 34 A DAMAGED WING COVER

CRACK DUE TO
3G LOAD
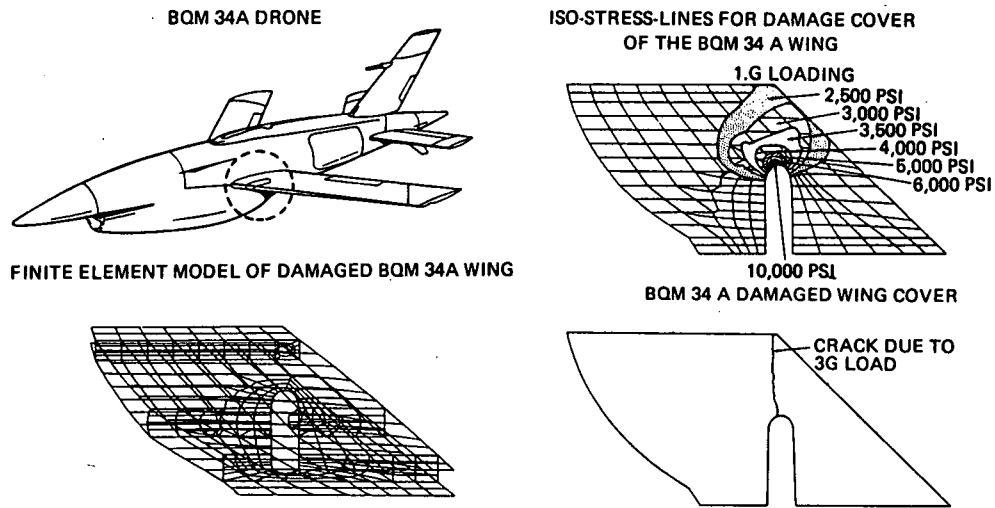
Figure 2-247. Vulnerability Study of a Damaged Missile Wing

The structural response of a damaged semimonocoque fuselage was analyzed from a model by the same patching technique. A vertical slot between the second and third frames near the tail end was cut in the fuselage skin. The cut extended from the crown down to a point at 108 degrees on each side. The patch had a width convering the last three bays of the fuselage and a circumferential length longer than that of the slot. As can be seen in Figure 2-248, much smaller elements are used in the patch especially around the tip region where high stress concentration is anticipated. This finite element model was subsequently analyzed by NASTRAN for a 1g load condition. Proper resultant forces were placed on the four cut boundaries to transmit air pressures from the nose, wings, and tail assembly which were omitted in this truncated fuselage. Stress concentrations were found around the slot tip area with sufficient intensity such that a crack would form at this point. Catastrophic failure seems certain to occur because there is no crack arresting structural member in the propagation path between frames, and the peak stress of 26000 psi shown in Figure 2-249 would increase rapidly as the crack enlarges.

To demonstrate the importance of the patching technique which provides stress concentration data, another analysis was made on a model obtained simply by removing the plate elements between the two frames to simulate the damage inflicted on the fuselage. This simple model, Figure 2-250, had a cutout wider than the slot but was bounded on four sides by smooth edges. NASTRAN analysis revealed much higher stresses than those of the undamaged model, however, no danger could be detected for any catastrophic failure in this analysis. This contradictory conclusion, of course, was not totally unexpected, especially when the simple model had a structurally sound configuration. However, it did point out the danger of under-modeling and the importance of a true simulation.

FINITE ELEMENT MODEL OF A SECTION OF A FUSELAGE

DAMAGE PATCH FOR FUSELAGE

FINITE ELEMENT MODEL OF
A DAMAGED FUSELAGE
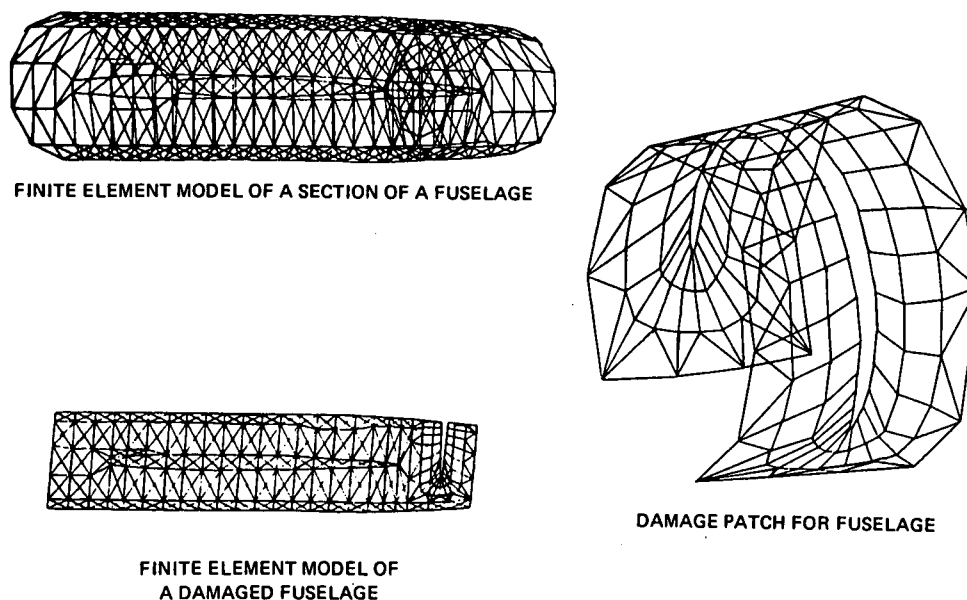
Figure 2-248. Development of Finite Element Model for a Damaged Fuselage

The study of structural vulnerability of battle-damaged aircraft by projectile hits can be conveniently treated in two phases. In the impact fracture phase damage criteria of instantaneous failure, i.e. the upper bound of vulnerability, are of interest. Then the assessment of local damages to the structure must be determined for subsequent survival analyses. The prediction methods in these areas are inadequate at the present time, however, some guidelines are available for a quick estimate. In the continued flight phase where residual strength, loss of control, dynamic and aerodynamic instabilities are a concern, the finite element techniques become extremely valuable. To attack these problems two distinct finite element models should be employed. A "Static Model" with sufficient damage details can be developed for residual strength anlaysis while a "Kinematic Model", being much simpler than the former, can be used in the anlayses of structural response. The Kinematic model is definitely the cheaper one to run, yet would yield sufficiently accurate results in stiffness or dynamic analysis. For completeness, many different analyses must be performed on a large structure, these models must be carefully designed for optimization in terms of accuracy and economy.

VERTICAL CUT BETWEEN FRAMES

ANALYTICAL MODEL GENERATED BY BING
FOR NASTRAN ANALYSIS

10,000 PSI   26,000 PSI
6,000 PSI
3,000 PSI

HIGH STRESS AT DAMAGED TIP INDICATES
CRITICAL CONDITION FOR CRACK PROPAGATION

DISTORTION OF DAMAGED AREA UNDER
1-G LOAD CONDITION
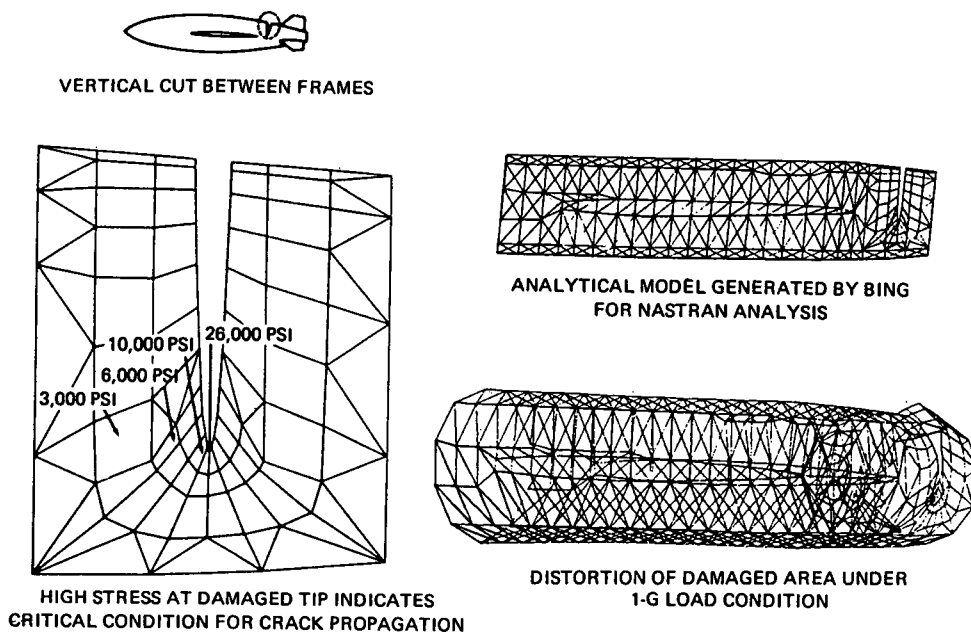
Figure 2-249. Vulnerability Study of a Damaged Missile Body

11,595 PSI
(MAX)   PRINCIPAL STRESS

☒ ≥ 10,000 PSI
⊞ ≥ 4,000 PSI
▨ ≥ 2,000 PSI
☐ ≥ 1,000 PSI
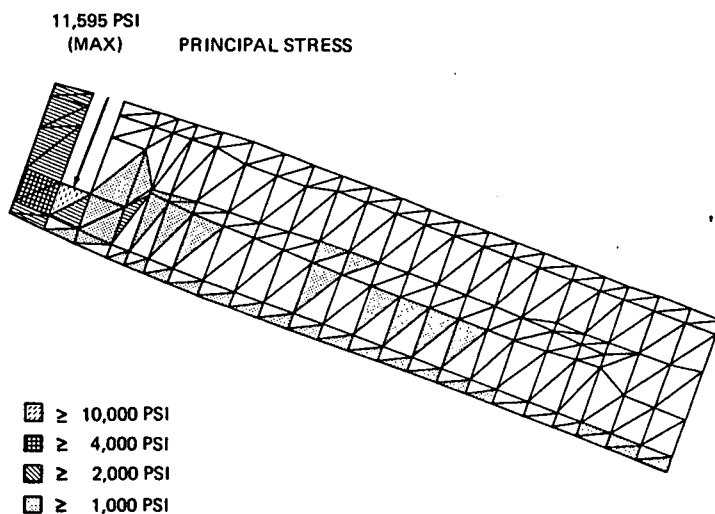
Figure 2-250. Damage Model with Smooth Sides

2.6 REFERENCES

2-1   J. Massmann, "Structural Response to Impact Damage", AGARD-Report No. 633, Sept. 1975.

2-2   J. G. Avery, G. T. Burch, Jr., "An Aircraft Structural Combat Damage Model," and "...Design Handbook," AFFDL-TR-70-115, and 116, Nov. 1970.

2-3   J. G. Avery, T. R. Porter, and R. W. Lauzze, "Structural Integrity Requirements for Projectile Impact Damage - An Overview", AGARD Conference Proceedings No. 186, Jan. 1976.

2-4   J. Massmann, "Investigation About Residual Strength of Damaged Structures," ICAF Conference 1973, LBF-Report S-108 ff.

2-5   J. Massmann, Schrittweise Entwicklung einer Berechnungs-, Pruf- und Konstruktionsvorschrift für luftstossbelastete Schutzraumtore, dritter Schritt, IABG-Bericht Nr. B-TF-411, Ottobrunn -August 30, 1973.

2-6   J. Massmann, Gasschlagmodell zur Berechnung der Munitionswirkung in Flugzeughohlräumen, IABG-Bericht Nr. B-TF-484, Ottobrunn - December 22, 1974.

2-7   J. G. Avery, T. R. Porter, "Survivable Combat Aircraft Structures Design Criteria and Guidelines, Final Report," and "... Design Handbook," AFFDL-TR-74-49 and -50, 1974.

2-8   J. Jensen, P. Thorndyke, M. Campbell, "Aircraft Wing Structural Concepts with Improved Ballistic Damage Tolerance," GDC-DDG69-002, General Dynamics, Convair Division, 1969.

2-9   J. A. Suarez, "Vulnerability of Composite Aircraft Structures," AFFDL-TR-72-8, February 1972.

2-10   "Advanced Development on Vulnerability/Survivability of Advanced Composite Structures," AFML-TR-73-152, May 1973.

2-11   E. F. Olster, H. A. Woodbury, "Evaluation of Ballistic Damage Resistance and Failure Mechanisms of Composite Materials," AFML-TR-72-79, April 1972.

2-12   J. G. Avery, S. J. Bradley and K. M. King, "Battle Damage Tolerant Wing Structural Development Program," Final Report, NASC Contract N00019-75-C-0178, Boeing Document D180-26069-1, 1979.

2-13   J. Brass, J. Yamane and M. Jacobson, "Effects of Internal Blast on Combat Aircraft Structures ," AFFDL-TR-73-136, Volumes I and II, January 1974.

2-14   M. J. Jacobson, J. Yamane, and M. Ratwani, "Effects of Internal Blast on Combat Aircraft Structures Effects of Detonations of High-Explosive Projectiles on Fracture of Metallic Aircraft Compartments," AFFDL-TR-75-73, Volume II, July 1975.

2-15   A. L. Dobyns, "Fiber Composite Blast Response Computer Program (BR-1FC) BR-1 Code Modification and Test Program", AFFDL-TR-78-29, JTCG/AS-76-T-008, October 1977.

2-16   R. D. Hayes, et al., "Flightworthy Graphite Fiber Reinforced Composite Aircraft Primary Structural Assemblies," AFML-TR-72-176, April 1972.

2-17   J. G. Avery, S. J. Bradley, R. J. Bristow, "Survivable Composite Structure for Combat Aircraft," AFFDL-TR-79-3132, 1979.

2-18   J. G. Avery, W. M. Herlin, "Development of a Proposed Military Specification for Survivable Aircraft Structures (Nonnuclear)," AFFDL Contract F33615-78-C-3423, September 1980.

2-19   R. Recht, "Equations for Predicting Penetration of AP and API Projectiles into Aircraft," Denver Research Institute, 1973.

2-20   Anon., "The Resistance of Various Metallic Materials to Perforation by Steel Fragments," Ballistic Research Laboratory, Project Thor Report 47.

2-21   "Ballistic Penetration Resistance for Selected Encounter Conditions", Boeing Memo No. L-7160-JGA-073.

2-22   "Penetration Equations Handbook - Draft" prepared by the JTCG/ME Penetration Equations Committee of the Aircraft Target Vulnerability Subgroup, 1975.

2-23   J. G. Avery, "Fracture Due to Damage from Projectile Impact," Engineering Fracture Mechanics, Vol. 4, pp749-763, 1972.

2-24   J. G. Avery, "Designing Fiber Composite Structure for Battle Damage Tolerance," 22nd National SAMPE Symposium, 1977.

2-25   J. G. Avery, T. R. Porter, "A Parametric Evaluation of Lightweight Metal and Composite Structure Exposed to Gunfire," Army Symposium on Solid Mechanics, Ocean City, Md., 1972.

2-26   J. G. Avery, S. J. Bradley, K. M. King, "Fracture Control in Ballistic Damaged Graphite/Epoxy Wing Structure," ASTM 13th National Symposium on Fracture Mechanics, June 1980.

2-27   J. G. Avery and T. R. Porter, "Comparisons of the Ballistic Impact Response of Metals and Composites for Military Aircraft Applications," Foreign Object Impact Damage to Composites, ASTM STP 568, 1975.

212

2-28   J. G. Avery, S. J. Bradley, K. M. King, "Developing Graphite/Epoxy Structure for Combat Damage Resistance and Tolerance," AIAA/ASME/ASCE/AHS 21st Structure, Structures Dynamics and Materials Conference, May 1980.

2-29   A. Dobyns, J. Avery, "Blast Response of Fiber Composites - Test and Analysis," 3rd Biennial JTCG/AS Aircraft Survivability Symposium, Monterey, Calif., 1978.

2-30   A. Dobyns, J. Avery, "The Response of Advanced Composite Structures to High-Explosive Blast" Army Symposium on Solid Mechanics, Cape Cod, Mass., October 1980.

2-31   T. R. Porter, "Effect of Low Velocity Impact on Static and Fatigue Properties," DOD/NASA Mini-Symposium on Effect of Impact Damage on the Behavior of Composite Materials, 2-4 November 1977.

2-32   J. F. Proctor, "Internal Blast Damage Mechanisms Computer Program," Report 61, JTCG/ME-73-3, Joint Technical Coordinating Group for Munitions Effectiveness, April 1973.

2-33   D. P. Ankeney, "Physical Vulnerability of Aircraft Due to Fluid Dynamic Effects," AGARD-AR-106, July 1977.

2-34   G. Kinney, "Explosive Shocks in Air," the MacMillan Company, New York, 1962.

2-35   G. Abrahamson, A. Florence, and H. Lindberg, "Radiation Damage Study Vol. XIII -Dynamic Response of Beams, Plates, and Shells to Pulse Loads," BSD TR 66-372, Ballistic Systems Division, Air Force Systems Command, 1966.

2-36   R. Sewell, G. Kinney, "Response of Structures to Blast: A New Criterion," NWC TP 4422, Naval Weapons Center, June 1968.

2-37   J. E. Greenspon, "Theoretical Calculation of Iso-Damage Characteristics," Technical Report No. 10, DAADOS-69-C-116 for BRL, Aberdeen Proving Grounds, Md., 1970.

2-38   R. W. H. Wu, E. A. Witmer, "Finite-Element Analysis of Large Elastic-Plastic Transient Deformations of Simple Structures," AIAA J., Vol. 9, No. 9, September 1971, pp. 1719-1724.

2-39   W. H. Chen, "Necking in a Bar," Technical Report No. ARPA-40, Division of Engineering and Applied Physics, Harvard University, March 1970.

2-41   R. S. Sandhu, "Ultimate Strength Analysis of Symmetric Laminates," AFFDL-TR-73-137, Feb, 1974.

2-42   J. E. Ashton, J. C. Halpin, O. H. Petit, "Primer on Composite Materials: Analysis," Technomic Publishing Co., Stamford, Conn., 1968.

2-43   D. McCarthy, "Definition of Engine Debris and Some Proposals for Reducing Potential Damage to Aircraft Structure," AGARD Conference Proceedings No. 186, January 1976.

2-44   T. W. Coombe, D. F. Vowles, "Structural Effects of Engine Burst Non- Containment," AGARD Conference Proceedings No. 186, January 1976.

2-45   E. A. Lundstrom, "Fluid Dynamic Analysis of Hydraulic Ram," NWC TP 5227, Naval Weapons Center, China Lake, California, July 1971.

2-46   E.A. Lundstrom, "Fluid/Structure Interaction in Hydraulic Ram," JTCG/AS Hydrodynamic Ram Seminar, AFFDL-TR-77-32/JTCG/AS-77-D-002, May 1977.

2-47   D.P. Ankeney, "Hydraulic Ram Structural Response Modification," Addendum to Hydraulic Ram IV, JTCG/AS-74-T-018, Naval Weapons Center Report, 25 May 1977.

2-48   E.A. Lundstrom, W.K. Fung, "Fluid Dynamic Analysis of Hydraulic Ram IV (User's Manual for Pressure Wave Generation Model)," JTCG/AS-74-T-018, Naval Weapon Center, China Lake, California, December 1974.

2-49   M. Helriegel, "Evaluation of Hydraulic Ram Pressure Prediction Analysis," Boeing Document D180-18807-1, August 1975.

2-50   R.J. Bristow, D.L. Henry, "Investigation of Ballistic-Damage-Tolerant Fuel Tanks," Boeing Document D180-17504-1, 1973.

2-51   E.A. Lundstrom, W.K. Fung, "Fluid Dynamic Analysis Hydraulic Ram III (Result of Analysis)," Naval Weapons Center, China Lake, California, (JTCG/AS TEAS P.E.5.1.1.11), October 1974.

2-52   "DEPROP, A Digital Computer Program for Predicting Dynamic Elastic-Plastic Response of Panels to Blast Loadings", AFATL-TR-76-71, June 1976.

2-53   M. Rosenblatt, G.E. Eggum, and L. De Angelo, "Numerical Analyses of Fuel Tank Penetration Dynamics," AFFDL-TR-76-31, July 1975.

2-54   D.F. Haskell, "Damage Tolerance of Semimonocoque Aircraft Structure," AGARD Conference Proceedings No. 186, January 1976.

2-55   R. G. Forman, et al, "Vulnerability of Aircraft Structures Exposed to Small Arms Fire Projectile Impact Damage," AFFDL-TR-67-157, 1967.

2-56   P. C. Paris, G. C. Sih, "Stress Analysis of Cracks," Fracture Toughness Testing and its Applications, ASTM STP 381, 1965.

2-57   D. P. Wilhem, "Fracture Mechanics Guidelines for Aircraft Structural Applications," AFFDL-TR-69-111, February 1970.

2-58   R. J. Engle, Jr., "CRACKS, A Fortran IV Digital Computer Program for Crack Propagation Analysis," AFFDL-TR-70-107, October 1970.

2-59   D. E. Piper, S. H. Smith, and R. V. Carter, "Corrosion Fatigue and Stress-Corrosion Cracking in Aqueous Environments," presented at Materials for Oceanspace Symposium at the National Metal Congress, 1966.

2-60   W. L. Engstrom, "Effect of Frequency on Fatigue Crack Growth Rates in 7075-T6 Aluminum," Boeing Document D6-20173.

2-61   J. C. McMillan and R. M. N. Pelloux, "Fatigue Crack Propagation Under Program and Random Loads," Fatigue Crack Propagation, ASTM STP 415, 1967.

2-62   T. R. Porter, "Method of Analysis and Prediction for Variable Amplitude Fatigue Crack Growth," Engineering Fracture Mechanics, Vol. 4, pp. 717-736, 1972.

2-63   M. McKinney, T. Porter and C. Sedlacek, "Battle Damage Tolerant Wing Study," Navy Contract N00019-72-C-0433, Final Report D180-15150-1, 1972.

2-64   D.P. Rooke, D. J. Cartwright, "A Compendium of Stress Intensity Factors," Her Majesty's Stationary Office, London, 1976.

2-65   M. D. Campbell, G. L. O'Barr and J. F. Haskins, "Correlation of Residual Strength of Ballistically Damaged Panels with Fracture Toughness Theory," GDC-ERR-1404, General Dynamics, Convair Division, 1969.

2-66   "NOVA-A Digital Computer Program for Calculating the Response of Aircraft to the Overpressure from a Nuclear Explosion," AFWL-TR-72-115, July 1973.

2-67   O. L. Bowie, "Analysis of an Infinite Plate Containing Radial Cracks Originating from the Boundary of an Internal Circular Hole," Journal of Mathematics and Physics, Vol. 35, 1956.

2-68   J. C. Newman, Jr., "An Improved Method of Collocation for the Stress Analysis of Cracked Plates with Various Shaped Boundaries," NASA TN D-6376, August 1971.

2-69   H. Tada, in cooperation with P. C. Paris and G. R. Irwin, "The Stress Analysis of Cracks Handbook," Del Research Corporation, Hellertown, Penn., 1973.

2-70   J. Massmann, "Structural Analysis of Impact Damage on Wings," AGARD Conference Proceedings No. 186, January 1976.

2-71   S. H. Smith, A. F. Liu, "Fracture Mechanics Application to Materials Evaluation and Selection for Aircraft Structure and Fracture Analysis," Boeing Document D6-17756, November 1966.

2-72   J. J. Horsley, "Stress Intensity Factors for Selected Alloys," Boeing Document D3-7326, January 1968.

2-73   S. H. Smith, T. R. Porter, W. D. Sump, "Fatigue Crack Propagation and Fracture Characteristics of 7075 Aluminum Alloy Sheet and Plate in Three Aged Conditions," Boeing Document D519523, (also NASA CR-996).

2-74   J. Viglione, "Fracture Toughness Properties of Some Alloy Steels and Aluminum and Titanium Alloys," NAEC-AML-2111, March 1965.

2-75   "Fracture Characteristics of Aluminum Alloys," ALCOA TR 18, 1965.

2-76   A. F. Liu, "Statistical Variation on Fracture Toughness Data of Airframe Materials," Boeing document D6-15784 TN, 1968.

2-77   "Titanium Development Program," Boeing document D6A-10065-1 Commercial SST Program Phase II-C Report, 1966.

2-78   "High Strength Steel Evaluation for Supersonic Aircraft," Boeing Document D6A-10093-2, Commercial SST Program Phase II-C Report, 1966.

2-79   M. V. Hyatt, "Effects of Residual Stresses on Stress-Corrosion Crack Growth Rates in Aluminum Alloys," Boeing document D6-24469, November 1969.

2-80   R. Roberts, T. Rich, "Stress Intensity Factors for Plate Bending," J. of Applied Mechanics, Vol. 34, Sept. 1967.

2-81   G. Sih, G. Embley, R. Ravera, "Impact Response of a Finite Crack in Plane Extension," International J. of Solids and Structures, Vol. 3, 1972.

2-82   G. Embley, G. Sih, "Sudden Appearance of a Crack in a Bent Plate," International Solids and Structures, Vol. 9, 1973.

2-83   M. McKinney, T. Porter, C. Sedlacek, "Battle Damage Tolerant Wing Study," Navy Contract N00019-72-C-0433, 1972.

2-84   J. Przemieniecki, "Theory of Matrix Structural Analysis," McGraw-Hill Book Company, 1968.

2-85   R. W. Walter et al., "Designing for Integrity in Long-Life Composite Aircraft Structures," Fatigue of Filamentary Composite Materials, ASTM STP 636, 1977.

2-87   C. C. Poe, "The Effect of Riveted and Uniformly Spaced Stringers on the Stress Intensity Factor of a Cracked Sheet," M.S. Thesis, Virginia Polytechnic Institute, April 1969.

2-88   H. Vlieger, "Residual Strength of Cracked Stiffened Panels," National Aerospace Laboratory NLR, NLR-TR-71004U, January 1971.

2-89   S. J. Bhatt, "Analysis of Load Transfer in Stiffened Skin Panels Under Various Conditions of Skin Fatigue Cracks," Boeing document D6-17821, June 1966.

2-90   C. W. Rogers, et al., "Structural Airframe Application of Advanced Composite Materials," Vol. 4, Sec. 4, AFML-TR-60-101, October 1969.

2-91   M. M. Ratwani, "Characterization and Residual Strength Predictions of Ballistically Damaged Aircraft Structures," JTCG/AS-76-T-010, Sept. 1977.

2-92   "Repair Technology for Boron/Epoxy Composites," Interim Report, Air Force Materials Laboratory Contract F33615-69-C-1498, Grumman Aircraft Engineering Corp.

2-93   R. W. Walter, "Investigation of Static and Fatigue Performance of 5208-T300T Graphite/Epoxy Laminates," Boeing document D180-20378-1, 1977.

2-94   J. Greenspon, "Elastic-Plastic Response of Structures to Blast and Impulse Loads," BRL Contract DA-18-001-AMC-1019, TR No. 7, 1967.

2-95   J. Proctor, "Aircraft Loading from an Internal Explosion," Naval Ordnance Laboratory, presented at Army Symposium on Solid Mechanics, Ocean City, Md., 1972.

2-96   H. Balmer, "Computer Programs to Calculate the Dynamic Elastic-Plastic Responses of Impulsively Loaded Simple Structures," MIT ASRL TR 1022, 1964.

2-97   W. Salus, Ip Ching-U, and J. Van Derlinden, "Design Considerations of Elastic-Plastic Structures Subjected to Dynamic Loads," AIAA/ASME 11th Structures, Structures Dynamics and Materials Conference, Denver, Colorado, 1970.

2-98   J. W. Leech, P. T. Hsu, and E. W. Mack, "Stability of a Finite Difference Method for Solving Matrix Equations", AIAA Journal, Vol. 3, No. 11, pp. 2172-2173, November 1965.

2-99   Rogers, Chitwood, and Ashton, "Structural Airframe Application of Advanced Composite Materials," Vol. IV., Section IV., AFML-TR-69-101.

2-100   E. F. Olster, H. A. Woodbury, "Evaluation of Ballistic Damage Resistance and Failure Mechanisms of Composite Materials," AFML-TR-72-79, April 1972.

2-101   R. D. Hayes, et al., "Flightworthy Graphite Fiber Reinforced Composite Aircraft Primary Structural Assemblies," AFML-TR-71-276, April 1972.

2-102   J. G. Avery, T. R. Porter, "Battle Damage Tolerance of Fiber Composites," Boeing document D180-17669-1, 1973.

2-103   J. R. Hancock, G. D. Swanson, "Toughness of Filamentary Boron/Aluminum Composites," Composite Materials Testing and Design (Second Conference), ASTM STP 497, pp. 299-310, 1972.

2-104   M. E. Waddoups, J. R. Eisemann and B. E. Kaminski, "Microscopic Fracture Mechanics of Advanced Composite Materials," Journal of Composite Materials, Vol. 5, October 1971.

2-105   J. M. Whitney, R. J. Nuismer, "Stress Fracture Criteria for Laminated Composites Containing Stress Concentrations," Journal of Composite Materials, Vol. 8, July 1974.

2-106   R. V. Sanga, "The 747 Fail-Safe Structural Verification Program," 7th ICAF Symposium, London, England, July 1973.

2-107   D. Broek, H. Vlieger, The Thickness Effect In Plane Stress Fracture Toughness, NLR TR 74032, 1974.

2-108   H. Vlieger, "Fail-safe Characteristics of Built-up Sheet Structures", presented to the 9th ICAS symposium, Haifa, Israel, August 1974.

2-109   H. Konish, et. al., "Method for Estimating Fracture Strength of Specially Orthotropic Composite Laminates," ASTM STP 521, 1973.

2-110   A. Cruse, "Tensile Strength of Notched Composites," Journal of Composite Materials, Vol. 7, April, 1973.

2-111   M. Ratwani, "Weckselwirkung von Rissen," Institut fur Festkorpermechanik, Freiburg, W. Germany, Research Report, May 1972.

2-112   M. Isida, "Analysis of Stress Intensity Factors for Plates Containing Random Array of Cracks," Japanese Society of Mechanical Engineering, Vol. 13, No. 59, 1970.

2-113   F. Erodogan, R. Roberts, "A Comparative Study of Crack Propagation in Plates Under Extension and Bending," Proceedings of First International Conference on Fracture (1965), Vol. I, pp 341.

2-114   P. C. Huang, "Finite Element Applications to Battle Damaged Structure," AGARD Report No. 648, April 1976.

2-115   P. C. Huang, J. P. Matra, "Planform Input Generator (PING)," NOLTR73-109 Naval Surface Weapons Center, White Oak Laboratory, Silver Spring, MD., March 1975.

2-116   P. C. Huang, J. P. Matra, "Missile Body Input Generator (BING)", NSWC/WOL/TR 75-9, Naval Surface Weapons Center, White Oak Laboratory, Silver Spring, MD., March 1975.

SECTION III

DESIGN GUIDELINES FOR IMPACT DAMAGE TOLERANCE

3.0 DESIGN GUIDELINES FOR IMPACT DAMAGE TOLERANCE

As indicated in Figure 3-1 aircraft must maintain structural integrity relative to many types of damaging mechanisms, including for example:

1. Fatigue,
2. Non-detectable initial defects,
3. In-flight damage, such as that inflicted by military and engine debris projectiles.

The objective in designing for fatigue is to prevent wear-out during the anticipated usage of the aircraft. The objective of the second structural integrity requirement is to prevent an airplane from unexpectedly failing as a result of an undetected flaw or defect. In both cases, the benefits of successful design are improved safety and economics.

With respect to projectile impact damage, the objective is to prevent structural failure from damage suddenly inflicted during flight. A substantial portion of combat aircraft attrition for example, has been caused by structure-related failures induced by projectile impact. Projectile damage may cause loss of strength and stiffness, often amplified by the interaction between primary structure and engine fuel storage, creating damage mechanisms such as hydrodynamic ram, vapor explosions and fire.

In spite of the importance of the projectile damage threat to combat aircraft, this category of damage is addressed in only a limited way by existing structural design guidelines and specifications. Although vulnerability analysts have always been concerned with the effects of projectiles, this often represents unfamiliar ground for structural designers. Because of this, effort is required to integrate projectile damage tolerance within the structural design process, along with related fatigue and fail-safe criteria, as indicated in Figure 3-2.

The remainder of this section presents an overview of a methodology for projectile damage tolerant design and certain of the techniques and guidelines available for implementation.

	FATIGUE (CRACK INITIATION)	NON-DETECTABLE INITIAL DEFECTS	INFLICTED DAMAGE
DESIGN REQUIREMENTS:	RELATED MIL SPECIFICATION: MIL 8860	RELATED MIL SPECIFICATION: MIL 83444	RELATED MIL SPECIFICATION: NONE GUIDELINES: AFFDL-TR-74-50 (BATTLE DAMAGE)
DESIGN OBJECTIVE:	PREVENT WEAR-OUT	PREVENT FAILURE FROM WORST-CASE INITIAL FLAWS	PREVENT FAILURE FROM INFLICTED DAMAGE
DESIGN CRITERIA:	DESIGN CRITERIA BASED ON STATISTICAL MATERIAL RESPONSES	DAMAGE CRITERIA BASED ON NDI CAPABILITIES	DAMAGE CRITERIA DETERMINED BY DAMAGE SIZE INFLICTED BY SPECIFIED THREAT

Figure 3-1. Aircraft Structural Integrity Requirements Include Several Types of Damage Mechanisms

Figure 3-2. Impact Damage Tolerance Can be Incorporated into Structural Design Procedures

3.1 DESIGN METHODOLOGY FOR ACHIEVING IMPACT DAMAGE TOLERANCE

Projectile impact damage tolerance can be achieved most efficiently by incorporating ballistic damage assessment, resistance, and tolerance analysis methods into existing structural design methodology. This entails developing these methods and requirements within a format which is compatible with existing structural damage tolerance procedures. An approach has been developed which accomplishes this, as summarized in the following paragraphs.

3.1.1 Design Methodology Overview

To achieve structural survivability with minimum weight and cost penalties, a quantitative assessment of structural survivability should be included during all design phases of the aircraft. This requires implementing a design and assessment methodology permitting designers to determine the survival capability of a current design. The objectives of the methodology are to evaluate the structural capability of the damaged airframe, and to compare this with structural performance requirements as dictated by mission criteria. Figure 3-3 is a flow diagram illustrating the steps required to evaluate the survivability level of a structural design using a methodology that is consistent with structures design methods.

Based on the conceptual goals for the aircraft, specific mission and threat requirements must be defined. These requirements are used as input data in establishing the detailed requirements and capabilities of the structure. The steps for implementation are described in the following paragraphs.

3.1.1.1 Determination of Structural Requirements

Structural requirements are determined by the operating environment of the aircraft as dictated by the mission. For survivability analysis, three basic types of load information are required for each structural component considered. These are:

(a) The loads and the physical environment at the time of projectile impact;

(b) The cyclic loading spectrum after projectile impact;

(c) The maximum load and the associated physical environment that will be encountered after projectile impact;

This information is obtained by constructing the anticipated operational history for the aircraft, including the 1-g loading conditions, gust loadings, and maneuver load factors for the prescribed missions. A sample stress/time history for a structural element is shown in Figure 3-4, determined from the loading assessment. From this information, and an assessment of probable encounter scenarios, stress level requirements can be defined for critical structural elements at the time of impact.

SYSTEM CONCEPTUAL GOALS

⬇

AIRCRAFT SYSTEM REQUIREMENTS

• AIRCRAFT MISSION
  REQUIREMENTS

• THREAT
  REQUIREMENTS

AIRCRAFT STRUCTURAL CONFIGURA-TION

DESIGN INTERACTION

STRUCTURAL REQUIREMENTS

• DETERMINE LOADS
  AND ENVIRONMENT
  AT IMPACT

• DETERMINE CYCLIC
  LOADING AFTER
  IMPACT

• DETERMINE MAXIMUM
  LOAD AND SPEED AFTER
  IMPACT

STRUCTURAL CAPABILITY

• DETERMINE DAMAGE

• DETERMINE CYCLIC
  LOADING EFFECTS

• DETERMINE

  • RESIDUAL STRENGTH

  • RESIDUAL STIFFNESS
    AND RIGIDITY

ASSESSMENT

COMPARE REQUIREMENTS
AND CAPABILITIES
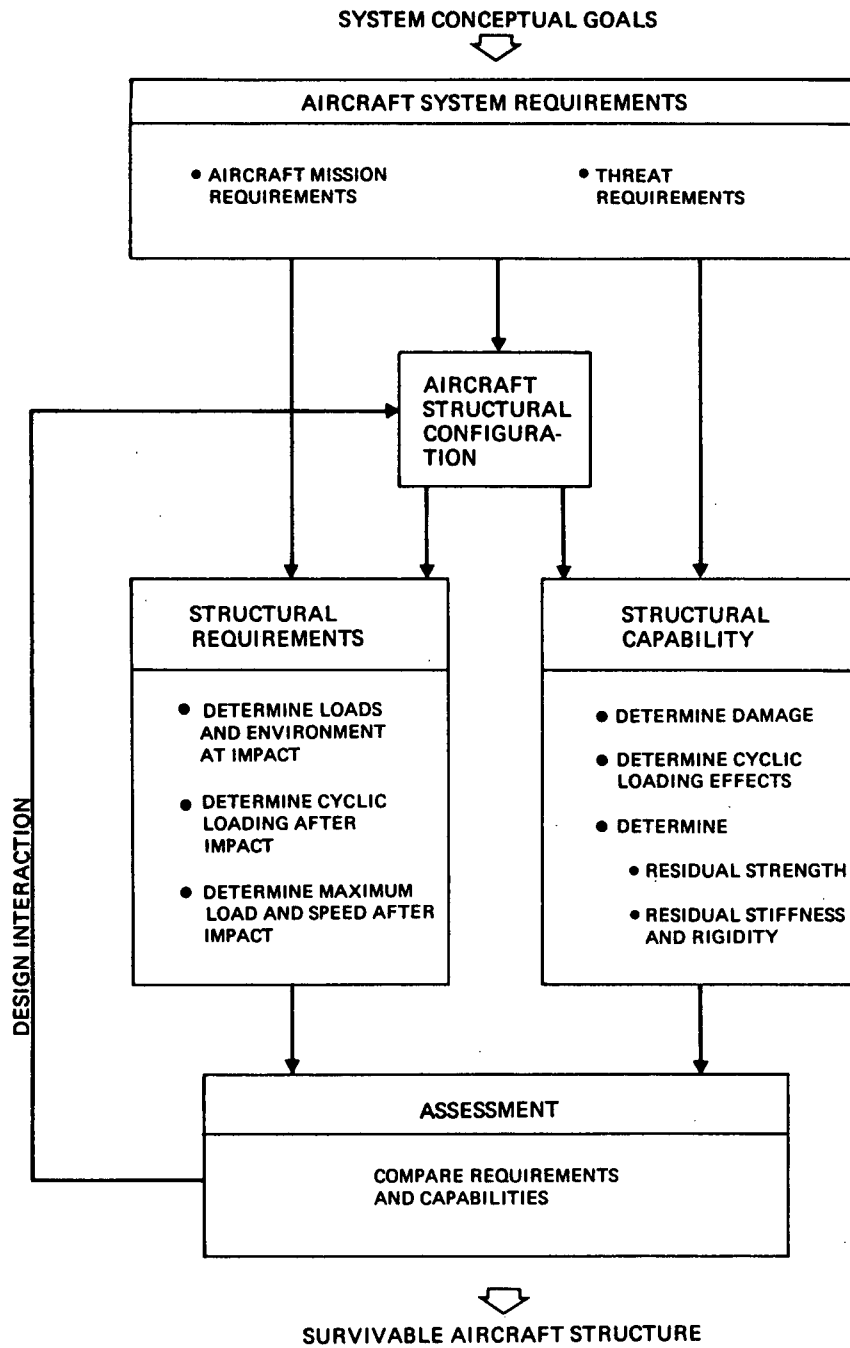
⬇

SURVIVABLE AIRCRAFT STRUCTURE

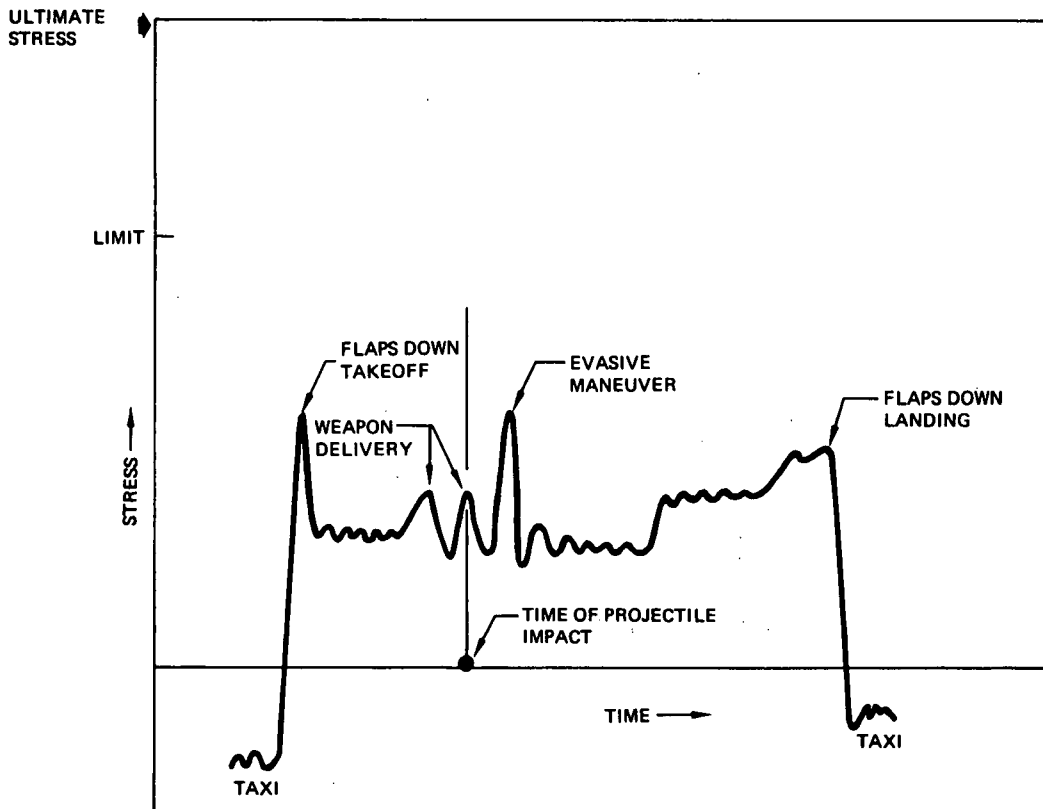*Figure 3-3. Survivable Structures Design Methodology*

Figure 3-4. Sample Stress-Time History for Structural Element,
Defining Stress Requirements for Mission Completion

The maximum loadings anticipated from the time of damage occurrence until mission completion or repair determine the residual strength requirements for the airplane. Likewise, the operating stresses from damage occurrence until the airplane is repaired define the cyclic loading requirements.

Physical environment, particularly temperature, can affect the residual strength of damaged structure because it influences the failure behavior of aircraft materials. Other possible degrading physical environments include: humidity, moisture, cleaning fluids, hydraulic fluids, and fuel, especially during the application of cyclic loads.

The requirements addressed above pertain to the probable loadings encountered during a sortie. This is one of the distinguishing features of projectile damage tolerance, as contrasted with fatigue or initial defect damage tolerance. The latter damage mechanisms are most often related to aircraft lifetimes or periods of time established by prescribed inspection intervals. Although deferral of combat damage repair can be an important factor, leading to the requirement for engaging in several sorties following damage, the operating intervals with projectile damage will always be short relative to the other damage mechanisms.

3.1.1.2 Determination of the Capability of Damaged Structure

Determining structural capability requires an evaluation of structural degradation due to weapon damage, using analysis techniques discussed in Section II. The required analysis steps were shown on the right side of Figure 3-3. Several unique technical disciplines come into operation at this point, because evaluating structural degradation due to projectile impact damage requires an understanding of the mechanics of projectile damage and damage tolerance.

The first step is to determine the type and extent of the damage inflicted by the projectile. This damage constitutes a flaw which reduces the remaining strength and stiffness of the structure. Structural damage from projectile impact is a function of the type of projectile and the engagement conditions, as well as physical environment, applied loads, and compounding effects such as hydrodynamic ram.

Damaged structure that does not fail at the time of impact is subjected to subsequent cyclic loading as a result of gust and maneuvers during continued flight. These cyclic loadings induce fatigue that can influence the damage size and character, thereby changing the severity of the induced flaw. In metal structure, cyclic stresses will generally increase the damage size and severity, thus reducing the strength of the ballistic-damaged structure during operation.

The damaged airframe must have sufficient residual strength to sustain the maximum flight loads subsequently encountered. This residual strength is related to damage size and the inherent damage tolerance of the structure as determined by material selection and design configuration. The stiffness of aircraft structure that has been damaged is also altered by projectile damage. Stiffness degradation can induce several failure mechanisms, including flutter, loss of control, or extensive internal load redistribution.

The final results of the structural capability determination can be presented in a manner analogous to the stress/time requirements history presented in Figure 3-4. This is termed the "strength-time" history (an example is shown in Figure 3-5). As shown in the figure, the structural capability is the design ultimate strength before encountering damage. After projectile impact, however, the structural capability may be severely degraded. The
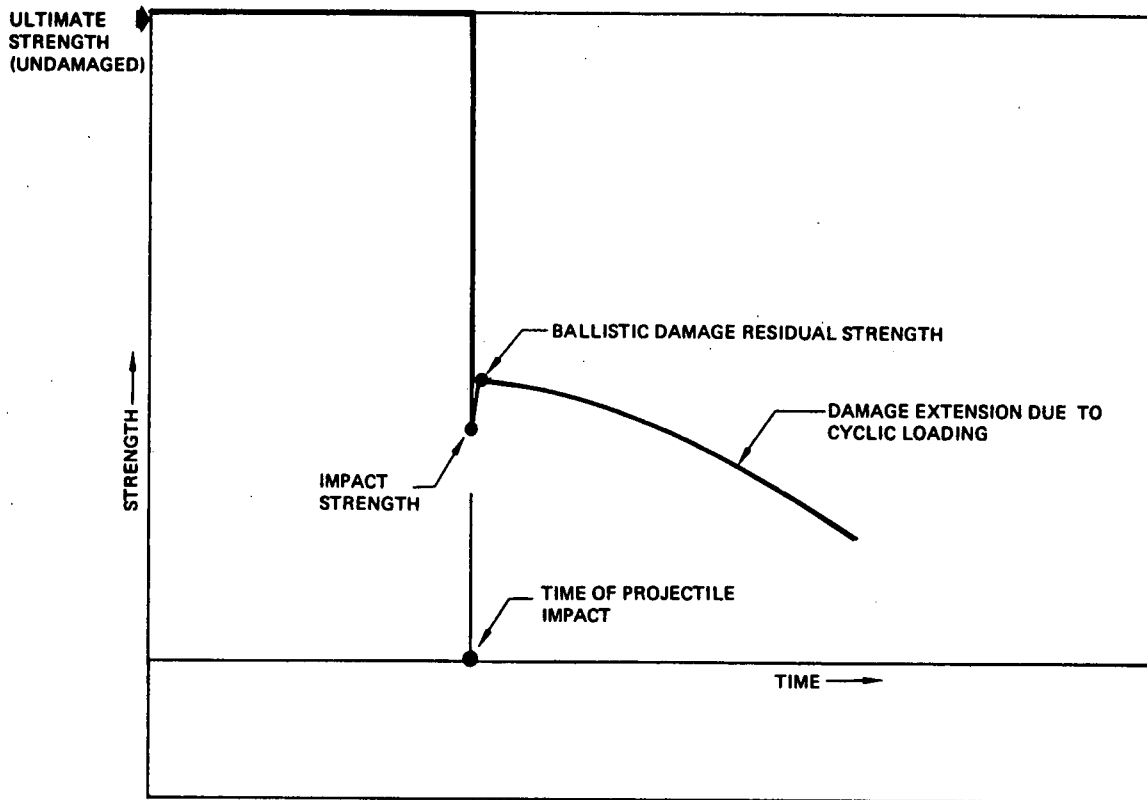
Figure 3-5. Strength-Time History for a Structural Element, Indicating Structural Capability

initial degradation is the strength at the instant of impact when dynamic effects are prominant. Immediately after impact, the structural capability is the static residual strength, which may degrade further due to the fatigue damage caused by cyclic loadings.

3.1.1.3 Structural Survivability Assessment

The final survivability assessment compares the stress/time and the strength/time histories; that is, the requirements and the capabilities. A typical comparison is shown in Figure 3-6. This figure shows the stress/time and strength/time histories for a wing structural element. At time "A", although the strength capability is reduced

Figure 3-6. Comparison of Stress-Time and Strength-Time Histories To Assess Requirements-vs-Capabilities

significantly due to damage inflicted by projectile impact, the structural element did not fall catastrophically. In this example, the strength requirements exceed the strength capability in the landing approach, and structural failure occurs at that time. A design iteration is required to correct the failure condition. The final assessment depends on the impact damage tolerance criteria selected for 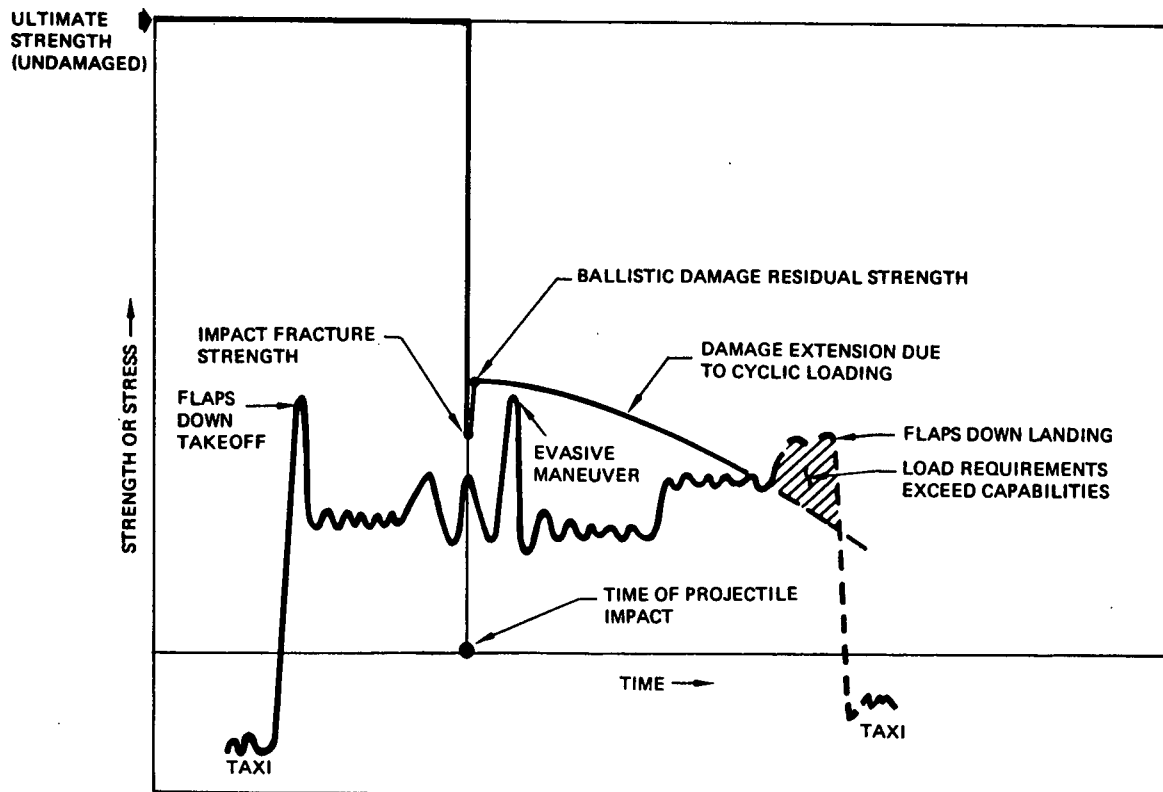the aircraft, and criteria selection and specification is an extremely important aspect of impact damage tolerant design.

3.1.2 Design Methodology Elements

As indicated in the overview above, the requirements for survivable structure must be integrated within the earliest phases of aircraft design by implementing a structural survivability assessment into the design process, and performing design iterations to achieve desired final results. To be effective, the procedures used must address the following factors:

o   The procedures must be applicable to each design phase (conceptual, preliminary and detail). The requirements imposed in each phase must also be achievable with the level of vehicle definition, analysis tools, resources, and verification techniques employed within that phase.

o   The procedures must be based on a well-defined design and analysis methodology that is consistent with current structural design procedures, including the methods employed in durability and damage tolerance.

o   The structural design parameters and measures implemented must be capable of being efficiently integrated into the assessment of total vehicle survivability. The measures of structural hardness adopted must be understandable to structural designers, survivability specialists, and system analysts. This requirement has become very important due to the increasing need to demonstrate the cost-effectiveness of alternate configurations and technology developments in terms of system life-cycle cost improvements.

Design procedures which incorporate these factors are presented below, defining the specific implementation of the survivable structure design methodology summarized in the previous paragraphs. These procedures include:

1.   Structural Survivability Assessment,

2.   Threat Definition,

3.   Mission Definition,

4.   Threat Encounter Definition,

5.   Critical Structure Identification,

6.   Damage Size Determination,

7.   Residual Strength,

8.   Cyclic Loading After Impact,

9.   Rigidity and Stiffness After Impact.

3.1.2.1 Structural Survivability Assessment

To verify that the damaged aircraft can sustain the speeds and load factors required for mission performance, the structural capability of the damaged aircraft must be greater than the structural requirements of the appropriate combat missions. Verification must be performed at each phase of system development. The methods used must be consistent in level of detail with the structural definition and sizing procedures used during each development phase. The verification must incorporate the probabilities associated with impact location, damage size, material performance, residual strength and stiffness capability, and external loading requirements. The elements defined below must be addressed.

3.1.2.2 Design Threat Definition

A design threat must be established for structural survivability assessment. The design threat is used to determine the specific projectile induced effects which the structure will be designed to survive. Selection of the design threat must be based on an assessment of the probable threats encountered in the intended operational environment of the aircraft. However, this is not the only consideration. An additional consideration is the capability to quantitatively define the effects of the threat. If there is insufficient available data to do this, the threat is unsuitable for use in conceptual and preliminary design. It must be kept in mind that the threat specification is for use in design, and does not represent a vulnerability level for the aircraft. For example, an aircraft structure designed using a single hit by a .50 caliber bullet as the design threat will have some level of survivability against multiple impacts, and against larger threats.

3.1.2.3 Mission Definition

The mission profile(s), defining aircraft altitude and air speed from take-off to base-return and landing, must be established for structural survivability assessment.

3.1.2.4 Threat Encounter Definition

Using the design threat and the established mission profile(s), the following must be established:

a.   Mission segments where the threat(s) will be encountered, including the weapon deployment density and the anticipated rate of fire at each encounter point.

b. Aircraft configuration at each projectile encounter point, including weight, distribution of fuel and depth of fuel in each tank, description and location of ordnance and external stores.

c. Aircraft altitude, speed, and physical environment at each projectile encounter.

d. Probable obliquity, projectile striking velocity, and apparent yaw relative to the aircraft coordinate system.

3.1.2.5 Critical Structure Identification

A failure modes and effects criticality analysis (FMECA) of the aircraft structure must be conducted to identify and classify all flight and mission critical structural elements with regard to level of criticality. Failure modes should be defined for each critical structural element relative to the damage mechanisms associated with the threat(s) defined in 3.1.2.2.

3.1.2.6 Damage Size Determination

A damage prediction analysis must be performed to estimate the extent of damage to critical structural elements resulting from the threat and encounter conditions determined in 3.1.2.2, 3.1.2.3, and 3.1.2.4. As a minimum, the analysis should include:

a. An estimation of the maximum damage, least damage, and mean damage, including their associated probabilities of occurrence resulting from uncertainties in encounter conditions and the locations of the impact. The damage estimates should include percent of section removed and the corresponding effective flaw size for determining residual strength for the primary loading conditions.

b. An assessment of the effects of projectile striking velocity and obliquity, structural material, configuration and thicknesses. Sensitivity factors should be determined. Interaction between penetrator damages should be considered if the analysis defined in 3.1.2.4 indicates a significant probability of multiple penetrator impacts. Interaction between projectile impact and blast pressure loading should be considered when applicable. Hydrodynamic ram effects should be assessed based on the results obtained from 3.1.2.4.

c. A consideration of the type of structure. Unless analysis demonstrates that the projectile damage will not propagate, the entire damaged load path shall be assumed destroyed in multiple load path structure and the damage shall be assumed to propagate to the next undamaged crack stopper for crack arrest type structure.

d. A consideration of the effects of impacting loaded structure. The damage size prediction should include the potential damage augmentation associated with the specified load level at impact.

3.1.2.7 Residual Strength

For each design threat, mission, and encounter condition, the residual strength capability of the damaged aircraft structure should be determined. The assessment results should be expressed in terms of probability of structural survival given a hit as a function of load factor, incorporating the probability associated with striking strength critical structure combined with the probability associated with the damage size resulting from the threat encounter. An example of this presentation is shown in Figure 3-7. Redistribution of the internal loads in the damaged structure should be determined where appropriate. The effects of transient and steady-state heating should be included. Unless other criteria are specified by the procuring activity, aircraft damaged by the design threat should sustain the loading requirements defined below.
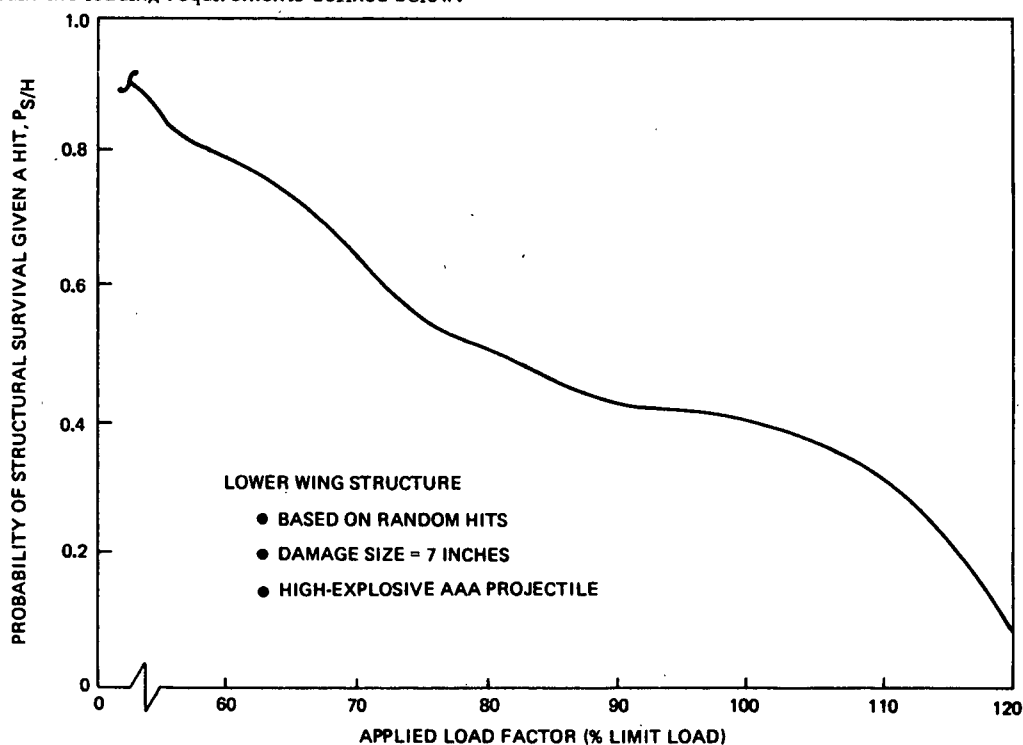

Figure 3-7. Typical Probability of Survival of a Structural Component Impacted by an AAA High-Explosive Projectile

3.1.2.7.1 Strength Requirements At Impact

The aircraft should be capable of sustaining a single impact by the design threat without failing strength critical structure when loaded at the time of impact to two-thirds of limit load.

3.1.2.7.2 Strength Requirements After Impact

The damaged aircraft should be capable of sustaining limit load without failing strength critical structure during the remaining mission profile.

3.1.2.8 Cyclic Loading After Impact

The alteration or extension of the projectile damage caused by the cyclic loading environment should be determined for the mission segment between projectile impact and return to base or sortie completion, and the effects of this alteration or extension should be considered in determining the strength requirement of 3.1.2.7.2, and the stiffness and rigidity requirements of 3.1.2.9.

3.1.2.9 Rigidity and Stiffness After Impact

After being damaged by the design threat, the aircraft should be free from flutter, divergence, and other aeroelastic instabilities at all speeds up to the limit speed for the remainder of the mission profile for each threat, mission and encounter condition specified. Freedom from flutter, divergence and other aeroelastic instabilities of the damaged aircraft should be verified for the minimum altitude at which the limit speed can be obtained and the minimum altitude at which the maximum dynamic pressure can be obtained. The effects of transient and steady-state heaing should be included. Verification should be based on measured vibration modes when available. A sufficient number of nodes should be used to assure accurate representation of the important dynamic characteristics of the damaged aircraft. Results should be expressed as a probability of structural survival, incorporating the probabilities associated with damaging stiffness critical structure combined with the probability of encountering aerodynamic conditions sufficient to cause the unacceptable degradation.

3.2 DESIGN TECHNIQUES FOR IMPROVING PROJECTILE IMPACT DAMAGE TOLERANCE

The previous paragraphs outlined procedures for assuring that the consequences of projectile damage are quantitatively considered in structural design. This section presents some design techniques which are useful in improving the survivability of structure to projectile impact. The designer can employ several techniques for improving the capability of aircraft structure impacted by projectiles, including:

a. Reducing the probability of hitting critical structural elements,
b. Improving the damage resistance of structure,
c. Improving the damage tolerance of structure.

Reducing the probability of hitting critical structural elements can be accomplished by reducing the size of critical elements, locating critical elements so that they are shielded by less critical components, or locating critical elements so that they are removed from a probable projectile flight path. These techniques can be highly effective, but they will not be discussed further here because they are too dependent upon design configuration to permit generalization.

The damage resistance of a structural element, as shown in Figure 3-8, is measured by the extent of damage inflicted by a given threat. The importance of damage size in the assessment of structural survivability cannot be over-emphasized, since failure criteria for structure depends on damage size. This is in contrast to failure criteria for many other aircraft system components that can often be rationally based solely on penetration. Material properties and geometric configuration determine damage resistance. For example, 2024-T3 aluminum is more damage resistant (exhibits less cracking) than 7075-76 aluminum when exposed to projectile impact. In general, the use of high-toughness materials will improve damage resistance.

Damage tolerance, on the other hand, is measured by the ability of the structure to contain or "tolerate" damage of a given size while completing mission requirements. A damage-tolerant structure is obtained by careful attention to both detail design and material selection. Multiple load paths, and multi-element configurations such as skin with stiffeners capable of limiting or containing damage extension contribute to improved damage tolerance. Damage tolerance should be considered in the design of every major primary structural component. Multiple-load-paths should be separated to minimize the possibility of critical damage from a single impact. Short load paths are recommended to minimize total vulnerable area. Flammable and/or explosive components should not be placed near primary load paths.

In areas where both members of a dual load path could be damaged by a single impact, and where design (geometry) limitations restrict the use of redundant structure, special effort should be made to provide damage resistance. This is achieved by minimizing the exposed area and using damage-resistant materials. Good damage resistance will also enhance repair capability, since repair times are frequently proportional to damage size.

The above general design considerations are deceptively simple. Their application in specific circumstances is complex, and requires both design awareness and inventiveness. Designers need analytical tools in order to implement the structural survivability design methodology, and these tools must be formulated in terms of design parameters, so that the effects of design alternatives can be evaluated. Basic design techniques which provide survivable structure are: 1) assuring that sufficient load paths remain after damage infliction, and 2) assuring that the damage is contained at the maximum loading condition following damage infliction.

The second technique makes use of damage tolerance approaches which are also applicable to fail-safe design relative to fatigue and/or initial defect damage, with the exception of inspection for damage, plus the additional need to consider dynamic effects. The first technique, however, entails some analysis approaches that are more unique to projectile damage, particularly when the design threat can impose large damage, causing significant internal load redistribution. The development of projectile damage resistant/tolerant load paths for a structural component might proceed in the following way during preliminary design:

1. Develop a damage size analytical model for the design threat impacting the structural materials being considered for the component.

2. Using the damage size model, define the layout of primary load paths in such a way that the destruction of load paths is minimized for a hit by the design threat. For example, spar spacing might be defined such that only one spar can be destroyed by the impact.

3. Use a finite-element structural analysis model of the component to determine the distribution of internal loads at the loading conditions corresponding to the projectile damage critical design requirements.

4. After the finite element model to incorporate the effects of the imposed projectile damage, and determine the internal loads existing in the damaged configuration. Resize structural elements, if necessary, to assure sufficient residual load-path capability.
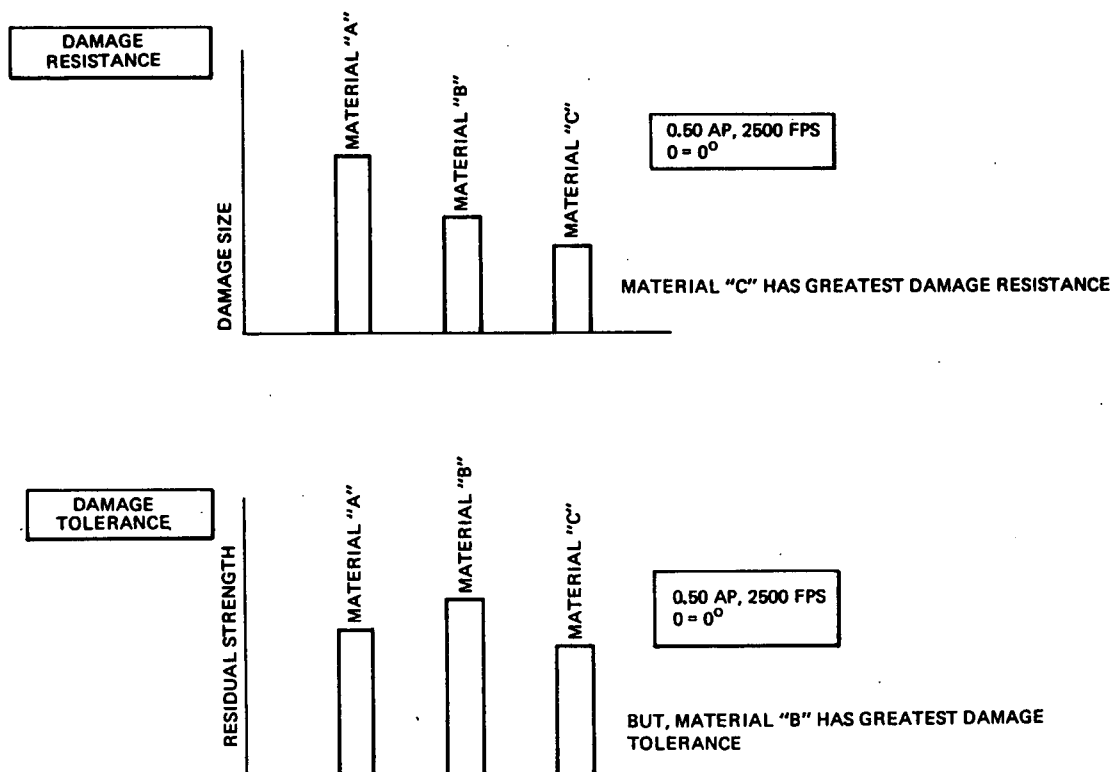

Figure 3-8. Damage Resistance and Tolerance

REPORT DOCUMENTATION PAGE

1.Recipient's Reference	2.Originator's Reference	3.Further Reference	4.Security Classification of Document
	AGARD-AG-238	ISBN 92-835-1403-3	UNCLASSIFIED

5.Originator	Advisory Group for Aerospace Research and Development North Atlantic Treaty Organization 7 Rue Ancelle, 92200 Nueilly sur Seine, France

6.Title	DESIGN MANUAL FOR IMPACT DAMAGE TOLERANT AIRCRAFT STRUCTURE

7.Presented at

8.Author(s)/Editor(s) John G.Avery	9.Date October 1981

10.Author's/Editor's Address	Boeing Military Airplane Company P.O.Box 3707, M/S 41-10 Seattle, Washington, USA 98124	11.Pages 240

12.Distribution Statement	This document is distributed in accordance with AGARD policies and regulations, which are outlined on the Outside Back Covers of all AGARD publications.

13.Keywords/Descriptors

Aircraft survivability	Weapon threats	Hydrodynamic ram
Structural survivability	Combat damage	Engine debris
Damage tolerance	Projectile impact	Fracture mechanics
Nonnuclear	Projectile damage	Advanced composites
Structural response	Blast damage	

14. Abstract

The Manual presents a methodology for integrating projectile impact damage tolerance into aircraft structural design. The information is presented in three sections:
(1) Description of Projectile Threats; (2) Analysis Methods for Predicting Structural Response to Projectile Impact; (3) Design Guidelines for Impact Damage Tolerance.

This report has been prepared at the request of the Structures and Materials Panel of AGARD.

AGARDograph No.238 Advisory Group for Aerospace Research and Development, NATO DESIGN MANUAL FOR IMPACT DAMAGE TOLERANT AIRCRAFT STRUCTURE by John G.Avery 240 Pages The Manual presents a methodology for integrating projectile impact damage tolerance into aircraft structural design. The information is presented in three sections: (1) Description of Projectile Threats; (2) Analysis Methods for Predicting Structural Response to Projectile Impact; (3) Design Guidelines for Impact Damage Tolerance. This report has been prepared at the request of the Structures and Materials Panel of AGARD. ISBN 92-835-1403-3	AGARD-AG-238 Aircraft survivability Structural survivability Damage tolerance Nonnuclear Structural response Weapon threats Combat damage Projectile impact Projectile damage Blast damage Hydrodynamic ram Engine debris Fracture mechanics Advanced composites
AGARDograph No.238 Advisory Group for Aerospace Research and Development, NATO DESIGN MANUAL FOR IMPACT DAMAGE TOLERANT AIRCRAFT STRUCTURE by John G.Avery 240 Pages The Manual presents a methodology for integrating projectile impact damage tolerance into aircraft structural design. The information is presented in three sections: (1) Description of Projectile Threats; (2) Analysis Methods for Predicting Structural Response to Projectile Impact; (3) Design Guidelines for Impact Damage Tolerance. This report has been prepared at the request of the Structures and Materials Panel of AGARD. ISBN 92-835-1403-3	AGARD-AG-238 Aircraft survivability Structural survivability Damage tolerance Nonnuclear Structural response Weapon threats Combat damage Projectile impact Projectile damage Blast damage Hydrodynamic ram Engine debris Fracture mechanics Advanced composites
AGARDograph No.238 Advisory Group for Aerospace Research and Development, NATO DESIGN MANUAL FOR IMPACT DAMAGE TOLERANT AIRCRAFT STRUCTURE by John G.Avery 240 Pages The Manual presents a methodology for integrating projectile impact damage tolerance into aircraft structural design. The information is presented in three sections: (1) Description of Projectile Threats; (2) Analysis Methods for Predicting Structural Response to Projectile Impact; (3) Design Guidelines for Impact Damage Tolerance. This report has been prepared at the request of the Structures and Materials Panel of AGARD. ISBN 92-835-1403-3	AGARD-AG-238 Aircraft survivability Structural survivability Damage tolerance Nonnuclear Structural response Weapon threats Combat damage Projectile impact Projectile damage Blast damage Hydrodynamic ram Engine debris Fracture mechanics Advanced composites
AGARDograph No.238 Advisory Group for Aerospace Research and Development, NATO DESIGN MANUAL FOR IMPACT DAMAGE TOLERANT AIRCRAFT STRUCTURE by John G.Avery 240 Pages The Manual presents a methodology for integrating projectile impact damage tolerance into aircraft structural design. The information is presented in three sections: (1) Description of Projectile Threats; (2) Analysis Methods for Predicting Structural Response to Projectile Impact; (3) Design Guidelines for Impact Damage Tolerance. This report has been prepared at the request of the Structures and Materials Panel of AGARD. ISBN 92-835-1403-3	AGARD-AG-238 Aircraft survivability Structural survivability Damage tolerance Nonnuclear Structural response Weapon threats Combat damage Projectile impact Projectile damage Blast damage Hydrodynamic ram Engine debris Fracture mechanics Advanced composites

AGARD

NATO ⊕ OTAN

7 RUE ANCELLE · 92200 NEUILLY-SUR-SEINE
FRANCE

Telephone 745.08.10 · Telex 610176

DISTRIBUTION OF UNCLASSIFIED AGARD PUBLICATIONS

AGARD does NOT hold stocks of AGARD publications at the above address for general distribution. Initial distribution of AGARD publications is made to AGARD Member Nations through the following National Distribution Centres. Further copies are sometimes available from these Centres, but if not may be purchased in Microfiche or Photocopy form from the Purchase Agencies listed below.

NATIONAL DISTRIBUTION CENTRES

BELGIUM
Coordonnateur AGARD – VSL
Etat-Major de la Force Aérienne.
Quartier Reine Elisabeth
Rue d'Evere, 1140 Bruxelles

CANADA
Defence Science Information Services
Department of National Defence
Ottawa, Ontario K1A OK2

DENMARK
Danish Defence Research Board
Østerbrogades Kaserne
Copenhagen Ø

FRANCE
O.N.E.R.A. (Direction)
29 Avenue de la Division Leclerc
92320 Châtillon sous Bagneux

GERMANY
Fachinformationszentrum Energie,
Physik, Mathematik GmbH
Kernforschungszentrum
D-7514 Eggenstein-Leopoldshafen 2

GREECE
Hellenic Air Force General Staff
Research and Development Directorate
Holargos, Athens

ICELAND
Director of Aviation
c/o Flugrad
Reykjavik

ITALY
Aeronautica Militare
Ufficio del Delegato Nazionale all'AGARD
3, Piazzale Adenauer
Roma/EUR

LUXEMBOURG
See Belgium

NETHERLANDS
Netherlands Delegation to AGARD
National Aerospace Laboratory, NLR
P.O. Box 126
2600 A.C. Delft

NORWAY
Norwegian Defence Research Establishment
Main Library
P.O. Box 25
N-2007 Kjeller

PORTUGAL
Direcção do Serviço de Material
da Forca Aerea
Rua da Escola Politécnica 42
Lisboa
Attn: AGARD National Delegate

TURKEY
Department of Research and Development (ARGE)
Ministry of National Defence, Ankara

UNITED KINGDOM
Defence Research Information Centre
Station Square House
St. Mary Cray
Orpington, Kent BR5 3RE

UNITED STATES
National Aeronautics and Space Administration (NASA)
Langley Field, Virginia 23365
Attn: Report Distribution and Storage Unit

THE UNITED STATES NATIONAL DISTRIBUTION CENTRE (NASA) DOES NOT HOLD
STOCKS OF AGARD PUBLICATIONS, AND APPLICATIONS FOR COPIES SHOULD BE MADE
DIRECT TO THE NATIONAL TECHNICAL INFORMATION SERVICE (NTIS) AT THE ADDRESS BELOW.

PURCHASE AGENCIES

Microfiche or Photocopy
National Technical
Information Service (NTIS)
5285 Port Royal Road
Springfield
Virginia 22161, USA

Microfiche
Space Documentation Service
European Space Agency
10, rue Mário Nikis
75015 Paris, France

Microfiche
Technology Reports
Centre (DTI)
Station Square House
St. Mary Cray
Orpington, Kent BR5 3RF
England

Requests for microfiche or photocopies of AGARD documents should include the AGARD serial number, title, author or editor, and publication date. Requests to NTIS should include the NASA accession report number. Full bibliographical references and abstracts of AGARD publications are given in the following journals:

Scientific and Technical Aerospace Reports (STAR)
published by NASA Scientific and Technical
Information Facility
Post Office Box 8757
Baltimore/Washington International Airport
Maryland 21240, USA

Government Reports Announcements (GRA)
published by the National Technical
Information Services, Springfield
Virginia 22161, USA